QUADRATIC POWER SYSTEM MODELING AND SIMULATION WITH APPLICATION TO VOLTAGE RECOVERY AND OPTIMAL ALLOCATION OF VAR SUPPORT

A Dissertation
Presented to
The Academic Faculty

by

Georgios Konstantinos Stefopoulos

In Partial Fulfillment
of the Requirements for the Degree
Doctor of Philosophy in the
School of Electrical and Computer Engineering

Georgia Institute of Technology
August 2009

QUADRATIC POWER SYSTEM MODELING AND SIMULATION WITH APPLICATION TO VOLTAGE RECOVERY AND OPTIMAL ALLOCATION OF VAR SUPPORT

Approved by:

Dr. A. P. Sakis Meliopoulos, Advisor
School of Electrical and Computer Engineering
Georgia Institute of Technology

Dr. Deepakraj M. Divan
School of Electrical and Computer Engineering
Georgia Institute of Technology

Dr. Ronald G. Harley
School of Electrical and Computer Engineering
Georgia Institute of Technology

Dr. Shijie Deng
School of Industrial and Systems Engineering
Georgia Institute of Technology

Dr. David G. Taylor
School of Electrical and Computer Engineering
Georgia Institute of Technology

Date Approved: June 12, 2009

To my beloved family: my father Konstantinos (Kostas), my mother Despoina (Nana), and my brother Vangelis.

To my grandparents George and Penelope (Pitsa) and George and Paraskevi (Voula).

ACKNOWLEDGEMENTS

"Σα βγεις στον πηγαιμό για την Ιθάκη,
να εύχεσαι νάναι μακρύς ο δρόμος,
γεμάτος περιπέτειες, γεμάτος γνώσεις."
[Κώνσταντίνος Καβάφης – Ιθάκη (1911)]

"As you set out for Ithaca,
hope that the journey is long,
full of adventure, full of knowledge."
[Konstantinos Kavafis – Ithaca (1911)]

In Odyssey, Odysseus' journey back to Ithaca lasted for ten years. This journey lasted a bit less, but still it was a long one, full of adventure, full of discovery, and full of knowledge. Eventually it got to a successful ending, attributed to a great extent to the many people who came into my life, helped me, and encouraged me during this period, making these eight years the most fascinating years of my life so far. Expressing my thanks and gratitude to all of them is the least I could do.

First of all, I would like to thank my Ph.D. advisor, Professor Sakis Meliopoulos. He is the reason I came to Georgia Tech in 2001 and his guidance and support provided me the main thrust for the successful completion of my work here. I am grateful to him for the many opportunities he gave me to expand my knowledge and experience, but above all I am grateful to him for supporting me not only academically, but also personally, especially during difficulties.

I would like to express my appreciation to Professor Ronald G. Harley, Professor David G. Taylor, Professor Deepak M. Divan, and Professor Shijie Deng for serving as my Ph.D. committee members and for the knowledge and support they provided to my

studies either by direct collaboration or through the classes they taught me. I would also like to thank Professor Yorai Wardi who served as a member of my proposal committee but, unfortunately, could not participate in my Ph.D. committee.

I would also like to extend my thanks to all the other professors of the electrical energy group of the school of ECE at Georgia Tech, namely Professor Miroslav M. Begovic and Professor Thomas G. Habetler, as well as all the professors who taught the many classes I attended here and to whom I owe all the new and exciting things I learned during my studies.

I owe many thanks to Dr. George J. Cokkinides for his constant help and support. His contribution to my research was invaluable and a large part of my work would not have been completed without my collaboration with him.

This journey would have not started at all without the encouragement and help from four of my undergraduate professors at the National Technical University of Athens, back in Greece. I would, therefore, like to express my appreciation to Professor Nikos Hatziargyriou, Professor Costas Vournas, and late Professors George Contaxis and Basil Papadias. I would like to thank them for believing in me, making this dream of mine become a reality, and for continuing helping and supporting me even during my time here.

Nevertheless, the persons who helped me the most in my studies and research are my fellow colleagues, lab mates, and friends in Professor Meliopoulos' research group and I would like to show my appreciation to every single one of them. First I would like to thank the people who welcomed me here in the group in August 2001: Sun-Wook Kang, Murad Asa'd, Wenzong Gao, Xi Zhu, Jeegar Bakhai and the visiting scholars Dr.

Deok Young Kim and Dr. Ramazan Caglar. I would also like to thank the other two visiting scholars that came to our lab later, Dr. Cha and Dr. Buhm Lee, whom I kept seeing in various conferences all over the world even after they left Atlanta.

However, above all I would like to thank my great colleagues and good friends Fang Yang, Ramiz Alaileh, Collin Brown, and especially Quang Binh Dam. They were always beside me, I had such a great collaboration with them, and our relationship extended to true friendship, way beyond the working environment. I wish all my colleagues in the future were just like them.

Furthermore, I am also pleased to finish my work leaving a great number of new members in the lab with whom I had the opportunity to work and exchange ideas during the last period of my studies. Among them I would like to mention Yongnam Cho, Sungyun Choi, Tao Ye, Renke Huang, Kyle Howells, Curtis Roe, Sandhya Madan, Darshit Shah, and especially Vangelis Farantatos who is also one of my great Greek friends in Atlanta and whom and his family I knew, even before meeting him in person here.

In addition, I would like to extend my thanks to all the old and new graduate students of the school of ECE electrical energy group, who were here when I arrived and graduated, who came later but left before me, or who are staying behind. I wish all of them the best in their studies and in their lives. Among them special thanks go to Salman Mohagheghi and his wife Neda, to Branislav Radibratovic and his wife Jelena, and to Satish Rajagopalan. These three were not only my closest colleagues, but also my best friends and I hope this remains true for the rest of my life. I would also like to mention namely Goker Ariyak, Afroz Imam, Joy Mazumdar, Zhi Gao, Ari Zachas, Jean Carlos

Hernandez Mejia, Yamille del Valle, Josh Perkel, Harjeet Johal, Jyoti Sastry, Anish Prasai, Stefan Grubic, Frank Kreikebaum, Debrup Das, Rohit Moghe, Jorge Hernandez, Jiaqi Liang, Pinjia Zhang, Jing Dai, Yao Duan, Yi Du, Siwei Cheng, Sang Taek Han, Prasad Rajendra Kandula, Song Yang. But among all the power-group students I would like to specially thank Yi Yang for being my dearest friend and moral supporter. Her amazing character and personality is invaluable for all the people in our group.

I am also thankful to all my friends at the Georgia Tech community and Atlanta, in general, and in particular to all my Greek friends who made me feel like being home, though thousands of miles away. In particular I would like to mention Michael Balchanos, George Georgoulas, Yorgos Mourlas, Nikolaos Vasiloglou, Vasilis Lakafosis, Yannis Doudalis, Stathis Bakolas, and Professors Manos Tentzeris and Christos Alexopoulos.

Furthermore, I would also like to thank all my friends and relatives back in Greece that supported me during all these years and were always so happy eager to see me every time I was visiting home. Especially I would like to thank Damianos Georgiadis, Akis Tsonos, and Professor Pavlos Georgilakis who was also a great support and consultant in my studies.

Last but not least among my friends I would like to thank Shalini Gupta for her friendship, support, and for being such an amazing person to me. Her contribution was fundamental, even though she might not have always realized it. I would also like to thank her for giving me, through her personal attitude, the incentive and thrust, to make the final and most important step to the end of this journey and out of Georgia Tech.

Also I have special thanks to all the people who stood by me and supported me during a tough period of my life at the beginning of 2007, when I had to face a serious medical issue. I would like to thank especially my advisor, Professor Meliopoulos, for supporting me as none else would have done, and all my friends here in Atlanta. I would also like to thank all the medical personnel who took care of me both in Athens and in Atlanta. Without their expertise, moral support, and encouragement this journey would have possibly ended unsuccessfully more than two years ago.

Finally, I would like to thank my parents, Kostas and Nana, and my brother, Vangelis, for their love, support, patience, and for making everything possible and every sacrifice required on their behalf to make this dream come true, as they have always done in the past. I hope one day I can also become as good as they are.

As this journey gets close to the end the joyful feeling of reaching the final destination and achieving the final goal may not seem any more as profound and intense as it was expected at the very beginning. However, I do know better by now that, at the end, it is the journey, not the destination that actually matters the most…

"Κι αν πτωχική την βρεις, η Ιθάκη δε σε γέλασε.
Έτσι σοφός που έγινες, με τόση πείρα,
ήδη θα το κατάλαβες οι Ιθάκες τι σημαίνουν."
[Κώνσταντίνος Καβάφης – Ιθάκη (1911)]

And if you find her poor, Ithaca won't have fooled you.
Wise as you will have become, so full of experience,
you must have already understood what these Ithacas really mean.
[Konstantinos Kavafis – Ithaca (1911)]

TABLE OF CONTENTS

LIST OF TABLES

LIST OF FIGURES

SUMMARY

The main objectives of this research are to simulate voltage-recovery phenomena (using improved, realistic system models and accurate solution techniques) and to develop methods for the mitigation of problems related to slow voltage recovery. Therefore, this work concentrates on the areas of voltage-recovery analysis in electric power systems, dynamic load modeling with emphasis on induction-motor models, dynamic simulation with emphasis on the numerical integration methods, and optimal allocation and operation of static and dynamic VAr resources.

Power-system modeling and power-system simulation, both steady-state and dynamic, are fundamental for any type of power-system analysis, and thus for the study of voltage-recovery phenomena. In the first part of this work, a general framework for power-system analysis is presented the main characteristics of which are (a) the utilization of full three-phase models, which provide a more realistic and high-fidelity type of analysis that can capture system asymmetries and imbalances, and (b) the use of a "quadratized" mathematical formulation, which models the system under study as a set of mathematical equations of order no more than two. The modeling approach is essentially the same for steady-state, quasi-steady-state, and dynamic analysis. Models are constructed for each system component and then the model of the entire system is constructed by applying the connectivity constraints between all the components. The solution methodology is based on Newton's method for nonlinear equations. For the analysis of voltage recovery the quasi-steady-state model is introduced and primarily used in this work.

Furthermore, a new approach for time-domain transient simulation of electric power systems and dynamical systems, in general, is introduced in this research. The new methodology has been named quadratic integration method. The method is based on a numerical integration scheme that assumes that the system states vary “quadraticaly” within an integration time step. The approach demonstrates superior behavior compared to traditionally used methods in power system simulation (such as the trapezoidal integration rule) in terms of accuracy without sacrificing the essential numerical stability properties.

Accurate modeling and simulation of voltage-recovery phenomena allows the development of ways for the mitigation of such problems via the optimal allocation and operation of static and dynamic VAr resources, which is the topic of the second part of this work. First the topic is approached using static and dynamic (trajectory) sensitivity analysis. The static and dynamic sensitivity analysis are utilized for the optimal selection of candidate locations for VAr additions based on steady-state and dynamic performance criteria, respectively. Furthermore, the trajectory sensitivities can provide information about the optimal operation of existing VAr sources during transients. Then an approach based on dynamic programming is proposed for the optimal allocation of static and dynamic reactive support. The optimal operation of installed dynamic VAr sources is also addressed utilizing concepts from the theory of applied optimal control and trajectory optimization.

CHAPTER 1

INTRODUCTION AND OBJECTIVES OF RESEARCH

1.1 Problem Statement

The August 2003 blackout in the US northeastern interconnected system brought into focus the importance of the VAr/voltage control problem in interconnected power systems. Two major issues were identified: (a) during transient stability swings, near-voltage collapse is experienced near the center of oscillations and (b) voltage recovery is delayed by the dynamics of the electric loads, such as induction motors, when not enough fast-responding reactive support sources (dynamic VAr sources) exist in the system. These issues are not new; electric power systems frequently experience a slow voltage recovery following disturbances. Although a plethora of publications exist that describe voltage phenomena, a comprehensive methodology and satisfactory analysis and design tools that address the issue of placement of static/dynamic VAr source mix are not readily available. It is also known that slow voltage-recovery phenomena have secondary effects such as unintentional operation of protective relays, electric load disruption, or motor stalling. It is important to note that electric utilities are aware of the potential VAr/voltage control problems from off-line studies and are preparing for averting such problems utilizing their own criteria. Indeed, the usual way to address these problems is by performing extensive simulations of system response and deciding on the amount of dynamic VAr sources, by trial and error, on the basis of the simulation results – a laborious procedure that may not encompass all possibilities.

Tools for studying voltage recovery are not as realistic as they need to be and are not as robust as is necessary. Most off-line studies are based on the traditional power-flow analysis, which does not take into account the dynamics of the load, while dynamic off-line studies that do consider the load dynamics are relatively few and depend on assumed data for the dynamics of the electric load. Real-time tools are almost exclusively based on traditional power-flow models and analysis techniques, which are not capable of capturing the voltage-recovery phenomena identified in this work. This practice leads to a disconnect between real-time models/tools and reality because, in general, the dynamics of the loads are not modeled – the majority of which are electric motors. The electric load characteristics play an important role in determining the voltage response and VAr requirements of a system following severe distress. Indeed, electric loads, which are predominantly induction motors, delay the voltage recovery of the system once the disturbance has been removed. The recovery of the voltage can be improved with dynamic VAr sources, i.e., VAr sources that have a fast response time, such as static VAr compensators (SVCs).

1.2 Objectives of Research

The objectives of this research work are (a) to develop realistic models that accurately model the dynamics of the system and realistically capture voltage-recovery phenomena and (b) to develop criteria for the selection of the optimal mix and placement of static and dynamic VAr resources in large power systems utilizing the tools from objective (a). The criteria include, but are not limited to, speed of voltage recovery, avoidance of unnecessary relay operations, avoidance of motor stalling, and avoidance of voltage collapse. These criteria are incorporated into a unified optimization model for

minimizing the deployment of static and dynamic VAr resources while meeting such performance criteria.

This work presents a method that can be used to study voltage-recovery events after a disturbance and proposes ways and methods to mitigate delayed voltage-recovery problems. More specifically, the problem is stated as follows: Assume a power system with dynamic loads, such as induction motors. A fault occurs at some place in the system and is cleared by the protection devices after some period of time. During the fault the voltage is suppressed in the vicinity of the fault, causing changes in the system such as deceleration of motors. Once the fault is cleared the voltage will tend to recover. In general, the voltage recovery is not instantaneous because of the system dynamics. The objective is to study the recovery of the voltage after the disturbance has been cleared at the buses where dynamic or other sensitive loads are connected and also determine how these loads affect the recovery process. Moreover, if the recovery rate is not satisfactory, based on specific criteria, ways are proposed to mitigate the problem and improve the voltage profile of the system.

In the presented work a hybrid approach is used for the study of voltage recovery that is based on static network modeling integrated with a quasi-dynamic model of the loads and generators. More specifically, the power network is assumed to operate in sinusoidal quasi-steady state, but the slow electromechanical dynamics of generating units and loads are explicitly included in the model. This approach provides a more realistic tool compared to the traditional static power-flow analysis, but avoiding the full-scale transient simulation, which requires detailed system and load dynamic models.

The proposed approach for the study of voltage recovery considering dynamic load representation is based on simulating the dynamical equations describing the dynamics of the motor and the generator rotor and solving them along with the network load-flow equations and the possible additional internal equations of the existing devices. This procedure is referred to as either quasi-steady-state analysis or quasi-static analysis.

More specifically, following a disturbance in the system, the electrical torque produced by any motor connected to the system will change because of the variation of the voltage at the motor terminals. This will cause a deviation in the torque balance between the electrical torque produced by the motor and the mechanical torque required by the load connected to the motor shaft. Because of this imbalance between the load torque and the motor torque, the rotor speed of the machine will transiently change in accordance with the equation of motion of the rotor.

Therefore, a typical scenario, which emphasizes the behavior of the induction motors, consists of the following phases:

1) Pre-fault phase: The system operates at steady-state conditions. The system state is obtained by performing a load-flow analysis with the motors operating in torque-equilibrium mode. This means that in steady state, the electric torque produced by each motor equals the mechanical torque required by the load served by the motor.

2) *During-fault phase:* When a fault (or a disturbance in general) takes place the motors of the system enter a transient operating phase. Typically, the motors are supplied by a considerably reduced voltage, resulting in a decrease in the electromechanical torque produced by the motors. Subsequently, the motors decelerate since their mechanical loading will be higher than the electromechanical torque they produce. Depending on the

voltage level and on the mechanical load characteristics (the load may be of constant torque or its torque may depend on the speed), the motors will decelerate and most likely stall unless the fault is cleared and the voltage is restored in time. The deceleration of each induction motor is computed based on the simulation procedure described next. Specifically, at each time step, the electromechanical motor torque and the mechanical load torque are computed and the deceleration of the motor over the time step is computed. Based on the deceleration, a new rotor speed is computed at the current time step. Then the process is repeated at the new operating point. The analysis procedure is applied throughout the duration of the fault. The final operating condition of the fault period provides the initial conditions for the post-fault period.

3) *Post-fault phase:* The same simulation approach is also applied to the post-contingency system. During this phase, the motors of the system may start accelerating again, or they may keep decelerating until they eventually stall. The procedure provides the voltage-recovery transient at each bus without using full-scale transient simulation during the longer post-fault period. As mentioned before, the final operating condition of the fault period determines the initial conditions of the post-fault system.

In the first part of this thesis, a literature review of the voltage-recovery phenomena in power systems is performed. In addition, a survey of the criteria for acceptable voltage recovery is included. Appropriate models are reviewed to determine their suitability for properly capturing the phenomena that affect voltage recovery. Criteria and models form the building blocks for the selection of the optimal mix and for the placement of static and dynamic VAr resources in large power systems to alleviate slow voltage recovery. The criteria include, but are not limited to (a) speed of voltage recovery, (b) avoidance of

unnecessary relay operations, (c) avoidance of motor stalling, and (d) avoidance of voltage collapse. These criteria are incorporated into an integrated optimization model for minimizing the deployment of static and dynamic VAr resources while meeting such operational criteria. Dynamic programming techniques, which are capable of incorporating the above criteria, are used for the solution of the optimization problem. The unique advantage of the developed approach is the ability of the new tools for power-system analysis to explicitly model the dynamics of the load while providing performance comparable to the usual power-flow models. These tools include (a) the single- and three-phase "quadratized" power flow, (b) the quasi-steady-state dynamic simulation, and (c) the static and dynamic sensitivity-based methods.

An important task of the presented work is the development of a suitable simulation method that allows modeling and analysis of voltage-related phenomena. For this purpose, the models and tools developed during this research were integrated with models and analysis methods previously developed by this research team. The overall methodology is capable of (a) modeling the dynamics of the electric load (i.e., each load may consist of a certain percentage of induction motors of various designs, certain percentage of synchronous motors, certain percentage of lighting load, certain percentage of regulated load) and (b) capturing the effects of system oscillations on voltage and on reactive-power absorption. For purposes of this work, a parameterized, dynamic electric load model was utilized from physical considerations, such as percentage of motor load, lighting, computers, etc. Note that the simulation methodology combines the advantages of the "quadratized" power flow and the quasi-steady-state (dynamic) simulation. The proposed load model permits routinely conducting simulations of various load scenarios.

In addition, trajectory sensitivity information quantifies the significance of the model parameters on the speed of voltage recovery. The proposed integrated methodology accurately simulates the voltage behavior of the system during disturbances. Specifically, it precisely predicts voltage dips and voltage-recovery rates, as well as determines the most sensitive parameters that affect voltage-recovery phenomena. It is also important to stress that the integrated simulation method is capable of determining the cause of slow voltage recovery, for example, load dynamics, system oscillations, or a combination of the two.

The major achievements of this work are (a) the development and implementation of appropriate models and analysis methodologies for the simulation and study of voltage-recovery phenomena; (b) the characterization of criteria for determining the optimal mix and placement of static and dynamic VAr sources (these criteria ensure better voltage recovery following a disturbance, avoidance of unintentional relay operations, avoidance of load disruption, and prevention of motor stalling); and (c) the development of a research tool for optimal selection of size and placement of static and dynamic VAr resources. From an operations perspective, the same tool may be used to determine the adequacy of available resources in real time. The development tool is flexible and capable of incorporating complex design and performance criteria such as maximum permissible voltage dip, maximum permissible voltage-dip duration, or a combination of both.

1.3 Thesis Outline

A brief outline of the remainder of the document is presenting in this section:

In Chapter 2, the origin and history of the research topic is described. First, a general description of the investigated issues is presented, followed by a substantial literature survey, organized by the various subtopics of this research work.

Then, in Chapter 3, a high-level, overall description of the proposed modeling approach is given. The “quadratized” power system model is presented and described along with the proposed solution methodologies that are used in this research.

Chapter 4 presents a description of the power system component models utilized in this work. Some of these models have been developed as part of this work, while others were developed in the past and are simply utilized in this work. Emphasis is given to the models that were developed during this work and a more detailed description is provided for them. The rest of the models are just referenced for completeness. A more detailed description of the newly developed and implemented models in this research work is presented in Appendix A.

Chapter 5 is a description of a numerical integration method that was developed in this work and is utilized as part of the analysis methodology associated with this research.

Chapter 6 describes the static and dynamic sensitivity analysis that is utilized extensively in this research. Sensitivity analysis methods are used for contingency ranking purposes and for the selection of the optimal locations of voltage-support devices. Furthermore, sensitivity analysis provides an insight on the system parameters that mostly affect the process of voltage recovery.

Chapter 7 elaborates on the proposed methodology for the optimal selection and allocation of voltage-control devices in transmission or distribution systems for the mitigation of slow voltage recovery.

Chapter 8 introduces the proposed methodology for the optimal operation of voltage-control devices that have already been installed in transmission or distribution systems for the mitigation of slow voltage recovery.

Chapter 9 presents some demonstrating examples and simulation results of the proposed modeling and analysis methodologies and optimization algorithms.

Finally, Chapter 10 concludes this thesis summarizing the main parts of this research work, as well as the main outcomes and contributions. Furthermore, it provides future research directions on the topics of this research.

There are two appendices at the end of this dissertation. Appendix A provides some more technical details on specific aspects of this work, and in particular on modeling issues. It presents a detailed description on the power system component models that were developed for this work. Some implementation details of these models are also included. Appendix B includes a brief description of the application of the quadratic power-system modeling, described in this work, in a probabilistic power-flow framework. The work described in this appendix is an extension of some of the topics presented in this dissertation, in particular the quadratic modeling and the sensitivity analysis, in a different area of power-system engineering.

CHAPTER 2

LITERATURE REVIEW AND BACKGROUND INFORMATION

2.1 Introduction

The main objectives of this work are to simulate voltage-recovery phenomena (using improved, realistic system models and accurate solution techniques) and to develop methods for the mitigation of problems related to slow voltage recovery. Emphasis is given to dynamic load modeling in particular. Therefore, the focus of this work mainly concentrates on the following topics:

- Study of voltage-recovery phenomena;
- Power-system modeling, with emphasis on dynamic load models, and in particular induction-motor loads;
- Power-system analysis and simulation methodologies;
- Optimal allocation and operation of voltage-support devices.

A concise review of previous work on these issues is presented in the next sections of this chapter. The last section of the chapter presents an overall description of the proposed research as an extension to the work that has been performed in the past.

2.2 Voltage Recovery and Dynamic Load Modeling

This section addresses the issue of voltage-stability and voltage-recovery phenomena following typical faults in a power system in the presence of dynamic loads. It is well known that the voltage recovery after a disturbance is delayed by the load

dynamics (such as the dynamics of induction motors), especially when insufficient fast-reacting reactive resources (dynamic VAr sources) exist [1] – [13]. The phenomenon is well known to utilities and is typically studied either using static load-flow techniques or with full-scale transient simulations. In addition, in case of transient oscillations among generating units after the successful clearance of a fault, voltages may collapse near the center of oscillation. During this period, motors decelerate and the dynamics of the load affect the speedy recovery of the voltage. Both these phenomena may trigger secondary effects such as motor tripping and other undesired relay operations.

Off-line studies of voltage issues are mainly based on the traditional load-flow analysis, which does not model the power system in detail or take into account the dynamics of the load, while studies that do consider the load dynamics are relatively few and depend on assumed data for the dynamic behavior of the electric load. On-line tools are almost exclusively based on traditional load-flow models as well, and they are not capable of capturing the dynamic nature of voltage-recovery phenomena. This practice leads to discrepancies between the analytical models and the real behavior of the system.

The issue of load modeling and the effects of dynamic loads on voltage phenomena have been studied to a significant extent in the literature [4] – [22]. In [4] the issues of voltage dips in three-phase systems after symmetric or asymmetric faults and the accurate modeling of voltage recovery are addressed. In [5] and [6] the voltage-recovery phenomena and the effect of induction-motor loads are studied from a practical point of view, based on actual events from utility experience. References [7] and [8] study the voltage recovery of wind turbines after short circuits. The issue of mitigating the delayed voltage recovery using fast VAr resources is addressed in [9] – [11] and [13]. The impact

of induction-motor loads on voltage phenomena has also been studied on a more general research basis. Reference [12] addresses the topic of oscillatory voltage instability caused by induction motors in isolated power systems in particular, while [14] refers to the impact of induction-motor loads on the system loadability margins and on the damping of inter-area oscillations. Finally, [15] – [35] are indicative of current research approaches and topics on the modeling of induction-motor loads in power systems. An extensive list of references on understanding and modeling load behavior can be found in [24].

The problem of transient voltage sags during disturbances and of recovery of voltage after the disturbance has been removed is quite well known. The importance of the problem has been well identified; its significance is increasing, especially in modern, restructured power systems, which may frequently operate close to their limits under heavy-loading conditions. Furthermore, the increased number of voltage-sensitive loads and the requirements for improved power-system reliability and power quality are imposing more strict criteria for voltage recovery after severe disturbances. It is well known that slow voltage-recovery phenomena have secondary effects such as unintended operation of protective relays, electric load disruption, motor stalling, etc. Many sensitive loads may have stricter settings of protective equipment and therefore will trip faster in the presence of slow voltage recovery, resulting in loss of load with severe economic consequences. A typical situation of voltage recovery following a disturbance is illustrated in Figure 2.1. Note that there is a fault during which the voltage collapses to a certain value. When the fault clears, the voltage recovers quickly to another level and then slowly builds up to the normal voltage level. The last period of slow recovery is mostly affected by the load dynamics and especially the behavior of induction motors.

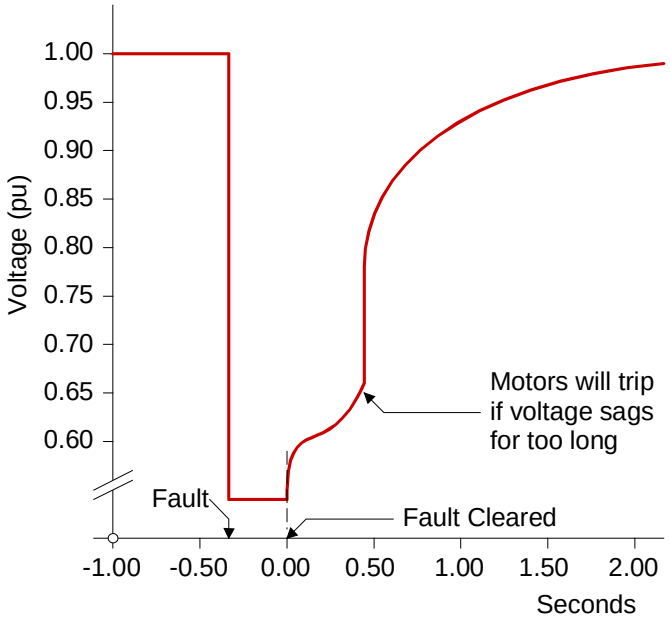

Figure 2.1: Typical behavior of voltage recovery during and after a disturbance.

2.3 Induction-Motor Models for Power-System Analysis

This section addresses the issues of induction-motor modeling for power-system analysis and estimation of model parameters. Load modeling in power systems is of great importance for both steady-state and dynamic analysis and has been addressed extensively in the literature [15] – [35]. Induction motors constitute the most significant part of industrial loads and their performance has a considerable impact on the behavior of a power system. Nevertheless, power-system studies usually refrain from explicitly representing induction-motor loads and from taking their behavior into consideration, especially at the generation and transmission levels. Constant-power or constant-impedance load models or voltage- and frequency-dependent models are commonly used in such cases. Such models provide adequately accurate results in many situations.

Typically, induction motors are represented in power-system studies as constant-power loads. Although this is a valid representation for steady-state operation under

certain conditions, induction motors do not always operate under constant-power conditions, especially when large deviations of voltage occur. In reality, in steady state, motors operate at a point where the electro-mechanical torque of the motor equals the mechanical torque of their load. As the voltage at the terminals of the induction motor changes, the operating point will change.

The significance of this is described with an example illustrated in Figure 2.2 and Figure 2.3. The IEEE 24-bus reliability test system (RTS) is used [36]. Figure 2.2 shows the voltage profile after a line contingency, assuming constant-power load representation. Green indicates voltage magnitudes within 5% of the nominal voltage; yellow indicates a voltage deviation of more than 5%, but less than 10% of the nominal voltage; red indicates a voltage deviation of more than 10%. Figure 2.3 illustrates the same condition assuming that half of the electric load at each bus has been replaced by induction-motor loads. The difference between the two figures (i.e., Figure 2.2 and Figure 2.3) is that the induction motors, included in the system of Figure 2.3, operate at a different slip (or speed) as dictated by the system solution (at the solution the electromechanical torque produced by the motor is equal to the mechanical torque of the load). The reactive-power absorption of the induction motors is different at different values of speed and, therefore, the motors greatly affect the voltage profile of the system.

This behavior cannot be captured by a simple, static, constant-power load model. Such models fail to capture all the phenomena, especially under highly stressed conditions, which deviate significantly from normal operation. Furthermore, this type of modeling is static, is suitable only for steady-state analysis, and cannot be accurately used for any sort of dynamic analysis.

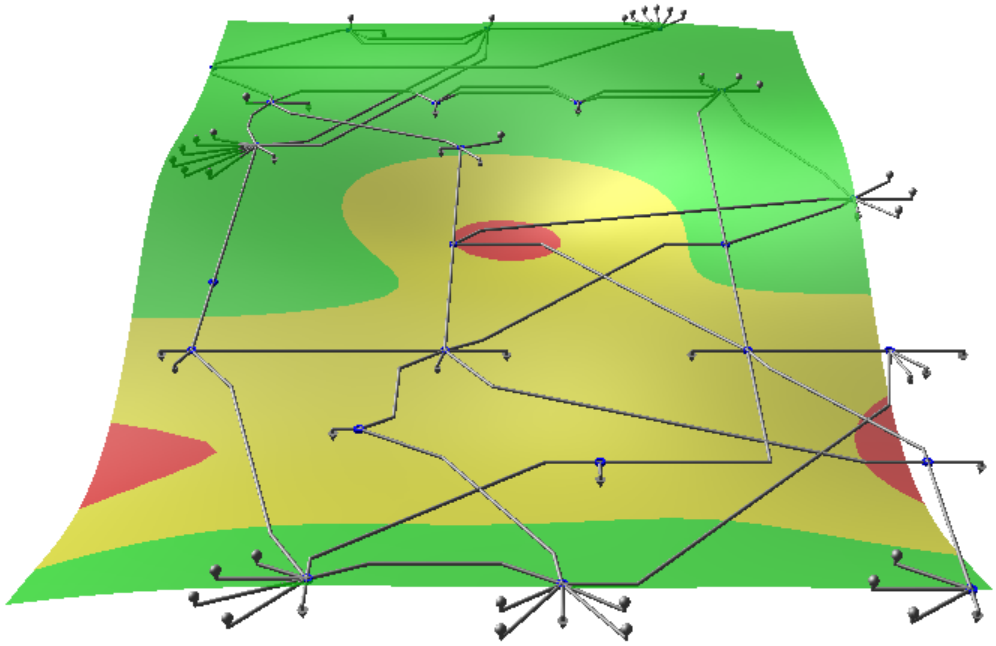

Figure 2.2: Voltage profile of the 24-bus RTS after a line contingency, with constant-power load representation.

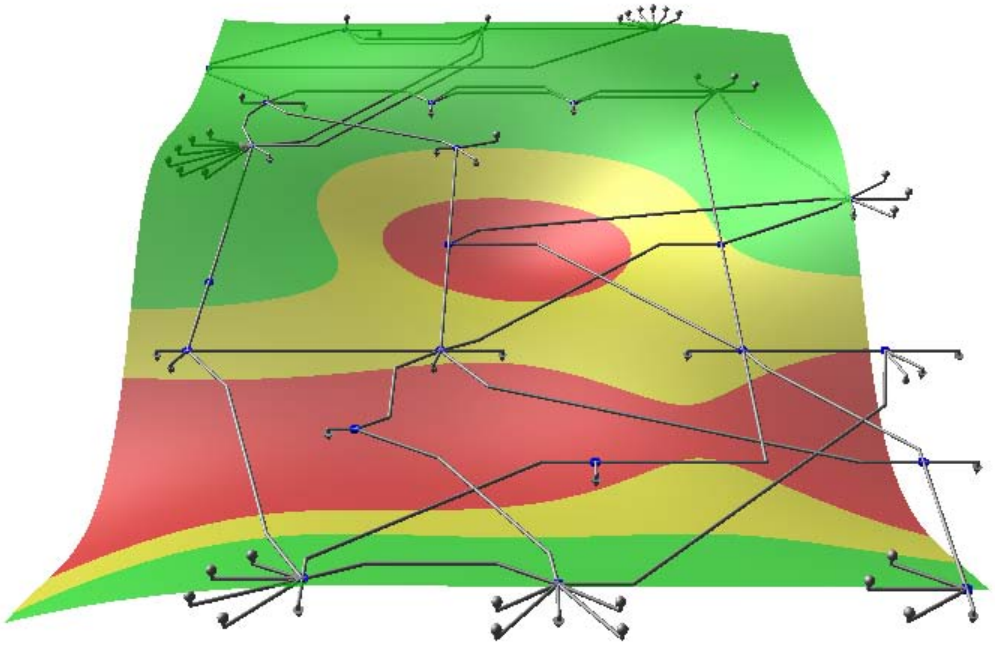

Figure 2.3: Voltage profile of the 24-bus RTS after line contingency, with induction motors assuming 2% slowdown.

Explicit representation of induction motors, however, is very infrequent in power-system studies, although induction-motor models have been established for many years in the literature for electric-machinery analysis. This is mainly due to issues of interfacing the induction-motor model with the rest of the power network while maintaining the traditional form of the power-flow equations that model the network behavior.

A single-phase-equivalent induction-motor model for power-system studies was developed earlier by this research group [35]. The model is cast in a form that can be immediately interfaced with the power-system model, thus alleviating many of the interconnection problems frequently addressed in the literature. Also, the model is in quadratic form, making it readily compatible with the single-phase "quadratized" power-flow model developed by this research group [35], [37] – [41].

Another main problem with induction-motor representation is the unavailability of parameter values to construct accurate models. This is one of the reasons motors are not usually explicitly represented in system studies. The issue of estimating the model parameters of an induction motor has been addressed by several researchers [42] – [57]. In many of these cases, high accuracy is required in the parameter determination, especially when the problem is viewed from the electric machinery point of view [42] – [49]. However, when load modeling is concerned for power-system-analysis applications (like load-flow analysis, stability analysis, dynamic simulation, or power-system-protection coordination), the level of accuracy needed is considerably less, on the order of 10-15% [50]. Field measurements obtained during specific tests can be used for the accurate identification of a motor model; however, such tests are usually difficult or impossible to perform in actual, operational industrial motors [51], [52]. Furthermore,

performing such tests makes little sense when the accuracy requirements are relatively low.

Therefore, several approaches have been presented for induction-motor-model identification based on data that can become easily available [50] – [55]. Almost all the approaches formulate the estimation problem as a nonlinear least squares minimization problem that estimates all the unknown parameters simultaneously. This problem is solved either by traditional mathematical numerical techniques (Newton type) [54] – [57] or by computational-intelligence-based techniques (like genetic algorithms) [50] – [53]. Numerical techniques are very efficient; however, they are reported to not be very robust and prone to providing suboptimal solutions or no solution at all, depending on the stiffness of the problem and on the initialization of the iterative solution algorithm [50] – [53]. Furthermore, they require good knowledge of the analytical models used [50] – [53]. Because of these drawbacks, computational-intelligence techniques have also been applied. Such techniques require less information on the underlying mathematical model and are more robust, usually at the expense of longer computational time and uncertainty in the accuracy of the underlying model [50] – [53].

2.4 Numerical Integration Methods in Power-System Analysis

Dynamic simulation is a very important tool in power-system transient analysis. The two key components of a dynamic simulation are (a) the system model and (b) the numerical integration technique used to solve the dynamical model equations. Numerical methods for ordinary differential equations (ODEs) are divided into two main categories: Runge-Kutta methods are one, the other being the class of linear multi-step methods. Runge-Kutta methods are one-step, multi-stage methods [58] – [60]. This means that in

order to evaluate the unknown function $x(t)$ at time t over the integration interval $[t-h, t]$, they use information only from one past value, $x(t-h)$, where h is the integration step, but they compute the new value $x(t)$ after several stages of calculations, estimating some intermediate values of x in the interval $[t-h, t]$. Thus, the value of $x(t)$ is computed based on $x(t-h)$ and intermediate values of x in $[t-h, t]$. Linear multi-step methods, on the other hand, use a series of past values of x ($x(t-h)$, $x(t-2h)$, $x(t-3h)$, etc) to compute the new value $x(t)$.

Another important categorization of numerical methods for ODEs is explicit and implicit methods [58] – [60]. Explicit methods do not use information at the unknown point, $x(t)$, for calculating the value $x(t)$, and the value of $x(t)$ and of x at any intermediate stages is explicitly computed based on previously known quantities. Implicit methods, on the other hand, also utilize information at the unknown point $x(t)$ for calculating the value $x(t)$. Although this may seem contradictory, the computation of $x(t)$ in this case is again simply done by solving a system of equations. In mathematical terms, explicit methods result in the solution of a triagonal system of equations at each integration step, which is performed explicitly via a backward and forward substitution. Implicit methods result in a full system requiring a matrix inversion or in practice a matrix factorization and then a forward and backward substitution. Therefore, it is evident that explicit methods are, in general, more efficient computationally. If n is the dimensionality of the system, then, in the general case, an explicit method requires an amount of computational time proportional to n^2, while an implicit method requires an amount of computational time proportional to n^3. This may improve significantly if the system is sparse (and sparsity techniques are utilized) or if it is of some other special

structure. On the other hand, implicit methods, because of the additional information they utilize, are, in general, much more accurate, more robust, and numerically stable. Therefore, they are more appropriate for difficult and stiff problems (defined in general as problems in which the system model has both very fast and slow modes), where explicit methods may fail completely to provide an accurate solution [58] – [60].

The majority of the more popular Runge-Kutta methods are explicit methods; therefore, they are only suitable for non-stiff and well-behaving problems and do not demonstrate good numerical stability properties. However, there is also a class of implicit Runge-Kutta methods that demonstrates superior stability properties and thus is very suitable for stiff problems and also for problems of differential-algebraic equations. The most important and commonly used of these methods are derived from collocation and are based on quadrature rules; that is, the points at which the intermediate stage approximations are taken are the same points used in certain classes of quadrature formulas [58] – [60].

A great number of numerical integration methods have been proposed and used for time-domain power-system simulation to transform the ordinary differential equations to algebraic equations at each time step [61] – [69]. Such methods include the backward Euler method, the trapezoidal rule, Simpson's rule, other explicit Runge-Kutta methods, Gear's method, or other linear multi-step methods, mainly of the backward differentiation formula (BDF) family. In many situations, the equations describing the operation of a power system are stiff and thus implicit methods are preferred, though they are more expensive in terms of computational time. Implicit, linear multi-step methods are in general the most widely used. Among these methods the trapezoidal integration is one of

the most popular in network transient analysis because of its merits of low distortion and absolute stability (A-stability). Absolute stability is a highly desired property. It implies that, for a linear, autonomous system, stable modes of the actual, continuous system will be represented as stable modes in the approximate, discrete system after the integration rule is applied. For example, the trapezoidal rule is used in EMTP [70] – [72], Spice [70], and Virtual Test Bed [70]. No implicit Runge-Kutta methods have ever been used so far in power-system applications.

However, the trapezoidal rule has several drawbacks that limit its applicability and indicate that some improvements in dynamic simulation methods are needed. Two major disadvantages of the trapezoidal integration scheme are its low accuracy compared to other existing methods (trapezoidal rule is second-order accurate) and the artificial numerical oscillations that are often encountered, especially in the simulation of power-electronic circuits, where switching events, and therefore discontinuities, occur. Specifically, the numerical values of certain variables oscillate around the true values. The magnitude and frequency of such numerical oscillations are directly related to the parameters of the energy storage elements of the model of the system and to the time step of the simulation. In several cases this problem is so severe that the simulation results are erroneous.

The problem has been studied in the literature and several solutions have been proposed [70] – [80]. The numerical oscillations associated with the trapezoidal integration have been identified as resulting from two different causes. One type of numerical oscillation is caused by an overly large simulation time step compared to the smallest time constant in the system [70]. This problem may occur when simulating a

stiff system such as a power system with electric machines and power electronic devices. Another type of numerical oscillation is caused by step changes in certain state variables, i.e., when the trapezoidal rule is used as a pure differentiator [70]. This kind of numerical oscillation is often observed in power electronic circuits when inductive or capacitive elements are present. Note that since a step change in a state variable can be considered as an infinitely small time constant in the system, the two types of numerical oscillations are not completely unrelated.

Several approaches have been proposed to suppress these numerical oscillations. One popular approach is to use the trapezoidal rule with damping [73]. However, this method introduces artificial elements in the system that may affect the true solution to some extent. Another interesting approach is to apply the critical damping adjustment (CDA) scheme, as proposed in [71] and [72]. This approach suggests switching from the trapezoidal integration rule to another integration method that does not have an oscillation problem, like backward Euler, for one time step after the discontinuity and then switching back to the trapezoidal rule again and continuing the simulation normally. This idea has been extensively studied and several similar approaches of a combination of trapezoidal and backward Euler rules have been proposed [74] – [77]. The choice of the implicit Euler method presents several implementation advantages and is, therefore, preferred.

However, the backward Euler method is order-one accurate and the trapezoidal method order-two, so the accuracy remains quite low. In addition, the use of one integration method instead of two would be preferable. Gear's second-order method has been proposed as an alternative. This method does eliminate such numerical oscillations;

however, it is as accurate as the trapezoidal method, so it does not provide any advantage in terms of accuracy. Furthermore it is not A-stable, which is a desired property. In [78] the issue is addressed for the very specific problem of power-electronics simulation in EMTP. A combination of the trapezoidal rule, as implemented in EMTP, and an algorithm that separates the switching circuit from the EMPT electric network is proposed. Filter interpolation is used in [79], and a method based on wave digital filters has also been suggested and studied [80].

2.5 Optimal Allocation of Static and Dynamic VAr Sources

Reactive or VAr support is a very important topic for the efficient and reliable operation of an electric power system. It relates directly to the voltage profile across a system. Synchronous generating units are the primary devices for producing and controlling reactive power and regulating the voltage level across the transmission network. However, reactive power is mainly consumed near major load centers and in particular large industrial sites, sometimes connected at the distribution side of the electric grid; therefore it is desirable to have reactive support devices close to such areas. Since in many cases power generating units are located relatively far from load centers, other reactive support devices need to be installed at various locations of the grid so that the system achieves and maintains the desired performance in terms of reactive power and voltage control.

Capacitor banks are the most commonly used method of local reactive support. They are installed either at transmission or distribution substations near areas where reactive power is needed. Capacitors can be either permanently connected to the grid, or they can be switched on and off using mechanical switches. The operating speed of such

switches is relatively low, on the order of hundreds of milliseconds or more just for the switching. Therefore, capacitors are considered static reactive support devices and are installed mainly considering criteria related to the steady-state performance of the system.

When capacitors are placed at the transmission side of the system, such criteria may include leveling the voltage profile across the network, increasing the power transfer capability, or increasing the voltage stability margin of the system. When capacitor placement is considered at the distribution side, such criteria may include the minimization of losses, the power factor correction, or the minimization of voltage drop. Note that in the case of a transient phenomenon, capacitors that are connected to the grid will instantaneously provide their reactive support to the grid without any control or feedback on their operation (therefore, in the case of a voltage drop, for example, this support will be less than the nominal power); furthermore, this support will also be provided during the steady-state operation before the transient occurs, thus affecting the power-system operation at steady state. Capacitors that are not connected cannot be efficiently switched on during a transient because of their slow response switching times and lack of fast automatic control. Therefore, it is reasonable to place capacitor banks in a system based on steady-state, rather than on dynamic, criteria.

The problem of optimal capacitor-bank placement in power systems based on several objectives, either one at a time or simultaneously, has been extensively studied in the literature and there is much ongoing research on this topic, as well. Although this particular topic is outside the scope of this research, it is closely related to it. Therefore, a brief literature review is presented in the next paragraph. A number of indicative

references are listed in the reference section at the end of this document [81] – [123]. A good survey of capacitor allocation in distribution feeders can be found in [123].

Capacitor placement is usually addressed separately, either at the distribution (most of the times) [81] – [102] or at the transmission [103] – [112] side of the grid. Little work has been done on addressing the issue in the entire system simultaneously [113] – [114]. An important issue that is addressed is the fact that at the distribution level, system asymmetries and imbalances are significant; therefore, they need to be accounted for [83], [88] – [91]. This means that the positive-sequence, single-phase-equivalent network models, which are commonly used in transmission networks, are not appropriate tools for analysis. Full, three-phase models should be used instead. In some cases, the optimal allocation problem is treated as a continuous, nonlinear optimization problem [82] – [85], but in most situations the problem is described as an integer or mixed integer, nonlinear, combinatorial optimization problem, as for example in [86] – [91], [106] – [112]. At the transmission level, the problem is, generally, formulated as an optimal power-flow problem incorporating operational constraints [106] – [112]. The main operational objectives considered are leveling of voltage profile [111], [112], maximization of voltage stability limits [108], [111], [112], minimization of system losses [108], and increase of available transfer capability [110], when transmission systems are studied [107]. When distribution systems are considered, the main objectives are the minimization of voltage drop [82], [83], [97] – [100], [102], the energy loss minimization [82]-[88], [92]-[96], [102], [106], the power factor correction [102], or the power quality improvement [114]. Such objectives are usually treated separately or combined in a single-objective function [86]-[91]. The minimization of installation and operation cost

are almost always taken into consideration as well [85] – [96], [102], [108] – [114]. Some attempts have also been presented recently using multi-objective optimization techniques [102], [113], [114]. The solution algorithms considered range from classical optimization algorithms [81] – [82], [85], like branch and bound [104], [110], [116] or Benders decomposition [109], (usually incorporating some kind of heuristic to minimize the search space [104], [117]) to modern, computational intelligence methods [118] like fuzzy logic [119], [120], genetic and evolutionary algorithms [96], [97], [100] – [114], particle swarm optimization [111], [112], [121], Taboo search [92], [93], [98], [99], [118], or even neural networks [122]. Many of these algorithms claim to be able to locate or, at least, approximate a global optimal solution, while others can only locate a local optimum.

Contrary to static VAr support, dynamic VAr sources present significant advantages in terms of controlling the power system performance during both steady-state and transient operation. Such advantages include much faster response times, continuously varying reactive-power injection (contrary to the capacitor banks, where the reactive injection is discretely varying as the modules are switched on and off), more efficient and smoother automatic control of the reactive-power injection based on feedback algorithms, and continuous operation of the device. This latter advantage means that the device can be continuously connected to the grid, providing the desired amount of reactive power based on the operation of its controller. Therefore, when a transient occurs and more reactive power is needed, the controller will detect this condition and respond automatically to adjust the output of the VAr source.

Nevertheless, because of their high cost and complex installations, dynamic VAr sources are almost exclusively installed based on dynamic criteria, in which case they offer considerable benefits in the control of voltage and reactive power. Once installed, they can also be used to regulate the system under steady-state conditions and criteria; however, such an operation cannot by itself justify the installation of a VAr source, since much less expensive capacitor banks can perform almost equally well.

The problem of optimal allocation of dynamic VAr sources has been less studied in the literature compared to capacitor placement or static VAr source allocation, especially when dynamic performance criteria are involved. In [124] the optimal placement of static VAr compensators (SVCs) is considered for improving power-system stability. More specifically, the objective is to damp voltage and power swings after the occurrence of a disturbance. The problem is addressed using linearization and modal analysis. In [125] the impact of generation mix on the placement of static VAr compensators is considered. This work addresses only steady-state system behavior and uses a standard power-flow system model. The objective is to provide maximum transfer capability for all possible generation mixes using SVCs. Sensitivity analysis is used for the determination of optimal locations for SVC placement. A similar topic is addressed in [126]. A static and dynamic VAr source scheduling problem is addressed for improving voltage stability margin. The main objective of the work is to reschedule the reactive injection of the machines from a perspective of improving voltage-stability margin, without impact on the active economic dispatch, using VAr sources. Only steady-state system behavior is considered. The effects of placing VAr support devices on the dynamic behavior of a realistic multi-machine power system are studied in [127] and [128]. A static

compensator, a series capacitive/reactive compensator, and a unified power-flow controller are considered. Detailed models of these devices and their controllers are used to simulate their effects on system transient performance under several operating scenarios. Particle-swarm optimization is employed in [129] for the optimal sizing and placement of static compensators in power systems, while the similar problem of SVC placement is addressed in [130] using genetic algorithms. In both cases only steady-state criteria and system performance are considered. Finally, in [131], the optimal placement of SVC is again addressed based on reactive-power spot prices. Again, the work addresses only static criteria and steady-state system behavior. The problem is presented and formulated in an optimal-power-flow setup. Static contingency screening is also used for contingency selection.

2.6 Summary

This chapter presented an overall description of the specific research topic of this dissertation in the context of related work that has been performed in the past. The main objective of this work is the study of voltage-recovery phenomena and the development of methodologies for the mitigation of problems related to slow voltage recovery. Therefore, the areas of this research include voltage-recovery analysis in electric power systems, dynamic load modeling with emphasis on induction-motor models, dynamic simulation with emphasis on the numerical integration methods, and optimal allocation and operation of static and dynamic VAr resources.

The problems related to voltage recovery are well known to electric utilities and have been observed for many years in power systems. However, this topic is still of great interest and importance since it directly affects the quality of provided power. Modeling

electric loads is one of the most important issues when studying voltage-recovery phenomena. The composition and the characteristics of the load as well as its dynamics determine the local behavior of the voltage during transient operation. This work focuses on the modeling of three- and single-phase induction-motor loads for power system analysis.

Analysis techniques, like power-flow analysis and dynamic simulation are the main tools for the study of voltage-related phenomena. This work utilizes the quadratic, three-phase modeling for both steady-state and dynamic analysis. Furthermore, it makes use of a quasi-steady-state analysis for the simulation of voltage recovery to capture the essential dynamics of the system, without significantly increasing the computational complexity. Emphasis is given to the numerical integration method that is utilized for the time-domain simulations. Significant work has been performed in the literature in the area of numerical integration for power-system analysis; however, the practically available options are limited and present specific disadvantages. A new numerical integration technique is introduced as part of this thesis and utilized throughout this work, attempting to address some of the problems of existing methods.

Finally, ways are proposed to mitigate problems caused by slow voltage-recovery by optimally installing and operating static and dynamic VAr sources. The topic of static reactive-source placement, like capacitor placement, has been extensively studied in the literature. Little work has been done when dynamic VAr sources are involved and, in particular, when the dynamical system behavior is taken into consideration. Furthermore, the issue of optimal operation of existing reactive-support devices has also been given

limited attention. This work attempts to provide more comprehensive insight into these issues than do previous works do.

CHAPTER 3

THREE-PHASE QUADRATIZED MODELING AND ANALYSIS

3.1 Overview

Because of the importance of the system modeling and simulation, both static and dynamic, as basic analysis tools in power systems, many attempts have been made to improve the efficiency and accuracy of modeling and solution techniques [37], [132] – [134]. These attempts range from different formulations of the power-flow or dynamic simulation problem to advanced sparsity methods and shortcuts for repeat solutions or even to attempts to obtain a direct non-iterative solution to the problem [37], [132] – [134]. In this section a method of reformulating the power system mathematical modeling in a way that will improve the efficiency of the solution method is presented. In this context it was observed in the early ‘70s that expressing the bus-voltage phasors in Cartesian coordinates results in a formulation of the model of the system that is less complex, since trigonometric functions are absent [37]. Going one step further, an improved idea is not only to use Cartesian coordinates for the phasor expressions, but also to “quadratize” the sytem equations, i.e., to express the equations as a set of equations with order no greater than two. It turns out that this can be achieved very easily with the introduction of additional state variables as needed. The advantage of this formulation is that the resulting equations of the system model are either linear or quadratic. Application of Newton’s method is ideally suited to quadratic equations. This results in the “quadratized” power flow (QPF) formulation for steady-state analysis or,

more generally, in the quadratized power system modeling for both steady-state and dynamic analysis [37] – [41], [135] – [137].

When network equations are considered, the traditional power-flow model consists of the power-balance equations at each bus of the system. Power-flow equations are expressed in the polar coordinates in terms of the systems states (bus voltage magnitudes and angles). Therefore, trigonometric terms exist in the formulated power-flow equations. In addition, induction-machine load models are very complicated and contain very high-order terms resulting from the complex load model. Consequently, the highest order of the equations in this traditional formulation is more than two.

Quadratic system modeling, however, is set up based on applying Kirchhoff's current law at each bus. In addition, the complex state variables are expressed in Cartesian coordinates. Additional state variables are introduced and, as a result, the system equations are "quadratized." Thus the equations are transformed in a set of equations that are linear or quadratic with order of no more than two. Also, trigonometric terms are absent, which makes the power-flow equations less complex. Such a quadratic formulation of a system model provides superior performance in two aspects: (a) faster convergence and (b) the ability to model complex load characteristics, various classes of loads, such as interruptible load or critical load, and in general complex devices without increasing the degree of nonlinearity of the whole system to more than two [37] – [41], [135] – [137].

Three-phase power-system modeling, with emphasis on network modeling, is another important issue that is being considered in this work. Typically, electric networks are modeled as single-phase equivalents, using the positive sequence network of the

system. This basic structure implies the following assumptions: (a) the system operates under balanced three-phase conditions and (b) the power system is a symmetric three-phase system, which is fully described by its positive sequence network. Although most of the time this is quite true in transmission-network analysis, in many cases these assumptions introduce deviations between the physical system and the mathematical model [37].

An actual transmission system operates in near-balanced conditions. The imbalance may be small or large depending on the design of the system. As an example, Figure 3.1 illustrates the voltages and currents of the three phases of an actual system at a selected bus. Note, for example, a significant difference in the currents of Phases A and B of the transmission line to bus EDIC UEI-7 and to bus VOLNEY. The voltage in this case has a significant difference between these two phases, as well.

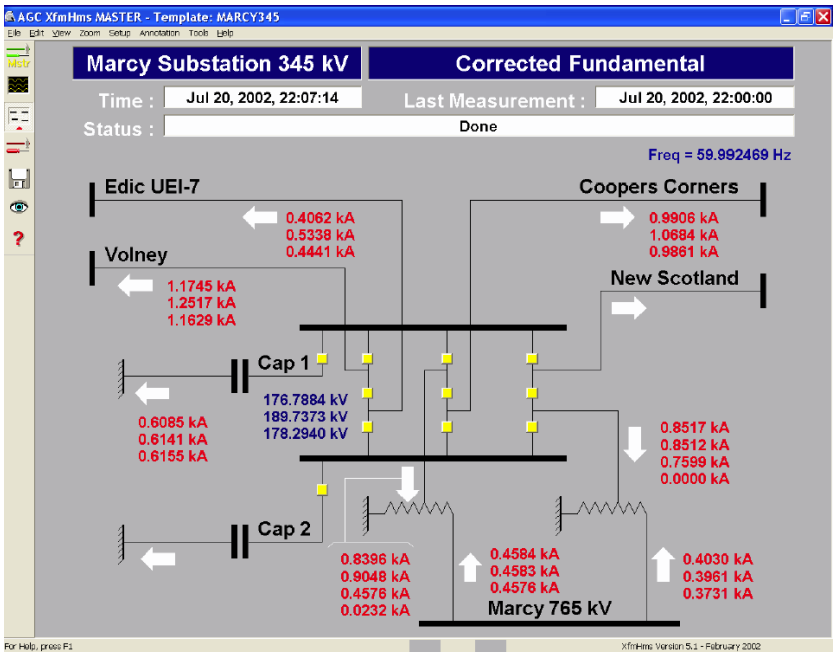

Figure 3.1: Actual three-phase voltages and currents at MARCY 345 kV substation of the New York Power Authority (NYPA). Screenshot from AGC XfmHms program, developed by this research group.

Furthermore, the imbalances become a very important issue when distribution feeders are modeled for distribution-system analysis [138] – [140]. The existence of single-phase loads at the distribution level make the system operate under unbalanced conditions and, therefore, full three-phase analysis is highly desired in these cases. Since most of the voltage problems may appear at the distribution level, close to load centers, and mainly affect sensitive loads at load centers, the ability to model and perform analysis at the distribution level is highly desired.

Moreover, an actual power transmission system is never symmetric. While some components are designed to be near-symmetric, some others are not. For example, transmission lines are never symmetric. The impedance of any phase is different than the impedance of any other phase. In many cases, this imbalance can be corrected with transposition; however, because of cost many lines are not transposed. The asymmetry may be small or large, depending on the design of the system. One power system component that contributes to the asymmetry is the untransposed three-phase line. As an example, Figure 3.2 illustrates an actual configuration of a three-phase line. For the purpose of quantifying the asymmetry of this line, two asymmetry metrics are defined:

$$S_1 = \frac{1}{2}\frac{|z_{max} - z_{min}|}{|z_1|}, \tag{3.1}$$

$$S_2 = \frac{1}{2}\frac{|y_{max} - y_{min}|}{|y_1|}, \tag{3.2}$$

where z_1 is the positive sequence series impedance of the line, z_{max} and z_{min} are the max and min series impedances of the individual phases, y_1 is the positive sequence shunt admittance of the line, y_{max} and y_{max} are the max and min shunt admittances of the individual phases. The above indices provide the level of asymmetry among phases of a

transmission line in a quantitative manner. As a numerical example, these metrics have been computed for the line of Figure 3.2 and are presented in Figure 3.3. Note that the asymmetry is on the order of 5 to 6%. For these reasons, explicit three-phase modeling has been adopted in this work for every power-system component.

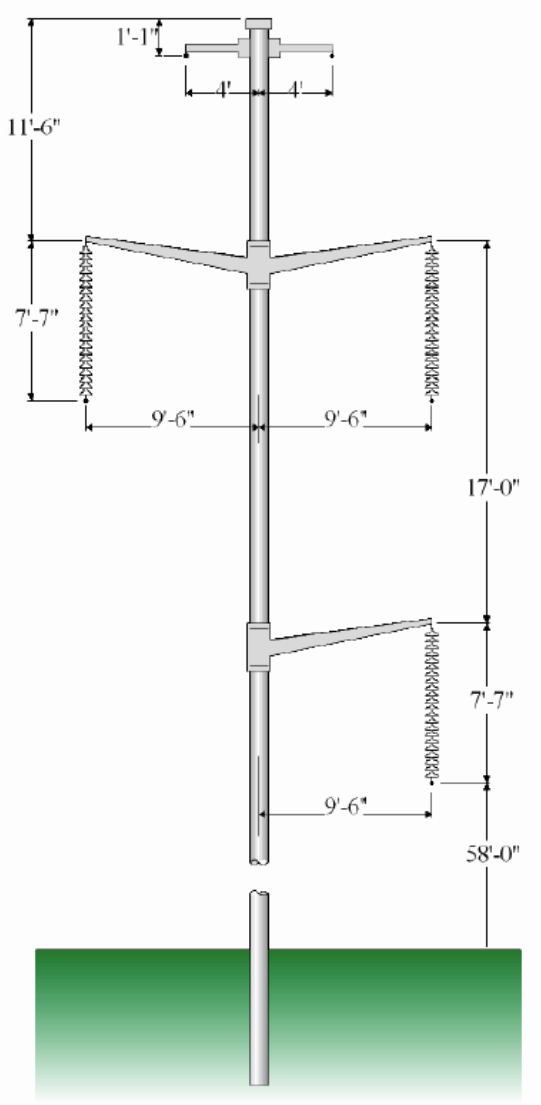

Figure 3.2: Configuration of a 230 kV, H-frame transmission tower (courtesy of Georgia Power Co.) [37].

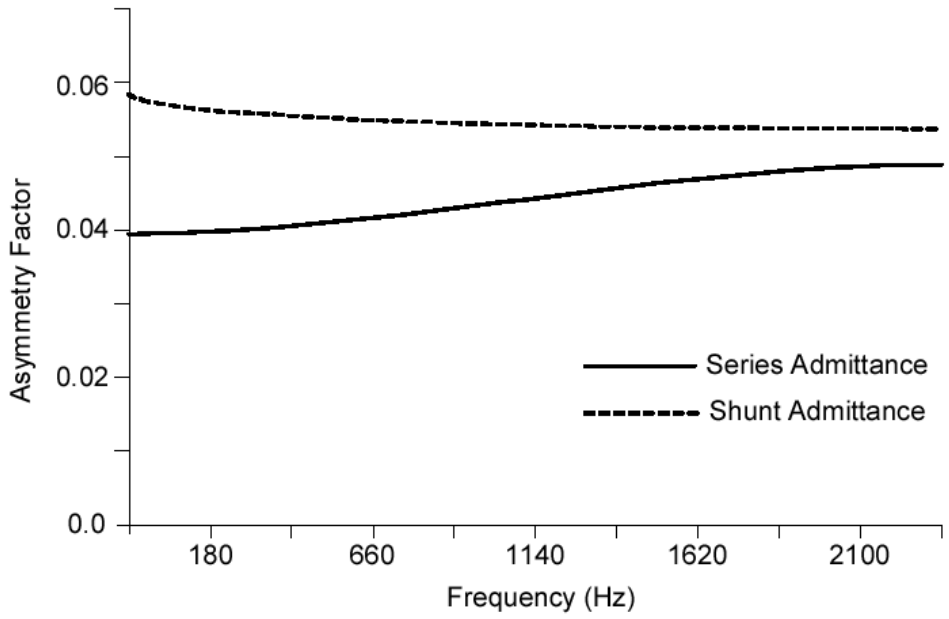

Figure 3.3: Line asymmetry indices (line of Figure 3.2).

3.2 Quadratic Three-Phase Modeling: Steady-State Analysis

At any location in a power system, referred to as a system bus, there may be many different connected components, like generating units, loads (of various types), circuits (overhead transmission lines, underground cables, power transformers), and shunt devices (of various types). The general bus of a system with several connected components is illustrated in Figure 3.4. While the circuits and most of the shunt devices are linear elements, the loads and generators may operate in such a way that imposes nonlinearities. Common loads models are (a) three-phase and single-phase constant-power load, (b) three-phase and single-phase constant-impedance load, and (c) three-phase and single-phase induction-motor loads. Common operating modes of generating units for steady-state analysis are (a) constant-voltage, constant-real-power operation and (b) constant-real-power, constant-power-factor operation.

The new quadratic modeling approach consists of writing Kirchoff's current law at each bus of the system. The models of loads and generators are expressed in terms of their terminal current and additional equations in additional internal state variables that define their operating mode. The additional equations may be nonlinear, but of order no higher than two. This can be achieved without any approximations by introducing additional state variables. Therefore, only the mathematical formulation is different; the physical models remain the same. The resulting set of equations is consistent meaning that the number of equations equals the number of unknowns. In addition, the set of equations is linear or quadratic in terms of the state variables. These equations are solved via Newton's method. The proposed model has two advantages: (a) the resulting model is more accurate than the usual models without increasing the complexity of the equations and (b) the convergence characteristics of the proposed model are superior to conventional methods.

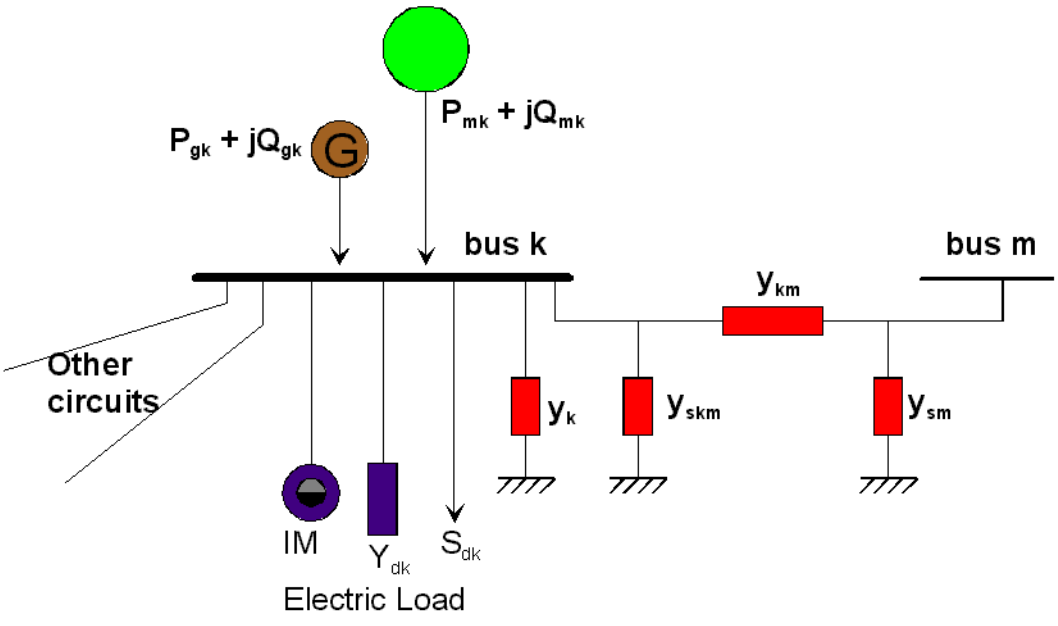

Figure 3.4: General power system bus [41].

As discussed earlier each component of the system can be represented with an appropriate set of linear or quadratic equations. By expressing the voltage and current phasors in terms of their Cartesian coordinates (i.e., $\tilde{I} = I_r + jI_i$ and $\tilde{V} = V_r + jV_i$), the following general form is obtained for any power system component:

$$\begin{bmatrix} I_r^k \\ I_i^k \\ 0 \end{bmatrix} = y_{eq\_real}^k \begin{bmatrix} V_r^k \\ V_i^k \\ y^k \end{bmatrix} + \begin{bmatrix} x^{k^T} f_{eq\_real_1}^k x^k \\ x^{k^T} f_{eq\_real_2}^k x^k \\ \dots \end{bmatrix} - b_{eq\_real}^k, \tag{3.3}$$

where $x^k = \begin{bmatrix} V_r^k \\ V_i^k \\ y^k \end{bmatrix}$ and $y_{eq\_real}^k$, $b_{eq\_real}^k$, and $f_{eq\_real}^k$ are vectors and matrices of appropriate dimensions. V_r^k and V_i^k are the real and imaginary parts of the device terminal voltage (for each terminal node) referred to as external device states, y^k are the internal device states, and I_r^k and I_i^k are the device terminal currents (for each terminal node) with direction into the device.

Application of Kirchoff's current law at each bus of the system, like bus k of Figure 3.4, eliminates the left-hand-side current variables and results in a quadratic set of equations for the whole system of the form:

$$\begin{bmatrix} 0 \\ 0 \\ 0 \end{bmatrix} = Y_{eq\_real} \begin{bmatrix} V_r \\ V_i \\ y \end{bmatrix} + \begin{bmatrix} x^T F_{eq\_real_1} x \\ x^T F_{eq\_real_2} x \\ \dots \end{bmatrix} - B_{eq\_real}\,. \tag{3.4}$$

Additional details on the quadratic power flow, as developed earlier by this research group, can be found in references [38] – [41].

3.3 Quadratic Three-Phase Modeling: Dynamic Analysis

Note that the mathematical form described in the previous section can be extended and is also directly applicable to dynamic component modeling after the differential equations have been converted to algebraic equations using some numerical integration rule. In our case the quadratic integration rule, developed as part of this work, is assumed, as presented in Chapter 5. This work extends previous work on this topic by this research group [135] – [137]. These notions for transient analysis of electric networks are based on the concepts first introduced in [61] about the resistive companion form of elements and used extensively in the literature. A recent description can be found in [77]. For this case, the following conventions have been used to construct the generalized, "quadratized," algebraic component form of each model.

The general model consists of differential and algebraic equations of the form:

$$\begin{aligned} \frac{dx(t)}{dt} &= f(x(t), y(t), t), \\ 0 &= g(x(t), y(t), t), \end{aligned} \tag{3.5}$$

where

$x(t)$ are the dynamical states ($x \in R^n$),

$y(t)$ are the algebraic states ($y \in R^m$),

f are the differential equations ($f: R^{n+m+1} \to R^n$),

g are the algebraic equations ($g: R^{n+m+1} \to R^m$),

t indicates the free variable representing time.

After applying the quadratic integration rule at the interval $[t-h, t]$, as described in detail in Chapter 5, the differential equations are transformed into algebraic equations

involving the values of the dynamical states at times $t-h$, t, and at the midpoint of the interval t_m. The compact expression of the rule for the dynamical system (3.5) is

$$\frac{h}{24}f(t,x(t),y(t))+x_m-\frac{h}{3}f(t_m,x_m,y_m)=x(t-h)+\frac{5h}{24}f(t-h,x(t-h),y(t-h)),$$
$$x(t)-\frac{h}{6}f(t,x(t),y(t))-\frac{2h}{3}f(t_m,x_m,y_m)=x(t-h)+\frac{h}{6}f\big(t-h,x(t-h),y(t-h)\big). \tag{3.6}$$

For the special case of a linear, time invariant system of the form:

$$\dot{x}(t)=Ax(t)+Bu(t)\ , \tag{3.7}$$

with

$x(t)$ the dynamical states ($x\in R^n$),

$u(t)$ the model input vector ($u\in R^p$),

A the linear matrix of the model ($A\in R^{n\times n}$),

B the input matrix of the model ($B\in R^{n\times p}$).

Equations (3.6) at each time step become

$$\begin{bmatrix} I_n-\frac{h}{6}A & -\frac{2h}{3}A \\ \frac{h}{24}A & I_n-\frac{h}{3}A \end{bmatrix}\cdot\begin{bmatrix} x(t) \\ x_m \end{bmatrix}=\begin{bmatrix} I_n+\frac{h}{6}A \\ I_n+\frac{5h}{24}A \end{bmatrix}\cdot x(t-h)+\begin{bmatrix} \frac{h}{6}B & \frac{h}{6}B & \frac{2h}{3}B \\ -\frac{h}{24}B & \frac{5h}{24}B & \frac{h}{3}B \end{bmatrix}\cdot\begin{bmatrix} u(t) \\ u(t-h) \\ u_m \end{bmatrix}. \tag{3.8}$$

I_n is the identity matrix of dimension n and h the length of the integration time step. Note that the right-hand side of (6) contains known quantities at the current integration step. The algebraic equations, g, are appended to the transformed differential equations at times t and t_m and this results in a consistent set of equations (equal number of equations and unknowns). The unknowns are the values of the states (dynamic x and algebraic y) at

times t and t_m. The values at $t - h$ are known values from the previous time step. These equations are solved for the unknown quantities at each time step.

Note now that via the "quadratization" process f and g are transformed to functions that are at most quadratic. Therefore, the model is transformed to a fully equivalent quadratic system of the form:

$$\begin{bmatrix} \dot{x}(t) \\ 0 \\ 0 \end{bmatrix} = [A_1(t) \quad A_2(t) \quad A_3(t)] \begin{bmatrix} x(t) \\ y(t) \\ z(t) \end{bmatrix} + \begin{bmatrix} X^T F_1(t) X \\ \dots \\ X^T F_N(t) X \end{bmatrix} + B(t)u(t) \,, \tag{3.9}$$

where

$x(t)$ are the dynamical states ($x \in R^n$),

$y(t)$ are the algebraic states ($y \in R^m$),

$z(t)$ are additional algebraic states introduced for the model quadratization ($z \in R^q$),

$X(t)$ is the total state vector ($X \in R^{N=n+m+q}$),

$u(t)$ is the model input vector ($u \in R^p$),

$A(t)$ is the linear matrix of the model ($A \in R^{N \times N}$),

$F(t)$ is the quadratic part of the model ($F_i \in R^{N \times N}$, $_{i = 1, \dots, N}$),

$B(t)$ is the input matrix of the model ($B \in R^{N \times p}$),

t indicates the free variable representing time.

In particular, $A(t) = [A_1(t) \quad A_2(t) \quad A_3(t)]$, where $A_1 \in R^{N \times n}$, $A_2 \in R^{N \times m}$, and $A_3 \in R^{N \times p}$. F is a set of matrices that define the quadratic terms in (3.9). It can be viewed as an array of matrices. All the model matrices can be either constant of time-dependent,

as indicated in (3.9). As an example, time-dependent models can be used to represent switching, or multi-stage systems. The model matrices are constant for the duration of a specific stage, but they change from stage to stage. When such a representation is used only the (constant) matrices A, F, B and the input vector u need to be defined for each model, irrespectively of the model complexity. This facilitates significantly the implementation. Furthermore, Jacobian matrix of the mathematical model can be easily computed as

$$J = A + \begin{bmatrix} X^T(F_1 + F_1^T) \\ \dots \\ X^T(F_N + F_N^T) \end{bmatrix}. \tag{3.10}$$

In fact, in the proposed formulation the dynamical equations can be modeled by a linear vector function and the algebraic equations by a quadratic vector function. That is, all nonlinearities can be moved to the algebraic part of the model. Any nonlinear power-system or power-electronics model can be transformed into a set of linear differential equations and a set of algebraic equations of degree no more than two (quadratic) by the introduction of additional appropriate state variables. This results in a model of the form:

$$\begin{aligned} \dot{x}(t) &= h(x(t), y(t), z(t), t) = A'_1 x(t) + A'_2 y(t) + A'_3 z(t) + B'u(t), \\ 0 &= q(x(t), y(t), z(t), t), \end{aligned} \tag{3.11}$$

where $x \in R^n$ is the vector of dynamic states, $y \in R^m$ is the vector of algebraic states, $z \in R^q$ is a vector of additional state variables for the quadratization, $u \in R^p$ is the input vector, h is a set of linear functions with respect to x, y, and z, and q is the set of quadratic functions consisting of the transformed (quadratized) functions g and of additional functions introduced to quadratize the model. Furthermore, $A'_1 \in R^{n \times n}$,

$A'_2 \in R^{n\times m}$, $A'_3 \in R^{n\times q}$, $B' \in R^{n\times p}$. Note the form of the quadratized equations comprises a set of linear differential equations and a set of quadratic algebraic equations.

Then, the linear differential equations are integrated as discussed above, resulting in an equation similar to (3.8) and the quadratic algebraic equations of the system (expressed at times t and t_m) are appended to the set of equations (3.8). The end result is a model that contains one subset of linear equations and another subset of quadratic equations as in (3.12):

$$\begin{bmatrix} I_n - \frac{h}{6}A_1 & -\frac{h}{6}A_2 & -\frac{h}{6}A_3 & -\frac{2h}{3}A_1 & -\frac{2h}{3}A_2 & -\frac{2h}{3}A_3 \\ \frac{h}{24}A_1 & \frac{h}{24}A_2 & \frac{h}{24}A_3 & I_n - \frac{h}{3}A_1 & -\frac{h}{3}A_2 & -\frac{h}{3}A_3 \end{bmatrix} \cdot \begin{bmatrix} x(t) \\ y(t) \\ z(t) \\ x_m \\ y_m \\ z_m \end{bmatrix} =$$

$$\begin{bmatrix} I_n + \frac{h}{6}A_1 & \frac{h}{6}A_2 & \frac{h}{6}A_3 \\ I_n + \frac{5h}{24}A_1 & \frac{5h}{24}A_2 & \frac{5h}{24}A_3 \end{bmatrix} \cdot \begin{bmatrix} x(t-h) \\ y(t-h) \\ z(t-h) \end{bmatrix} + \begin{bmatrix} \frac{h}{6}B & \frac{h}{6}B & \frac{2h}{3}B \\ -\frac{h}{24}B & \frac{5h}{24}B & \frac{h}{3}B \end{bmatrix} \cdot \begin{bmatrix} u(t) \\ u(t-h) \\ u_m \end{bmatrix}, \qquad (3.12)$$

$$0 = q(x(t), y(t), z(t), t),$$
$$0 = q(x_m, y_m, z_m, t).$$

Solution of the above system $(2 \times (m + n + q)$ equations in $2 \times (m + n + q)$ unknowns) via Newton's method yields the value of the state vector $x(t)$. Note that the values at the midpoint, x_m, y_m, and z_m, are simply intermediate results and are discarded at the end of the calculations at each step.

For the construction and solution of the network equations, the resulting set of algebraic equations for each component needs to be written in an algebraic companion form, using the notions presented so far. This form contains the equations for the through variables of the model (in our case terminal currents for each device terminal) along with

the additional model equations. The equations of the through variables are referred to as external or interface equations, while the rest of the model equations are internal. The through variables are not unknowns, but are just used as a means of connecting the device to the rest of the network. They are eliminated after the application of the connectivity constraints (in our case Kirchoff's current law). The generalized, quadratic component companion form at each time step $[t-h, t]$ has the general form:

$$\begin{bmatrix} I \\ 0 \end{bmatrix} = A.X + \begin{bmatrix} X^T F_1 X \\ \dots \\ X^T F_n X \end{bmatrix} - b, \tag{3.13}$$

where

I denotes the through variables,

X denotes the total state vector,

A is the coefficient matrix for the linear terms,

F_i is the coefficient matrix for the quadratic terms for each equation i,

n is the total number of equations and also unknowns,

b is the vector of past history terms and constant or state independent terms (e.g. inputs).

The ordering of the model equations is as follows: The equations are separated into two main groups, i.e., equations at time t and equations at time t_m. Equations at time t are listed first, followed by equations at time t_m. First, the external equations (terminal currents) are listed. The algebraic equations resulting from discretizing the differential equations, by applying the quadratic integration rule from time $t-h$ to time t, are listed

next. Finally, the remaining internal algebraic equations at time t are appended, listing the linear equations first and the nonlinear (quadratic) next. The further ordering of the internal equations (and states) is arbitrary and is done in such a way that the resulting equations have diagonal dominance. The same ordering is used for the second group of equations at time t_m. The external equations at time t_m are first, followed by the discretized differential equations after integrating from $t-h$ to time t_m, and then followed by the internal algebraic equations at time t_m.

The ordering of the total state vector X follows the equation ordering. It should be noted again that since application of the quadratic integration yields the values of the states at times t and t_m, each state variable exists at two time instants in the state vector. The ordering used in the state vector assumes two groups of variables: each variable at time t is first, followed by the variables at time t_m in the same order. The terminal device voltages v are called external states, since they interface the device with the rest of the network and they are states shared by other devices as well (connected to the same nodes). Other variables can also be external states. These variables at time t appear first in the state vector in correspondence with the equations for the though variables. The rest of the states are referred to as internal device states. They correspond to equations with zero left-hand side. The dynamic states at time t are listed next, followed by the algebraic states at time t, first the linear and then the nonlinear. Then the group of variables at time t_m follows with the same ordering.

For implementation reasons, it is preferable to convert all the differential equations to linear equations of the very simple form $\frac{dx(t)}{dt} = x'(t)$, (where $x'(t)$ is part of the internal states and can be either linear or nonlinear) and then move all the nonlinearities

to the algebraic equations. Therefore, based on the ordering and grouping described above in compact matrix notation, the device model can be cast in the generalized form:

$$
\begin{aligned}
i(t) &= A_1(t)v(t) + A_2(t)x(t) + A_3(t)y(t) + A_4(t)z(t), && \text{[external equations]} \\
0 &= \frac{dx(t)}{dt} + B_1(t)v(t) + B_2(t)x(t) + B_3(t)y(t) + B_4(t)z(t), && \text{[differential equations]}
\end{aligned}
\tag{3.14}
$$

$$
\begin{aligned}
0 &= C_1(t)v(t) + C_2(t)x(t) + C_3(t)y(t) + C_4(t)z(t), && \text{[linear internal equations]} \\
0 &= q(v(t), x(t), y(t), z(t), t), && \text{[nonlinear internal equations]}
\end{aligned}
$$

where

$v(t)$ are the external states,

$x(t)$ are the internal dynamic states,

$y(t)$ are the internal linear algebraic states, and

$z(t)$ are the internal nonlinear algebraic states.

The coefficient matrices A_1 to A_4, B_1 to B_4, C_1 to C_4 can be constant or time-varying in the general case (like, for example, when the system configuration is changing, there are discrete switchings in the system, or limits exist). The equations involving the function q in (3.12) are the nonlinear equations of the system.

Therefore, after applying the quadratic integration rule, the differential equations become algebraic and the state vector at each time step is [assuming i external equations (and states), k internal dynamic equations (and states), j internal algebraic linear

equations (and corresponding states), and l internal algebraic nonlinear equations (and corresponding states)]

$\mathrm{X} = [\mathrm{X^T(t)} \quad \mathrm{X^T(t_m)}]$,

with $X(t) = [v^T(t) \quad x^T(t) \quad y^T(t) \quad z^T(t)]^T$ and

$X(t_m) = [v^T(t_m) \quad x^T(t_m) \quad y^T(t_m) \quad z^T(t_m)]^T$,

where

$v(t) = [v_1(t) \quad ... \quad v_i(t)]^T$,

$x(t) = [x_1(t) \quad ... \quad x_k(t)]^T$,

$y(t) = [y_1(t) \quad ... \quad y_j(t)]^T$,

$z(t) = [z_1(t) \quad ... \quad z_l(t)]^T$,

$v(t_m) = [v_1(t_m) \quad ... \quad v_i(t_m)]^T$,

$x(t_m) = [x_1(t_m) \quad ... \quad x_k(t_m)]^T$,

$y(t_m) = [y_1(t_m) \quad ... \quad y_j(t_m)]^T$,

$z(t_m) = [z_1(t_m) \quad ... \quad z_l(t_m)]^T$,

and the equations in quadratic form are

$$\begin{bmatrix} i_1(t) \\ \dots \\ i_i(t) \\ 0 \\ \dots \\ 0 \\ i_1(t_m) \\ \dots \\ i_i(t_m) \\ 0 \\ \dots \\ 0 \end{bmatrix} = A. \begin{bmatrix} v(t) \\ x(t) \\ y(t) \\ z(t) \\ v(t_m) \\ x(t_m) \\ y(t_m) \\ z(t_m) \end{bmatrix} + \begin{bmatrix} X^T F_1 X \\ \dots \\ X^T F_n X \end{bmatrix} - b. \tag{3.15}$$

External states: $v_1(t),\dots, v_i(t)$, $v_1(t_m)$,…, $v_i(t_m)$.

Internal dynamical states: $x_1(t),\dots, x_k(t)$, $x_1(t_m)$,…, $x_k(t_m)$.

Internal linear algebraic states: $y_1(t),\dots, y_j(t)$, $y_1(t_m)$,…, $y_j(t_m)$.

Internal nonlinear algebraic states: $z_1(t),\dots, z_l(t)$, $z_1(t_m),\dots, z_l(t_m)$.

Through variables: $i_1(t),\dots, i_i(t)$, $i_1(t_m)$,…, $i_i(t_m)$.

The presented framework for dynamic simulation is quite general and can be applied to any network or any dynamical system in general. For power-system dynamic analysis the approach is essentially the same for both the full transient simulation and the proposed quasi-steady-state or quasi-static analysis, described in Chapter 1. The quasi-static approach, which is developed in this work, is based on simulating the essential dynamical equations describing the dynamics of the system motors and the rotors of the generators and solving them along with the network load-flow equations and the possible additional internal equations of the existing devices. This is based on the valid assumption that the electrical network quantities change much faster compared to the mechanical quantities of the machines. Therefore, the network is assumed to operate under sinusoidal, quasi-steady-state conditions. The voltages and currents at any node of

the grid are considered sinusoidal quantities at the fundamental frequency and phasor representation is utilized for them, as opposed to instantaneous values used for the slow changing mechanical quantities. This results in a mixed system model comprising both instantaneous and phasor quantities. However, the magnitude and phase of these phasors are changing in time. As a result, the representation is base on time-varying phasors (with varying magnitude and phase), as opposed to the constant phasors of the steady-state analysis.

This is essentially a reduced-order dynamical model of the system that preserves the essential dynamic behavior of the system, while maintaining a computational complexity similar to the steady-state power-flow analysis. This is due to the fact that the vast majority of the system-model equations are the network power-flow equations that are solved repeatedly at each time step of the dynamic simulation. Therefore, the quasi-static analysis is an intermediate solution between the steady-state analysis and the full transient simulation.

Regarding the analysis of voltage recovery phenomena, when using the quasi-static analysis the phenomena are considered from a macroscopic level. In this case, fast electrical transients are ignored and the analysis is focused on the transient behavior of the voltage phasors, i.e. the transient behavior of the magnitude of the voltage. The electrical network is considered to operate under sinusoidal, quasi-steady-state conditions at the fundamental frequency, subject to similar to the standard load flow assumptions. Therefore, frequency-domain, phasor representation is utilized for the electrical network model. The dynamic behavior of the system is imposed only by the slow

electromechanical dynamics of the load (induction motors) and the generators. The analysis is based on time-varying phasor representation.

On the other hand, in the full transient analysis all the electrical transients as well as the full time-domain waveform distortion (from sinusoidal) of the electrical quantities, if any, are of concern. In this case, electrical transients resulting from the interaction of capacitors and inductance of the system are of concern as well as electrical transients from magnetic core saturation (in-rush currents). In general, there is an interaction between the load dynamics and the electrical transients. This model captures these interactions. No assumptions are made in this modeling approach and the full time-domain waveforms are obtained as a result of the dynamic simulation. Thus, the full time-domain transient analysis is a high-fidelity type of analysis that can capture any type of phenomena in the system and incorporates all the fast system dynamics. There are no assumptions made on the waveforms of the electrical quantities. Therefore, full time-domain representation is used for any quantity and the transient behavior of the full time-domain waveforms is obtained. The system dynamic behavior is driven by all the dynamics of the generating units and the dynamic loads, like induction motors, including the fast stator dynamics of the electric machinery, as well as the electrical transients due to the interactions of the network inductances and capacitances. This type of analysis results in very accurate, high-fidelity type of analysis and can capture phenomena that occur due to nonlinearities in the system components and due to saturation. However, studies of this type are computationally demanding and, therefore, the analysis can be limited to relatively small system sizes.

3.4 Solution Method

The solution method is the same for both steady-state and dynamic (quasi-steady-state and full transient) analysis once the differential equations of the dynamical system are converted to algebraic equations, by the application of some numerical integration rule. The network solution is obtained by application of Newton's method to the "quadratized" form of the network equations [37], [38], [41], [132] – [135], [137], [141]. The "quadratized" network equations are generated as follows: Consider the general form of equations for any model of the system (linear or nonlinear). Note that this form includes two major sets of equations, which are called external equations, or current equations, and internal equations respectively. The electric currents at the terminals of the component appear only in the external equations. Similarly, the device states consist of two variable sets: external states (i.e., bus voltage $\tilde{V}^k = V_r^k + jV_i^k$ if phasor notation is used) and internal state variables y^k (if any). The set of equations is consistent in the sense that the number of external states and the number of internal states equal the number of external and internal equations, respectively.

The entire network equations are obtained by applying the connectivity constraints among the system components, i.e., Kirchoff's current law at each system bus. Specifically, utilizing phasor notation Kirchoff's current law applied to all buses of the system yields

$$\sum_k A^k \tilde{I}^k = 0, \tag{3.16}$$

where $\tilde{I}^k = I_r^k + jI_i^k$ is the device k node current injections (for all nodes associated with that device), and A^k is a component incidence matrix with

$$\{A_{ij}^k\} = \begin{cases} 1, & \text{if node j of device k is connected to node i.} \\ 0, & \text{otherwise.} \end{cases} \quad (3.17)$$

Similarly, for instantaneous quantities Kirchoff's current law applied to all buses of the system yields

$$\sum_k A^k i^k(t) = 0, \quad (3.18)$$

where $i^k(t)$ is the device k node current injections (for all nodes associated with that device), and A^k is a component incidence matrix with

$$\{A_{ij}^k\} = \begin{cases} 1, & \text{if node j of device k is connected to node i.} \\ 0, & \text{otherwise.} \end{cases} \quad (3.19)$$

All the internal equations from all devices should be added to the (3.16) or (3.18), yielding the following set of equations:

$$\begin{cases} \sum_k A^k \tilde{I}^k = 0, \\ [\text{internal equations of all devices}], \end{cases} \quad (3.20)$$

or

$$\begin{cases} \sum_k A^k i^k(t) = 0, \\ [\text{internal equations of all devices}]. \end{cases} \quad (3.21)$$

Let $\tilde{V} = V_r + jV_i$, for phasor quantities, or $V(t)$, for instantaneous values, be the vector of all node voltages. Then, the following relationships hold respectively:

$$\tilde{V}^k = (A^k)^T \tilde{V}, \quad (3.22)$$

$$V^k(t) = (A^k)^T V(t), \quad (3.23)$$

where $\tilde{V}^k$ or $V^k(t)$ is device k bus voltage.

The complex phasor equations can be separated into two sets of real equations by expressing the voltages and currents with their Cartesian coordinates. Then the device currents can be eliminated with the use of (3.16) or (3.18). This procedure will yield a set of equations in terms of the voltage variables and the internal device state variables. If all the state variables are represented with the vector x, then the equations can be written in the following form:

$$G(x) = Y_{real}x + \begin{bmatrix} x^T f_1 x \\ x^T f_2 x \\ \dots \end{bmatrix} - B_{real} = 0, \tag{3.24}$$

where x is the vector of all the state variables and Y_{real}, f, B_{real} are matrices of appropriate dimensions. The simultaneous solution of these equations is obtained via Newton's method. Specifically, the solution is given by the following algorithm:

$$x^{v+1} = x^v - J_G^{-1}\left\{ Y_{real}x^v + \begin{bmatrix} x^{v^T} f_1 x^v \\ x^{v^T} f_2 x^v \\ \dots \end{bmatrix} - B_{real} \right\}, \tag{3.25}$$

where v is the iteration step number; J_G is the Jacobian matrix of the function $G(x)$ in (3.24). In particular, the Jacobian matrix takes the following form:

$$J_G = Y_{real} + \begin{bmatrix} x^{v^T}(f_1 + f_1^T) \\ x^{v^T}(f_2 + f_2^T) \\ \dots \end{bmatrix}. \tag{3.26}$$

It is important to note that Newton's method is ideally suited for the solution of quadratic equations.

3.5 Summary

Power-system modeling and power-system simulation, both steady-state and dynamic, are fundamental for any type of power-system analysis. These topics comprise a large part of the work conducted in this research. The general framework for power-system analysis that is utilized throughout this work is presented in this chapter. Full three-phase modeling is used to provide a more realistic and high-fidelity analysis that can capture system asymmetries and imbalances can be accounted for.

The proposed modeling and simulation approach is based on the "quadratized" formulation, which models the system under study as a set of mathematical equations of order no more than two. The framework of the modeling approach is essentially the same for both steady-state and dynamic analysis. The dynamic analysis can be either quasi-steady-state or full transient analysis. Appropriate models, based on the type of analysis, are constructed for each system component and then the model of the entire system is constructed by applying the connectivity constraints between all the components. The solution methodology is based on Newton's method for nonlinear equations.

CHAPTER 4

POWER-SYSTEM COMPONENT MODELING

4.1 Introduction

The modeling principles and methodologies presented in Chapter 3 are utilized in the development and implementation of appropriate mathematical models for power system components. This chapter presents a description of the most important component models that were developed as part of this work. These models include dynamic load models, in the form of induction machines, generating unit models, and models of voltage-support devices. Since the analysis of primary interest for the studies performed within this research is the quasi-steady-state analysis, the models utilized for this type of analysis are highlighted. A more thorough description of all the newly developed and implemented models in this research work is presented in Appendix A, along with implementation details for each model.

4.2 Synchronous Single- and Two-Axis Generating-Unit Model

4.2.1 Overview

The dynamics of the generating units, including their control subsystems, are of great importance in the study of voltage recovery. Furthermore, the synchronous generator is the main VAr source in power systems, and thus the main control device of voltage phenomena. Therefore, part of this work is dedicated to describing and implementing models of the generating unit, along with its excitation system and prime mover [132] – [136].

Since the synchronous generator is the main device for controlling reactive power, emphasis has been given to modeling synchronous generators for both steady-state and dynamic analysis. A three-phase, single-axis model has been implemented for steady-state analysis. This model is being augmented to include the dynamic characteristics of the synchronous generator for quasi-steady-state analysis. In addition a physically-based, two-axis model is implemented for full transient analysis. Furthermore, exciter and turbine-governor models are also incorporated. Realistic modeling of the exciter system, as well as the generator and excitation system limits, is important for voltage support studies, since they can be used to construct the actual unit capability curves, which may change based on the configuration and operating data of the electric grid where the unit is connected.

4.2.2 Single-Axis Steady-State Model

The steady-state model of a single-axis synchronous generator is presented in this section. The model includes three control options:

- PQ mode;
- PV mode;
- Slack bus mode.

The generator model also includes the following features:

- Internal impedance;
- Voltage control at user specified node;
- Real and reactive power limits;

- Reactive power allocation factor;
- Quadratic operating cost model;
- Failure/repair rate model.

However, it should be noted that not all these feature are essential for this work.

The unit is electrically described as a source (controlled by its subsystems) behind an equivalent impedance, as illustrated in the equivalent circuit of Figure 4.1. The internal sources provide a set of balanced three-phase voltages, described with the state variables of emf magnitude, E, and internal angle, δ or equivalently by the real and imaginary parts of the emf phasor $\tilde{E} = E_r + jE_i$. The state vector is, therefore, defined as $x = [V_{ar} \quad V_{ai} \quad V_{br} \quad V_{bi} \quad V_{cr} \quad V_{ci} \quad V_{nr} \quad V_{ni} \quad E_r \quad E_i]^T$, where the subscripts r and i denote real and imaginary parts respectively and the subscripts a, b, c denote the three phases. The detailed model equations are presented in Appendix A.

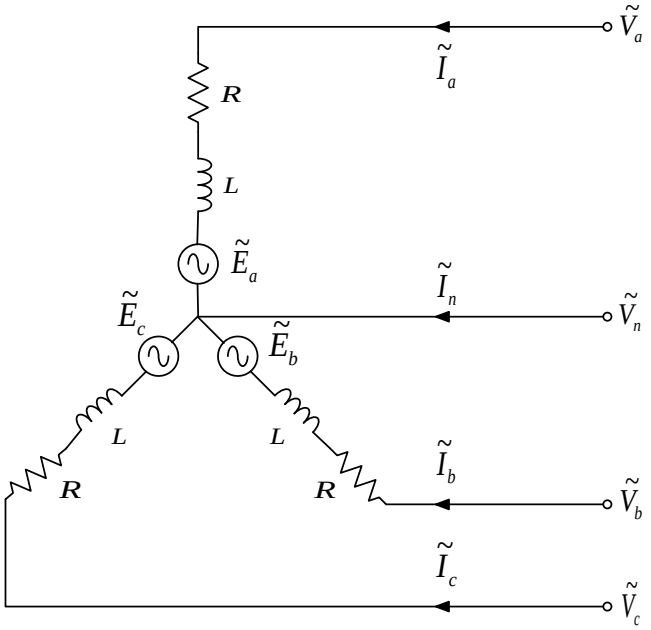

Figure 4.1: Equivalent circuit of single-axis synchronous generator model.

4.2.3 Single-Axis Quasi-Static Model

The dynamic model is based on a quasi-steady-state model that assumes that the generator is operating under sinusoidal steady-state conditions as far as the electrical system is concerned. Only the dynamics of the mechanical system of the rotor are assumed; therefore, the steady-state equations also hold, with the augmentation of the system with the swing equation of the rotor rotational movement. This equation defines the mechanical rotational speed $\omega(t)$ as well as the internal voltage angle $\delta(t)$, which is now a time-varying quantity defined via the swing equation. In this case, the state vector is $x(\mathrm{t}) = [V_{ar} \quad V_{ai} \quad V_{br} \quad V_{bi} \quad V_{cr} \quad V_{ci} \quad V_{nr} \quad V_{ni} \quad \delta(\mathrm{t}) \quad \omega(\mathrm{t}) \quad \mathrm{P_e(t)} \quad \mathrm{T_e(t)} \quad \mathrm{E(t)}]^{\mathrm{T}}$.

The internal voltage magnitude $E(t)$ is specified by the excitation system or may have a constant value. The mechanical torque applied to the rotor $T_m(t)$ is provided by a prime-mover system (turbine-governor) or may have a constant value. Some generic models are used for the excitation and prime-mover systems, based on the standard IEEE models [132] – [134]. The difference in this work is that the nonlinearities in these models are also "quadratized" and the models are casted in the form of equations (3.14) and, eventually, (3.15), assuming that the quadratic integration rule is used. The models are presented in more detail in Appendix A.

4.2.4 Two-Axis Full Transient Model

This model is used for full time-domain transient simulation of a synchronous generator [132] – [136]. The model is based on a linear flux current relation; however, it can be easily extended to include nonlinear effects and harmonics. Figure 4.2 illustrates the electrical subsystem model of a synchronous machine with two damper windings as a set of mutually coupled circuits [134] – [136]. The mechanical system is modeled as a

rotating mass subject to a mechanical torque as well as an electromagnetic torque [134] – [136]. Analysis on these systems taking into consideration the time-varying mutual inductances between stator and rotor windings yields the equations of the generator model [134] – [136]. These equations are subsequently "quadratized" to yield the quadratic model. The model is a phase-frame-based model that directly utilizes the phase quantities, without making use of Park's transformation. The model is presented in detail in Appendix A. Details can also be found in [135], [136] as part of previous work performed by this research group. The work presented in Appendix A is a new and more accurate formulation compared to the one in [135] and [136].

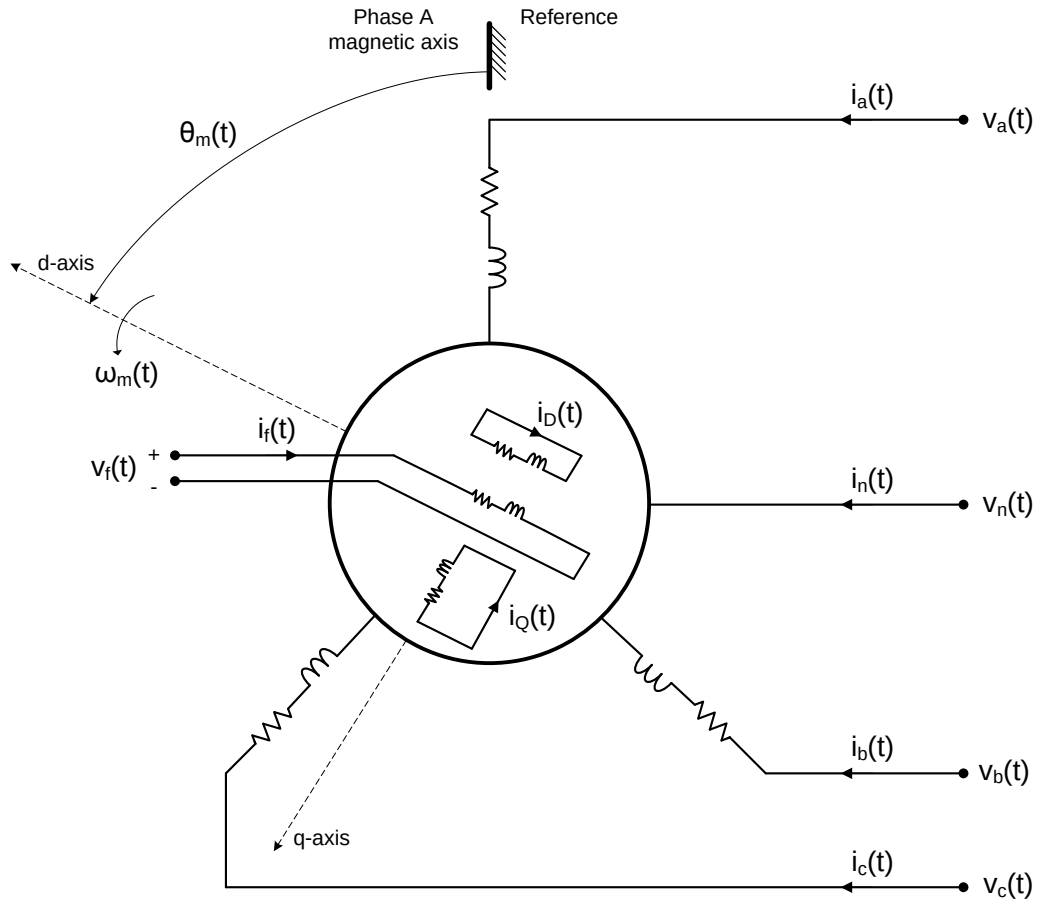

Figure 4.2: Electrical model of a synchronous machine as a set of mutually coupled windings [135].

4.3 Three-Phase Induction-Motor Model

4.3.1 Overview

A quadratic, three-phase induction-machine model has been developed as an extension of a similar single-phase-equivalent model [35], [142] – [148]. Physically, the model is based on the typical steady-state sequence circuits of the induction motor [132], [138]-[140], shown in Figure 4.3. Note that induction motors have in general little or no asymmetry, so their representation with sequence networks is valid and accurate.

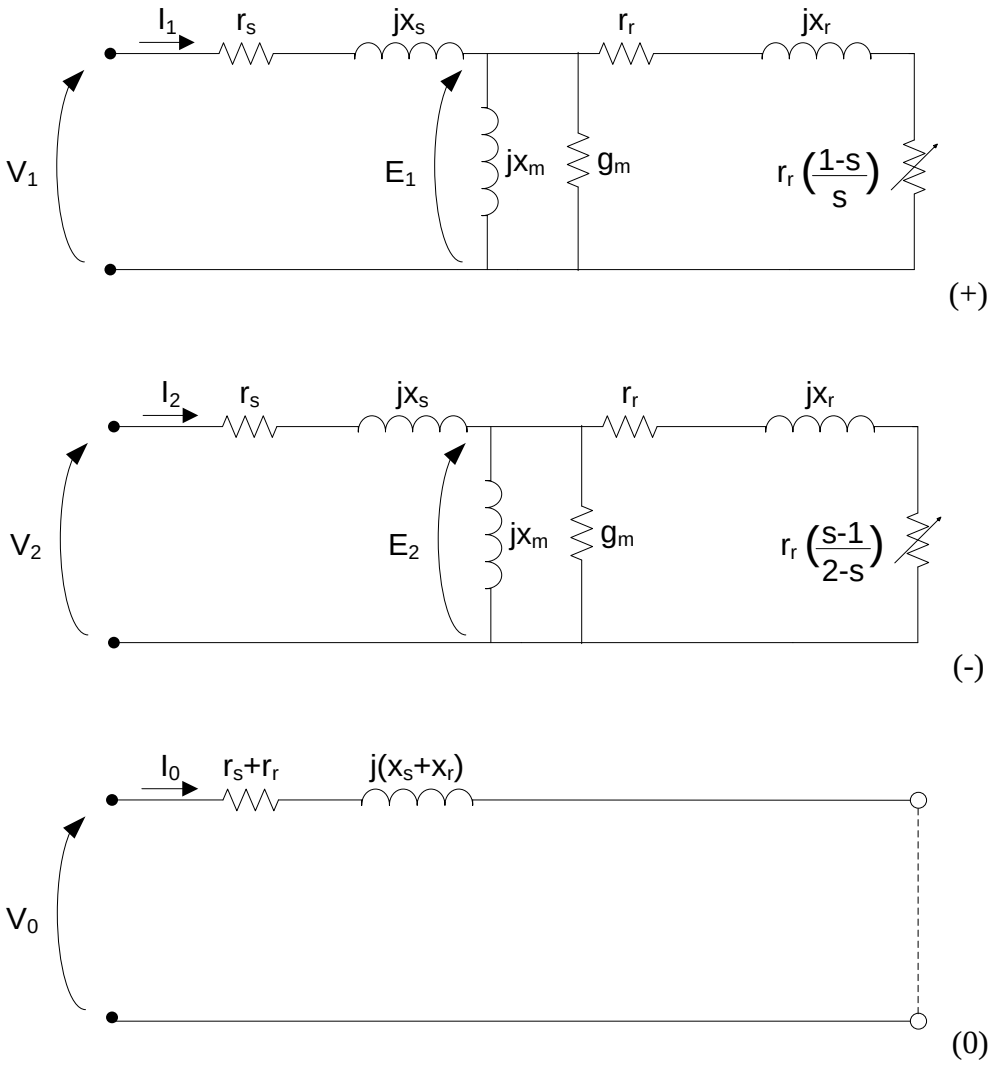

Figure 4.3: Induction motor sequence networks.

The model input data include typical motor nominal (nameplate) data, plus electrical parameters and mechanical-load data. The user interface of the model is presented in Figure 4.4 and shows the model implementation details. More details on the model implementation can be found in Appendix A.

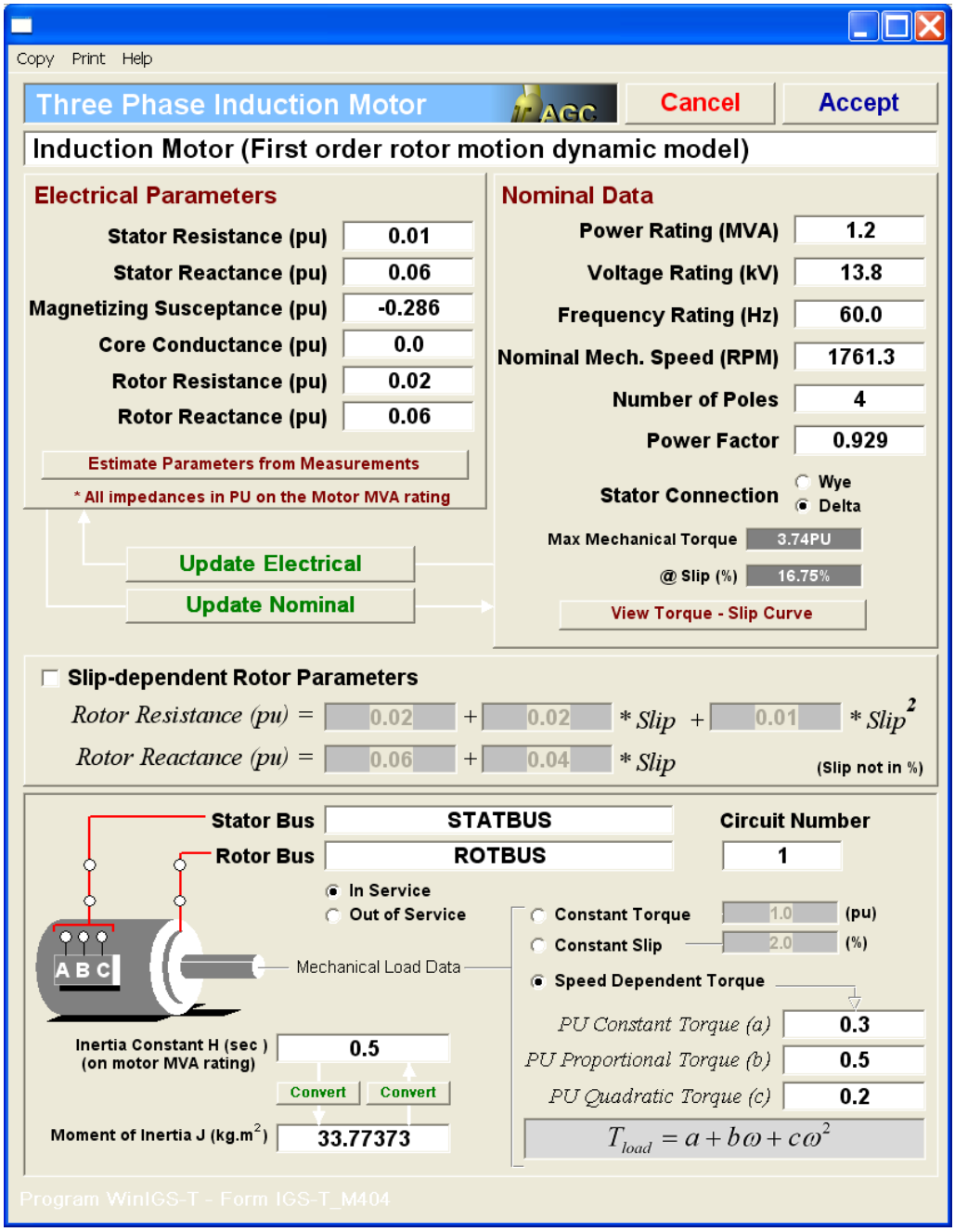

Figure 4.4: Induction motor input data form.

4.3.2 Steady-State Model

The model supports two mechanical loading modes in steady state: (a) torque equilibrium and (b) constant slip. In the torque-equilibrium mode, the mechanical torque can be either constant or depend linearly or quadratically on the mechanical speed. In this mode the motor operating point is defined as the point at which the mechanical torque of the load is equal to the electrical torque produced by the motor. In the constant slip mode, the motor operates at a specific constant speed.

Circuit analysis of the sequence networks of Figure 4.3 yields the electrical equations of the model. An additional equation links the electrical state variables to the mechanical torque. This equation is derived by equating the mechanical power (torque times mechanical frequency) to the power consumed by the variable resistors in the positive and negative circuits of Figure 4.3. In the constant-slip mode, the motor operates at constant speed. The value of the slip is known from the operating speed and, therefore, the model is linear. In the torque-equilibrium model, the motor electromechanical torque is equal to the mechanical load torque. The slip is not a known constant and thus it becomes part of the state vector. In this mode, the model becomes nonlinear and is "quadratized" based on the procedure described in Chapter 3. The detailed model equations are presented in Appendix A.

The model described above is based on the standard equivalent circuit of an induction machine. This model is in general capable of representing a wide variety of motors; however, there are several motor types that cannot be adequately represented, for example, motors with double-cage or deep-bar rotors. For the representation of such motors a slightly modified equivalent circuit has been used [50], [52]-[55], [132]. Here, a

generalized model is proposed that assumes the rotor parameters are not constant, but depend on the slip the motor is operating at. A quadratic dependence is assumed for the rotor resistance and a linear dependence for the rotor reactance. Therefore, the rotor parameters are

$$r_r(s) = \alpha + \beta.s + \gamma.s^2,$$
$$x_r(s) = \delta + \varepsilon.s, \tag{4.1}$$

where s is the operating slip. These equations are included in the motor model. Note that in the constant-slip operating mode, the model is not significantly affected since the slip is known and thus the rotor impedance is simply computed for this slip value. In the torque-equilibrium mode, however, the rotor parameters become part of the state vector after the inclusion of equations (4.1). The variation of the rotor parameters is graphically shown in Figure 4.5. The value of the resistance reduces significantly as the speed increases, while the reactance may have rather small variation with speed. In fact, the reactance value changes slightly and remains mainly constant, as it is also linearly related to the stator reactance, which can be assumed to be constant. A similar change could also be assumed for the stator reactance to make the model more precise.

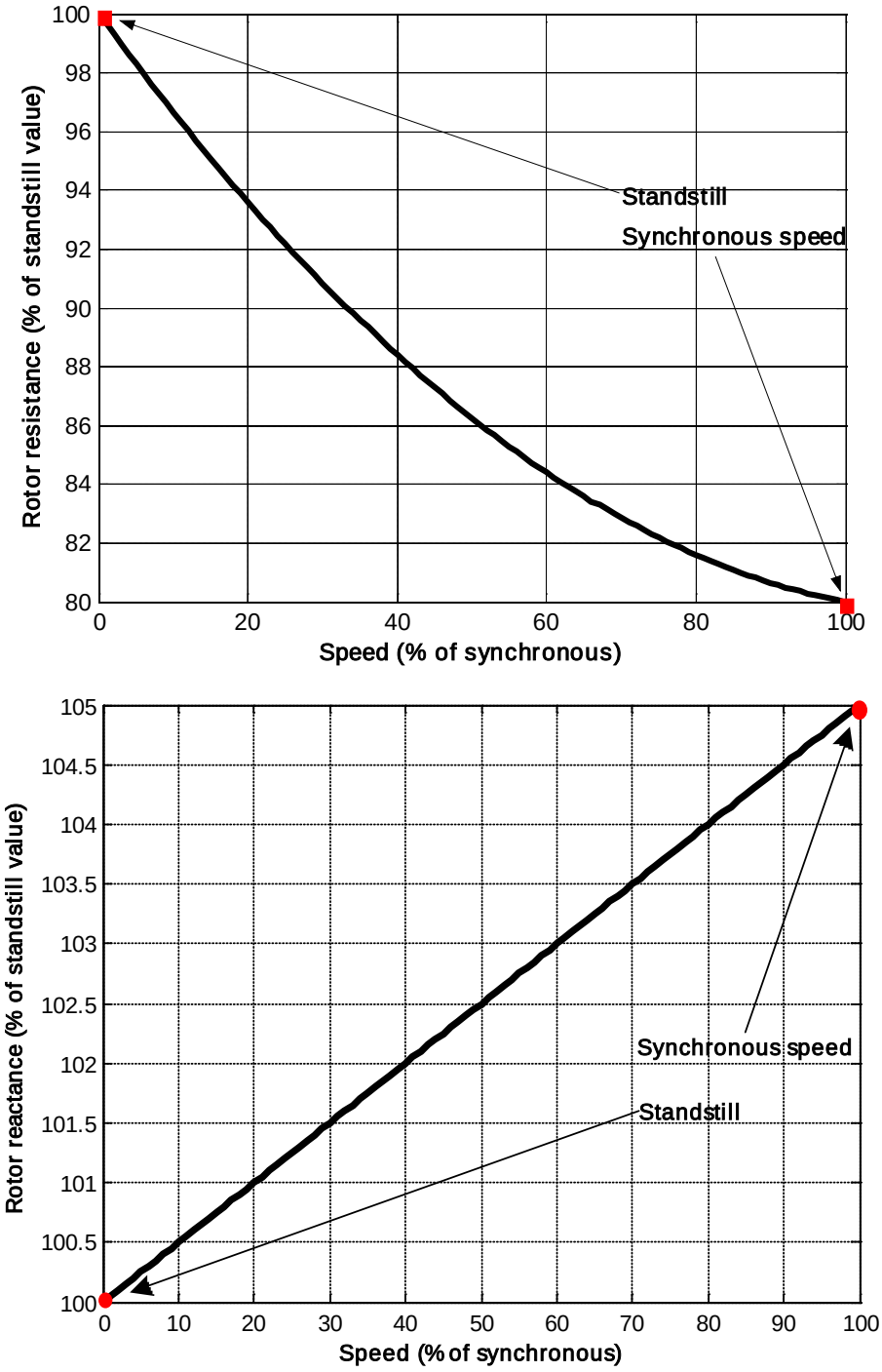

Figure 4.5: Qualitative representation of slip-dependent rotor impedance.

A model with slip-dependent rotor parameters can adequately represent, in a unified way, motors of every type and every NEMA design (A, B, C or D), including motors

with a double-cage or deep-bar rotor. Figure 4.6 shows the slip-torque characteristics of four main NEMA motor designs. Designs A and D can be accurately represented using constant-parameter models; for designs B and C the slip-dependent model is used for more realistic representation.

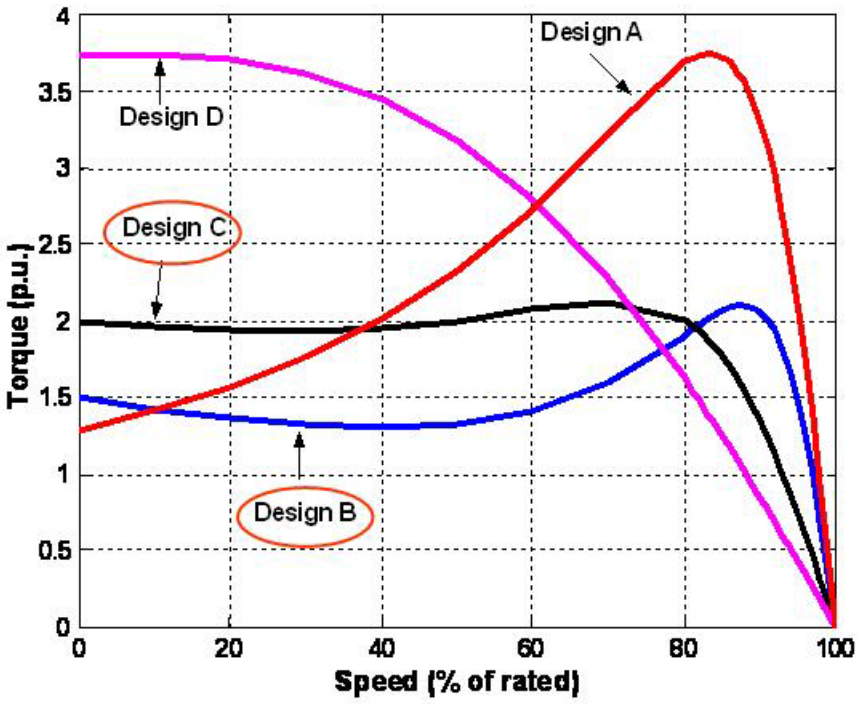

Figure 4.6: NEMA designs for AC induction motors. Designs B and C cannot be accurately represented using the classical equivalent circuit.

4.3.3 Quasi-Static Model

To capture the essential dynamic behavior of induction-motor loads, the model described in the previous section is augmented by the dynamical Equation (4.2) describing the rotor motion:

$$J\frac{d\omega_m}{dt} = T_{em} - T_m \,, \tag{4.2}$$

where

J is the rotor-load moment of inertia,

ω_m is the rotor mechanical speed,

T_{em} is the electrical motor torque,

T_m is the mechanical load torque,

and Equation (4.3) relates the speed and slip as

$$0 = \omega_m - s.\omega_s - \omega_s. \tag{4.3}$$

This simplified transient model can capture the effects of the motor in the voltage profile of the power system. The electrical transients in the motor are neglected, as they do not have significant effect on the network solution, especially for the time scales of interest, which are very long compared to the time scales of the electrical transients. Phasor representation is therefore used for the electrical quantities. The elimination of stator electrical transients makes it possible to interface the motor with the network that is assumed to operate in quasi-steady-state conditions.

4.3.4 Full Transient Model

The transient model is based on representing an induction motor as a set of six mutually coupled windings, three for the phases of the stator and three for the rotor phases, as illustrated in Figure 4.7. The mutual inductances between the stator and rotor windings are time-varying and are considered state variables. The model is a time-varying, nonlinear model and is subsequently “quadratized”. It is a phase-frame-based model that utilizes the actual phase quantities without making use of the d-q transformation, as is the case with all the induction motor models found in the literature. The detailed model equations are presented in Appendix A.

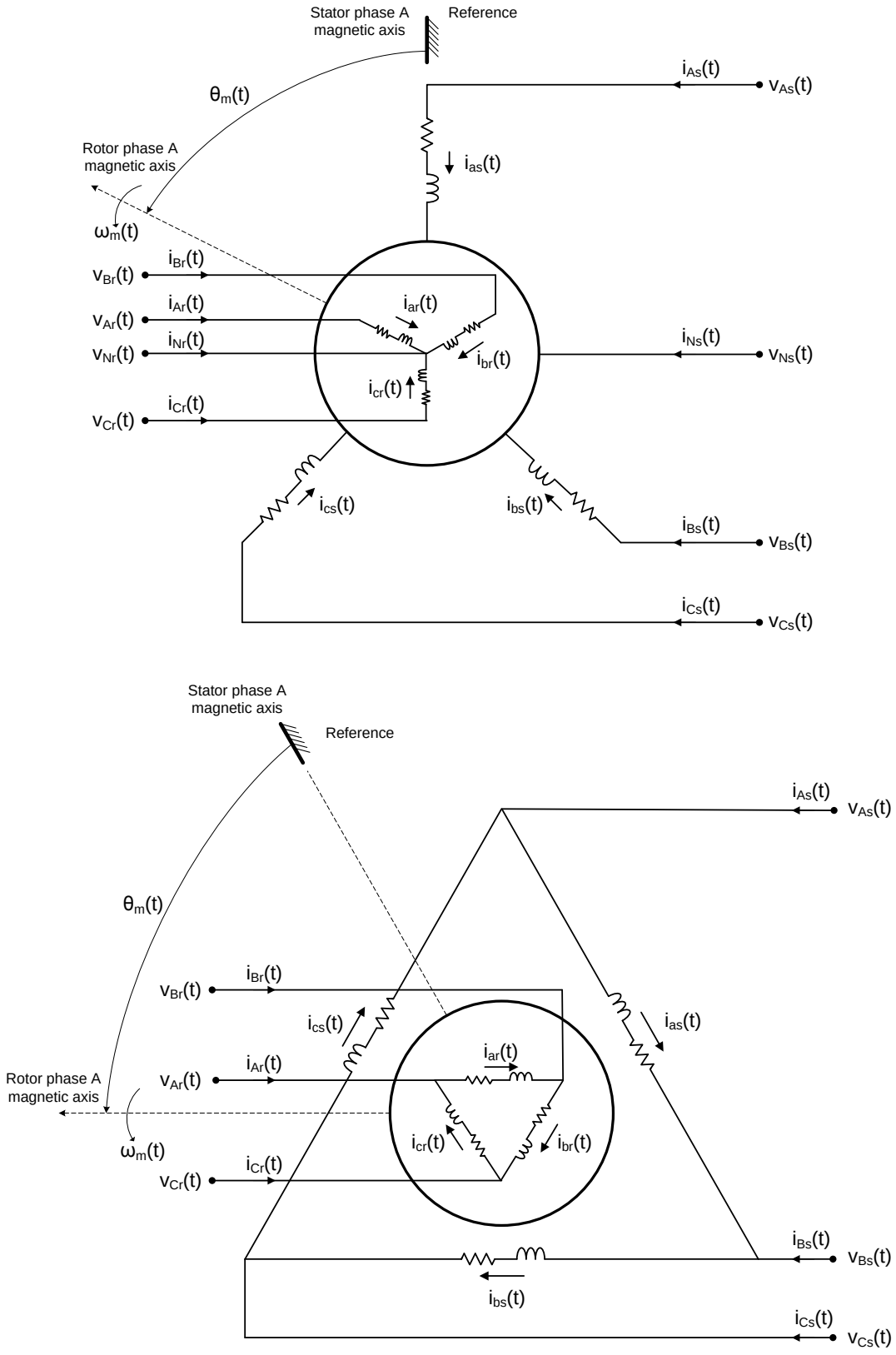

Figure 4.7: Induction motor model for wye and delta motor connections.

4.3.5 Model Parameter Estimation

4.3.5.1 Problem Formulation

Explicit induction-motor representation in power-system studies requires some basic information regarding the electrical and mechanical parameters of the specific motors that are represented, like the ones shown in the form of Figure 4.4. Such data need not be of very high accuracy, but in general they are difficult to obtain, especially when aggregate models are used to represent groups of machines. Methods for load composition identification can be used in such cases to identify the load composition and the load parameters. In this thesis a simple approach is proposed for estimating the equivalent circuit parameters of a specific induction motor. This methodology makes use of data that, in general, are available from the motor manufacturer, like the slip-torque characteristic or the slip-current or slip-power factor characteristics. Such curves are shown in Figure 4.8 and Figure 4.9. These graphs also illustrate the high sensitivity of motor reactive power consumption with respect to speed. A parameter estimation procedure becomes even more important when a slip-dependent parameter model is used. In this case, the model coefficients of (4.1) are difficult or impossible to evaluate without the use of an estimation procedure.

When the rotor circuit parameters are to be estimated, assuming that the stator and core parameters are known, the slip-torque characteristic of the motor provides adequate information. However, when all the equivalent-circuit parameters are to be estimated (six in total if constant rotor parameters are assumed and nine if slip-dependent rotor parameters are used), the slip-torque characteristic itself is not enough and some additional information is necessary. Such information can be provided using, for

example, the slip-current characteristic of the motor along with the slip-torque curve. In this paper the estimation problem will be formulated in its general form, assuming that all the equivalent circuit parameters are to be estimated; however, the methodology will be demonstrated for the estimation of just the rotor parameters using only the slip-torque curve.

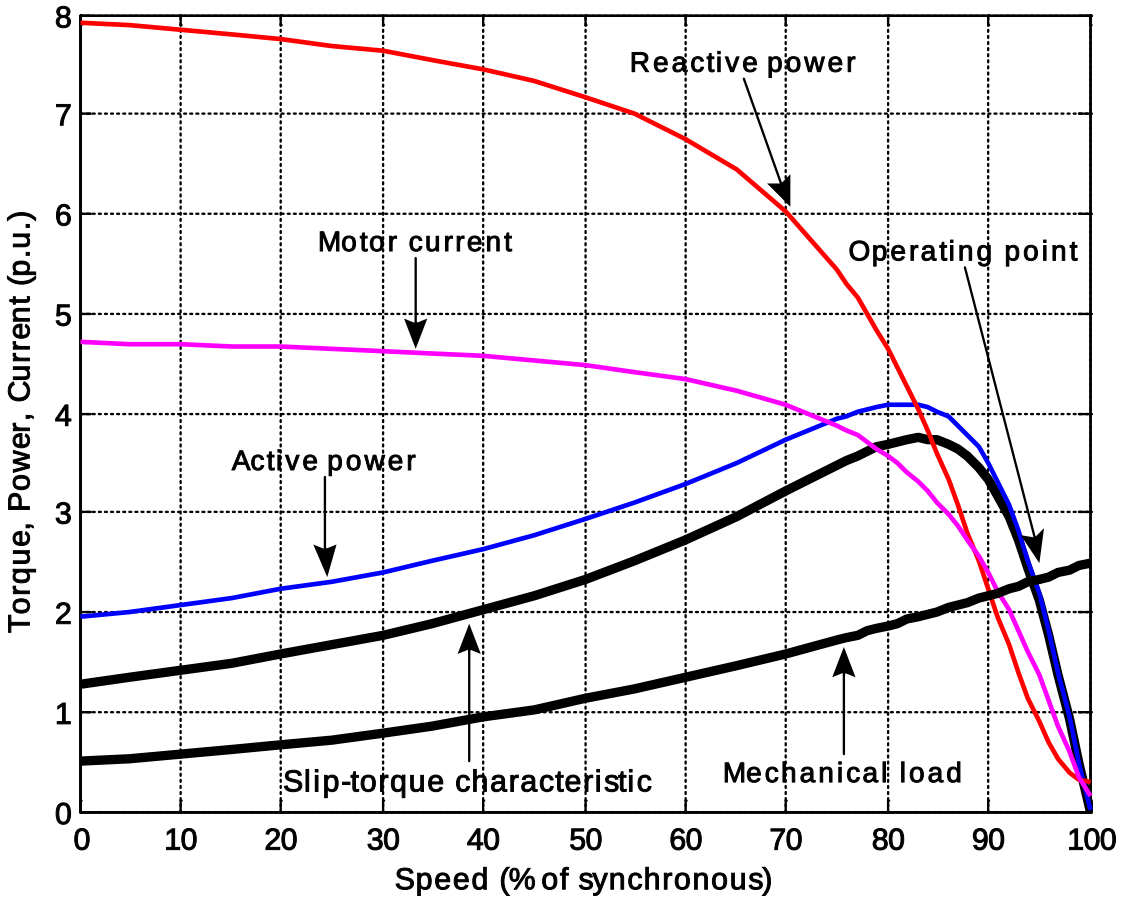

Figure 4.8: Motor operating conditions for various operating speeds (Design A).

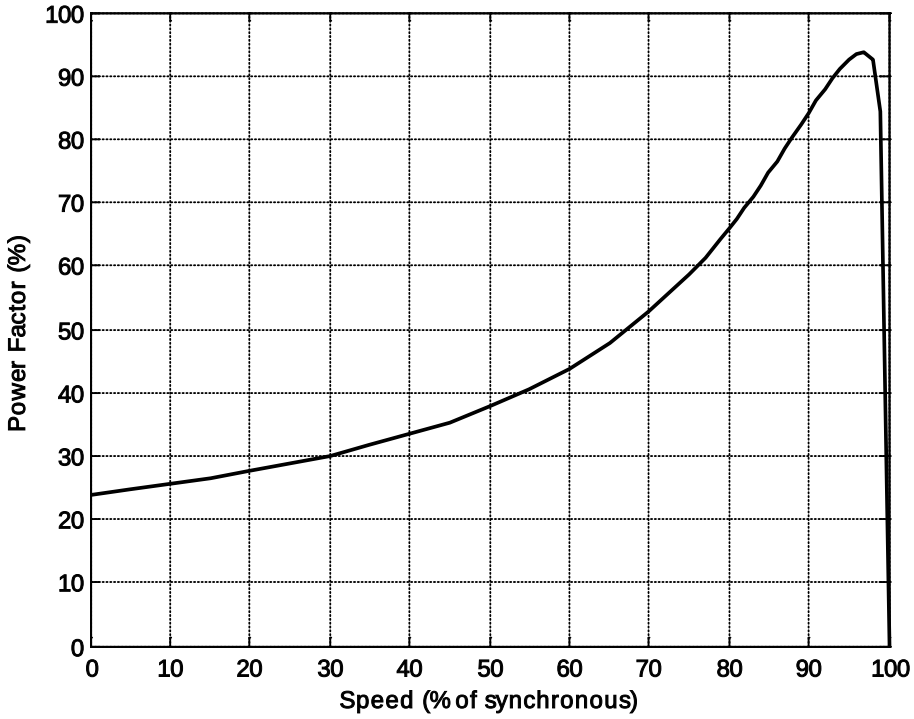

Figure 4.9: Motor power factor for various operating speeds (Design A).

The parameter-estimation problem can be formulated as a least-squares optimization problem, the objective being the minimization of the deviation between the measured torque and current curves and the model generated curves, as illustrated in Figure 4.10. These curves are known as a set of discrete measurement points.

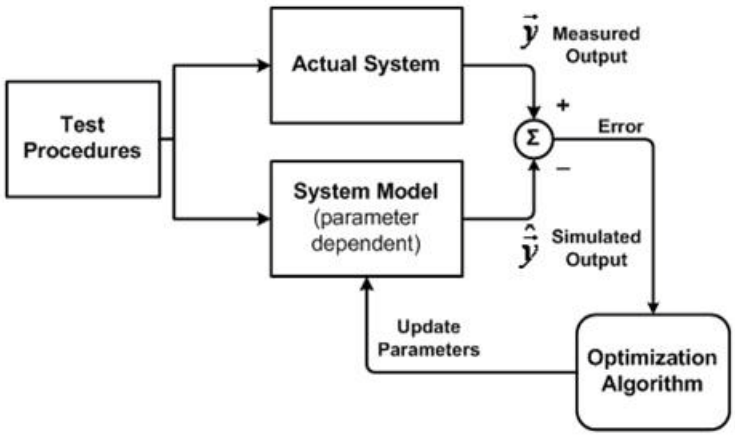

Figure 4.10: Block diagram of estimation procedure.

The mathematical problem formulation is as follows:

$$\min J = \sum_{i=1}^{m} w_i r_i^2 = r^T W r, \tag{4.4}$$

subject to:

$$\tilde{I} = (g_s + jb_s)\tilde{V} - (g_s + jb_s)\tilde{E} ,$$

$$T_{em} = U.s.r_r/\omega_s,$$

$$0 = \widetilde{W}_n - \tilde{Y}_n \tilde{E}_n, \tag{4.5}$$

$$0 = U - \widetilde{W}_n \widetilde{W}_n^*,$$

$$0 = -(g_1 + jb_1)\tilde{V}_k + (g_1 + j(b_1 + b_m))\tilde{E}_n + \widetilde{W}_n s,$$

$$0 = r_2 \tilde{Y}_n + jx_2 s\tilde{Y}_n - 1,$$

where

$$r_i = \begin{cases} T_{em,i}(p) - T_{measured,i} & \text{, if i is a torque measurement,} \\ I_i(p) - I_{measured,i} & \text{, if i is a current measurement,} \end{cases}$$

w_i is the weight of measurement i,

m is the total number of measurements,

p is the parameter vector.

The equations in (4.5) are the single-phase equivalent equations of the induction motor model. They can be derived from the full model equations, presented in Appendix A, assuming that the motor is operating under balanced conditions, and thus only the positive sequence network is active. These equations are used in the estimation procedure because the motor curves and thus the measurement data are obtained under

nominal operating conditions. Therefore, the estimation is performed under nominal conditions.

4.3.5.2 Solution Methodology

The above optimization problem is a nonlinear least squares minimization problem. The solution of such a problem can only be approximated (no analytical solution exists) using some numerical method. The most commonly used approach is the Gauss-Newton method, which is a Newton-type iterative process for the solution of over-determined systems of equations [141]. Application of this method to a least squares optimization problem as the one described above yields the following iterative algorithm:

$$p^{n+1} = p^n - \left(H(p^n)^T W H(p^n)\right)^{-1} H(p^n)^T W r(p^n), \tag{4.6}$$

where

p is the parameter vector to be estimated,

r is the residual vector with elements as described earlier,

W is the weight matrix with elements as described above,

n is the iteration index,

H is the Jacobian matrix of measurement equations with respect to parameters, i.e., in general, assuming that torque and current measurements are used it holds that $H(p^n) = \left[\frac{\partial T_{em}}{\partial p}^T \quad \frac{\partial I}{\partial p}^T\right]^T\Big|_{p=p^n}$.

The Jacobian matrix can be easily computed based on the model equations (4.5) using the chain rule of differentiation.

It has been observed in the literature [50]-[53], [141] that Newton-type numerical methods are very efficient and can provide accurate results provided that a good initial guess of the solution is available; otherwise, the algorithm may converge to an incorrect solution, or may even diverge, providing no solution at all. To mitigate such problems to some extent, two global convergence strategies are implemented and are optionally used along with the Gauss-Newton solution procedure. Such strategies guarantee the convergence of the algorithm to a solution, irrespectively of the initial guess. Therefore, the implemented algorithm is not prone to divergence. The solution is not guaranteed to be the global optimum, but the inclusion of such strategies increases the robustness of the estimation algorithm and the probability of providing the correct solution, even with a less accurate initial estimate.

Two global convergence strategies have been implemented: the line-search algorithm and the trust-region algorithm. For the trust region algorithm, the Levenberg-Marquardt method with a locally-constrained optimal step has been used [141]. The two strategies are employed if the simple Gauss-Newton procedure (without global convergence) fails to provide a reasonable solution or a solution at all.

The basic idea of the line-search method is that the search in the solution space should always proceed at steps that result in a continuous decrease of the objective function (for minimization problems). That is, the objective function should not be allowed to increase at a new estimate, compared to the previous one. The search always follows the Newton direction, as computed by the standard Newton method, but the full Newton step is not taken if it does not result in a decrease in the objective function. Instead, a smaller step is taken along the Newton line until the step size is such that the

new estimate results in a lower value of the objective function. This eliminates the possibility of taking a large Newton step at an early stage of the algorithm that would overshoot the solution and take the search far away from the neighborhood of the solution. This is one of the main reasons that may cause divergence of the Newton method and, therefore, the line-search algorithm provides very good results most of the times.

Contrary to the line-search algorithm, the trust-region approach does not limit the search only along the Newton direction. A local, quadratic model of the system is constructed at each iteration, and the search direction is defined based on this model. The size of the step is defined based on a computed trust-region radius, which is an estimation of the radius of validity of the quadratic model. The locally constrained optimal step approach is used [141]. More detailed mathematical background on the underling theory can be found in [141].

4.4 Single- and Two-Phase Induction Motor Model

4.4.1 Overview

This paragraph describes a single-phase induction-machine model used for three-phase network analysis. The motor can be connected either between a phase and neutral or between two phases of the system. Models for steady-state, quasi-static and full transient analysis are developed. The purpose of this model is to allow a more realistic and accurate, yet computationally simple, representation of unbalanced loading condition in power-system analysis, especially in distribution networks. Normally, loads are represented either as static or as dynamic loads. Static loads can be constant-power loads,

constant-impedance loads, constant-current loads, voltage-, or frequency-dependent loads. While these representations can capture quite effectively the general load behavior, they are not exact representations of the actual load. Therefore, more precise load models may be needed. In dynamic studies, induction motors are usually represented as dynamic loads; however, usually very detailed, time-domain motor models are employed (originally developed for electric machinery analysis and not analysis of large scale power systems) that make computations intensive, especially when large power networks are involved, and therefore are not practical for applications like, for example, voltage-recovery or voltage-stability analysis.

The model input data include typical nominal (nameplate) data plus electrical parameters and mechanical-load data. The model supports four mechanical loading modes in steady state: (a) constant torque, (b) constant power, (c) constant slip, and (d) speed-dependent torque. For dynamic analysis the constant-power and constant-slip modes have no meaning and therefore only the constant torque or slip-dependent torque modes are used. The model also supports the options of including a running and a starting capacitor. The model incorporates four starting methods: (a) split phase, (b) capacitor start, (c) permanent split capacitor, and (d) capacitor start capacitor run. The input data form is illustrated in Figure 4.11.

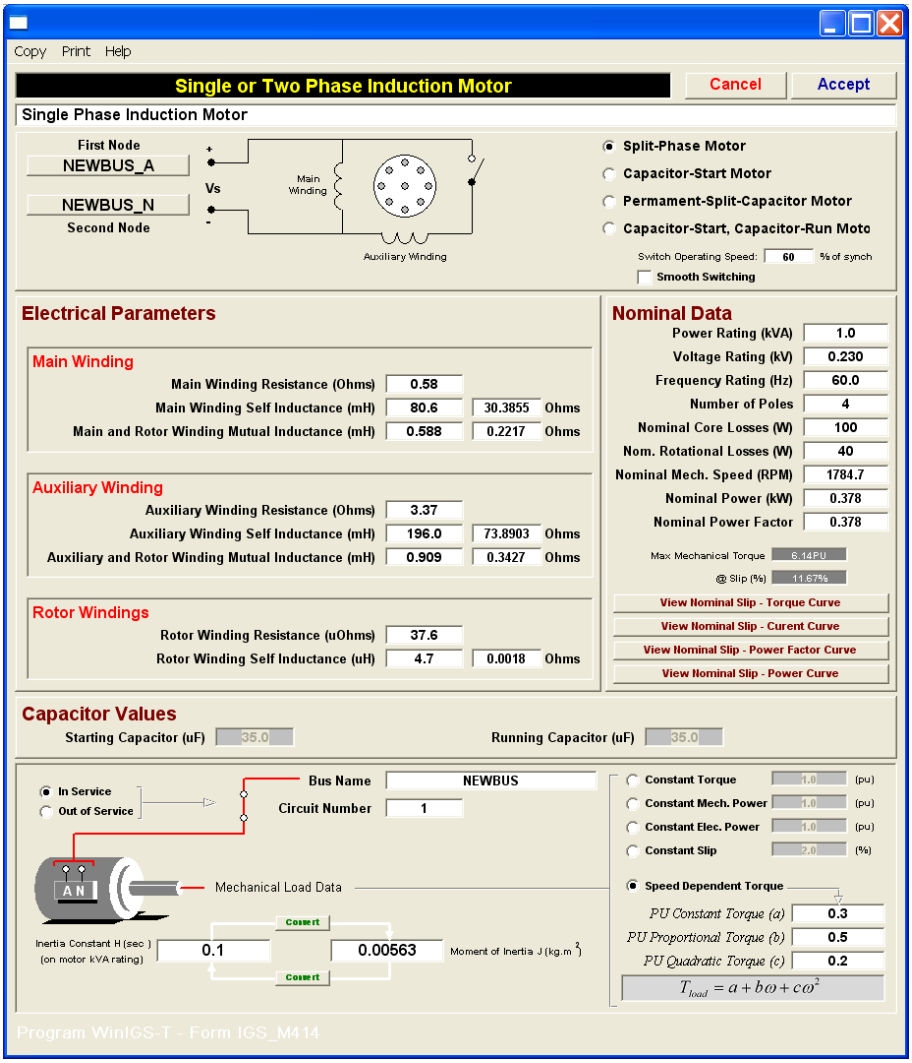

Figure 4.11: Single-phase induction-motor input data form.

4.4.2 Steady-State Model

The compact model is based on the revolving field theory of a single-phase induction motor [149]. The physical circuit is presented in Figure 4.12, showing the case of both main and auxiliary windings and starting and running capacitors [149]. Circuit analysis yields the steady-state model of the motor, depending on the starting method and the mechanical loading mode. Detailed presentation of the model equations can be found in Appendix A.

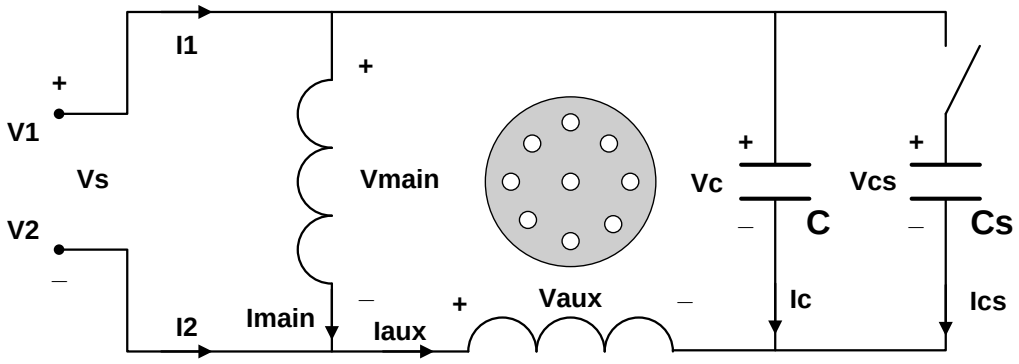

Figure 4.12: Single-phase induction-motor physical circuit (capacitor-start, capacitor-run case) [149].

4.4.3 Quasi-Static Model

The model is based on the frequency-domain, steady-state model for the electrical quantities, with the addition of a dynamic equation to describe the rotor motion. The mechanical-load torque, T_L, can be either constant or related to the motor mechanical speed, ω_m. This leads to two models based on the motor loading: (a) constant torque model and (b) speed-dependent torque model. Note that the second model can contain the first as a special case. The motor speed is linearly related to the slip, s. The model is appended with an additional differential equation describing the motor rotor acceleration, i.e., a swing equation of the form of (4.2). Notice that the model is a switching model with two states (starting state and operational state), depending on the status of the starting switch, which relates to the speed of the motor. The detailed mathematical model is presented in Appendix A.

4.4.4 Full Transient Model

The model is based on the time-domain analysis of the schematic diagram of Figure 4.12 [149]. The rotor is represented by two perpendicular windings. The model equations are presented, in detail, in Appendix A.

4.5 Dynamic and Static VAr Source Modeling

4.5.1 Dynamic VAr Source Modeling

4.5.1.1 Overview

In the area of dynamic VAr source modeling the presented work concentrates on the implementation of a generic model of a static VAr compensator (SVC), since such systems constitute the major representative of voltage-support devices in practical power systems. The system model is a thyristor-controlled reactor (TCR), a thyristor-switched capacitor (TSC), or a combination of a TCS in parallel with TSC modules. The implementation is based on references [132], [150] – [153] and more details can be found there. Here, emphasis will be given on the implementation of a TCR in parallel with fixed capacitor banks, i.e., a TCR-FC SVC configuration as illustrated in Figure 4.13 [154]. For simplicity the filter is not considered at this stage.

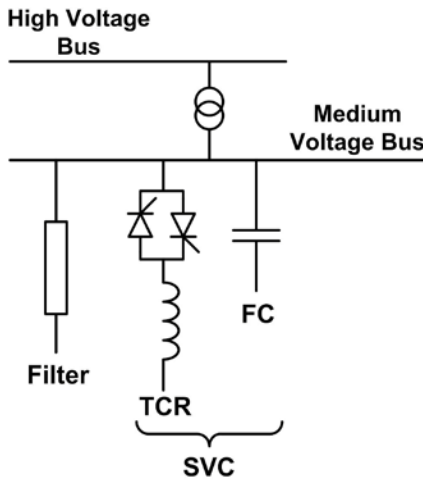

Figure 4.13: Illustration of TCR-FC SVC configuration [154].

The basic elements of a TCR are a reactor in series with a bidirectional thyristor switch. The thyristors conduct on alternate half-cycles of the supply voltage frequency

depending on the firing angle α, which is measured from a zero crossing of voltage. Full conductance is obtained with a firing angle of 90^0. The current is essentially reactive and sinusoidal. Partial conduction is obtained with firing angles between 90^0 and 180^0. Firing angles between 0^0 and 90^0 are not allowed as they produce asymmetrical currents with a DC component [132]. The conductance angle σ is related to α by $\sigma = 2(\pi - \alpha)$. The instantaneous current is given by

$$i(t) = \begin{cases} \frac{\sqrt{2}V}{X_L}(cos\alpha - cos\omega t) & ,\alpha < \omega t < \alpha + \sigma, \\ 0 & ,\alpha + \sigma < \omega t < a + \pi. \end{cases} \tag{4.7}$$

By applying Fourier analysis, the RMS value of the fundamental component I_1 of the TCR current can be expressed as

$$I_1 = \frac{V}{X_L}\frac{\sigma - sin\sigma}{\pi}, \tag{4.8}$$

where I_1 and V are RMS values, and X_L is the reactance of the reactor at foundamental frequency.

The effect of increasing α (i.e., decreasing σ) is to reduce the fundamental component I_1. This is equivalent to increasing the effective inductance of the reactor. In effect, as far as the fundamental frequency current component is concerned, the TCR is a controllable susceptance. The effective susceptance as a function of α is

$$B(a) = \frac{I_1}{V} = \frac{\sigma - sin\sigma}{\pi X_L} = \frac{2(\pi - \alpha) + sin2\alpha}{\pi X_L}. \tag{4.9}$$

The maximum value of the effective susceptance occurs at full conduction ($\alpha = 90^0$,$\sigma = 180^0$), and it is equal to $\frac{1}{X_L}$; the minimum value is zero, obtained with $a = 180^0$ or $\sigma = 0^0$. This susceptance-control principle is known as phase control. The susceptance

is switched into the system for a controllable fraction of every half cycle. The variation in susceptance as well as the TCR current is smooth or continuous.

The TCR requires a control system, which determines the firing instants, i.e., the firing angle a, measured from the last zero crossing of the voltage. In some designs the control system responds to a signal that directly represents susceptance. In others the control responds to error signals such as voltage deviation. The result is a steady-state V/I-characteristic, which can be described by

$$V = V_{REF.} + X_{SL} I_1, \tag{4.10}$$

where X_{SL} is the slope reactance determined by the control system gain.

The voltage-control characteristic of the system can be extended into the capacitive region by adding fixed or switched capacitor banks in parallel, as illustrated in Figure 4.13.

For three-phase systems, the single-phase legs described above can be connected either in wye or in delta. Delta connection is preferable because at balanced conditions all triple harmonics generated by the TCR circulate within the closed delta and are, therefore, absent from the line currents.

A proportional-integral controller is used to provide the firing angles a or equivalently the conductance angles σ. The inputs of the controller are the actual voltage across the SVS and a voltage reference value, as illustrated in Figure 4.14. For a three-phase system, usually all single-phase SVSs are controlled by the same controller, although each single-phase leg can also be controlled independently by its own controller. In the case of a single controller the sensed voltage can be one particular phase

voltage, the line-to-line voltage of two phases, or, preferably, the positive-sequence voltage value.

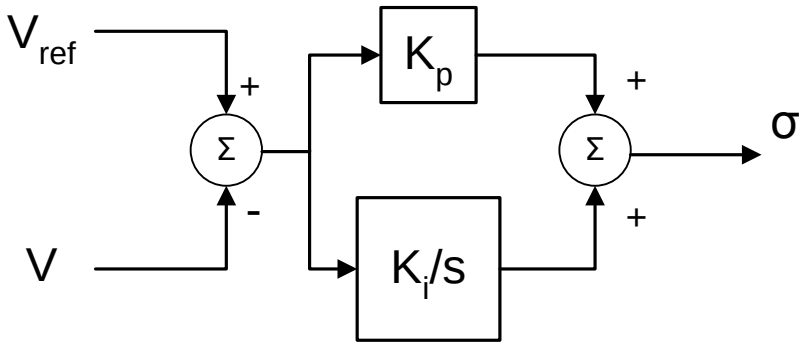

Figure 4.14: Schematic of SVS PI control scheme.

4.5.1.2 Steady-State Model

The steady-state model represents the SVS configuration as (a) a total variable succeptance of all the modules making up the system at the fundamental frequency or (b) an equivalent susceptance consisting of the parallel combination of a thyristor-controlled rector equivalent admittance, which is a function of the firing angle, and a fixed capacitive susceptance [132], [151]. The detailed model can be found in Appendix A.

4.5.1.3 Quasi-Static Model

The quasi-steady-state model represents the SVS configuration as variable sucpeptance, like in steady state, but a time delay is introduced by the integral control of the controller of Figure 4.14. The detailed model can be found in Appendix A.

4.5.2 Static VAr Source Modeling

4.5.2.1 Overview

In addition, there are traditional VAr support devices that cannot respond as fast as SVCs. For example, mechanically switched capacitor banks provide reactive-power support, but they cannot respond within the time frame of the desired voltage recovery. The reason is that their switching depends on mechanical switches that have a relatively long response time. If the static VAr sources are fixed, and thus constantly connected to the grid, then they can respond very fast, but their existence will also affect the steady-state behavior of the system. Therefore, static VAr sources are usually placed in an electric power grid based on steady-state criteria (like, for example, leveling the system voltage profile, minimizing system losses, increasing loadability limits). It is important to note that in general, static VAr support devices are relatively low cost, while the dynamic VAr support devices are of relative high cost. Therefore, the issue of designing the system to provide dynamic VAr support and fast voltage recovery at minimal cost arises. These problems will be addressed via an optimization procedure that accounts for the technical characteristics of dynamic and static VAr sources, their cost, and the requirements for fast voltage recovery. The optimization problem is described in Chapter 7 of this thesis.

Shunt capacitors are the static VAr sources considered in this work. Their mathematical model is presented next.

4.5.2.2 Steady-State Model

The steady-state model is the standard linear capacitor (reactor) model of specific capacitance (inductance) and, therefore, of specific impedance. The equivalent Y-leg capacitance or inductance is computed based on the provided nominal operating conditions, i.e., rated voltage V_R and rated reactive power Q_R as in (4.11). Note that it is assumed that Q_R has a negative value for inductors and positive for capacitors.

$$C = \frac{Q_R}{V_R^2 \omega} \text{ and } L = -\frac{V_R^2}{Q_R \omega}. \tag{4.11}$$

The equivalent Y-leg impedance is computed as

$$\tilde{Y}_s = j\omega C \text{ for capacitor banks and } \tilde{Y}_s = \frac{1}{j\omega L} \text{ for reactors.} \tag{4.12}$$

4.5.2.3 Quasi-Static Model

For the quasi-steady-state type of analysis sinusoidal steady-state network conditions are assumed and the model of the capacitor or inductor bank for this type of analysis is the same as the steady-state model. No dynamics are included, since the capacitor charging or discharging dynamics are very fast to be considered for this type of analysis.

4.5.2.4 Full Transient Model

The full transient model is the standard linear capacitor (reactor) model of specific capacitance (inductance) and, therefore, of specific impedance. The equivalent Y-leg capacitance or inductance is computed based on the provided nominal operating conditions, i.e., rated voltage V_R and rated reactive power Q_R as in (4.13). Note that it is assumed that Q_R has a negative value for inductors and positive for capacitors.

$C = \frac{Q_R}{V_R^2 \omega}$ and $L = -\frac{V_R^2}{Q_R \omega}$. (4.13)

Each equivalent Y-leg capacitor or inductor is represented by a linear differential equation of the form:

$C \frac{dv_c(t)}{dt} = i_c(t)$, for capacitor banks and (4.14)

$L \frac{di_L(t)}{dt} = v_L(t)$, for inductors, (4.15)

where

v_c is the voltage across the capacitor,

i_c is the current through the capacitor,

v_L is the voltage across the inductor,

i_L is the current through the inductor.

A nonlinear inductor model has also been implemented, for full transient analysis, as part of this work. This model is presented in detail in Appendix A.

4.6 Three-Phase Electric Network Model

In this work, a three-phase, four-wire, physically based, breaker oriented model is utilized to represent the electric power network [155]. Transmission lines are modeled in detail as three phase systems, based on their physical parameters. Substations are also modeled in detail including their internal configuration, with explicit representation of breakers, switches and transformers. For both steady-state and quasi-steady-state analysis the network is assumed to be operating under sinusoidal steady-state conditions. Therefore, phasor representation is used in all cases, and the models of network devices

are the same. The difference between the two types of analysis is that the phasors in the quasi-steady-state analysis are time-varying phasors. All of these models have been developed in the past by this research group and were simply used in this work; thus, no detailed description of each one is presented here.

A typical example of a small system, containing most of the devices described in this section, is illustrated in Figure 4.15.

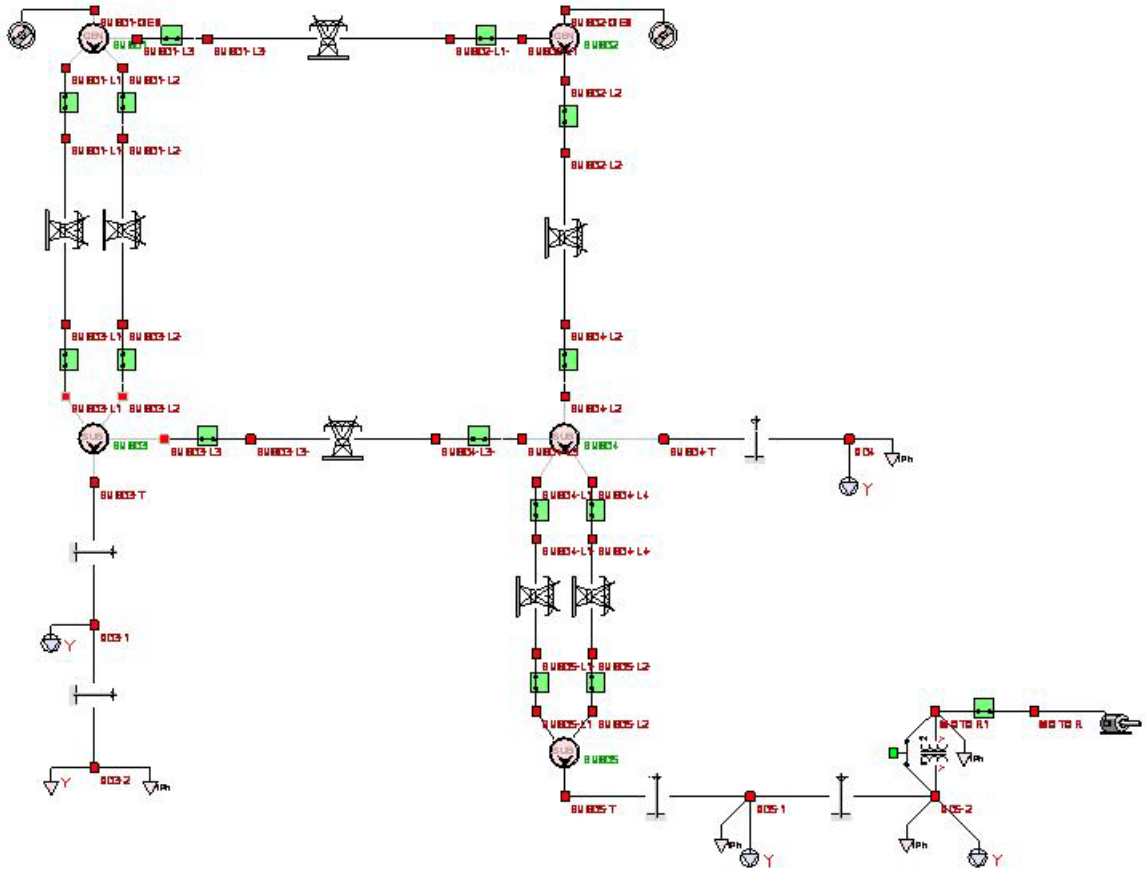

Figure 4.15: One-line diagram of a small electric power system.

4.7 Substation Model

In this work, a detailed system representation is adopted based on the physical configuration of the system, as explained in the previous paragraph. Therefore, each

system substation is modeled in detailed configuration using breaker and switch models. This results in a breaker-oriented system representation [155]. Since this may result in additional complication of the system one-line diagram, even in small systems, a substation model is used that generates additional editor layers of the one line diagram, keeping therefore the whole system layer relatively simple. All of the internal substation devices can be viewed and accessed by going to the substation layer. An interface device connects devices in the substation layer to devices at the top layer. Geographic information data of the substation location can be entered in the model, if available, and the substation can be placed at the appropriate location if a GPS map is available at the top network level. The substation model and its interface are illustrated in Figure 4.16. An example substation configuration is illustrated in Figure 4.17.

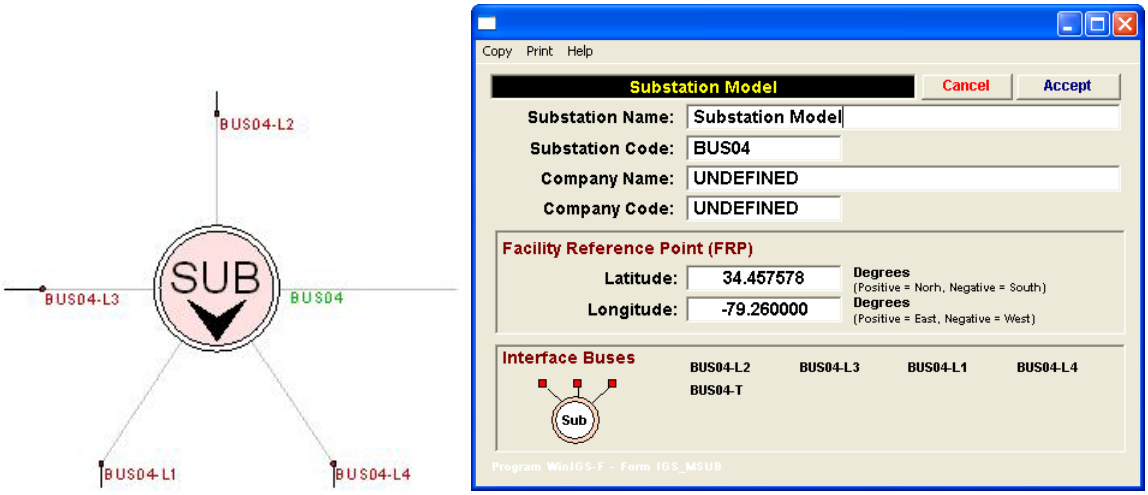

Figure 4.16: Substation model interface and data.

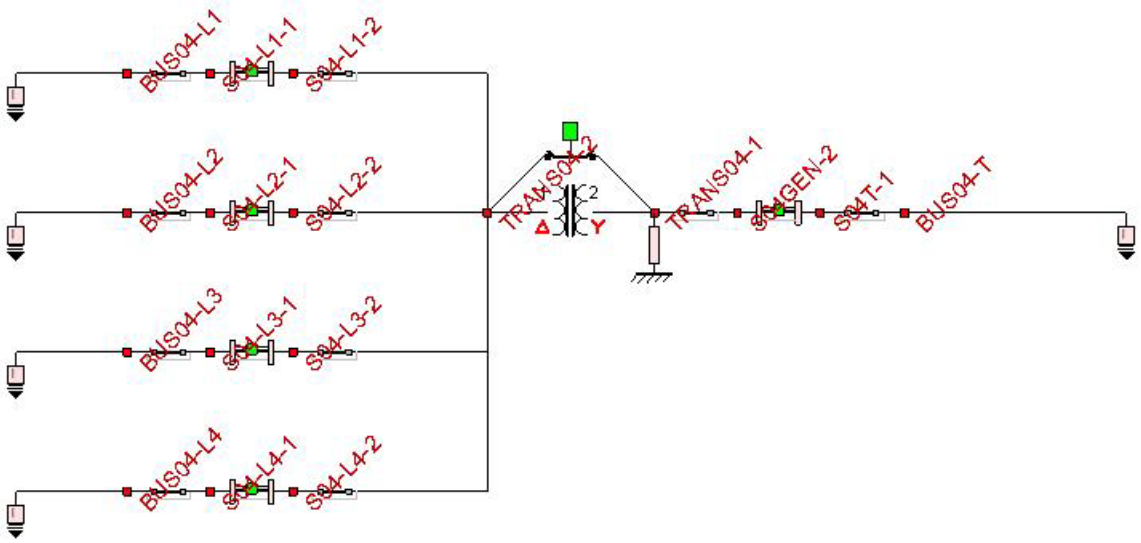

Figure 4.17: Example substation configuration. The arrow symbol is the interface to the rest of the network.

4.8 Summary

This chapter presented an overview of the models of various power system components that were developed during this work. All the models are based on the modeling approach described in Chapter 3. More details on these models can be found in Appendix A.

CHAPTER 5

QUADRATIC INTEGRATION METHOD

5.1 Overview

This chapter of the thesis describes a new approach for the time-domain simulation of power systems and dynamical systems in general [156] – [160]. The new methodology, referred to as quadratic integration method, is based on the following two innovations: (a) the nonlinear equations of the system model (nonlinear differential or differential-algebraic equations) are reformulated to a fully equivalent system of linear differential and quadratic algebraic equations (by introducing additional state variables and algebraic equations) and (b) the model equations are integrated using a numerical integration scheme that assumes that the system states vary quadratically within an integration time step, as functions of time (quadratic integration). As a comparison, in the trapezoidal rule it is assumed that the system states vary linearly throughout a time step. The first innovation was described in detail in Chapter 3 of the thesis; this chapter is dedicated to the description of the proposed numerical integration scheme.

This basic concept in the derivation of the quadratic integration method is illustrated in Figure 5.1. Note that within an integration time step of length h, defined by the interval $[t-h, t]$, the two end points, $x(t-h)$ and $x(t)$, and the midpoint, $x(t_m) = x(t-\frac{h}{2})$, fully define the quadratic function in the interval $[t-h, t]$. Assume that the function x varies quadratically in time within the integration time step $[t-h, t]$ as

$$x(\tau) = a + b\tau + c\tau^2,\ 0 \le \tau \le h, \tag{5.1}$$

where the three parameters a, b, and c fully define the quadratic function within a time step. These parameters can be expressed in terms of the values of the unknown function of time, $x(\tau)$, at the two ends of the interval $x(t-h)$ and $x(t)$ and at a third, internal point of the interval, like the midpoint, $x(t-h/2)$. For simplicity in the notation we will use the symbol t_m for the value of time at the midpoint and the symbol x_m for the value of the function x at the midpoint, i.e, $t_m = t - h/2$ and $x_m = x(t_m)$. If the new variable τ is used instead of t, then it holds that $x(t-h) = x(\tau = 0)$, $x(t) = x(\tau = h)$, and $x_m = x(t_m) = x(t - h/2) = x(\tau = h/2)$.

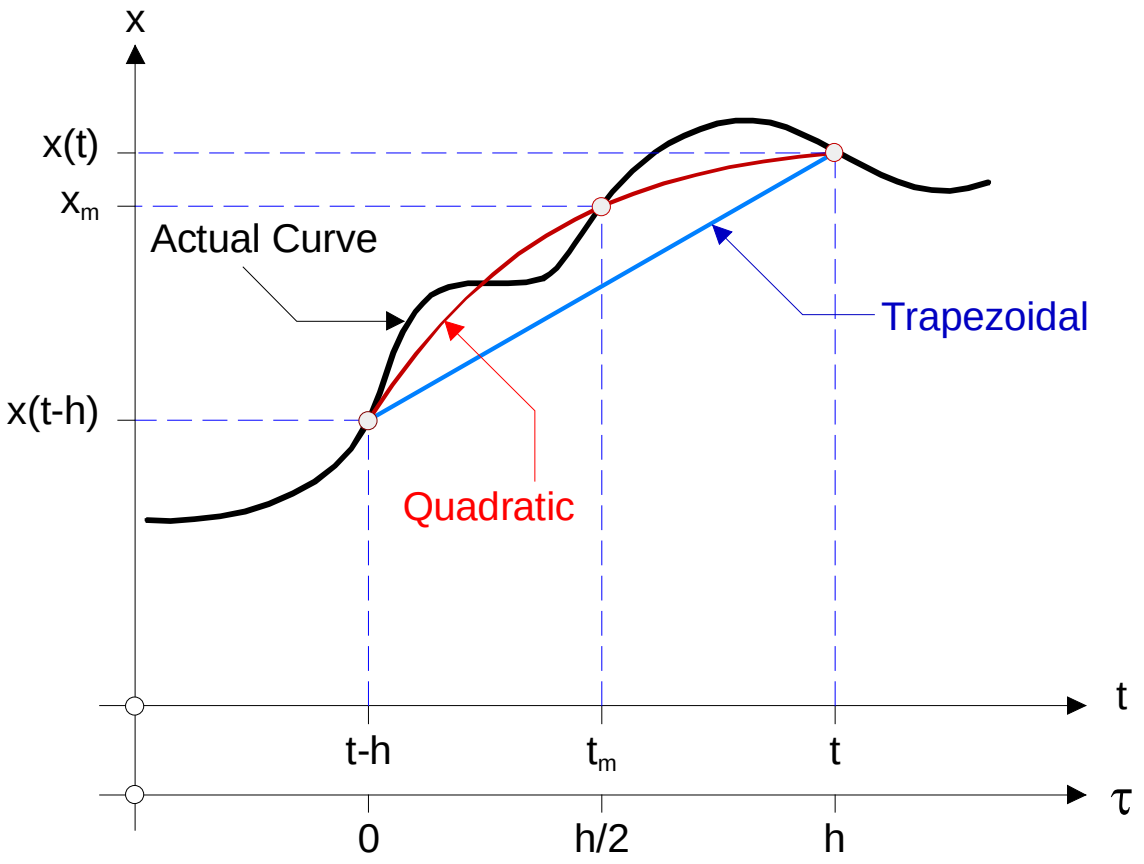

Figure 5.1: Illustration of the quadratic integration method; basic assumption.

The procedure for obtaining the parameters of (5.1) is described next. It is required that the quadratic function interpolates the actual function x at the two endpoints of the interval and at the midpoint. This is described by the following three equations:

At time $t-h$, i.e., for $\tau = 0$: $x(t-h) = a$.

At time t, i.e., for $\tau = h$: $x(t) = a + bh + ch^2$.

At time t_m, i.e., for $\tau = h/2$: $x_m = a + b\frac{h}{2} + c\frac{h^2}{4}$.

Substituting the first equation into the other two yields

$$x(t) = x(t-h) + bh + ch^2, \tag{5.2}$$

$$x_m = x(t-h) + b\frac{h}{2} + c\frac{h^2}{4}. \tag{5.3}$$

This is a linear, 2x2 system in the unknowns b and c

$$\begin{bmatrix} h & h^2 \\ h/2 & h^2/4 \end{bmatrix} \cdot \begin{bmatrix} b \\ c \end{bmatrix} = \begin{bmatrix} x(t) - x(t-h) \\ x_m - x(t-h) \end{bmatrix}. \tag{5.4}$$

Solution of the system yields

$$\begin{bmatrix} b \\ c \end{bmatrix} = \begin{bmatrix} -1/h & 4/h \\ 2/h^2 & -4/h^2 \end{bmatrix} \cdot \begin{bmatrix} x(t) - x(t-h) \\ x_m - x(t-h) \end{bmatrix}. \tag{5.5}$$

Therefore, the three parameters a, b, and c are expressed as

$$a = x(t-h), \tag{5.6}$$

$$b = \frac{1}{h}(-3x(t-h) + 4x_m - x(t)), \tag{5.7}$$

$$c = \frac{2}{h^2}(x(t-h) - 2x_m + x(t)). \tag{5.8}$$

The general expression $x(\tau) = a + b\tau + c\tau^2$ with the above values for a, b, and c is used to perform the integration within the time interval $[t-h, t]$.

This quadratic function is integrated in the time interval $[t-h, t]$ resulting in a set of algebraic equations for this integration step. The solution of the equations is obtained via Newton's method, in the general, nonlinear case, or via a direct solution in the linear case. Note that by virtue of the first step of "quadratization" the resulting algebraic equations are either linear or quadratic. These two cases are illustrated in the following paragraphs.

5.1.1 Linear System Integration

Assume a linear, autonomous, dynamical system of ordinary differential equations (ODE's) of the form

$$\dot{x} = Ax, \tag{5.9}$$

where A is a constant square matrix of the same dimension as the state vector x, say n. Discretizing time and integrating the equations with respect to time over a time step $[t-h, h]$ yields

$$x(t) - x(t-h) = A\int_{t-h}^{t} x(T)dT \Rightarrow x(t) = x(t-h) + A\int_{t-h}^{t} x(T)dT = x(t-h) + A\int_{0}^{h} x(\tau)d\tau. \tag{5.10}$$

The way this integral is calculated defines the numerical method for the solution of the ODEs. Assuming that x is a quadratic function in $[t-h, t]$, as described in the previous section, and analytically integrating this function yields the following results:

Integration over time interval $[t-h, t_m]$ yields:

$$\int_{t-h}^{t_m} x(T)dT = \int_0^{h/2} x(\tau)d\tau = \frac{5h}{24}x(t-h) + \frac{h}{3}x_m - \frac{h}{24}x(t); \quad (5.11)$$

Integration over time interval $[t-h, t]$ yields:

$$\int_{t-h}^{t} x(T)dT = \int_0^{h} x(\tau)d\tau = \frac{h}{6}x(t-h) + \frac{2h}{3}x_m - \frac{h}{6}x(t); \quad (5.12)$$

Integration over time interval $[t_m, t]$ yields:

$$\int_{t_m}^{t} x(T)dT = \int_{h/2}^{h} x(\tau)d\tau = -\frac{h}{24}x(t-h) + \frac{h}{3}x_m + \frac{5h}{24}x(t). \quad (5.13)$$

Since x is in fact an n-dimensional vector, the above equations are in fact systems of n equations, rather than simple scalar equations. Using the first two of these equations (or any other combination of two) it holds that

$$x_m = x(t-h) + A\left(\frac{5h}{24}x(t-h) + \frac{h}{3}x_m - \frac{h}{24}x(t)\right), \quad (5.14)$$

$$x(t) = x(t-h) + A\left(\frac{h}{6}x(t-h) + \frac{2h}{3}x_m + \frac{h}{6}x(t)\right). \quad (5.15)$$

Note that $x(t-h)$ has a known value, therefore, the above equations comprise a consistent system of equations in the unknown vectors $x(t)$ and x_m. Also note that the value of $x(t)$ is the value of interest and x_m is just an intermediate computation. The linear system of equations is

$$\frac{h}{24}Ax(t) + \left(I - \frac{h}{3}A\right)x_m = \left(I + \frac{5h}{24}A\right)x(t-h), \quad (5.16)$$

$$\left(I - \frac{h}{6}A\right)x(t) - \frac{2h}{3}Ax_m = \left(I + \frac{h}{6}A\right)x(t-h), \quad (5.17)$$

or in compact matrix form:

$$\begin{bmatrix} \frac{h}{24}A & I - \frac{h}{3}A \\ I - \frac{h}{6}A & -\frac{2h}{3}A \end{bmatrix} \cdot \begin{bmatrix} x(t) \\ x_m \end{bmatrix} = \begin{bmatrix} \left(I + \frac{5h}{24}A\right) \\ \left(I + \frac{h}{6}A\right) \end{bmatrix} x(t-h). \quad (5.18)$$

Note that I is the n-dimensional identity matrix and the total number of equations and unknowns is equal to $2n$. The dimensions of the specific matrices are

I: n x n;

A: n x n;

$x(t)$: n x 1;

x_m: n x 1;

$x(t-h)$: n x 1;

$$\begin{bmatrix} \frac{h}{24}A & I-\frac{h}{3}A \\ I-\frac{h}{6}A & -\frac{2h}{3}A \end{bmatrix}: 2n \text{ x } 2n;$$

$$\begin{bmatrix} x(t) \\ x_m \end{bmatrix}: 2n \text{ x } 1;$$

$$\begin{bmatrix} \left(I+\frac{5h}{24}A\right) \\ \left(I+\frac{h}{6}A\right) \end{bmatrix}: 2n \text{ x } 2n.$$

In the more general case, where the linear system is of the form $\dot{x}(t) = Ax(t) + Bu(t)$ (where A is a constant, square, n x n matrix, u is a k-dimensional input vector of known functions of time, and B is an n x k matrix), the final equations have only minor differences compared to the ones derived above. Discretizing time and integrating the equations with respect to time over a time step $[t-h, t]$ yields

$$x(t) - x(t-h) = A\int_{t-h}^{t} x(T)dT + B\int_{t-h}^{t} u(T)dT \Rightarrow$$

$$x(t) = x(t-h) + A\int_{0}^{h} x(\tau)d\tau + B\int_{0}^{h} u(\tau)d\tau. \quad (5.19)$$

However, since u is a vector of known input function, independent of the states, the computation of the integral $\int_{t-h}^{t} u(T)dT$ is straightforward and provides a constant value at each integration step. This computation is, in general, also performed numerically. Therefore, the equation becomes $x(t) = x(t-h) + A\int_0^h x(t)d\tau + b$, where b is a known n x 1 vector at each integration interval. Consequently, only a constant term b needs to be added to the previously derived equations that are to be solved at every time step.

$$\begin{bmatrix} \frac{h}{24}A & I - \frac{h}{3}A \\ I - \frac{h}{6}A & -\frac{2h}{3}A \end{bmatrix} \cdot \begin{bmatrix} x(t) \\ x_m \end{bmatrix} = \begin{bmatrix} \left(I + \frac{5h}{24}A\right) \\ \left(I + \frac{h}{6}A\right) \end{bmatrix} x(t-h) + \begin{bmatrix} b \\ b \end{bmatrix}. \tag{5.20}$$

All the definitions and dimensions are as above. The constant $b = B\int_{t-h}^{t} u(T)dT$ is an n-dimensional vector.

Note that if the assumption that the function x varies linearly in the interval $[t-h, t]$ is made, then the trapezoidal integration rule will be derived, following the same reasoning and a similar analysis.

5.1.2 Nonlinear System Integration

Based on this approach of introducing the quadratic integration method it is not possible to formally derive the expressions for a general nonlinear system. It is easier, however, to derive equations assuming that the dynamical system is quadratic. Since this research work only deals with quadratic systems, this is enough. Furthermore, it is possible to transform a system of nonlinear differential equations into a system of differential-algebraic equations with linear differential equations and nonlinear algebraic

equations. These two observations cover all the nonlinear cases that will be encountered in this research.

However, an expression for the quadratic integration for the general form of a nonlinear system $\dot{x}(t) = f(t, x(t))$ can be intuitively guessed based on the analysis so far. More specifically, in the special case of a linear system it holds that $f(t, x) = Ax(t)$ (or $f(t, x) = Ax(t) + Bu(t)$ in a more general case, which was shown, however, not to introduce any major differences). Therefore, it is intuitive to assume that since in the linear case the quadratic integration is expressed by the system of equations

$$\frac{h}{24}Ax(t) + \left(I - \frac{h}{3}A\right)x_m = \left(I + \frac{5h}{24}A\right)x(t-h)\,, \tag{5.21}$$

$$\left(I - \frac{h}{6}A\right)x(t) - \frac{2h}{3}Ax_m = \left(I + \frac{h}{6}A\right)x(t-h)\,, \tag{5.22}$$

and since $Ax(t) = f(t, x)$, then in the general nolinear case the quadratic integration rule will consist of the equations

$$\frac{h}{24}f\big(t, x(t)\big) + x_m - \frac{h}{3}f(t_m, x_m) = x(t-h) + \frac{5h}{24}f(t-h, x(t-h))\,, \tag{5.23}$$

$$x(t) - \frac{h}{6}f\big(t, x(t)\big) - \frac{2h}{3}f(t_m, x_m) = x(t-h) + \frac{h}{6}f(t-h, x(t-h))\,. \tag{5.24}$$

Conveniently enough, this turns out to be the case, as will be shown in the next section. Furthermore, the proposed quadratic integration method can be introduced in a more formal mathematical way, which will make it easy to obtain a general expression for the method for any nonlinear system. This new approach will be discussed in section 5.3.

The proposed method demonstrates improved convergence characteristics of the iterative solution algorithm. It is an implicit numerical integration method (it can be easily observed that it makes use of information at the unknown point, $x(t)$), and,

therefore, it demonstrates the desired, advanced, numerical-stability properties compared to explicit methods. It is also fourth order accurate and, therefore, much more precise compared to all the traditionally used methods in power-system applications. Furthermore, the proposed method does not suffer from the problem of numerical oscillations, contrary to the trapezoidal rule.

5.2 Description of the Quadratic Integration Method

This section presents the key features of the quadratic integration method. The method is based on two innovations: First, the nonlinear system-model equations (nonlinear differential or differential-algebraic equations) are reformulated to a fully equivalent system of linear differential and quadratic algebraic equations, by introducing additional state variables and additional algebraic equations. This step aims in reducing the nonlinearity of the system to at most quadratic in an attempt to improve the efficiency of the solution algorithm, as well as facilitate the implementation of the method, especially for large and complex models. It is independent of the integration method and, thus, can be applied in combination with any numerical integration scheme. Second, the system-model equations are integrated using the implicit numerical scheme that was conceptually described in the introductory section, 5.1, of this chapter.

The quadratic integration method belongs to the category of implicit, one-step, Runge-Kutta methods. More specifically, it is an implicit Runge-Kutta method based on collocation and it can be alternatively derived based on the collocation theory. The basic idea is to choose a function from a simple space, like the polynomial space, and a set of collocation points and require that the function satisfy the given problem equations at the collocation points [58] – [60]. The method has three collocation points at $x(t-h)$,

$x_m = x(t_m)$, and $x(t)$. It uses the Lobatto quadrature rules and is a member of the family of Lobatto methods. Any Lobatto method with s collocation points has an order of accuracy of $2s - 2$, therefore, this method is order-four accurate [58] – [60].

Assuming the general, nonlinear, non-autonomous, dynamical system

$$\dot{x}(t) = f(t, x), \tag{5.25}$$

the algebraic equations at each integration step of length h, resulting from the quadratic integration method, are

$$\begin{aligned} x_m - \tfrac{h}{3} f(t_m, x_m) + \tfrac{h}{24} f\big(t, x(t)\big) &= x(t-h) + \tfrac{5h}{24} f\big(t-h, x(t-h)\big), \\ x(t) - \tfrac{2h}{3} f(t_m, x_m) - \tfrac{h}{6} f\big(t, x(t)\big) &= x(t-h) + \tfrac{h}{6} f\big(t-h, x(t-h)\big). \end{aligned} \tag{5.26}$$

Solution of the system, via Newton's method, yields the value of the state vector $x(t)$. Note that the value at the midpoint, x_m, is simply an intermediate result and it is discarded at the end of the calculations at each step. For the special case of a linear system of the form

$$\dot{x}(t) = Ax(t) + Bu(t), \tag{5.27}$$

the algebraic equations at each time step become

$$\begin{bmatrix} \frac{h}{24}A & I - \frac{h}{3}A \\ I - \frac{h}{6}A & -\frac{2h}{3}A \end{bmatrix} \begin{bmatrix} x(t) \\ x_m \end{bmatrix} = \begin{bmatrix} \left(I + \frac{5h}{24}A\right) \\ \left(I + \frac{h}{6}A\right) \end{bmatrix} x(t-h) + \begin{bmatrix} -\frac{h}{24}B & \frac{5h}{24}B & \frac{h}{3}\mathrm{B} \\ \frac{\mathrm{h}}{6}\mathrm{B} & \frac{\mathrm{h}}{6}\mathrm{B} & \frac{2\mathrm{h}}{3}\mathrm{B} \end{bmatrix} \begin{bmatrix} \mathrm{u(t)} \\ \mathrm{u(t-h)} \\ \mathrm{u_m} \end{bmatrix}, \tag{5.28}$$

where I is the identity matrix of proper dimension and h the length of the integration step.

The proposed integration approach has the following advantages: (a) improved accuracy and desired numerical stability and (b) absence of fictitious numerical

oscillations. Details about the numerical properties of the method are discussed next, in section 5.4.

5.3 Formal Mathematical Derivation of Quadratic Integration Method

5.3.1 Introduction

The proposed quadratic integration method is a member of the family of implicit Runge-Kutta methods that are based on collocation. Runge-Kutta methods are one of the two main categories of numerical method for ordinary differential equations (ODEs), the other being the class of linear, multi-step methods. Runge-Kutta methods are one-step, multi-stage methods. This means that in order to evaluate the unknown function, $x(t)$, at time t, they use information only from one past value, $x(t-h)$, where h is the integration step, but they compute the new value $x(t)$ after several stages of calculations, estimating some intermediate values of x in the interval $[t-h, t]$. Thus the value of $x(t)$ is computed based on $x(t-h)$ and intermediate values of x in $[t-h, t]$.

The most popular Runge-Kutta methods are explicit methods (they do not use information at the unknown point $x(t)$, for the calculation of the value $x(t)$ and the value of $x(t)$ and of x at any intermediate stages is explicitly computed based on previously known quantities); therefore, they are only suitable for non-stiff and well behaving problems and do not demonstrate good numerical stability properties. However, there is also a class of implicit Runge-Kutta methods, most of which demonstrate superior stability properties and are very suitable for stiff problems and also for problems of differential-algebraic equations. The most important and commonly used of these methods are derived from collocation and are based on quadrature methods; that is, the

points at which the intermediate stage approximations are taken are the same points used in certain classes of quadrature formulas [58].

5.3.2 Basic Quadrature Rules

Given the task of evaluating an integral $\int_a^b f(t)dt$ for some function $f(t)$ in an interval $[a, b]$, the basic quadrature rules are derived by replacing $f(t)$ with an interpolating polynomial, $\phi(t)$, and integrating the latter exactly. If there are s distinct interpolation points, $c_1, \dots, c_s$, the interpolating polynomial of degree less than s can be expressed in Lagrange form as

$$\phi(t) = \sum_{j=1}^{s} f(c_j) L_j(t), \tag{5.29}$$

where $L_j(t) = \prod_{i=1, i\neq j}^{s} \frac{(t-c_i)}{(c_j-c_i)}$.

Then $\int_a^b f(t)dt \approx \sum_{j=1}^{s} w_j f(c_j)$, where the weights w_j are given by $w_j = \int_a^b L_j(t)dt$. The precision of the quadrature rule is p if the rule is exact for all polynomials of degree up to p, i.e., if for any polynomial f of degree less than p, $\int_a^b f(t)dt = \sum_{j=1}^{s} w_j f(c_j)$. If $b - a = O(h)$ then the error in a quadrature rule of precision p is $O(h^{p+1})$. Obviously, $p \geq s$, but p may be significantly larger than s if the points c_j are chosen carefully. The midpoint and trapezoidal rules (the latter used by the trapezoidal integration) have precision $p = 2$. Simpson's rule (used by the popular 4$^{\text{th}}$-order Runge-Kutta method) has precision $p = 4$. Gaussian quadrature at s points has the highest possible precision $p = 2s$.

5.3.3 Implicit Runge-Kutta Methods Based on Collocation

For the representation of each presented method the Bucher array formulation will be used. The Bucher array is a matrix structure as shown below

c_1	a_{11}	a_{12}	…	a_{1s}
c_2	a_{21}	a_{22}	…	a_{2s}
…	…	…		…
c_s	a_{s1}	a_{s2}	…	a_{ss}
	b_1	b_2	…	b_s

or, in shorthand notation

c	A
	b^T

where $c = \begin{bmatrix} c_1 \\ c_2 \\ \dots \\ c_s \end{bmatrix}$, $b = \begin{bmatrix} b_1 \\ b_2 \\ \dots \\ b_s \end{bmatrix}$, $A = \begin{bmatrix} a_{11} & a_{12} & \dots & a_{1s} \\ a_{21} & a_{22} & \dots & a_{2s} \\ \dots & \dots & & \dots \\ a_{s1} & a_{s2} & \dots & a_{ss} \end{bmatrix}$, and s is the number of internal interval points used by the method, also known as stages of the method. Using this notations, in general, an s-stage Runge-Kutta method for the ODE system $\dot{x}(t) = f(t, x)$ can be written (for each integration step $[t-h, t]$) in the form

$$X_i = x(t-h) + h\sum_{j=1}^{s} a_{ij} f(t-h+c_j h, X_j),\ 1 \le i \le s, \tag{5.30}$$

$$x(t) = x(t-h) + h\sum_{i=1}^{s} b_i f(t-h+c_i h, X_i). \tag{5.31}$$

The representation holds for all Runge-Kutta methods. In the case of collocation methods, s is also the number of interpolation points in $[t-h, t]$ and the values of **c** provide these points. Although it is not necessary, in practice however, it holds that for all the methods $c_i = \sum_{j=1}^{s} a_{ij}$, $i = 1, \dots, s$. A Runge-Kutta method is explicit iff $a_{ij} = 0$ for $j \ge i$ (A is strictly lower triangular), because then each X_i is given in terms of known quantities; otherwise, it is implicit.

Gauss methods: These are the maximum order methods; an s-stage Gauss method has an order of $2s$. The first two members of this class are

1. Implicit midpoint method ($s = 1, p = 2$):

$$\begin{array}{c|c} \frac{1}{2} & \frac{1}{2} \\ \hline & 1 \end{array}$$

2. $s = 2, p = 4$:

$$\begin{array}{c|cc} \frac{3-\sqrt{3}}{6} & \frac{1}{4} & \frac{3-2\sqrt{3}}{12} \\ \frac{3+\sqrt{3}}{6} & \frac{3+2\sqrt{3}}{12} & \frac{1}{4} \\ \hline & \frac{1}{2} & \frac{1}{2} \end{array}$$

Radau methods: These methods correspond to quadrature rules where one end of the time interval $[t-h, t]$ is included ($c_1 = 0$ or $c_s = 1$) and they attain order $2s - 1$. The choice $c_1 = 0$ makes no sense (implicit methods that use information at time t are of interest), so only the case $c_s = 1$ is considered. These methods are best suited for differential-algebraic equation problems. The first two members of this class are

1. Backward Euler ($s = 1, p = 1$):

$$\begin{array}{c|c} 1 & 1 \\ \hline & 1 \end{array}$$

2. $s = 2, p = 3$:

$\frac{1}{3}$	$\frac{5}{12}$	$-\frac{1}{12}$
1	$\frac{3}{4}$	$\frac{1}{4}$
	$\frac{3}{4}$	$\frac{1}{4}$

Lobatto methods: These methods correspond to quadrature rules where the function is sampled at both ends of the interval. The order of accuracy is $2s - 2$. Quadratic integration belongs to this class of methods. The same holds for trapezoidal integration. The first two members of this class are

1. Trapezoidal method ($s = 2, p = 2$):

0	0	0
1	$\frac{1}{2}$	$\frac{1}{2}$
	$\frac{1}{2}$	$\frac{1}{2}$

2. Quadratic integration ($s = 3, p = 4$):

0	0	0	0
$\frac{1}{2}$	$\frac{5}{24}$	$\frac{1}{3}$	$-\frac{1}{24}$
1	$\frac{1}{6}$	$\frac{2}{3}$	$\frac{1}{6}$
	$\frac{1}{6}$	$\frac{2}{3}$	$\frac{1}{6}$

Expanding the Bucher array notation, the full set of equations defining the quadratic integration rule for the system $\dot{x} = f(t,x)$ are (in the interval $[t-h, t]$)

$$X_1 = x(t-h), \tag{5.32}$$

$$X_2 = x(t-h) + \frac{5h}{24} f(t-h, X_1) + \frac{h}{3} f\left(t - \frac{h}{2}, X_2\right) - \frac{h}{24} f(t, X_3), \tag{5.33}$$

$$X_3 = x(t-h) + \frac{h}{6} f(t-h, X_1) + \frac{2h}{3} f\left(t - \frac{h}{2}, X_2\right) + \frac{h}{6} f(t, X_3), \tag{5.34}$$

$$x(t) = x(t-h) + \frac{h}{6} f(t-h, X_1) + \frac{2h}{3} f\left(t - \frac{h}{2}, X_2\right) + \frac{h}{6} f(t, X_3). \tag{5.35}$$

Note that X_1 is simply $x(t-h)$ and also the last two equations imply that $X_3 = x(t)$. In addition X_2 is the value of x at the midpoint of the interval, i.e., $X_2 = x\left(t - \frac{h}{2}\right) = x(t_m)$, which is called x_m for simplicity. Therefore, the equations can be reduced and rewritten as

$$x_m = x(t-h) + \frac{5h}{24} f\big(t-h, x(t-h)\big) + \frac{h}{3} f(t_m, x_m) - \frac{h}{24} f(t, x(t)) , \tag{5.36}$$

$$x(t) = x(t-h) + \frac{h}{6} f\big(t-h, x(t-h)\big) + \frac{2h}{3} f(t_m, x_m) + \frac{h}{6} f(t, x(t)) , \tag{5.37}$$

which yield the system of nonlinear equations for the unknowns, $x(t)$ and x_m:

$$x_m - \frac{h}{3} f(t_m, x_m) + \frac{h}{24} f\big(t, x(t)\big) = x(t-h) + \frac{5h}{24} f(t-h, x(t-h)) , \tag{5.38}$$

$$x(t) - \frac{2h}{3} f(t_m, x_m) - \frac{h}{6} f\big(t, x(t)\big) = x(t-h) + \frac{h}{6} f(t-h, x(t-h)) . \tag{5.39}$$

These are the equations of the quadratic integration method for any nonlinear system of the general form $\dot{x}(t) = f(t,x)$ and are the same with the equations derived based on intuition in the section 5.1.2.

In the case of a linear, autonomous system of the form $\dot{x}(t) = Ax(t)$, $f(t,x) = Ax$ and, thus, the equations become

$$\frac{h}{24}Ax(t) + \left(I - \frac{h}{3}A\right)x_m = \left(I + \frac{5h}{24}A\right)x(t-h), \tag{5.40}$$

$$\left(I - \frac{h}{6}A\right)x(t) - \frac{2h}{3}Ax_m = \left(I + \frac{h}{6}A\right)x(t-h)\ . \tag{5.41}$$

Note these equations are the exact same equations as the ones derived in section 5.1.1 for the linear system integration.

A Runge-Kutta method with a nonsingular coefficient matrix A that satisfies $a_{sj} = b_j,\ j = 1, \dots, s$, is called *stiffly accurate*. This property gives stiff decay to the method. Neither the trapezoidal nor the quadratic integration have this property (matrix A is singular). The two Radau methods described previously in this section do have this property.

The basic idea of collocation is to choose a function from a simple space (usually a polynomial) and a set of collocation points, in every integration interval $[t-h, t]$, and require that the function satisfies the given problem equations at the collocation points. Starting with a set of s distinct points, $0 \le c_1 < c_2 < \cdots < c_s \le 1$, (if $c_1 = 0$ this is the point at $t-h$ and if $c_s = 1$ this corresponds to the point at t) and considering, for simplicity, a scalar ODE $\dot{x}(t) = f(t,x)$ first, the objective is to find the polynomial $\phi(t)$ of degree at most s that collocates the ODE in $[t-h, t]$ as follows:

$$\phi(t-h) = x(t-h)\ , \tag{5.42}$$

$$\dot{\phi}(t_i) = f(t_i, \phi(t_i)),\ i = 1,2, \dots, s, \tag{5.43}$$

where $t_i = t - h + c_i h = t - (1 - c_i)h$ are the collocation points. This defines $\phi(t)$ uniquely and it holds that the numerical solution at time t, which is the value to be calculated, is equal to $\phi(t)$. Note that if the polynomial pieces defined this way on each step interval $[t - h, t]$ are collected into a single function defined on the whole solution interval, then a continuous, piecewise-polynomial approximation of the actual solution, $x(t)$, is obtained.

This provides an s-stage, implicit Runge-Kutta method. $\dot{\phi}$ is a polynomial of degree at most $s - 1$, which interpolates s data points, $f\big(t_i, \phi(t_i)\big)$. Defining $K_i = \dot{\phi}(t_i)$ $\dot{\phi}$ can be expressed as a Lagrange interpolation formula

$$\dot{\phi}(t - h + \tau h) = \sum_{j=1}^{s} L_j(t - h + \tau h) K_j, \tag{5.44}$$

where $L_j(t - h + \tau h) = \prod_{i=1, i \neq j}^{s} \frac{(\tau - c_i)}{(c_j - c_i)}$. Since $\dot{\phi}$ is a polynomial of degree less than s, it agrees with its s-points interpolant identically. Integrating $\dot{\phi}$ with respect to t from $t - h$ to t_i, $i = 1,2, \ldots, s$, and from $t - h$ to t, it is obtained that

$$\phi(t_i) - \phi(t - h) = h \sum_{j=1}^{s} \Big(\int_0^c L_j(r) dr \Big) K_j, \tag{5.45}$$

$$\phi(t) - \phi(t - h) = h \sum_{j=1}^{s} \left(\int_0^1 L_j(r) dr \right) K_j. \tag{5.46}$$

Now define

$$a_{ij} = \int_0^c L_j(r) dr, \tag{5.47}$$

$$b_j = \int_0^1 L_j(r) dr. \tag{5.48}$$

Thus, $K_i = f\big(t_i, \phi(t_i)\big) = f\big(t_i, x(t - h) + h \sum_{j=1}^{s} a_{ij} K_j\big)$ and $x(t) = x(t - h) + h \sum_{i=1}^{s} b_i K_i$. The obtained formula is, therefore, a Runge-Kutta method. Finally, note that

for the general ODE system $\dot{x} = f(t, x)$, where x is a vector and f a vector function precisely, the same argument can be repeated, where now a vector of collocation polynomials exists.

The Gauss, Radau, and Lobatto methods introduced earlier in this chapter are collocation methods. That is, given the quadrature points c_i for each case, all the other coefficients of the method are determined. The order of such collocation-based Runge-Kutta methods is at least s and is determined only as a result of quadrature theory. The maximum order of an s-stage Runge-Kutta method is $2s$. This maximum order is achieved by collocation at Gaussian points.

5.3.4 Derivation of Quadratic Integration Method

Assume a 3rd-degree polynomial, $\phi(\tau)$, defined in the interval $[t-h, t]$ via the equation $\phi(\tau) = a + b\tau + c\tau^2 + d\tau^3$, where $0 \leq \tau \leq h$ ($\tau = 0$ corresponds to time $t-h$ and $\tau = h$ corresponds to time t). Assume three collocation points ($s = 3$) defined as $c_1 = 0$, $c_2 = 1/2$, and $c_3 = 1$. The scalar case will be assumed here, but the general case is identical, assuming vectors for each quantity instead of scalar values, as explained earlier. Thus for the scalar ODE $\dot{x}(t) = f(t, x)$, a polynomial $\phi(\tau)$ is defined of degree at most $s = 3$ that collocates the ODE in the interval $[t-h, t]$ as

$$\phi(t-h) = x(t-h)\,, \tag{5.49}$$

$$\dot{\phi}(t_1) = \dot{\phi}(t-h) = f(t-h, \phi(t-h))\,, \tag{5.50}$$

$$\dot{\phi}(t_2) = \dot{\phi}\left(t - \frac{h}{2}\right) = \dot{\phi}(t_m) = f(t_m, \phi(t_m))\,, \tag{5.51}$$

$$\dot{\phi}(t_3) = \dot{\phi}(t) = f(t, \phi(t))\,. \tag{5.52}$$

Because of the assumed cubic dependence on time it holds that $\dot{\phi}(\tau) = b + 2c\tau + 3d\tau^2$. Expressing the previous equations in terms of τ being the argument of ϕ results in

$$\phi(0) = x(t-h)\ , \tag{5.53}$$

$$\dot{\phi}(0) = f(t-h, \phi(0))\ , \tag{5.54}$$

$$\dot{\phi}\left(\frac{h}{2}\right) = f(t_m, \phi(\frac{h}{2}))\ , \tag{5.55}$$

$$\dot{\phi}(h) = f(t, \phi(h))\ . \tag{5.56}$$

From these equations it can be derived that

$$a = x(t-h)\ , \tag{5.57}$$

$$b = f\big(t-h, \phi(0)\big) = f(t-h, a) = f(t-h, x(t-h))\ , \tag{5.58}$$

$$b + ch + \tfrac{3}{4}dh^2 = f(t_m, a + b\tfrac{h}{2} + c\tfrac{h^2}{4} + d\tfrac{h^3}{8})\ , \tag{5.59}$$

$$b + 2ch + 3dh^2 = f(t, a + bh + ch^2 + dh^3)\ . \tag{5.60}$$

Note that these four equations fully define the polynomial ϕ. The parameters a and b are explicitly defined in terms of x as $a = x(t-h)$ and $b = f(t-h, x(t-h))$; c and d are defined by solving the system of the last two equations.

Define

$$K_1 = \dot{\phi}(t_1) = \dot{\phi}(t-h), \tag{5.61}$$

$$K_2 = \dot{\phi}(t_2) = \dot{\phi}(t_m), \tag{5.62}$$

$$K_3 = \dot{\phi}(t_3) = \dot{\phi}(t). \tag{5.63}$$

$\dot{\phi}$ can be written as a Lagrange interpolation formula:

$\dot{\phi}(t-h+\tau h)=\sum_{j=1}^{3}L_j(t-h+\tau h)K_j \;= L_1(t-h+\tau h)K_1+L_2(t-h+\tau h)K_2+$

$L_3(t-h+\tau h)K_3,$ (5.64)

where $L_j(t-h+\tau h)=\prod_{i=1,i\neq j}^{s}\frac{(\tau-c_i)}{(c_j-c_i)}$, i.e.,

$L_1(t-h+\tau h)=\frac{(\tau-c_2)}{(c_1-c_2)}\frac{(\tau-c_3)}{(c_1-c_3)}=2\left(\tau-\frac{1}{2}\right)(\tau-1)=2\tau^2-3\tau+1\,,$ (5.65)

$L_2(t-h+\tau h)=\frac{(\tau-c_1)}{(c_2-c_1)}\frac{(\tau-c_3)}{(c_2-c_3)}=-4(\tau^2-\tau)\,,$ (5.66)

$L_3(t-h+\tau h)=\frac{(\tau-c_1)}{(c_3-c_1)}\frac{(\tau-c_2)}{(c_3-c_2)}=2\tau^2-\tau\,.$ (5.67)

Integrating $\dot{\phi}$ with respect to t from $t-h$ to t_i, $i=1,2,3$, and from $t-h$ to t, the following expressions are obtained:

$\phi(t_1)-\phi(t-h)=h\sum_{j=1}^{3}\left(\int_0^0 L_j(r)dr\right)K_j \Rightarrow 0=0,$ (5.68)

$\phi(t_2)-\phi(t-h)=$

$h\sum_{j=1}^{3}\left(\int_0^{1/2} L_j(r)dr\right)K_j \Rightarrow \phi(t_m)-\phi(t-h)=h\sum_{j=1}^{3}\left(\int_0^{1/2} L_j(r)dr\right)K_j,$ (5.69)

$\phi(t_3)-\phi(t-h)=$

$h\sum_{j=1}^{3}\left(\int_0^{1} L_j(r)dr\right)K_j \Rightarrow \phi(t)-\phi(t-h)=h\sum_{j=1}^{3}\left(\int_0^{1} L_j(r)dr\right)K_j,$ (5.70)

$\phi(t)-\phi(t-h)=h\sum_{j=1}^{3}\left(\int_0^{1} L_j(r)dr\right)K_j.$ (5.71)

Note that the first equation vanishes since it is just an identity and the last two coincide. Therefore, the ones left are the second and third equations. Now define

$a_{11}=\int_0^{c_1}L_1(r)dr=\int_0^0 L_1(r)dr=0,$ (5.72)

$a_{12}=\int_0^{c_1}L_2(r)dr=\int_0^0 L_2(r)dr=0,$ (5.73)

$$a_{13} = \int_0^{c_1} L_3(r)dr = \int_0^0 L_3(r)dr = 0, \tag{5.74}$$

$$a_{21} = \int_0^{c_2} L_1(r)dr = \int_0^{1/2}(2r^2 - 3r + 1)dr = \frac{1}{12} - \frac{3}{8} + \frac{1}{2} = \frac{5}{24}, \tag{5.75}$$

$$a_{22} = \int_0^{c_2} L_2(r)dr = -4\int_0^{1/2}(r^2 - r)dr = -4\left(\frac{1}{24} - \frac{1}{8}\right) = \frac{1}{2} - \frac{1}{6} = \frac{1}{3}, \tag{5.76}$$

$$a_{23} = \int_0^{c_2} L_3(r)dr = \int_0^{1/2}(2r^2 - r)dr = \frac{1}{12} - \frac{1}{8} = -\frac{1}{24}, \tag{5.77}$$

$$a_{31} = \int_0^{c_3} L_1(r)dr = \int_0^{1}(2r^2 - 3r + 1)dr = \frac{2}{3} - \frac{3}{2} + 1 = \frac{1}{6}, \tag{5.78}$$

$$a_{32} = \int_0^{c_3} L_2(r)dr = -4\int_0^{1}(r^2 - r)dr = -4\left(\frac{1}{3} - \frac{1}{2}\right) = \frac{2}{3}, \tag{5.79}$$

$$a_{33} = \int_0^{c_3} L_3(r)dr = \int_0^{1}(2r^2 - r)dr = \frac{2}{3} - \frac{1}{2} = \frac{1}{6}, \tag{5.80}$$

$$b_1 = \int_0^1(2r^2 - 3r + 1)dr = \frac{1}{6}, \tag{5.81}$$

$$b_2 = -4\int_0^1(r^2 - r)dr = \frac{2}{3}, \tag{5.82}$$

$$b_3 = \int_0^1(2r^2 - r)dr = \frac{1}{6}. \tag{5.83}$$

Using these definitions it is obtained that

$$\phi(t_m) - \phi(t - h) = h\sum_{j=1}^3 a_{2j}K_j, \tag{5.84}$$

$$\phi(t) - \phi(t - h) = h\sum_{j=1}^3 a_{3j}K_j = h\sum_{j=1}^3 b_jK_j, \tag{5.85}$$

where

$$K_1 = \dot{\phi}(t - h) = f(t - h, \phi(t - h)), \tag{5.86}$$

$$K_2 = \dot{\phi}(t_m) = f(t_m, \phi(t_m)), \tag{5.87}$$

$$K = \dot{\phi}(t) = f(t, \phi(t)). \tag{5.88}$$

Therefore, the quadratic integration is defined by the following system of equations:

$$\phi(t_m) - \phi(t-h) = \frac{5h}{24} f\big(t-h, \phi(t-h)\big) + \frac{h}{3} f\big(t_m, \phi(t_m)\big) - \frac{h}{24} f(t, \phi(t)), \qquad (5.89)$$

$$\phi(t) - \phi(t-h) = \frac{h}{6} f\big(t-h, \phi(t-h)\big) + \frac{2h}{3} f\big(t_m, \phi(t_m)\big) + \frac{h}{6} f(t, \phi(t)). \qquad (5.90)$$

The values of ϕ at the various stages represent the estimated values of the unknown state x and based on the collocation is also holds that $\phi(t-h) = x(t-h)$. Thus, we can change our notation from ϕ to x and the method becomes

$$\frac{h}{24} f\big(t, x(t)\big) + x_m - \frac{h}{3} f(t_m, x_m) = x(t-h) + \frac{5h}{24} f(t-h, x(t-h)), \qquad (5.91)$$

$$x(t) - \frac{h}{6} f\big(t, x(t)\big) - \frac{2h}{3} f(t_m, x_m) = x(t-h) + \frac{h}{6} f(t-h, x(t-h)). \qquad (5.92)$$

Notes:

The polynomial assumed at the beginning of the section has to be of degree at most three and that is the reason a third-degree polynomial was assumed. In this case the parameters a, b, c, and d could be uniquely identified from the collocation points. A lower-degree polynomial, like 2nd degree, could have been assumed, but then for three collocation points the last two equations defining the collocation would have to be consistent with each other.

Since information from both ends of the integration interval is used ($c_1 = 0$ and $c_s = c_3 = 1$) the method belongs to the Lobatto class.

5.4 Numerical Stability Properties of Quadratic Integration Method

5.4.1 Numerical Properties of Implicit Runge-Kutta Methods

The order of the quadratic integration method is $p = 4$. This means that the method is very nice in terms of accuracy, since the error at each step is $O(h^5)$. The order is twice that of the commonly used trapezoidal integration method, thus, as far as accuracy is concerned, the method is preferable to trapezoidal. In general, all one-step methods (Runge-Kutta) are zero-stable [58], so quadratic integration is also zero-stable.

With regard to studying the absolute stability, the test equation $\dot{x}(t) = \lambda x(t)$ is used, which is the most commonly used equation to test absolute stability. The region of absolute stability is obtained for a given method by determining for what values of $z = h\lambda$, where h is the integration step, it holds that $|x(t)| \leq |x(t-h)|$ when applying the method to the test equation. It can be easily verified that for the test equation a Runge-Kutta method reads $x(t) = R(z)x(t-h)$, where $z = h\lambda$ and $R(z) = 1 + zb^T(I - zA)^{-1}I1$ [58]. $A = [a_{ij}]$ is the coefficient matrix of the Runge-Kutta method and $b = [b_1, \dots, b_s]^T$ is the coefficient vector of the method. $I1$ is defined as $I1 = [1,1, \dots, 1]^T$.

The region of absolute stability is given by the set of values z such that $|R(z)| \leq 1$. For an explicit method is can be shown that $R(z)$ is a polynomial and hence the method cannot be A-stable [58]. As stated earlier a method is called A-stable if the region of absolute stability in the complex z-plane contains the entire left half-plain. This means that independently of the step size $h > 0$, a stable eigenvalue λ of the original, continuous-time system, with $Re(\lambda) < 0$, will be still represented as a stable mode in the

discrete-time system and, thus, the discrete system mimics accurately the behavior of the original system. For implicit Runge-Kutta methods, in contrast to explicit methods, $R(z)$ is a rational function, i.e., it is a quotient of two polynomials $R(z) = \frac{P(z)}{Q(z)}$ and, therefore, it is easy to design A-stable implicit methods. All the implicit Runge-Kutta methods that have been presented so far, including the trapezoidal and the quadratic integration, turn out to be A-stable.

For a method to have stiff decay, it is needed that $R(z) \to 0$ as $Re(z) \to \infty$ (the problem becomes very stiff). For this it must hold that $R(z)|_{z\to-\infty} = 0$, which is achieved if $P(z)$ has a lower degree than $Q(z)$. Note that if A is non-singular, then $R(z)|_{z\to-\infty} = 1 - b^T A^{-1} I1$, so $R(z)|_{z\to-\infty} = 0$ if the last row of A coincides with b^T. For a collocation Runge-Kutta method, this happens when $c_1 > 0$ and $c_s = 1$. In particular, Radau methods (extending Backward Euler) have stiff decay; Gauss and Lobatto methods (which extend midpoint and the trapezoidal) do not have stiff decay, although they are A-stable.

5.4.2 Numerical Properties of Quadratic Integration

The basic numerical stability properties of a numerical integration method are studied using the first order test equation

$$\dot{x}(t) = ax(t). \tag{5.93}$$

Applying the quadratic integration method yields at each time step

$$\begin{bmatrix} x(t) \\ x_m \end{bmatrix} = \begin{bmatrix} \left(\frac{12+6ah+a^2h^2}{12-6ah+a^2h^2}\right) \\ \left(\frac{12-0.5a^2h^2}{12-6ah+a^2h^2}\right) \end{bmatrix} x(t-h) \tag{5.94}$$

and, therefore,

$$x(t) = \frac{12+6ah+a^2h^2}{12-6ah+a^2h^2}x(t-h), \tag{5.95}$$

where h is the integration step. Setting $z = ah$ yields the characteristic polynomial, $R(z)$, of the method as

$$R(z) = \frac{z^2+6z+12}{z^2-6z+12}. \tag{5.96}$$

Note that the eigenvalue a of the system can be complex, so z is in general a complex number.

Alternatively the characteristic polynomial can be obtained by the Butcher array notation. For the quadratic integration it holds that

$A = \begin{bmatrix} 0 & 0 & 0 \\ \frac{5}{24} & \frac{1}{3} & -\frac{1}{24} \\ \frac{1}{6} & \frac{2}{3} & \frac{1}{6} \end{bmatrix}$, $b = \begin{bmatrix} \frac{1}{6} \\ \frac{2}{3} \\ \frac{1}{6} \end{bmatrix}$, $c = \begin{bmatrix} 0 \\ \frac{1}{2} \\ 1 \end{bmatrix}$. The characteristic polynomial is given by

$$R(z) = 1 + zb^T(I - zA)^{-1}I1 = 1 + z\begin{bmatrix} \frac{1}{6} & \frac{2}{3} & \frac{1}{6} \end{bmatrix}\left(I - z\begin{bmatrix} 0 & 0 & 0 \\ \frac{5}{24} & \frac{1}{3} & -\frac{1}{24} \\ \frac{1}{6} & \frac{2}{3} & \frac{1}{6} \end{bmatrix}\right)^{-1}\begin{bmatrix} 1 \\ 1 \\ 1 \end{bmatrix} = 1 +$$

$$z\begin{bmatrix} \frac{1}{6} & \frac{2}{3} & \frac{1}{6} \end{bmatrix}\begin{bmatrix} 1 & 0 & 0 \\ -\frac{5}{24}z & 1-\frac{1}{3}z & \frac{1}{24}z \\ -\frac{1}{6}z & -\frac{2}{3}z & 1-\frac{1}{6}z \end{bmatrix}^{-1}\begin{bmatrix} 1 \\ 1 \\ 1 \end{bmatrix} = \cdots = \frac{z^2+6z+12}{z^2-6z+12}. \tag{5.97}$$

The region of absolute stability is given by the set of values z such that $|R(z)| \leq 1$. A method is called A-stable if the region of absolute stability in the complex z-plane contains the entire left half-plane. This means that, independently of the step size $h > 0$, a stable eigenvalue a of the original, continuous-time system, with $Re(a) < 0$, will be

still represented as a stable mode in the discrete-time system, and thus the discrete system mimics accurately the behavior of the original system, in terms of stability. Note that for $Re(z) < 0$ it follows that $|R(z)| \leq 1$. For the characteristic polynomial above it holds that $|R(z)| \leq 1$ for any value of z in the left half-plane. This is illustrated in Figure 5.2 and Figure 5.3. Therefore, the proposed method is A-stable.

Furthermore, the absolute stability region is exactly the left complex half-plane, as illustrated in Figure 5.4. This property is called strict A-stability. If the dynamical system under study includes an unstable mode, then this mode will remain unstable in the descretized system, irrespectively of the size of the integration step. This is not the case for other methods like the backward Euler or the BDF, linear, multi-step methods, where the numerical stability domain extends in the right half-plane, where $Re(z) > 0$. In this case, if the real dynamical system includes an unstable mode, this mode could appear as stable in the discrete system for some value of the step size.

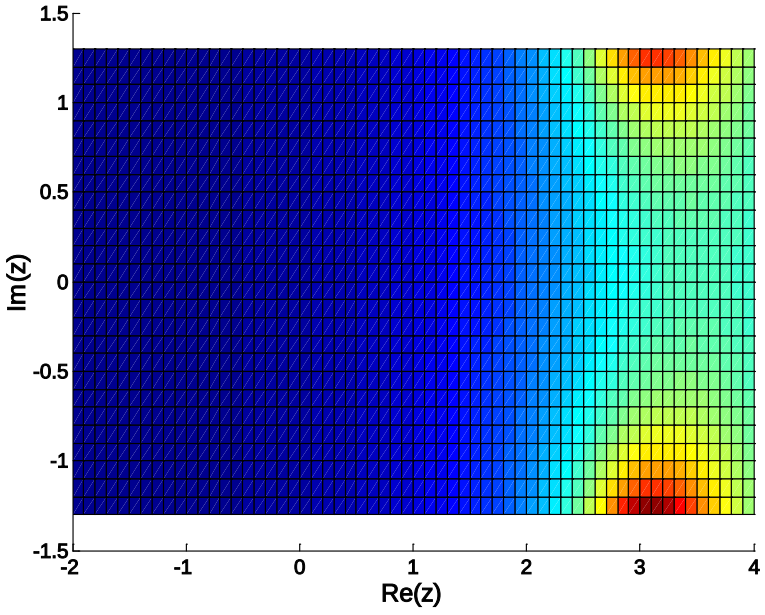

Figure 5.2: Plot of $|R(z)|$ for quadratic integration.

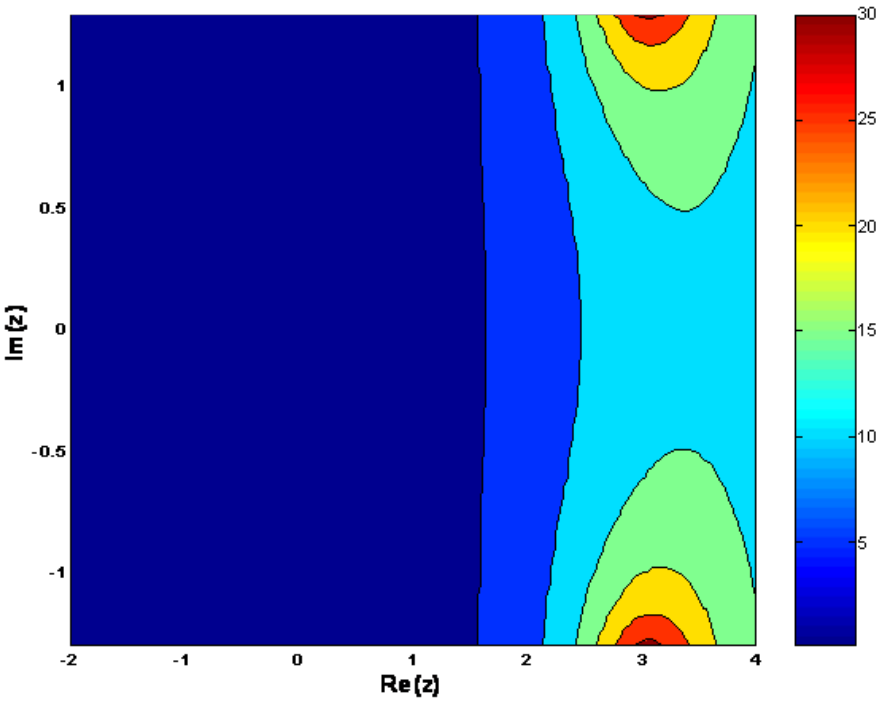

Figure 5.3: Contour plot of $|R(z)|$ for quadratic integration.

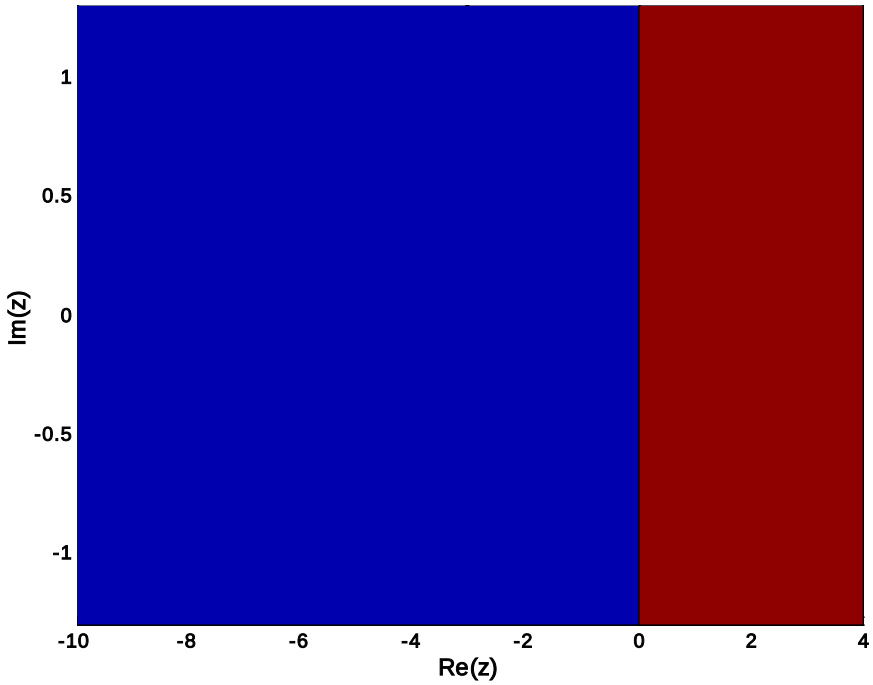

Figure 5.4: Absolute stability region of quadratic integration method (blue region).

5.4.3 Comparison of the Trapezoidal Method and the Quadratic Integration Method

Comparing the quadratic and the trapezoidal integration methods the following hold:

Both the trapezoidal method and the quadratic integration method are strictly A-stable. The characteristic polynomial of the trapezoidal method is $R(z) = \frac{2+z}{2-z}$ and it holds that $|R(z)| \leq 1$ in the whole complex left half-plane, where $Re(z) < 0$. This can be computed from the method's Butcher array as

$$R(z) = 1 + zb^T(I - zA)^{-1}I1 = 1 + z\begin{bmatrix}\frac{1}{2} & \frac{1}{2}\end{bmatrix}\left(I - z\begin{bmatrix}0 & 0\\ \frac{1}{2} & \frac{1}{2}\end{bmatrix}\right)^{-1}\begin{bmatrix}1\\1\end{bmatrix} =$$

$$1 + z\begin{bmatrix}\frac{1}{2} & \frac{1}{2}\end{bmatrix}\begin{bmatrix}1 & 0\\ -z\frac{1}{2} & 1 - z\frac{1}{2}\end{bmatrix}^{-1}\begin{bmatrix}1\\1\end{bmatrix} = 1 + \frac{z}{1-\frac{z}{2}}\begin{bmatrix}\frac{1}{2} & \frac{1}{2}\end{bmatrix}\begin{bmatrix}1 - z\frac{1}{2} & 0\\ z\frac{1}{2} & 1\end{bmatrix}\begin{bmatrix}1\\1\end{bmatrix} = 1 + \frac{z}{1-\frac{z}{2}} = \frac{1+\frac{z}{2}}{1-\frac{z}{2}}. \quad (5.98)$$

For $R(z) = \frac{1+\frac{z}{2}}{1-\frac{z}{2}}$, it holds that $|R(z)| \leq 1$ in the whole left half-plane and, thus, the method is A-stable. This is illustrated in Figure 5.5 and Figure 5.6.

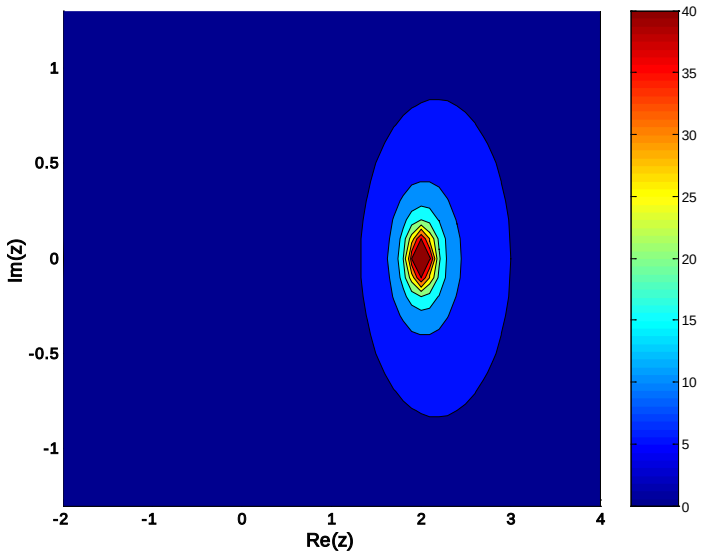

Figure 5.5: Contour plot of $|R(z)|$ for trapezoidal method.

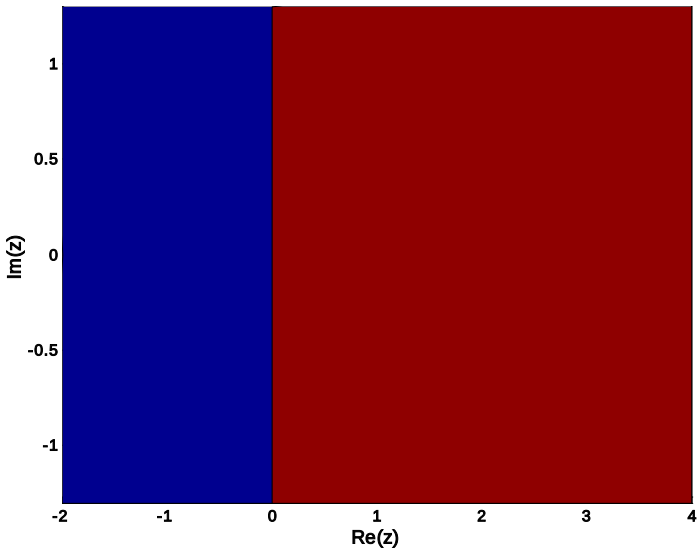

Figure 5.6: Absolute stability region of trapezoidal integration method (blue region).

The trapezoidal method is second-order accurate. The quadratic integration is a fourth-order method. Therefore, in terms of accuracy, quadratic integration is much preferable. This, however, comes with the drawback of additional computational expense.

It has been observed in applications that the trapezoidal method can provide an oscillatory solution even for systems that have exponential solutions, as the simple test equation above. This is apparent if one considers the term $R(z) = \frac{2+z}{2-z}$ for a physically stable system. Note that it is possible to select the integration time step ($z = ah$) so that this term is negative (for example any real value for z, with $Z < -2$). This can occur when larger integration steps are selected. In this case, the solution will be oscillatory, oscillating around the true solution of the problem. In the case of the quadratic integration, the corresponding term $R(z) = \frac{z^2+6z+12}{z^2-6z+12}$ can never be negative as long as $Re(z)$ is negative, that is, as long as the physical system is stable. Therefore, it appears that this method is free of such fictitious oscillations. This can be a very nice

characteristic in many applications. The behavior of the quadratic integration method in terms of this issue is still under investigation and will be part of the future work associated with this research.

As described earlier, the proposed quadratic integration method is an implicit Runge-Kutta method based on collocation. The trapezoidal integration method can be also viewed as a member of this category; however, trapezoidal rule uses two collocation points, while the proposed method uses three. This provides a great advantage in terms of accuracy. As every numerical integration method, the quadratic integration directly converts the system of differential equations to a set of algebraic equations, at each integration step. The formulation of these equations is straightforward and the procedure can be automated. This can facilitate the process in more complicated models. However, the number of algebraic equations of the quadratic integration scheme is double compared to that of the trapezoidal rule, due to the additional collocation point. The end-result is increased computational effort compared to the trapezoidal method per iteration (approximately double when sparsity techniques are used). Nonetheless, the improved method accuracy (order-four, compared to order-two of the trapezoidal method) allows the use of larger time steps, so that the total computational effort becomes less than that of trapezoidal integration, while the accuracy remains significantly higher. The tradeoff between accuracy and computational speed applies also to higher-order, implicit Runge-Kutta methods. As the number of collocation points, and thus the order, increases, the computational effort also increases. It appears that the quadratic integration method achieves a good balance between accuracy and computational speed.

The proposed method also appears to possess better numerical properties and be more accurate when compared to linear, multi-step methods commonly used in power system transient analysis. The use of such methods is usually restricted to order-two accurate methods. Detailed comparison of the quadratic integration and linear, multi-step methods commonly used could be investigated as future work of this research.

5.5 Summary

This section of the dissertation describes a new approach for time-domain transient simulation of electric power systems and dynamical systems in general. The new methodology has been named quadratic integration method. The method is based on a numerical integration scheme that assumes that the system states vary quadratically within an integration time step.

The proposed method yields an implicit numerical integration scheme that belongs to the category of Runge-Kutta methods based on collocation and, in particular, the Lobatto family. The approach demonstrates superior behavior compared to traditionally used methods in power system simulation (such as the trapezoidal integration rule) in terms of accuracy without sacrificing the essential numerical stability properties. The method also appears to be free of artificial numerical oscillations, which comprise a common problem of the trapezoidal rule.

CHAPTER 6

STATIC AND DYNAMIC SENSITIVITY ANALYSIS

6.1 Overview

Sensitivity analysis is an important tool commonly used in power system computations, either in an optimization context or in filtering and estimation processes [37] – [41]. In this work, sensitivity analysis is used for the selection of the best candidate locations for installation of voltage-support devices (as described in section 6.2) and also as part of a contingency ranking algorithm (as described later in section 7.5). Under steady-state conditions sensitivity analysis is based on the computation of the derivative of a quantity with respect to a system state, a control variable, or a parameter. This notion has been extended to time-domain analysis, in the concept of dynamic sensitivity or trajectory sensitivity [161] – [177]. Sensitivities are computed through time along a system trajectory, resulting in a time waveform (or sequence in practice) of derivative values.

6.2 Static Sensitivity Analysis

Static sensitivity analysis is used to determine the best candidate locations of VAr source additions, based on steady-state performance criteria and installation cost. The sensitivity of the defined objective function with respect to the addition of a specific VAr module at a specific system location can be efficiently computed using the co-state method [37] – [41], [178]-[181].

More specifically, assume an objective function aiming to the leveling of the system voltage profile at selected load buses in the system, where voltage sensitive loads are connected, like the one defined by (6.1) as

$$J_V = \sum_{k=1}^{N} w_k \left(\frac{V_k - V_{k,mean}}{V_{k,step}} \right)^{2n}, \quad (6.1)$$

where

w_k is a weighting factor, $0 < w_k < 1$,

$V_{k,mean}$ is the nominal bus voltage value (typically 1.0 p.u.), (it is in general the mean value in the desired range, i.e., $\frac{1}{2}\left(V_k^{max} + V_k^{min}\right)$),

$V_{k,step}$ is the voltage deviation tolerance (i.e., $\frac{1}{2}\left(V_k^{max} - V_k^{min}\right)$),

V_k is the actual voltage magnitude at bus k,

n is a positive integer parameter defining the exponent,

N is the total number of PQ buses.

Several other performance indices can be defined, based on the desired performance and cost criteria. By including a control parameter Q_i defining the addition of a VAr support device of rating Q at location i in the system model the defined performance index J can be expressed as a function of the state vector and of the control variables, $J(x, Q_i)$. The change of the performance index due to the addition is

$$\Delta J = J(x^{new}, Q_i) - J(x^0, Q_i = 0.0), \quad (6.2)$$

where x^0 is the initial state, prior to the addition, x^{new} is the state after the addition, and the control variable Q_i changes from 0.0 to some specific value Q_i, modeling the

additional VAr support component (either capacitor module, or any type of dynamic source).

6.2.1 First-Order Sensitivity Analysis for Candidate Location Selection

The first order approximation of the objective function variation is provided by the derivative of the objective function with respect to the control variable

$$\Delta J = \frac{dJ}{dQ_i}\Delta Q_i, \tag{6.3}$$

and for a change in the control parameter from 0.0 to a value Q_i it holds that

$$\Delta J = -\frac{dJ}{dQ_i}Q_i. \tag{6.4}$$

The value of Q_i represents the specific minimum value of modules of reactive support that are added each time.

It is therefore expected that the derivative of the objective function with respect to the control parameter Q_i at the present operating point will provide a measure of the improvement achieved by the addition. Therefore, candidate locations are ranked based on the values of $\frac{dJ}{dQ_i}$, which express the first order change of the performance index. The values of these derivatives can be calculated using the co-state method as

$$\frac{dJ}{dQ_i} = \frac{\partial J}{\partial Q_i} - \hat{x}^T \frac{\partial g(x,Q_i)}{\partial Q_i}, \tag{6.5}$$

$$\hat{x}^T = \left[\frac{\partial J(x,Q_i)}{\partial x}\right]\left[\frac{\partial g(x,Q_i)}{\partial x}\right]^{-1}. \tag{6.6}$$

$J(x, Q_i)$ is the performance index, $g(x, Q_i) = 0$ are the power-flow equations, with the control parameter Q_i incorporated in them, x is the state vector, and $\hat{x}^T$ is the co-state vector.

Note that the objective function may depend explicitly on the control parameters and it also depends implicitly on them through the power-flow equations. The explicit dependence is captured by the partial derivative $\frac{\partial J}{\partial Q_i}$ and the implicit by the term $\hat{x}^T \frac{\partial g(x,Q_i)}{\partial Q_i}$. Furthermore, the co-state vector is invariant for all additions in all possible candidate locations; therefore, it is pre-computed at the present operating condition, resulting in extremely fast computations, even for large-scale power systems. After the co-state vector is computed, the sensitivity of the objective function for each addition is simply a vector-vector multiplication, with one of the vectors being very sparse.

6.2.2 Higher-Order Sensitivity Analysis for Candidate Location Selection

The state-linearization approach, described in this section, is a variation of the objective-function-linearization algorithm for selection of candidate locations. In this method, instead of linearizing the objective function directly, the system states are linearized with respect to the VAr module addition control parameter; the objective function J is then calculated as

$$J = J\left(x^0 + \frac{dx}{dQ_i}\Delta Q_i, Q_i\right), \tag{6.7}$$

where

x^0 is the present operating condition,

x is the system state vector,

Q_i is the reactive support control parameter.

The utilization of the linearized system states in calculating the objective function provides contributions from higher-order terms in the Taylor series expansion of the

objective function with respect to the control variables. The unique potential of this method has been proven in some previous work by this research group described in [38] – [39], [41], [181]. The state-linearization sensitivity method provides the traces of objective function with curvature, which can follow the highly nonlinear variations of the original objective functions to some extent, while the objective-function-linearization method provides only the straight line. Therefore, the higher order sensitivity method is superior to the simple objective-function-linearization-based method.

The location selection is based on the computation of the objective function improvement due to a reactive support module addition and on subsequent ranking of the candidate locations on the basis of this change. Consider the objective function J. The change of J due to the addition is

$$\Delta J = J\left(x^0 + \frac{dx}{dQ_i}\Delta Q_i, Q_i\right) - J(x^0, Q_i = 0.0), \tag{6.8}$$

where x^0 is the present operating condition. The sensitivity of the state with respect to the control parameter can be easily computed as

$$\frac{dx}{dQ_i} = -\left[\frac{\partial G(x,Q_i)}{\partial x}\right]^{-1}\left[\frac{\partial G(x,Q_i)}{\partial Q_i}\right]. \tag{6.9}$$

Note that $\frac{\partial G(x,Q_i)}{\partial x}$ is the Jacobian of the system and, therefore, it is pre-computed at the present operating condition and remains invariant for all computations involving different locations. Thus for each possible location, only the partial derivatives of the power-flow equation $G(x, Q_i)$ with respect to the reactive-support control parameter need to be computed. This vector has only few nonzero entries and, therefore, the computations are extremely fast. Taking into account the sparsity of this vector can

greatly improve the efficiency of the method. It should also be noted that $\frac{dx}{dQ_i}$ is a vector of the same size as the state vector and each one of its elements is the derivative of the corresponding state with respect to the control parameter. Once the new state is computed via this linear approximation, the calculation of the new value of the objective function is a straightforward operation.

6.3 Trajectory Sensitivity Analysis

Trajectory sensitivity analysis, [161] – [177], is used in this work to determine the best candidate locations of VAr source additions, based on dynamic performance criteria and installation cost. The sensitivity of a defined objective function J with respect to the addition of a specific VAr module at a specific system location is computed along the trajectory of the dynamical system following a disturbance. This computation can be efficiently executed using again the co-state method, [37] – [41], [178] – [181], at each time step of the simulation. Utilization of trajectory sensitivities can provide information about the best candidate locations for installing additional reactive support devices, considering criteria based on the dynamic behavior of the system, as well as information about the best way of operating existing VAr sources. The sensitivities may indicate that at specific instants of time it is more beneficial to inject reactive power at a specific location (where VAr sources exist), while injection at some other location may be more advantageous at a later time.

The dynamic simulation is performed numerically using some numerical integration technique. The value of the objective function J is also computed numerically along the simulation and its final value is obtained after the simulation is finished. The numerical

technique employed in this work is the quadratic integration rule, which is more accurate and appears to have significant numerical advantages compared to other existing and commonly used techniques, while maintaining the basic desired properties. This numerical integration method is described in Chapter 5. Application of the integration rule yields a set of algebraic equations to be solved at each time step. The numerical computation of the trajectory sensitivities is based on applying the co-state method at each time step observing the set of algebraic system equations at each time step. Therefore, the problem is converted to a static problem and the actual computations are similar to the ones described in the static sensitivity analysis section, where now each time step is assumed to be an operating point, around which the linearizations are performed. These computations are described next.

First a more theoretical approach is presented. The general form of the power system equations are as in (6.10)

$$\begin{aligned} 0 &= \frac{dx(t)}{dt} - f(x(t), y(t), t, u), \\ 0 &= g(x(t), y(t), t, u), \end{aligned} \tag{6.10}$$

where

$x(t)$ is the n-dimensional vector of dynamical states,

$y(t)$ is the m-dimensional vector of algebraic states,

u is the p-dimensional vector of control variables (in this case reactive support control parameters at possible system locations),

f is the n-dimensional vector function of system dynamic equations,

g is the m-dimensional vector function of system algebraic equations.

Assume a function $h(t,x,y,u)$, the sensitivity of which is to be computed with respect to the controls, $\frac{dh}{du}$. Using the chain rule it is obtained that

$$\frac{dh}{du} = \frac{\partial h}{\partial u} + \frac{\partial h}{\partial x}\frac{dx}{du} + \frac{\partial h}{\partial y}\frac{dy}{du}. \tag{6.11}$$

The values of $\frac{dh}{du}$, $\frac{\partial h}{\partial x}$, and $\frac{\partial h}{\partial y}$ are computable analytically assuming that $h(t,x,y,u)$ is a known function. The only terms that require further computations are the trajectory sensitivities $x_u = \frac{dx}{du}$ and $y_u = \frac{dy}{du}$.

Differentiating (6.10) with respect to the control u it is obtained that

$$\frac{d}{dt}\left(\frac{dx}{du}\right) = \frac{\partial f}{\partial u} + \frac{\partial f}{\partial x}\left(\frac{dx}{du}\right) + \frac{\partial f}{\partial y}\left(\frac{dy}{du}\right)$$

or

$$\frac{dx_u(t)}{dt} = \frac{\partial f}{\partial u} + \frac{\partial f}{\partial x}x_u(t) + \frac{\partial f}{\partial y}y_u(t) \tag{6.12}$$

and

$$0 = \frac{\partial g}{\partial u} + \frac{\partial g}{\partial x}\left(\frac{dx}{du}\right) + \frac{\partial g}{\partial y}\left(\frac{dy}{du}\right)$$

or

$$0 = \frac{\partial g}{\partial u} + \frac{\partial g}{\partial x}x_u(t) + \frac{\partial g}{\partial y}y_u(t). \tag{6.13}$$

Equations (6.12) and (6.13) form a system of linear differential algebraic equations (though time-varying) in the trajectory sensitivities $x_u = \frac{dx}{du}$ and $y_u = \frac{dy}{du}$. x_u is the dynamical state of this system and y_u the algebraic. One way of performing this computational procedure is the following:

Step 0: Initialize time, $t = 0$, and the variables $x(t)$, $y(t)$, $x_u(t)$, and $y_u(t)$.

Step 1: Solve equation (6.10) for the interval $[t, t + h]$ using quadratic integration.

Step 2: Solve equations (6.12) and (6.13) for the interval $[t, t + h]$ using quadratic integration.

Step 3: Compute the sensitivity of the function h from:

$$\frac{dh}{du} = \frac{\partial h}{\partial u} + \frac{\partial h}{\partial x} x_u(t + h) + \frac{\partial h}{\partial y} y_u(t + h).$$

Step 4: Advance time $t \to t + h$ and repeat process from step 1.

Equation (6.13) can be re-written as

$$\frac{\partial g}{\partial y} y_u = -\frac{\partial g}{\partial u} - \frac{\partial g}{\partial x} x_u \Rightarrow y_u = -\left(\frac{\partial g}{\partial y}\right)^{-1} \frac{\partial g}{\partial u} - \left(\frac{\partial g}{\partial y}\right)^{-1} \frac{\partial g}{\partial x} x_u. \tag{6.14}$$

Substituting (6.14) into (6.12) yields the following equation:

$$\dot{x}_u = \frac{\partial f}{\partial u} + \frac{\partial f}{\partial x} x_u + \frac{\partial f}{\partial y}\left[-\left(\frac{\partial g}{\partial y}\right)^{-1} \frac{\partial g}{\partial u} - \left(\frac{\partial g}{\partial y}\right)^{-1} \frac{\partial g}{\partial x} x_u\right]$$

or

$$\dot{x}_u = \frac{\partial f}{\partial u} + \frac{\partial f}{\partial x} x_u - \frac{\partial f}{\partial y}\left(\frac{\partial g}{\partial y}\right)^{-1} \frac{\partial g}{\partial u} - \frac{\partial f}{\partial y}\left(\frac{\partial g}{\partial y}\right)^{-1} \frac{\partial g}{\partial x} x_u \Rightarrow$$

$$\dot{x}_u = \left[\frac{\partial f}{\partial x} - \frac{\partial f}{\partial y}\left(\frac{\partial g}{\partial y}\right)^{-1} \frac{\partial g}{\partial x}\right] x_u - \frac{\partial f}{\partial y}\left(\frac{\partial g}{\partial y}\right)^{-1} \frac{\partial g}{\partial u} + \frac{\partial f}{\partial u}.$$

Therefore, the trajectory sensitivities can be computed by the equations:

$$\begin{aligned} \dot{x}_u &= \left[\frac{\partial f}{\partial x} - \frac{\partial f}{\partial y}\left(\frac{\partial g}{\partial y}\right)^{-1} \frac{\partial g}{\partial x}\right] x_u - \frac{\partial f}{\partial y}\left(\frac{\partial g}{\partial y}\right)^{-1} \frac{\partial g}{\partial u} + \frac{\partial f}{\partial u}, \\ y_u &= -\left(\frac{\partial g}{\partial y}\right)^{-1} \left[\frac{\partial g}{\partial u} + \frac{\partial g}{\partial x} x_u\right], \end{aligned} \tag{6.15}$$

where

$\frac{\partial f}{\partial x}$: nxn Jacobian matrix of partial derivatives of f wrt x,

$\frac{\partial f}{\partial y}$: nxm Jacobian matrix of partial derivatives of f wrt y,

$\frac{\partial f}{\partial u}$: nxp matrix of partial derivatives of f wrt controls u,

$\frac{\partial g}{\partial x}$: mxn Jacobian matrix of partial derivatives of g wrt x,

$\frac{\partial g}{\partial y}$: mxm Jacobian matrix of partial derivatives of g wrt y,

$\frac{\partial g}{\partial u}$: mxp matrix of partial derivatives of g wrt controls u,

x_u : nxp matrix of trajectory sensitivities of dynamic states wrt controls,

y_u : mxp matrix of trajectory sensitivities of dynamic states wrt controls.

Equations (6.15) are of the form:

$$\dot{x}_u = A(t)x_u + B(t),$$
$$y_u = C(t)x_u + D(t),$$

with

$A = \frac{\partial f}{\partial x} - \frac{\partial f}{\partial y}\left(\frac{\partial g}{\partial y}\right)^{-1}\frac{\partial g}{\partial x}$: nxn matrix,

$B = -\frac{\partial f}{\partial y}\left(\frac{\partial g}{\partial y}\right)^{-1}\frac{\partial g}{\partial u} + \frac{\partial f}{\partial u}$: nxp matrix,

$C = -\left(\frac{\partial g}{\partial y}\right)^{-1}\frac{\partial g}{\partial x}$: mxn matrix,

$D = -\left(\frac{\partial g}{\partial y}\right)^{-1}\frac{\partial g}{\partial u}$: mxp matrix.

Note that if the control is a scalar quantity (p=1) the dimensionality of the equations is considerably reduced.

The above computation of the trajectory sensitivity can be modified and simplified if the co-state method is employed, as explained at the beginning of this section. More specifically, consider again the general nonlinear system of differential algebraic equations describing the power system behavior, as in (6.10):

$$\begin{aligned} 0 &= \frac{dx(t)}{dt} - f(x(t), y(t), t, u), \\ 0 &= g(x(t), y(t), t, u), \end{aligned} \tag{6.16}$$

where

$x(t)$ is the n-dimensional vector of dynamical states,

$y(t)$ is the m-dimensional vector of algebraic states,

u is the p-dimensional vector of control variables,

f is an n-dimensional vector function,

g is an m-dimensional vector function.

To compute the solution of (6.16) through time, equations (6.16) are solved numerically using some numerical integration rule. It is assumed that an implicit integration rule is used and in particular the quadratic integration rule. Therefore, at each time step from $t - h$ to t, the differential equations are replaced by a set of discrete difference equations and the algebraic equations $g(t, x, y, u)$ are appended to this set. Therefore, at each time step a set of algebraic equations,

$$0 = G(X, u), \tag{6.17}$$

is solved, where the new state vector X, of dimension N, contains all the unknown states, both differential and algebraic, at the time step from $t-h$ to t. Assume a function $h(t,x,y,u)$, the sensitivity of which is to be computed with respect to the controls, $\frac{dh}{du}$, at each time step, along the solution trajectory. Using the chain rule:

$$\frac{dh}{du}=\frac{\partial h}{\partial u}+\frac{\partial h}{\partial X}\frac{dX}{du}. \tag{6.18}$$

Differentiating (6.17) with respect to u the following can be obtained at each time step:

$$0=\frac{\partial G}{\partial u}+\frac{\partial G}{\partial X}\frac{\partial X}{\partial u} \tag{6.19}$$

or

$$\frac{\partial X}{\partial u}=-\left(\frac{\partial G}{\partial X}\right)^{-1}\frac{\partial G}{\partial u}. \tag{6.20}$$

Substituting (6.20) into (6.18) yields:

$$\frac{dh}{du}=\frac{\partial h}{\partial u}-\frac{\partial h}{\partial X}\left(\frac{\partial G}{\partial X}\right)^{-1}\frac{\partial G}{\partial u}. \tag{6.21}$$

By defining the co-state vector $\hat{X}^T=\frac{\partial h}{\partial X}\left(\frac{\partial G}{\partial X}\right)^{-1}$(N-dimensional), (6.21) can be re-written as

$$\frac{dh}{du}=\frac{\partial h}{\partial u}-\hat{X}^T\frac{\partial G}{\partial u}. \tag{6.22}$$

The co-state vector is independent of the control parameter u and needs to be computed at each time step. However, its computation is quite straightforward when an implicit numerical integration scheme is used for the solution of the differential-algebraic system, as is usually the case. More specifically,

$$\hat{X}^T = \frac{\partial h}{\partial X}\left(\frac{\partial G}{\partial X}\right)^{-1} \Rightarrow \hat{X}^T\left(\frac{\partial G}{\partial X}\right) = \frac{\partial h}{\partial X}. \quad (6.23)$$

The co-state vector can be computed from the solution of the above system, where

$\hat{X}^T$: N-dimensional row state vector,

$\frac{\partial h}{\partial X}$: N-dimensional row vector of the partial derivatives of h with respect to X,

$\frac{\partial G}{\partial X}$: NxN Jacobian matrix of the system (6.17).

Note that $\frac{\partial G}{\partial X}$ has been already computed and factored as part of the solution of (6.17) at each simulation step and, therefore, it is readily available after (6.17) is solved; therefore, the solution of (6.23) only needs a backward and forward substitution (slightly modified because of the row instead of column vectors). This means that computation of the co-state vector does not impose significant additional cost at each time step.

Once the co-state vector is computed the computation of the sensitivity $\frac{\partial h}{\partial u}$ is quite straightforward and very fast for any control u. The co-state vector is the same irrespectively of the control. Therefore, for a scalar u it holds that $\frac{dh}{du} = \frac{\partial h}{\partial u} - \hat{X}^T\frac{\partial G}{\partial u}$, where $\frac{\partial h}{\partial u}$ is a scalar value easily computable and $\frac{\partial G}{\partial u}$ is an N-dimensional vector of the partial of the algebraic equations at each time step with respect to the control. Thus, the sensitivity can be computed by only a vector-vector multiplication at linear cost with respect to the system dimensionality. This inexpensive procedure is the only one that is repeated for all the controls. Furthermore, $\frac{\partial G}{\partial u}$ is a very sparse vector with constant number of non-zero elements, therefore, in practice the cost is not linear in terms of the system dimensionality, but it is constant and independent of the system dimensionality. This is

an extremely important property. Thus, the total cost of computing the sensitivities of some quantity with respect to all the system controls is mainly defined by the cost of computing the co-state vector at each step, which is the cost of a backward and forward substitution. Nevertheless, this cost is minor compared to the cost of solving the nonlinear system of equations at each time step, resulting from the numerical integration. Thus, sensitivities along the solution trajectory are computed at minor additional cost, along with the system simulation.

For the study and mitigation of voltage recovery phenomena the control parameters u consist of additional VAr support of rating Q placed at candidate location i, therefore, denoted as Q_i. Thus, the control vector u is defined as

$$u = [Q_1 \quad Q_2 \quad \dots \quad Q_i \quad \dots \quad Q_p]^T,$$

where p is the number of candidate locations considered. In this case, the function $h(t, x, y, u)$ is defined as an objective function describing the system performance that is to be minimized. This will be denoted as J. A possible definition of J can be related to the duration of a voltage dip at a specific load bus. In this case,

$$J_{dip}(v(t)) = t_1 - t_2, \tag{6.24}$$

where

t_1 : transition time at which the voltage fall below threshold ($v(t) < V^{min}$),

t_2 : transition time at which the voltage recovers above threshold ($v(t) > V^{min}$).

A more general performance objective function that takes into account both the duration and magnitude of the voltage dip can be defined via the area between the voltage

curve and the threshold, during the time that the voltage is below the threshold value. This is illustrated in Figure 6.1. Such a function is mathematically defined is (6.25). A more general assumption is made here, that the quantities under consideration can be any defined system quantities, not just specific voltage magnitudes, but also some other functions or combinations of the voltages. Such quantities are generally defined as $z(t)$. Therefore,

$$J(z(t)) = \int_{t_1}^{t_2} (z_{thres.} - z(t))dt, \tag{6.25}$$

where

$z(t)$: output of interest (scalar or vector), e.g. the voltage at specific load bus(es),

$z_{thres.}$: threshold level for performance criteria, e.g. minimum acceptable voltage level,

t_1 : time at which the observation quantity of interest falls below the threshold value,

t_2 : time at which the observation quantity of interest recovers above the threshold.

The value of $J(z(t))$ is computed numerically during the system simulation, using again the quadratic integration rule, and it is know when the simulation has been completed. The sensitivity of $J(z(t))$ with respect to the controls u, $\frac{dJ}{du}$, is also computed numerically along the simulation using the co-state method, as explained earlier. The final value of the sensitivity is also computed after the simulation has been completed based on the fact that

$$\frac{dJ(z(t))}{du} = \frac{d}{du}\int_{t_1}^{t_2} (z_{thres.} - z(t))dt = \int_{t_1}^{t_2} \frac{d}{du}(z_{thres.} - z(t))dt = -\int_{t_1}^{t_2} \frac{dz(t)}{du}dt. \tag{6.26}$$

Therefore, the sensitivity value $\frac{dJ(z(t))}{du}$ is computed numerically as a summation of sensitivity values computed at each simulation step.

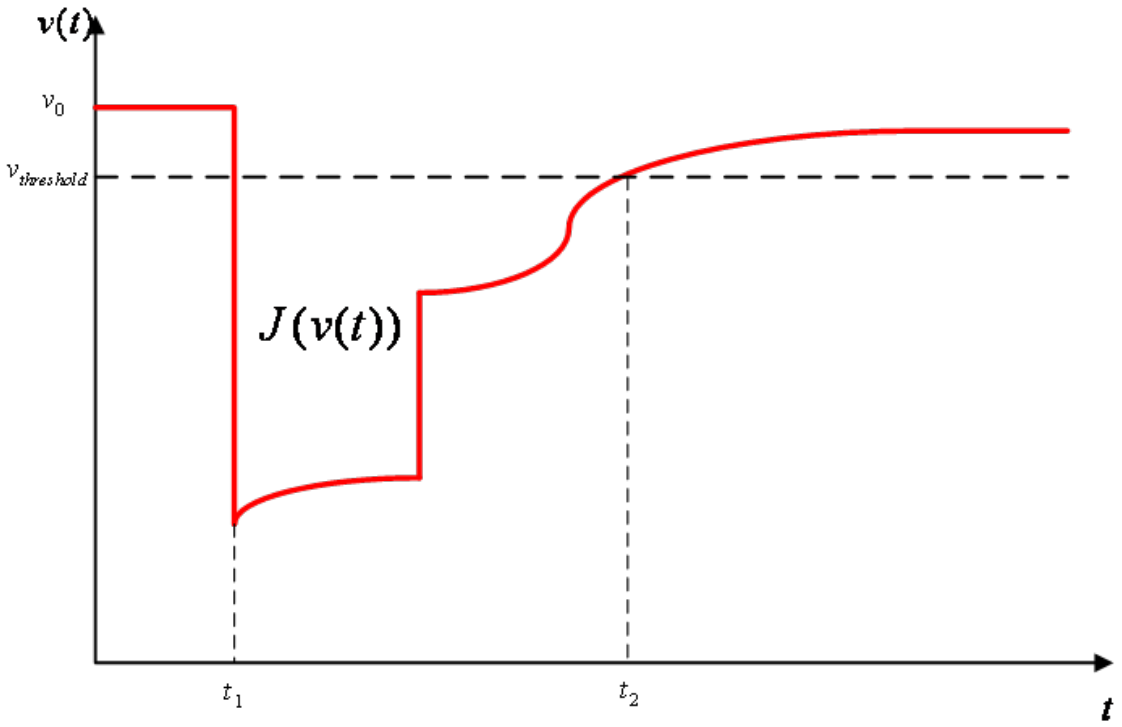

Figure 6.1: Illustration of voltage recovery and defined performance objective function.

6.4 Summary

This section of the dissertation describes the fundamentals of applied sensitivity analysis methods. In this work, sensitivity analysis is utilized for the selection of the best candidate locations for installation of additional voltage-support devices and for the implementation of a contingency ranking algorithm. This section addresses the installation of VAr sources issue; the contingency ranking is address in Chapter 7.

Under steady-state conditions sensitivity analysis is based on the computation of the derivative of an objective function or performance index with respect to a system state,

control variable, or parameter. This computation can be efficiently performed utilizing the co-state method. The static sensitivity analysis is used to select the optimal candidate locations for VAr additions based on steady-state performance criteria.

This notion has been extended to time-domain analysis, in the concept of dynamic sensitivity or trajectory sensitivity. In this case, sensitivities are computed through time along a system trajectory, resulting in a time waveform (or sequence in practice) of derivative values. The computation can be again efficiently performed at each time step of the dynamic simulation utilizing an extension of the co-state method. The resulting computational cost is small compared to the cost of the numerical integration; therefore, the computation of trajectory sensitivities does not significantly increase the computational burden of the simulation. The trajectory sensitivity analysis is used to select the optimal candidate locations for VAr additions based on dynamic performance criteria. Furthermore, the trajectory sensitivities can provide information about the optimal operation of existing VAr sources and about the most important system parameters affecting dynamic voltage problems, like the problem of slow voltage recovery.

CHAPTER 7

OPTIMAL ALLOCATION OF VOLTAGE-CONTROL DEVICES

7.1 Overview

The models and tools described in the previous sections are used for the formulation and solution of the optimization problem of allocation of voltage-control devices for the mitigation of voltage problems. While the system dynamic behavior is of primary interest in this work, standard static performance criteria can be also included, as described in the next paragraphs. Section 7.2 presents a brief overview of typical design criteria under consideration for the development of a voltage support system consisting both of static and dynamic VAr resources. Section 7.3 describes the problem and its formulation in some detail, while section 7.4 presents an overview of the proposed solution approach, based on dynamic programming. Section 7.5 describes the contingency-selection algorithm utilized in the problem formulation to account for various system contingencies.

7.2 Design Criteria

The dynamics of the system, consisting of generator response, load dynamics, and VAr support devices leads to the phenomenon of non-instantaneous recovery of the voltage following the clearance of a disturbance. The rate of voltage recovery depends on the parameters of the load, the parameters of the transmission system, the parameters of the generators and the exciter, and the parameters (type – dynamic/static and quantity) of the VAr support devices. The slow recovery of the voltage may have secondary,

unintended effects, related mainly to prolonged, abnormal system operation, undesired relay operation, or load tripping. For example, large motors are equipped with protection systems that protect them against a variety of abnormal conditions. Such protective system may trip the motor if this is deemed necessary.

One abnormal condition is low voltage for a prolonged period of time. In this case, motors overheat, because they tend to operate at higher currents and lower speeds. Furthermore, low voltage prevents motors from reaching rated speed or causes them to lose speed and draw heavy overloads. While the overload protection will eventually detect this condition, in many installations the low voltage may jeopardize production or affect electronic or digital controls, in which case the motor should be quickly disconnected. Protection from low voltage is a standard feature of AC motor controllers. The protective relay will trip instantaneously when the voltage drops below a certain value, like 50% to 70% of rated voltage. If immediate loss of the motor is not acceptable, for example in manufacturing plants, a time-delay undervoltage relay is preferred [182]. This also helps avoiding motor tripping on momentary voltage dips. In any case motors should be disconnected when severe low-voltage conditions persist for more than a few seconds [183].

Therefore, in general, the settings of motor protective systems are such that may trip the electric motor in case of the voltage remaining below a specified threshold for a pre-specified period of time. A review of present practices indicates that the protective device settings can be as strict as tripping the motor if the voltage remains below 90% of nominal for a period of more than 30 cycles.

7.3 Optimization Problem Formulation

The overall optimization methodology consists of three main parts: a) determination of the optimal location for reactive support, b) computation of amount of support, and c) determination of the optimal mix of static and dynamic support. The amount of reactive support can be, in general, computed by the solution of an optimization problem. Typically, such a problem is defined in the existing literature as a non-dynamic resource allocation problem, as described in Chapter 2. A specific snapshot of the power system under study is considered, operating under specific conditions and the problem is formulated as a static problem, not requiring a sequence of decisions, but one allocation decision for these particular system conditions. No time evolution of the system is considered.

In this proposed approach, the problem is viewed from dynamic perspective taking into consideration the evolution of the system over a particular planning horizon, and therefore requiring a sequence of decisions. In particular, the problem is formulated as follows:

Given:

- A particular power system comprising of generating units, transmission network, electric loads with specific load composition and an expected daily variation (mainly peak, shoulder, and valley load levels);
- A number of candidate buses for reactive-source placement;
- Capacitor modules of capacity Q_c MVAr, operating at specific voltage level, at cost $C_c(Q_c)$ (consisting of operating cost and installation cost);

- Dynamic VAr sources of capacity $Q_{D,min}$, $Q_{D,max}$, operating at specific voltage level, at cost $C_D(Q_{D,min}, Q_{D,max})$ (consisting of operating cost and installation cost);
- Voltage limits and voltage recovery criteria;
- A planning time-period for the study along with system changes over the planning horizon (e.g. load growth).

Compute:

The optimal selection of Q_i's for each candidate bus, i, where $Q_i = \sum Q_c$, and of $(Q_{D,min}, Q_{D,max})_i$ that minimizes the total cost, observes the voltage limits, and meets the voltage-recovery criteria.

A planning time period is defined for the study. Depending on the actual objectives, this period can be a single day, a month, or several years. When installation of new VAr sources is considered, years is the time period of interest. For other types of problems, for example operation of existing sources, shorter periods of time, such as a day or several hours, should be the total period of study. The study period is divided into smaller periods of time, for example one-year intervals, which comprise the stages of the problem. Expected load variations for these stages should be available, such as daily load curves, for a single day period, or load growth for periods of few years. Therefore, a representative load level and basic power-system configuration is defined for each stage. Transitions from stage to stage include expected load variations and other expected system configuration changes (change in load composition, commissioning of new substation, generating units, transmission lines, etc).

For each stage of the problem a series of states are defined based on VAr source additions. The state 0 is the base case (existing system) with no VAr source additions. The rest of the states are the new states after the addition of some VAr source configuration in the system. Note that it is assumed that VAr sources are added in specific, discrete module sizes and specific locations. Thus, state 1 denotes the state after the addition of one module at some place in the system, state 2 is the state after the addition of a second VAr module at a different or the same location and so on, until, theoretically, all N possible location and module combinations are considered (up to the available amount of modules or up to a certain level of modules per location). When this exhaustive enumeration is completed for the current stage, each state is evaluated in terms of a defined objective function. The objective function includes operational cost, static performance measures, as well as dynamic performance measures (such as voltage-recovery criteria) under all credible system contingencies. Then, a transition is performed to the next stage of the problem. There the procedure is repeated assuming the new operating conditions and system configuration and taking again into consideration all possible candidate locations and contingencies. The problem then moves to the next stage and this procedure keeps going until the end of the study period is reached.

Once all the states for each stage are defined the objective is to transition among states of successive stages in an optimal way, so that at the end of the study period a path of VAr source additions at each stage during the study period is defined that optimizes the total value of the defined objective function. This path is the optimal path. This procedure is illustrated in Figure 7.1. The term $Cost$ in the figure refers to the total objective function used to evaluate each state, as described later in this chapter.

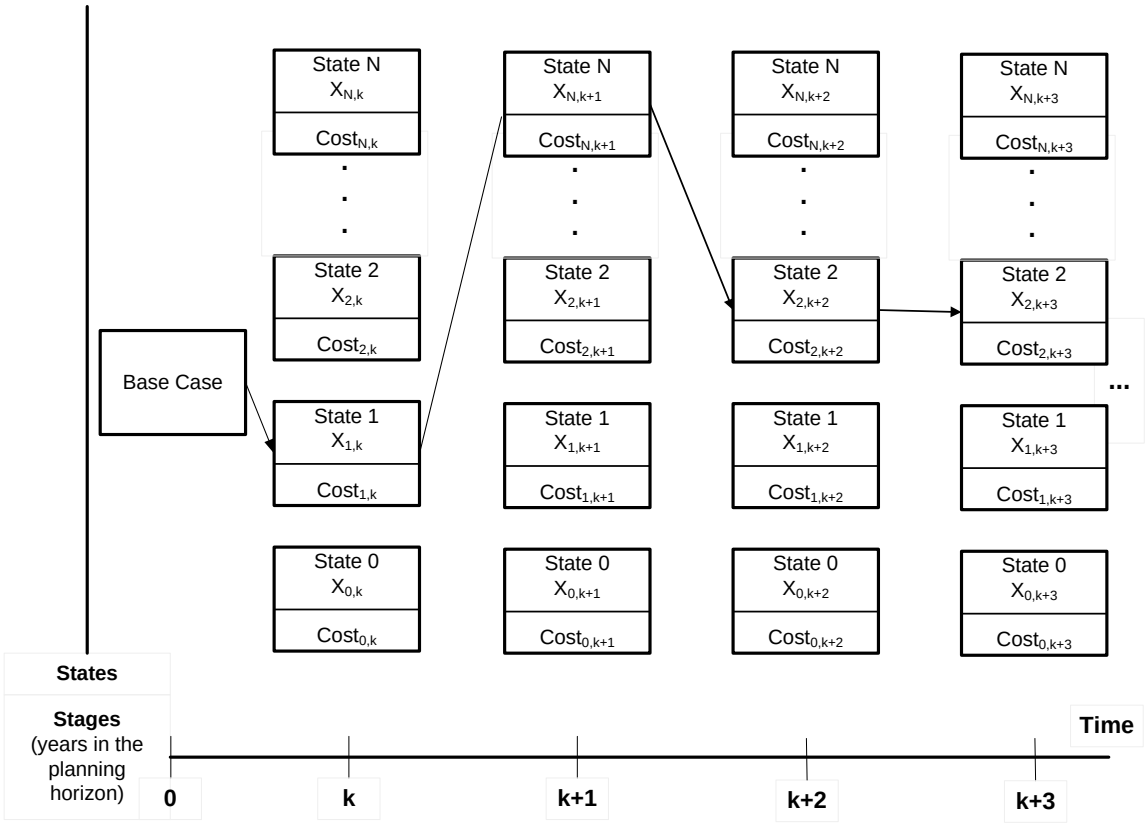

Figure 7.1: Illustration of planning problem for allocation of reactive resources.

The transitions from state to state from one stage to the next stage are performed based on specific rules. Only transitions (forward) that add VAr sources are allowed. If a resource is added at some point it cannot be removed at a later stage. Therefore, such a transition is not allowed. A state, X_i, at stage, T_k, is acceptable only if it meets both static and dynamic performance criteria, like voltage-recovery criteria. A penalty function is applied to the cost function, for states that do not satisfy the performance criteria, based on the deviation of these criteria. Theperformance criteria were discussed in Chapter 6 and they are briefly repeated here.

Steady-state voltage magnitude at load buses (of interest):

This can be expressed by utilizing a voltage index defined as

$$J_V = \sum_{k=1}^{N} w_k \left(\frac{V_k - V_{k,mean}}{V_{k,step}} \right), \tag{7.1}$$

where

w_k : weighting factor, $0 < w_k < 1$,

$V_{k,mean}$: nominal bus voltage value (typically 1.0 p.u.),

(it is in general the mean value in the desired range, i.e. $0.5\left(V_k^{max} + V_k^{min}\right)$),

$V_{k,step}$: voltage deviation tolerance (i.e. $0.5\left(V_k^{max} - V_k^{min}\right)$),

V_k : actual voltage magnitude at bus k,

n : positive integer parameter defining the exponent,

N : total number of buses of interest.

Voltage-sag magnitude and duration below a predefined value, or equivalently, voltage-recovery rate at certain load buses of interest.

This can be expressed by utilizing a functional of the form

$$J_{dip}(v(t)) = t_1 - t_2, \tag{7.2}$$

where

t_1 : transition time at which the voltage fall below threshold ($v(t) < V^{min}$),

t_2 : transition time at which the voltage recovers above threshold ($v(t) > V^{min}$),

or more generally of the form (recovery index)

$$J_R(z(t)) = \int_{t_1}^{t_2} (z_{thres.} - z(t))dt, \tag{7.3}$$

with

$z(t)$: output of interest (scalar or vector), e.g., voltage at specific load bus(es),

$z_{thres.}$: threshold level for performance criteria, e.g., minimum acceptable voltage level,

t_1 : time at which the observation quantity of interest fall below threshold value,

t_2 : time at which the observation quantity of interest recovers above threshold.

The annualized cost $C(X)$ of installing and operating VAr sources depends on the type of VAr support device, the rated power, and the location of placement (included in the X vector representing specific VAr source addition).

Therefore, the problem is a multi-objective optimization problem. A typical way of approaching the problem is by combining all the objectives in one composite objective. Thus, a typical expression of the objective function to be minimized would be a weighted sum of the above components:

$$J(X) = W_1 C(X) + W_2 f_V\left(\sum_{i=1}^{n} J_{V,i}\right) + W_3 f_{dip}\left(\sum_{i=1}^{n} J_{dip,i}\right) + W_4 f_R\left(\sum_{i=1}^{n} J_{R,i}\right), \quad (7.4)$$

where

W_j : objective weights,

C : annualized cost of installation and operation,

f : performance penalty functions,

n : total number of considered cases (base case plus selected contingencies).

This objective function is used for defining the $Cost$ function of Figure 7.1. Furthermore, the components of the objective function may also provide valuable information about

the type of VAr source additions. The value of the J_V component and its sensitivity with respect to a specific VAr addition reflects the improvement on steady-state network conditions and, therefore, towards capacitor placement. The value of the J_R (or J_{dip}) component and its sensitivity with respect to a specific VAr addition reflects the improvement on dynamic behavior and, therefore, towards dynamic VAr source placement.

7.4 Solution Method

7.4.1 Overview

The above problem is a nonlinear, discrete, optimization problem that can be viewed as an optimal path problem requiring a sequence of decisions. Due to the dynamic nature of the problem dynamic programming [184], [185] is the solution approach considered, in combination with sensitivity analysis.

7.4.2 Dynamic Programming

Dynamic programming is an optimization procedure that is particularly applicable to problems requiring a sequence of interrelated decisions. Each decision transforms the current situation into a new situation. A sequence of decisions, which in turn yields a sequence of situations, is sought that maximizes (or minimizes) some measure of value. The value of a sequence of decisions depends on the values of the individual decisions and situations in the sequence [185].

The power of dynamic programming is based on two simple key ideas: The principle of optimality and the notion of recursion. The principle of optimality states that the best sequence of situations from situation A to situation B, referred also as a path

from A to B, has the property that, whatever the initial decision at A, the remaining path to B, starting from the next point after A, must be the best path from that point to B. Alternatively, the principle of optimality can state that the best path from A to any situation B has the property that whatever the situation before B, call it C, the path must be the best path from A to C [185]. The first statement is the basis for the backward dynamic programming formulation, while the second is the basis for the forward dynamic programming formulation. Recursion is a methodology that suggests that the solution of a problem depends on solutions to smaller instances of the same problem. Thus, recursion operates by repeatedly solving the same problem of smaller size or dimensionality, until the problem becomes very simple and its solution becomes trivial. A recursive process is defined by its recurrence relation, which relates a problem of certain size to one or more problems of smaller size, and by the termination conditions, which are the solutions of the trivially simple subproblems. Therefore, a given problem can be solved using dynamic programming if the values of the best solutions of certain subproblems can be determined and at some point at or near the end of the "whole problem" the subproblems are so simple as to have trivial solutions [185].

In the terminology of dynamic programming the rule that assigns values to the various subproblems is called the optimal value function. This function can have several arguments that describe the current situation and thus uniquely define a particular subproblem. In general, one of these arguments (variable) describes how many decisions have thus far been made and it is one larger on the right-hand side of the recurrence relation than on the left, regardless of the particular decision. For some definitions of the arguments of the optimal value function, this variable might decrease instead of increase

by one after each decision. This particular monotonic variable is called the stage variable. All the remaining variables needed to describe the current situation, given the stage variable, are called state variables. The values of the stage and state variables constitute a description of the situation adequate to allow a dynamic programming solution. The rule that associates the best first decision with each subproblem is called the optimal policy function. The principle of optimality yields a formula or set of formulas relating various values of the optimal value function. This formula is called a recurrence relation. Finally, the value of the optimal value function for certain arguments is assumed obvious from the statement of the problem and from the definition of the function with no computation required. These obvious values are called the boundary conditions on the optimal value function [185].

Using this terminology, to solve a problem by means of dynamic programming the arguments of the optimal value function are chosen and hat function is defined in such a way as to allow the use of the principle of optimality to write a recurrence relation. Starting with the boundary conditions, the recurrence relation is then used to determine concurrently the optimal value and policy functions. When the optimal value and decision are known for the value of the argument that represents the original whole problem, the solution is completed and the best path can be traced out, by backtracking, using the optimal policy function alone [185].

7.4.3 Truncation of Search Space – Successive Approximations

Conceptually, the methodology described in 7.4.2 can be applied to the problem formulation described in section 7.3 in a way that will consider all possible states at every stage and all possible contingencies. Dynamic programming can be applied to find the

optimal path when all the states are evaluated. Each stage is defined as a time instant, like a year; a state is defined as a specific combination of locations with specific VAr source additions. The optimal value function of the i^{th} state of stage *k*, denoted as state $X_{i,k}$, is defined, in a forward dynamic programming formulation, as the minimum value of the objective function $Cost(X_{i,k})$ (based on the definition in (7.4)) that can be attained from the starting base case, at stage 0 to the current state $X_{i,k}$ and is denoted by $Cost^*(X_{i,k})$. The transition from state to state is based on the recurrence relation:

$$Cost^*(X_{i,k+1}) = \min_j\left[Cost^*(X_{j,k}) + T(X_{j,k} \rightarrow X_{i,k+1})\right], \tag{7.5}$$

where $T(X_{j,k} \rightarrow X_{i,k+1})$ is the transition cost from state $X_{j,k}$ of stage *k*, to state $X_{i,k+1}$ of stage *k+1* and the minimization is performed over all possible states *j* of stage *k* that can transition to state *i* of stage *k+1*. This transition cost is computed based on the objective function defined in equation (7.4) and includes the performance functions of the new state, the operating cost of the new state, plus the installation cost of the additional VAr sources from one state to the other. Finally, the boundary condition for the dynamic programming recursion is that at the initial base case it holds that $Cost^*(X_{0,0}) = Cost(X_{0,0})$. This cost can also be set to zero, since it is a common part of all the subsequent states and stages and its absolute value is not of interest. This approach is graphically illustrated in Figure 7.2.

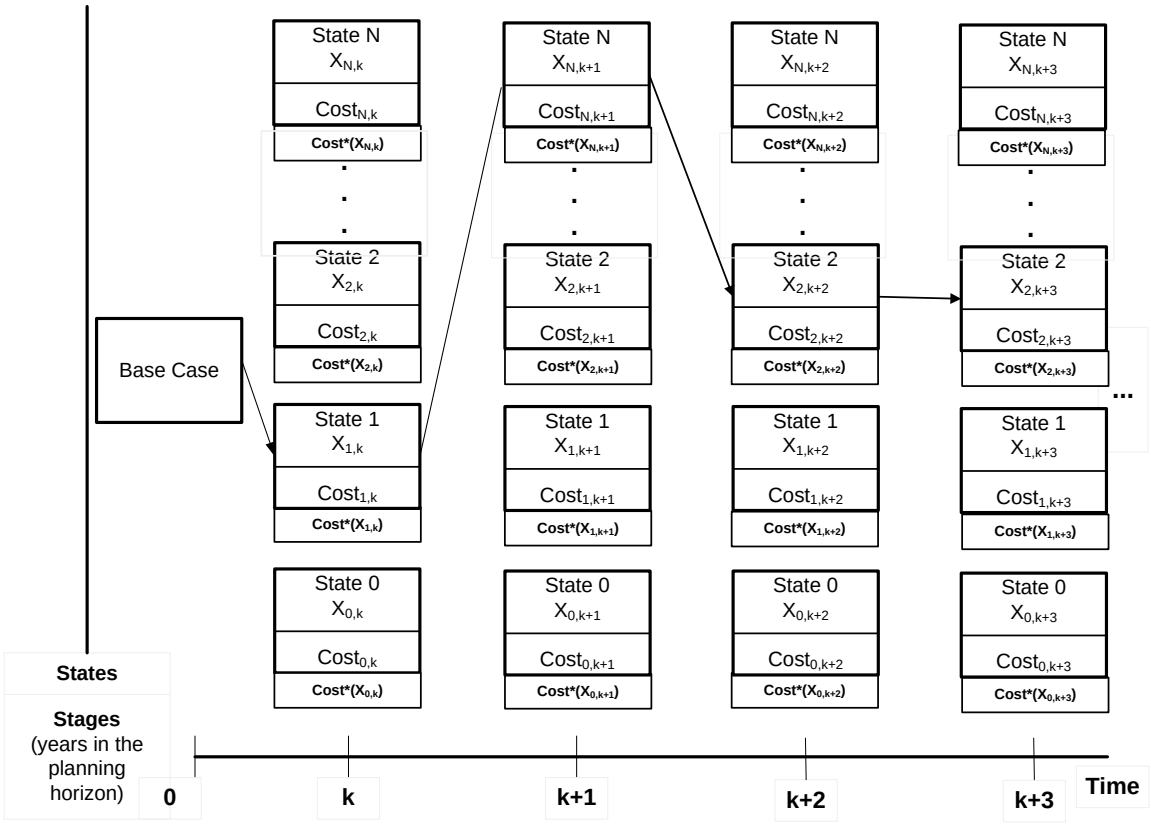

Figure 7.2: Illustration of planning problem for allocation of reactive resources considering the dynamic programming solution approach.

However, this approach that considers all possible states at every stage and all possible contingencies makes the problem computationally intractable, even theoretically, because of the huge number of possible states. For example if one considers the possibility of adding VAr sources at n_{VS} buses at up to m_{VS} different sizes per location (including no addition), then the number of possible states per stage will be ${m_{VS}}^{n_{VS}}$. Even for a very small test system of 10 possible locations with two possible additions per locations (i.e. three states per location: 0 additions, 1 addition, 2 additions) the total number of possible combinations will be $3^{10} = 59049$ states per stage! Alternatively, if one considers a slightly different problem and assumes the possibility of adding VAr

sources at n_{VS} locations having a total of l_{VS} modules available (having the possibility that all could be installed in a single location), then the number of possible states per stage will be $\binom{n_{VS}+l_{VS}-1}{n_{VS}-1}$. Again even for a small test system of 10 possible locations with a total of 10 modules available the total number of possible combination would be $\binom{19}{9} = 92378$ states per stage! This makes the problem practically intractable. If in addition all possible contingencies are to be considered at each state, say up to level 2 the number of contingencies per state will be approximately $(n_L + n_G)^2$ where n_L is the number of circuits in the system and n_G is the number of units in the system. For even a small system the product of this number and the total number of states, which indicates the number of simulations needed, will be humongous.

However, one does not need to take this brute force approach (and cannot take it in practice). The method of successive dynamic programming has been developed to address the dimensionality problem. Specifically, the basic idea of successive dynamic programming is to limit the number of states at every stage to a very small number. The small number of the states is selected with sensitivity methods that guarantee that these states will provide the states that will be part of the optimal solution. For this problem, the states are defined in terms of the most effective additions of dynamic or static VAr sources, and each state also includes only the most critical contingencies. Therefore, a small number of states are defined around the present iterate of the system trajectory (defined with the sequence of decisions to add static/dynamic VAr sources to the various system buses). The pass among all the problem stages is repeated successively, until the

computed series of optimal states has converged to a unique path (sequence of optimal states through the problem stages).

Referring to Figure 7.2, for each stage of the problem a series of states is defined based on combinations of VAr source additions. Only the first few best candidate locations are considered, based on static and dynamic sensitivity analysis. The state 0 is the base case with no VAr source additions. The state 1 is the new state after the addition of a VAr source module at some location in the system, and so on. Note again that it is assumed that VAr sources are added in specific, discrete module sizes. When this procedure is completed for the selected locations for the each stage the whole search space of states for all stages is created. Then each state is evaluated in terms again of the defined objective function, as in (7.4). As it was explained in the previous section as well, this objective function includes static performance measures, installation and operational cost, as well as dynamic performance measures (like voltage-recovery time) under a few specific system critical contingencies, selected via sensitivity methods. Once all the states are evaluated the dynamic programming recursion (7.5) is applied. Starting for the base case stage a transition is performed to the next stage of the problem, and subsequently, all the following stages, and this procedure keeps going until the end of the study period is reached. Note that after the end of the study period is reached a path of VAr source additions at each stage during the study period is defined. However, this path might not be optimal, due to the fact that only a small subset of locations and contingencies were considered and also only one addition per location per stage was assumed. Therefore, the procedure is repeated successively starting form the first state of the path that was computed during the first iterate. The states of this path are now the base cases of every

stage and all the sensitivity analyses of the next iterate is based on the operating conditions of these new bases cases belonging to the path computed during the previous iterate.

Again if one considers the possibility of adding VAr sources at n_{VS} location at up to m_{VS} different sizes per location (including no addition), then the number of possible states per stage will be ${m_{VS}}^{nvs}$. If now n_{VS} is only the 2 most favorable possible locations, selected via sensitivity analysis with two possible additions per locations (i.e., three states per location: 0 additions, 1 addition, 2 additions) the total number of possible combinations will be $3^2 = 9$ states per stage! This makes the problem very tractable in practice. If in addition only the two or three most important first level contingencies are to be considered at each state, chosen via sensitivity-based contingency screening, then the number of computations per state also stays within low and tractable values.

A set of feasible locations for reactive support can be determined based on the system topology and the physical constraints of the system under study. Such a procedure selects a small number of system buses where support can actually be installed and is based on system data, utility practices, preferences, and experience. Then, the best candidate locations are selected based on sensitivity analysis. Static sensitivity analysis can be used to determine locations based on steady-state performance criteria. Trajectory sensitivity analysis methods can be applied to determine locations based on dynamic criteria and also to illustrate optimal operation and control strategies for such devices during voltage recovery or other transient phenomena. A methodology for efficient computation of static and dynamic sensitivities was presented in Chapter 6. Since the results of sensitivity analysis depend on the system configuration, the system operating

point (mainly determined by the load level), the performance criteria, and the disturbances into consideration, some prescreening has to be performed in advance in such a way that the most common system operating states are considered and the most important disturbances are studied, for the desired performance criteria (for example, voltage-recovery criteria). Sensitivity analysis, in particular dynamic trajectory sensitivities, can be also used to determine the optimal mix of static and dynamic support, based on voltage-recovery criteria, once the amount of total compensation for a location is determined.

A flow diagram of the successive dynamic programming approach is presented in Figure 7.3.

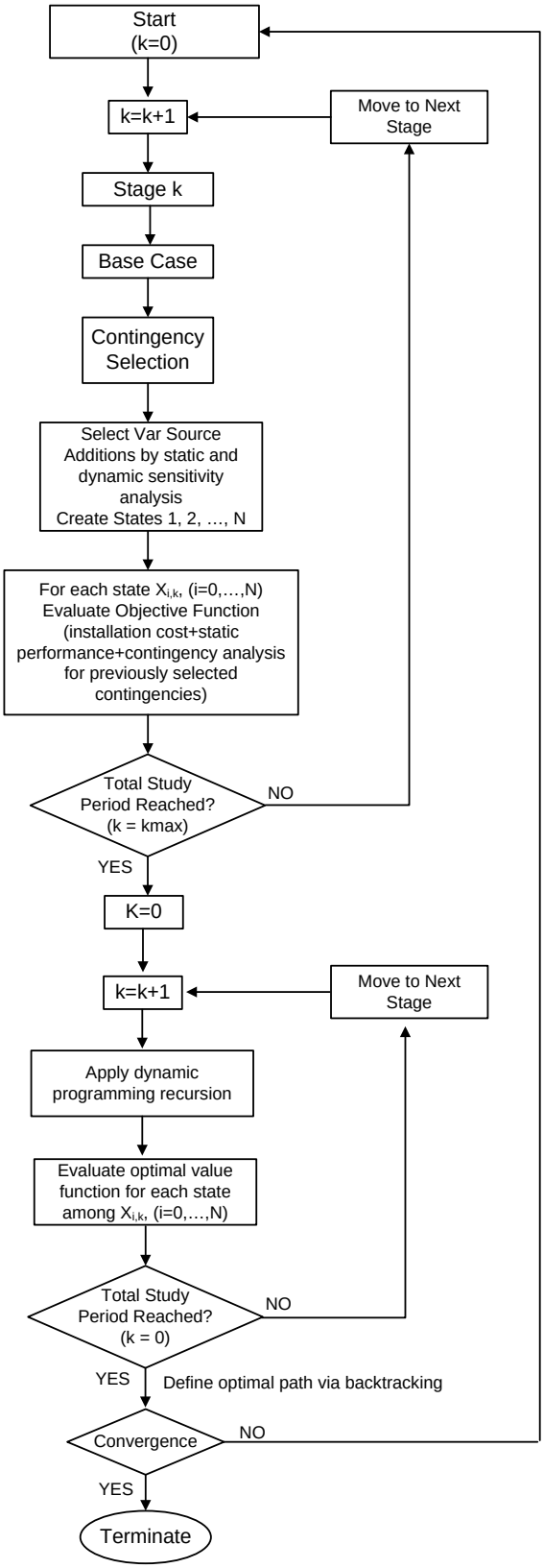

Figure 7.3: Flow diagram of proposed successive dynamic programming approach.

7.4.4 Single-Stage Resource Allocation

This paragraph addresses the issue of allocating specific reactive resources to a particular system configuration at some particular time. This problem can be formulated as a resource allocation problem assuming that the power system operates under specific operating conditions, like assuming only one stage of the planning problem described in section 7.3. This is usually the way the reactive support allocation problem is formulated in the literature, as explained in Chapter 2. In this section a procedure to address this resource-allocation problem will be presented, based again on dynamic programming. Thus, this section will also illustrate the application of dynamic programming to a problem that is not really dynamic, in the sense of requiring a sequence of decisions.

The resource allocation problem, in its simplest form, is described as follows: Assume N units of resource are available (dynamic VAr modules or capacitor modules) and need to be allocated among P candidate locations. An objective function J is also given, as described previously, representing the cost and performance realized by a particular allocation of resources. The problem is to allocate all of the N units of resource at specific locations so as to minimize the combined performance index, i.e. to choose P nonnegative integers $n_i,\ i = 1, \dots, P$ that maximize the performance index (objective function) J subject to the constraint $\sum_{i=1}^{P} n_i = N$ [185].

Although, as stated, the choice of the solution set $n_i,\ i = 1, \dots, P$ seems to be a single decision made at a particular time, to use dynamic programming the problem is viewed differently. Having designated the candidate locations by arbitrary but fixed numbers from 1 to P, from the N units of resource an amount n_1 is first allocated to the first location. Then n_2 units of the remaining $N - n_1$ units of resource are allocated to the

second location, then n_3 units of resource to the third location and so on. Viewed in this sequential fashion and assuming that several allocations have already been made at some particular point in the decision sequence the essential knowledge to proceed is the location that is currently under consideration and how much of the available resource is still unallocated. Therefore, for the backward dynamic programming formulation a stage is defined as the current location under consideration and the state as the remaining units of resource to be allocated at the current stage. The optimal value function, $f_k(n)$, is defined as the minimum value of the defined objective function that can be obtained from locations k through P, given n units of resource remaining to be allocated. Utilizing the principle of optimality the appropriate recurrence relation is

$$f_k(n) = \min_{n_k=0,1,\dots,n}[J([n_k|p_{k+1}(N-n_k)])]\,, \tag{7.6}$$

where n_k is the allocation to location k and $f_k(n)$ must be computed for $n = 0, \dots, N$. $p_k(n)$ is the optimal policy function at stage k, state n. That is, $p_k(n)$ denotes the optimal allocation to location k if there are n units of resource to distribute to locations k, $k+1$, …, P. Hence, $p_k(n)$ is the value of n_k that minimizes the right-hand side of (7.6). The minimization term $J([n_k|p_{k+1}(N-n_k)])$ is the value of the objective function for the allocation n_k to location k, given that the optimal allocation policy will be applied from the next stage on. The boundary conditions are $f_P(n) = J(n_p = n)$, for $n = 0, \dots, N$. The answer to the problem is given by $f_1(N)$ and the optimal policy is $p_1(N)$ [185]. The described procedure is illustrated in Figure 7.4.

In terms of computational effort it can be computed that the dynamic programming approach requires a total number of $(P-2)\sum_{i=1}^{N} i + 2N$ cases to be evaluated and thus

the same number of calculation of the defined objective function. The full enumeration requires $\binom{N+P-1}{P-1}$ cases to be evaluated for assigning N resources to P different locations. For a small case of $P = 10$ locations and $N = 5$ resources the full enumeration requires $\binom{14}{9} = 2002$ objective function evaluations, while the dynamic programming requires $8 * 15 + 10 = 130$ evaluations. This improved computational efficiency is illustrated in Figure 7.5 and Figure 7.6. Figure 7.5 shows two plots (linear and logarithmic vertical scales) of the required number of cases to be evaluated versus the dimensionality of the problem for $N = P = M$ and for values of M ranging from 1 to 15. The computational effort of the complete enumeration approach grows exponentially, while the dynamic programming approach remains within tractable limits. For $M = 15$ the difference in computational effort is almost 5 orders of magnitude.

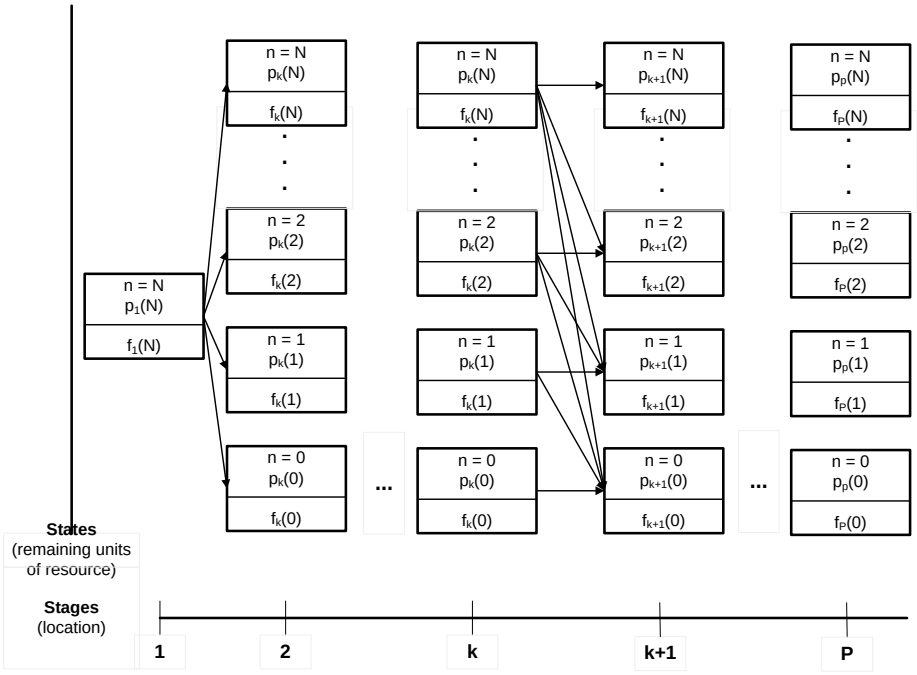

Figure 7.4. Illustration dynamic programming solution approach for the resource allocation problem.

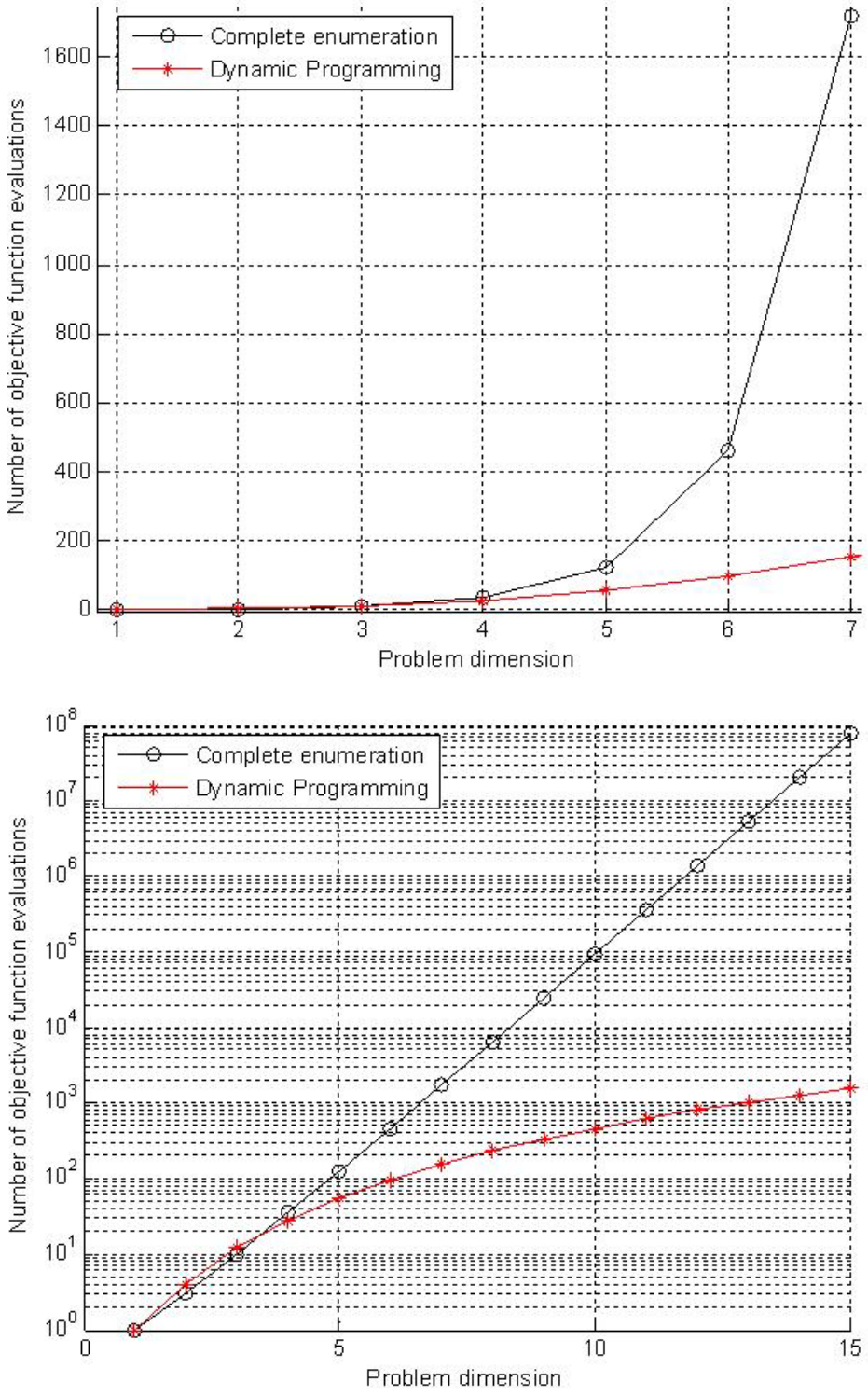

Figure 7.5: Comparison of direct enumeration and dynamic programming approach for the resource allocation problem (for equal number of resources and locations).

These conclusions are also verified by Figure 7.6, which shows again two three-dimensional plots (linear and logarithmic) of the required number of cases to be evaluated versus the dimensionality of the problem for all the different possible combinations of values of resources (N) and locations (P), for values of both parameters ranging from 1 to 15.

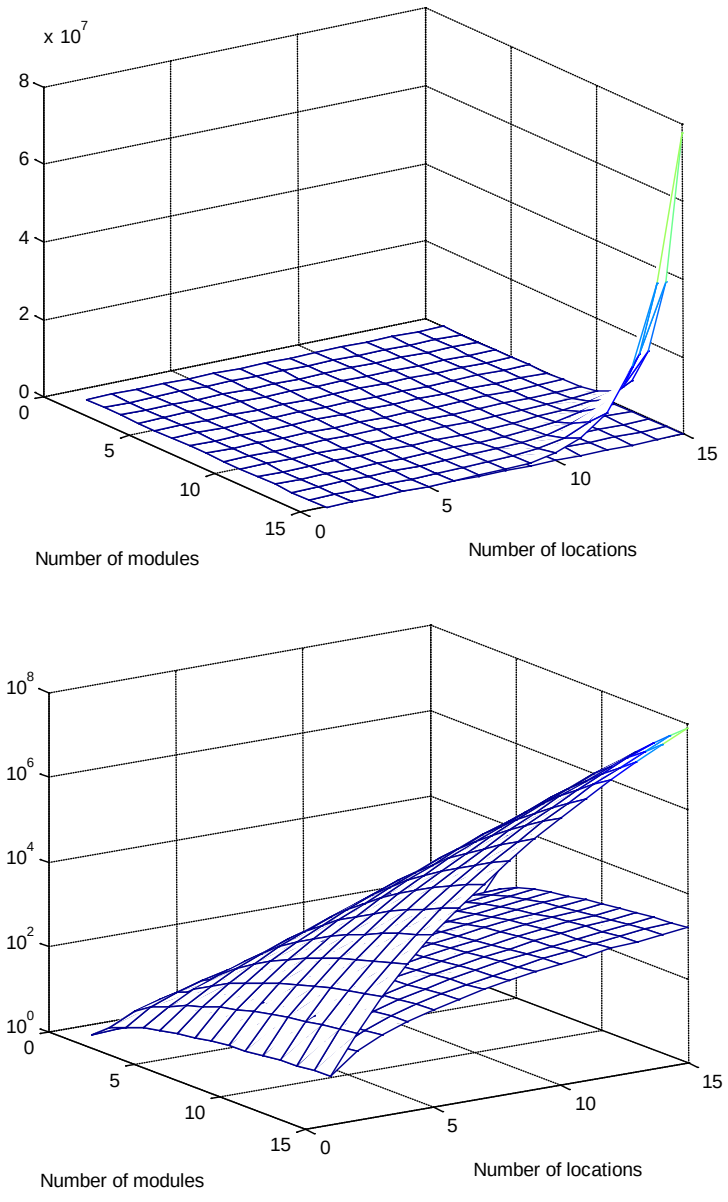

Figure 7.6: Comparison of direct enumeration and dynamic programming approach for the resource allocation problem (all combinations for up to 15 resources and locations).

A more complicated variation of this problem assumes that there are two types of resource to be allocated to the P locations with N_1 units of resource-type 1 and N_2 units of resource-type 2. These two types of resource can represent static and dynamic VAr sources. The problem is approached in a similar way. The stage is again defined as the location currently under consideration and the state as the remaining units or resources, for both types 1 and 2, to be allocated at the current location. Note that two arguments are needed in this case to define the state. Therefore, for the backward dynamic programming formulation the optimal value function, $f_k(n_1, n_2)$, is defined again as the minimum value of the defined objective function that can be obtained from locations k through P, given n_1 units of resource 1 and n_2 units of resource 2. The appropriate recurrence relation is

$$f_k(n_1, n_2) = \min_{\substack{n_{1k}=0,1,\ldots,n_1 \\ n_{2k}=0,1,\ldots,n_2}} [J([(n_{1k}, n_{2k})|p_{k+1}(N_1 - n_{1k}, N_2 - n_{2k})])] \,, \tag{7.7}$$

where n_{1k} and n_{2k} are the allocations to location k and $f_k(n_1, n_2)$ must be computed for $n_1 = 0, \ldots, N_1$ and $n_2 = 0, \ldots, N_2$. $p_k(n_1, n_2)$ is the optimal policy function at stage k, state (n_1, n_2) and the term $J([(n_{1k}, n_{2k})|p_{k+1}(N_1 - n_{1k}, N_2 - n_{2k})])$ is the value of the objective function for the allocation (n_{1k}, n_{2k}) to location k, given that the optimal allocation policy will be applied from the next stage on. The boundary condition is $f_P(n_1, n_2) = J(n_{1p} = n_1, n_{2p} = n_2)$, for $n_1 = 0, \ldots, N_1$ and $n_2 = 0, \ldots, N_2$. The answer to the problem is given by $f_1(N_1, N_2)$ and the optimal policy is $p_1(N_1, N_2)$.

7.5 Contingency Selection

The selection of the optimal mix of static and dynamic VAr sources should yield a system that will provide voltage regulation for the normal operating conditions of the

system and all credible contingencies. Contingencies mainly include systems faults that result in line outages and loss of generation. Such faults may be symmetric or asymmetric. Furthermore, more detailed contingencies can be considered, like specific breaker operation or disoperation, protective relaying operation or disoperation and so on. This work will not go into detail on specific types of contingencies and will mainly concentrate on system short circuits and line outages. However, the work performed during this thesis and the models developed have laid the foundation for easily modeling very detailed type of system contingencies, both symmetric and asymmetric. The optimal selection for the static and dynamic VAr sources should be such that the system performance/constraints are met for any credible contingency of the system. Therefore, a procedure is described below for selecting the credible contingencies and then the overall optimization problem is defined in the space of the selected contingencies.

One of the main computational issues in voltage-recovery studies is the selection of simulation scenarios, to be studied. Clearly not all possibly contingencies and faults can be considered in a system; therefore, contingency ranking and selection are of uttermost importance, to limit the analysis space. Specifically, the most critical contingencies, in terms of voltage problems, from all possible contingencies need to be identified and analyzed. For large-scale systems, the process imposes a substantial computational burden. For this reason, there have been consistent efforts to invent fast contingency selection algorithms and subsequent contingency analysis. Significant developments in the area of contingency selection include (a) contingency ranking with performance indices (PI) [186], (b) local solutions based on concentric relaxation [187], and (c) bounding methods [188], [189]. In addition, significant developments for contingency

analysis include the introduction of the fast decoupled power flow [190], the sparsity-oriented compensation method [191], the sparse vector methods [192], and the partial refactorization method [193].

Much attention on this issue has been focused on subnetwork solutions, which solve for a subset of state variables, using sparse vector methods. A typical application of subnetwork solutions to contingency selection is the bounding method [188], [189]. The subnetwork solution method had been also generalized with the zero-mismatch approach [194], which is an iterative solution method for AC power flow and is effective for both contingency screening and analysis.

Typical contingency selection methods consist of either ranking methods using a performance index (PI) or screening methods based on approximate power-flow solutions. It is widely recognized that PI-based methods are efficient, but vulnerable to misrankings, while screening methods are more accurate but inefficient. It has been also identified that the inaccuracies of the PI-based methods are mainly due to (a) nonlinearities of the system model [195] and (b) discontinuities of the system model arising from generator reactive-power limits and regulator tap limits [178], [179].

A hybrid contingency selection method had been proposed in the past, which takes advantage of the best features of the two approaches [178]. This method utilizes a procedure based on the concept of contingency stiffness index to identify “nonlinear contingencies” and a performance index method to identify contingencies causing discontinuities. While the hybrid method performs very well, the computational burden is significantly greater than pure PI-based methods.

This section describes the development and implementation of contingency ranking and selection algorithms as part of a power-system analysis program [41], [180], [181]. The implementation is based on PI-based methods and on the use of the "quadratized" power-flow system model. Each contingency is modeled with the introduction of a contingency or outage control variable. The ranking is based on the value of the sensitivity of the performance index with respect to the contingency control variable for each contingency. The computation of the sensitivities is performed using the very efficient co-state method. Moreover, this work introduces some new concepts as a way for improving the accuracy of the PI-based contingency ranking methods. The basic concept is the use of state-linearization rather than performance-index-linearization with respect to the outage variable and it appears to provide more accurate results in contingency ranking and selection, at the expense of slightly increased computational time. However, with the appropriate use of sparsity techniques this increase can become minimal. The methodology implementation is demonstrated with two simple systems. The PI-contingency selection is implemented as part of a power-system-analysis program and it is used in combination with compensation-based contingency-analysis method for steady-state security assessment and as a pre-filter for contingency ranking in power-system voltage-recovery analysis.

7.5.1 First-Order Index-Linearization PI Methods for Contingency Ranking

PI-based contingency-ranking methods reported in the literature are based on the evaluation of the PI gradient with respect to an outage. In [178] – [181] a rigorous definition of an outage has been proposed with the use of the outage (or contingency) control variable u_c, which has the following property [178] – [181]:

$$u_c = \begin{cases} 1.0, \text{ if the component is in operation,} \\ 0.0, \text{ if the component is outaged.} \end{cases} \tag{7.8}$$

The outage control variable is used in the component modeling of a power system, as illustrated in Figure 7.7 and Figure 7.8.

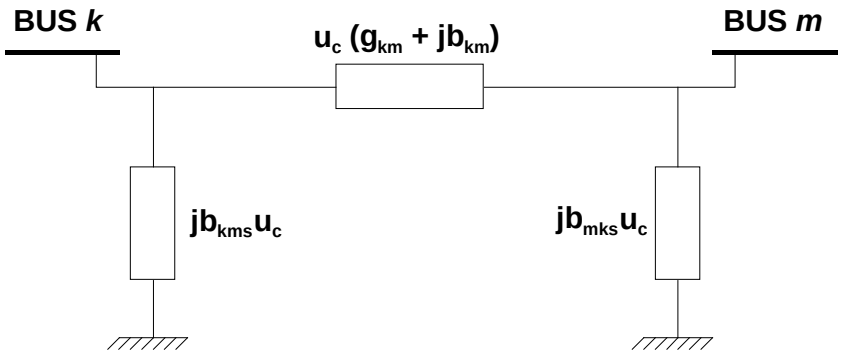

Figure 7.7: Circuit outage control variable u_c [37], [38].

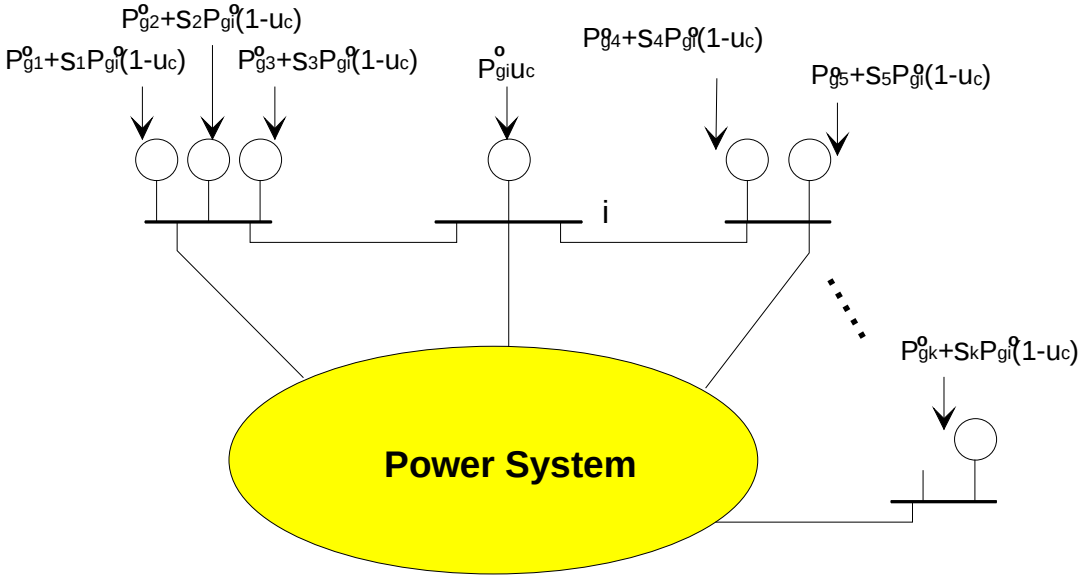

Figure 7.8: Generating unit outage control variable u_c [37].

Note that in the case of a generator outage, the outage control variable not only affects the power produced by the outaged unit, but also indicates the re-dispatch of its produced power to the remaining units, via a re-dispatch algorithm (Figure 7.8 illustrates a linear

re-dispatch, based on participation factors). The contingency control variable can not only model independent contingencies, like the ones indicated above, but can be also effectively used to model common mode contingencies, i.e., contingencies that are dependent upon each other. Such a situation is illustrated in Figure 7.9.

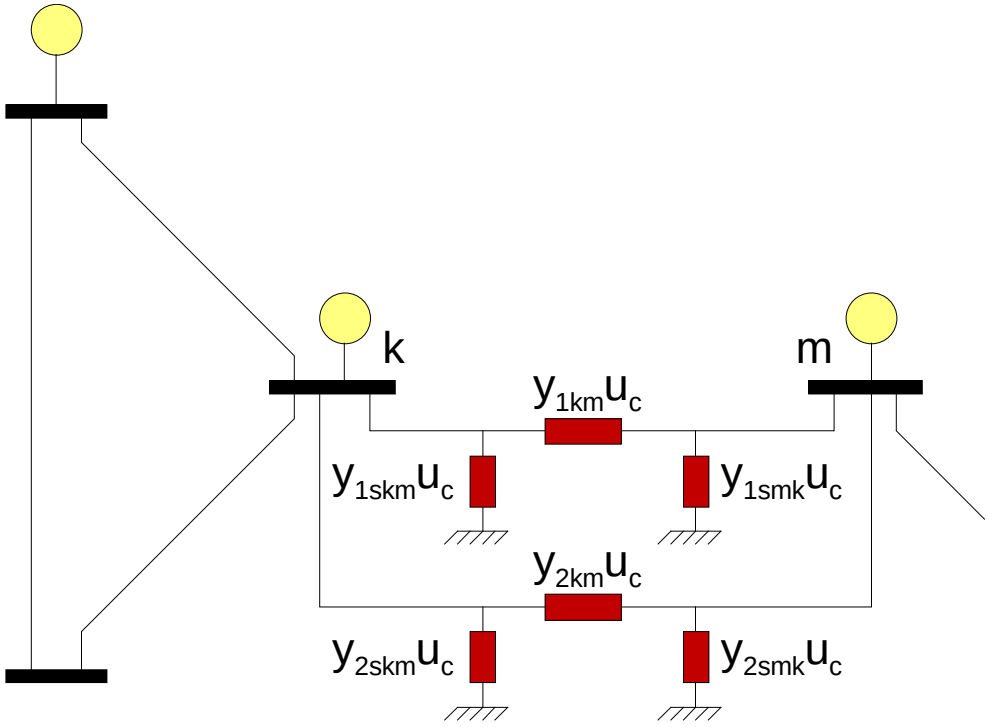

Figure 7.9: Representation of common mode outages with control variable u_c.

Depending on the purpose of contingency selection, a variety of performance indices can be utilized:

- *Circuit current-based index:*

$$J_C = \sum_j w_j \left(\frac{I_j}{I_{N,j}}\right)^{2n}, \tag{7.9}$$

where

w_j : weighting factor, $0 < w_j < 1$,

$I_{N,j}$: current-based thermal limit of the line,

I_j : magnitude of actual current through circuit j,

n : positive integer parameter defining the exponent.

- *Circuit power-based index:*

$$J_S = \sum_j w_j \left(\frac{S_j}{S_{N,j}}\right)^{2n}, \tag{7.10}$$

where

w_j : weighting factor, $0 < w_j < 1$,

$S_{N,j}$: power-based thermal limit of the line,

S_j : apparent power through circuit j,

n : positive integer parameter defining the exponent.

- *Voltage index:*

$$J_V = \sum_{k=1}^{N} w_k \left(\frac{V_k - V_{k,mean}}{V_{k,step}}\right)^{2n}, \tag{7.11}$$

where

w_k : weighting factor, $0 < w_k < 1$,

$V_{k,mean}$: nominal bus voltage value (typically 1.0 p.u.), (it is in general the mean value in the desired range, i.e. $0.5(V_k^{max} + V_k^{mean})$),

$V_{k,step}$: voltage deviation tolerance (i.e. $0.5(V_k^{max} - V_k^{mean})$),

V_k : actual voltage magnitude at bus k,

n : positive integer parameter defining the exponent,

N : total number of PQ buses.

- *Generation reactive power index*:

$$J_Q = \sum_{j=1}^{L} w_j \left(\frac{Q_j - Q_{j,mean}}{Q_{j,step}}\right)^{2n}, \quad (7.12)$$

where

w_j : weighting factor, $0 < w_j < 1$,

$Q_{j,mean}$: expected generated reactive power value; this is the mean value of the allowable range for each generator, i.e., $0.5\left(Q_{j,max} + Q_{j,mean}\right)$,

$Q_{j,step}$: reactive-power deviation tolerance; this is half of the allowable range for each generator , i.e., $0.5\left(Q_{j,max} - Q_{j,mean}\right)$,

Q_j : actual reactive power generated by unit j,

n : positive integer parameter defining the exponent,

L : total number of generating units.

Several other performance indices can be defined. In this work voltage-based indices are mainly considered. By including the outage control variable in the system modeling the defined performance index J can be expressed as a function of the state vector and of the control variables, $J(x, u_c)$. The change of the performance index due to the contingency is

$$\Delta J = J(x^{new}, u_c = 0.0) - J(x^0, u_c = 1.0), \quad (7.13)$$

where x^0 is the initial state, prior to the contingency, x^{new} is the state after the contingency and the control variable u_c changes from 1.0 to 0.0, modeling the component

outage. The first order approximation of the performance index variation is provided by the derivative of the PI with respect to the control variable

$$\Delta J = \frac{dJ}{du_c}\Delta u_c = \frac{dJ}{du_c}(u_c - 1), \tag{7.14}$$

and for a change in u_c from 1.0 to 0.0

$$\Delta J = -\frac{dJ}{du_c}. \tag{7.15}$$

It is, therefore, expected that the derivative of the performance index with respect to the outage control variable at the present operating point will provide a measure of the severity of a disturbance. Therefore, contingencies are ranked based on the values of $\frac{dJ}{du_c}$, which expresses the first-order change of the performance index. The values of these derivatives can be calculated using the co-state method as

$$\frac{dJ}{du_c} = \frac{\partial J}{\partial u_c} - \hat{x}^T \frac{\partial g(x,u_c)}{\partial u_c}, \tag{7.16}$$

$$\hat{x}^T = \left[\frac{\partial J(x,u_c)}{\partial x}\right]\left[\frac{\partial g(x,u_c)}{\partial x}\right]. \tag{7.17}$$

$J(x,u_c)$ is the performance index, $g(x,u_c) = 0$ are the power flow equations, with the outage control variable incorporated in them, u_c is the vector of the control variables of interest, x is the state vector, $\hat{x}^T$ is the co-state vector. Note that the performance index may depend explicitly on the control variables and it also depends implicitly on them through the power flow equations. The explicit dependence is captured by the partial derivative $\frac{\partial J}{\partial u_c}$ and the implicit by the term $\hat{x}^T \frac{\partial g(x,u_c)}{\partial u_c}$. Furthermore, the co-state vector is invariant for all contingencies; therefore it is pre-computed at the present operating condition, resulting in extremely fast computations, even for large scale power systems.

After the co-state vector is computed the sensitivity of the performance index for each contingency is simply a vector-vector multiplication, with one of the vectors being very sparse.

The contingency ranking algorithm based on the co-state method is efficient and precise as a first-order method. The computational requirements are equivalent to one iteration of the power-flow solution algorithm for the entire set of contingencies (cost of computing the co-state vector). However, for contingencies that trigger severe nonlinearities the method may lead to misrankings. This is because the behavior of the performance index around the present operating point may be significantly different from the behavior as one moves away from the current operating point. This issue has been addressed with the hybrid method, which separates contingencies into those that trigger sever nonlinearities and those that do not. The former are processed with more accurate and computationally demanding contingency selection methods and the latter (which represent the majority of contingencies) are ranked with the above described PI based method. The processing of a small number of contingencies via selection methods adds to the computational burden. Therefore, it is important to be able to use PI based methods on all contingencies. The following proposed method in this paper provides a promising approach towards this goal.

7.5.2 Higher-Order State-Linearization PI-Based Contingency Ranking

The proposed state-linearization approach is a variation of the PI-based contingency-ranking algorithm. In this method, instead of linearizing the performance indices directly, the system states are linearized with respect to the contingency control variable; the performance index J is then calculated as

$$J = J\left(x^0 + \frac{dx}{du_c}(u_c - 1), u_c\right), \tag{7.18}$$

where

x^0 is the present operating condition,

x is the system state vector,

u is the contingency control variable.

The utilization of the linearized system states in calculating the system performance index provides higher-order terms in the Taylor's series expansion. The unique potential of this method has been proven in some preliminary work by members of this research group described in [38], [39], [41], [181]. The state-linearization sensitivity method provides the traces of indices with curvature, which can follow the highly nonlinear variations of the original indices to some extent, while the PI-linearization method provides only the straight line. Therefore, the higher order sensitivity method is superior to the simple PI-linearization-based method.

The contingency selection is based on the computation of the performance index change due to a contingency and subsequent ranking of the contingencies on the basis of the change. Mathematically, one can view the outage of a circuit as a reduction of the admittance of the circuit to zero. The outage control variable, u_c, is again employed as illustrated in Figure 7.7 through Figure 7.9. Consider the performance index, J. The change of the performance index due to the contingency is

$$\Delta J = J\left(x^0 + \frac{dx}{du_c}(u_c - 1), u_c\right) - J(x^0, u_c = 1.0), \tag{7.19}$$

where x^0 is the present operating condition. The sensitivity of the state with respect to the control variable can be easily computed as

$$\frac{dx}{du_c} = -\left[\frac{\partial G(x,u_c)}{\partial x}\right]^{-1}\left[\frac{\partial G(x,u_c)}{\partial u_c}\right]. \tag{7.20}$$

Note that $\frac{\partial G(x,u_c)}{\partial x}$ is the Jacobian of the system and, therefore, it is pre-computed at the present operating condition and remains invariant for all contingencies. Thus, for each contingency only the partial derivatives of the power-flow equation $G(x,u_c)$ need to be computed, with respect to the contingency contrl variable. This vector has only few nonzero entries and, therefore, the computations are extremely fast. Taking into account the sparsity of this vector can greatly improve the efficiency of the method. It should also be noted that $\frac{dx}{du_c}$ is a vector of the same size as the state vector, each element of which is the derivative of the corresponding state with respect to the control variable. Once the new state is computed via this linear approximation, the calculation of the new value of the performance index is a straightforward operation.

The concept of the approach is illustrated graphically in Figure 7.10 and Figure 7.11 based on results obtained from the application of the method to a small test system. The first-order-analysis curve represents the PI-sensitivity linear curve after performing the linearization of the index with respect to the contingency control variable. The higher-order-analysis curve is the state-linearization curve with respect to the contingency control variable.

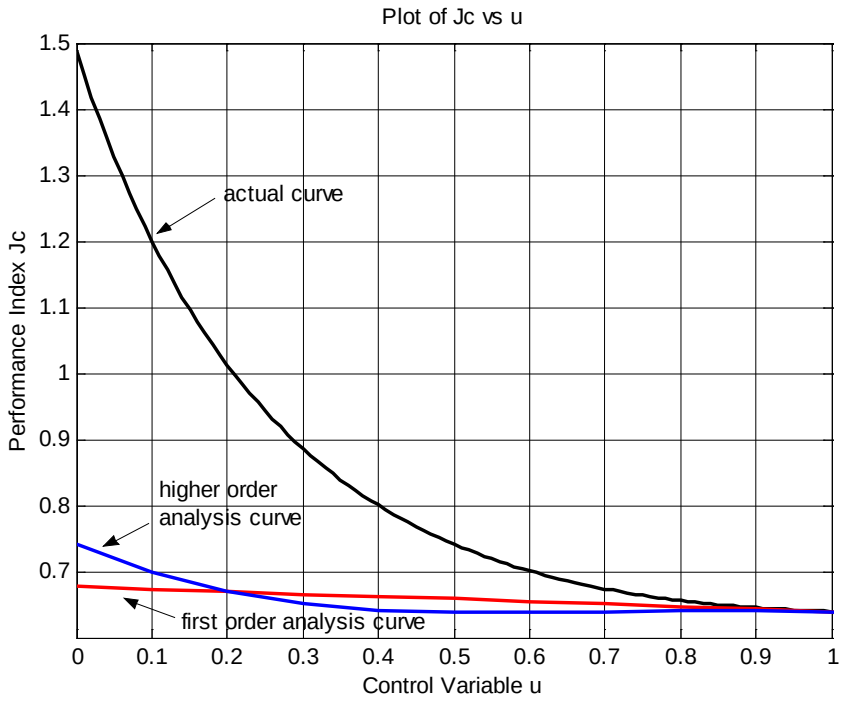

Figure 7.10: Plots of circuit-loading index vs. the contingency control variable u_c.

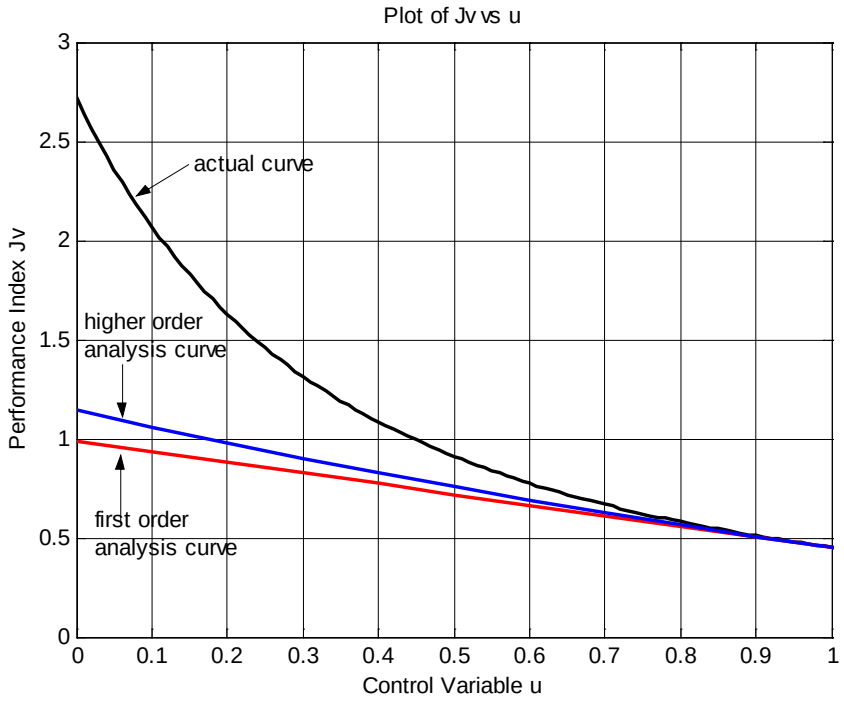

Figure 7.11: Plots of voltage index vs. the contingency control variable u_c.

7.6 Summary

The models and simulation tools developed in this work are used for the study of voltage-recovery phenomena and the identification of voltage-related problems cause by delayed recovery of the system voltage to acceptable level. Once such problems are identified and understood ways for possible mitigation of such problems can be developed. This chapter presented the formulation and solution approach of the optimization problem of allocation of voltage-control devices for the mitigation of voltage problems. The system dynamic behavior was of primary interest in this work; however, standard static performance criteria can also be included, as described in this chapter. The proposed approach defines the problem of optimal allocation of VAr resources as a planning problem over a pre-defined planning horizon and addresses it as a sequence of decisions. A dynamic-programming-based approach is developed for the solution of the problem coupled with sensitivity analysis.

CHAPTER 8

OPTIMAL OPERATION OF VOLTAGE-CONTROL DEVICES

8.1 Overview

This chapter addresses the topic of mitigation of delayed-voltage-recovery phenomena following typical faults in a power system by utilization of dynamic VAr sources of the system. It is well known that voltage recovery, after a disturbance, is affected or delayed by load dynamics (such as the dynamics of induction motors), especially when not enough fast reacting reactive resources (dynamic VAR sources) exist [4] – [12]. During this period, motors decelerate and the dynamics of the load affect the speedy recovery of the voltage. Such phenomena may trigger secondary effects, such as motor tripping and other undesired relay operations and have been studied to a significant extent in the literature [4] – [12], as presented in Chapters 1 and 2, and have also been reported as part of this research work [143] – [147].

Fast responding reactive support devices, referred to as dynamic VAr sources are used for improving system performance related to such phenomena. Installation and operation of such devices provide the means of locally controlling the voltage during transients in real time and, thus, alleviating or even eliminating such problems. The focus of this part of this work is the optimal operation of installed VAr resources for speeding up the transient voltage recovery and minimizing the impact of these transients.

The problem is formulated as an optimal control problem that determines the minimum control effort that provides the desired system behavior, based on specific

operational criteria. Such criteria are associated with the rate of recovery and the minimum time to recovery. Direct transcription methods are used to create a discrete numerical approximation of the continuous optimal-control problem, using an implicit Runge-Kutta discretization scheme. The mathematical problem formulation is presented considering a quasi-steady-state dynamic model of the power system, operational path constraints, and specific objective functions. The end result provides insight of the optimal operation and control of reactive support resources, under such transient phenomena.

8.2 Problem Description

A typical simulation scenario can be described as follows. Assume an electric power system operating under normal steady-state conditions. The system is subject to a wide variety of exogenous disturbances, like for example, short circuits. When such a disturbance takes place the system moves from its normal operating state, to the faulted state. For a specific disturbance the protection system will respond and will take the system through specific switching operations, moving it from the faulted state to the post-fault state. During this period the system will experience transients that may include voltage recovery transients and possible voltage instability. For this sequence of events, the needed control, via specific controlling devices, needs to be determined to ensure that the system will not experience any instability and will promptly return to acceptable operating conditions.

More specifically a typical scenario consists of the following phases:

1) Pre-fault phase: The system is operating at steady-state conditions.

2) During-fault phase: When a fault (or a disturbance in general) takes place the system enters a transient operating condition. Typically, the during-fault phase is characterized by severely abnormal operating conditions, like for example, very low voltage levels or significant frequency excursions.

3) Post-fault phase: This is the most important and interesting phase of the analysis. The fault is cleared by the protective system (or in general the disturbance is removed). This is, in general, associated with a change in the system configuration, which may now move to a new acceptable or unacceptable steady-state or even become unstable, depending on the control action applied to the system. The final operating conditions at the end of the fault period are the initial conditions of the post-fault system.

Voltage recovery following short circuits in electric power systems is one such phenomenon. Short circuits of various types (three-phase, two-phase, two-phase to ground, single-phase to ground) are common events in electric transmission or distribution systems. Such faults can cause significant voltage dips in their vicinity. They are usually cleared by the operation of protective circuit breakers and possibly the isolation of the fault location from the rest of the system (for example, removal of faulted line). However, the voltage built-up after such a fault may be slow and even exhibit a strong oscillatory behavior, depending on the dynamic characteristics of the system, and in particular the characteristics of the synchronous generating units and the dynamic loads, like, for example, motor loads. Such slow voltage recovery can result in system-wide problems, like voltage instability and voltage collapse or local problems in particularly weak areas in the system. That is, the system as a whole may recover and appear to reach an acceptable new steady-state; however, specific load areas of the

system may continue experiencing unacceptable operating conditions. This might result from the fact that slow voltage recovery may have other secondary effects and result in undesired protective relay operation, like tripping of sensitive loads.

Voltage behavior in a power system is mainly controlled via the synchronous generating units or via reactive support devices (VAr devices), like switched capacitors deployed throughout the system. However, generators cannot provide local support, while capacitors have to be switched on and off mechanically and, thus, cannot provide continuous and fast real-time response. They are, therefore, mainly used for controlling the voltage based on steady-state criteria, rather than during transients. They are also passive elements, and their control ability depends on the system voltage at their locations. Hence, their response might not be considerable, especially during faults that result in significant voltage dips.

For that reason, dynamic VAr sources, in the form of FACTS devices, are the only practical way of locally controlling the voltage. Such devices use power-electronics technology to control the reactive power they inject into the system. This allows fast response times and, hence, practically real-time control of the system, in the form of continuous, rather than discrete, control action.

8.3 Mathematical Problem Formulation

An electric power system can be modeled as a set of nonlinear differential-algebraic equations (DAEs) of the general form:

$$\begin{aligned} \dot{x}(t) &= f(x(t), y(t), u(t), p, t), \\ 0 &= g(x(t), y(t), u(t), p, t), \end{aligned} \tag{8.1}$$

where

$x(t)$ are the dynamical system states;

$y(t)$ are the algebraic system states;

$u(t)$ are the system control variables;

p is the system parameter vector;

f is the vector function of the dynamic system equations;

g is the vector function of the algebraic system equations.

The number of dynamical states is n_x, of algebraic states n_y, and of control variables n_u. The number of differential equations is n_f and the number of algebraic equations n_g. For implementation purposes it is convenient, and possible for most of the power system applications, to convert f to a set of linear equations and move all the nonlinearities to the algebraic equations, g. Furthermore, g is assumed to be a set of at most quadratic equations. This can be, in general, achieved by introducing some additional, algebraic state variables to "quadratize" the model, without any approximations, as presented in Chapter 3. Functions f and g, in general, also contain switching functions, which represent elements that are switched on and off (or change their operating mode) or modifications in the system configuration during different stages of the analysis and during the various scenarios under study. Changes in f and g define different topologies of the problem. Within a single topology the system dynamics are considered unmodified.

The control vector can contain any available controls of interest, like for example, generator controls or load controls (if available), both continuous and discrete. In our case, as described in the previous section, the control variables are the desired reactive-

power injections from existing dynamic VAr sources of interest. Mathematically, this can be represented by a reference input to the controller of the device. This is a continuous control, in the form of a trajectory of reactive-power injection or the reference input during the during-fault and post-fault phases of the analysis. During the pre-fault phase the controller input is some specific reference value that keeps the system operating under the desired steady-state conditions.

The problem is to define the optimal (minimum effort) control trajectory for dynamic VAr source injections that satisfies specific recovery criteria, associated with the rate of recovery. The approach presented in [196], [197] is followed. Specifically, the control functions $u(t)$ are to be chosen to minimize the objective function

$$J = \varphi[x(t_F), y(t_F), t_F], \tag{8.2}$$

subject to the state equations (8.1) and the boundary conditions

$$\psi[x(t_F), y(t_F), \mathrm{p}, t_F] = 0, \tag{8.3}$$

where the initial conditions $x(t_i) = x_i$ and $y(t_I) = y_I$ are given at the fixed initial time t_I and the final time t_F is free. The modified objective function of the problem is defined as

$$\hat{J} = [\varphi + v^T\psi]_{t_F} - \int_{t_I}^{t_F}\{\mu^T(t)g + \lambda^T(t)[\dot{x}(t) - f]\}dt. \tag{8.4}$$

Vector v is the vector of Lagrange multipliers for the discrete constraints, while vectors $\lambda(t)$ and $\mu(t)$ are the multipliers for the continuous constraints, referred to as adjoint or co-state variables. The necessary conditions for a constraint optimum are obtained by setting the first variation $\delta\hat{J} = 0$. The system Hamiltonian is defined as in (8.5), assuming that the differential-algebraic system (8.1) is of index one.

$$H = \lambda^T f + \mu^T g \tag{8.5}$$

and the auxiliary function is defined as

$$\Phi = \phi + v^T \psi. \tag{8.6}$$

The resulting necessary conditions are

$$[\dot{\lambda} \quad \dot{\mu}] = \left[-H_x^T \quad -H_y^T\right], \qquad \text{(adjoint equations)} \tag{8.7}$$

$$0 = H_u^T, \qquad \text{(control equations)} \tag{8.8}$$

$$\begin{aligned} &\lambda(t_F) = \Phi_x^T\big|_{t=t_F}, \\ &\mu(t_F) = \Phi_y^T\big|_{t=t_F}, \\ &0 = \left(\Phi_y + H\right)\big|_{t=t_F}, \\ &0 = \lambda(t_I), \\ &0 = \mu(t_I). \end{aligned} \qquad \text{(transversality conditions)} \tag{8.9}$$

Equations (8.1), (8.5), and (8.8) comprise a DAE system with boundary conditions at both t_I and t_F provided by (8.3) and (8.9). Altogether they form a two-point boundary value problem.

Furthermore, additional equality or inequality path constraints can be imposed within each phase of the general form:

$$h_l \leq h(x(t), y(t), u(t), p, t) \leq h_u, \tag{8.10}$$

as well as simple bounds on the state and control variables, representing, for example, upper and lower limits of specific device outputs:

$$\begin{aligned} &x_l \leq x(t) \leq x_u, \\ &y_l \leq y(t) \leq y_u, \\ &u_l \leq u(t) \leq u_u. \end{aligned} \tag{8.11}$$

8.4 Solution Methodology

Direct transcription is used to convert the infinite-dimensional, continuous-time, optimal-control problem to an approximate, finite-dimensional, discrete, nonlinear-programming (NLP) problem. Assume a specific topology of the problem, such as the post-fault conditions. The time duration of interest is divided into M intervals:

$$t_I = t_0 < t_1 < \cdots < t_M = t_F.$$

The number of grid points is $N = M + 1$. The values of the state and control variables are treated as a set of NLP variables. The differential equations are replaced by a finite set of discretized equations, at each grid point, based on some numerical integration scheme. For the trapezoidal scheme the NLP variables are

$$X^T = [x_1^T \quad y_1^T \quad u_1^T \quad \ldots \quad x_M^T \quad y_M^T \quad u_M^T],$$

and the discretization equations are

$$x_k = x_{k-1} + \frac{h_k}{2}(f_k + f_{k-1}) \tag{8.12}$$

or

$$0 = \left[x_k - \frac{h_k}{2} f_k\right] + \left[-x_{k-1} - \frac{h_k}{2} f_{k-1}\right], \tag{8.13}$$

where the subscripts k and $k-1$ denote the values at the current time t_k and the previous time $t_{k-1} = t_k - h_k$, respectively and h_k is the discretization step at the grid point k. Usually, the time step is constant; however, this notation also accommodates the case where the time step is variable. The step size can be defined as

$$h_k = \tau_k(t_F - t_I) = \tau_k \Delta t, \tag{8.14}$$

with $0 < t_k < 1$.

Therefore, $x_k = x(t_k)$, $y_k = y(t_k)$, $u_k = u(t_k)$, $f_k = f(x_k, y_k, u_k, p, t_k)$ and similarly at $k-1$. For the Hermite-Simpson discretization (also referred to as quadratic integration scheme for conciseness [196], [197]) the NLP variables are

$$X^T = \begin{bmatrix} x_1^T & y_1^T & u_1^T & x_{2m}^T & y_{2m}^T & u_{2m}^T & x_2^T & y_2^T & u_2^T & \dots \\ x_{Mm}^T & y_{Mm}^T & u_{Mm}^T & x_M^T & y_M^T & u_M^T & & & & \end{bmatrix}$$

and the discretization equations are

$$x_m - \frac{h}{3} f_m + \frac{h}{24} f_k = x_{k-1} + \frac{5h}{24} f_{k-1} \tag{8.15}$$

and

$$x_k - \frac{2h}{3} f_m + \frac{h}{6} f_k = x_{k-1} + \frac{h}{6} f_{k-1}$$

or

$$\begin{aligned} 0 &= \frac{h}{24} f_k + \left[x_m - \frac{h}{3} f_m \right] + \left[-x_{k-1} - \frac{5h}{24} f_{k-1} \right], \\ 0 &= \left[x_k + \frac{h}{6} f_k \right] - \frac{2h}{3} f_m + \left[-x_{k-1} - \frac{h}{6} f_{k-1} \right]. \end{aligned} \tag{8.16}$$

The subscript m denotes the midpoint of the segment with endpoints $k-1$ and k. All the algebraic equations are enforced at the grid points and appended to the "algebraized" differential equations. This means that the equations (8.17) and (8.18) are appended for the trapezoidal and quadratic discretization schemes, respectively, as derived from (8.1), (8.10), and (8.11):

$$\begin{aligned} &0 = g(x_k, y_k, u_k, p, t_k), \\ &h_l \le h(x_k, y_k, u_k, p, t_k) \le h_u, \\ &x_l \le x_k \le x_u, \\ &y_l \le y_k \le y_u, \\ &u_l \le u_k \le u_u, \end{aligned} \tag{8.17}$$

$$
\begin{aligned}
&0 = g(x_k, y_k, u_k, p, t_k),\\
&h_l \le h(x_k, y_k, u_k, p, t_k) \le h_u,\\
&x_l \le x_k \le x_u,\\
&y_l \le y_k \le y_u,\\
&u_l \le u_k \le u_u,\\
&0 = g(x_m, y_m, u_m, p, t_m),\\
&h_l \le h(x_m, y_m, u_m, p, t_m) \le h_u,\\
&x_l \le x_m \le x_u,\\
&y_l \le y_m \le y_u,\\
&u_l \le u_m \le u_u.
\end{aligned}
\tag{8.18}
$$

Inequality constraints are treated by the introduction of slack variables, which convert them to equality constraints.

Therefore, the resulting equality constraint NLP problem is to chose the decision variables X, as defined earlier, to minimize the objective function

$$F(X) = \phi(x_M, y_M), \tag{8.19}$$

as derived from (8.2), subject to the constraints

$$c(X) = 0, \tag{8.20}$$

which in this case are defined by equations (8.13) and (8.17) or (8.16) and (8.18) for $k = 1$ to $M = N - 1$, depending on the discretization scheme. It is assumed that the provided initial conditions, referring to the first grid point (at t_0) are consistent with all the algebraic constraints.

The form of (8.19), though it appears simplistic and restrictive, is quite general and can also accommodate objective functions or constraints defined via quadrature forms. This can be done by introducing additional dynamical states and casting the optimization problem in Mayer form [196]. So, for example, for an objective function defined as

$$J = \int_{t_I}^{t_F} w(x(t), y(t), u(t), p, t)dt, \tag{8.21}$$

an additional dynamic state variable, $\zeta(t)$, can be introduced along with the differential equation

$$\dot{\zeta} = w(x(t), y(t), u(t), p, t) \tag{8.22}$$

and the initial condition $\zeta(t_I) = 0$.

In this case, the objective function simply becomes

$$J = \zeta(t_F) = \phi(x_M, y_M). \tag{8.23}$$

The Lagrangian of the NLP is given by

$$L(X, \xi) = F(X) - \xi^T c(X) = \phi(x_M, y_M) - \sum_{k=1}^{M} \xi_k^T c_k(X). \tag{8.24}$$

The necessary conditions for this problem are

$$\frac{\partial L}{\partial \xi_k} = 0 = c(X), \tag{8.25}$$

$$\frac{\partial L}{\partial X_k} = 0. \tag{8.26}$$

The solution of the NLP problem is obtained via Newton's method.

8.5 Summary

This chapter presented some basic concepts and groundwork issues on the optimal operation of installed dynamic VAr sources for control of voltage-recovery phenomena in electric power systems. Concepts from the theory of applied optimal control and trajectory optimization were used to calculate the best and minimum-effort control strategy of such devices to improve the dynamic system performance. Such strategy is to be applied as reference input to the controller of a reactive support device, usually implemented as PI-controller in installed systems.

CHAPTER 9

DEMONSTRATIVE EXAMPLES

9.1 Introduction

Results from the implementation of the methodologies developed in this work are presented in this chapter. First, in section 9.2, simulation results utilizing the developed modeling and analysis tools are presented. The “quatratized” power system modeling is used along with the quadratic integration method for transient simulation. Some simple test cases are presented to demonstrate the quadratic modeling approach compared to traditional system modeling and the behavior of the quadratic integration method in comparison with the trapezoidal rule.

Then, in sections 9.3 and 9.4, the modeling and simulation tools developed in this work are demonstrated, for both steady-state and transient operation, in two power systems. The cases involve numerical examples from two artificial test systems, a transmission system and a distribution feeder. The voltage recovery after typical system faults is the main focus of the analysis.

In the following section, 9.5, the proposed contingency ranking approaches are presented and evaluated. Four examples are presented utilizing four different systems of increasing complexity.

Finally, the proposed methodologies for mitigation of voltage recovery problems by optimal installation and operation of dynamic VAr sources are demonstrated utilizing the same simple example systems in section 9.6.

9.2 Quadratic Modeling and Simulation of Dynamical Systems

This section presents the application of the "quadratized" modeling approach and the quadratic integration method to some simple dynamical systems. The examples are relatively simple since the goal is to clearly demonstrate the application and the advantages of the methodology, in comparison with the current practice, which concentrates on the trapezoidal integration rule. Furthermore, the purpose of the presented results is to quantify the behavior of the proposed methodology, as compared again to the current approaches.

9.2.1 Linear R-L-C Circuit with AC Excitation

The first example is a simple series R-L-C circuit, as illustrated in Figure 9.1. An AC voltage source of 10 V rms value and of 60 Hz frequency is the input of the circuit. Using the capacitor voltage and the circuit current as the two system states the system equations in the standard state-space representation are

$$\frac{d}{dt}\begin{bmatrix} v_C(t) \\ i(t) \end{bmatrix} = \begin{bmatrix} 0 & \frac{1}{C} \\ -\frac{1}{L} & -\frac{R}{L} \end{bmatrix}\begin{bmatrix} v_C(t) \\ i(t) \end{bmatrix} + \begin{bmatrix} 0 \\ \frac{1}{L} \end{bmatrix} u(t) = A\begin{bmatrix} v_C(t) \\ i(t) \end{bmatrix} + Bu(t), \tag{9.1}$$

where $v_C(t)$ is the capacitor voltage and $i(t)$ the circuit current. The input $u(t)$ is defined as $u(t) = 10\sqrt{2}\sin(120\pi t)$ in volts.

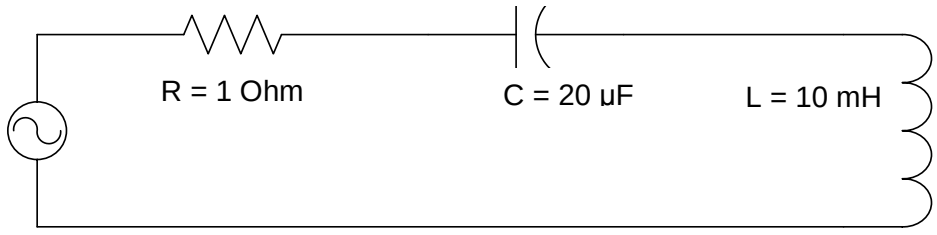

Figure 9.1: Series RLC circuit.

The system is simulated using the trapezoidal rule and the quadratic integration method. The results are also compared to the analytical solution of the system, so that the improved accuracy of the quadratic integration compared to the trapezoidal method is demonstrated. The trapezoidal rule yields the system defined by equations (9.2), at each time step:

$$\left(I - \frac{h}{2}A\right)\begin{bmatrix} v_C(t) \\ i(t) \end{bmatrix} = \left(I + \frac{h}{2}A\right)\begin{bmatrix} v_C(t-h) \\ i(t-h) \end{bmatrix} + \frac{h}{2}B(u(t) + u(t-h)). \tag{9.2}$$

The quadratic integration yields equations (9.3):

$$\begin{bmatrix} \frac{h}{24}A & I - \frac{h}{3}A \\ I - \frac{h}{6}A & -\frac{2h}{3}A \end{bmatrix}\begin{bmatrix} v_C(t) \\ i(t) \\ v_C(t_m) \\ i(t_m) \end{bmatrix} =$$

$$\begin{bmatrix} \left(I + \frac{5h}{24}A\right) \\ \left(I + \frac{h}{6}A\right) \end{bmatrix}\begin{bmatrix} v_C(t-h) \\ i(t-h) \end{bmatrix} + \begin{bmatrix} -\frac{h}{24}B & \frac{5h}{24}B & \frac{h}{3}B \\ \frac{h}{6}B & \frac{h}{6}B & \frac{2h}{3}B \end{bmatrix}\begin{bmatrix} u(t) \\ u(t-h) \\ u(t_m) \end{bmatrix}. \tag{9.3}$$

Figure 9.2 presents a graph of the capacitor voltage for the first 60 Hz-period. Figure 9.3 shows one period of the circuit current, while Figure 9.4 shows the inductor voltage for the duration of the simulation, until steady-state is reached. A time step of 0.1 ms was used. Note that the results of both integration method and the analytical solution are very close and therefore cannot be distinguished in the graphs.

Figure 9.5 presents the absolute error of the circuit current for the two methods, compared to the analytical solution, for the duration of the simulation. The current axis is logarithmic. Note that the quadratic integration method is almost three orders of magnitude more accurate compared to the trapezoidal.

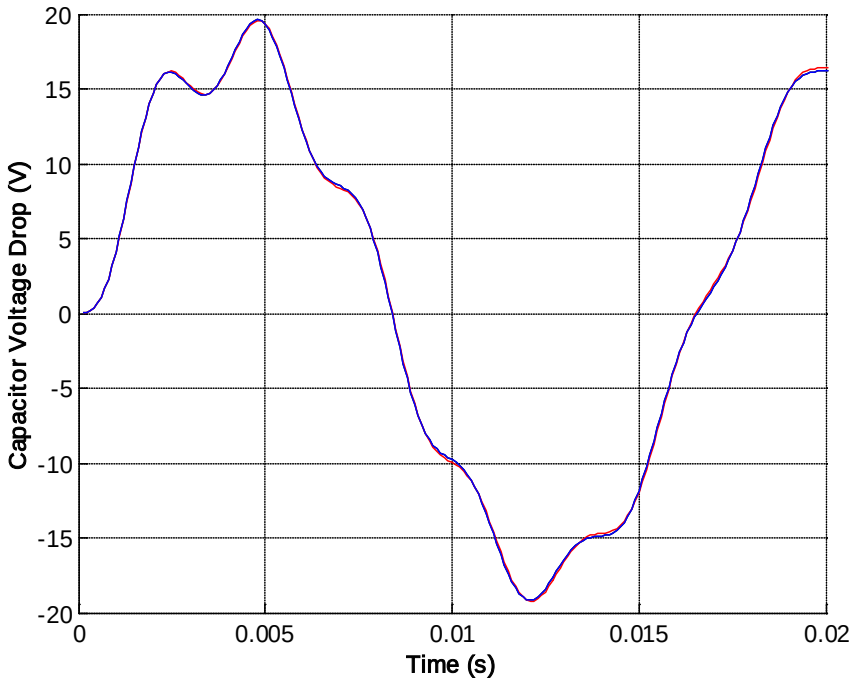

Figure 9.2: Capacitor voltage computed using trapezoidal (red) and quadratic (blue) integration (waveforms are too close to be distinguished in the graph).

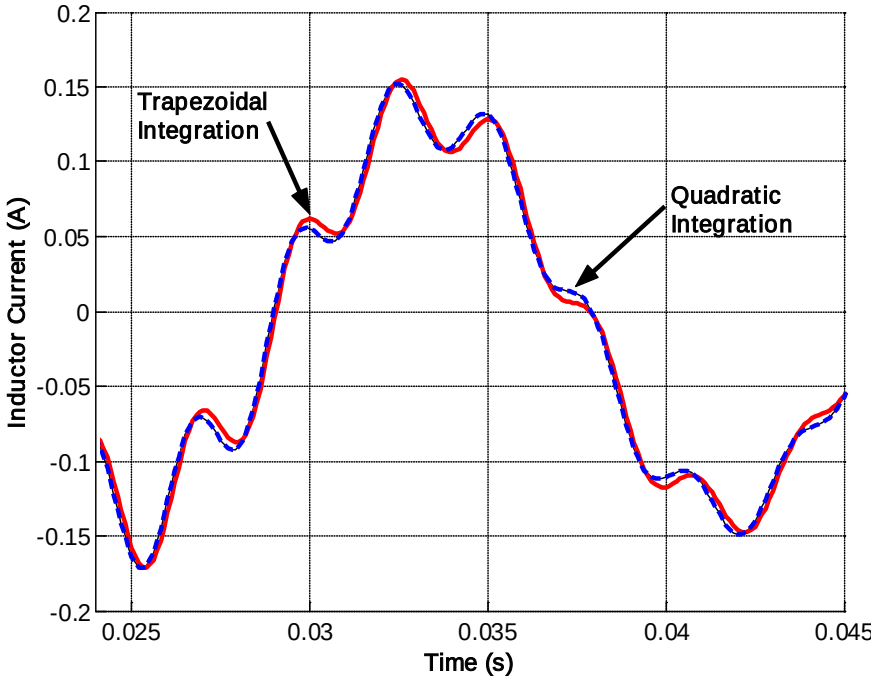

Figure 9.3: Circuit current computed using trapezoidal (red) and quadratic (blue) integration.

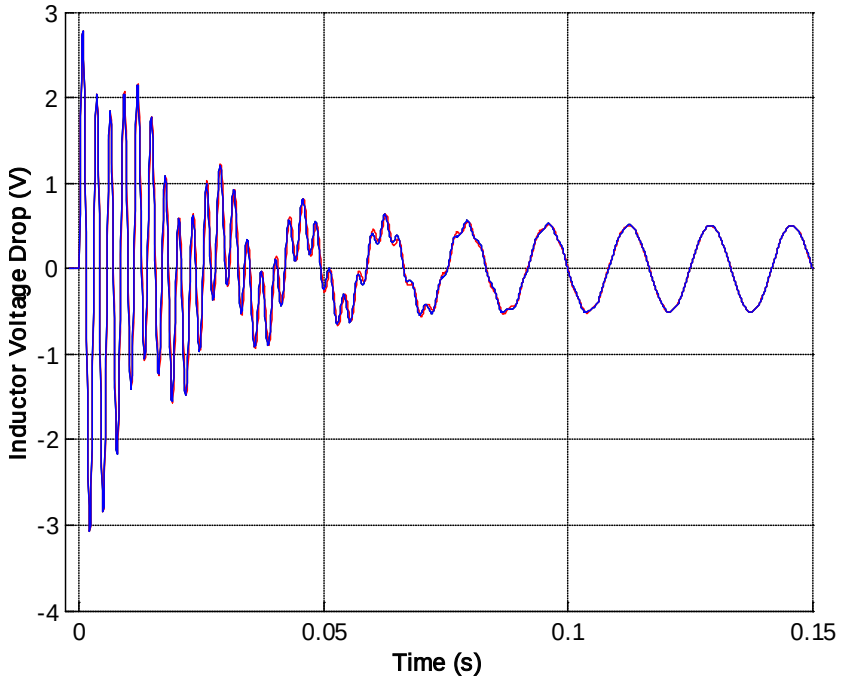

Figure 9.4: Inductor voltage using trapezoidal (red) and quadratic (blue) integration.

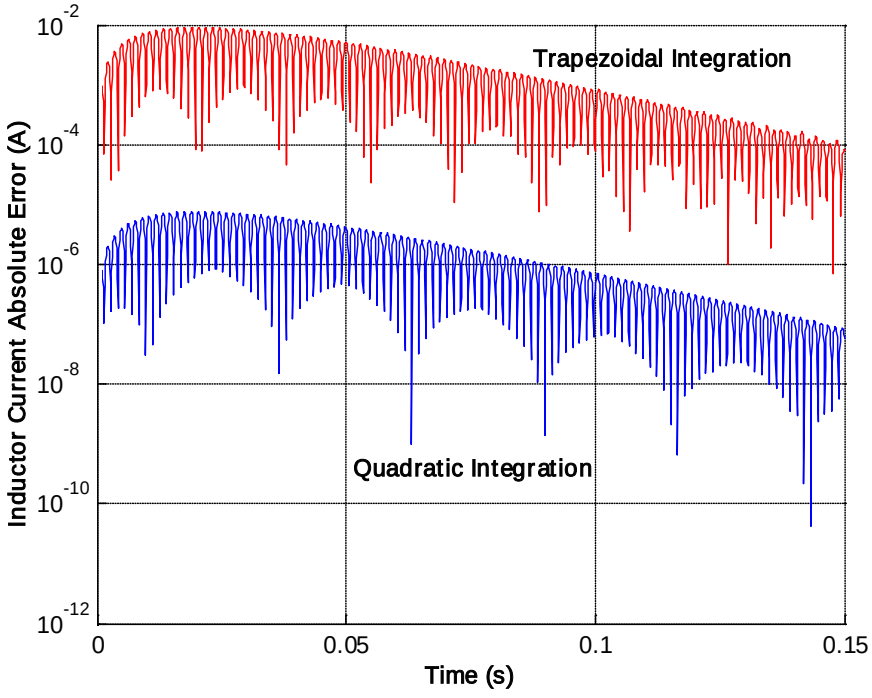

Figure 9.5: Absolute error of circuit current of trapezoidal (red) and quadratic (blue) integration.

9.2.2 Simple Converter Model

This example is illustrated in Figure 9.6. It consists of a 60 Hz AC voltage source in series with a linear inductor, a thyristor switch, and a capacitor with a parallel resistor.

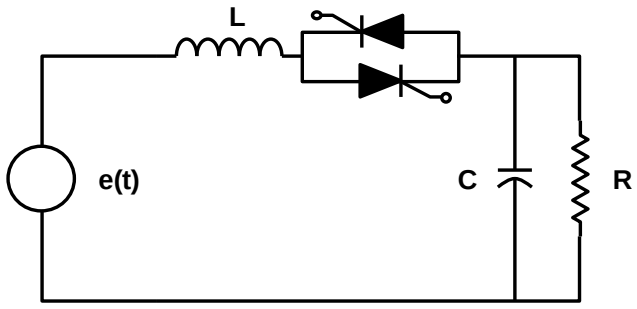

Figure 9.6: Simple converter model.

The system is linear and relatively simple, thus it is solved analytically. The capacitor voltage solution is presented in Figure 9.7. The analytical (exact) solution of the system output (capacitor voltage) is then compared with the numerical solutions obtained using the trapezoidal and quadratic integration rules, with various integration time steps. The results are presented in Figure 9.8.

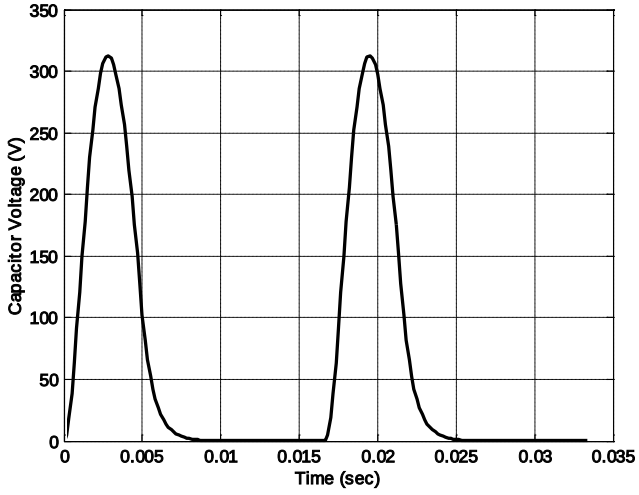

Figure 9.7: Capacitor voltage waveform.

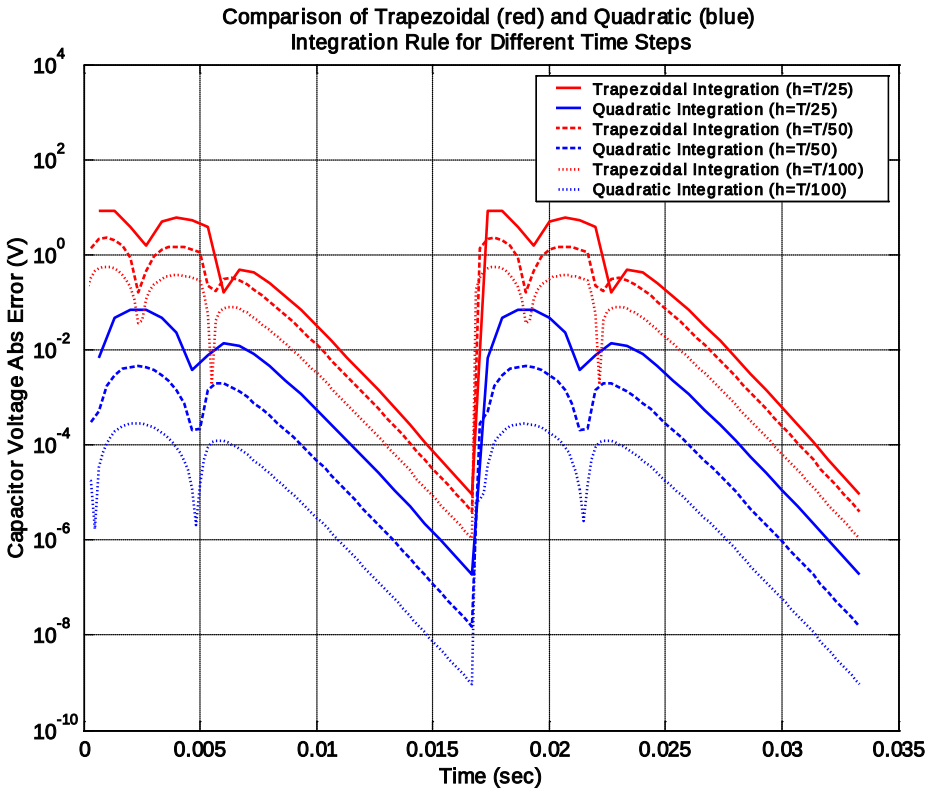

Figure 9.8: Comparison of trapezoidal and quadratic integration errors for various integration time steps.

The time steps in Figure 9.8 are indicated as fractions of the fundamental frequency T (T/25, T/50, T/100). The blue color lines indicate the quadratic and the red the trapezoidal integration method. Figure 9.8 indicates that the quadratic method is two orders of magnitude more accurate than the trapezoidal for the same time step, as imposed by its two-times higher order. It can be also concluded that the quadratic integration method can achieve similar accuracy as the trapezoidal for much larger integration time steps. In fact, in this particular example, the quadratic method is even more accurate than the trapezoidal for a four times larger time step. This feature could be used to alleviate the higher computation burden of the quadratic method compared to the trapezoidal, if the model under study permits utilization of larger time steps.

9.2.3 R-L Circuit with Diode

The third test case is a simple switching system, as illustrated in Figure 9.9. A sinusoidal voltage source of 10 V rms and 60 Hz frequency drives an inductive load through a diode. This scenario is often encountered in the simulation of power electronic systems. The diode is modeled using a piecewise linear model, as described by (9.4):

$$i_D(t) = \begin{cases} \frac{1}{R_D} v_D(t) & , v_D(t) \le V_{D0}, \\ \frac{1}{r_D} v_D(t) + V_{D0}\left(\frac{1}{R_D} - \frac{1}{r_D}\right), & v_D(t) > V_{D0}, \end{cases} \tag{9.4}$$

where i_D and v_D are the diode current and voltage respectively. V_{D0} is the voltage at which the diode starts conducting and R_D and r_D are the diode resistances. The numerical values of the above constant are $R_D = 10^6\ Ohm,\ r_D = 10^{-1}\ Ohm,\ V_{D0} = 0.7\ V$. The inductance value is $L = 1\ mH$. Using the diode voltage as state variable the system equations are

$$\frac{dv_D(t)}{dt} = \begin{cases} -\frac{R+R_D}{L} v_D(t) + \frac{R_D}{L} V_{AC}(t) & , v_D(t) \le V_{D0}, \\ -\frac{R+r_D}{L} v_D(t) + \frac{r_D}{L} V_{AC}(t) + \frac{V_{D0}}{L}\left((R + r_D)\left(1 - \frac{r_D}{R_D}\right) + r_D\left(1 + \frac{r_D}{R_D}\right)\right), & v_D(t) > V_{D0}. \end{cases} \tag{9.5}$$

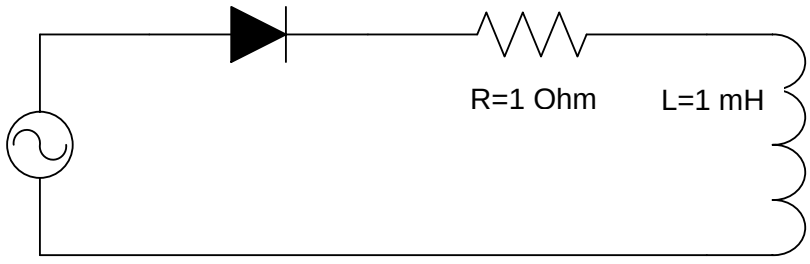

Figure 9.9: R-L Circuit with diode.

Figure 9.10 shows the voltage across the inductor and the diode voltage as computed using the trapezoidal integration method with a time step of 2 μs. Figure 9.11

shows the same waveforms as computed using the proposed integration method with a time step of 2 μs (same as in the case of trapezoidal integration). Note that when the trapezoidal integration is used severe numerical oscillations appear each time the diode is turned off. The quadratic integration successfully eliminates these oscillations.

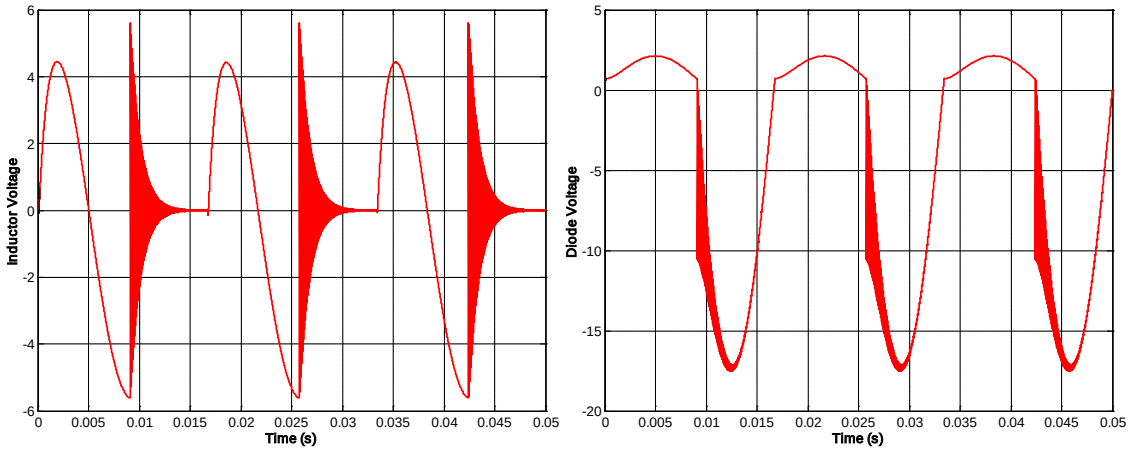

Figure 9.10: Inductor and diode voltage calculated using the trapezoidal integration.

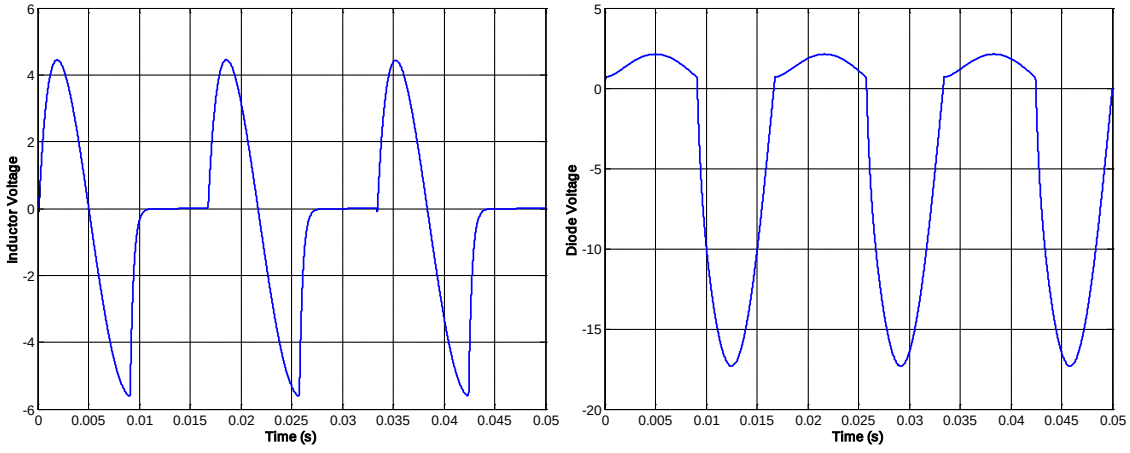

Figure 9.11: Inductor and diode voltage calculated using the quadratic integration.

9.2.4 Nonlinear Inductor

This test-case is an R-L circuit with a nonlinear inductor. Two cases of nonlinear inductor model are studied: (a) a piecewise linear inductor with two linear segments and (b) a saturable-core inductor with a high-order nonlinear flux-current characteristic. The circuit in both cases is as in Figure 9.12.

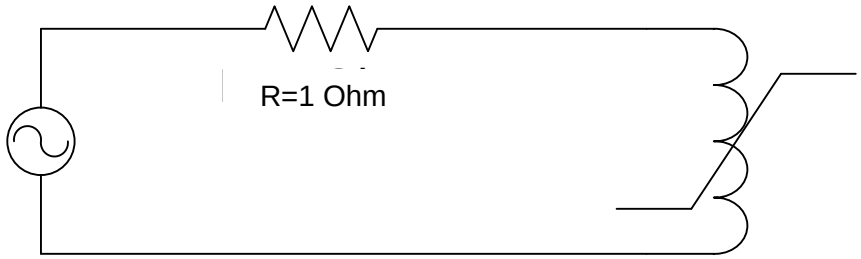

Figure 9.12: R-L Circuit with nonlinear inductor.

9.2.4.1 Piecewise Linear Inductor

In this case the circuit equations are

$$\frac{di(t)}{dt} = \begin{cases} -\frac{R}{L_1} i(t) + \frac{1}{L_1} V_{AC}(t), |i(t)| \leq i_0, \\ -\frac{R}{L_2} i(t) + \frac{1}{L_2} V_{AC}(t), |i(t)| > i_0. \end{cases} \tag{9.6}$$

The inductance values are $L_1 = 1\, mH$ and $L_2 = 0.1\, \mu H$. The switching occurs at $i_0 = 12\, A$. The voltage source is a sinusoidal AC source of 60 Hz frequency and 10 V rms. Figure 9.13 show the waveforms of the inductor voltage and current when computed using the trapezoidal rule with a time step of 10 μs. Note that the results contain numerical oscillations when switching from the first to the second model. Figure 9.14 show the same voltage and current waveforms when the system is simulated using

quadratic integration with the same time step. Note that the oscillations are eliminated, when this method is used.

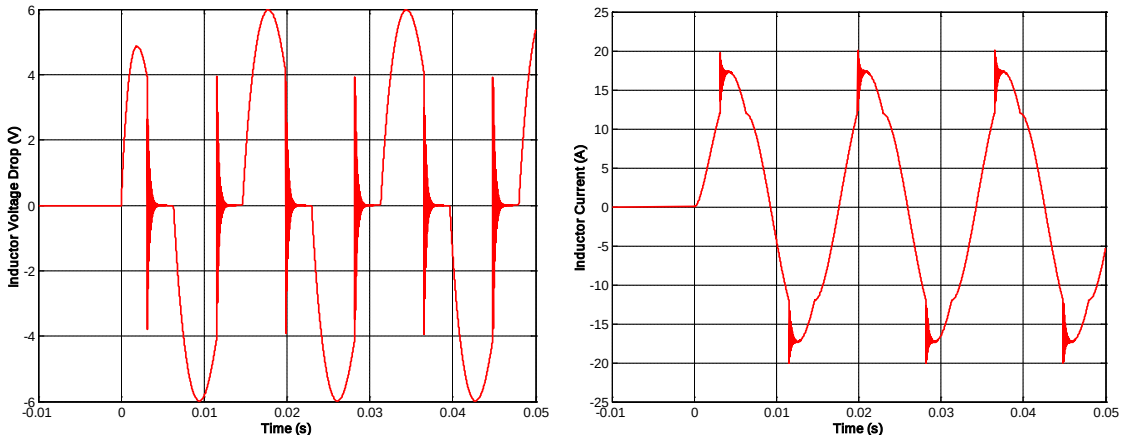

Figure 9.13: Voltage and current of piecewise linear inductor computed using the trapezoidal integration.

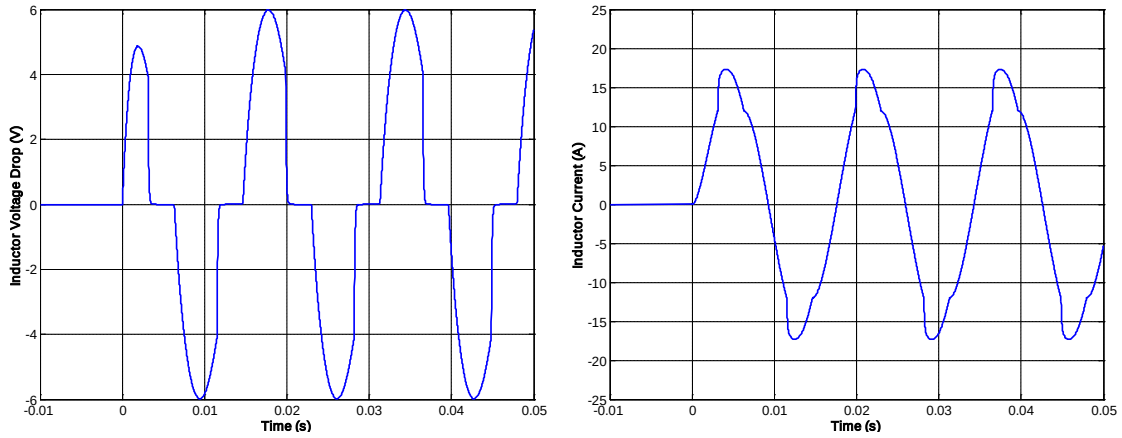

Figure 9.14: Voltage and current of piecewise linear inductor computed using the quadratic integration.

9.2.4.2 High-Order Saturable-Core Inductor

In this case the nonlinear inductor is represented by a high-order, nonlinear flux-current characteristic. The electrical circuit is the same as in Figure 9.12. The voltage source is a sinusoidal AC source of 60 Hz and of 100 V peak.

The current-flux characteristic is modeled by an analytical polynomial function of high degree according to equations (9.7) though (9.9), as illustrated in Figure 9.15. A detailed description of this model can be found in Appendix A.

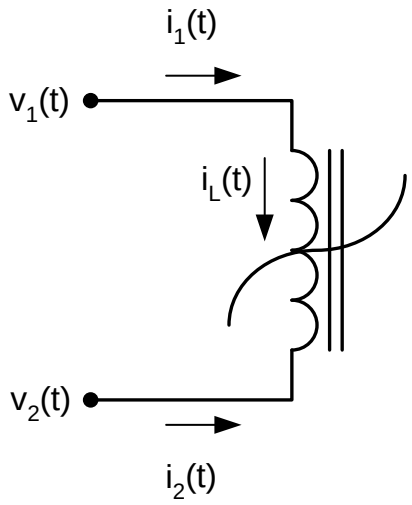

Figure 9.15: Saturable-core inductor model.

$$\frac{d\lambda(t)}{dt} = v_1(t) - v_2(t) = v_L(t), \tag{9.7}$$

$$i_1(t) = i_0 \cdot \left|\frac{\lambda(t)}{\lambda_0}\right|^n \cdot sgn\big(\lambda(t)\big) = i_L(t), \tag{9.8}$$

$$i_2(t) = -i_1(t), \tag{9.9}$$

where

$\lambda(t)$ is the inductor flux,

$v_1(t)$ is the voltage at the first terminal,

$v_2(t)$ is the voltage at the second terminal,

$v_L(t)$ is the voltage across the inductor,

$i_1(t)$ is the current into the first terminal,

$i_2(t)$ is the current into the second terminal,

$i_L(t)$ is the current through the inductor,

i_0, λ_0, and n are model parameters that define the degree of nonlinearity of the model.

The values of the system parameters are set to $i_0 = 1.0\ A$ and $\lambda_0 = 0.1\ Wb$. The used values of the exponent are 2, 4, 8, 16, 32, 64 and 128 and a parametric study is conducted gradually increasing the nonlinearity of the system. The inductor flux, current, and voltage are defined as the system outputs.

The original equations describing the circuit of Figure 9.12 are

$$\begin{aligned} &\dot{\lambda}(t) = -R \cdot i_L(t) + V_{AC}(t), \\ &0 = i_L(t) - i_0 \cdot \left|\frac{\lambda(t)}{\lambda_0}\right|^n \cdot sgn\big(\lambda(t)\big). \end{aligned} \tag{9.10}$$

The model is "quadratized" by introducing additional state variables, so that the resulting quadratic model consists of linear differential and quadratic algebraic equations. The procedure for "quadratizing" this model is described in more detail in Appendix A. As an example, for $n = 16$, four new variables are introduced for the "quadratization", z_1, z_2, z_3, and z_4 and the quadratic model of the circuit of Figure 9.12 is of the form:

$$\begin{aligned} &\dot{\lambda}(t) = v_L(t), \\ &0 = v_L(t) + R \cdot i_L(t) - V_{AC}(t), \\ &0 = i_L(t) - i_0 \cdot z_4(t) \cdot sgn\big(\lambda(t)\big), \\ &0 = z_1(t) - \left(\frac{\lambda(t)}{\lambda_0}\right)^2, \\ &0 = z_2(t) - z_1^2(t), \\ &0 = z_3(t) - z_2^2(t), \\ &0 = z_4(t) - z_3^2(t). \end{aligned} \tag{9.11}$$

Results from the seven test cases defined above (for the various exponent values) are presented in Figure 9.16 through Figure 9.43. For each exponent value, four methodologies are considered: (a) the original system with trapezoidal integration (current practice), (b) the original system with quadratic integration, (c) the "quadratized" system with trapezoidal integration, and (d) the "quadratized" system with quadratic integration (proposed methodology). The integration time step used for all the cases is set to 200μs. The waveforms or the inductor flux, voltage and current are shown, along with the number of Newton iterations required to solve the resulting algebraic equations at each time step to a predefined tolerance (constant for all cases). The value of the state vector at the previous time step is used as initial guess of the Newton's iterative algorithm at each time step. The Jacobian matrices for the test systems are analytically computed and supplied to the program, though finite-difference approximations were also used (to verify the analytically computed Jacobian values) yielding the same results.

Note that as the system nonlinearity increases the flux and especially voltage and current waveforms become more and more distorted and harmonics are introduced to the pure sinusoidal signals. Such phenomena are captured by both the trapezoidal and the quadratic integration method, however, the quadratic method is in general two orders of magnitude more accurate than the trapezoidal. Furthermore, as the nonlinearity increases to very high levels (n = 32, 64, 128) the trapezoidal method engages to artificial numerical oscillations, which in some cases make the whole simulation results erroneous. The quadratic method appears to be free of such oscillations and the only artifact is some overshooting of the solution (spike) for a very short period (in general one sample), which does not greatly affect the simulation results.

1) Exponent n = 2

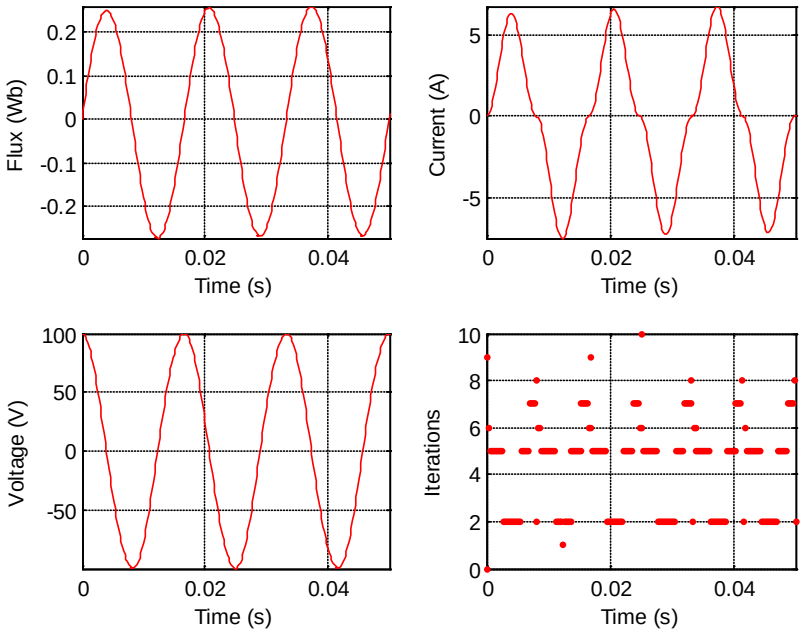

Figure 9.16: Simulation results from original system with trapezoidal integration (n=2).

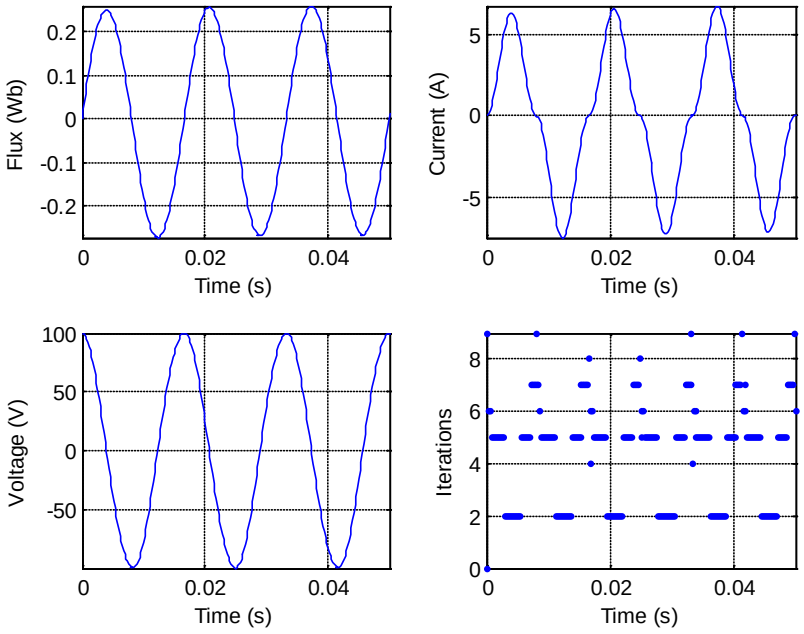

Figure 9.17: Simulation results from original system with quadratic integration (n=2).

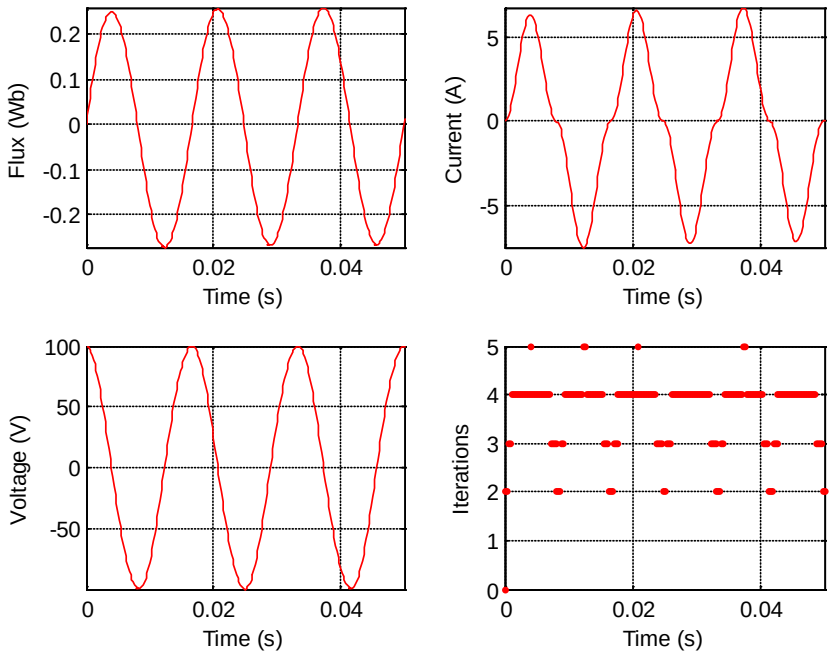

Figure 9.18: Simulation results from quadratic system with trapezoidal integration (n=2).

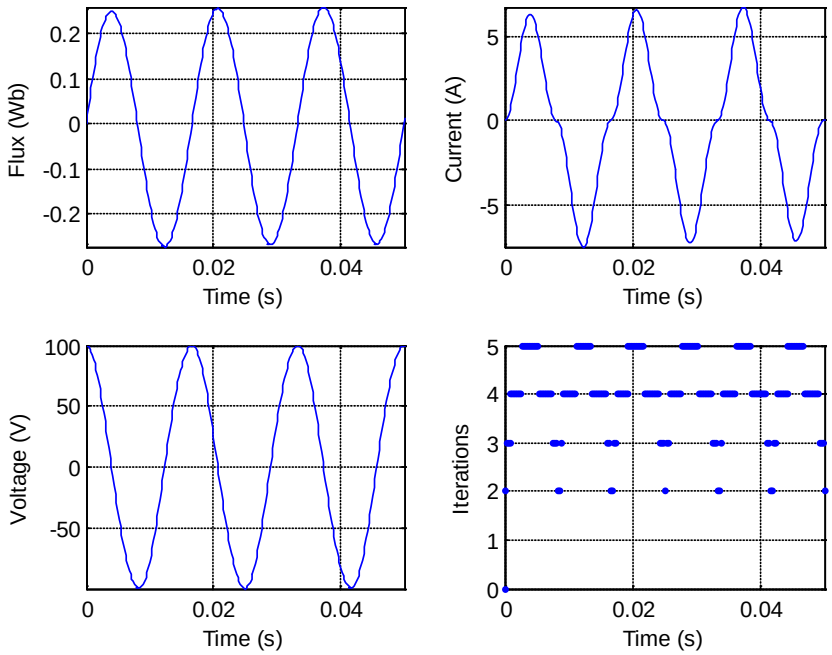

Figure 9.19: Simulation results from quadratic system with quadratic integration (n=2).

2) Exponent n = 4

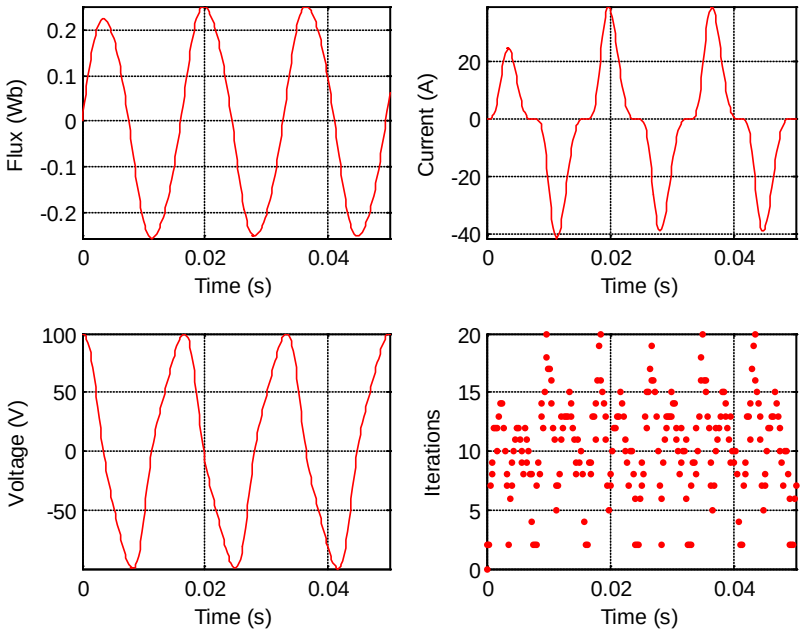

Figure 9.20: Simulation results from original system with trapezoidal integration (n=4).

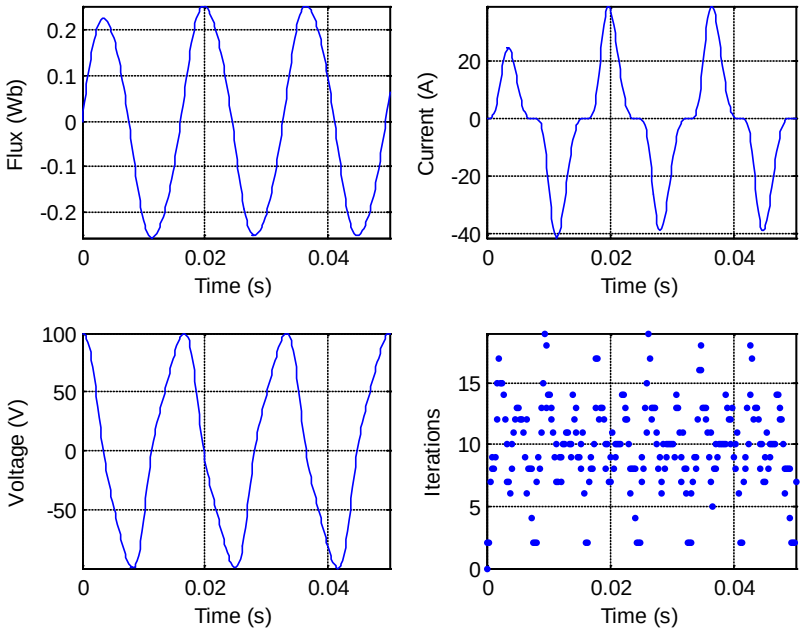

Figure 9.21: Simulation results from original system with quadratic integration (n=4).

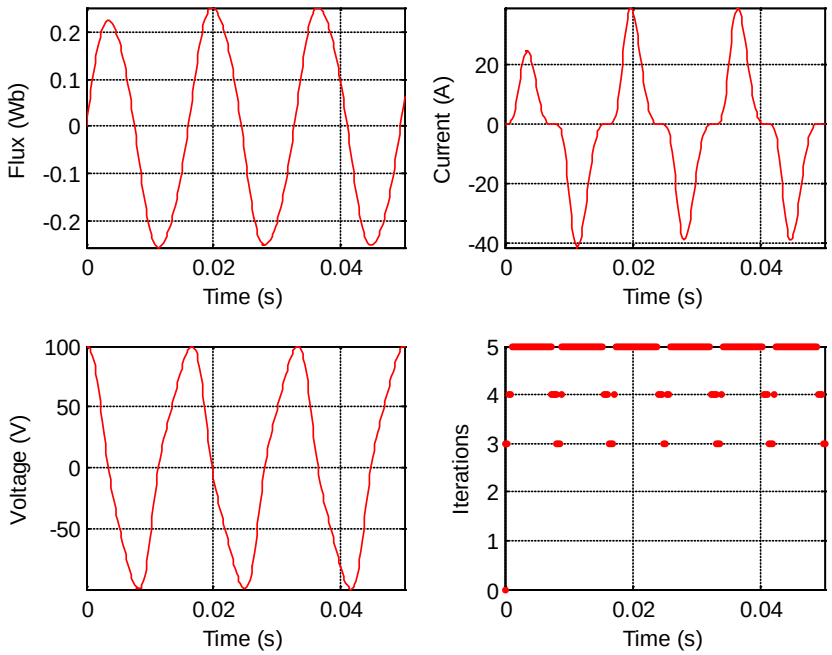

Figure 9.22: Simulation results from quadratic system with trapezoidal integration (n=4).

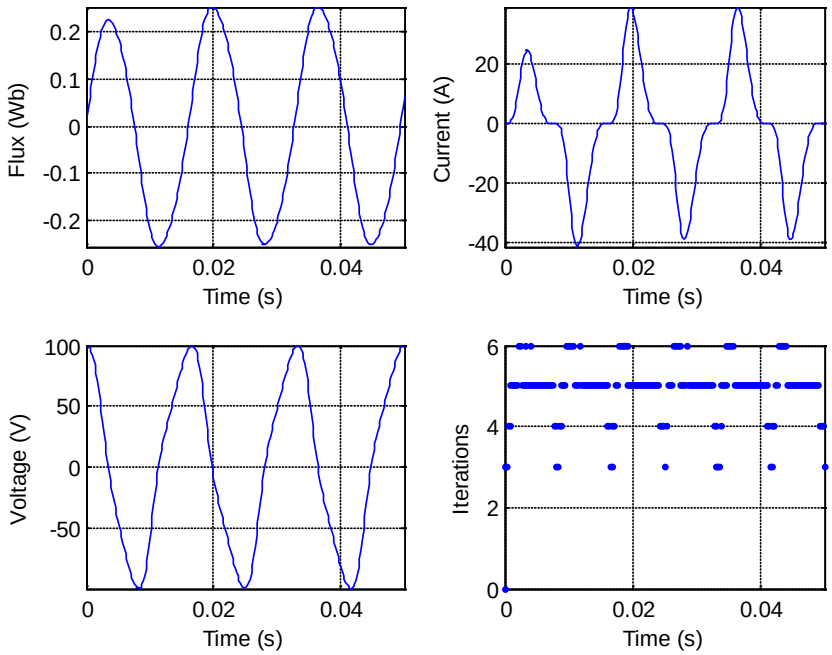

Figure 9.23: Simulation results from quadratic system with quadratic integration (n=4).

3) Exponent n = 8

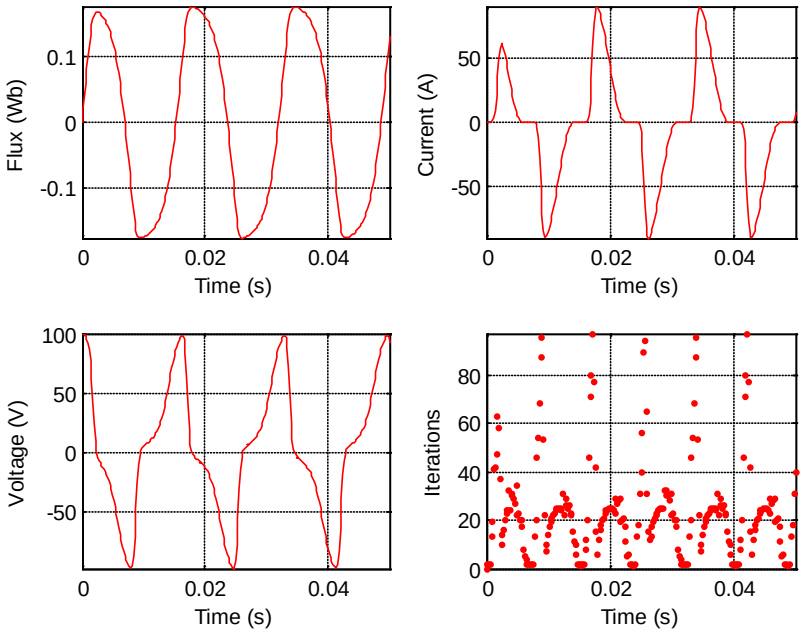

Figure 9.24: Simulation results from original system with trapezoidal integration (n=8).

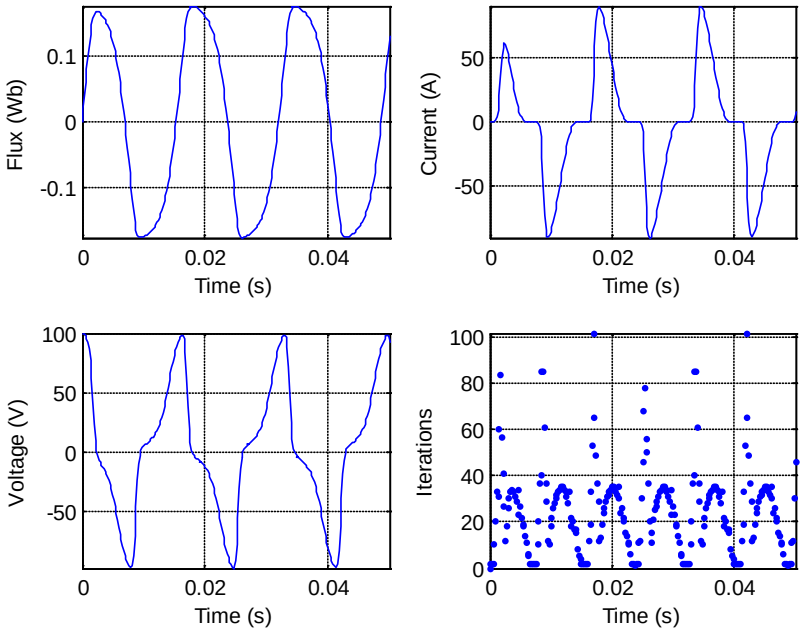

Figure 9.25: Simulation results from original system with quadratic integration (n=8).

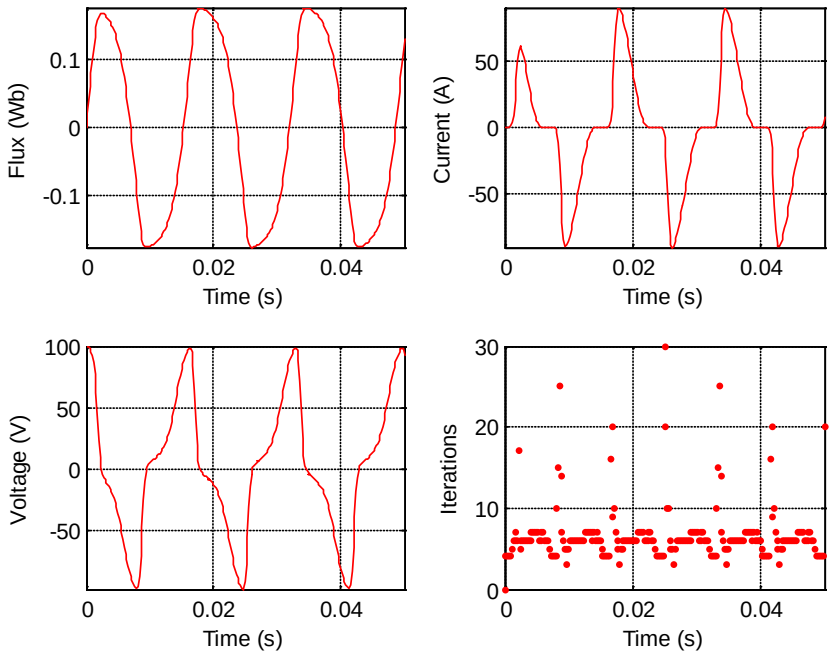

Figure 9.26: Simulation results from quadratic system with trapezoidal integration (n=8).

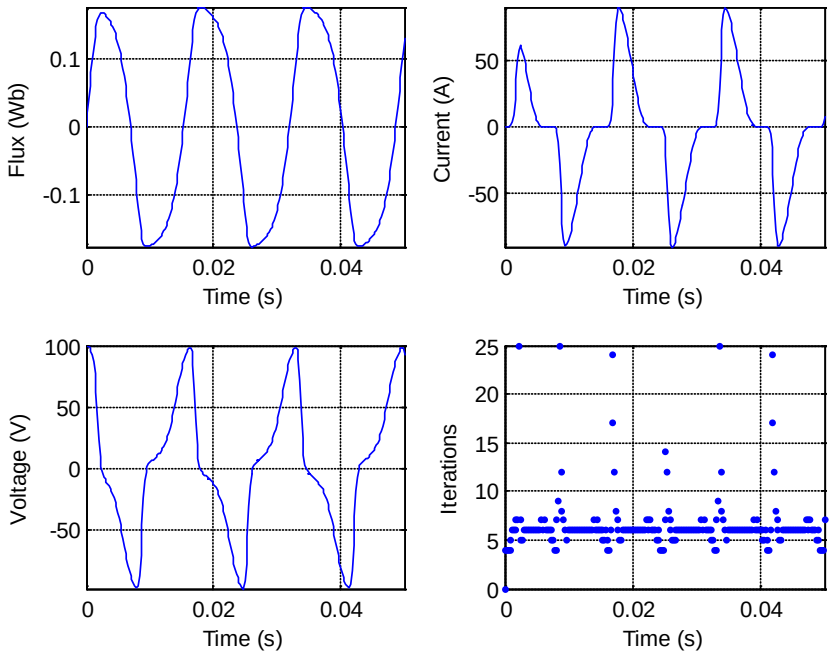

Figure 9.27: Simulation results from quadratic system with quadratic integration (n=8).

4) Exponent n = 16

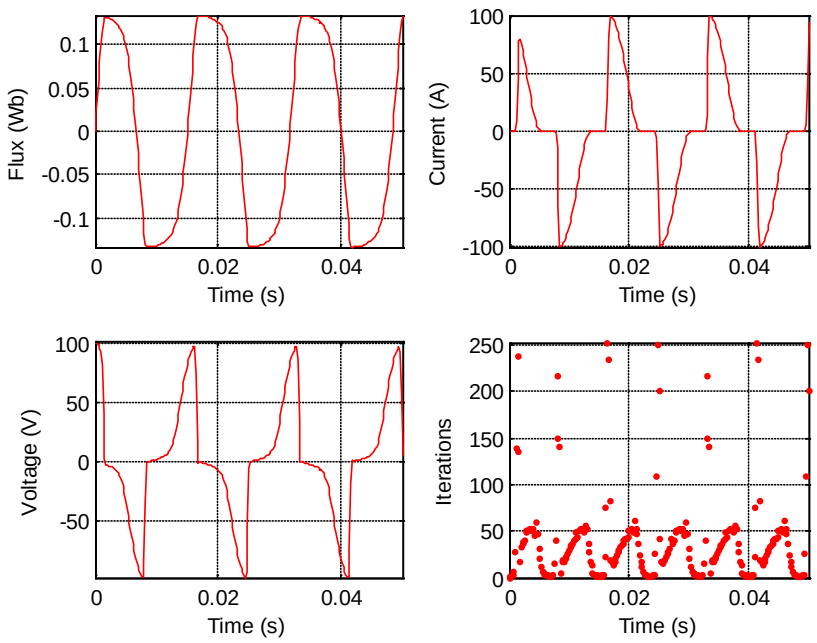

Figure 9.28: Simulation results from original system with trapezoidal integration (n=16).

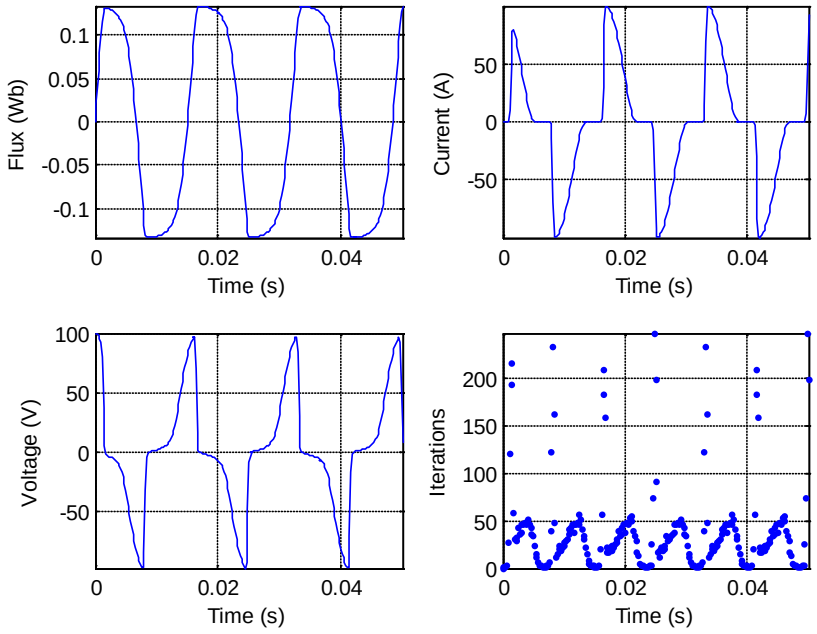

Figure 9.29: Simulation results from original system with quadratic integration (n=16).

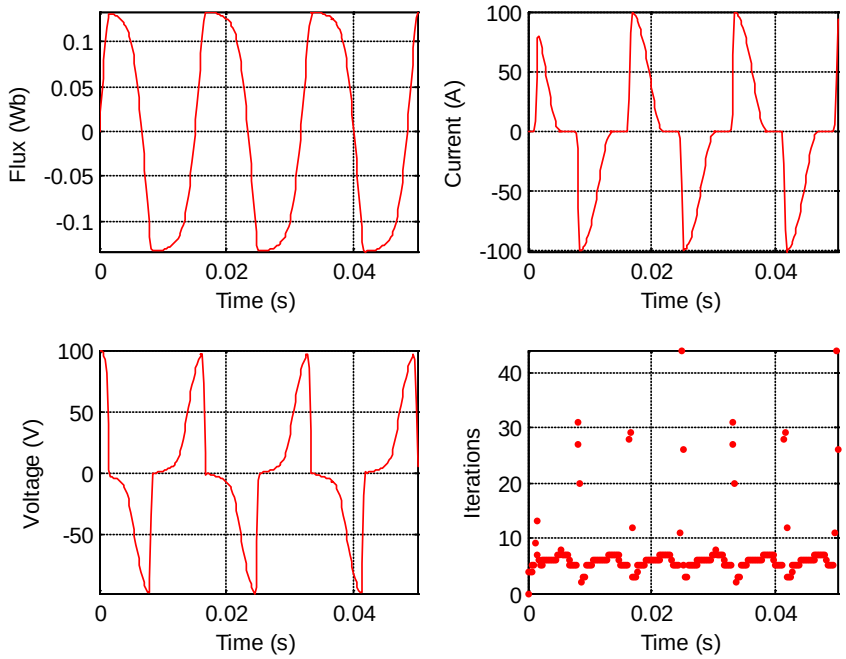

Figure 9.30: Simulation results from quadratic system with trapezoidal integration (n=16).

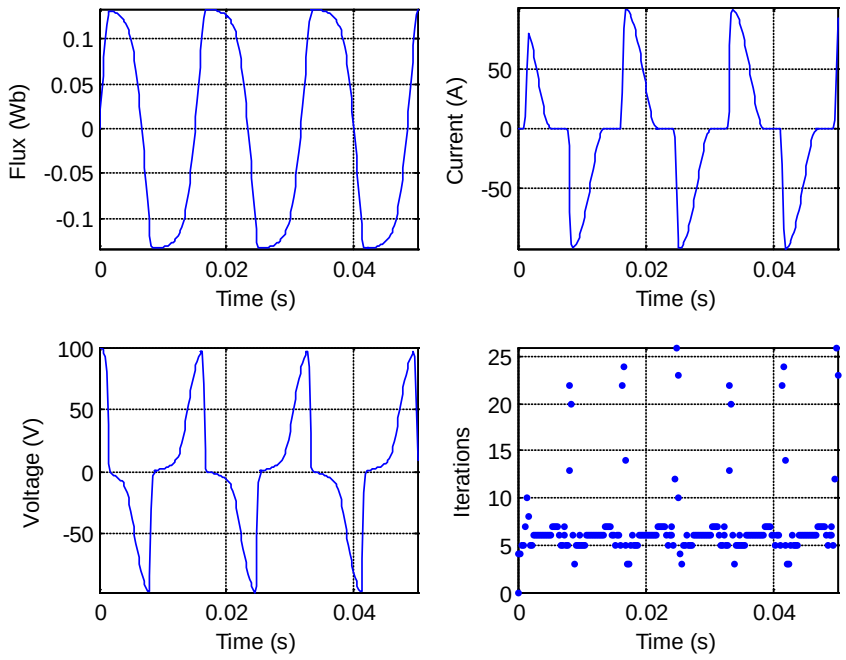

Figure 9.31: Simulation results from quadratic system with quadratic integration (n=16).

5) Exponent n = 32

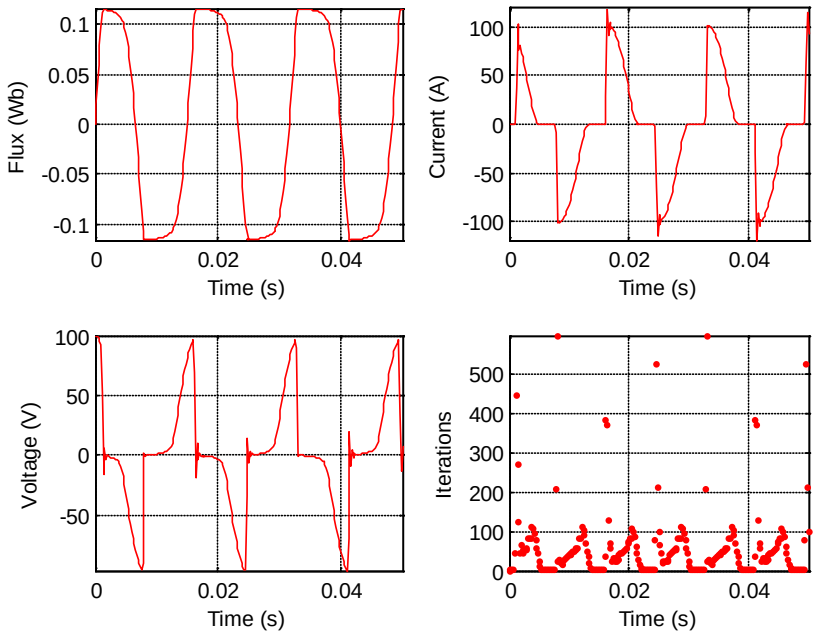

Figure 9.32: Simulation results from original system with trapezoidal integration (n=32).

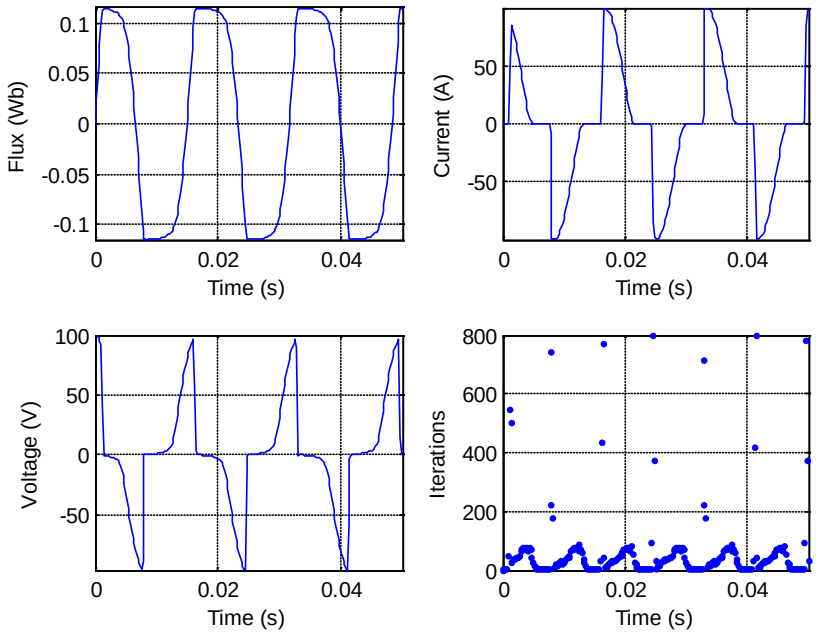

Figure 9.33: Simulation results from original system with quadratic integration (n=32).

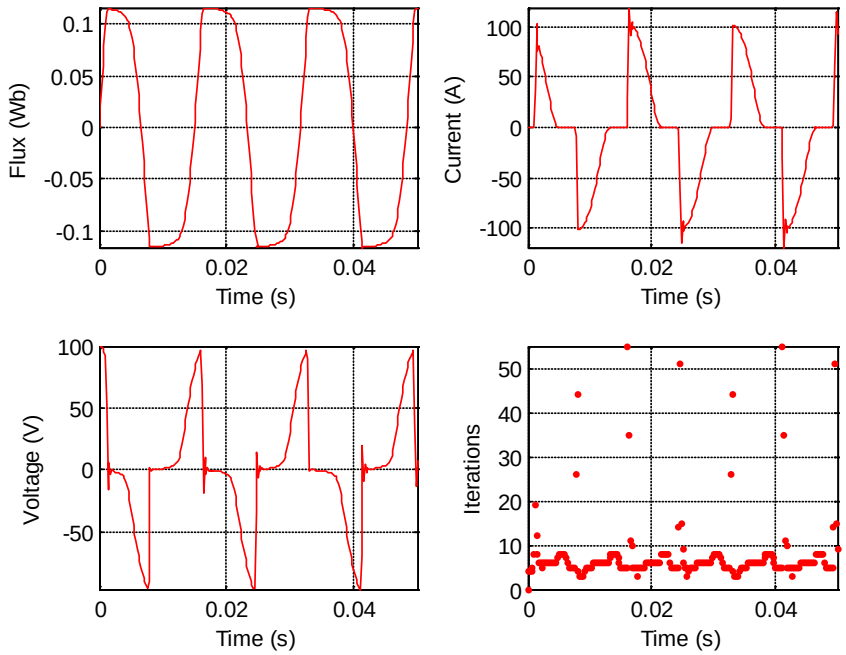

Figure 9.34: Simulation results from quadratic system with trapezoidal integration (n=32).

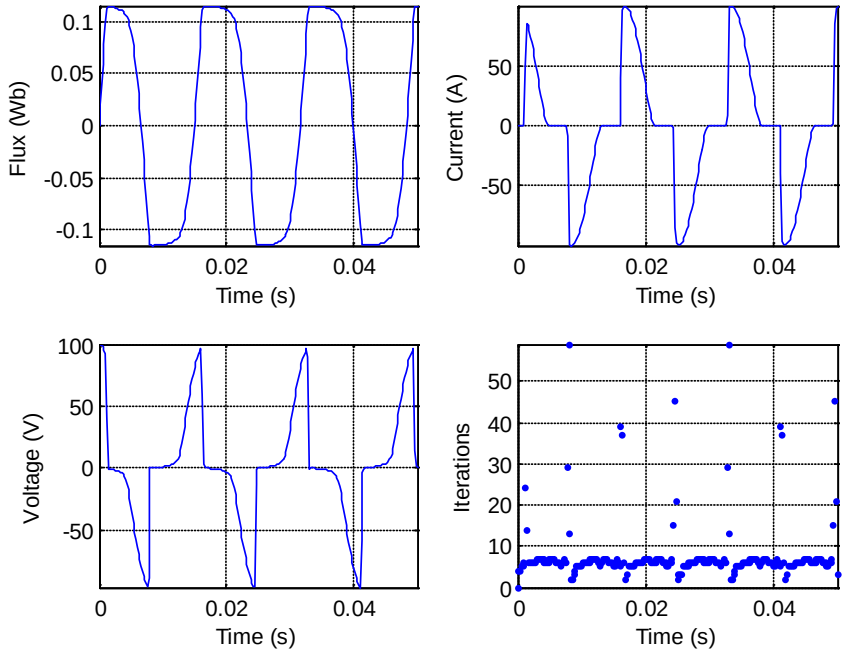

Figure 9.35: Simulation results from quadratic system with quadratic integration (n=32).

6) Exponent n = 64

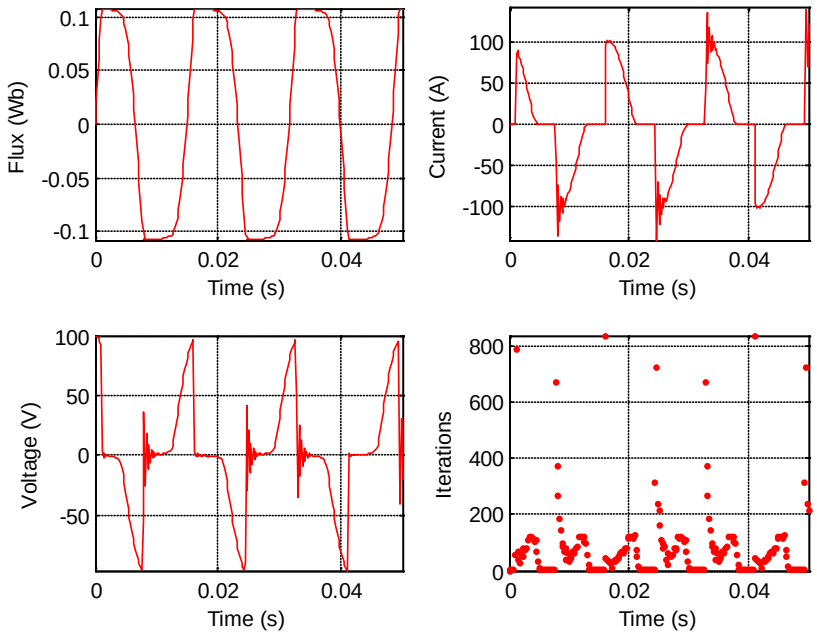

Figure 9.36: Simulation results from original system with trapezoidal integration (n=64).

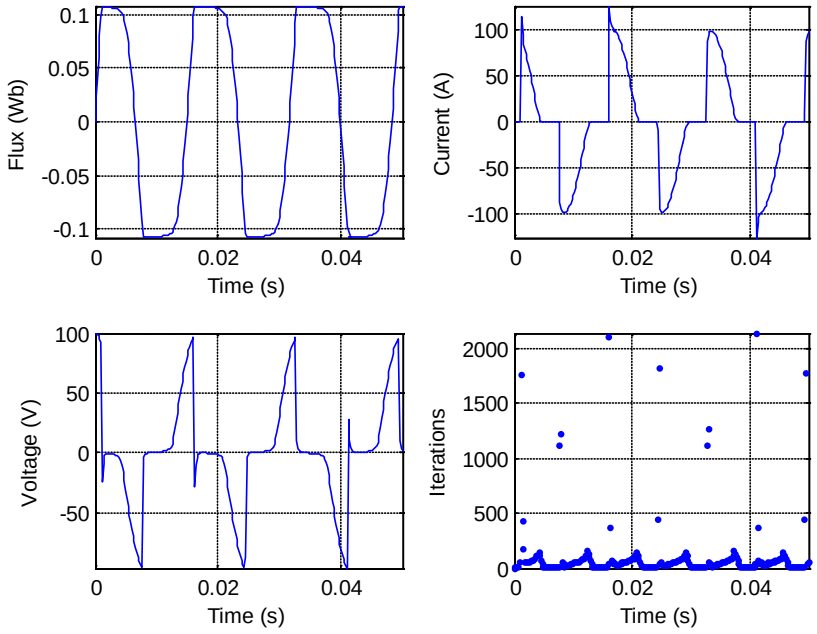

Figure 9.37: Simulation results from original system with quadratic integration (n=64).

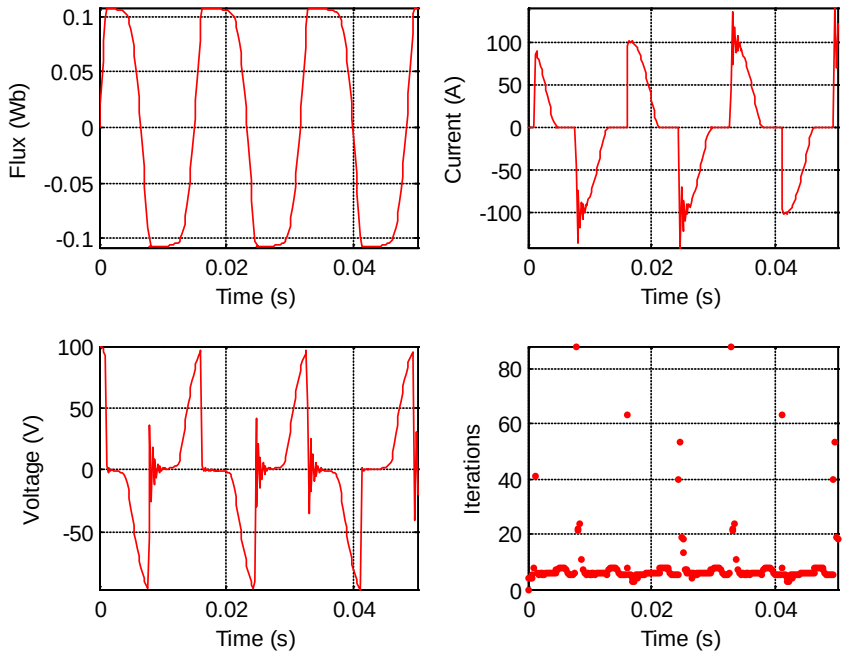

Figure 9.38: Simulation results from quadratic system with trapezoidal integration (n=64).

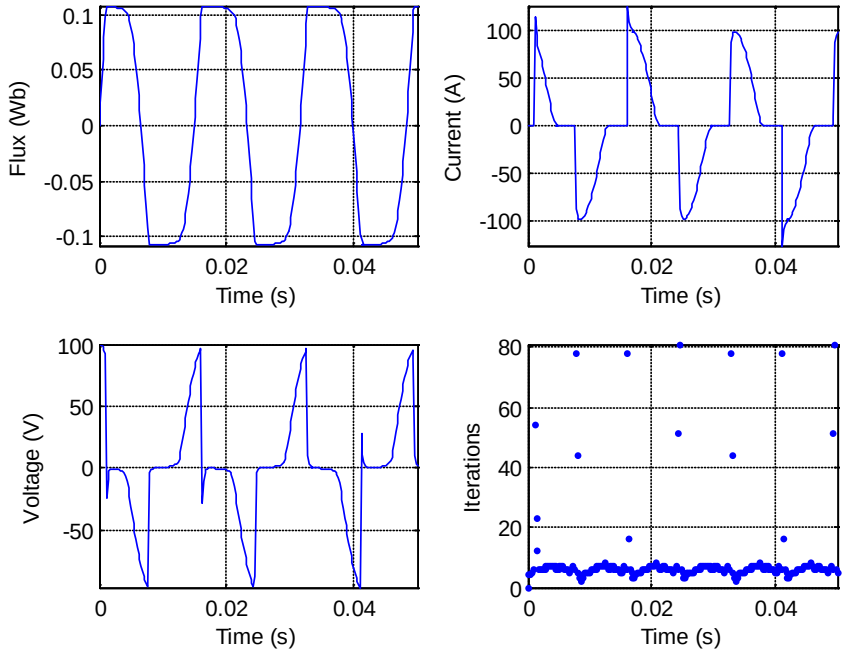

Figure 9.39: Simulation results from quadratic system with quadratic integration (n=64).

7) Exponent n = 128

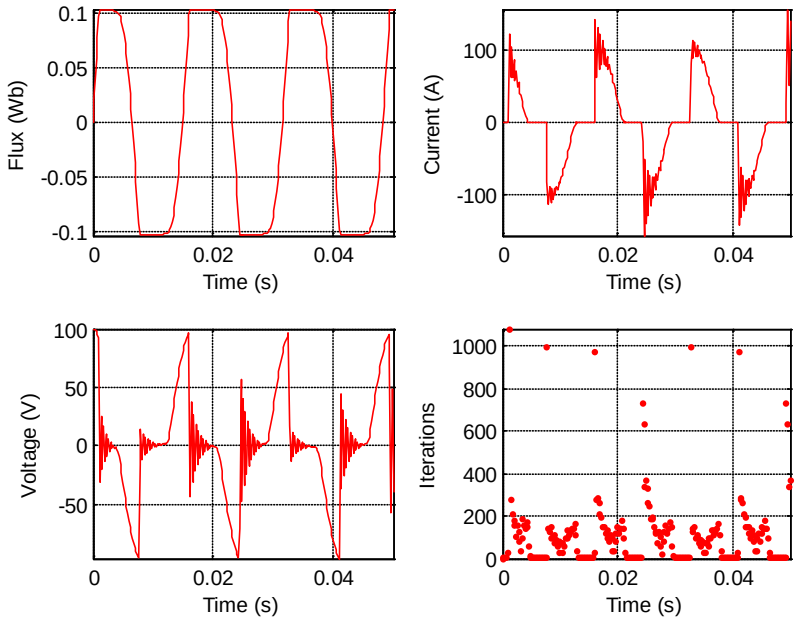

Figure 9.40: Simulation results from original system with trapezoidal integration (n=128).

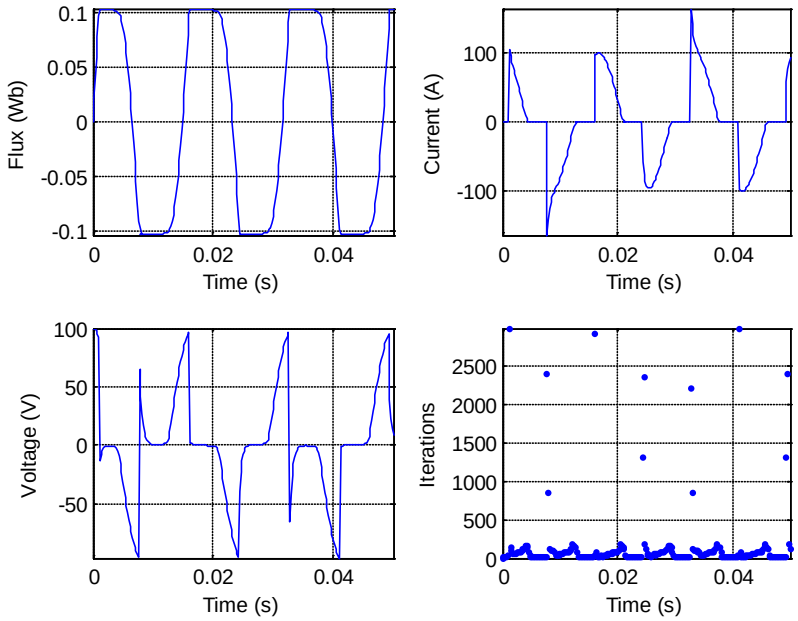

Figure 9.41: Simulation results from original system with quadratic integration (n=128).

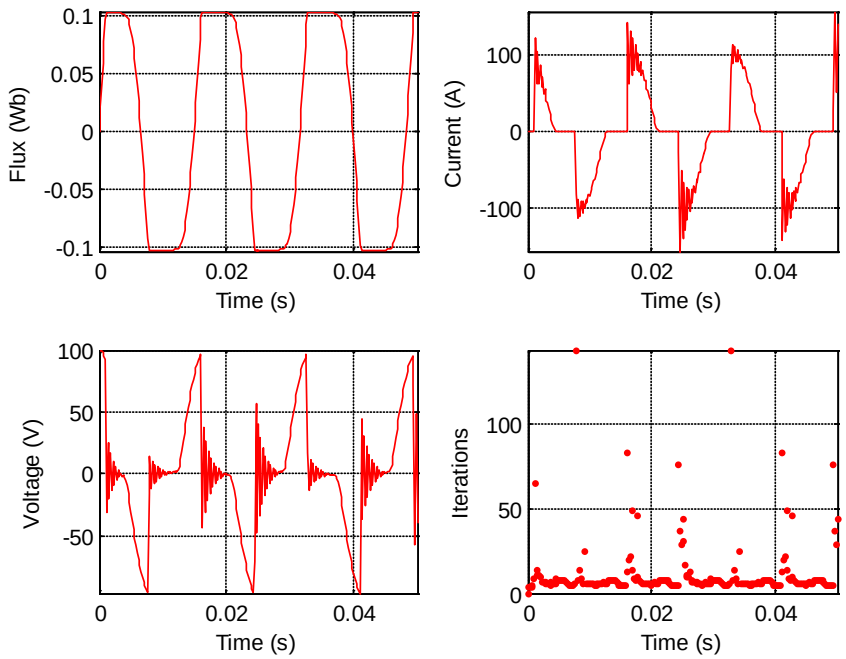

Figure 9.42: Simulation results from quadratic system with trapezoidal integration (n=128).

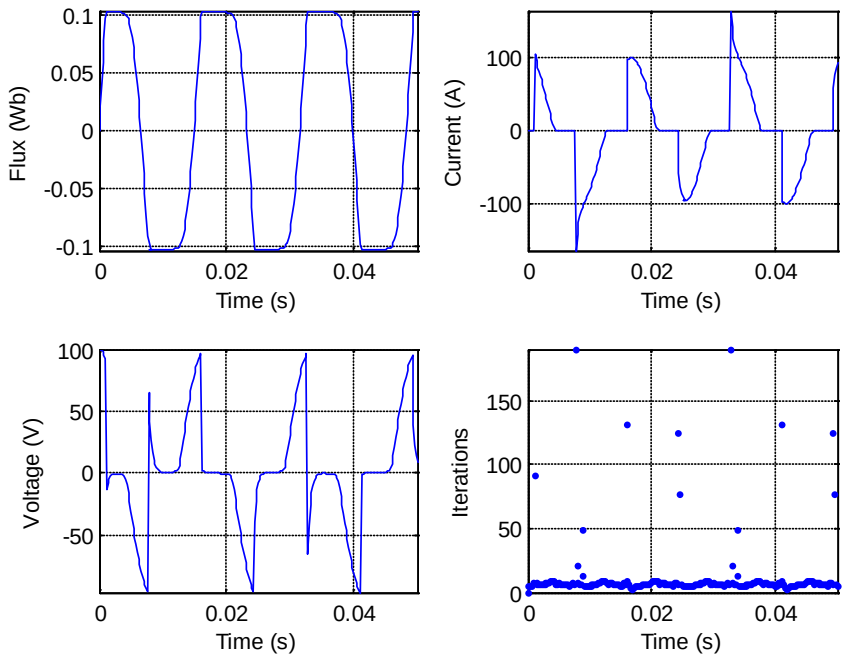

Figure 9.43: Simulation results from quadratic system with quadratic integration (n=128).

Some comparative results of the computational effort required by each one of the cases considered are presented next. This is mainly defined by the number of Newton iterations required at each integration time step, for each case. This is illustrated in all the previous figures, along with the simulation results. Table 9.1 through Table 9.3 provide some more details about the computational time and the average and maximum number of iterations required by each methodology for solving each case. The average number of iterations is the average over all the time steps of the simulation period. The maximum number refers to the maximum number of iterations that were required at some time step of the entire simulation period. Figure 9.44 to Figure 9.46 graphically illustrate these results.

Table 9.1: Simulation execution time for each methodology.

n	Execution time (s)			
	Original Trapezoidal	Original Quadratic	Quadratized Trapezoidal	Quadratized Quadratic
2	1.640	1.625	1.219	1.657
4	3.515	3.282	1.985	2.063
8	7.422	7.953	2.828	2.625
16	12.312	11.984	2.953	2.782
32	17.469	19.250	3.188	3.219
64	24.203	32.468	3.610	3.813
128	33.578	42.531	4.719	4.875

Table 9.2: Average number (over all time steps) of required Newton iterations for each methodology.

n	Average # of iterations			
	Original Trapezoidal	Original Quadratic	Quadratized Trapezoidal	Quadratized Quadratic
2	4.4	4.4	3.7	4.0
4	10.4	9.7	4.7	4.9
8	23.5	24.7	6.6	6.5
16	39.2	37.5	7.1	6.8
32	56.5	61.2	7.6	7.6
64	78.0	102.8	8.6	8.7
128	108.8	136.1	11.2	10.9

Table 9.3: Maximum number (over entire simulation time) of required Newton iterations for each methodology.

n	Max # of iterations			
	Original Trapezoidal	Original Quadratic	Quadratized Trapezoidal	Quadratized Quadratic
2	10	9	5	5
4	20	19	5	6
8	97	102	30	25
16	253	247	44	26
32	599	801	55	59
64	840	2139	88	81
128	1080	2997	143	190

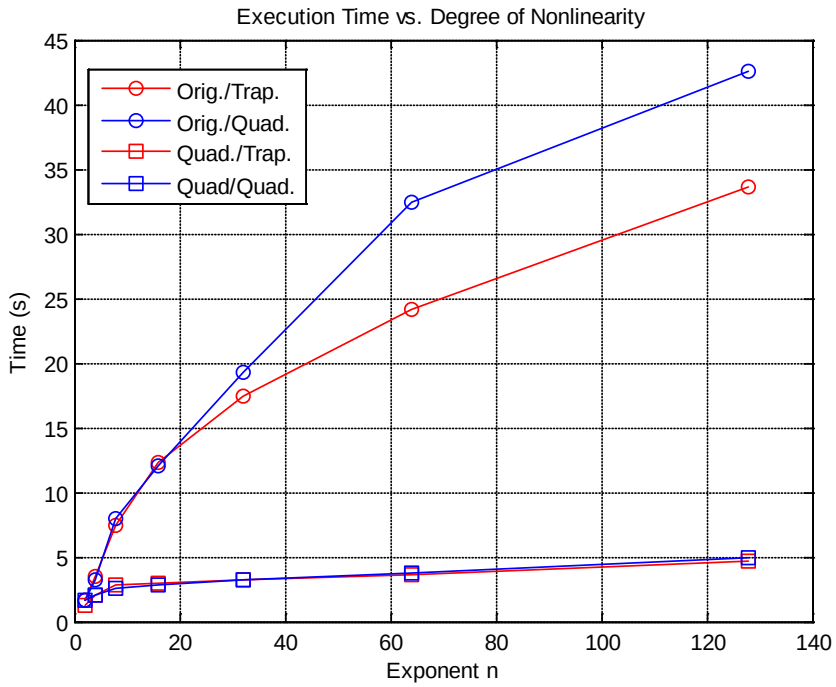

Figure 9.44: Execution time for the entire simulation for each methodology for each test case.

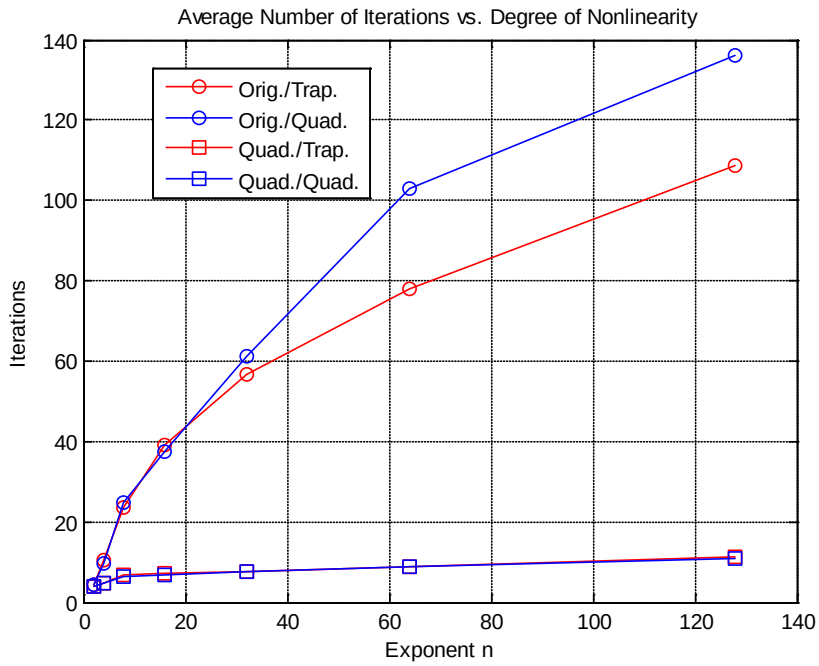

Figure 9.45: Average number of Newton iterations (at each time step) over the entire simulation period for each methodology for each test case.

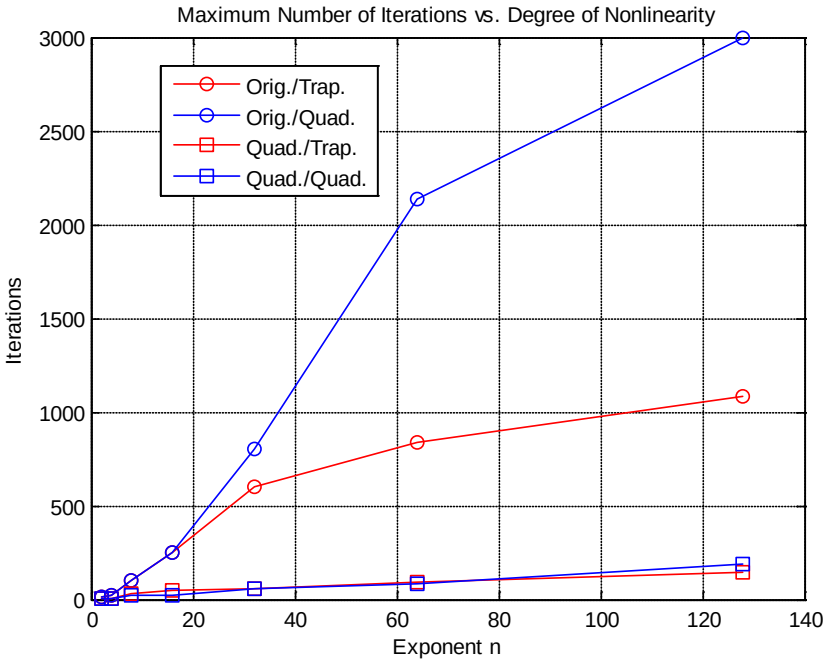

Figure 9.46: Maximum number of Newton iterations that were needed at some time step, for each methodology for each test case.

9.2.5 Single-Phase, Saturable-Core Transformer

The nonlinear inductor model described in the previous section is utilized to model a single-phase, saturable-core transformer. The model is used to represent nonlinearities that might occur during energization of transformers. Such condition may appear during cold load pick-up after severe disturbances and during transients in distribution feeders.

The transformer model is illustrated in Figure 9.47. The transformer core branch is modeled as an equivalent, nonlinear, saturable reactor. The system model in compact form is

$$\frac{d\lambda(t)}{dt} = e_1(t)\ , \tag{9.12}$$

$$v_1(t) - v_2(t) = r_1 i_1(t) + L_1 \frac{di_1(t)}{dt} + e_1(t), \tag{9.13}$$

$$v_3(t) - v_4(t) = r_2 i_3(t) + L_2 \frac{di_3(t)}{dt} + te_1(t), \tag{9.14}$$

$$i_m(t) = i_0 \cdot \left|\frac{\lambda(t)}{\lambda_0}\right|^n \cdot sgn(\lambda(t)) + g_L e_1(t), \tag{9.15}$$

$$i_1(t) - ti_3(t) - i_m(t) = 0, \tag{9.16}$$

$$i_2(t) = -i_1(t), \tag{9.17}$$

$$i_4(t) = -i_3(t), \tag{9.18}$$

where the symbols are as illustrated in Figure 9.47. More details on the model development can be found in Appendix A.

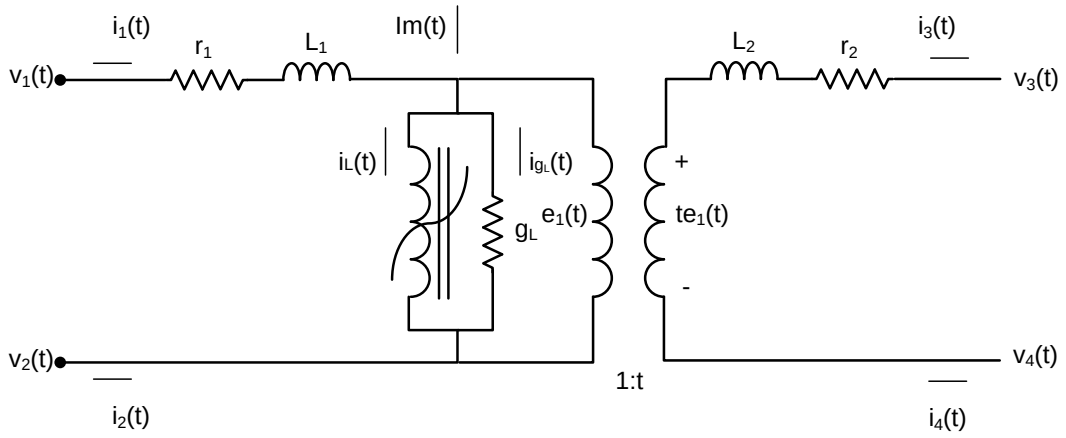

Figure 9.47: Saturable-core, single-phase transformer model.

Bringing the model into its standard form and quadratizing it yields:

$$i_1 = i_1(t), \tag{9.19}$$

$$i_2 = -i_1(t), \tag{9.20}$$

$$i_3 = i_3(t), \tag{9.21}$$

$$i_4 = -i_3(t), \tag{9.22}$$

$$L_1 \frac{di_1(t)}{dt} = v_{L1}(t), \tag{9.23}$$

$$L_2 \frac{di_3(t)}{dt} = v_{L2}(t), \tag{9.24}$$

$$\frac{d\lambda(t)}{dt} = e_1(t), \tag{9.25}$$

$$0 = i_L(t) + i_{g_L}(t) - i_m(t), \tag{9.26}$$

$$0 = g_L e_1(t) - i_{g_L}(t), \tag{9.27}$$

$$0 = i_m(t) - i_1(t) + t i_3(t), \tag{9.28}$$

$$0 = r_1 i_1(t) + v_{L1}(t) + e_1(t) - v_1(t) + v_2(t), \tag{9.29}$$

$$0 = r_2 i_3(t) + v_{L2}(t) + te_1(t) - v_3(t) + v_4(t), \tag{9.30}$$

$$0 = i_L(t) - i_0 \cdot z_m(t) \cdot [sgn(\lambda(t))]^{n+1}, \tag{9.31}$$

$$0 = z_1(t) - \left(\frac{\lambda(t)}{\lambda_0}\right)^2, \tag{9.32}$$

$$0 = z_2(t) - z_1^2(t), \tag{9.33}$$

…

$$0 = z_{m_1}(t) - z_{m_1-1}^2(t), \tag{9.31+m_1}$$

$$0 = z_{m_1+1}(t) - z_{i_1}(t) \cdot z_{j_1}(t), \tag{9.31+m_1+1}$$

$$0 = z_{m_1+2}(t) - z_{m_1+1}(t) \cdot z_{j_2}(t), \tag{9.31+m_1+2}$$

…

$$\begin{cases} 0 = z_m(t) - z_{m-1}(t) \cdot z_{j_{m2}}(t), & if\ n\ even, \\ 0 = z_m(t) - z_{m-1}(t) \cdot \lambda(t), & if\ n\ odd. \end{cases} \tag{9.31+m_1+m_2}$$

More details on the "quadratization" procedure for this model are presented in Appendix A. The symbols i_1, i_2, i_3, and i_4 that appear on the left-hand side of (9.19) to (9.22) do not represent state variables and they will the eliminated once the device is connected to the rest of the network and the connectivity constraints (Kirchhoff's current law) are applied. After applying the discretization rule (trapezoidal or quadratic integration) to the three differential equations the algebraic companion form of the transformer model is obtained, at each time step, as described in Appendix A.

The values of the system parameters are set to $r_1 = r_2 = 0.1\ Ohm$, $L_1 = L_2 = 0.5\ mH$, $g_L = 10^{-4}\ Mho$, $i_0 = 0.5\ A$ and $\lambda_0 = 0.4\ Wb$. The used values of the exponent *n* are set to 2, 4, 8, and 16 and a parametric study is conducted gradually increasing the

nonlinearity of the system. A sinusoidal AC voltage $v_{AC}(t)$ of 60 Hz and of 110 V rms value is applied to the primary side of the transformer ($v_{AC}(t) = v_1(t) - v_2(t) = \sqrt{2} \cdot 110 \cdot \cos(120\pi t)$). The secondary side voltage is defined as the system output, i.e. $v_{out}(t) = v_3(t) - v_4(t)$. A resistive load $R = 1\ Ohm$ is connected to the secondary side of the transformer. A time step of 200 μs is used for the simulations and the Matlab nonlinear equation solver is used for solving the set of resulting algebraic equations at each time step.

Results from the system simulation for various degrees of nonlinearity are shown in Figure 9.48 through Figure 9.63. The primary, secondary, and magnetizing currents, the output voltage, and the nonlinear inductor flux and emf are shown for each case. The magnetizing current of the transformer is the quantity that is primarily affected by the nonlinear inductor and contains a third harmonic component along with the fundamental frequency. As the degree of nonlinearity increases the third harmonic component becomes more evident and a fifth harmonic component also appears. The primary current is also polluted by these harmonics to a lesser extent, since the magnetizing current is a small component of it. The secondary voltage and current, as well as the magnetizing inductor flux and emf are not affected and they are of sinusoidal form at 60 Hz, even for high degrees of nonlinearity.

Comparing the model formulation and solution methodologies the standard approach of utilizing the original formulation with trapezoidal integration has the significant disadvantage of engaging to artificial numerical oscillations. More specifically the nonlinear inductor emf waveform is significantly corrupted by such oscillations. The oscillations decay very slowly, making the emf waveform inaccurate. The magnetizing

current is also affected, especially as the degree of nonlinearity increases, but to a much lesser extent. The rest of the outputs appear to be unaffected of such oscillations or of inaccuracies due to these oscillations in other system quantities. These numerical issues have a significant effect on the computational efficiency of the approach, which appears to be the worse in terms of computational burden.

The original formulation with quadratic integration is free of fictitious oscillations; however there is a bias in the nonlinear inductor emf waveform that decays rapidly with time. Therefore, this approach exhibits some transient inaccuracy in the emf waveform. The rest of the results are accurate. The quadratized system with trapezoidal integration has a very good behavior for low degrees of nonlinearity. The system does not engage into numerical oscillations, although the trapezoidal rule is used. It thus look as if the quadratization has eliminated the oscillation problem. However, for high degrees on nonlinearity an artificially bias is introduced to the magnetizing current. The form of the waveform is correct, but it is biased. This error also affects to a small extent the primary current. The rest of the outputs are very accurate. Finally, the quadratic system with quadratic integration is completely free of fictitious oscillations and exhibits a much lesser (but existing in high nonlinearities) bias in the magnetizing current. In terms of accuracy it provides the more precise results.

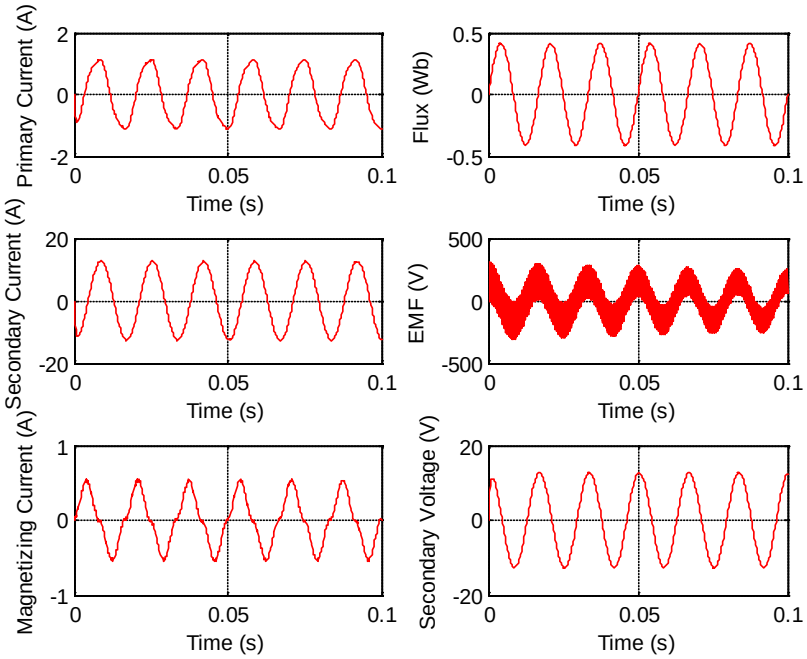

Figure 9.48: Simulation results from original system with trapezoidal integration (n=2).

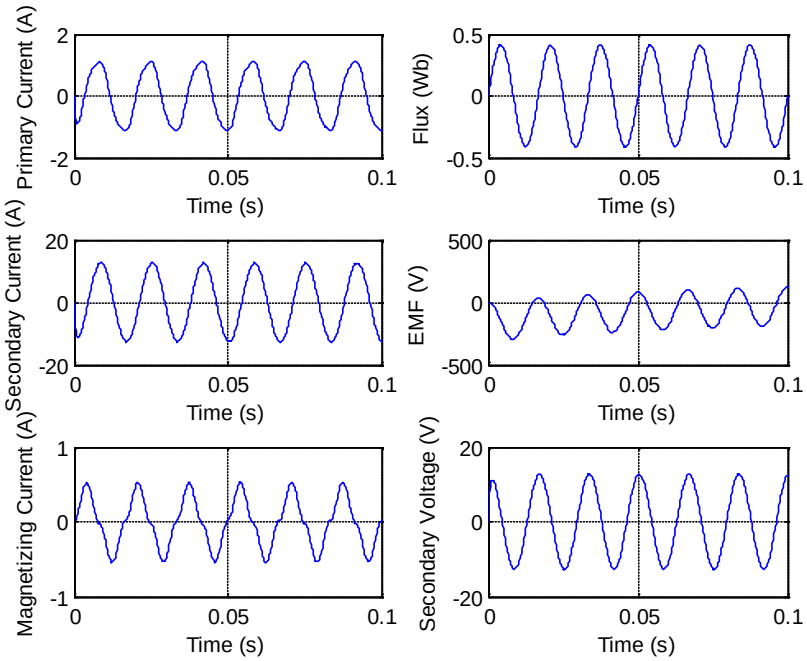

Figure 9.49: Simulation results from original system with quadratic integration (n=2).

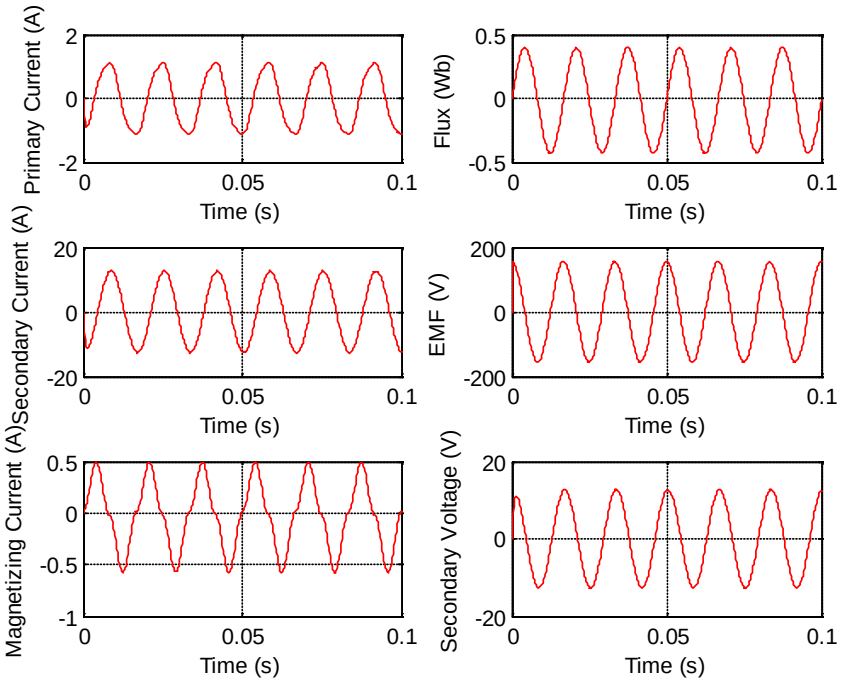

Figure 9.50: Simulation results from quadratic system with trapezoidal integration (n=2).

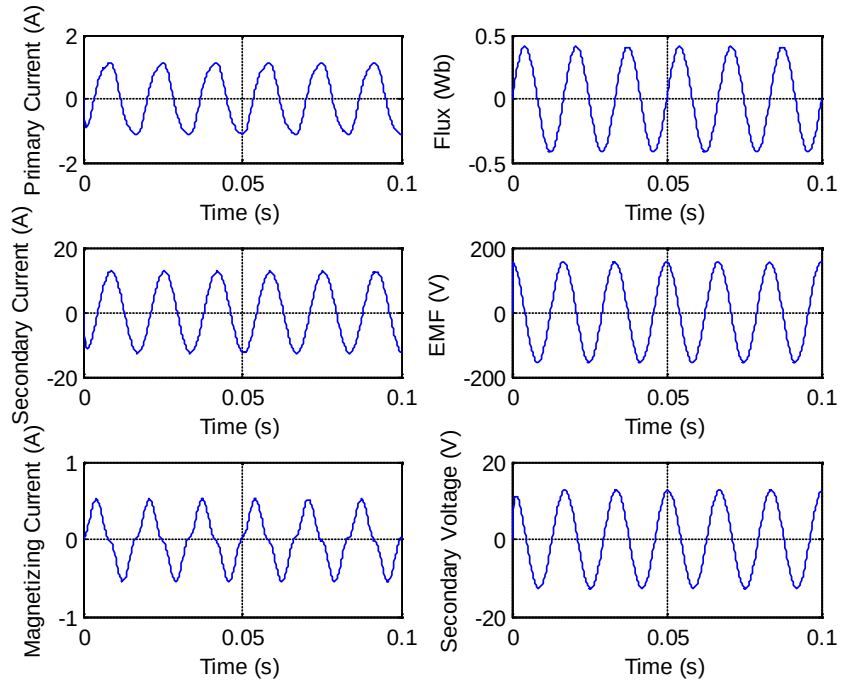

Figure 9.51: Simulation results from quadratic system with quadratic integration (n=2).

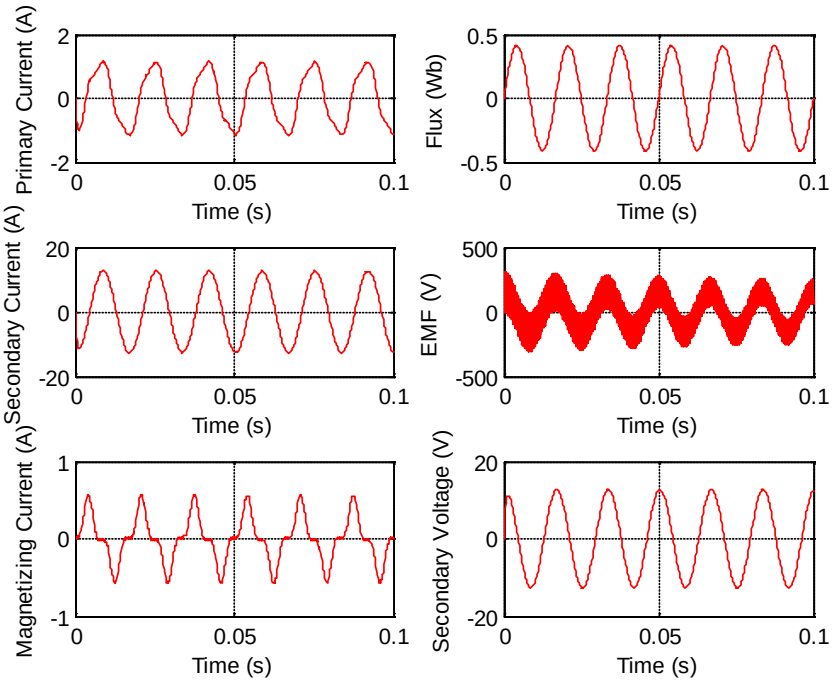

Figure 9.52: Simulation results from original system with trapezoidal integration (n=4).

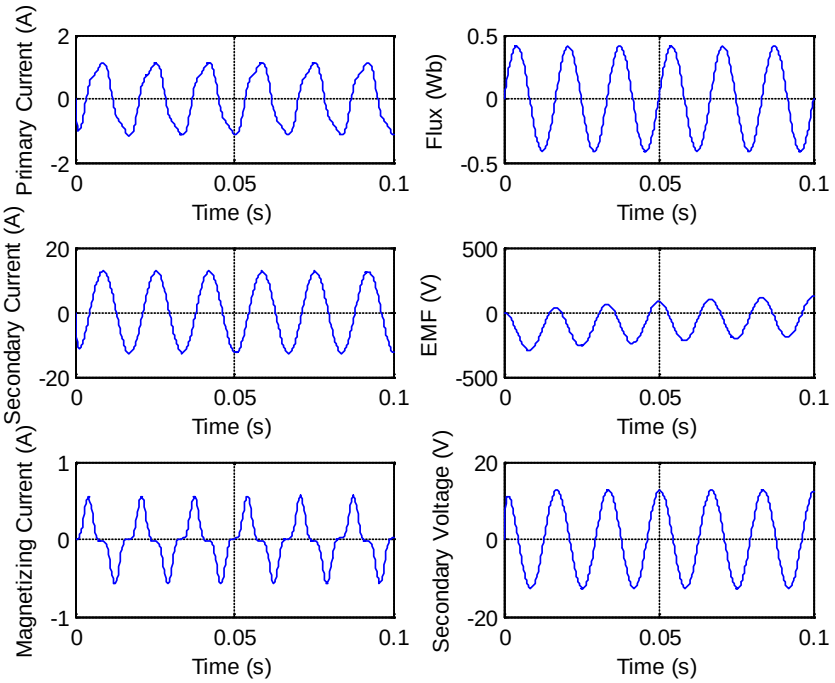

Figure 9.53: Simulation results from original system with quadratic integration (n=4).

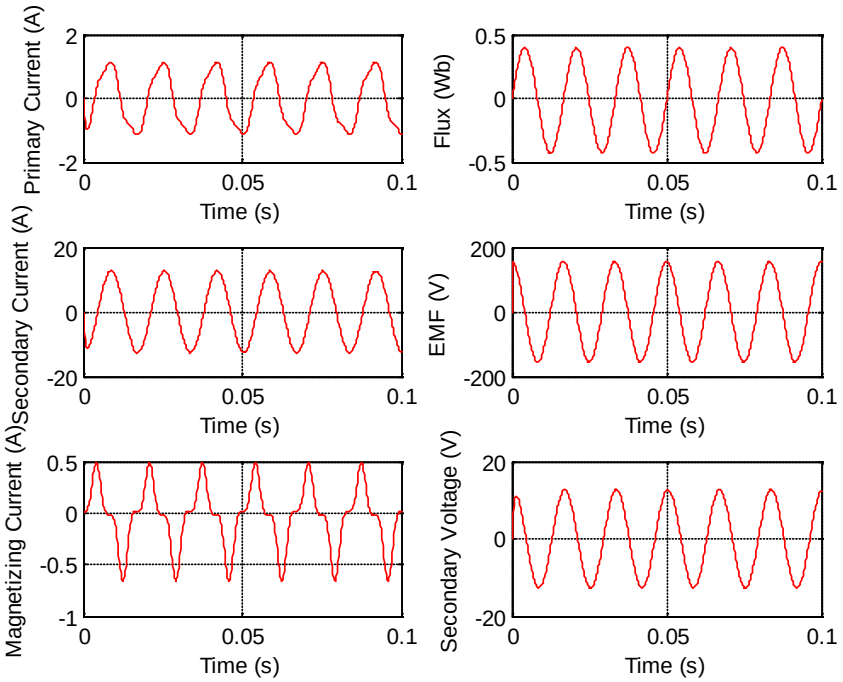

Figure 9.54: Simulation results from quadratic system with trapezoidal integration (n=4).

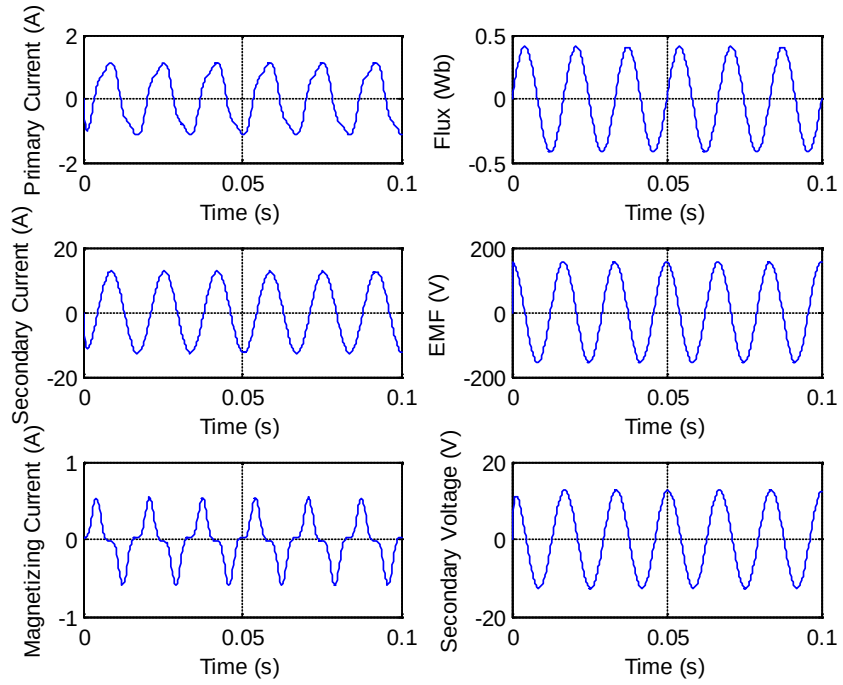

Figure 9.55: Simulation results from quadratic system with quadratic integration (n=4).

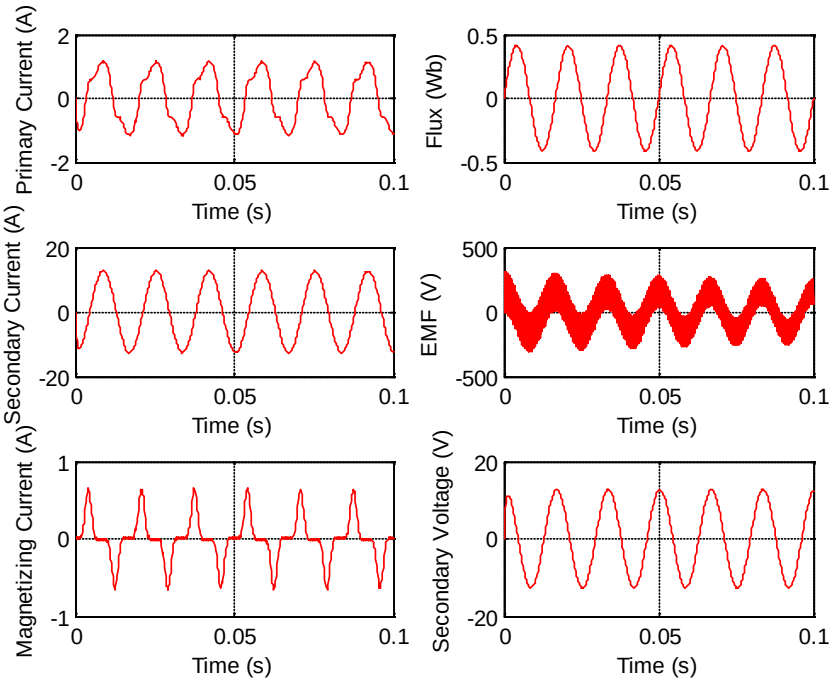

Figure 9.56: Simulation results from original system with trapezoidal integration (n=8).

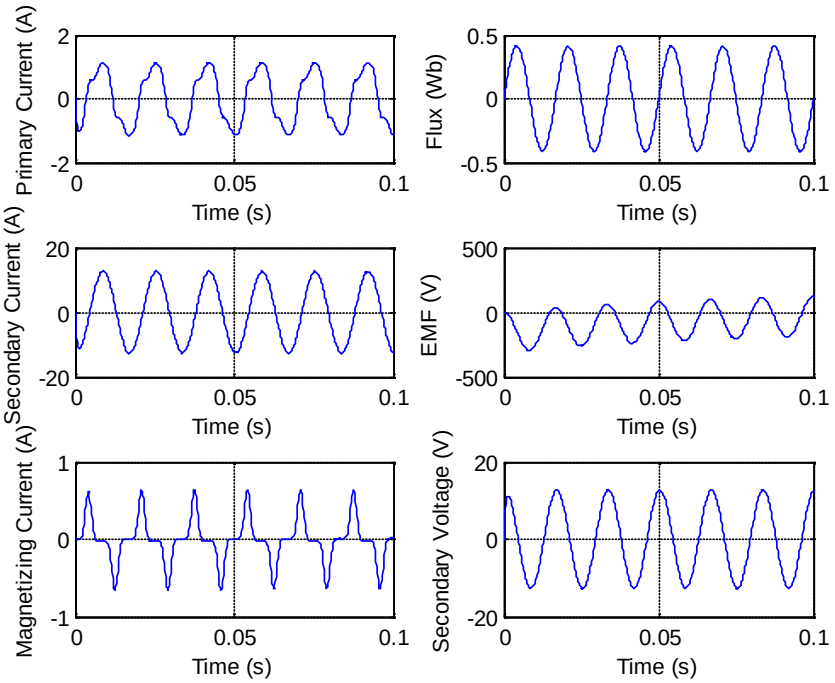

Figure 9.57: Simulation results from original system with quadratic integration (n=8).

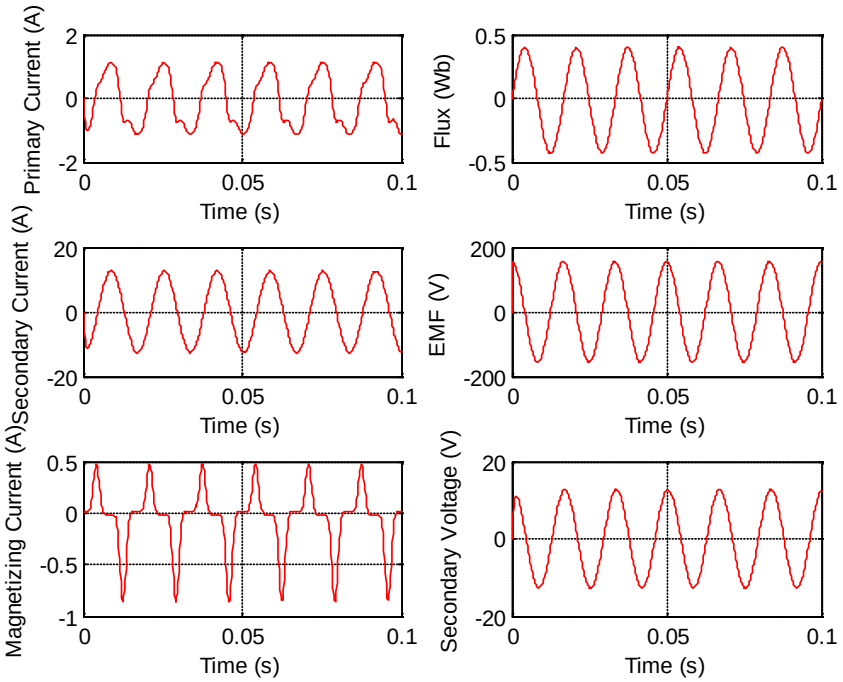

Figure 9.58: Simulation results from quadratic system with trapezoidal integration (n=8).

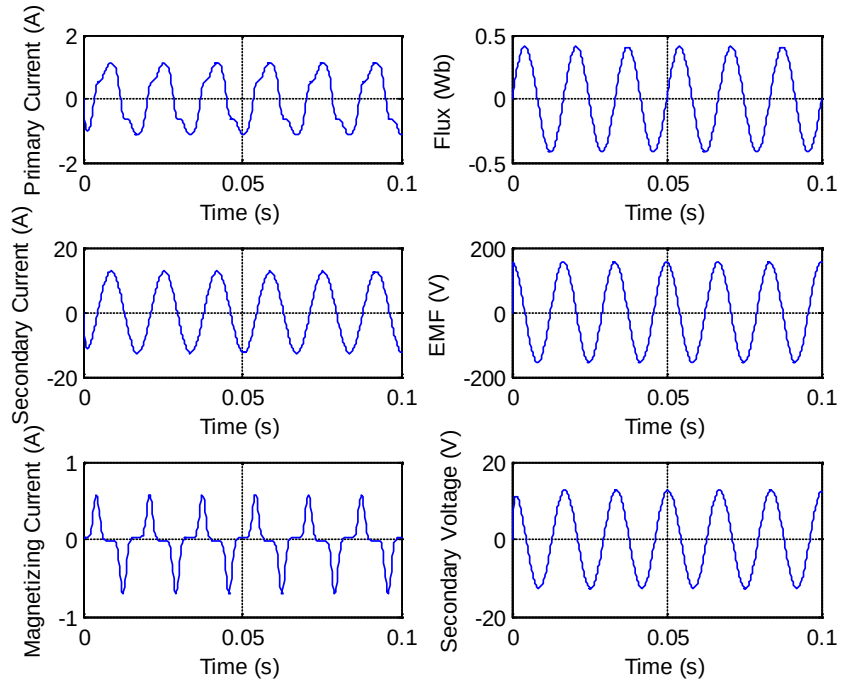

Figure 9.59: Simulation results from quadratic system with quadratic integration (n=8).

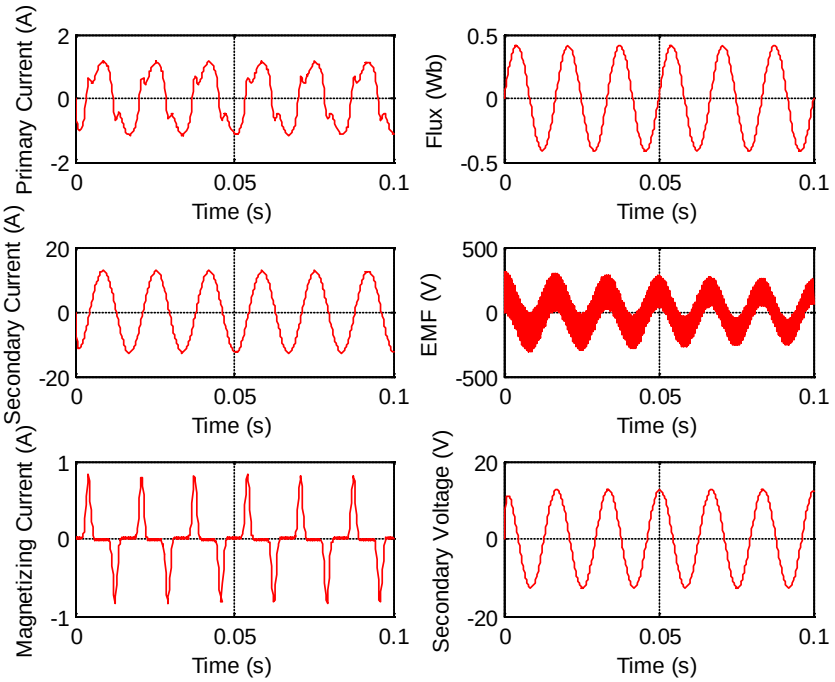

Figure 9.60: Simulation results from original system with trapezoidal integration (n=16).

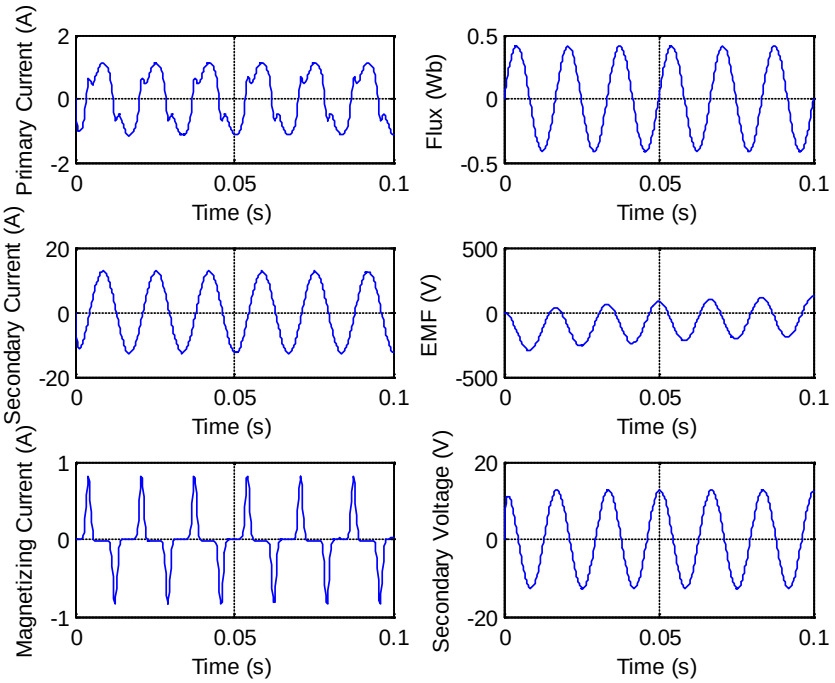

Figure 9.61: Simulation results from original system with quadratic integration (n=16).

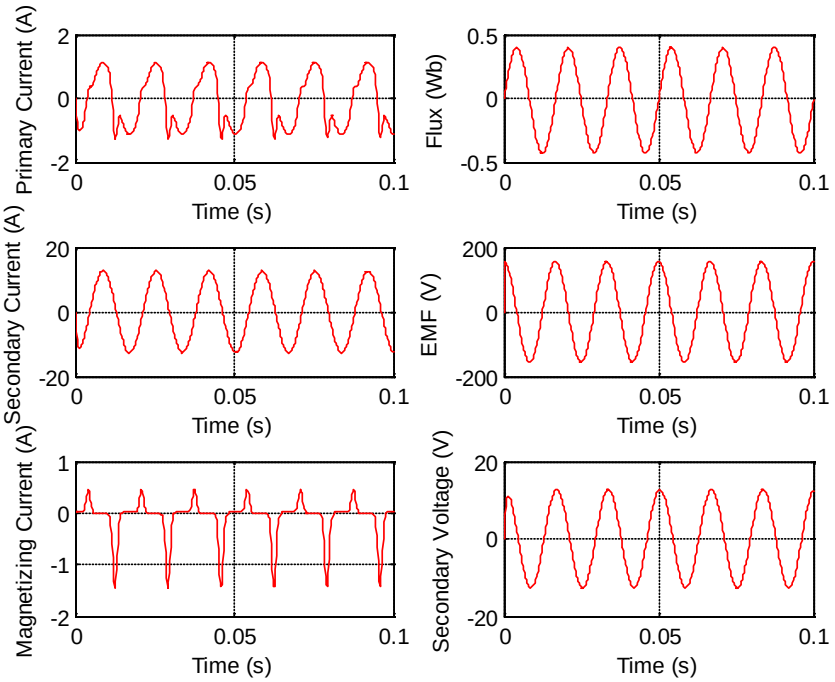

Figure 9.62: Simulation results from quadratic system with trapezoidal integration (n=16).

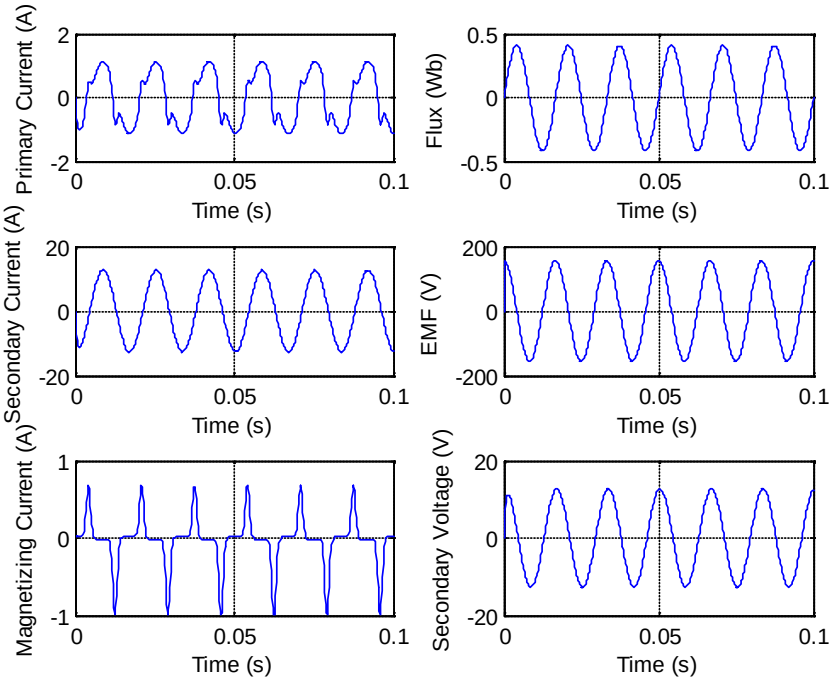

Figure 9.63: Simulation results from quadratic system with quadratic integration (n=16).

Table 9.4 through Table 9.6 and Figure 9.64 to Figure 9.66 present information about the computational efficiency of each approach. The standard approach of trapezoidal integration is the least efficient for this test case. The "quadratized" system with trapezoidal integration is the most efficient, while the original system with quadratic integration performs very well in terms of execution time. However, both these systems provide some inaccuracies and biases in the results. The proposed approach of quadratic system with quadratic integration appears to be the best combination of performance and accuracy. Furthermore, the quadratic systems exhibit a more robust behavior, in general.

Table 9.4: Simulation execution time for each methodology.

n	Execution time (s)			
	Original Trapezoidal	Original Quadratic	Quadratized Trapezoidal	Quadratized Quadratic
2	7.157	3.578	2.875	3.125
4	8.781	3.625	3.250	3.610
8	10.547	4.250	3.219	3.875
16	11.281	3.719	3.485	4.015

Table 9.5: Average number (over all time steps) of required Newton iterations for each methodology.

n	Average # of iterations			
	Original Trapezoidal	Original Quadratic	Quadratized Trapezoidal	Quadratized Quadratic
2	12.13	4.48	4.25	4.52
4	15.45	4.59	4.67	4.99
8	20.68	5.91	4.68	5.26
16	23.44	5.09	4.98	5.32

Table 9.6: Maximum number (over entire simulation time) of required Newton iterations for each methodology.

n	Average # of iterations			
	Original Trapezoidal	Original Quadratic	Quadratized Trapezoidal	Quadratized Quadratic
2	23	8	8	8
4	42	8	8	9
8	120	86	8	9
16	238	109	8	9

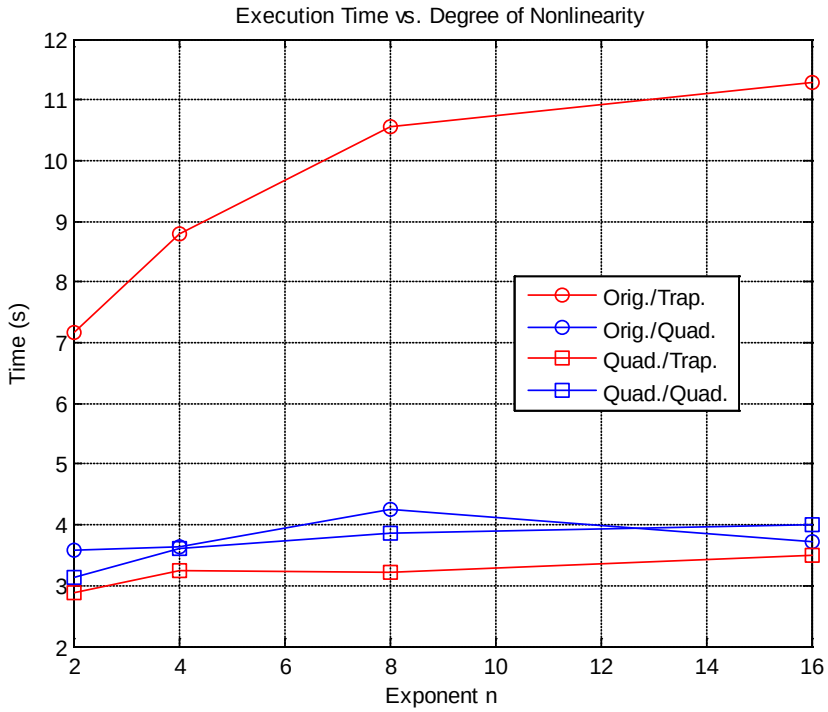

Figure 9.64: Execution time for the entire simulation for each methodology for each test case.

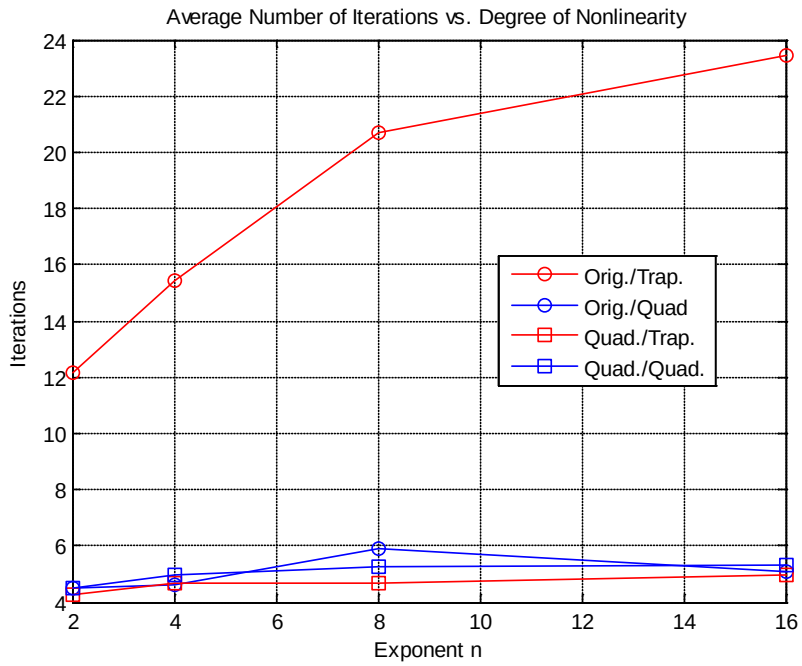

Figure 9.65: Average number of Newton iterations (at each time step) over the entire simulation period for each methodology for each test case.

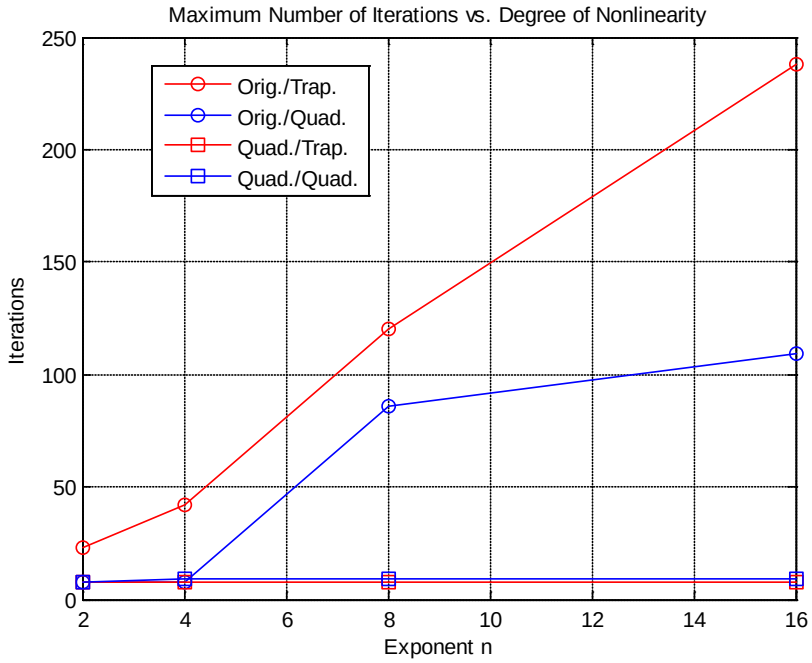

Figure 9.66: Maximum number of Newton iterations that were needed at some time step, for each methodology for each test case.

9.2.6 Single- and Three-Phase Induction Motor Startup

This example involves demonstration of the developed three- and single-phase induction motor models for full transient analysis. In particular the startup of two induction motors is simulated based on the methodology presented in this dissertation. The models are described in detail in Appendix A. The example also includes the implemented three- and single-phase saturable-core transformer models, which are again described in Appendix A.

The test system is presented in Figure 9.67. The system comprises of a generating unit at 18 kV, modeled as an equivalent three-phase source, a 18/115 kV step-up transformer, a transmission line, a 115/25 kV step-down transformer, two distribution lines, two distribution transformers from 25 kV to 480 V (one three-phase, one single-phase) and two induction-motor loads, one three-phase motor and one single-phase. The breakers of the system are also modeled. All the transformers are saturable-core transformers. Details on the data of all the system components and the type and loading of the motors are shown in Figure 9.68 through Figure 9.72.

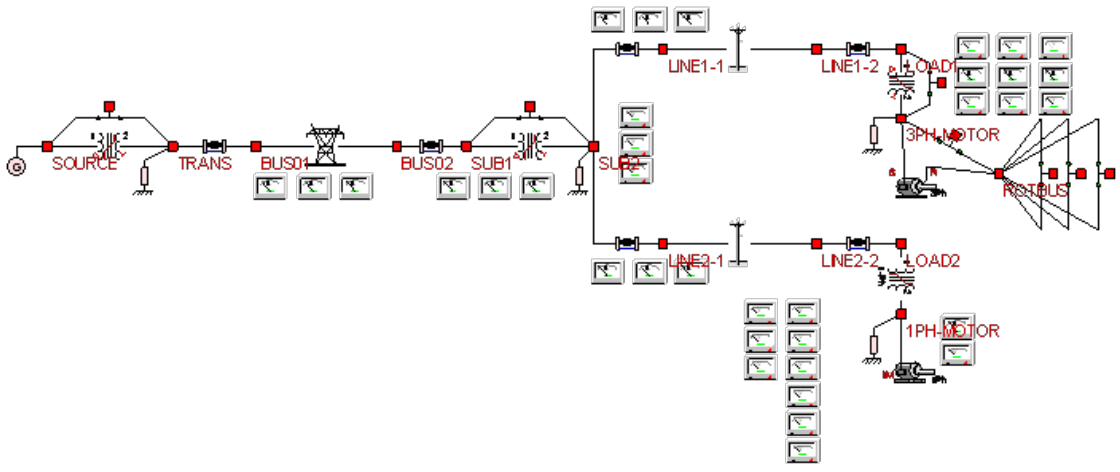

Figure 9.67: One-line diagram of test system for simulation of motor startup transients.

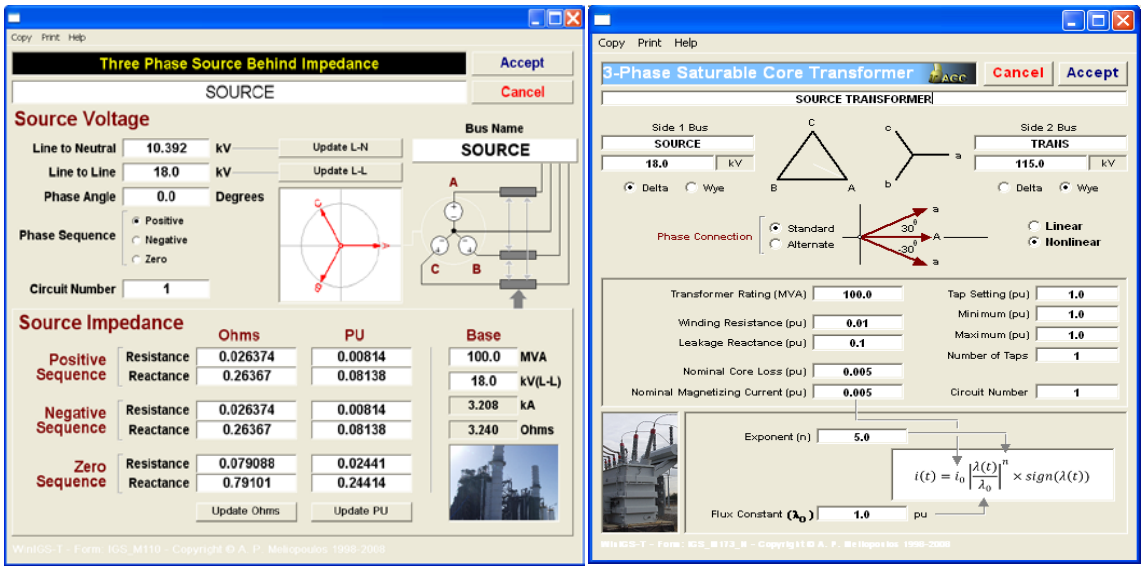

Figure 9.68: Data of equivalent source and step-up transformer.

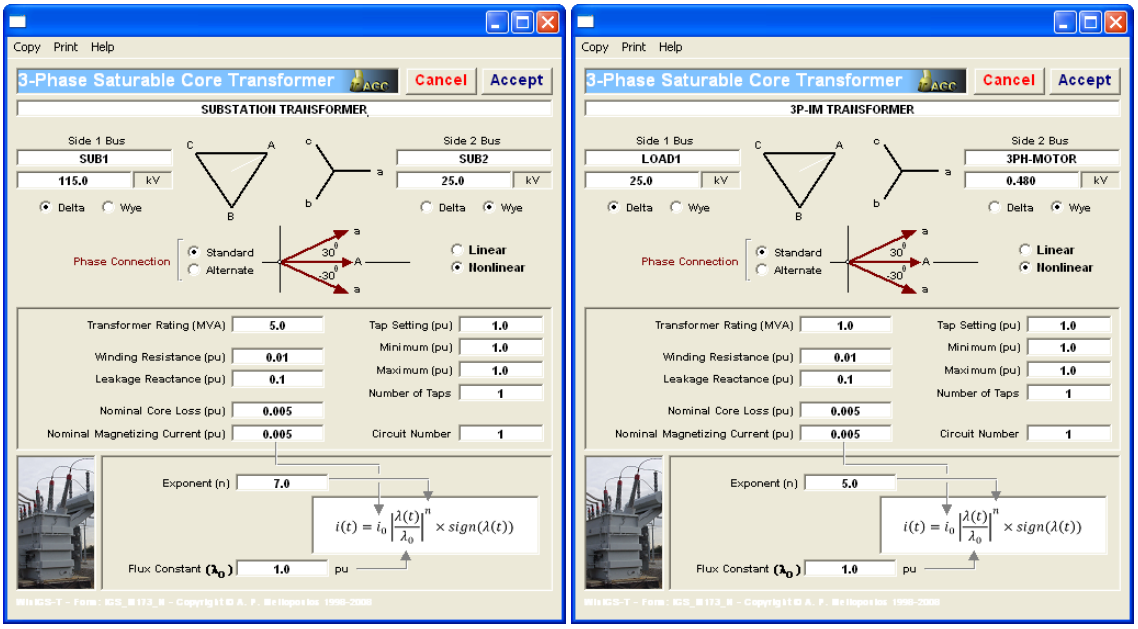

Figure 9.69: Data of substation and distribution three-phase transformers.

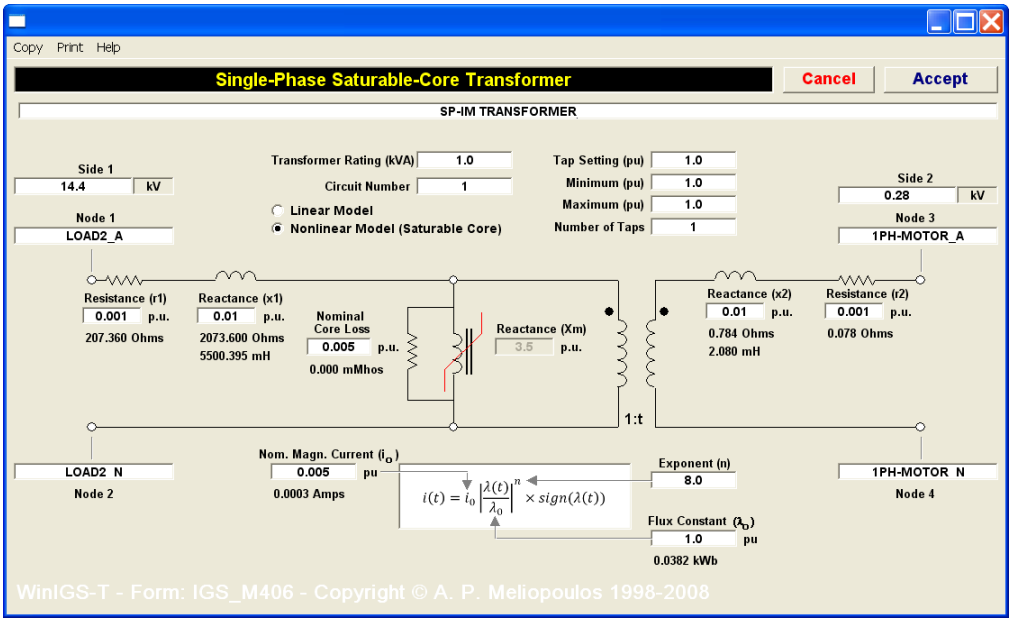

Figure 9.70: Data of single-phase-transformer.

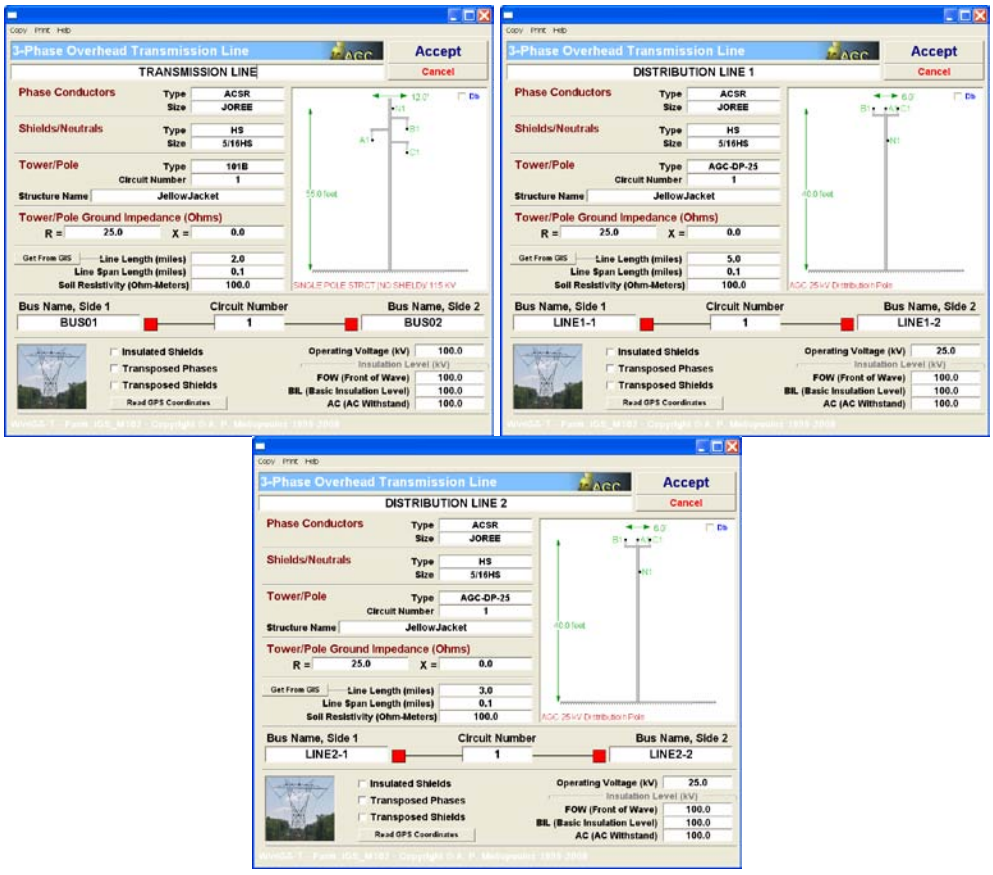

Figure 9.71: Data of transmission and distribution lines.

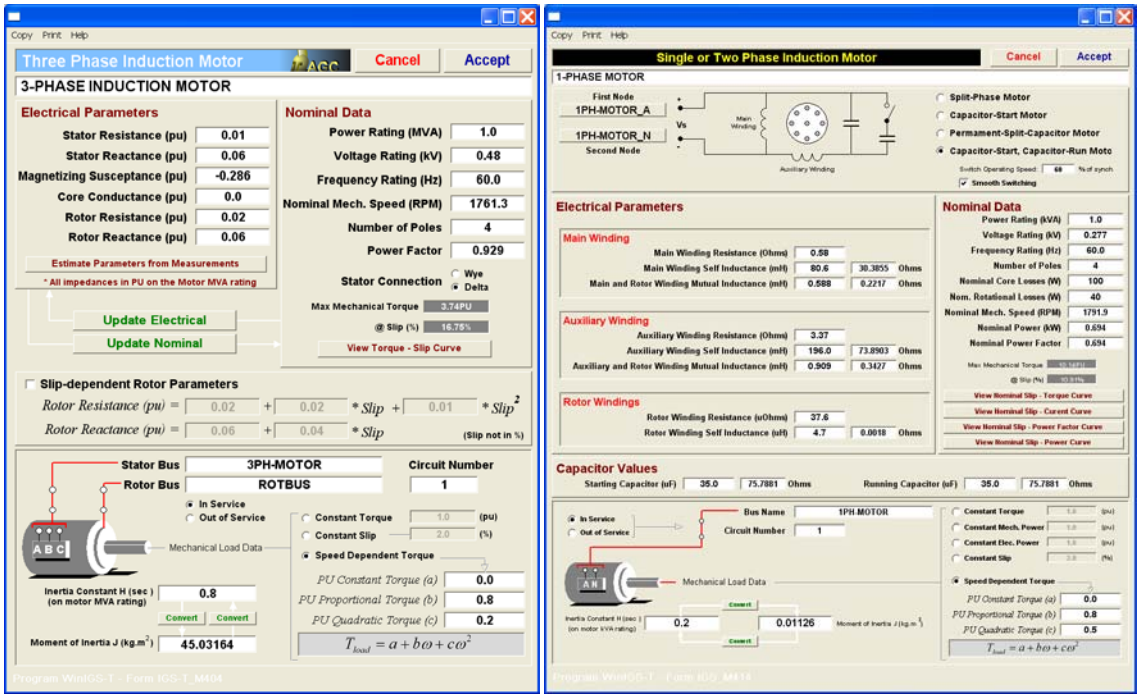

Figure 9.72: Data of three- and single-phase phase induction motors.

The system energization is simulated, which includes the starting up of the two motors (cold load pickup). The simulation results are presented in Figure 9.73 through Figure 9.76. Figure 9.73 shows the mechanical response of the motors in terms of speed and torque. The single-phase motor accelerates much faster, because of its small size and reaches steady state in about 0.7 s, while the three-phase motor takes almost 2 s to reach its final speed. The single-phase motor produces a pulsating torque, even at steady state that oscillates around the load torque. The three-phase motor, on the other hand, produces a constant electric torque. Figure 9.74 illustrates the voltages and currents at the motor terminals, while Figure 9.75 and Figure 9.76 illustrate the main and auxiliary winding currents of the single-phase motor and the currents through the substation transformer respectively. It is evident that the current consumption is large during the start-up and the voltages are suppressed during this period, until the motors reach their steady state.

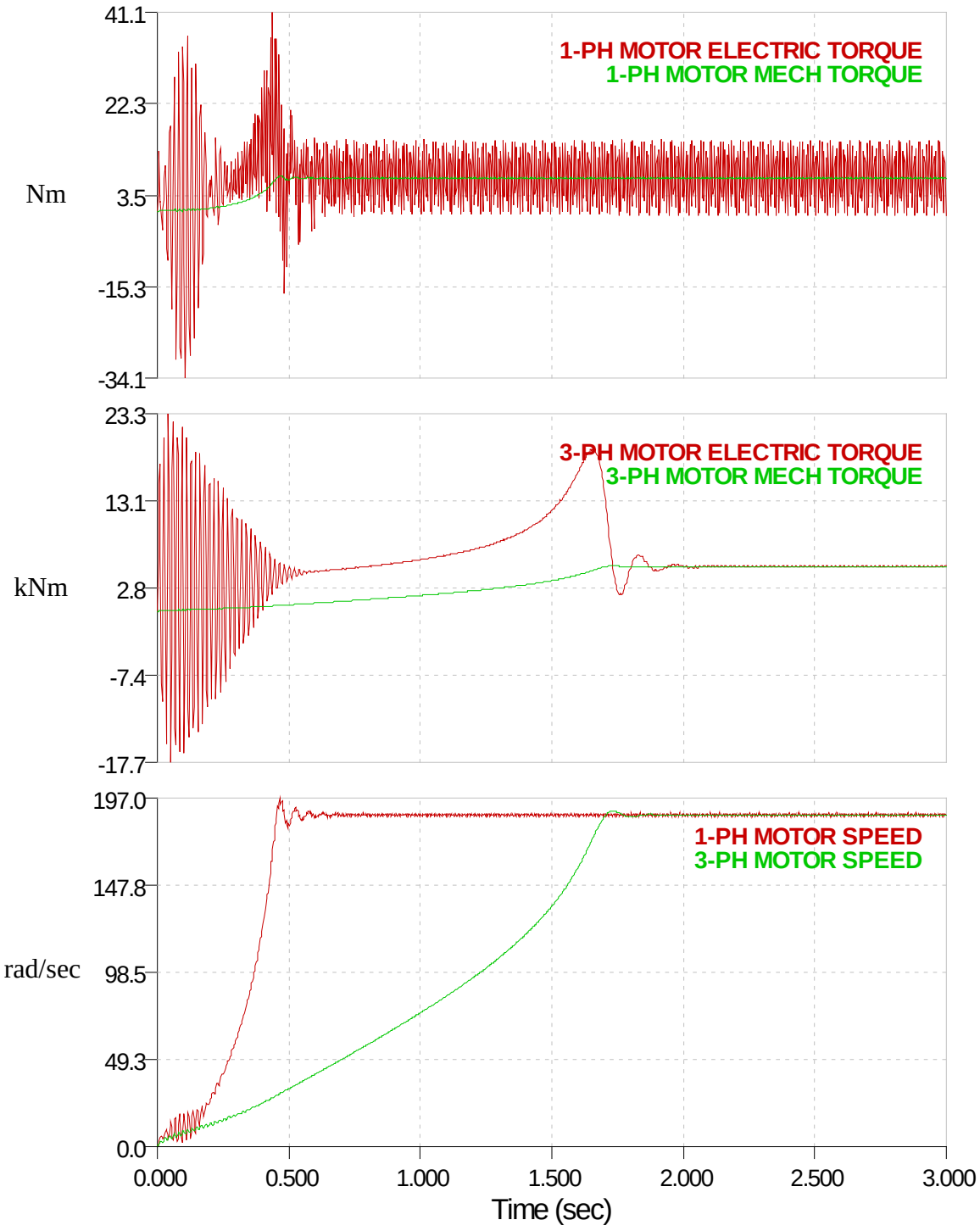

Figure 9.73: Mechanical and electrical torque and induction motor speed during start-up.

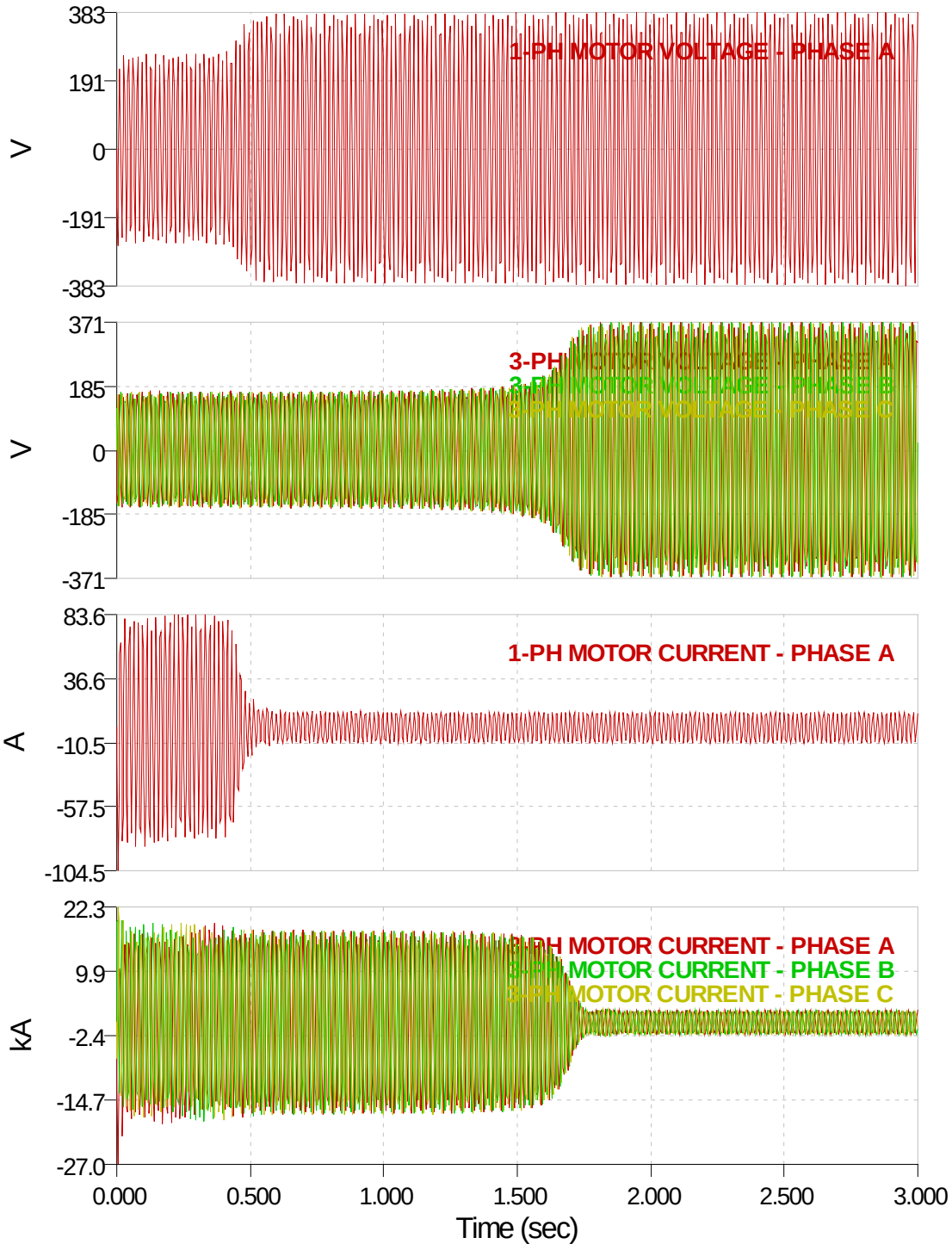

Figure 9.74: Single- and three-phase induction motor voltages and currents during start-up. Phases A, B, and C are shown for the three-phase motor and phase A for the single-phase.

Figure 9.75: Main- and auxiliary-winding currents of the single-phase induction motor during start up.

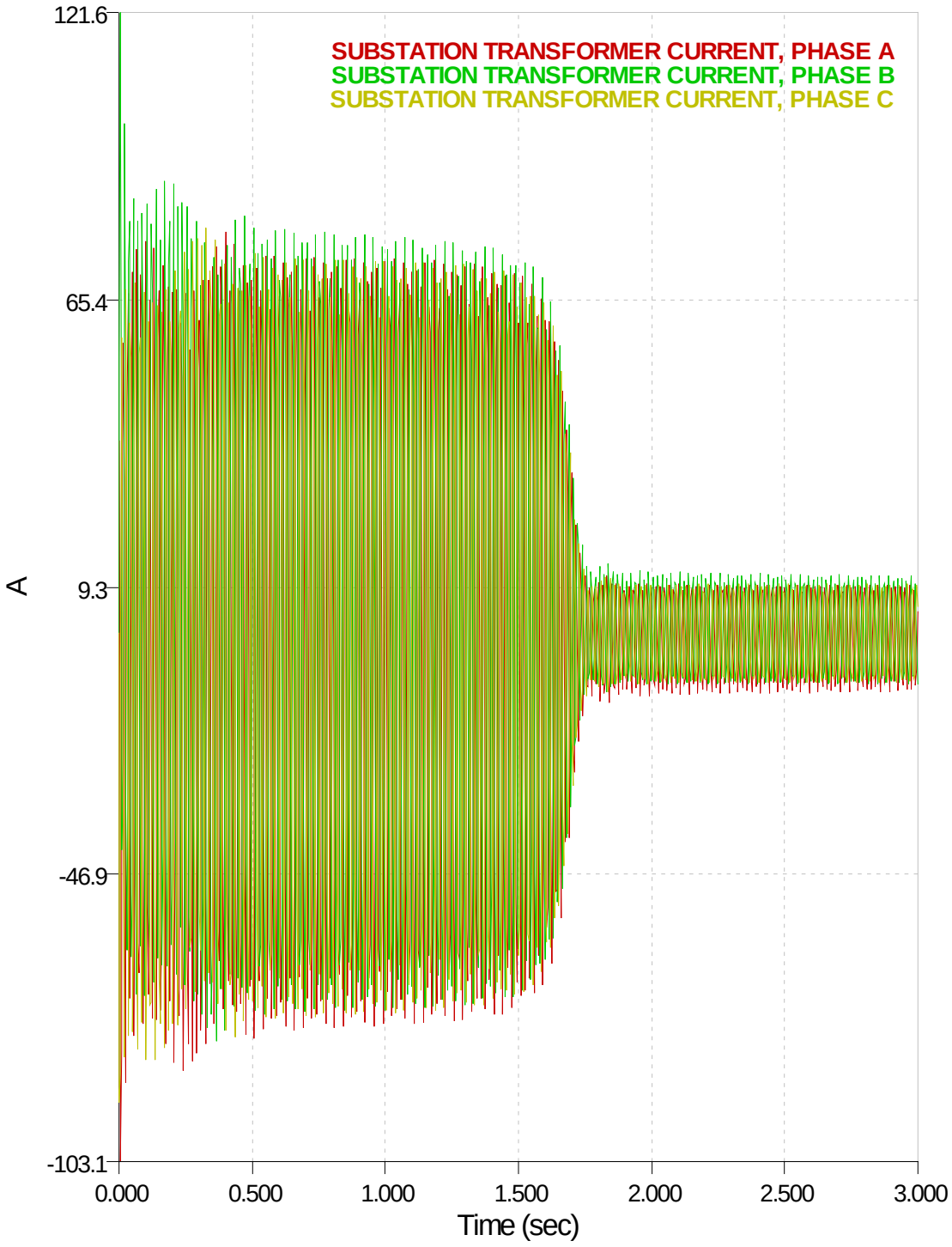

Figure 9.76: Substation transformer current during system energization.

9.3 Transmission-System Voltage Recovery

This numerical example involves the bulk power system shown in Figure 9.77. The system consists of two generating units at two different generator substations connected to the rest of the grid via step-up transformers. Apart from the generating substation, there are three main high-voltage transmission substations. Note that the system is represented using physically-based, three phase modeling, as described throughout this work. The configuration of each substation is explicitly represented, using the breaker-oriented modeling approach, as illustrated in Figure 9.78. The breakers and switches are explicitly represented and the system transformers are included in the substation models.

The system also includes small sections of the medium-voltage, distribution feeders. Distribution lines are modeled and single-phase loads, both constant impedance and constant power, are also included, to introduce load imbalance in the system. Induction motors are also connected, via step-down transformers at the ends of the distribution feeders at load buses. Four different motors are used, each one of a different NEMA design, and their operation is compared.

Furthermore, the motor-model estimation procedure is demonstrated for the estimation of the rotor parameters for each one of the motors. The slip-torque characteristic is generated using some specific parameters and then these curves are used as input to the estimation algorithm. The estimated values are compared with the actual values, which in this artificial example are known.

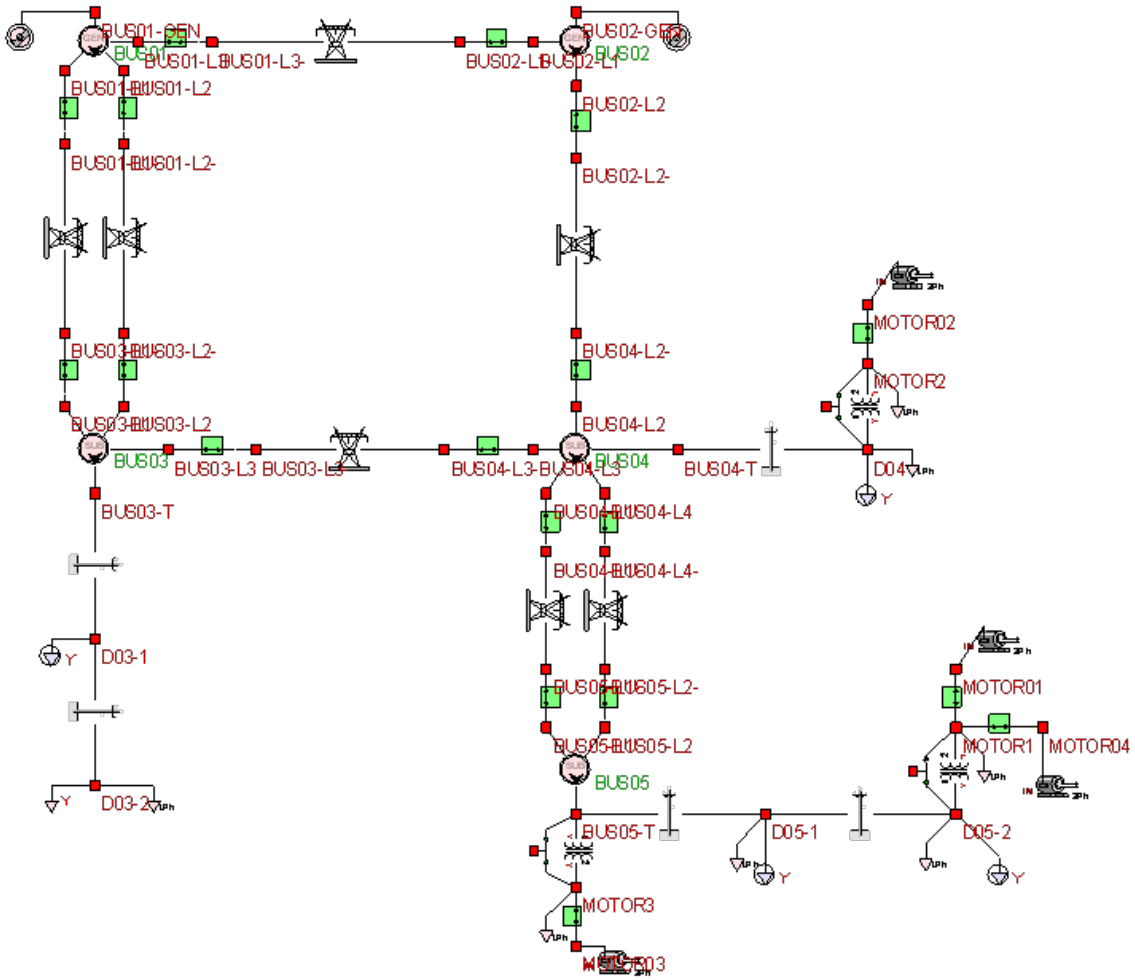

Figure 9.77: One-line diagram of three-phase model of transmission test system.

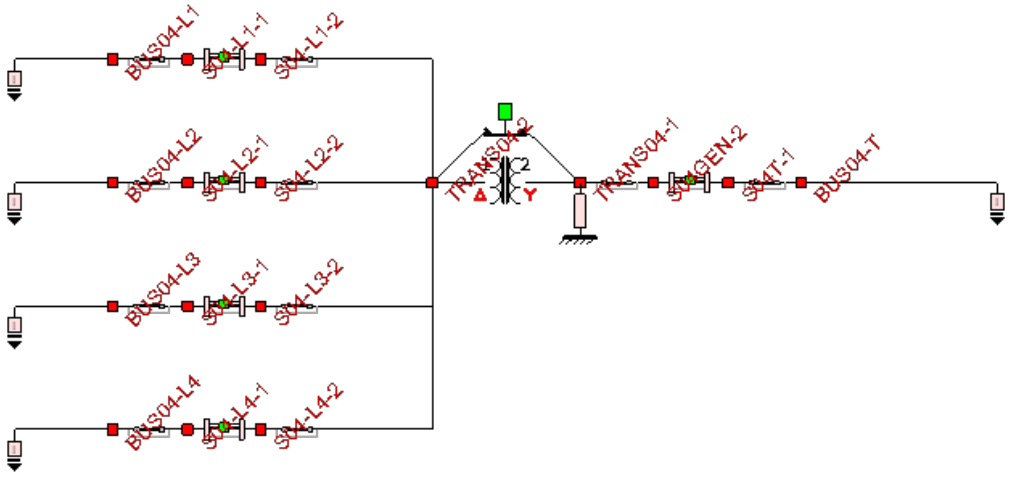

Figure 9.78: One-line diagram of distribution substation configuration.

9.3.1 Motor-Model Estimation

All the motors in the system are rated at 1 MVA. Their stator electrical parameters are $r_s = 0.01$, $x_s = 0.06$, $x_m = 3.5$, $g_m = 0$. All values are in p.u. at the motor ratings (1 MVA, 13.8 kV). The rotor parameters are used to test the estimation procedure. The slip-torque characteristic of each motor is generated and is provided as input to the model estimator. These nominal slip-torque characteristics are presented for each motor in Figure 9.79.

The estimated values are compared with the actual values used to generate the characteristics. A constant rotor parameter model is used for type A and D motors, while a slip-dependent model is used for type B and C motors. The initial value for all the parameters, for both the two-parameter model and the five-parameter model, was set to 0.01 p.u. The actual parameter values along with the estimation results are presented in Table 9.7 through Table 9.10. These tables also show the number of Newton iterations required by the solution algorithm, the execution time, and the absolute maximum deviation between the estimated and the actual slip-torque curve. Figure 9.80 shows the deviation between the actual and estimated slip-torque characteristic, for each motor type. This would be the only measure of the estimation error, if the parameter values were not known in advance, as would be the case in a realistic situation.

In all cases the estimation algorithm provided practically exact values of the model parameters. For the motors of designs A, B, and D the simple Gauss-Newton based algorithm (without a global convergence strategy) was enough to provide satisfactory results. In the case of motor C, the simple Gauss-Newton algorithm and the line-search algorithm failed to provide the solution; therefore, the trust-region algorithm was

employed, as a global convergence strategy, along with the Gauss-Newton solution process to provide a result. The convergence of the algorithm for the type C motor is illustrated in Figure 9.81. The objective function tolerance was set to 10^{-4}. The actual value achieved at the 5^{th} iteration was 1.25×10^{-6}.

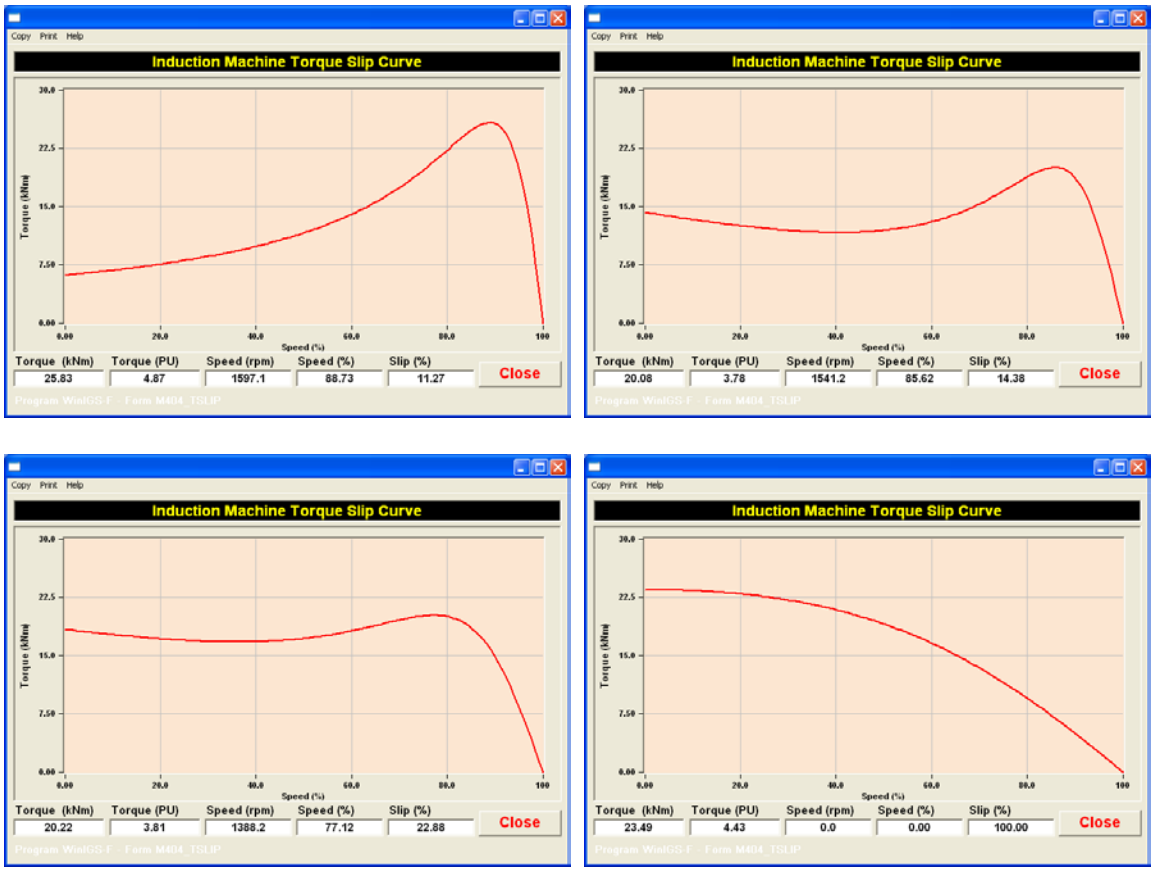

Figure 9.79: Nominal slip-torque characteristic of the four induction motor designs.

Table 9.7: Estimation results for design A motor.

Parameter	Actual Value (p.u.)	Estimated Value (p.u.)	Number of Iterations	Execution Time (s)	Max. Torque Deviation (p.u.)
r_r	0.01	0.01			
x_r	0.03	0.03	4	0.05	3.05×10^{-5}

Table 9.8: Estimation results for design B motor.

Parameter	Actual Value (p.u.)	Estimated Value (p.u.)	Number of Iterations	Execution Time (s)	Max. Torque Deviation (p.u.)
α	0.02	0.02			
β	-0.03	-0.03			
γ	0.05	0.05	5	0.16	4.13×10^{-4}
δ	0.06	0.06			
ε	-0.01	-0.01			

Table 9.9: Estimation results for design C motor.

Parameter	Actual Value (p.u.)	Estimated Value (p.u.)	Number of Iterations	Execution Time (s)	Max. Torque Deviation (p.u.)
α	0.03	0.03			
β	-0.03	-0.03			
γ	0.06	0.06	5	0.08	8.95×10^{-4}
δ	0.06	0.06			
ε	-0.01	-0.01			
Simple Gauss-Newton algorithm and Gauss-Newton with line search failed to converge; Levenberg-Marquardt trust-region algorithm was used.					

Table 9.10: Estimation results for design D motor.

Parameter	Actual Value (p.u.)	Estimated Value (p.u.)	Number of Iterations	Execution Time (s)	Max. Torque Deviation (p.u.)
r_r	0.1	0.1			
x_r	0.04	0.04	6	0.08	3.29×10^{-4}

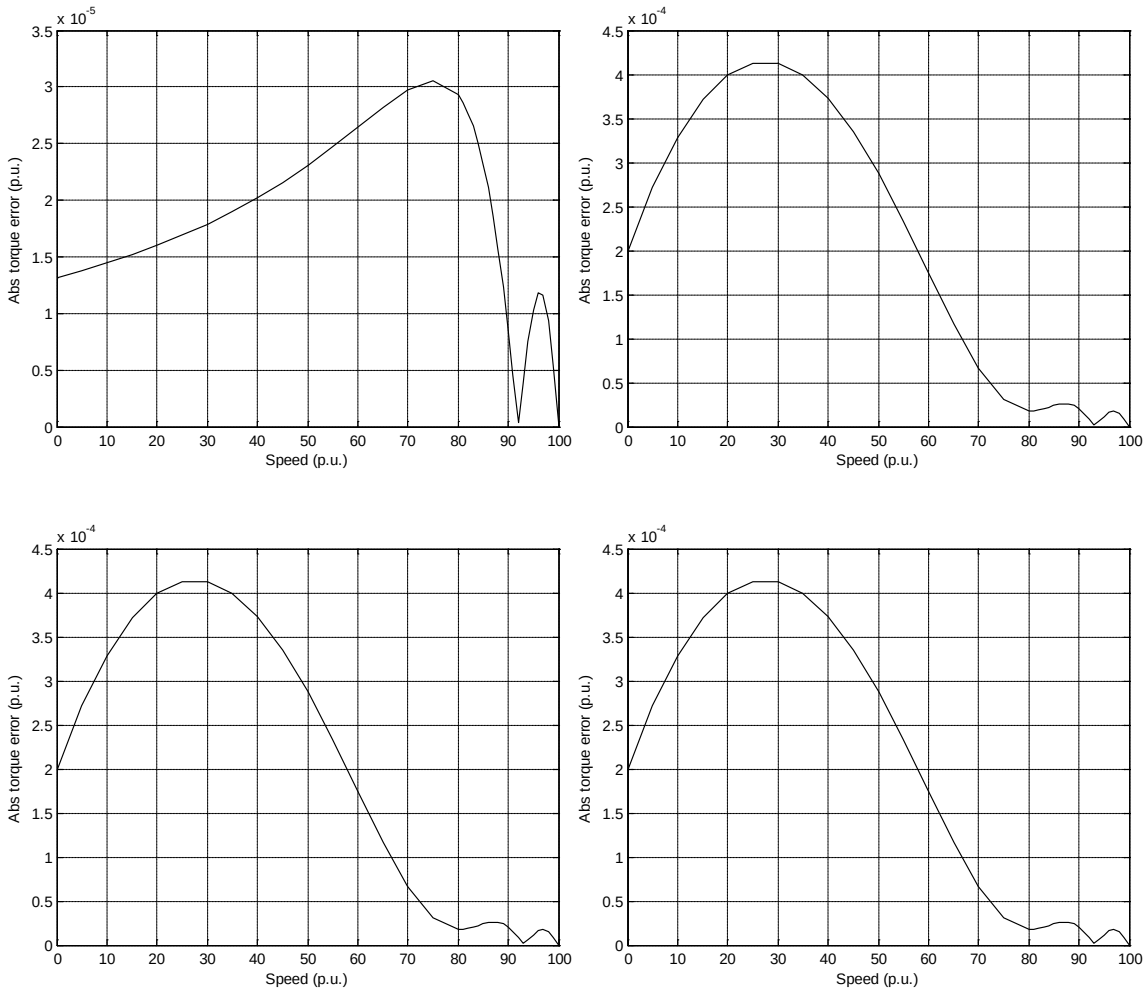

Figure 9.80: Error between actual and estimated slip-torque characteristic, for motor designs A, B, C and D respectively.

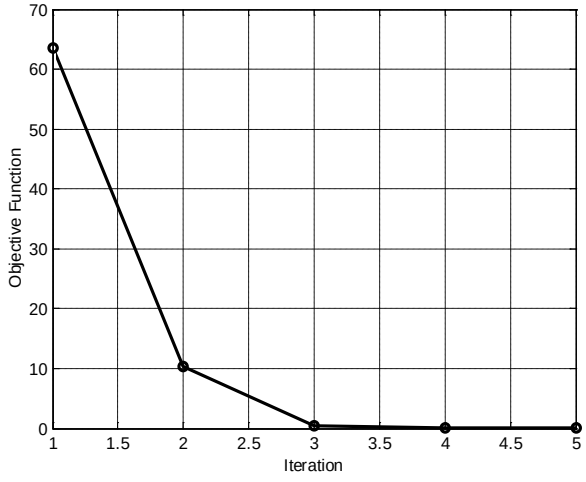

Figure 9.81: Convergence of iterative estimation process for design C motor.

9.3.2 Steady-State Analysis

The steady-state analysis results for the four different motor types are illustrated in Figure 9.82. The motors are operating at torque-equilibrium mode and they all have the same load torque that depends quadratically on speed based on the equation

$$T_m = 0.5 + 0.5\omega + 0.2\omega^2, \tag{9.34}$$

with

T_m : mechanical load torque in p.u.,

ω : mechanical speed in p.u.

Note that this load model results in overloading conditions at steady-state of about 10 to 15% for each motor. The model output provides information about the terminal voltage of the motor, the absorbed current and power per phase, the motor speed, the internal voltages of the motor, the power losses, and the produced mechanical torque. It also provides, graphically, the operating slip-torque characteristic of the motor at the current operating point.

It is interesting to notice the different behavior of the four different motor designs. The motor of design A operates with the smallest slip value and the best power factor of 95%. Design A also has the least amount of losses. Design D has a similarly high power factor, but operates at reduced speed, at a slip value of close to 14%. Design D also produces lower torque compared to design A, although their terminal voltage is the same, and also has significantly higher losses compared to all other designs. Designs B and C operate at the worse power factor, which is still, however, quite high at about 93%. Of course, the operating point of each motor also depends on the network bus it is connected

to. Additional network quantities are presented in the figures below. Figure 9.83 displays a general solution report for the system. Figure 9.84 illustrates graphically the voltage profile of the system. The bulk side of the system (generation and transmission) operates under elevated voltage conditions because the second generating unit regulars its output at 1.02 p.u. Note, however, the low voltage profile at the load areas, where the voltage drops as low as 0.9 p.u.

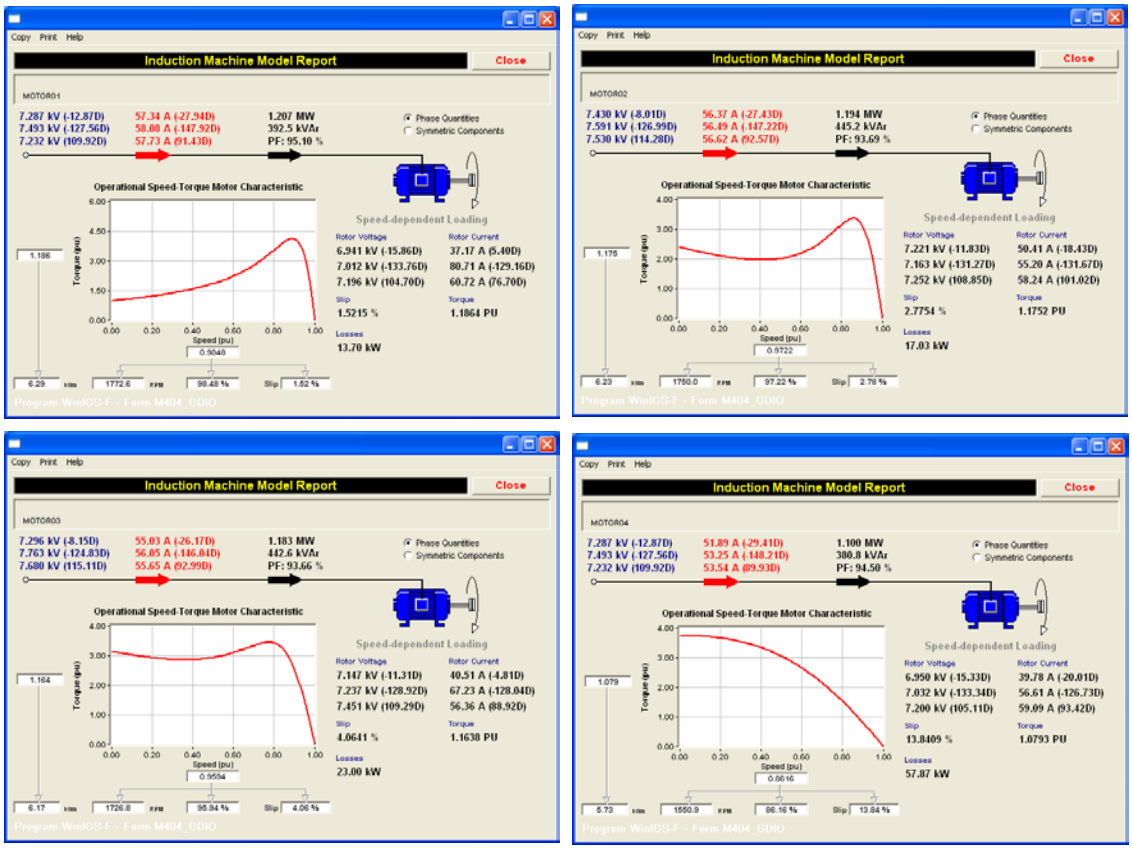

Figure 9.82: Steady-state-analysis results for four NEMA class A, B, C, and D motors.

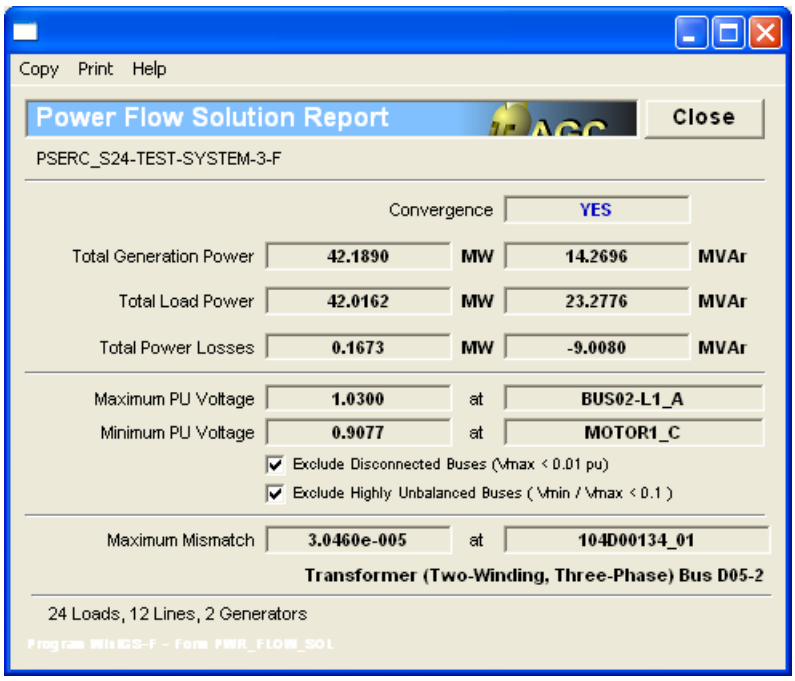

Figure 9.83: Steady-state solution report at base case.

Bus Voltage – Min = 0.9077 p.u. Max = 1.03 p.u.

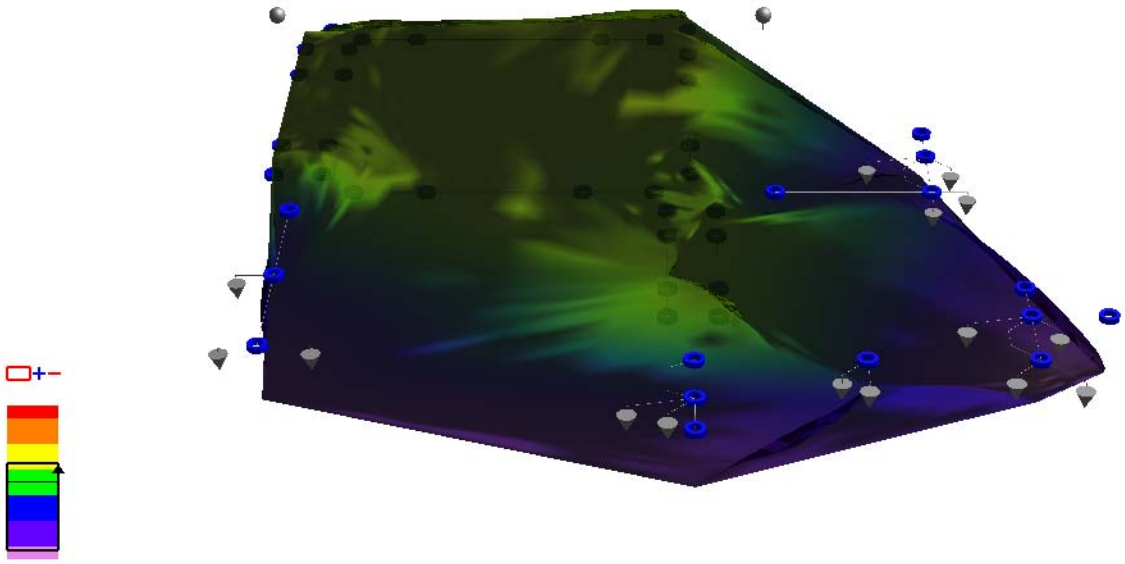

Figure 9.84: Surface plot of system voltage profile (positive sequence). Green color indicates normal voltage within ±1.8%. Yellow, orange, and red indicate overvoltage up to 5.4%, up to 9%, and above 9% respectively. Blue, light blue, and purple indicate undervoltage down to 5.4%, down to 9%, and below 9% respectively.

9.3.3 Quasi-Steady-State Analysis

Results from dynamic analysis are presented next. First, a line-to-line fault, between phases A and B is applied to the system at the line BUS03-L3 – BUS04-L3 very close to the BUS03 terminal. The fault is cleared after 300ms by removing the line. A quasi-steady-state analysis is performed, assuming that the network is operating under sinusoidal steady-state conditions. The motor inertia constants are set as follows:

Motor 1 (design A) 0.5 sec (moment of inertia of 28.14 $kg.m^2$);

Motor 2 (design B) 1.0 sec (moment of inertia of 56.29 $kg.m^2$);

Motor 3 (design C) 0.1 sec (moment of inertia of 5.63 $kg.m^2$);

Motor 4 (design D) 0.5 sec (moment of inertia of 28.14 $kg.m^2$).

Simulation results with emphasis on monitoring the voltage recovery at the induction-motor terminals are presented in Figure 9.85. Note that because of the delta-wye transformers between the fault location and the monitoring buses, the faulted phases at the load buses may not necessarily appear to be the same as at the fault location.

Next, a three-phase fault is applied to the system at the same line BUS03-L3 – BUS04-L3 very close to the BUS03 terminal. The fault is cleared after 300ms by removing the line. The dynamic simulation results from this test case are presented in Figure 9.86.

Finally, a line-to-line fault is considered again at the same line BUS03-L3 – BUS04-L3 very close to the BUS03 terminal. The fault is cleared after 300ms by removing the line. However, now motors 3 and 4 are disconnected after a specific time following the fault, when their speed falls below a certain value; the motors are

reconnected to the system following the fault clearance. In particular, motor 3 disconnects at 0.2 seconds after the fault and reconnects 0.05 seconds following the fault clearance and motor 4 trips 0.15 seconds after the fault and reconnects 0.3 seconds after the fault is cleared. The dynamic simulation results from this test case are presented in Figure 9.87.

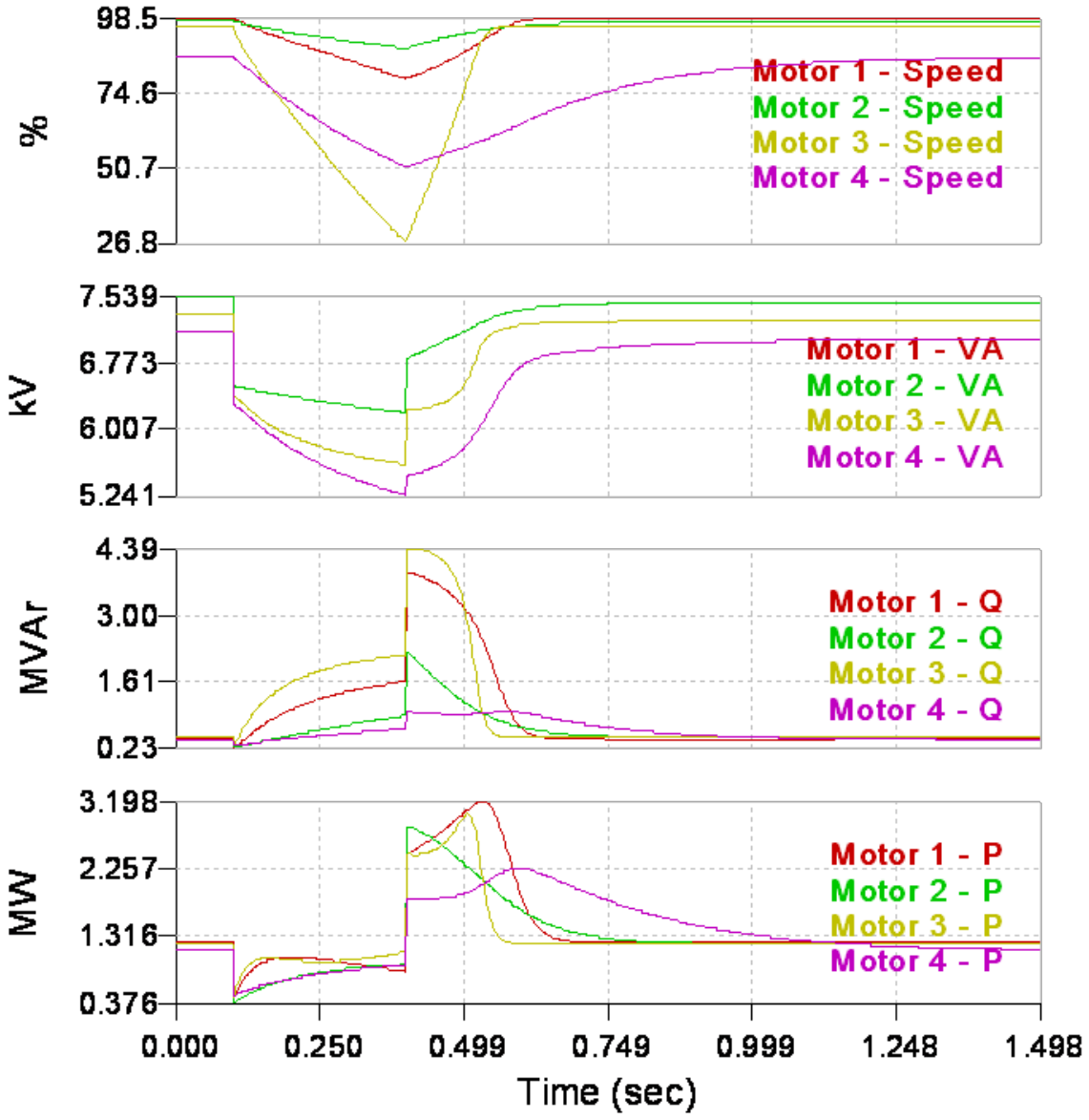

Figure 9.85: Motor speeds, terminal-voltage recovery (phase A), and reactive and active power absorption during fault and post-fault period after a line-to-line fault, cleared by line removal.

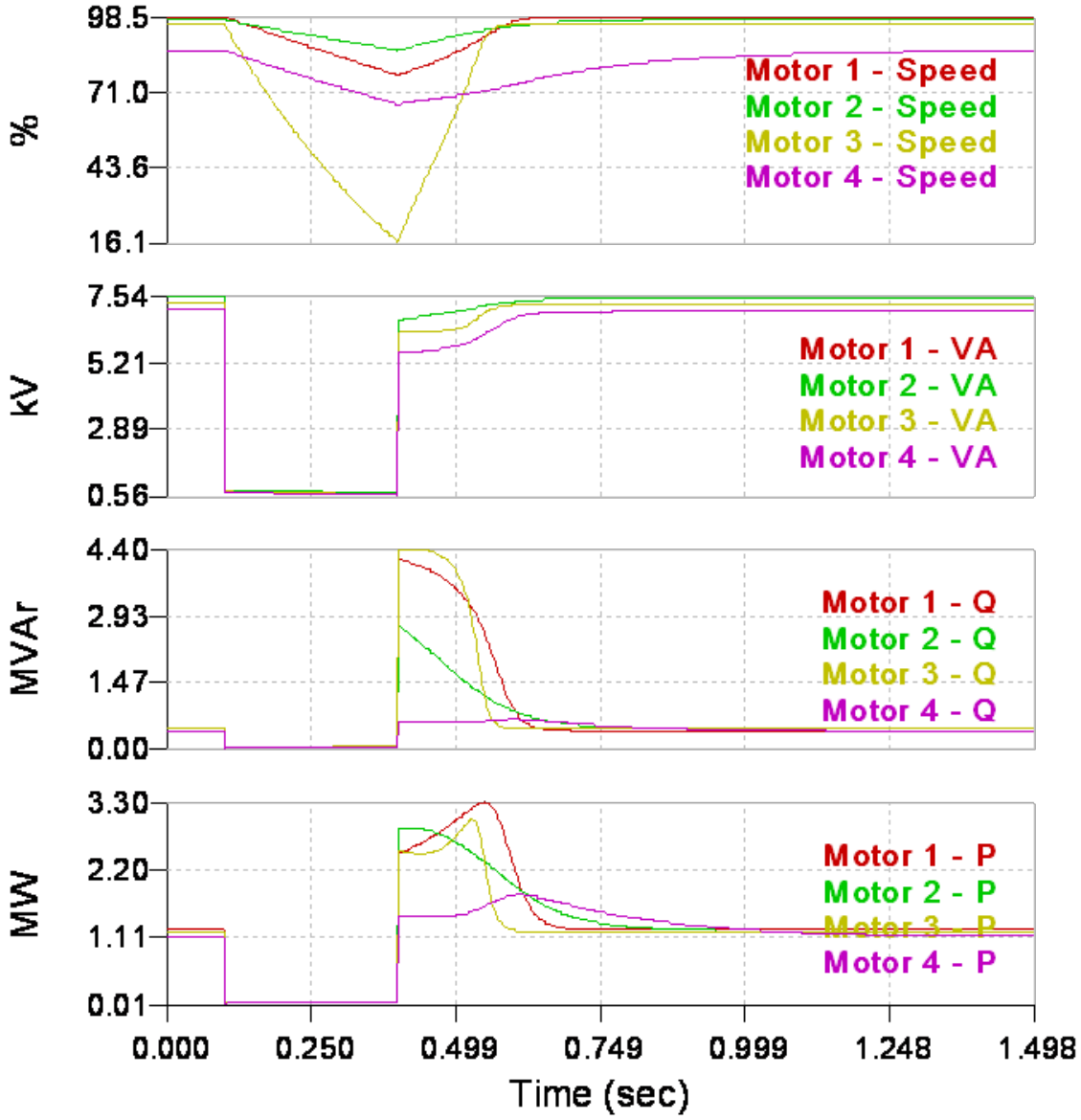

Figure 9.86: Motor speeds, terminal-voltage recovery (phase A), and reactive and active power absorption during fault and post-fault period after a three-phase fault, cleared by line removal.

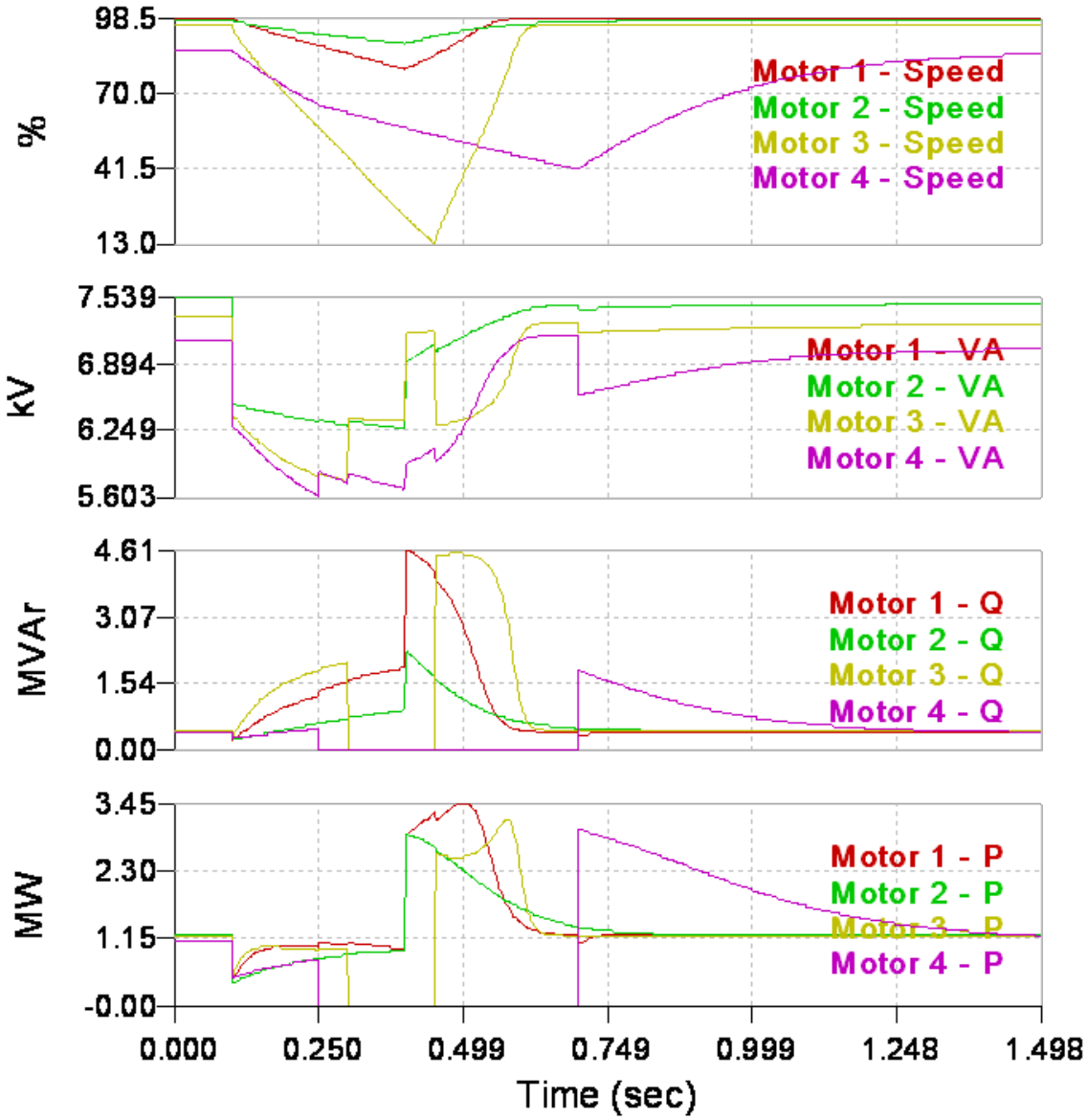

Figure 9.87: Motor speeds, terminal-voltage recovery (phase A), and reactive and active power absorption during fault and post-fault period after a line-to-line fault, cleared by line removal, including motor tripping and reconnection.

9.4 Distribution-System Voltage Recovery

9.4.1 Introduction

This example presents a voltage-recovery simulation and study using a more realistic system comprising of a small part of a transmission system and a distribution system comprising of two feeders. The system is a 13.8 kV distribution system comprising overhead and underground distribution. There are distributed loads of houses (including air conditioners), commercial buildings, and industrial facilities. There are voltage correction capacitors along the circuit. Figure 9.88 shows the overall single-line diagram of the system.

The transmission part of the system is represented by two equivalent generating units, connected via step-up transformers to the transmission grid. Unit 1 is a 35 MVA unit, operating at 18 kV, with a 2.0 sec inertia constant, while unit 2 is a 45 MVA unit , operating at 15 kV, with a 3.5 sec inertia constant. Both units regulate their output voltage at 1.02 p.u. The distribution substation is connected to the rest of the network via three overhead transmission lines: two parallel lines to the equivalent generating unit 1 and one line to the equivalent unit 2. The main component of the distribution substation is a three-phase, two-winding transformer. The transformer is rated at 7.5 MVA with a transformation ratio 115/13.8 kV. Three types of three-phase load models are utilized: (a) constant-power loads, (b) constant-impedance loads, and (c) dynamic loads in the form of three-phase induction motors. All the loads can be either wye or delta connected. Three-phase motors of various designs are connected at buses MCC1 and MCC5 of the top feeder part and buses MCC3, MCC6, MCC8, MCC-P2, MCC-P3, and MCC-P8A of the bottom feeder part. Unbalanced loading is typical in distribution systems. Single-phase

loads are used throughout the feeder to model loads connected between two phases and between a phase and neutral. Three types of single- or two-phase loads are considered: (a) constant-power loads, (b) constant-impedance loads, and (c) dynamic loads in the form of single-phase induction motors. Single-phase motors are connected at buses MCC-P2, MCC-P3, and MCC-P8 of the system. The motors are capacitor-start, capacitor-run motors. Finally, reactive support, in the form of capacitor banks is also used to improve the power factor of the feeder, connected at the high side of the transmission transformer.

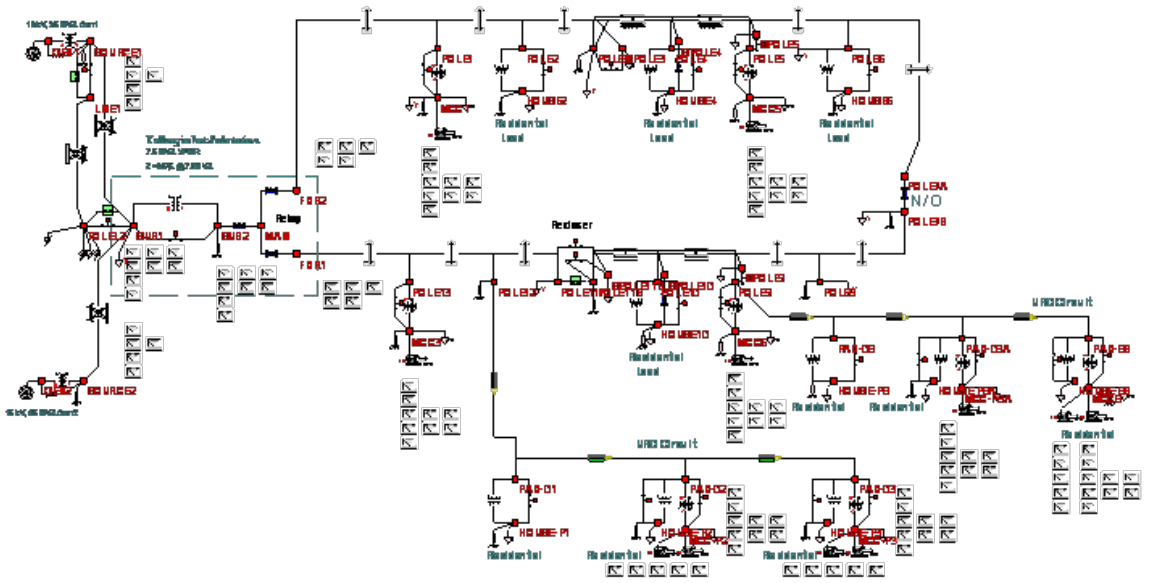

Figure 9.88: Single-line diagram of a 13.8 kV example system.

9.4.2 Quasi-Static Analysis

First the quasi-static analysis is presented. This type of analysis takes into account only the mechanical dynamics of the induction motors of the system. A steady-state, load-flow simulation is performed first to initialize the system at a specific operating point. Then a three-phase fault takes place at the transmission side of the substation on

the first line connecting the substation to the first generating unit. The fault is cleared after 0.3 seconds by removing the faulted line. The voltage recovery of the system is studied and presented in the figures below.

Figure 9.89 and Figure 9.90 show the voltage recovery at the low side of the substation transformer, which is the feeder voltage at the beginning of the feeder. The voltage at steady state is at 0.980 p.u., 0.991 p.u., and 1.015 p.u. for phases A, B, and C respectively, before the fault occurs. It drops at approximately 19 V for all three phases during the fault, for a period of 18 cycles, until the fault is cleared by the line relays. When the faulted line is removed from the system the voltage jumps to 0.800 p.u., 0.807 p.u., and 0.819 p.u., for phases A, B, and C respectively and it starts building up slowly. It reaches the value of 0.9 p.u. in about 87 cycles after the fault it cleared for phase A, 85 cycles for phase B, and 80 for phase C. There is a noticeable imbalance between the three phases due to the existence of single-phase loading in the system.

Figure 9.91 illustrates the current variations at the substation transformer and the two feeder sections before, during, and after the fault. Only the phase A currents are illustrated The transformer current magnitude transiently increases almost 1.8 times immediately after the clearance of the fault, then slowly reduces and reaches a value close the pre-fault value almost one second after the fault clearance. The first section of the feeder demonstrates a higher increase and more severe response and this section determines the behavior of the whole feeder. This is because of the fact that this feeder includes the larger amount of induction machines, which predominately define the transient behavior of the system.

Figure 9.92 to Figure 9.98 present the induction motor behavior during the simulation period and provide better insight on the system behavior. Figure 9.92 and Figure 9.93 demonstrate the voltage recovery at the 480 V (L-L) buses, where the motors are connected. Phase A voltages are presented. Initially all the voltages range from 0.97 p.u. down to 0.91 p.u. As at the substation level, the fault-induced voltage recovery demonstrates a slow rate at all the buses and none of the motors recovers above 90% of the nominal voltage level. Motor MCC1 recovers faster, but it does reach 85% of the nominal voltage level in about 83 cycles, after the fault clearance. Therefore, the motor voltage remains below 0.85 p.u. for a period of more than 100 cycles, including the fault period. The terminal voltage stabilizes eventually at a value close to 88%. Most of the other motors exhibit similar behavior; however, no other motor manages to recover above 0.86 p.u. even after two seconds from the clearance of the fault. Their terminal voltage is, however, stabilized at a value between 0.82 p.u. and 0.86 p.u. Motors MCC-P8A and MCC5 are the two exceptions that do not manage to recover. Their voltage remains at around 0.63 p.u. and 0.60 p.u. even after 120 cycles after the fault clearance. This is an indication that these motors do not recover and they stall. This phenomenon is clearly illustrated in Figure 9.94 and Figure 9.95, where the speed of each motor is presented. Motors MCC1, MCC6, MCC8, and MCC-P3 have a similar response and they recover quickly without losing much of their speed during the fault period. In fact, none of these motors slows down to less than 90% of their synchronous speed. The single-phase motors almost stall during the fault period and they restart when the fault is cleared. However, because of their small size and inertia they accelerate fast and reach an acceptable speed quickly. Ten they slowly speed up more to their new steady-state speed. Motors MCC3

and MCC-P2 slow down considerably, at about 75%, but they respond fairly quickly and manage to recover to their nominal value at a relatively slow way, in terms of speed. In particular motor MCC-P2 is the last motor to reach its steady-state speed. Motors MCC5 and MCC-P8A are the two exceptions that do not recover and stall.

Figure 9.96 to Figure 9.98 present the current and power absorption of the eleven system motors. It is important to note the high current and reactive-power values that are transiently absorbed by the motors during the post-fault period. In particular, the reactive power reaches a level of four up to eight times the nominal value of the motor, driving also the current to similar levels. The active power also increases considerably, but does not reach more than two times the nominal power. It is also important to note that for the two motors that stall, the reactive power and the absorbed current remain to a level close to five times their nominal value during the whole post-fault period and never come back to lower levels. The active power absorbed by these motor remains low, even lower than the nominal, and the motors cannot accelerate back to their nominal speed.

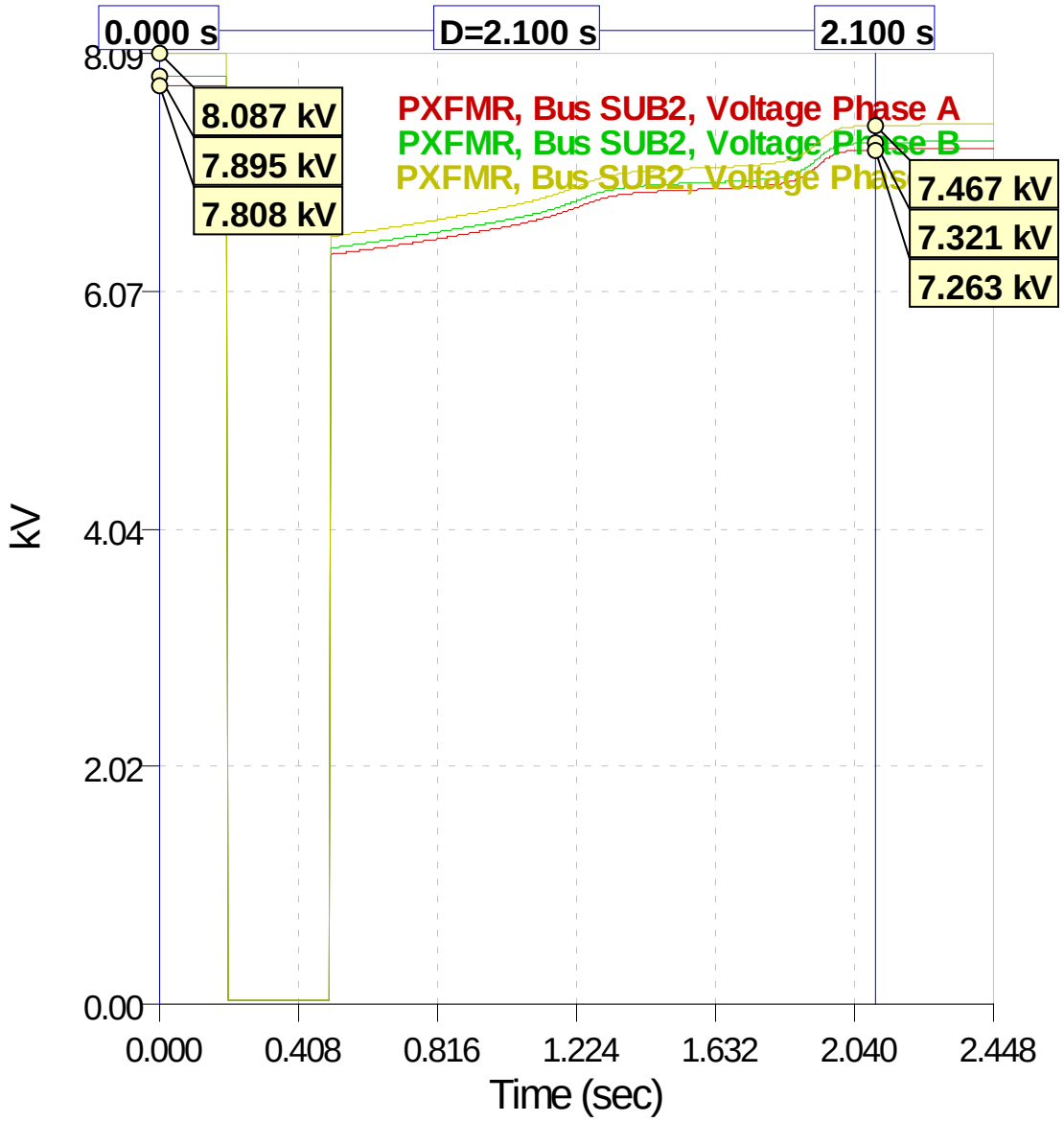

Figure 9.89: Voltage recovery at secondary side of distribution substation after a three-phase fault at the transmission system side (voltage in volts, time in seconds). Initial and final voltage values for each phase.

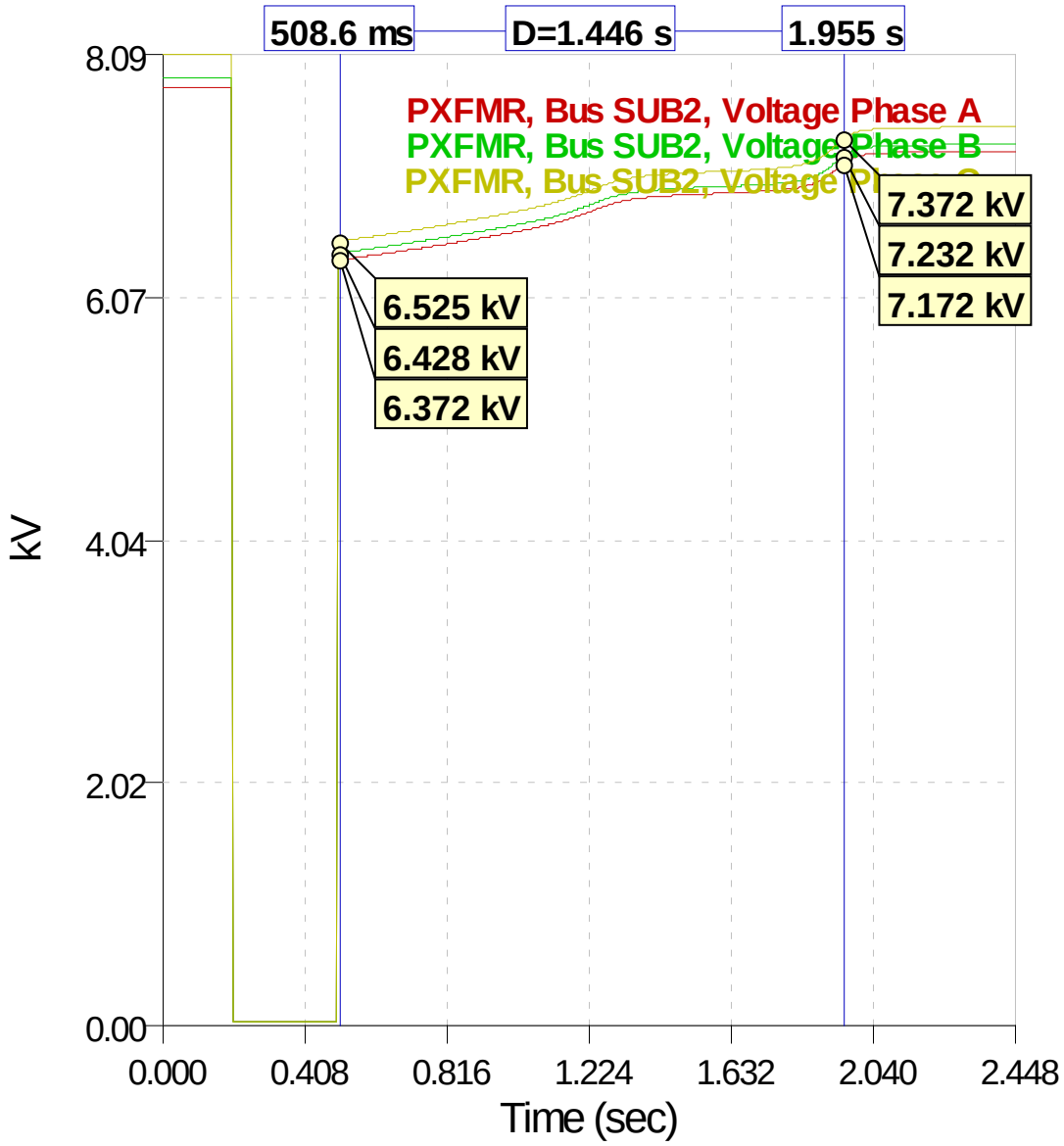

Figure 9.90: Voltage recovery at secondary side of distribution substation after a three-phase fault at the transmission system side (voltage in volts, time in seconds). Voltage recovery until all three phases reach level of 0.9 p.u.

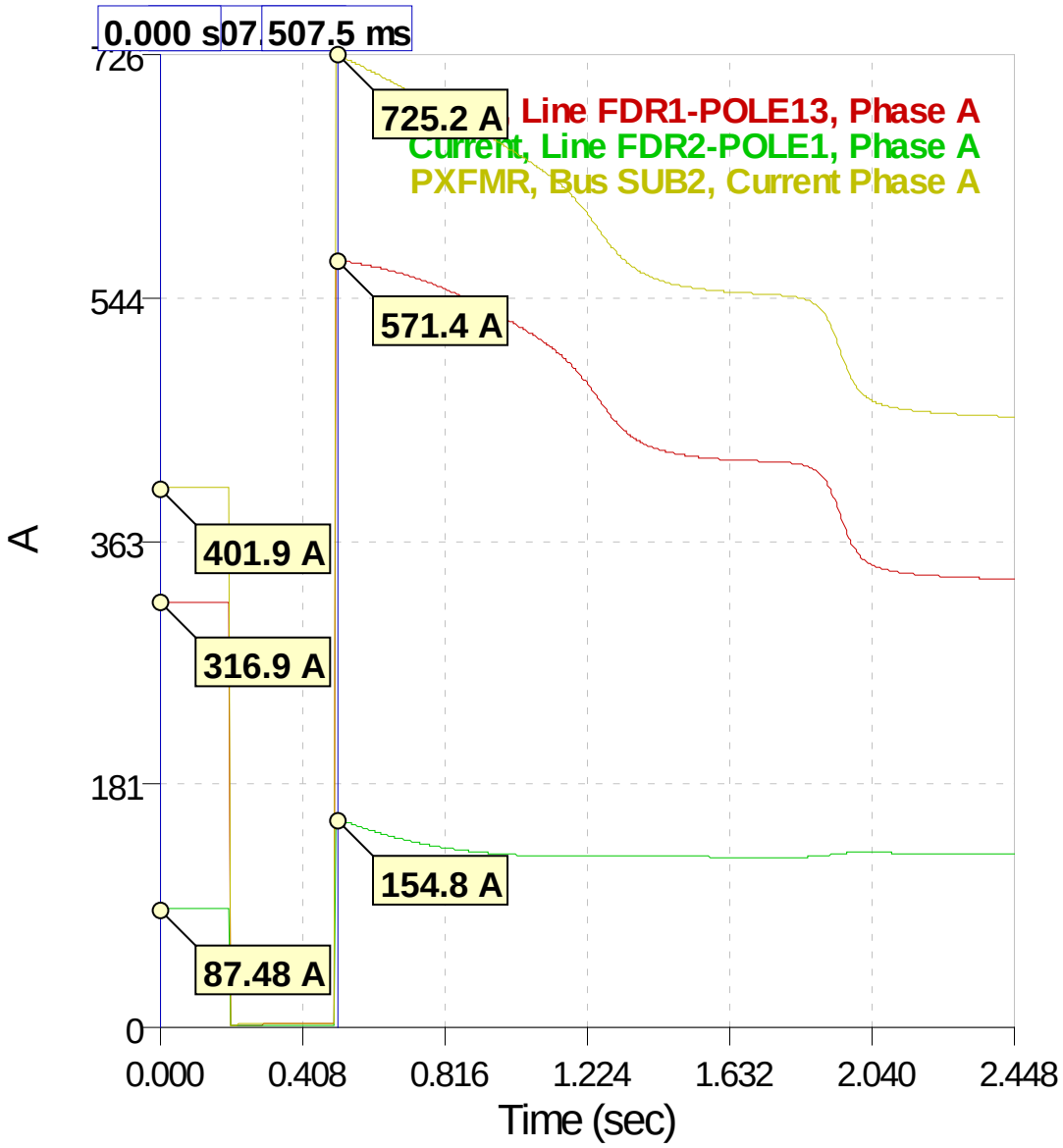

Figure 9.91: Substation-transformer (low side) and feeder currents (phase A) (current in Amps, time in seconds). Steady-state values and values immediately after the clearance of the fault.

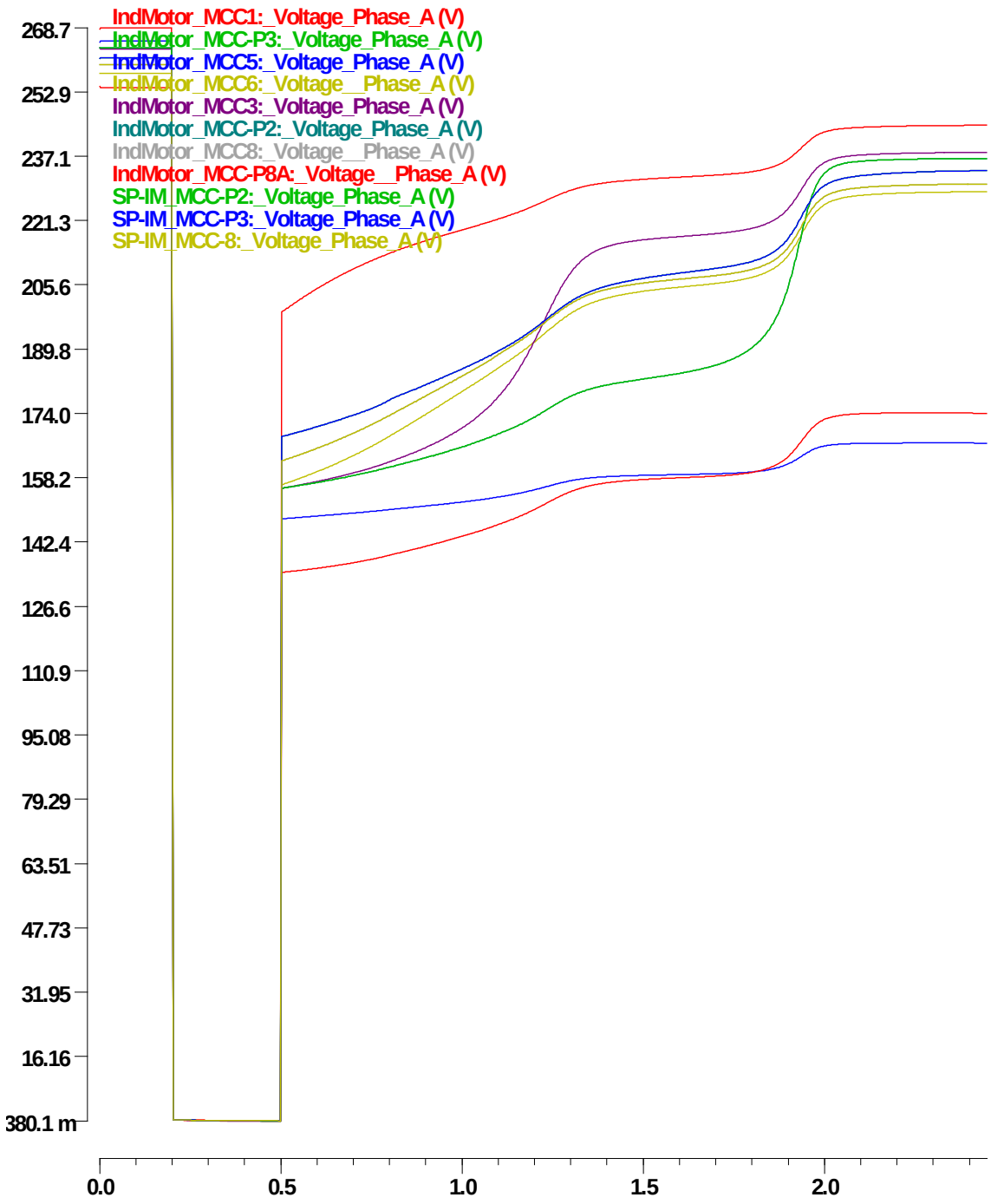

Figure 9.92: Voltage recovery at induction-motor buses (phase A) after a three phase fault at the transmission-system side (voltage in volts, time in seconds).

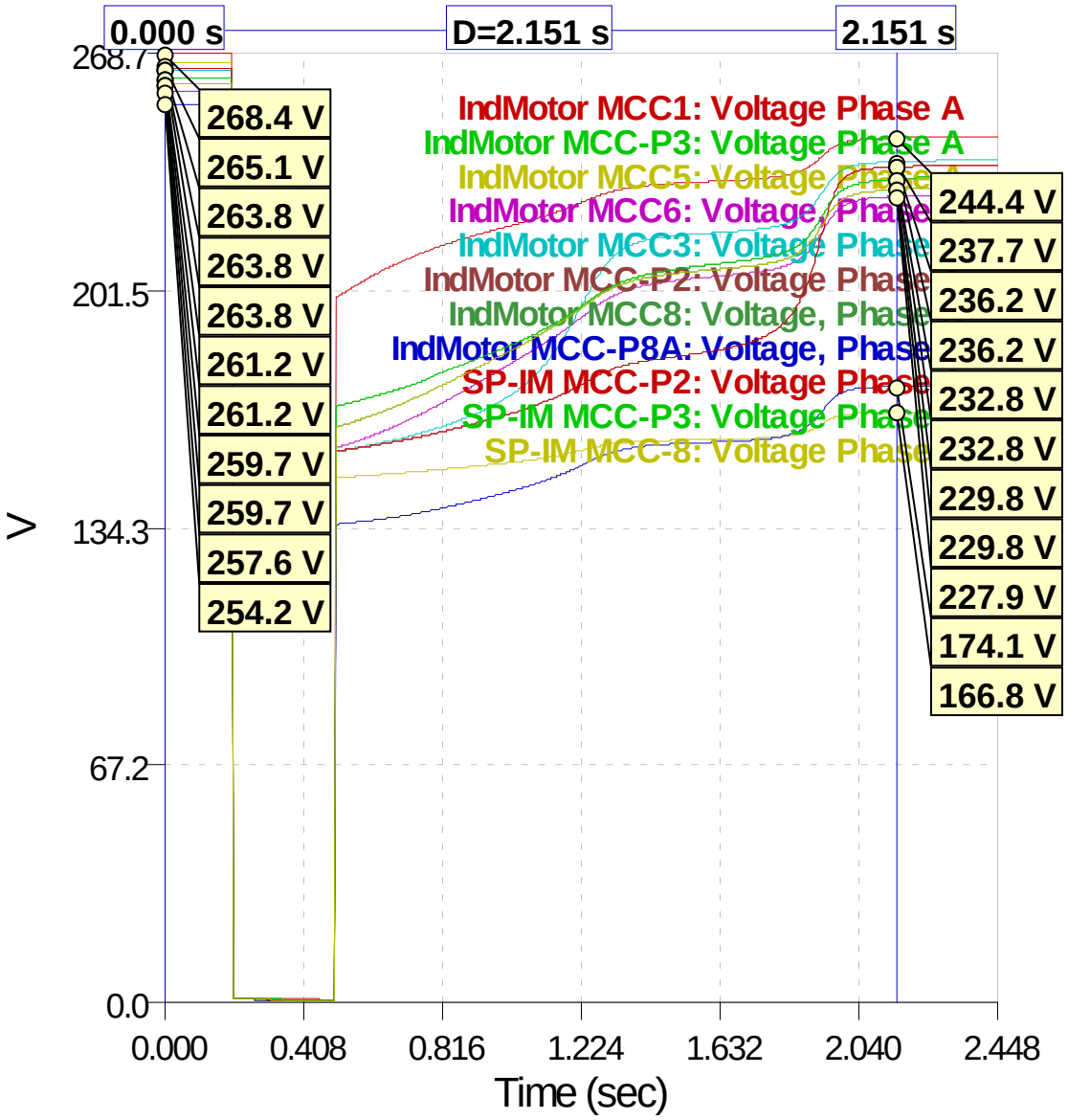

Figure 9.93: Voltage recovery at induction-motor buses (phase A) after a three phase fault at the transmission-system side (voltage in volts, time in seconds). Pre-fault values and final voltage levels after the recovery phase.

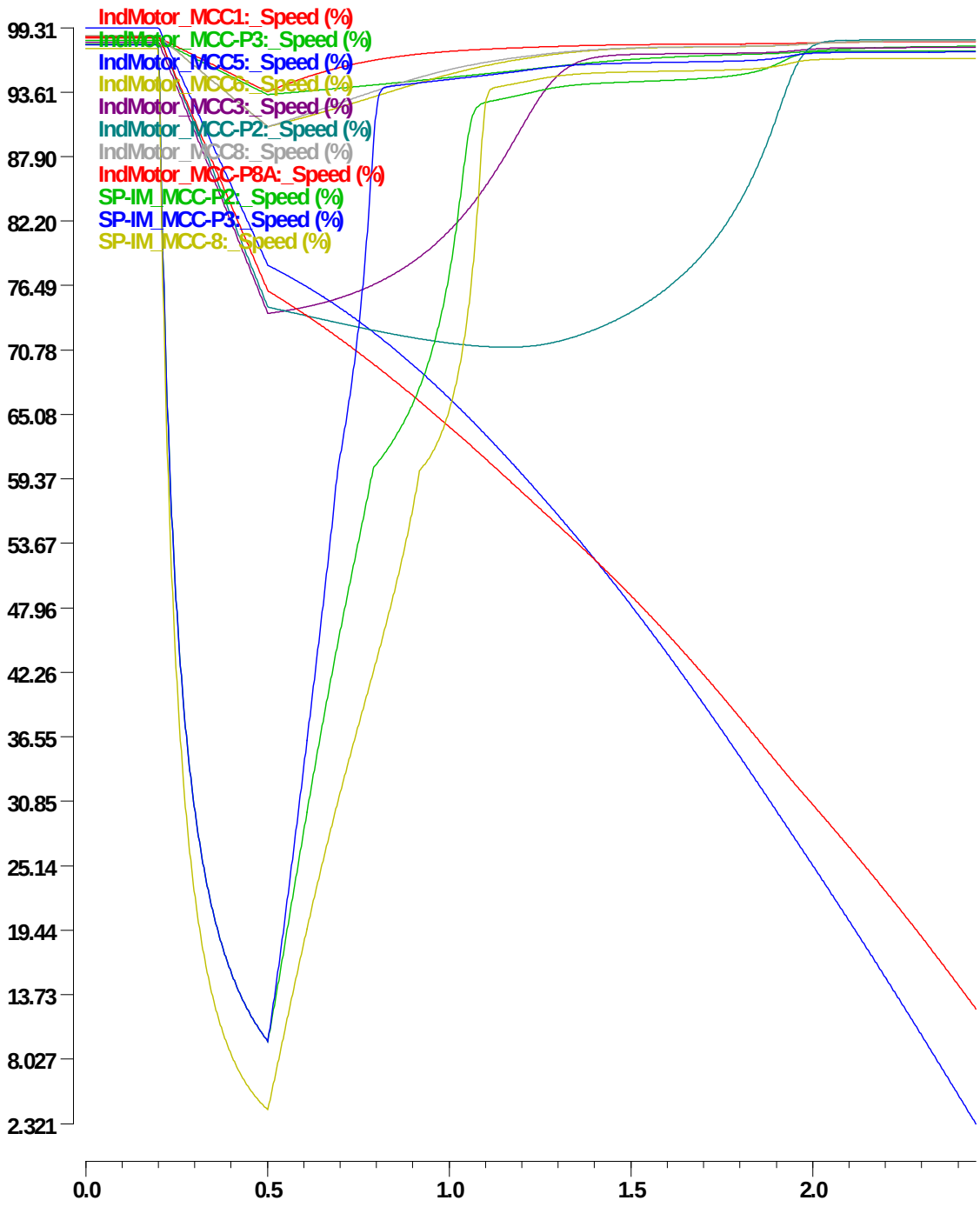

Figure 9.94: Induction-motor speed after a three-phase fault at the transmission-system side (speed in % of synchronous, time in seconds).

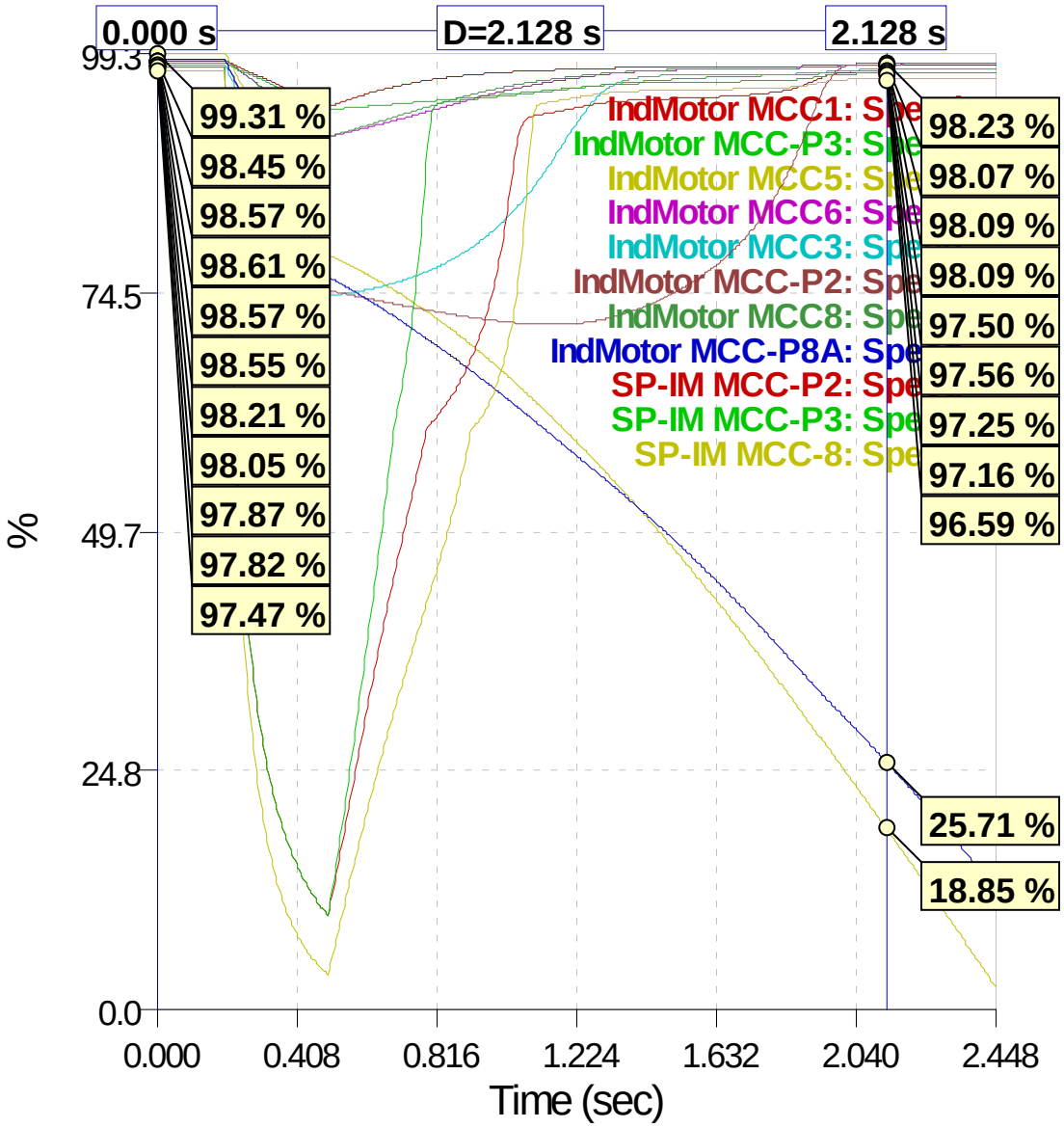

Figure 9.95: Induction-motor speed after a three-phase fault at the transmission-system side (speed in % of synchronous, time in seconds). Initial and approximate final speed values.

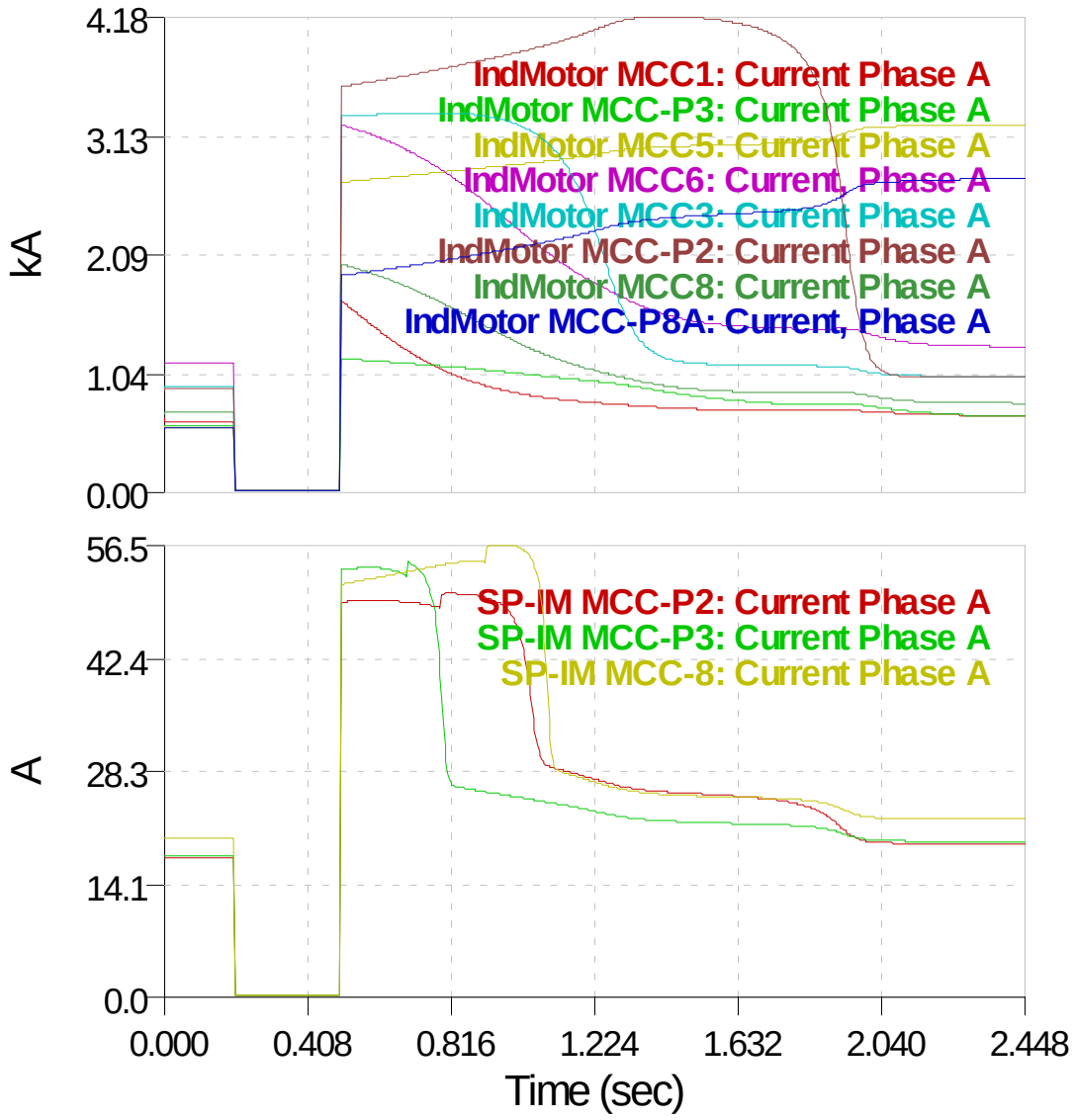

Figure 9.96: Current absorption by induction motors (phase A) after a three-phase fault at the transmission-system side (current in Amps, time in seconds). Single-phase motors are shown separately.

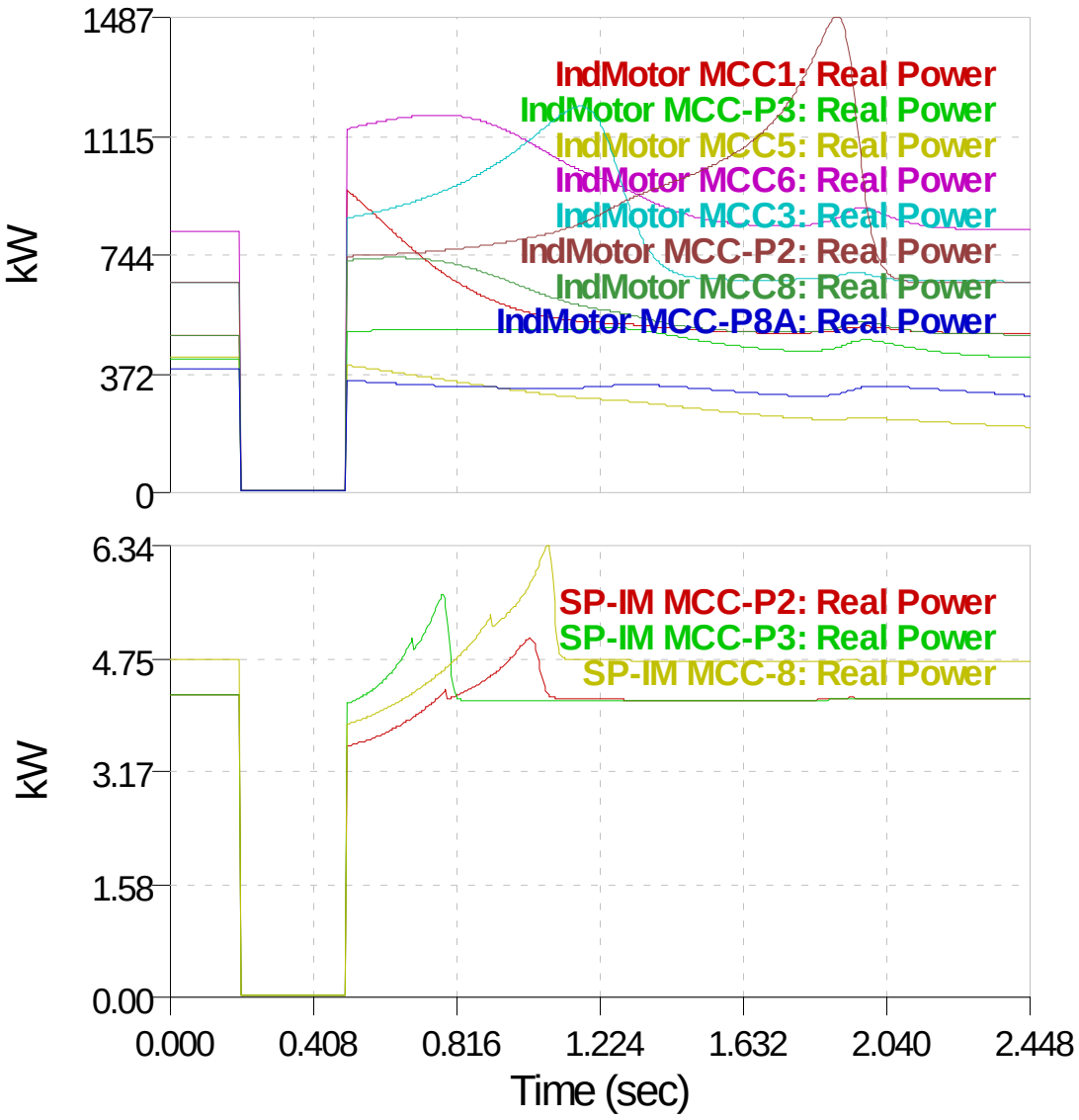

Figure 9.97: Active-power absorption by induction motors after a three-phase fault at the transmission-system side (active power in Watts, time in seconds). Single-phase motors are shown separately.

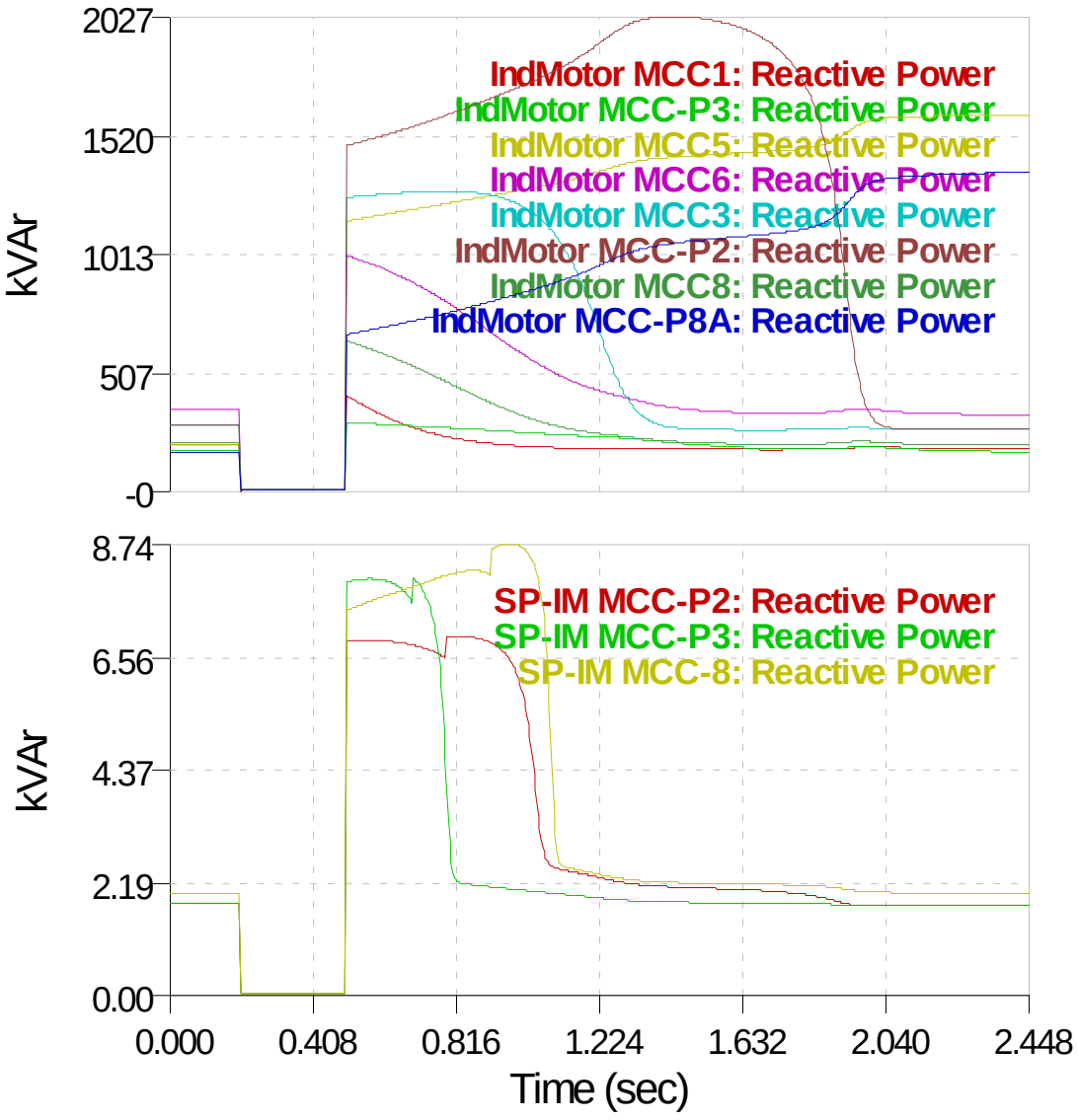

Figure 9.98: Reactive-power absorption by induction motors after a three-phase fault at the transmission system side (reactive power in VAr, time in seconds). Single-phase motors are shown separately.

9.4.3 Full Transient Analysis

In this section results are presented obtained by full transient analysis on the same system of Figure 9.88. A slightly modified version of the system is used for this type of analysis. The system has the exact same topology and components; however the loading of the induction motors is slightly modified. In particular, the loading of all the motors is

speed-dependent with zero constant-torque part and the single-phase motors are now of permanent-split-capacitor type. This modification was done to allow the motors to start-up during the feeder energization phase, which is simulated with this kind of analysis. This, however, results in a milder system response and lower loading of the machines during the transient operation. Furthermore, saturation data are also included for all the system transformers. The remainder of the system is unchanged.

This type of analysis takes into account all the transients, both mechanical and electrical. In addition to the motor dynamics, the transformer saturation and inrush currents are also modeled and can be taken into account. The system initializes from zero initial conditions and thus the whole system energization and motor start-up is simulated including the cold load pickup of the feeders. Once the system reaches a steady-state, the same three-phase fault at the transmission line takes place, lasting for 0.3 s. Therefore, in this case it is of interest to observe the start-up transients of the system, as well as the voltage-recovery transients. The simulation results of the full transient analysis are shown in Figure 9.99 through Figure 9.107. The figures show full time-domain waveforms as well as the rms values of voltages and currents, as computed by analyzing the time-domain waveforms.

The feeder-energization phase lasts for 9.5 seconds. Then the three-phase fault is applied from 9.5 to 9.8 seconds. The fault is cleared at that point by removing the faulted line and the system reaches a new steady state after another 1.5 to 2 seconds. The total simulation time is 12 seconds. Figure 9.99 presents the mechanical speed in % of the synchronous speed of all the eleven induction motors of the system (both three-phase and single-phase) for the duration of the simulation. The following two figures, Figure 9.100

and Figure 9.101, present the motor speed during the start-up phase and during the fault and voltage-recovery period respectively. Notice that all motors are four-pole machines.

The acceleration varies for each motor and depends on the motor design, loading, and location. The three-phase motor MCC3 reaches steady-state first, in less than two seconds. This motor is located away from the rest of the loads, at the beginning of the first feeder (bottom feeder in single-line diagram). Three-phase motor MCC-P2 follows along with motors MCC1 and MCC5. These two motors are the only two motors of the second feeder and they exhibit similar behavior during the acceleration phase. All these three motors reach their steady state in about 3.5 seconds. Once motor MCC-P2 has reached steady state, the single-phase motor MCC-P2 starts accelerating rapidly and reaches a value close to steady state in about four seconds. Then it slowly keeps accelerating to its final steady-state speed. It is evident from Figure 9.100 that this single-phase motor was delayed because of the acceleration of the larger three-phase motor connected at the same bus and, in particular, because the suppressed voltage at its location. Once the three-phase motor reached its steady state and the voltage was restored to a greater level, the smaller motor also accelerated rapidly. The group of motors MCC8, MCC6, and MCC-P3 exhibit a slower rate and takes them seven to eight seconds to reach their steady-state. Once this happens the other two single-phase motors, which are connected at the same buses as these ones, accelerate fast and reach their steady-state speed. Within eight seconds all the motors of the system have reached their normal operating speed, except for motor MCC-P8A, which takes more than nine seconds to reach steady state. This motor is greatly affected by the behavior of all the rest motors and cannot accelerate until all the other motors have reached their steady state.

Once all the motors reach steady state a three-phase fault is applied at one of the transmission lines connecting generator 1 and the substation. The fault is applied at 9.5 s and is cleared after 0.3 s by removing the faulted line. The three single-phase motors decelerate rapidly and practically stall until the fault is cleared. They restart when the voltage is restored immediately after the removal of the fault and rapidly accelerate to a new steady-state speed. Motor MCC8 is mostly affected and requires more time to recover. Most of the three-phase induction motors are not greatly affected by the fault. Motors MCC3 and MCC-P2 exhibit a significant slow-down, close to 65% of synchronous speed, but pick up speed fast after the fault it removed. Motor MCC5 slows down to close to 40% speed and requires close to a second to reach a new steady state after the fault is cleared. All the motors have reached a new steady state by that time, except for motor MCC-P8A, which requires a much greater time to recover. In any case all the system motors require after the fault is cleared and the system goes back to normal operation within less than two seconds. Figure 9.102 illustrates the electrical torque produced by each one of the three-phase motors during the entire study period. The torque of each motor peaks, during the energization phase and during the voltage-recovery phase when the motor is closed to reaching its steady-state speed and match the speed of the mechanical load it drives.

Figure 9.103 illustrates the time-domain waveform of the current loading of the substation transformer and each one of the two system feeders. The situation is similar in all three cases. The current absorption is high during the energization phase because of the high motor starting currents. Then it reaches a low, steady-state value when the system reaches its normal operating conditions. Notice that feeder 2 reaches a steady state

much faster than feeder 1 and also has much lower current values. This is due to the fact that feeder 1 is much more heavily loaded, while feeder 2 only has two motors connected to it. A similar situation is observed after the fault is cleared. The current reduces to almost zero shortly after the fault, because of the almost zero voltage at the high-side of the substation. Then increases dramatically during the recovery period since all the motors have lost speed during the fault and are now accelerating. Once the motor operation is restored the currents reduce again.

This is illustrated in more detail in Figure 9.104 through Figure 9.107. These figures present the current absorption by each of the induction motors of the system, for the entire simulation period (Figure 9.104 and Figure 9.105) and for the post-fault phase (Figure 9.106 and Figure 9.107). Both time-domain waveforms (Figure 9.104 and Figure 9.106) and rms values (Figure 9.105 and Figure 9.107) are presented. The rms waveforms clearly indicate the high reactive current absorption during the motor acceleration. These waveforms of the rms values are in accordance with the results obtained by the quasi-static analysis presented in the previous section. It is also of interest to observe that, as can be seen more clearly in Figure 9.107, immediately after the occurrence of the fault and for a short period of time the motor current transiently increases, and then goes to a very low value for the duration of the fault. This is because of the fact that there is trapped flux in the motor and thus when the terminal voltage is lost the induction machine transiently acts as a generator feeding the fault. When this flux decays the current reduces rapidly. This phenomenon could not be caught with the simplified, reduced-order model of the induction machine used for quasi-static analysis.

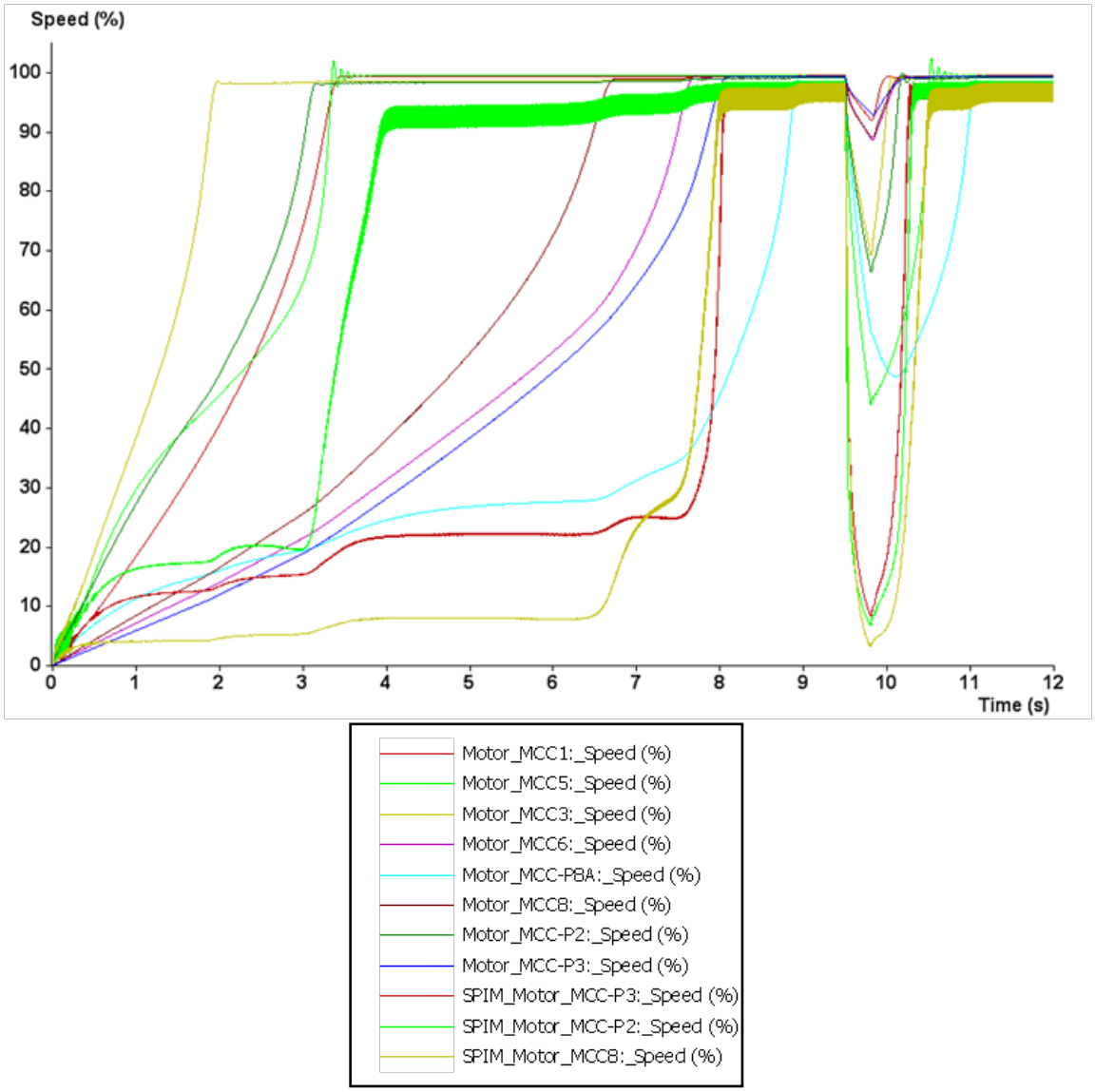

Figure 9.99: Induction motor speed for all system motors during the entire simulation (speed in % of synchronous, time in seconds).

Finally, Figure 9.108 to Figure 9.111 illustrate the voltage behavior at the terminals of all the induction motors. There is a slow voltage built-up during the energization phase, which follows closely the acceleration of each corresponding motor. Notice that the built-up is taking place in stages, depending not only on the motor connected at the particular bus, but also on the motors existing nearby. A similar situation is observed

during the recovery phase following the removal of the fault. All the results obtained using the detailed full transient analysis are verifying the results obtained using the quasi-static approach and similar phenomena and type of behavior are observed in both cases.

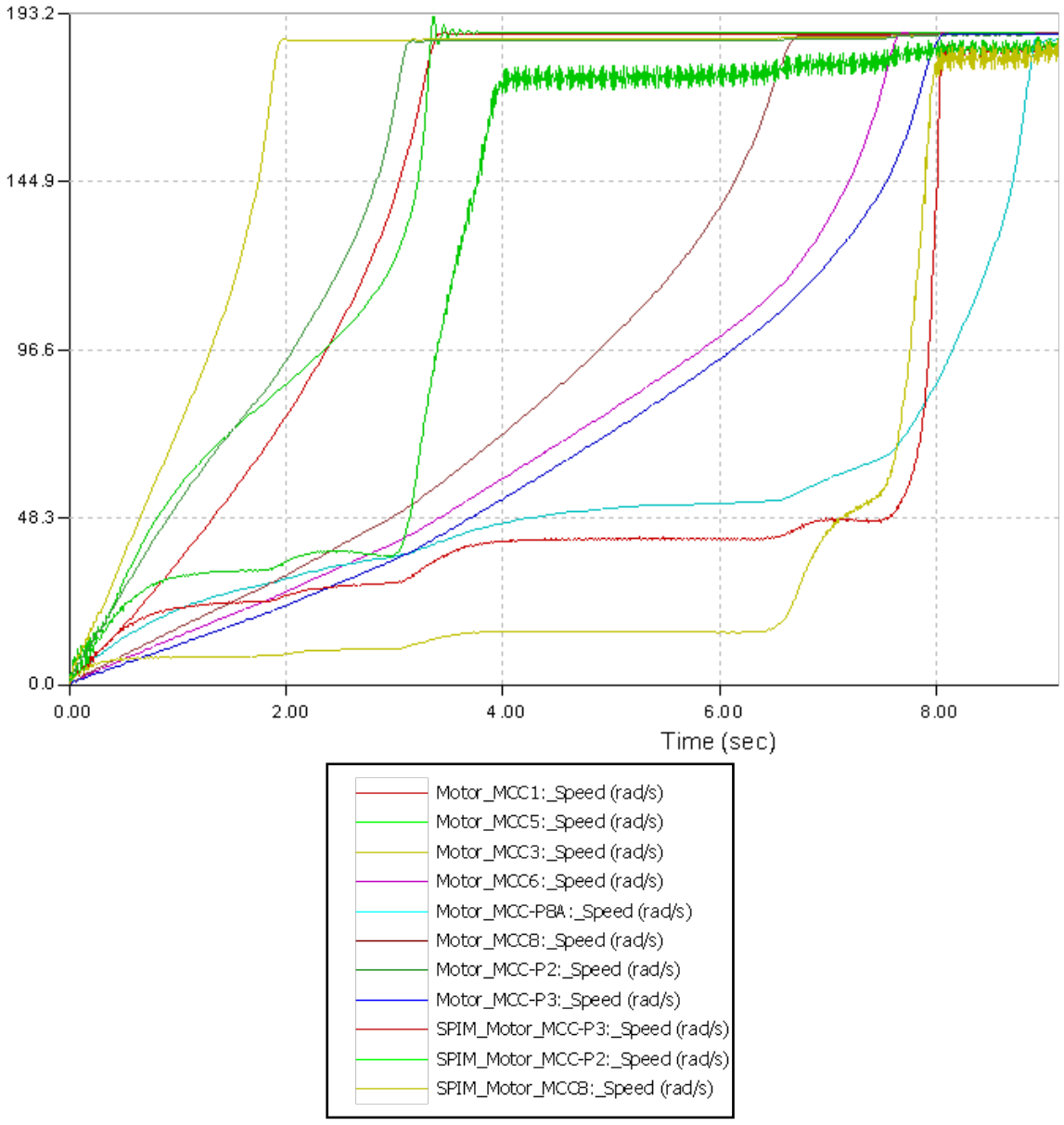

Figure 9.100: Induction motor speed for all system motors during the system-energization phase (speed in rad/s, time in seconds).

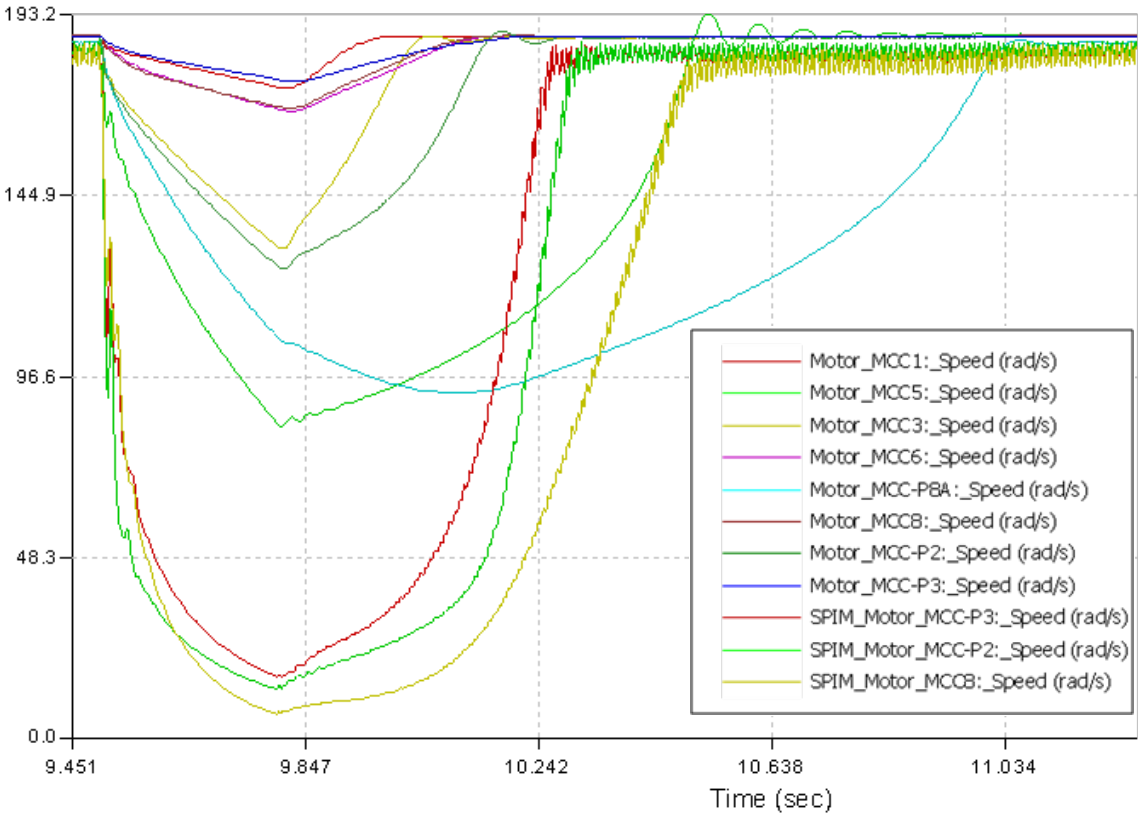

Figure 9.101: Induction motor speed for all system motors during fault and voltage-recovery period (speed in rad/s, time in seconds).

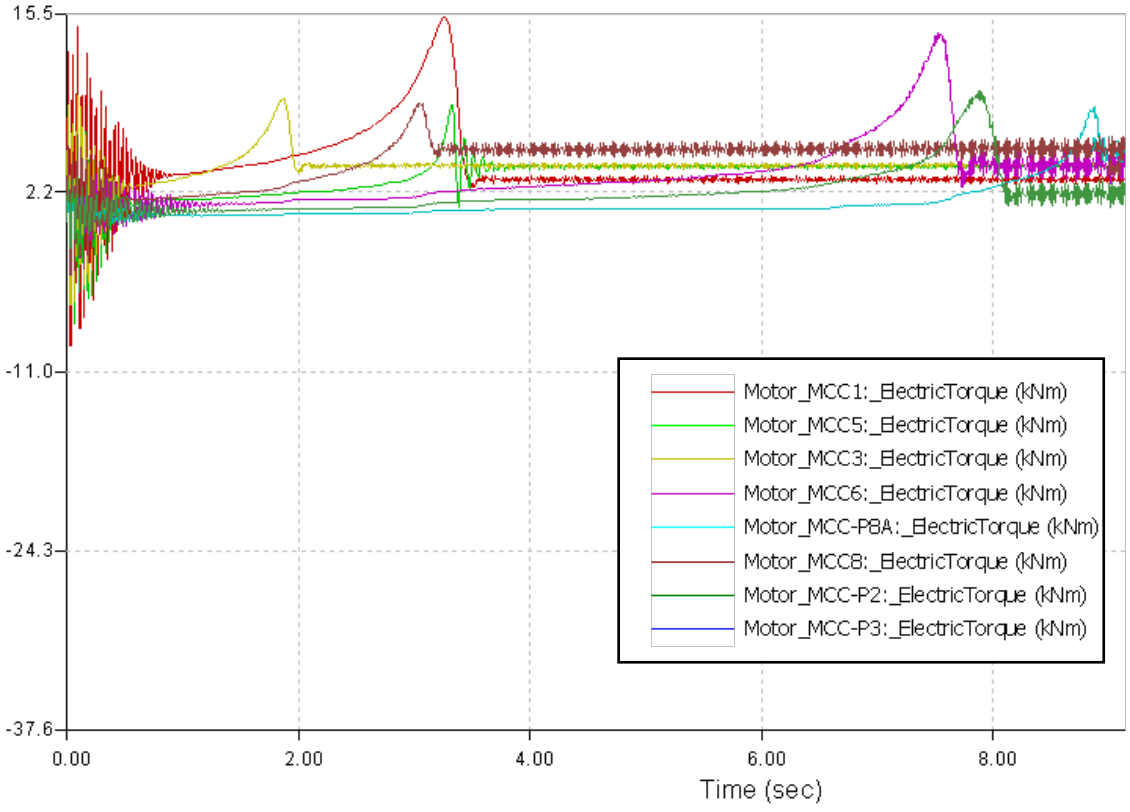

Figure 9.102: Developed electrical torque by the three-phase motors of the system during the system energization phase (torque in kNm, time in seconds).

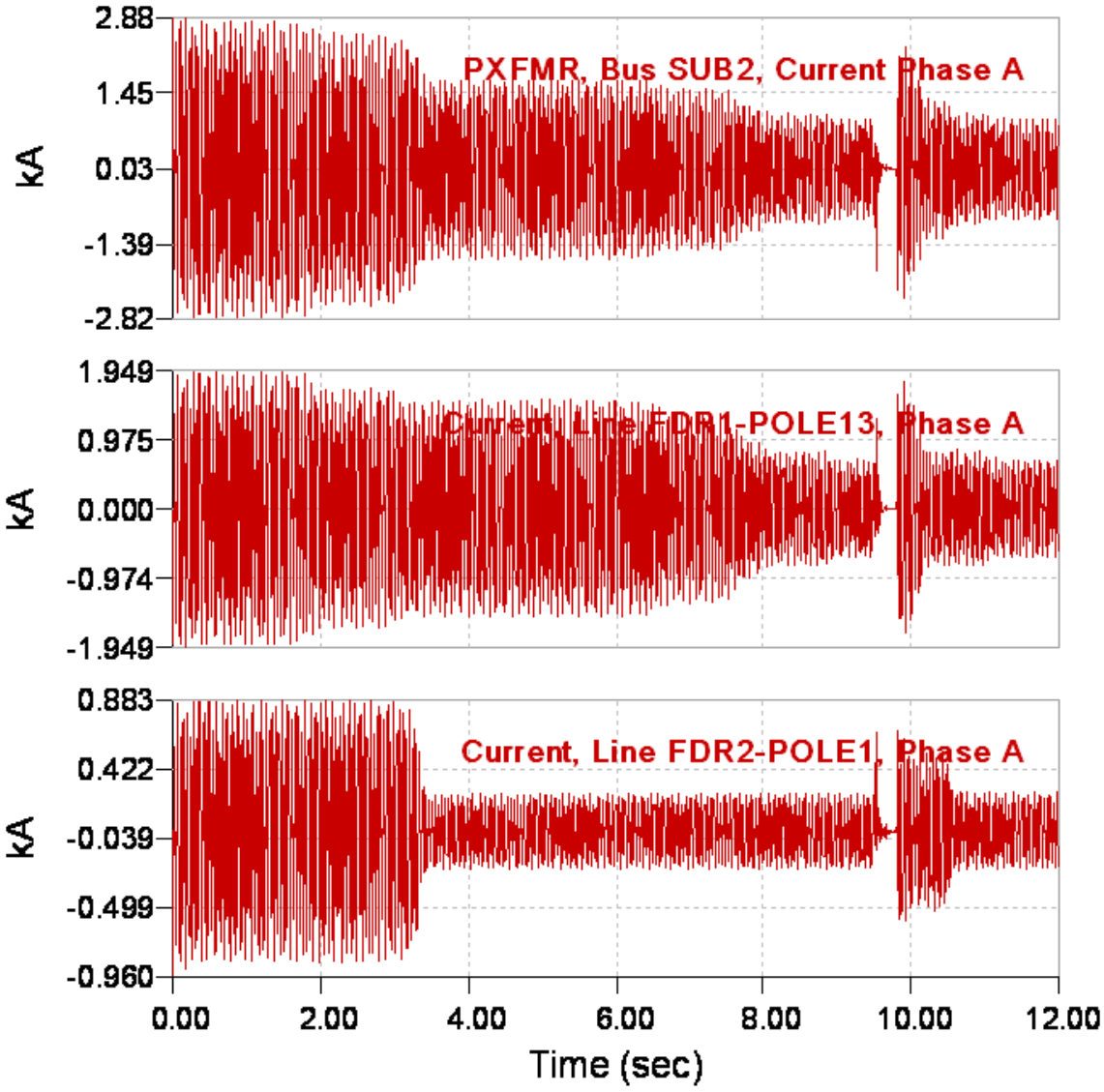

Figure 9.103: Current loading (phase A) of substation transformer and each of the two distribution feeders (current in kA, time in seconds).

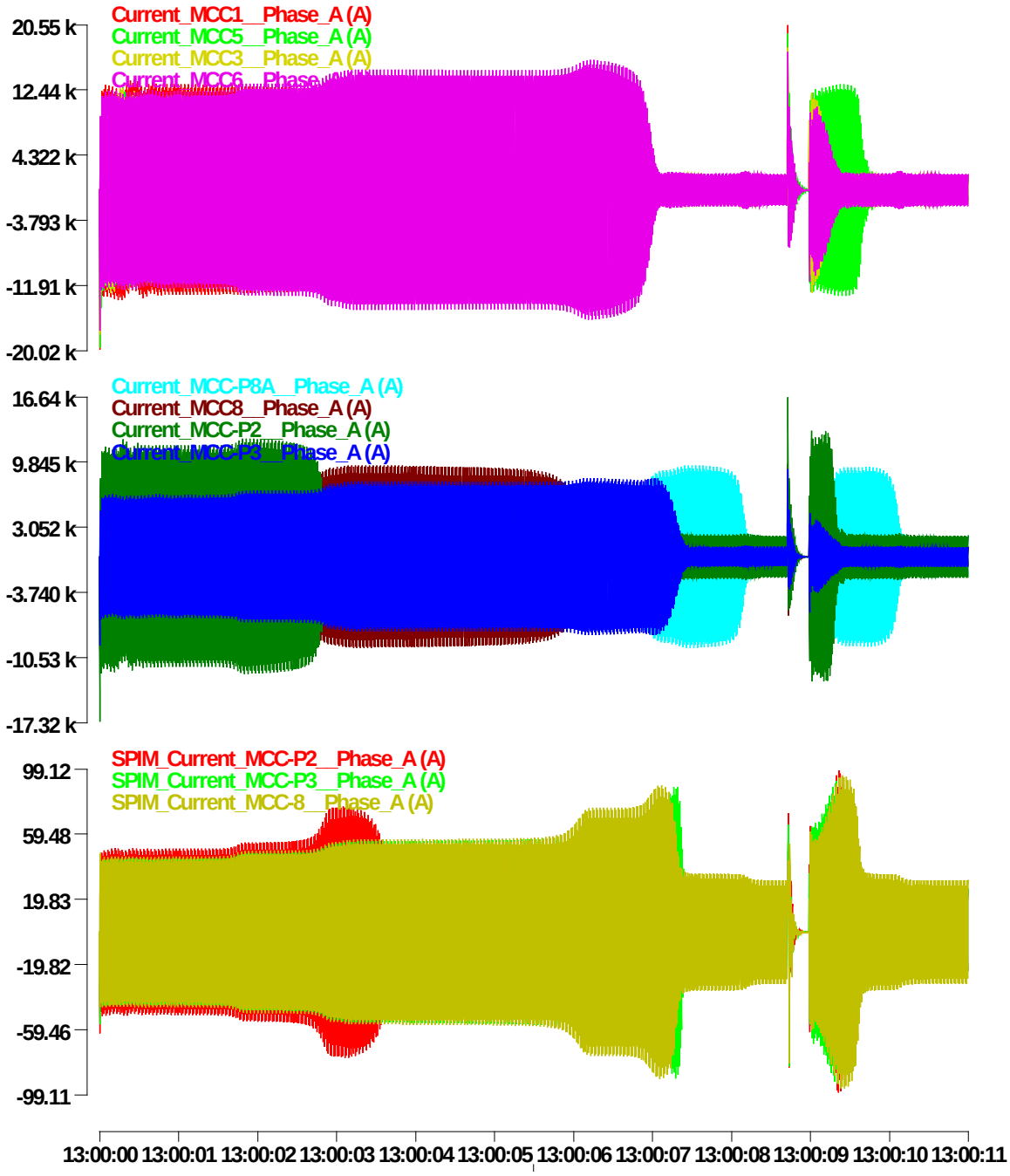

Figure 9.104: Current absorption waveforms (phase A) for each induction motor during the entire simulation period (current in Amps, time in hh:mm:ss format). Single-phase motors are shown separately at the bottom graph.

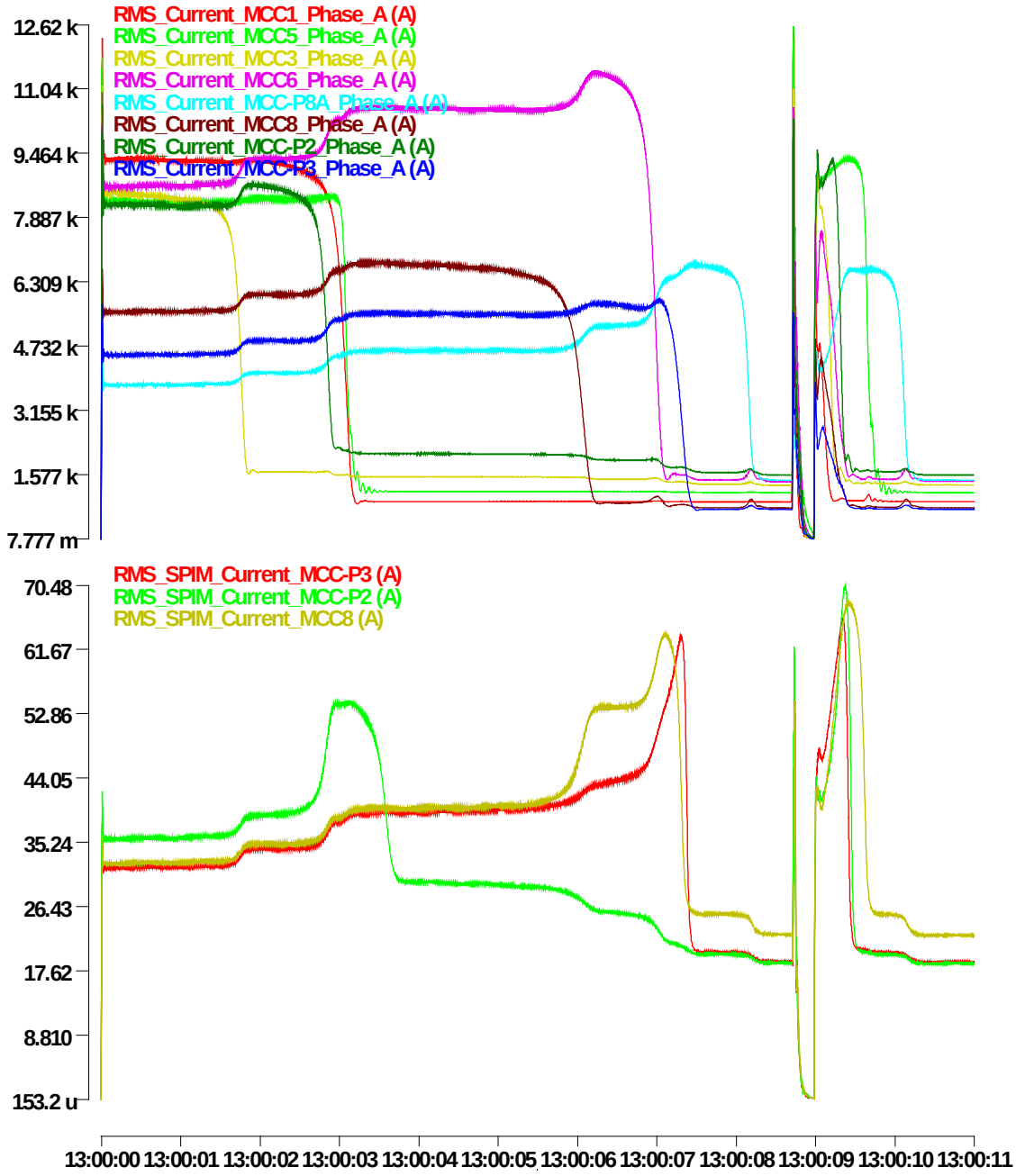

Figure 9.105: Rms value of current absorption (phase A) by each induction motor during the entire simulation period (current in Amps, time in hh:mm:ss format).

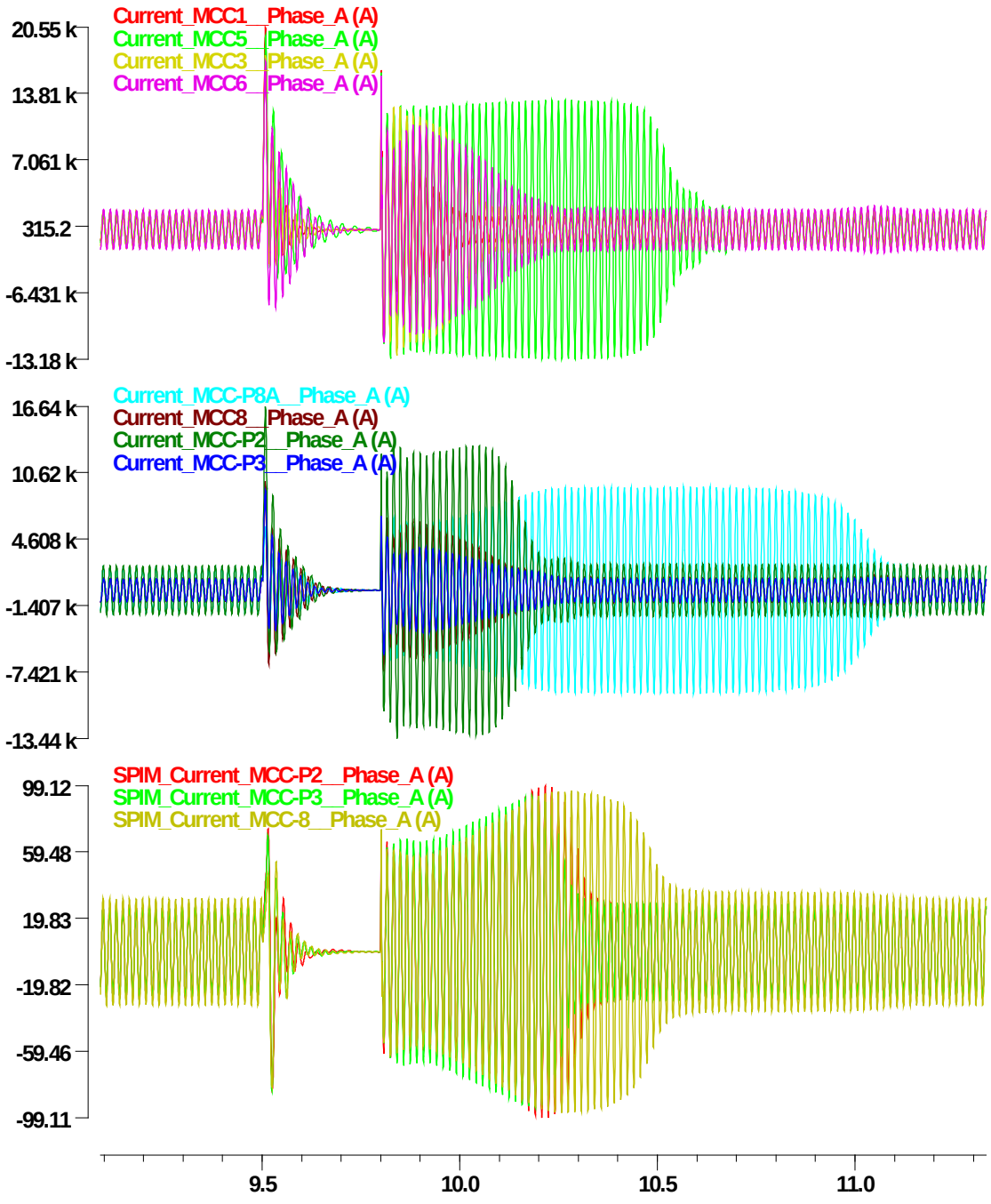

Figure 9.106: Current absorption waveforms (phase A) for each induction motor during the fault and voltage-recovery period (current in Amps, time in seconds). Single-phase motors are shown separately at the bottom graph.

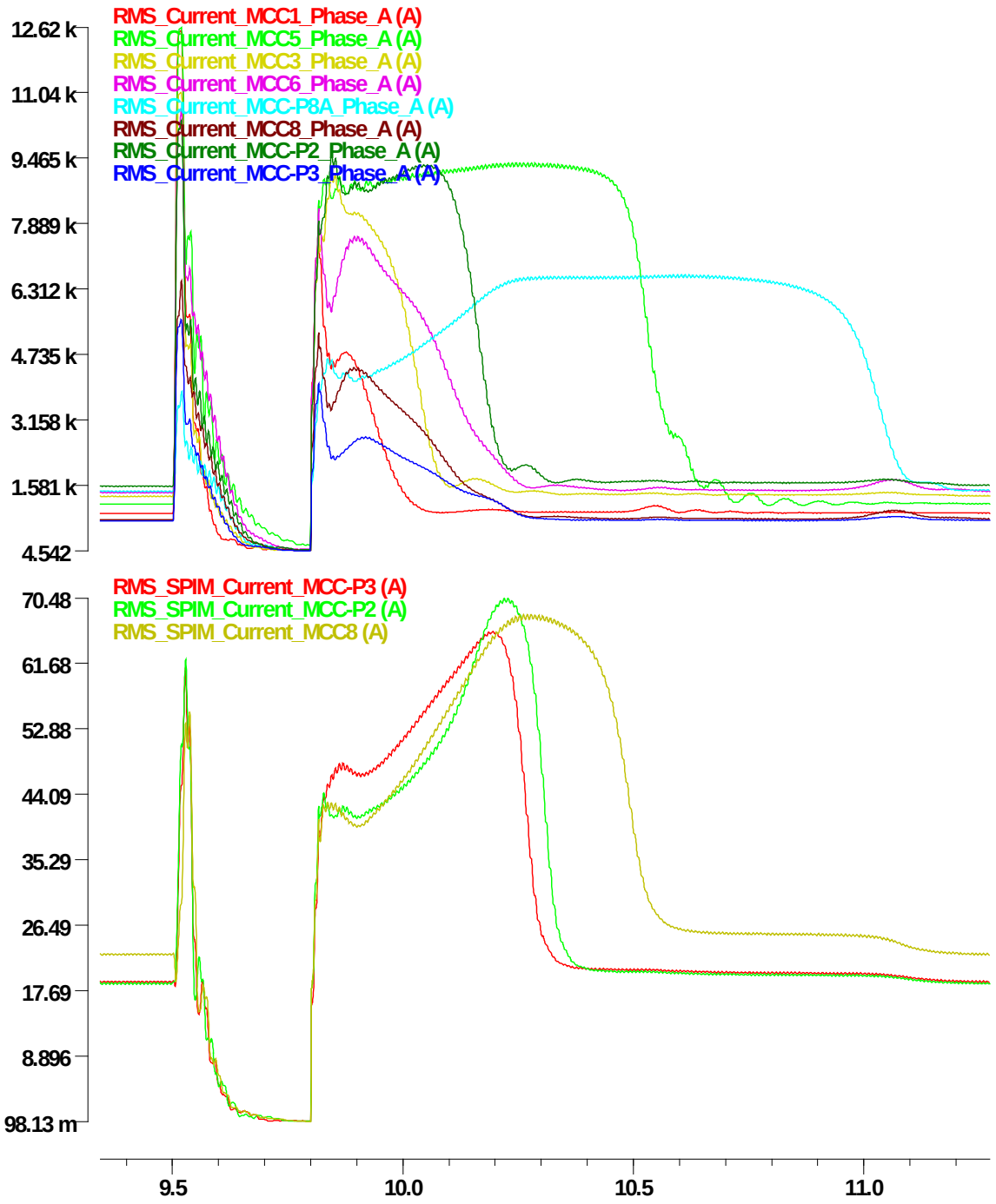

Figure 9.107: Rms value of current absorption (phase A) by each induction motor during the fault and voltage-recovery period (current in Amps, time in seconds).

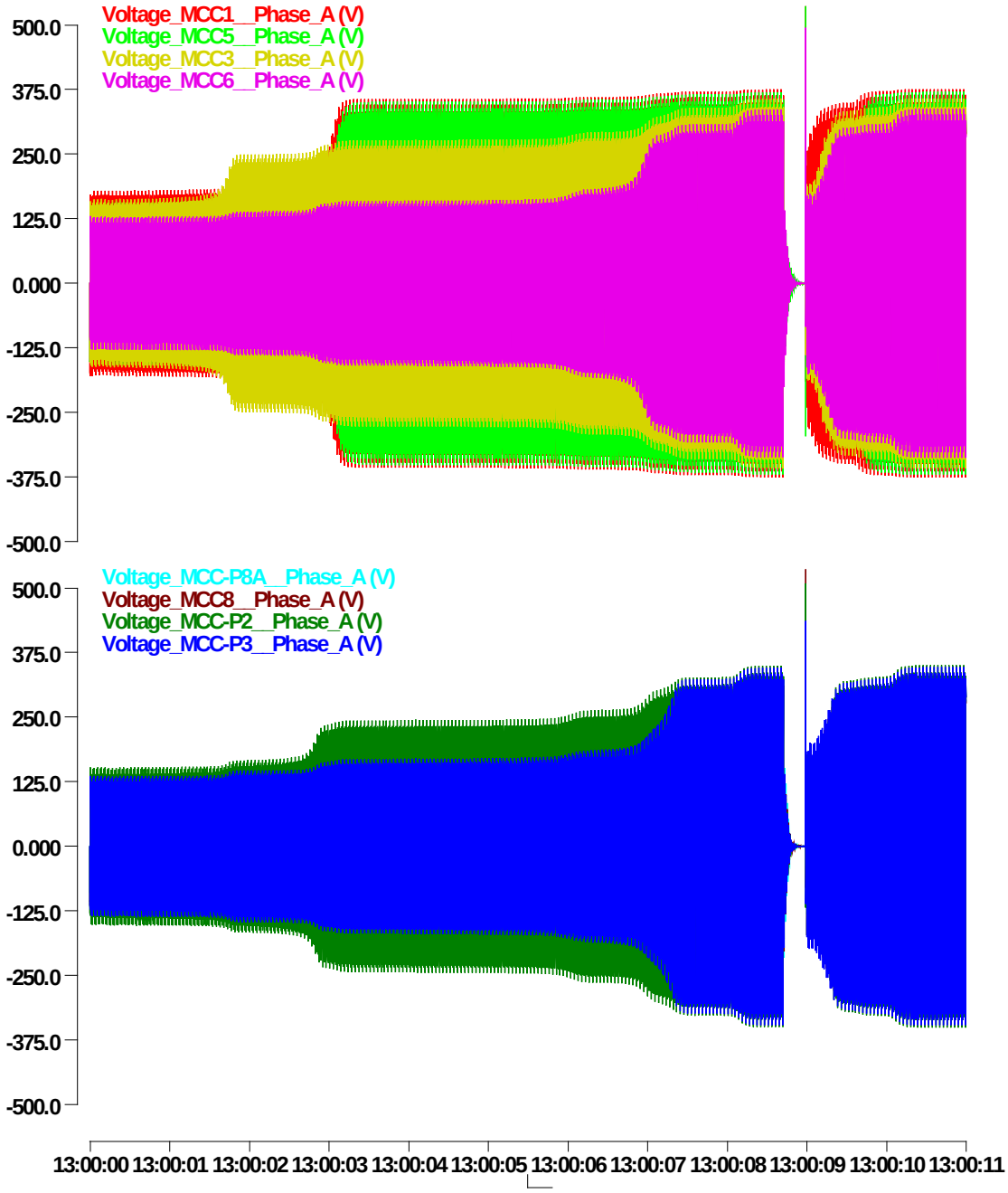

Figure 9.108: Terminal voltage waveforms (phase A) at induction motor terminals during the entire simulation period (voltage in volts, time in hh:mm:ss format).

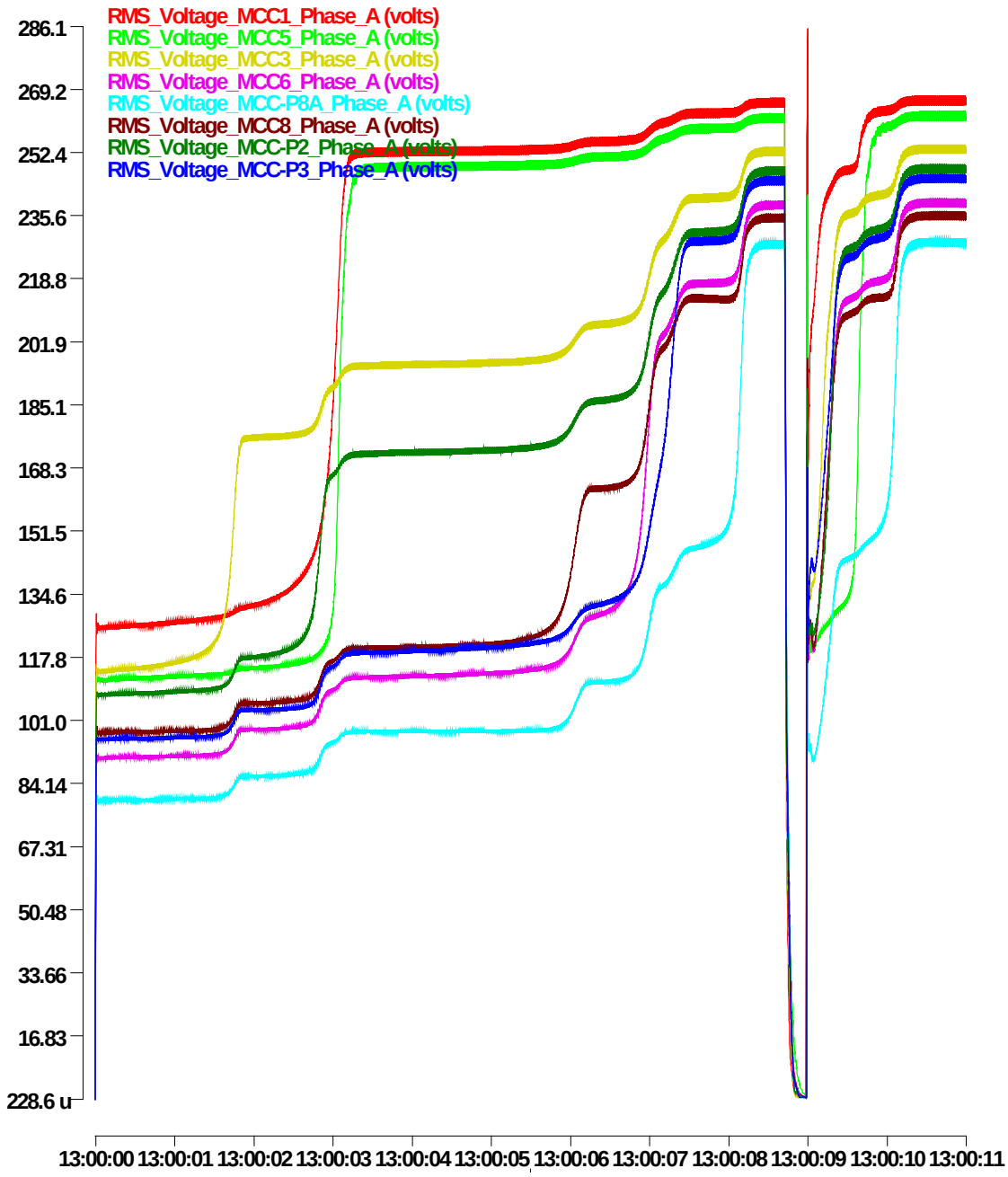

Figure 9.109: Rms value of terminal voltage (phase A) at induction motor terminals during the entire simulation period (voltage in volts, time in hh:mm:ss format).

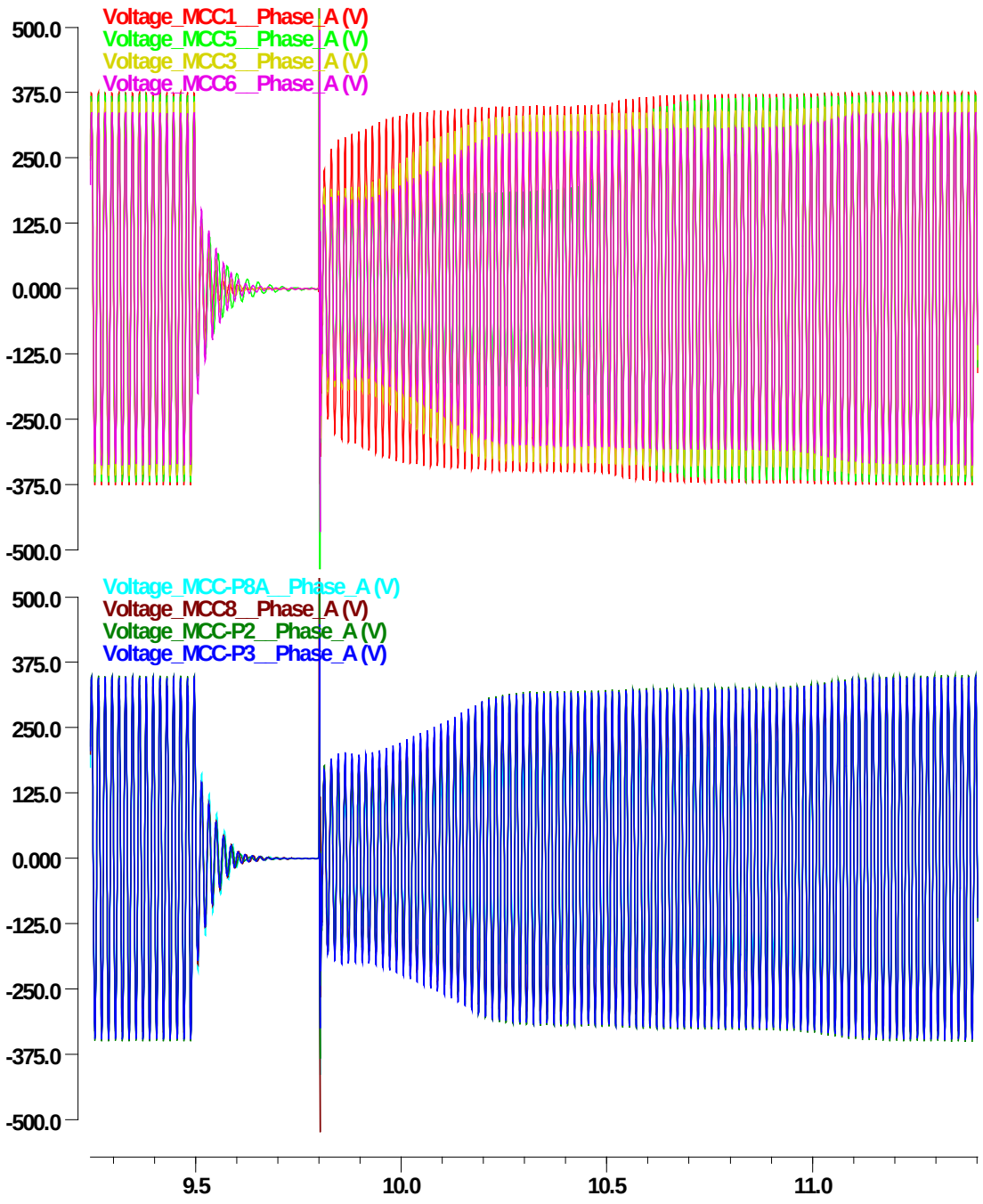

Figure 9.110: Terminal voltage waveforms (phase A) at induction motor terminals during the fault and voltage-recovery period (voltage in volts, time in seconds).

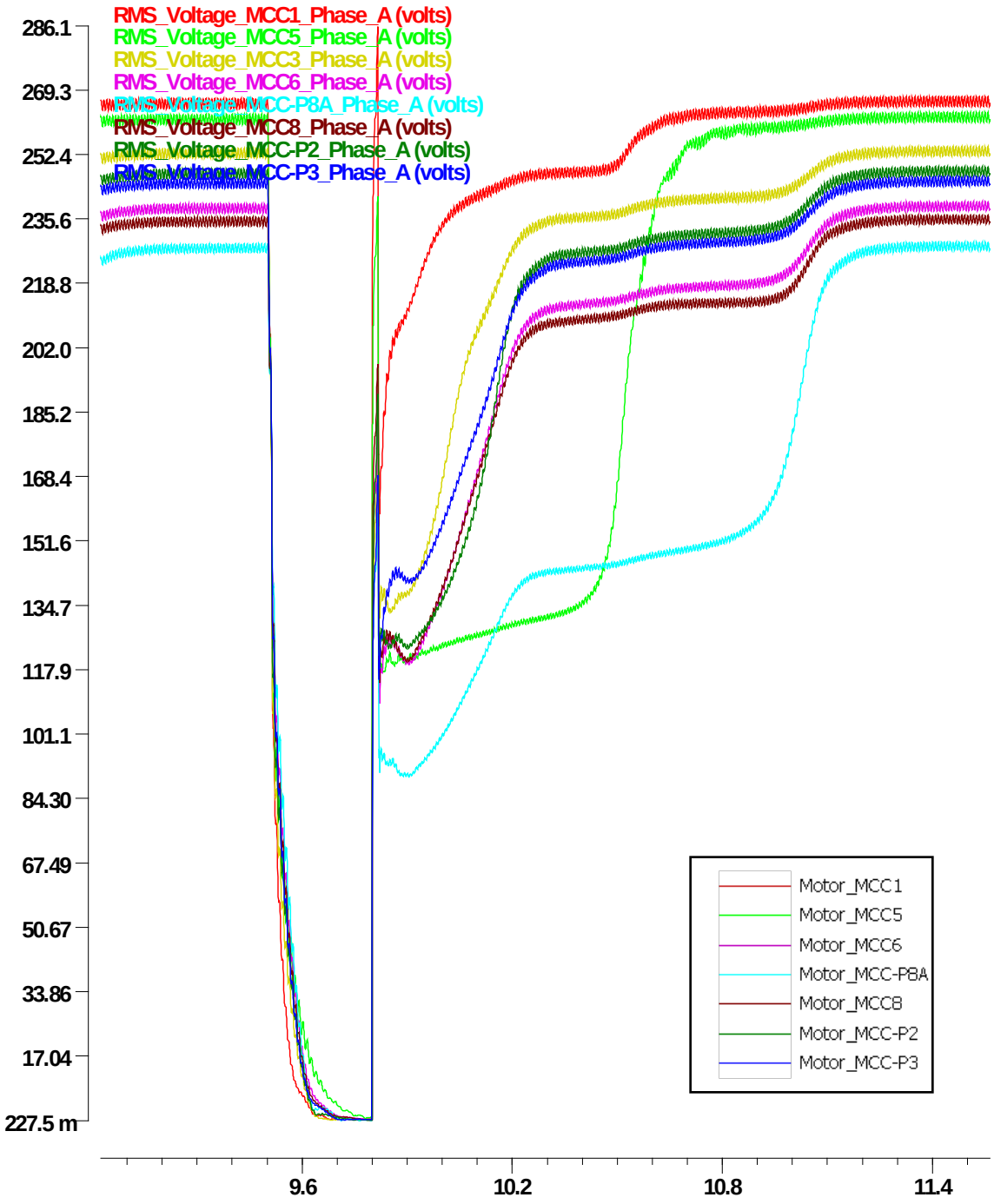

Figure 9.111: Rms value of terminal voltage (phase A) at induction motor terminals during the fault and voltage-recovery period (voltage in volts, time in seconds).

9.5 Contingency Ranking

9.5.1 Introduction

This section demonstrates the implementation and application of the contingency ranking methodology based on sensitivity analysis, as described in section 7.6. The proposed methodology is implemented in a Visual C++ environment using object-oriented techniques as part of existing power system analysis software, developed by the this research group. Both the first-order, PI-linearization and the higher-order, state-linearization approaches are integrated in the same environment. An additional option of calculating the sensitivity of the PI wrt to the outage control variable numerically, using a secant approximation is also available and mainly used for debugging purposes.

A graphical user interface has been developed to facilitate the input of data. The user defines the performance index to be used, the contingencies to be considered and the desired solution approach (i.e. first-order analysis with PI-linearization, higher-order analysis with state-linearization and if numerical check with secant approximation will be performed) along with the required solution parameters. The results provided are the estimation of the performance index change, ΔJ, based on which the ranking is performed. The results are presented to the user in a numerical form. The user interface of the program is shown in Figure 9.112. The described indices correspond to the indices defined in section 7.5.

The method has been applied to three small power systems: a four-bus system, a nine-bus system, and the IEEE 24-bus reliability test system (RTS) [36]. The proposed state-linearization method is compared to the PI-linearization method and both of the method are compared to the full load-flow analysis.

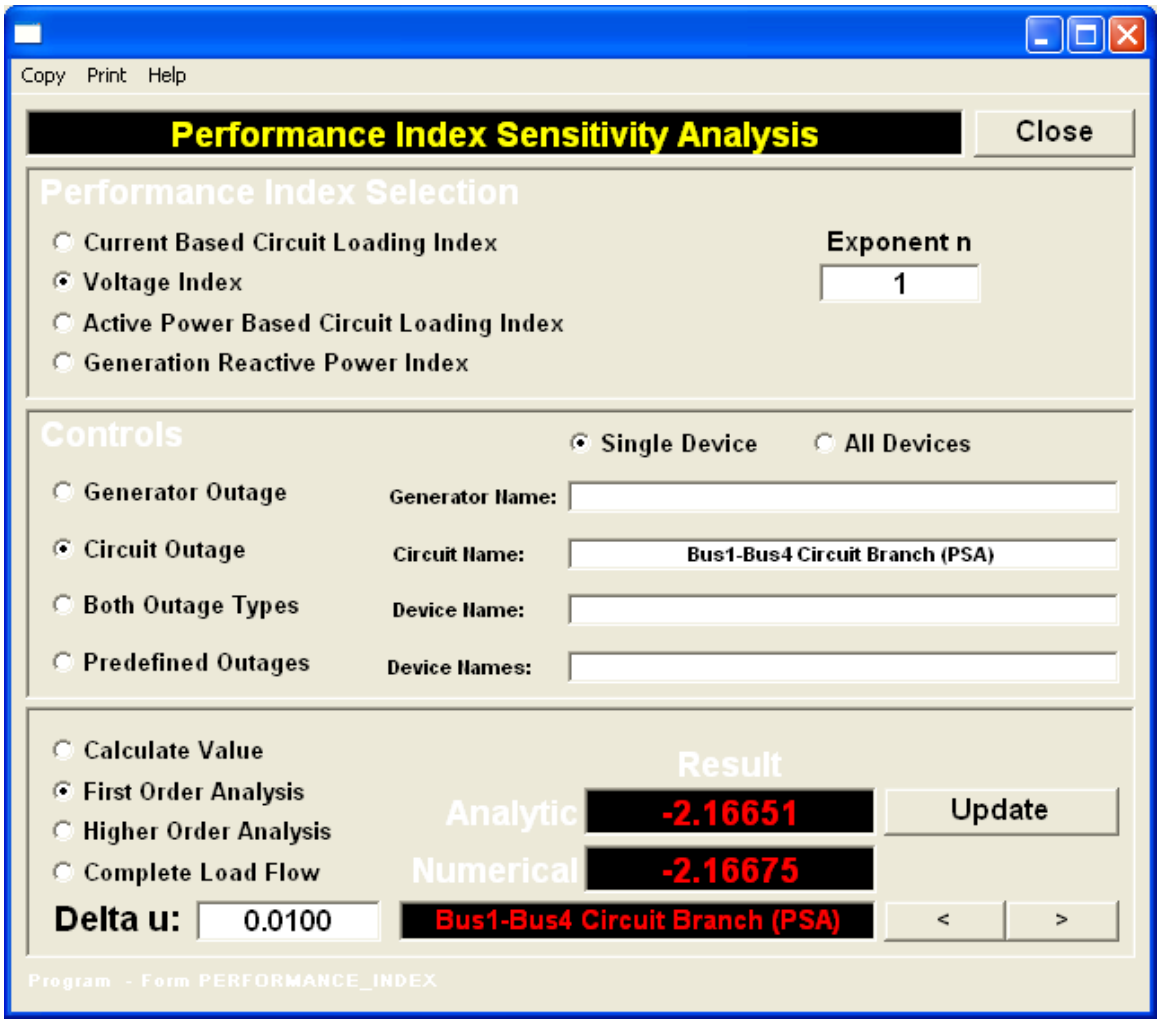

Figure 9.112: Main user interface for contingency ranking.

9.5.2 Four-Bus System

The four-bus test system is depicted in Figure 9.113. It consists of three constant-power loads, two generators, and four transmission lines represented with pi-equivalent circuits. Table 9.11 presents comparative results from contingency ranking using the PI-linearization approach, the state-linearization approach and the full load-flow solution, for the voltage index. The exponent value in the index definition is chosen to be two. All buses are equally weighted. Note that the actual absolute value of the performance index

change does not provide any significant information, when compared between the various methodologies. Only the relative ranking is of interest. Note that both methods achieve perfect ranking of contingencies. The outage of line between buses 10 and 30 is the most severe contingency and in fact there is no load-flow solution for this contingency.

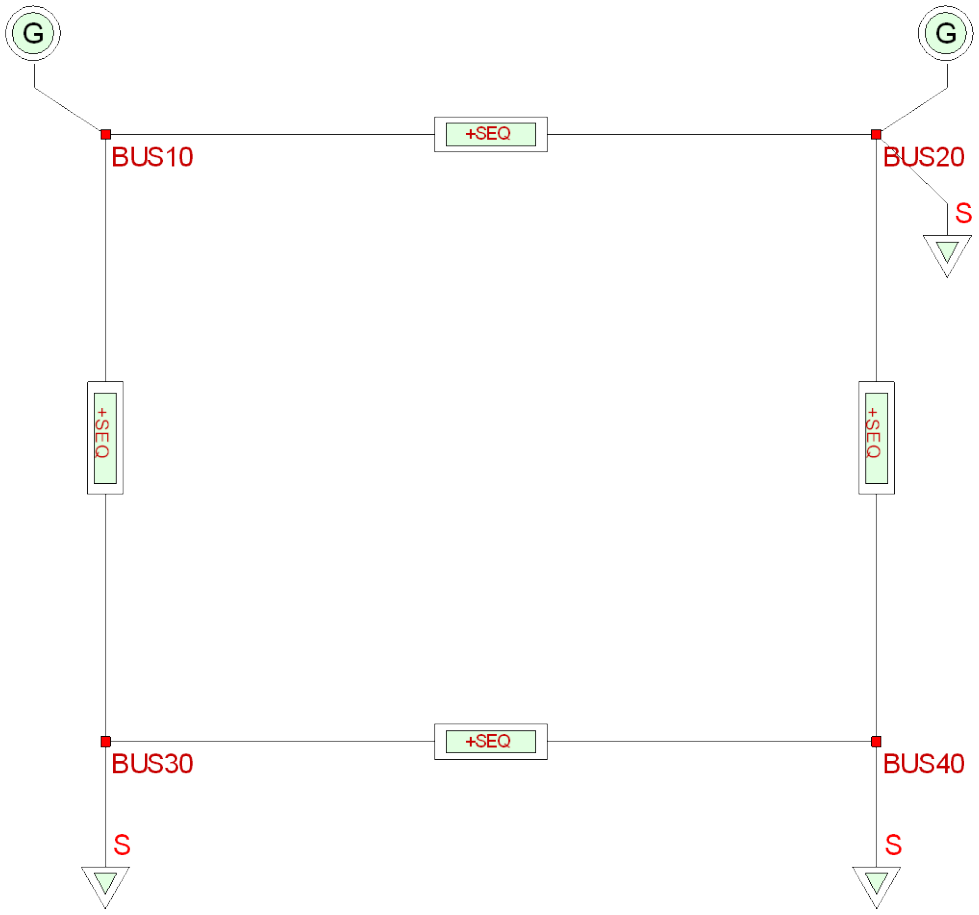

Figure 9.113: Four-bus test system used for contingency-ranking evaluation.

Table 9.11: Ranking results using the voltage-index for the four-bus system. The NLF note indicated there is no load-flow solution.

Circuit Name	First-order Analysis		Higher-order Analysis		Full Load-flow Analysis	
	ΔJ	Rank	ΔJ	Rank	ΔJ	Rank
BUS10 – BUS30	6.12	1	7.01	1	NLF	1
BUS20 – BUS40	5.31	2	6.29	2	185.36	2
BUS30 – BUS40	0.05	3	0.05	3	0.44	3
BUS10 – BUS20	0.0004	4	0.0002	4	0.04	4

9.5.3 Nine-Bus System

The nine-bus test system is depicted in Figure 9.114. It consists of three constant-power loads, three generators, and nine transmission lines. Table 9.12 presents comparative results from contingency ranking using the PI-linearization approach, the state-linearization approach and the full load-flow solution, for the voltage index. The exponent value in the index definition is chosen to be two. As in the previous example, all buses are equally weighted.

Note that there are some misrankings of both the linearization methods compared to the full load-flow analysis. The most severe of these misranking result from the fact that the removal of the lines between BUS1 and BUS4, BUS3 and BUS6, and BUS2 and BUS8 also results in the loss of a corresponding generating unit and thus significant change in the system topology. This common mode outage was not taken into account when performing the index- or state-linearization and thus it is not expected to be caught by the two methods. It is simulated, however, in the load-flow solution. Thus, a more fair comparison of the ranking results would be if these three contingencies are excluded. The ranking of the remaining 6 line-contingencies is shown in Table 9.13 and the ranking results now look much closer to the results obtained via full load-flow. It can be seen from Table 9.13 that the higher-order ranking method achieves a better can more consistent ranking compared to the first-order linearization, resulting only in minor misrakings compared to the more severe ones of the first-order, state linearization.

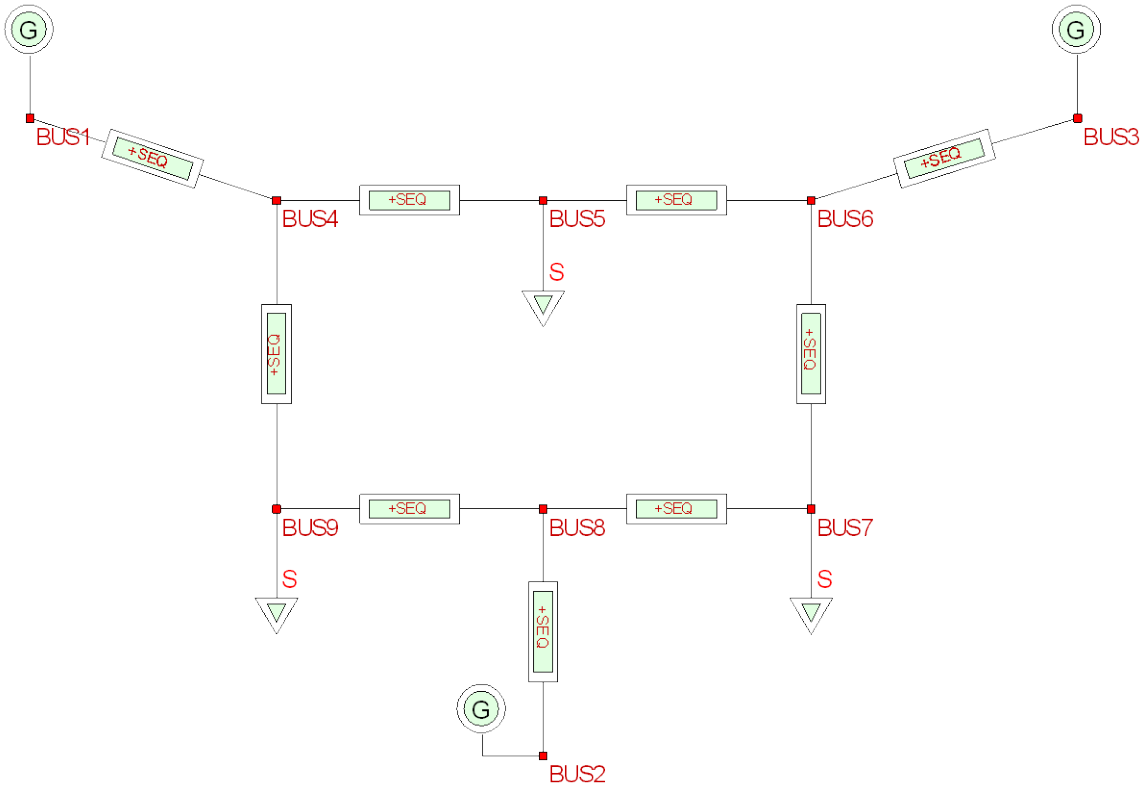

Figure 9.114: Nine-bus test system used for contingency-ranking evaluation.

Table 9.12: Ranking results using the voltage-index for the nine-bus system.

Circuit Name	First-order Analysis		Higher-order Analysis		Full Load-flow Analysis	
	ΔJ	Rank	ΔJ	Rank	ΔJ	Rank
BUS1 – BUS4	2.22	2	2.48	2	434.76	1
BUS8 – BUS2	1.27	5	1.43	5	405.96	2
BUS3 – BUS6	0.55	9	0.48	9	403.04	3
BUS9 – BUS4	1.83	4	2.21	3	24.32	4
BUS8 – BUS9	2.58	1	2.51	1	8.84	5
BUS4 – BUS5	0.84	6	1.06	6	5.64	6
BUS5 – BUS6	1.92	3	1.78	4	3.10	7
BUS7 – BUS8	0.66	8	0.86	7	4.70	8
BUS6 – BUS7	0.71	7	0.79	8	1.72	9

Table 9.13: Ranking results using the voltage-index for the nine-bus system. Contingencies that result in loss of generators have been excluded.

Circuit Name	First-order Analysis		Higher-order Analysis		Full Load-flow Analysis	
	ΔJ	Rank	ΔJ	Rank	ΔJ	Rank
BUS9 – BUS4	1.83	3	2.21	2	24.32	1
BUS8 – BUS9	2.58	1	2.51	1	8.84	2
BUS4 – BUS5	0.84	4	1.06	4	5.64	3
BUS5 – BUS6	1.92	2	1.78	3	3.10	4
BUS7 – BUS8	0.66	6	0.86	5	4.70	5
BUS6 – BUS7	0.71	5	0.79	6	1.72	6

9.5.4 18-Bus System

The test system utilized in section 9.3 for demonstrating a transmission system voltage recovery example is considered next. The system is illustrated in Figure 9.77. Circuit contingencies are only considered in the form of line outages. Table 9.14 presents comparative results from contingency ranking using the PI-linearization approach, the state-linearization approach and the full load-flow solution, for the voltage index. The exponent value in the index definition is chosen to be two. As in the previous examples, all buses are equally weighted.

Table 9.14: Contingency ranking for the test system utilizing the voltage index.

Name	First-order Analysis		Higher-order Analysis		Full Load-flow Analysis	
	ΔJ	Rank	ΔJ	Rank	ΔJ	Rank
TRANSFORMER BUS05	52.60	3	60.25	3	1897.13	1
TRANSFORMER BUS03	0.42	16	0.42	16	1185.23	2
TRANSFORMER BUS04	0.84	14	0.85	14	1038.24	3
LINE BUS05-T TO D05-1	67.14	2	77.43	2	948.47	4
LINE BUS03-T TO D03-1	0.03	20	0.03	20	789.42	5
LINE BUS04-T TO D04	0.36	17	0.37	17	777.43	6
LINE D05-1 TO D05-2	149.32	1	179.16	1	682.89	7
TRANSFORMER GEN2	16.32	4	17.69	4	569.08	8
TRANSFORMER GEN1	10.13	6	9.67	7	424.79	9
LINE D03-1 TO D03-2	0.04	19	0.04	19	399.11	10
TRANSFORMER MOTOR3	1.04	13	1.05	13	376.77	11
TRANSFORMER MOTOR1-4	2.26	12	2.28	12	305.97	12
LINE BUS02 TO BUS04	15.64	5	16.56	5	210.33	13
LINE BUS03 TO BUS04	9.95	7	10.33	6	102.84	14
LINE1 BUS04 TO BUS05	4.45	8	4.52	8	12.22	15
LINE2 BUS04 TO BUS05	3.44	9	3.48	9	4.77	16
TRANSFORMER MOTOR2	0.60	15	0.60	15	4.26	17
LINE2 BUS01 TO BUS03	2.89	11	2.94	11	4.42	18
LINE1 BUS01 TO BUS03	2.90	10	2.95	10	4.02	19
LINE BUS01 TO BUS02	0.17	18	0.17	18	0.67	20

Some significant misrankings can be observed for this test system. However, a more thorough examination of the outages that cause the misrankings and of the system diagram reveals that all these misrankings are caused by contingencies that result in loss of additional system components to the outaged circuit. These are components that are connected to that circuit in radial configuration. Such contingencies, which result in major changes in the system configuration, cannot be correctly assessed by the proposed

linearization techniques unless these common mode outages are also taken into consideration. Since this is not the case in the current ranking, such misrankings are expected. However, when removing these contingencies from the list of Table 9.14 and mainly consider only the transmission level outages, it can be observed by the results shown in Table 9.15 that both methods achieve perfect contingency ranking for all the remaining cases.

Table 9.15: Contingency ranking for the test system utilizing the voltage index and excluding contingencies that cause additional component outage.

Name	First-order Analysis		Higher-order Analysis		Full Load-flow Analysis	
	ΔJ	Rank	ΔJ	Rank	ΔJ	Rank
LINE BUS02 TO BUS04	15.64	1	16.56	1	210.33	1
LINE BUS03 TO BUS04	9.95	2	10.33	2	102.84	2
LINE1 BUS04 TO BUS05	4.45	3	4.52	3	12.22	3
LINE2 BUS04 TO BUS05	3.44	4	3.48	4	4.77	4
LINE1 BUS01 TO BUS03	2.90	5	2.95	5	4.02	6
LINE2 BUS01 TO BUS03	2.89	6	2.94	6	4.42	5
LINE BUS01 TO BUS02	0.17	7	0.17	7	0.67	7

9.5.5 IEEE 24-Bus Reliability Test System

The 24-bus reliability test system is depicted in Figure 9.115. Detailed data for the system can be found in [36]. The contingencies are ranked in terms of voltage deviation using the same voltage index as in the previous examples with an exponent of two. The ranking for all methods is presented in Table 9.16. Both linearization methods result in some misranking, but the misrankings are, in general, not severe. So, for example the top ten most severe contingencies (based on the full load-flow analysis) are accurately identified by both methods with only the 10^{th} contingency not being included in the list, having been replaced by the 11^{th}. The actual ranking of the ten most important contingencies is not exact, but for prescreening, filtering purposes this is acceptable. A similar situation holds for the next ten contingencies. Again all of them are identified by

both methods, with minor misrankings within the group. The main goal of these ranking methodologies is to obtain a quick first estimate the group of the most severe contingencies and then proceed using full load-flow analysis to analyze each one of the few ones selected, instead of performing a full load-flow analysis for every possible contingency. This can prove very efficient in large-scale systems.

Table 9.16: Ranking results using the voltage index for the IEEE 24-bus system.

Name	First-order Analysis		Higher-order Analysis		Full Load-flow Analysis	
	ΔJ	Rank	ΔJ	Rank	ΔJ	Rank
Circuit 138kV, BUS70 to BUS80	2.54	2	3.06	2	416.11	1
Circuit 138kV, BUS60 to BUS100 - Cable	5.38	1	7.45	1	165.91	2
Circuit 230kV, BUS150 to BUS240	1.88	4	2.11	3	15.01	3
Transformer 138/230kV, BUS240/BUS30	1.36	9	1.35	11	8.67	4
Circuit 230kV, BUS140 to BUS160	1.49	8	1.69	8	7.93	5
Circuit 230kV, BUS110 to BUS130	2.20	3	2.06	4	5.27	6
Circuit 138kV, BUS20 to BUS40	1.57	7	1.85	6	5.04	7
Circuit 138kV, BUS10 to BUS50	1.21	11	1.41	9	4.85	8
Circuit 230kV, BUS120 to BUS130	1.76	6	1.75	7	4.17	9
Circuit 138kV, BUS20 to BUS60	1.79	5	2.05	5	3.59	10
Transformer 138/230kV, BUS100/BUS120	1.21	12	1.01	13	3.43	11
Transformer 138/230kV, BUS90/BUS120	1.05	14	1.00	14	2.69	12
Transformer 138/230kV, BUS100/BUS110	0.94	15	0.81	15	2.66	13
Circuit 138kV, BUS10 to BUS30	1.27	10	1.40	10	1.98	14
Transformer 138/230kV, BUS90/BUS110	0.80	16	0.78	16	2.05	15
Circuit 230kV, BUS120 to BUS230	1.11	13	1.16	12	1.50	16
Circuit 230kV, BUS110 to BUS140	0.22	17	0.22	17	0.39	17
Circuit 138kV, BUS40 to BUS90	0.22	18	0.20	18	0.38	18
Circuit 138kV, BUS80 to BUS90	0.21	19	0.19	20	0.30	19
Circuit 138kV, BUS30 to BUS90	0.18	20	0.20	19	0.30	20
Circuit 138kV, BUS50 to BUS100	0.16	21	0.16	21	0.28	21
Circuit 230kV, BUS130 to BUS230	0.09	23	0.06	23	0.26	22
Circuit 138kV, BUS80 to BUS100	0.12	22	0.12	22	0.13	23
Circuit 230kV, BUS160 to BUS170	0.02	24	0.03	24	0.07	24
Circuit 230kV, BUS160 to BUS190	0.008	25	0.01	25	0.07	25
Circuit 230kV, BUS150 to BUS160	0.003	28	0.003	30	0.018	26
Circuit 230kV, BUS200 to BUS230	-0.003	32	0.002	31	0.017	27
Circuit 230kV, BUS200 to BUS230	-0.003	33	0.002	32	0.017	28
Circuit 230kV, BUS190 to BUS200	0.006	26	0.007	26	0.016	29
Circuit 230kV, BUS190 to BUS200	0.006	27	0.007	27	0.016	30
Circuit 138kV, BUS10 to BUS20 - Cable	0.0003	31	0.0003	35	0.0092	31
Circuit 230kV, BUS180 to BUS210	0.0009	29	0.001	33	0.0015	32
Circuit 230kV, BUS180 to BUS210	0.0009	30	0.001	34	0.0015	33
Circuit 230kV, BUS170 to BUS220	-0.005	34	0.005	29	-0.002	34
Circuit 230kV, BUS170 to BUS180	-0.095	36	-0.007	36	-0.006	35
Circuit 230kV, BUS150 to BUS210	-0.096	37	-0.051	37	-0.014	36
Circuit 230kV, BUS150 to BUS210	-0.096	38	-0.051	38	-0.014	37
Circuit 230kV, BUS210 to BUS220	-0.006	35	0.006	28	-0.019	38

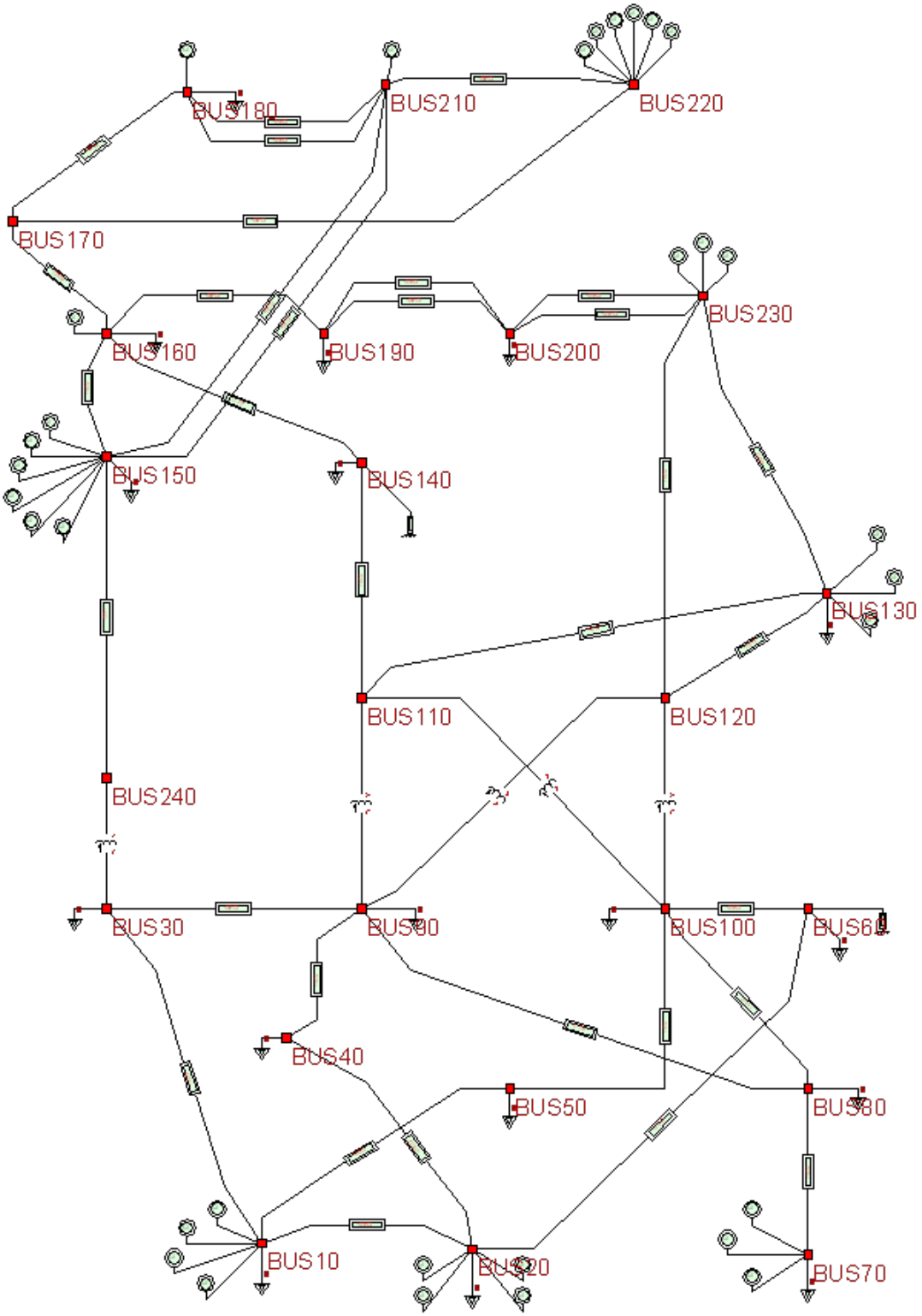

Figure 9.115: The IEEE 24-bus reliability test system.

9.6 Optimal Allocation of VAr Resources

9.6.1 Introduction

This section involves a step-by-step demonstration of the application of dynamic programming for the optimal allocation of VAr sources. Both the planning problem over a predefined time horizon and the static, single-state allocation problem, as described in sections 7.3 and 7.4 respectively will be illustrated utilizing the proposed dynamic programming approach. The approach will be demonstrated utilizing some simple examples that are easily presented in detail.

9.6.2 Multi-Stage Planning Problem

The system that is being used for the study is the simple transmission system illustrated in Figure 9.116. The system consists of two generating units and a third generator (acting as slack unit in steady state) representing the equivalent external network, where the system is connected to, via a transmission line. There are two generating substations (BUS01 and BUS02), equipped with step-up transformers, two transmission substations (BUS03 and BUS04), two distribution substations (BUS05 and BUS06), with step down transformers, seven transmission lines and two distribution lines in the system. Loads are connected to the system at the ends of the distribution lines via transformers. Portion of the load is represented as constant impedance load and another portion as induction motor loads. In particular there are two motors connected to the system, at buses BUS08-L and BUS07-L, rated at 1.0 and 0.5 MVAr respectively. Motor 1, at BUS08-L, has an inertia constant of 0.5 s and drives a fan-type load, while motor 2, at BUS07-L, has an inertia constant of 1.5 s and drives a constant power load of 1.0 p.u. Note that the system is represented using physically-based, three phase modeling, as

described throughout this work. The configuration of each substation is explicitly represented, using the breaker-oriented modeling approach. The breakers and switches are explicitly represented and the system transformers are included in the substation models. The bulk side of the system is, in general, symmetric. Small asymmetries are introduced due to the transmission-line structures.

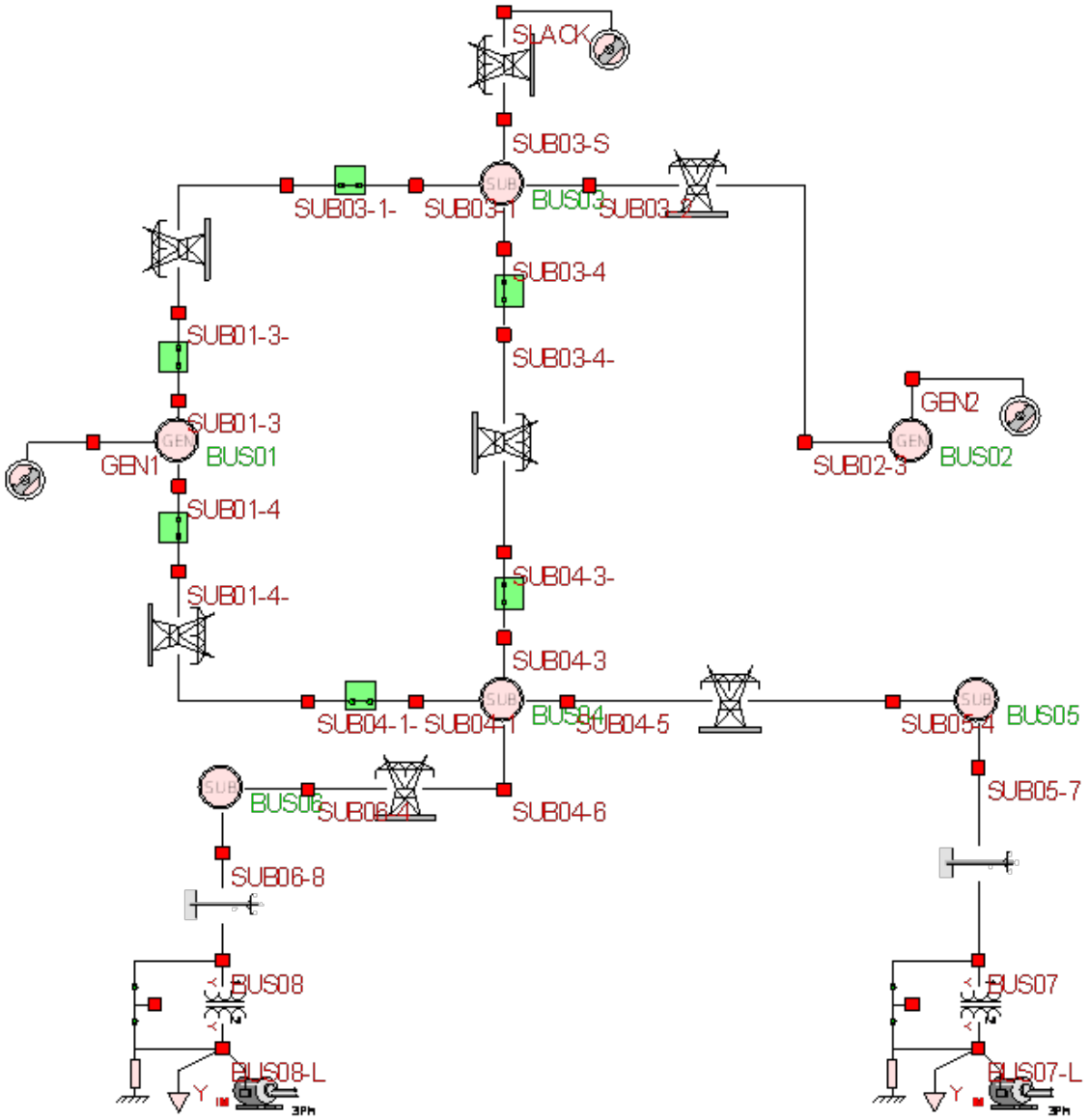

Figure 9.116: One-line diagram of transmission test system.

The steady-state behavior of the system is illustrated in Figure 9.117 through Figure 9.119. Figure 9.117 shows some general information on the system condition after the load-flow analysis. Figure 9.118 presents an illustration of the voltage profile across the system. Note that the generation and transmission side of the system maintain a voltage profile close to the nominal voltage values, however, the voltages start deviating considerably closer to the load areas and fall down to 90% at the locations where major loads are connected. Finally, Figure 9.119 illustrates the steady-state conditions of the two induction motors of the system.

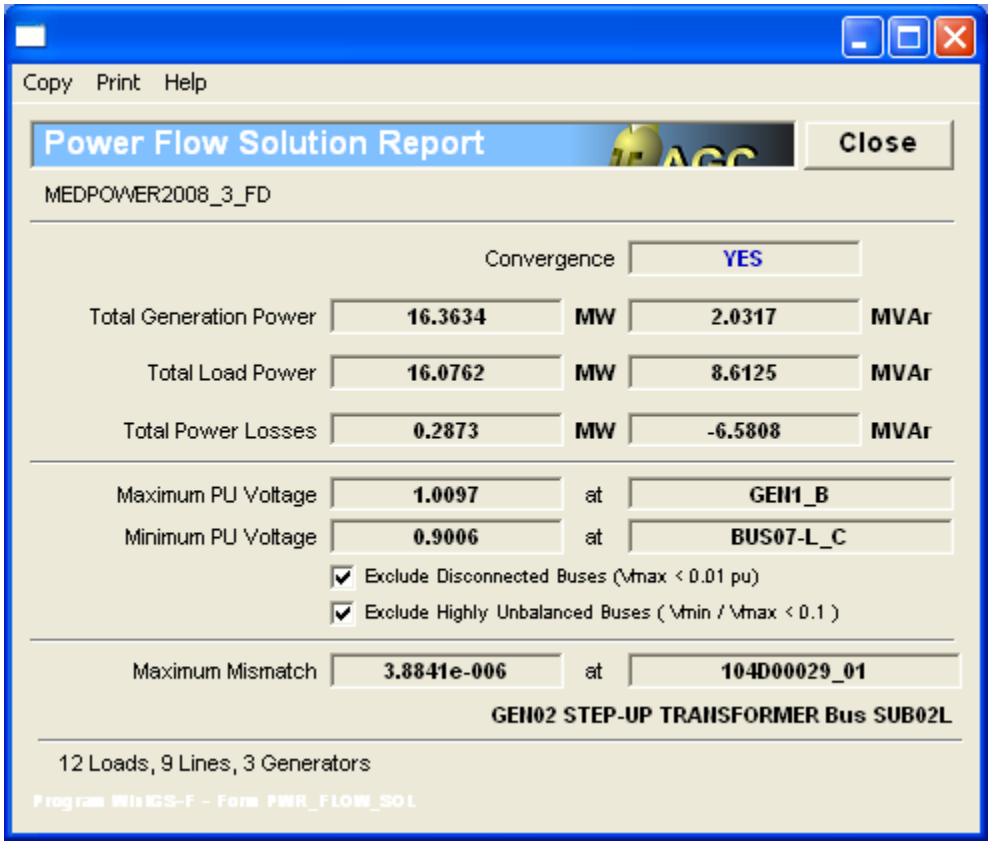

Figure 9.117: Steady-state solution report.

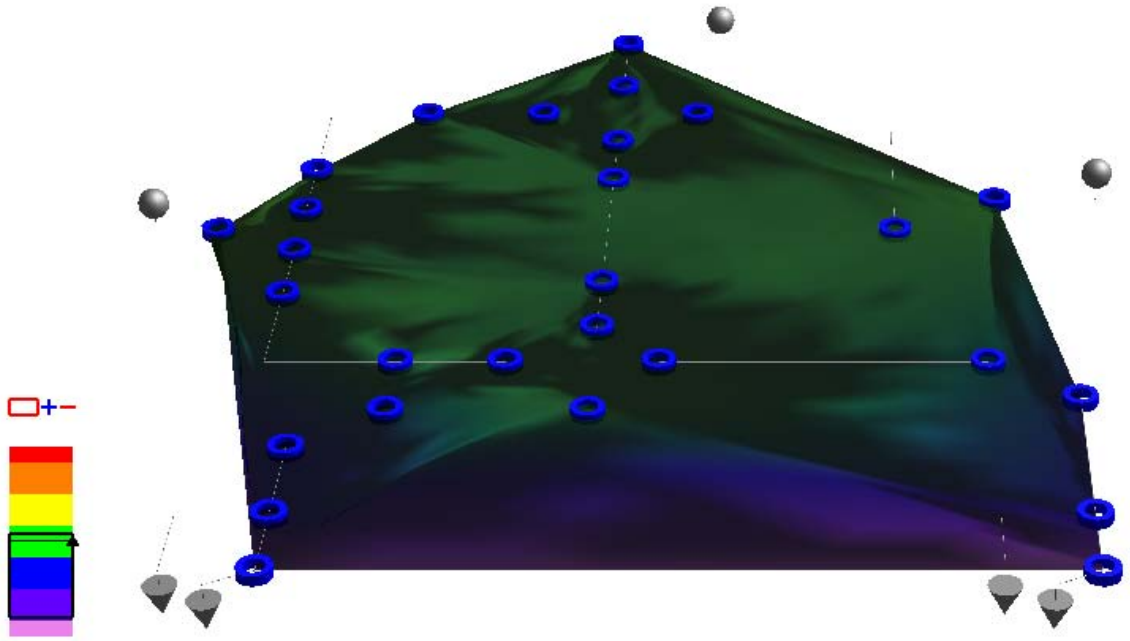

Figure 9.118: Surface plot of voltage profile (positive sequence) across the system at steady-state conditions. Green indicates normal voltage within ±1.8%. Yellow, orange, and red indicate overvoltage up to 5.4%, up to 9%, and above 9% respectively. Blue, light blue, and purple indicate undervoltage down to 5.4%, 9%, and below 9% respectively.

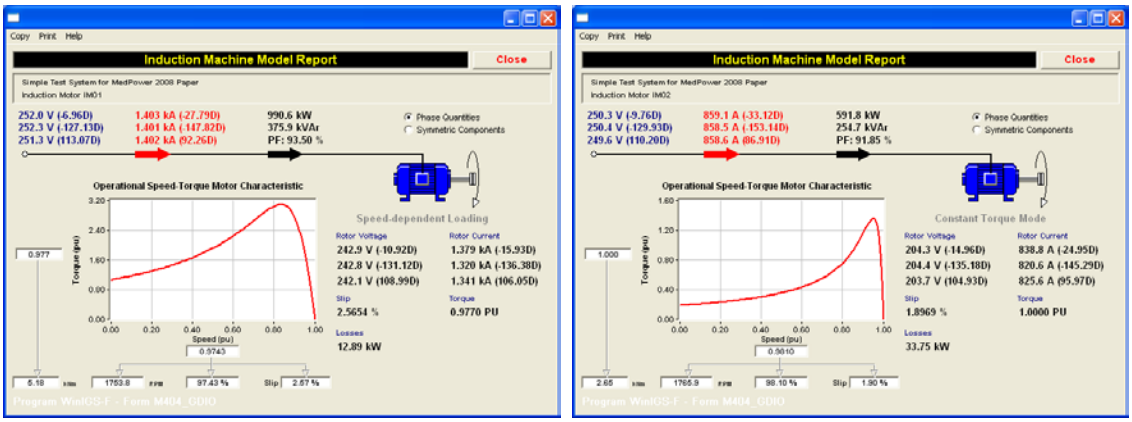

Figure 9.119: Steady-state-analysis results for two motors in the system.

Then the dynamic behavior of the system is studied utilizing the quasi-steady-state analysis. A three-phase fault it considered on the line connecting buses 3 and 4, very close to BUS04. The fault is cleared after 0.2 s by removing the faulted line. The

simulation results of this scenario are presented in Figure 9.120 and Figure 9.121. The same observation that have been made for other voltage recovery cases analyzed previously also hold. It is apparent, however, that the dynamic behavior of this system is not very satisfactory. More specifically, the first induction motor recovers quickly and gets back to a new acceptable steady-state condition. The voltage at its terminals also recovers quickly. However, this is not the case with the second motor, which does not manage to recover and stalls.

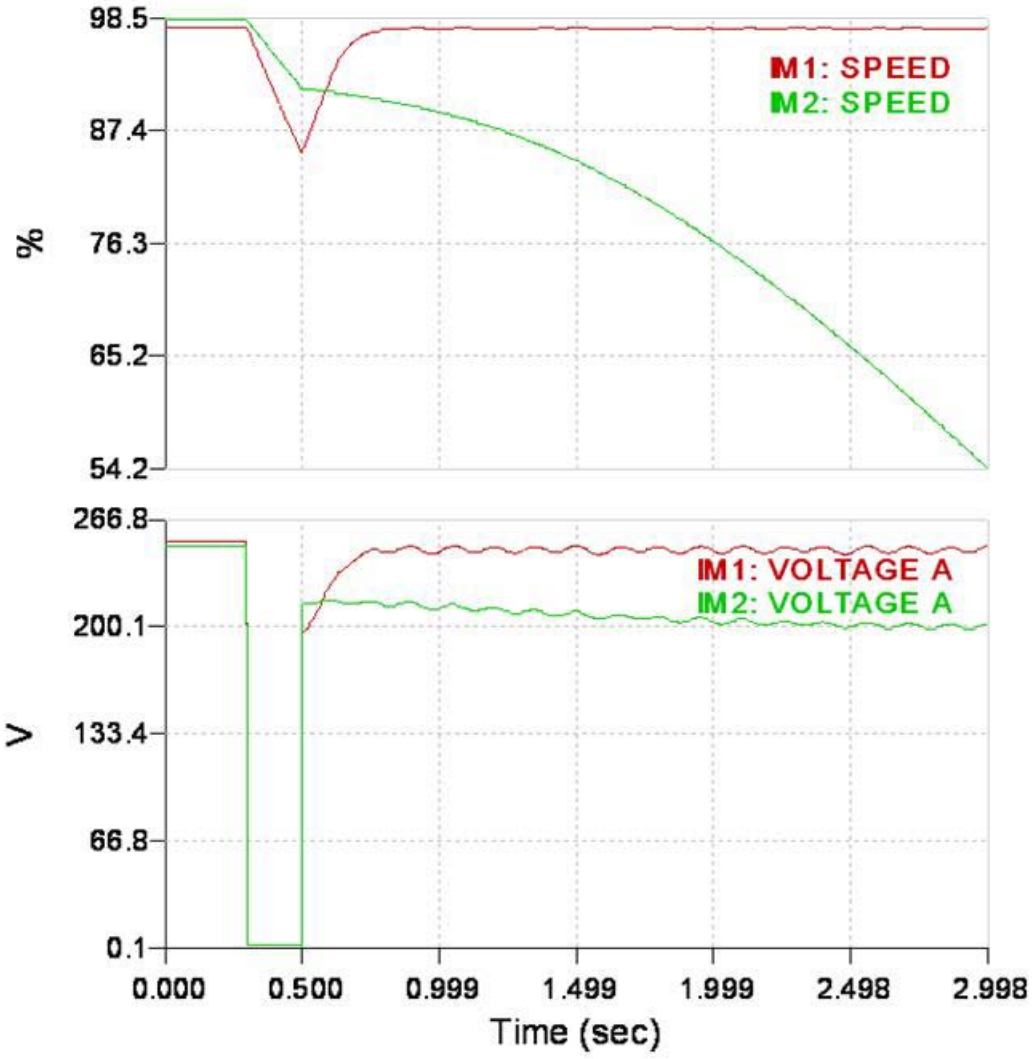

Figure 9.120: Motor speed and terminal voltage (phase A) of the two three-phase induction motors of the system during the simulation period.

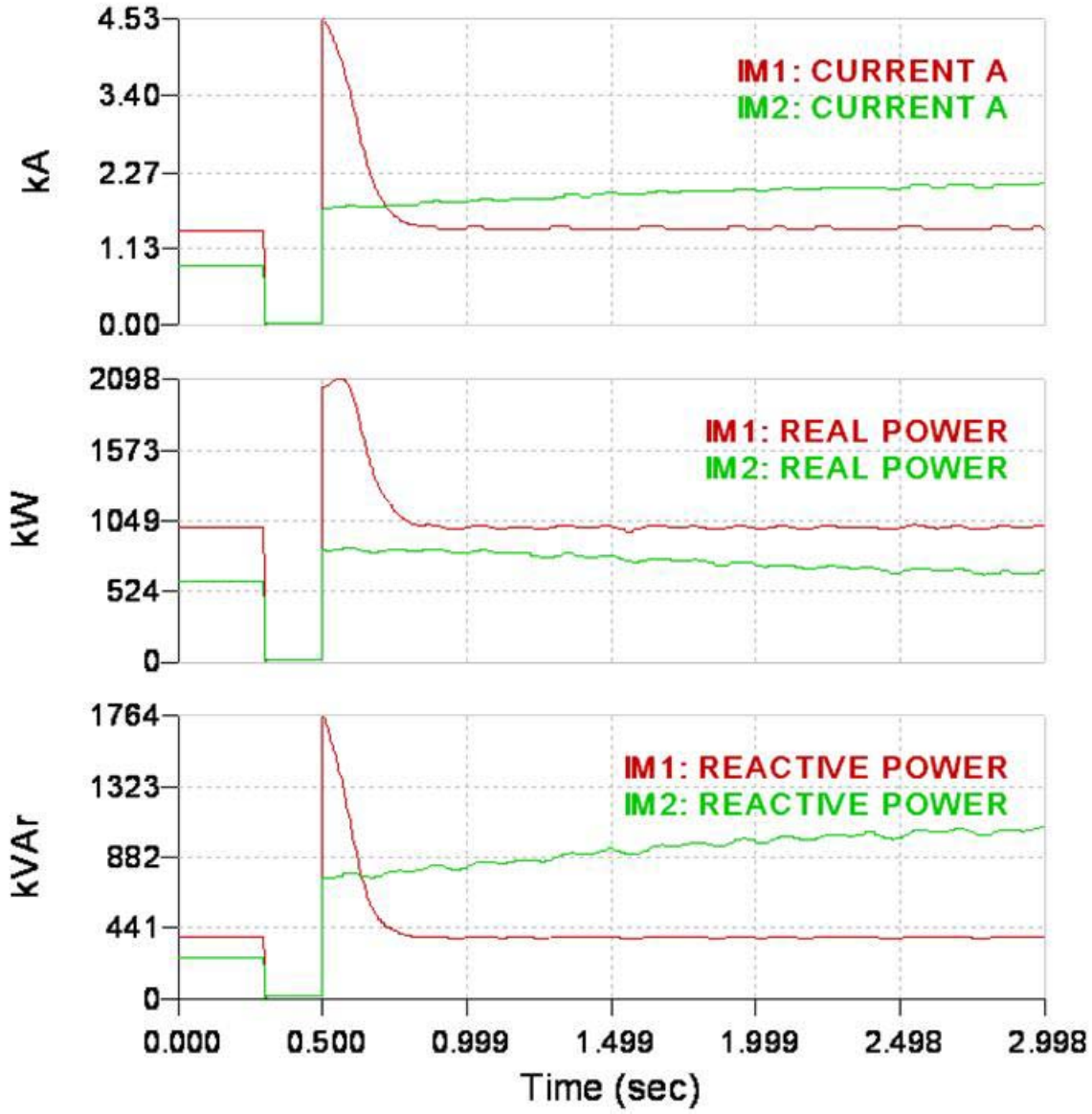

Figure 9.121: Motor current (phase A) and power absorption of the two three-phase induction motors of the system during the simulation period.

Therefore, the objective is to improve the behavior of the system and mitigate the voltage-related problems, both at steady-state and during transients by optimally allocating reactive support in the system over a pre-defined planning horizon.

A total number of three stages will be considered, representing a three-year period of time. At each year the system is considered at its peak load. The base case is the case presented above and the current loading conditions are the peak loading conditions of the base case. The peak loading conditions are the only ones assumed for this simple example and it is assumed that they are representative of the system behavior. Furthermore, the nonconforming static load model (described in Appendix B) is used to represent the load growth and variations between the time stages of the problem. Two load variables are considered and a 3% load growth per year is assumed for the static loads. The two motor loads are considered unchanged.

VAr support modules are assumed to be connected to the system at increments of 500 kVAr. Their cost is defined as a combination of installation and operating cost. The cost varies from year to year. In particular operating cost increases per year, while installation cost decreases. The operating cost depends quadratically on the rated power of the unit. The installation cost depends linearly on the unit rating and also has a term that depends on the installation location. Location cost is arbitrary defined based on the system zones, defined below, and is fixed over the entire planning period. Installation cost is also arbitrary defined as 500$/kVAr for the first year, 450$/kVAr for the second, and 300$/kVAr for the third. The assumed quadratic relation for the operating cost of the form:

$$C_{op}(X) = aX^2 + bX + c\ , \tag{9.35}$$

and the relation for the installation cost is

$$C_{in}(X) = dX + C_L(X)\ , \tag{9.36}$$

where

X : is the amount of reactive support in kVAr,

$C_{op}(X)$: is the cost of operation in $,

$C_{in}(X)$: is the installation cost in $,

$C_L(X)$: is the additional installation cost depending on the location.

The location cost is also assumed to depend linearly on X and is defined as

Zone 1: 100 $/kVAr (Transmission side, buses 1 through 6);

Zone 2: 200 $/kVAr (First distribution feeder, buses BUS06-8, BUS08, BUS08-L) ;

Zone 3: 300 $/kVAr (Second distribution feeder, buses BUS05-7, BUS07, BUS07-L).

The operation and installation cost parameters for each year are defined in Table 9.17.

Table 9.17: Operation and installation cost of reactive support.

Year	Operating Cost a ($/kVAr²)	b ($/kVAr)	c ($)	Installation Cost d ($/kVAr)
1	0.01	100	10000	500
2	0.01	110	12000	450
3	0.01	120	15000	300

The system performance is evaluated utilizing the performance indices defined in Chapter 6, and a combined objective function is constructed. The voltage index defined in (6.1) is used as part of the objective function to represent static performance. This performance index is also used for the contingency selection, as described in Chapter 7. The positive sequence voltage value is considered for the evaluation of the index and an exponent of 2 (n=1) is used.

The functional (6.24) is used as part of the objective function to represent dynamic performance, denoted here as J_R. In this case this functional measures the time, in ms, after the fault clearance for the voltage to recover above 0.8 p.u. The voltage sag duration at the load buses of interest (in this case the two buses where motors are connected) is being monitored. The functional is evaluated for the worse of the buses where the voltage recovers and for the worse of the three phases. Buses that do not recover are not considered, however such situations are captured by a penalty factor that is assigned to the objective function for states that, under some of the selected contingencies, do not satisfy voltage recovery criteria, based again on a functional of the form (6.24). The criterion used is the voltage remaining below 80% of nominal for a period of more than 30 cycles of the fundamental, which is approximately 0.5 s. This functional is denoted by J_{dip} and measures the time, in seconds, above the 30 cycles that the voltage stays below 0.8 p.u. If more than one buses do not satisfy this criterion then the durations of all violating buses are added.

A weight is assigned at each component of the objective function, so that no component has an overwhelming effect on it, apart from the penalty factor. The weights are chosen in such a way that the objective function values are normalized to a value close to 1.0. The operating and installation cost are also annualized to the value of the current operating cost.

Circuit contingencies are only considered in the form of line outages. In steady-state a contingency is analyzed by load-flow analysis after removing the corresponding circuit. For the dynamic analysis they are simulated as outages after three-phase faults, since these kinds of faults are the most severe ones. The base case screening of circuit

contingencies, based on the voltage index is illustrated in Table 9.18 for the two proposed sensitivity analysis methods. The methods are also compared with the exact ranking obtained via the full load-flow solution.

Table 9.18: Contingency ranking for the test system utilizing the voltage index.

Name	First-order Analysis		Higher-order Analysis		Full Load-flow Analysis	
	ΔJ	Rank	ΔJ	Rank	ΔJ	Rank
LINE BUS04 TO BUS05	2.84287	5	3.27002	5	21664.0885	1
LINE BUS04 TO BUS06	3.46852	3	4.15371	3	1401.4125	2
TRANSFORMER BUS06	2.82734	6	3.21753	6	933.2587	3
LINE BUS03 TO BUS02	0.34883	11	0.35404	11	800.5281	4
LINE BUS06 TO BUS08	0.20269	13	0.20489	13	669.6886	5
TRANSFORMER BUS08	3.85593	2	4.57119	2	566.7377	6
LINE BUS05 TO BUS07	0.59693	9	0.61454	9	529.2390	7
TRANSFORMER BUS07	6.06383	1	7.38301	1	485.2079	8
TRANSFORMER BUS05	3.24339	4	3.73930	4	458.2996	9
LINE BUS03 TO SLACK	1.02442	7	1.05873	7	404.2067	10
TRANSFORMER GEN01	0.75063	8	0.78146	8	400.6475	11
TRANSFORMER GEN02	0.17099	15	0.17244	15	400.1115	12
LINE BUS03 TO BUS04	0.57717	10	0.58870	10	1.6227	13
LINE BUS01 TO BUS04	0.27753	12	0.28027	12	0.2354	14
LINE BUS01 TO BUS03	0.18152	14	0.18314	14	0.1711	15

Note that both the linearization methods provide the exact same ranking. The top ten contingencies are adequately identified, however, significant misrankings can be observed for this system when compared to the ranking based on the load-flow solution. But, as in a previous case, a more thorough examination of the outages that cause the misrankings and of the system diagram reveals that all these misrankings are caused by contingencies that result in loss of additional system components than just the outaged circuit. These components are connected to that circuit in radial configuration. Since the voltage behavior at the load points is of interest and in particular the voltage recovery at the induction motor terminals, such contingencies, which remove the motors and other components of the system, are not of interest. In addition unit outages are not considered and, thus, the outages of the two generating-unit step-up transformers are also excluded, as well as the line that connects the system to the equivalent slack bus. Therefore, all

these contingencies are not currently of interest and thus by removing them from the list of Table 9.18, mainly only the transmission level outages are considered. The results of the ranking of these three outages are shown in Table 9.19 and it can be seen from these results that both methods achieve perfect contingency ranking in this case.

Table 9.19: Contingency ranking for the test system utilizing the voltage index and excluding contingencies that cause additional component outage.

Name	First-order Analysis		Higher-order Analysis		Full Load-flow Analysis	
	ΔJ	Rank	ΔJ	Rank	ΔJ	Rank
LINE BUS03 TO BUS04	0.57717	1	0.58870	1	1.6227	1
LINE BUS01 TO BUS04	0.27753	2	0.28027	2	0.2354	2
LINE BUS01 TO BUS03	0.18152	3	0.18314	3	0.1711	3

Therefore, the contingencies to be considered are the outage of lines connecting BUS03 and BUS04, BUS01 and BUS04, and BUS01 and BUS03. These three contingencies will be considered, both for steady-state analysis and dynamic analysis. For the dynamic, quasi-static analysis a three-phase fault will be assumed at each line, very close to BUS04, close to BUS01, and close to BUS03, respectively, cleared by the corresponding circuit removal from the system after 0.2 seconds.

Load buses and transmission or distribution substations are mainly considered for VAr support installation, since there is no point in placing VAr sources at generating stations. The two most favorable locations for VAr source additions are determined, based on static sensitivity analysis. The sensitivity analysis results are presented in Table 9.20. The ranking is performed based on the absolute value of the sensitivity. The negative sign comes from the fact that the performance index value decreases with the VAr source additions, indicating improvement on the system performance. Note that the most favorable locations are the terminal buses where the loads are connected. The top two locations are the induction motor buses. The performance index becomes less and

less sensitive to VAr additions when moving away from the load areas towards the bulk side of the system.

Table 9.20: Sensitivity-based candidate location ranking for VAr source additions.

Ranking	Bus Name	Sensitivity
1	BUS07-L	-0.013670
2	BUS08-L	-0.006440
3	BUS07	-0.006350
4	BUS08	-0.003400
5	BUS05-7	-0.005530
6	BUS06-8	-0.003240
7	BUS05	-0.000710
8	BUS06	-0.000550
9	BUS04	-0.000400
10	BUS01	-0.000370
11	BUS03	-0.000340
12	BUS02	-0.000300

Therefore, the two most favorable locations are BUS07-L and BUS08-L, and, for simplicity, up to only two modules are considered for installation per location. That is, each location can have zero, one, or two modules. As a result, the truncated space (based on the sensitivity analysis) includes $3^2 = 9$ states per stage and a total of three stages.

The initial system state, without any VAr source additions is evaluated first. The details of the evaluation are shown in Table 9.21. The values of each component of the objective function at this initial base case are used to normalize the values at each state at later stages. The operating cost is part of the objective function; the rest of the components are evaluated based on the static and dynamic performance for each state under base case and contingencies. There is no cost associated with the initial state, since no new VAr resources exist in the system. So, all costs are arbitrarily normalized with respect to \$100,000. Note that the static performance index J_V includes contributions for the base case and the three contingencies under consideration. All these values are

normalized with respect to the value at the initial base case. J_R and J_{dip} are both dynamic indices and include contributions from the system dynamic behavior under the three contingencies. J_{dip} introduces a penalty function for voltage below 0.8 p.u. for more than 30 cycles. The value of this duration index is normalized with respect to the 30 cycles period, with is about 0.5 s. The J_R index is normalized with respect to 100. Subsequently, the normalized objective function value is computed for each state at each stage. The value the total index J at the initial base case is used to normalize the values at all the states at the all the stages. The detailed values of the objective function and its components are shown along with each state for all the three stages in Table 9.22 through Table 9.24. Each state is denoted by an array of numbers. Each position of the array indicates a location and each number indicates the number of modules installed in that specific locations. Location 1 is BUS07-L and location 2 is BUS08-L in this example. The possible transition among states of successive stages and the installation cost associated with each such transition is show in Table 9.25 through Table 9.27.

Table 9.21: Evaluation of total performance of initial base case.

J_V			J_R			J_{dip}			J
	Actual Value	**Norm. Value**		**Actual Value**	**Norm. Value**		**Actual Value**	**Norm. Value**	
J_{VBC}	4010.02674	1.0000							
J_{V1}	4011.64950	1.0004	J_{R1}	90.1	0.9010	J_{dip1}	2.2	4.4	
J_{V2}	4010.26212	1.0000	J_{R2}	81.3	0.8130	J_{dip2}	2.2	4.4	
J_{V3}	4010.19785	1.0000	J_{R3}	82.4	0.8240	J_{dip3}	2.2	4.4	
		4.0004			**2.538**			**13.2**	**19.7384**

Table 9.22: State definition and evaluation for the first year of the problem.

State #	State	Operating Cost ($)	Operating Cost (norm)	J_V	J_R	J_{dip}	J
0	(0,0)	0	0	4.0010	2.6090	13.2	19.8100
1	(0,1)	62,500	0.6250	3.9981	1.8020	13.2	19.6251
2	(0,2)	120,000	1.2000	3.9962	1.1420	13.2	19.5382
3	(1,0)	62,500	0.6250	3.9961	2.5920	0.0	7.2130
4	(1,1)	120,000	1.2000	3.9933	1.7960	0.0	6.9893
5	(1,2)	182,500	1.8250	3.9916	1.1250	0.0	6.9416
6	(2,0)	120,000	1.2000	3.9967	2.5730	0.0	7.7697
7	(2,1)	182,500	1.8250	3.9940	1.7810	0.0	7.6000
8	(2,2)	250,000	2.5000	3.9924	1.1130	0.0	7.6054

Table 9.23: State definition and evaluation for the second year of the problem.

State #	State	Operating Cost ($)	Operating Cost (norm)	J_V	J_R	J_{dip}	J
0	(0,0)	0	0	4.0014	2.6450	13.2	19.8464
1	(0,1)	69,500	0.6950	3.9985	1.8500	13.2	19.7435
2	(0,2)	132,000	1.3200	3.9966	1.1790	13.2	19.6956
3	(1,0)	69,500	0.6950	3.9964	2.6330	0.0	7.3244
4	(1,1)	132,000	1.3200	3.9936	1.8430	0.0	7.1566
5	(1,2)	199,500	1.9950	3.9917	1.1670	0.0	7.1537
6	(2,0)	132,000	1.3200	3.9969	2.6200	0.0	7.9369
7	(2,1)	199,500	1.9950	3.9941	1.8280	0.0	7.8171
8	(2,2)	272,000	2.7200	3.9924	1.1580	0.0	7.8704

Table 9.24: State definition and evaluation for the third year of the problem.

State #	State	Operating Cost ($)	Operating Cost (norm)	J_V	J_R	J_{dip}	J
0	(0,0)	0	0	4.0019	2.7030	13.2	19.9049
1	(0,1)	77,500	0.7750	3.9989	1.8990	13.2	19.8729
2	(0,2)	145,000	1.4500	3.9969	1.2180	13.2	19.8649
3	(1,0)	77,500	0.7750	3.9968	2.6920	0.0	7.4638
4	(1,1)	145,000	1.4500	3.9938	1.8870	0.0	7.3308
5	(1,2)	217,500	2.1750	3.9919	1.2100	0.0	7.3769
6	(2,0)	145,000	1.4500	3.9970	2.6810	0.0	8.1280
7	(2,1)	217,500	2.1750	3.9942	1.8760	0.0	8.0452
8	(2,2)	295,000	2.9500	3.9924	1.1980	0.0	8.1404

Table 9.25: Normalized installation cost for transition between states from the initial base case to the first year. The dash symbol indicates impossible transition.

From\To	(0,0)	(0,1)	(0,2)	(1,0)	(1,1)	(1,2)	(2,0)	(2,1)	(2,2)
(0,0)	0	3.5	7.0	4.0	7.5	11.0	8.0	11.5	15.0
(0,1)	-	0	3.5	-	4.0	7.5	-	8.0	11.5
(0,2)	-	-	0	-	-	4.0	-	-	8.0
(1,0)	-	-	-	0	-	7.0	4.0	7.5	11.0
(1,1)	-	-	-	-	0	3.5	-	4.0	7.5
(1,2)	-	-	-	-	-	0	-	-	4.0
(2,0)	-	-	-	-	-	-	0	3.5	7.0
(2,1)	-	-	-	-	-	-	-	0	3.5
(2,2)	-	-	-	-	-	-	-	-	0

Table 9.26: Normalized installation cost for transition between states from the first to the second year. The dash symbol indicates impossible transition.

From\To	(0,0)	(0,1)	(0,2)	(1,0)	(1,1)	(1,2)	(2,0)	(2,1)	(2,2)
(0,0)	0	3.25	6.5	3.75	7.0	10.25	7.5	10.75	14
(0,1)	-	0	3.25	-	3.75	7.0	-	7.5	10.75
(0,2)	-	-	0	-	-	3.75	-	-	7.5
(1,0)	-	-	-	0	-	6.5	3.75	7.0	10.25
(1,1)	-	-	-	-	0	3.25	-	3.75	7.0
(1,2)	-	-	-	-	-	0	-	-	3.75
(2,0)	-	-	-	-	-	-	0	3.25	6.5
(2,1)	-	-	-	-	-	-	-	0	3.25
(2,2)	-	-	-	-	-	-	-	-	0

Table 9.27: Normalized installation cost for transition between states from the second to the third year. The dash symbol indicates impossible transition.

From\To	(0,0)	(0,1)	(0,2)	(1,0)	(1,1)	(1,2)	(2,0)	(2,1)	(2,2)
(0,0)	0	2.5	5.0	3.0	5.5	8.0	6.0	8.5	11.0
(0,1)	-	0	2.5	-	3.0	5.5	-	6.0	8.5
(0,2)	-	-	0	-	-	3.0	-	-	6.0
(1,0)	-	-	-	0	-	5.0	3.0	5.5	8.0
(1,1)	-	-	-	-	0	2.5	-	3.0	5.5
(1,2)	-	-	-	-	-	0	-	-	3.0
(2,0)	-	-	-	-	-	-	0	2.5	5.0
(2,1)	-	-	-	-	-	-	-	0	2.5
(2,2)	-	-	-	-	-	-	-	-	0

The optimal value function of the i^{th} state of stage k, denoted as state $X_{i,k}$, is defined, in a forward dynamic programming formulation, as the minimum value of the objective function $J(X_{i,k})$ (based on the definition above) that can be attained from the starting base case, at stage 0 to the current state $X_{i,k}$ and is denoted by $J^*(X_{i,k})$. A more convenient notation will be used for representing the states of this problem, as was also done earlier in the tables above. Each state will be denoted using a pair of numbers indicating the number of VAr modules at each one of the two locations. Therefore, the first (state 0) state of first stage is denoted as $X_{0,1} = (0,0)_1$. The transition from state to state is based on the recurrence relation:

$$J^*\left(X_{i,k+1}\right) = \min_j\left[J^*\left(X_{j,k}\right) + T(X_{j,k} \rightarrow X_{i,k+1})\right], \tag{9.37}$$

where $T(X_{j,k} \rightarrow X_{i,k+1})$ is the transition cost from state $X_{j,k}$ of stage *k*, to state $X_{i,k+1}$ of stage *k+1* and the minimization is performed over all possible states *j* of stage *k* that can transition to state *i* of stage *k+1*. This transition cost is computed based on the objective function and includes the performance functions of the new state, the operating cost of the new state, plus the installation cost of the additional VAr sources from one state to the other. Finally, the boundary condition for the dynamic programming recursion is that at the initial base case it holds that $J^*\left(X_{0,0}\right) = J\left(X_{0,0}\right)$. In this case it holds that $J^*\left(X_{0,0}\right) = J((0,0)_0) = 19.7384$ as it was computed in Table 9.21. This cost can also be set to zero, since it is a common part of all the subsequent states and stages and its absolute value is not of interest. The computations for each stage are described below. This approach is graphically illustrated in Figure 9.122. The optimal policy function p_k indicates the state of the previous stage, $k-1$, that is selected based on the recurrence relation and provides

the computed minimum value of the optimal value function. For the first stage this state is trivially the initial base case.

Stage 1

$J^*((0,0)_1) = 19.7384 + 19.8100 + 0.0 = 39.5484,\ p_1((0,0)_1) = (0,0)_0,$

$J^*((0,1)_1) = 19.7384 + 19.6251 + 3.5 = 42.8635, p_1((0,1)_1) = (0,0)_0,$

$J^*((0,2)_1) = 19.7384 + 19.5382 + 7.0 = 46.2766, p_1((0,2)_1) = (0,0)_0,$

$J^*((1,0)_1) = 19.7384 + 7.2130 + 4.0 = 30.9514, p_1((1,0)_1) = (0,0)_0,$

$J^*((1,1)_1) = 19.7384 + 6.9893 + 7.5 = 34.2277, p_1((1,1)_1) = (0,0)_0$

$J^*((1,2)_1) = 19.7384 + 6.9416 + 11.0 = 37.6800, p_1((1,2)_1) = (0,0)_0,$

$J^*((2,0)_1) = 19.7384 + 7.7697 + 8.0 = 35.5081, p_1((2,0)_1) = (0,0)_0$

$J^*((2,1)_1) = 19.7384 + 7.6000 + 11.5 = 38.8384, p_1((2,1)_1) = (0,0)_0,$

$J^*((2,2)_1) = 19.7384 + 7.6054 + 15.0 = 42.3438, p_1((2,2)_1) = (0,0)_0.$

Stage 2:

$J^*((0,0)_2) = J^*((0,0)_1) + J((0,0)_2) = 39.5484 + 19.8464 = 59.3948,$

$p_2((0,0)_2) = (0,0)_1,$

$J^*((0,1)_2) = \min\{39.5484 + 19.7435 + 3.25, 42.8635 + 19.7435 + 0\} =$

$\min\{62.5419,62.607\} = 62.5419,$

$p_2((0,1)_2) = (0,0)_1,$

$J^*((0,2)_2) = \min\{39.5484 + 19.6956 + 6.5, 42.8635 + 19.6956 + 3.25, 46.2766 +$

$19.6956 + 0\} = \min\{65.7440, 65.8091, 65.9722\} = 65.7440,$

$p_2((0,2)_2) = (0,0)_1,$

$J^*((1,0)_2) = \min\{39.5484 + 7.3244 + 3.75, 30.9514 + 7.3244 + 0\} =$

$\min\{50.6228, 38.2758\} = 38.2758,$

$p_2((1,0)_2) = (1,0)_1,$

$J^*((1,1)_2) = \min\{39.5484 + 7.1566 + 7.0, 42.8635 + 7.1566 + 3.75, 34.2277 +$

$7.1566 + 0\} = \min\{53.7050, 53.7701, 41.3843\} = 41.3843,$

$p_2((1,1)_2) = (1,1)_1,$

$J^*((1,2)_2) = \min\{39.5484 + 7.1537 + 10.25, 42.8635 + 7.1537 + 7.0, 46.2766 +$

$7.1537 + 3.75, 30.9514 + 7.1537 + 6.5, 34.2277 + 7.1537 + 3.25, 37.6800 +$

$7.1537 + 0\} = \min\{56.9521, 57.0172, 57.1803, 44.6051, 44.6314, 44.8337\} =$

$44.6051,$

$p_2((1,2)_2) = (1,0)_1,$

$J^*((2,0)_2) = \min\{39.5484 + 7.9369 + 7.5, 30.9514 + 7.9369 + 3.75, 35.5081 +$

$7.9369 + 0\} = \min\{54.9853, 42.6383, 43.4450\} = 42.6383,$

$p_2((2,0)_2) = (1,0)_1,$

$J^*((2,1)_2) = \min\{39.5484 + 7.8171 + 10.75, 42.8635 + 7.8171 + 7.5, 30.9514 +$

$7.8171 + 7.0, 34.2277 + 7.8171 + 3.75, 35.5081 + 7.8171 + 3.25, 38.8384 +$

$7.8171 + 0\} = \min\{58.1155, 61.4306, 45.7685, 45.7941, 46.5752, 46.6555\} =$

$45.7685,$

$p_2((2,1)_2) = (1,0)_1,$

$J^*((2,2)_2) = \min\{39.5484 + 7.8704 + 14, 42.8635 + 7.8704 + 10.75, 46.2766 + 7.8704 + 7.5, 30.9514 + 7.8704 + 10.25, 34.2277 + 7.8704 + 7.0, 37.6800 + 7.8704 + 3.75, 35.5081 + 7.8704 + 6.5, 38.8384 + 7.8704 + 3.25, 42.3438 + 7.8704 + 0\} = \min\{61.4188, 61.4839, 61.6470, 49.0718, 49.0981, 49.3004, 49.8785, 49.9588, 50.2142\} = 49.0718,$

$p_2((2,2)_2) = (1,0)_1.$

Stage 3:

$J^*((0,0)_3) = 59.3948 + 19.9049 = 79.2997,$

$p_3((0,0)_3) = (0,0)_2,$

$J^*((0,1)_3) = \min\{81.7677, 82.4148\} = 81.7677,$

$p_2((0,1)_3) = (0,0)_2,$

$J^*((0,2)_3) = \min\{84.2597, 84.9068, 85.6089\} = 84.2597,$

$p_2((0,2)_3) = (0,0)_2,$

$J^*((1,0)_3) = \min\{69.8586, 45.7396\} = 45.7396,$

$p_2((1,0)_3) = (1,0)_2,$

$J^*((1,1)_3) = \min\{72.2256, 72.8727, 48.7151\} = 48.7151,$

$p_2((1,1)_3) = (1,1)_2,$

$J^*((1,2)_3) = \min\{74.7717, 75.4188, 76.1209, 50.6527, 51.2612, 51.9820\} = 50.6527,$

$p_2((1,2)_3) = (1,0)_2,$

$J^*((2,0)_3) = \min\{73.5228, 49.4038, 50.7663\} = 49.4038,$

$p_2((2,0)_3) = (1,0)_2,$

$J^*((2,1)_3) = \min\{75.9400, 76.5871, 51.8210, 52.4295, 53.1835, 53.8137\} = 51.821,$

$p_2((2,1)_3) = (1,0)_2,$

$J^*((2,2)_3) =$

$\min\{78.5352, 79.1823, 79.8844, 54.4162, 55.0247, 55.7455, 55.7787, 56.4089, 57.2122\} =$

$54.4162,$

$p_2((2,2)_3) = (1,0)_2.$

Therefore, the computed path involves installing one 500-kVAr-module of reactive support at BUS07-L at the beginning of the first year. This configuration is kept unchanged until the end of the third year without adding any more support. For this simple system and for the defined criteria this is the optimal solution. However, this path might not be optimal, in general, because only a truncated search space was searched, utilizing sensitivity analysis. In this case the process moves to the next iterate and sensitivity analysis is used again chose locations assuming the states of the defined path (with the defined additions) as base case for each year. The process repeats until it converges to a single path.

Simulation of the system after the installation of reactive support confirms the improved behavior of the system. Simulation results for both steady-state and dynamic analysis are presented in Figure 9.123 and Figure 9.124 for the third-year configuration of the system with the VAr module addition. Only the most severe contingency, which is a three-phase fault on line BUS03-BUS04 close to BUS04 cleared by the removal of the

line, is simulated and presented. In steady-state the system behavior was acceptable even before the VAr source addition and remains within acceptable levels. There is, however, great improvement in terms of dynamic behavior, since now both system motors manage to recover within acceptable time after the fault removal.

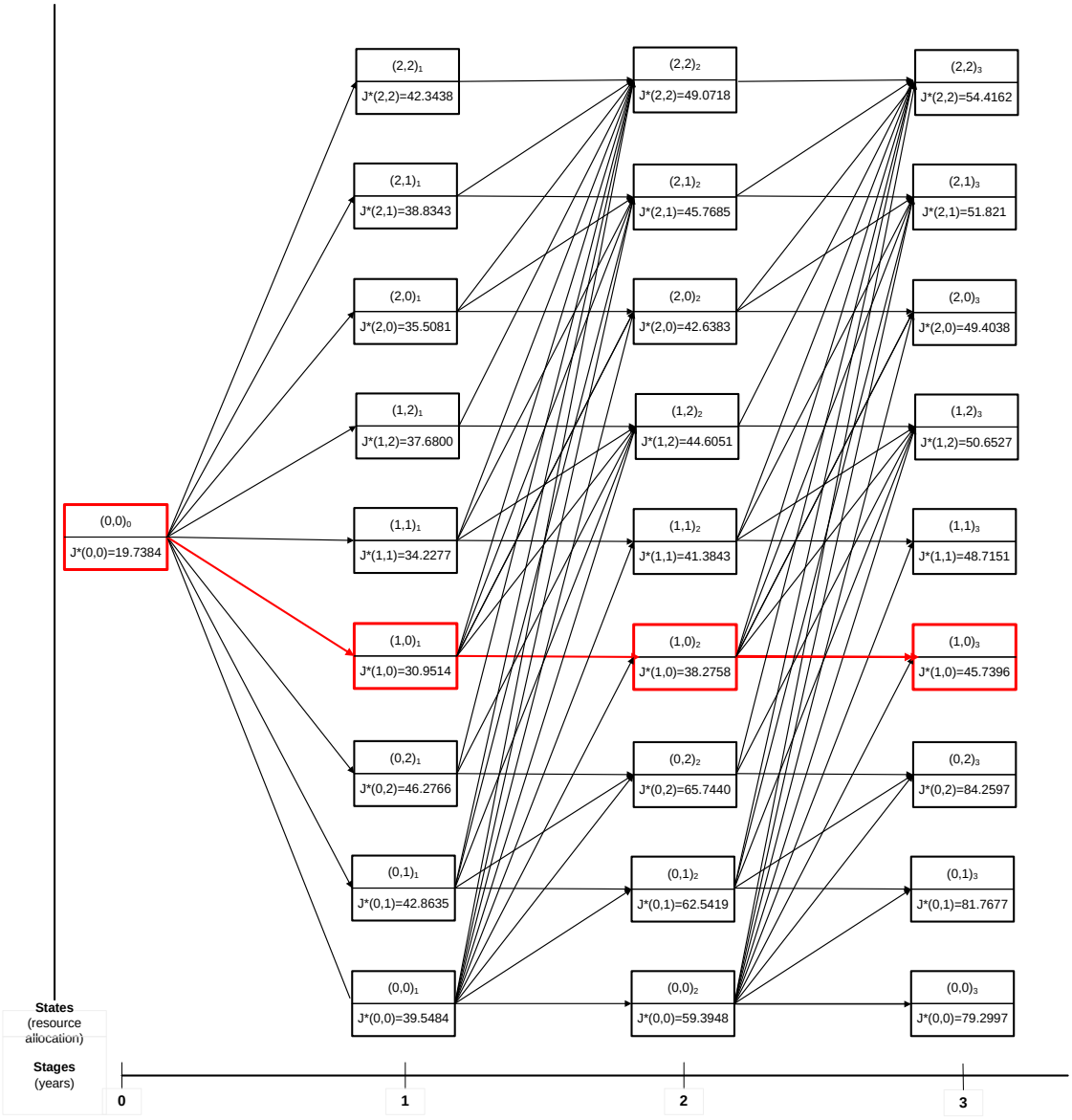

Figure 9.122: Illustration of dynamic programming solution.

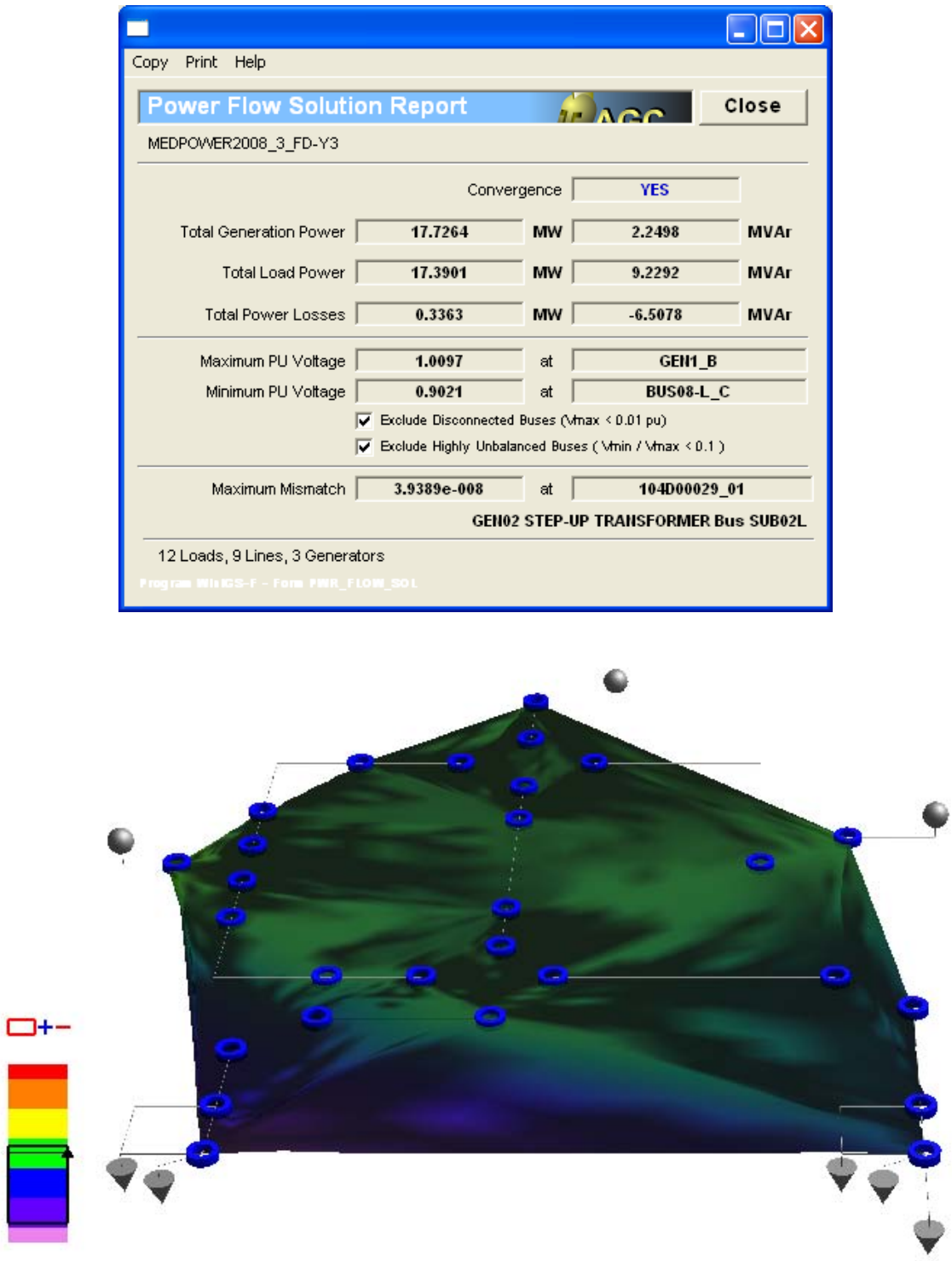

Figure 9.123: Steady-state system solution and voltage profile (positive sequence) after the installation of VAr support. Green indicates normal voltage within ±1.8%. Yellow, orange, and red indicate overvoltage up to 5.4%, up to 9%, and above 9% respectively. Blue, light blue, and purple indicate undervoltage down to 5.4%, 9%, and below 9% respectively.

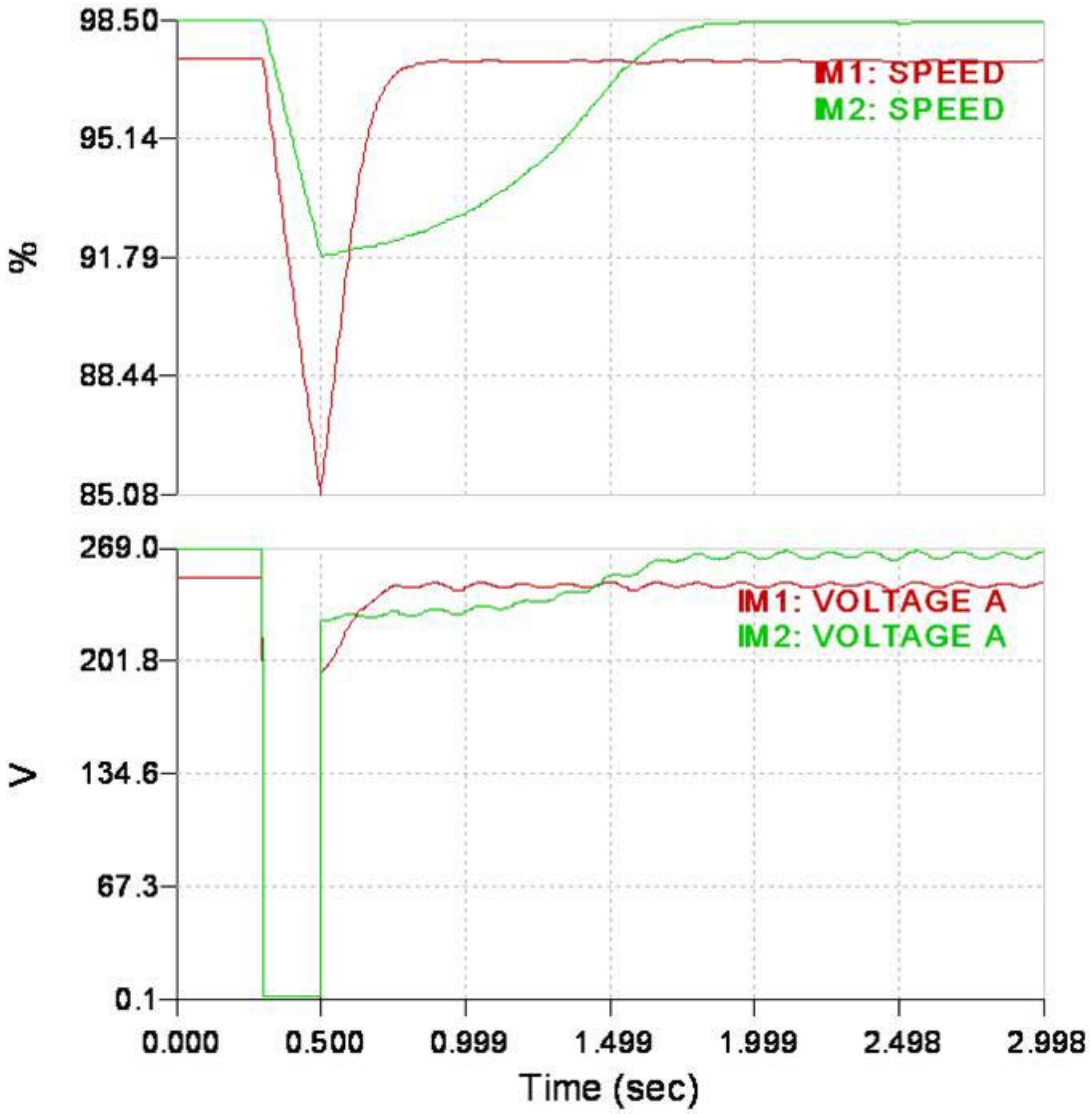

Figure 9.124: Induction motor speed and terminal voltage recover following a three-phase fault cleared by line removal after the installation of reactive support.

It should be mentioned, however, that the solution obtained is the most economical solution that achieves acceptable system behavior. That is, this is the minimum support that can be installed and the solution is greatly affected by the installation and operation cost. I was thus observed during the solution process that if the cost factor was not considered and only the system performance was of interest, while all the other problem parameters remained the same, the optimal solution at the end of the third year would be

to install 1000 kVAr (two modules) of support at BUS08-L and 500 kVAr (one module) at BUS07-L. This configuration provides the best system performance. This is illustrated for the third year and for the same contingency in Figure 9.125 and Figure 9.126.

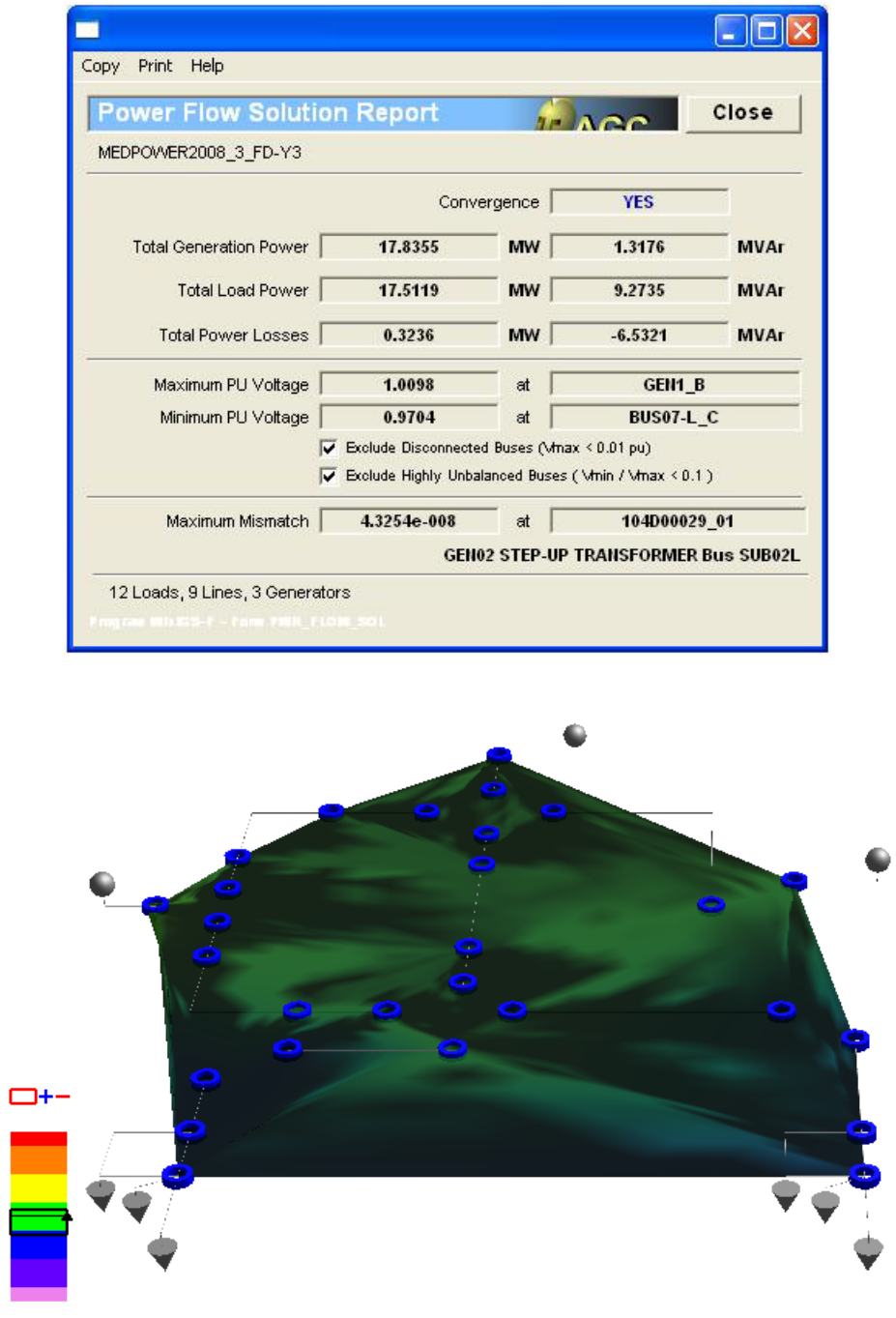

Figure 9.125: Steady-state system solution and voltage profile (positive sequence) after the installation of additional VAr support.

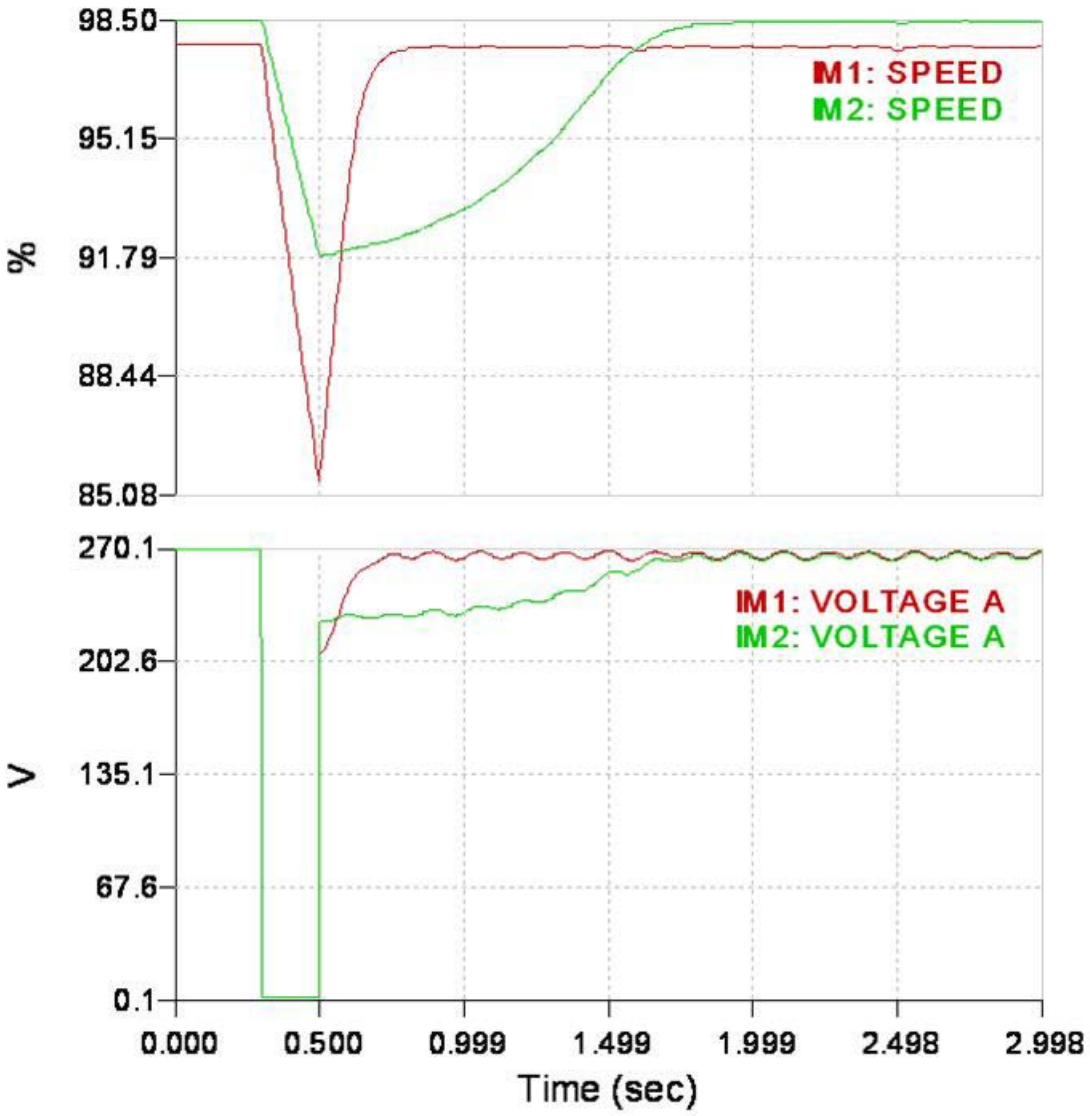

Figure 9.126: Induction motor speed and terminal voltage recover following a three-phase fault cleared by line removal after the installation of additional reactive support.

Note that in this case the steady-state voltage profile is improved and levelized and also the recovery rate after the clearance of the fault is much higher. However, although this solution achieved better performance, it is also much more expensive and therefore not optimal from an economical point of view based on the defined objectives.

9.6.3 Single-Stage Allocation Problem

This section presents a demonstrating example of the dynamic-programming-based methodology for resource allocation as described in section 7.4.4. The problem being considered is a static problem not requiring a sequence of decisions, but a single decision for the installation of N reactive support modules at P possible candidate locations. A simple example is presented to clearly demonstrate the approach step by step. The simple power system of Figure 9.77 is used again as test system. The steady-state and quasi-steady-state behavior of the system was analyzed in section 9.3. The system consists of a much higher number of distinct buses than can be seen from the diagram, since the configuration of each substation is also taken into account. In total, excluding the substation configurations, 18 main buses can be identified in the system. However, not all the buses are candidate locations for installation of reactive support. So, for example, it is not meaningful to consider the generating-unit substations as possible locations for VAr support additions.

The performance of each allocation configuration is evaluated based on static criteria only, since also only static resources are considered. Additional dynamic criteria and contingencies can also be included, as explain in Chapter 7 and demonstrated in the previous example; however, this example will be kept fairly simple. Therefore, only the voltage index, J_V, as defined in Chapter 6 and used extensively in this chapter, will be considered, and only the base case will be evaluated for each configuration. The exponent of the index is chosen to be two and all the buses of the system are considered with equal weight. Each state evaluation requires a load-flow solution and the computation of the performance index. The objective is to find the allocation that minimizes this

performance index. The base-case value of this index, for the original system without any VAr source additions has a computed value $J_{V,BaseCase} = 9.28549$. This value will be used to normalize all the subsequent values and the normalized value of the optimal value function, as defined in a following paragraph, will be used.

The best candidate locations are selected via sensitivity analysis, utilizing the above mentioned performance index. More specifically the sensitivity of the index with respect to VAr source addition at the specific location is computed for each system bus (excluding the generating unit and substation buses). The results are shown in Table 9.28.

Table 9.28: Sensitivity-based candidate location ranking for VAr source additions.

Ranking	Bus Name	Sensitivity
1	MOTOR1	-0.002200
2	MOTOR2	-0.001450
3	MOTOR3	-0.001290
4	D03-2	-0.001170
5	D03-1	-0.001120
6	D05-2	-0.001110
7	BUS03-T	-0.001080
8	D05-1	-0.000910
9	BUS05-T	-0.000730
10	D04	-0.000640
11	BUS04-T	-0.000530
12	BUS05	-0.000380
13	BUS04	-0.000350
14	BUS03	-0.000270

The ranking is performed based on the absolute value of the sensitivity. The negative sign comes from the fact that the performance index value decreases with the VAr source additions, indicating improvement on the system performance. Note that the most favorable locations are the terminal buses where the loads are connected. The top three locations are the induction motor buses. The performance index becomes less and less

sensitive to VAr additions when moving away from the load areas towards the bulk side of the system.

Thus, four candidate locations are identified utilizing the above analysis. All of them are at the distribution side of the system. Three of these locations are at the buses where the motor loads are connected, namely MOTOR1, MOTOR2, and MOTOR3 and the fourth one is the load bus D03-2. For this problem only static VAr source allocation will be considered, in the form of capacitor modules of 500 kVAr each. A single type of resource is considered for simplicity, although two types could also be considered (static and dynamic) could also be considered as described in section 7.4.4. Eight such modules are available, so the problem is to optimally allocate $N = 8$ units of resource to $P = 4$ candidate locations. The full enumeration approach would require 165 different combinations to be evaluated. The proposed dynamic programming approach requires 88 cases to be evaluated, roughly half compared to the full enumeration approach. The gain for this simple example is not that great, but the example is kept simple for demonstrating purposes. It was explained in section 7.4.4 that the gain is much greater as the problem size increases.

Therefore, following the approach of section 7.4.4, each stage of the problem represents a candidate location and each state is the remaining amount of VAr modules to be placed at this location, at the corresponding stage. Thus the problem is defined as a four-stage, eight-state (per stage) problem. The stage (location numbering) is as follows: 1. MOTOR1, 2. MOTOR2, 3. MOTOR3, and 4. D03-2. The optimal value function, denoted by $f_k(n)$ is defined as the minimum value of the defined objective function, J_V,

that can be obtained from locations k through $P = 4$, given n units of resource remaining to be allocated. Utilizing the principle of optimality the appropriate recurrence relation is

$$f_k(n) = \min_{n_k=0,1,\dots,n}[J([n_k|p_{k+1}(8-n_k)])] \,, \tag{9.38}$$

where n_k is the allocation to location k and $f_k(n)$ must be computed for $n = 0, \dots, 8$. $p_k(n)$ is the optimal policy function at stage k and state n, and the minimization term $J([n_k|p_{k+1}(8-n_k)])$ is the value of the objective function for the allocation n_k to location k, given that the optimal allocation policy will be applied from the next stage on. The answer to the problem is given by $f_1(8)$ and the optimal policy is $p_1(8)$. The boundary condition can be easily computed for stage 4, via load-flow, and are (normalized values, as explained earlier)

$f_4(0) = 1.0000$,

$f_4(1) = 0.9399$,

$f_4(2) = 0.8851$,

$f_4(3) = 0.8358$,

$f_4(4) = 0.7922$,

$f_4(5) = 0.7544$,

$f_4(6) = 0.7227$,

$f_4(7) = 0.6972$,

$f_4(8) = 0.6783$.

Using the recurrence relation (9.38) and the transition depicted in Figure 9.127 the following results are obtained:

Stage 3

$f_3(0) = 1.0000, p_3(0) = 0,$

$f_3(1) = \min\{0.9345, 0.9399\} = 0.9345$, $p_3(1) = 1,$

$f_3(2) = \min\{0.8767, 0.8753, 0.8851\} = 0.8753, p_3(2) = 1,$

$f_3(3) = \min\{0.8269, 0.8182, 0.8213, 0.8358\} = 0.8182, p_3(3) = 2,$

$f_3(4) = \min\{0.7857, 0.7693, 0.7651, 0.7728, 0.7922\} = 0.7651, p_3(4) = 2,$

$f_3(5) = \min\{0.7536, 0.7290, 0.7170, 0.7175, 0.7300, 0.7544\} = 0.7170, p_3(5) = 3,$

$f_3(6) = \min\{0.7312, 0.6978, 0.6776, 0.6703, 0.6756, 0.6931, 0.7227\} = 0.6703,$
$p_3(6) = 3,$

$f_3(7) = \min\{0.7191, 0.6763, 0.6473, 0.6318, 0.6293, 0.6395, 0.6623, 0.6972\} =$
$0.6293, p_3(7) = 3,$

$f_3(8) =$
$\min\{0.7180, 0.6652, 0.6268, 0.6024, 0.5916, 0.5941, 0.6096, 0.6377, 0.6783\} =$
$0.5916, p_3(8) = 4.$

Stage 2

$f_2(0) = 1.0000, p_2(0) = 0,$

$f_2(1) = \min\{0.9274, 0.9345\} = 0.9274, p_2(1) = 1,$

$f_2(2) = \min\{0.8664, 0.8632, 0.8753\} = 0.8632, p_2(2) = 1,$

$f_2(3) = \min\{0.8180, 0.8036\ 0.8048, 0.8182\} = 0.8036$, $p_2(3) = 2$,

$f_2(4) = \min\{0.7832, 0.7566, 0.7461, 0.7491, 0.7651\} = 0.7461$, $p_2(4) = 2$,

$f_2(5) = \min\{0.7631, 0.7233, 0.7000, 0.6918, 0.6969, 0.7170\} = 0.6918$, $p_2(5) = 2$,

$f_2(6) = \min\{0.7588, 0.7046, 0.6676, 0.6471, 0.6404, 0.6502, 0.6703\} = 0.6404$,

$p_2(6) = 2$,

$f_2(7) = \min\{0.7716, 0.7019, 0.6500, 0.6162, 0.5967, 0.5952, 0.6043, 0.6293\} =$

0.5952, $P_2(7) = 2$,

$f_2(8) =$

$\min\{0.8029, 0.7163, 0.6483, 0.6001, 0.5668, 0.5529, 0.5502, 0.5642, 0.5916\} =$

0.5502, $p_2(8) = 2$.

Stage 1

$f_1(8) = \min\{0.5523, 0.4813, 0.4516, 0.4264, 0.4159, 0.4329, 0.4552, 0.4995,$

$0.5502\} = 0.4159$, $p_1(8) = 4$.

(Since 8 resources are available at the beginning, the values of $f_1(7)$, $f_1(6)$, etc need not be computed.)

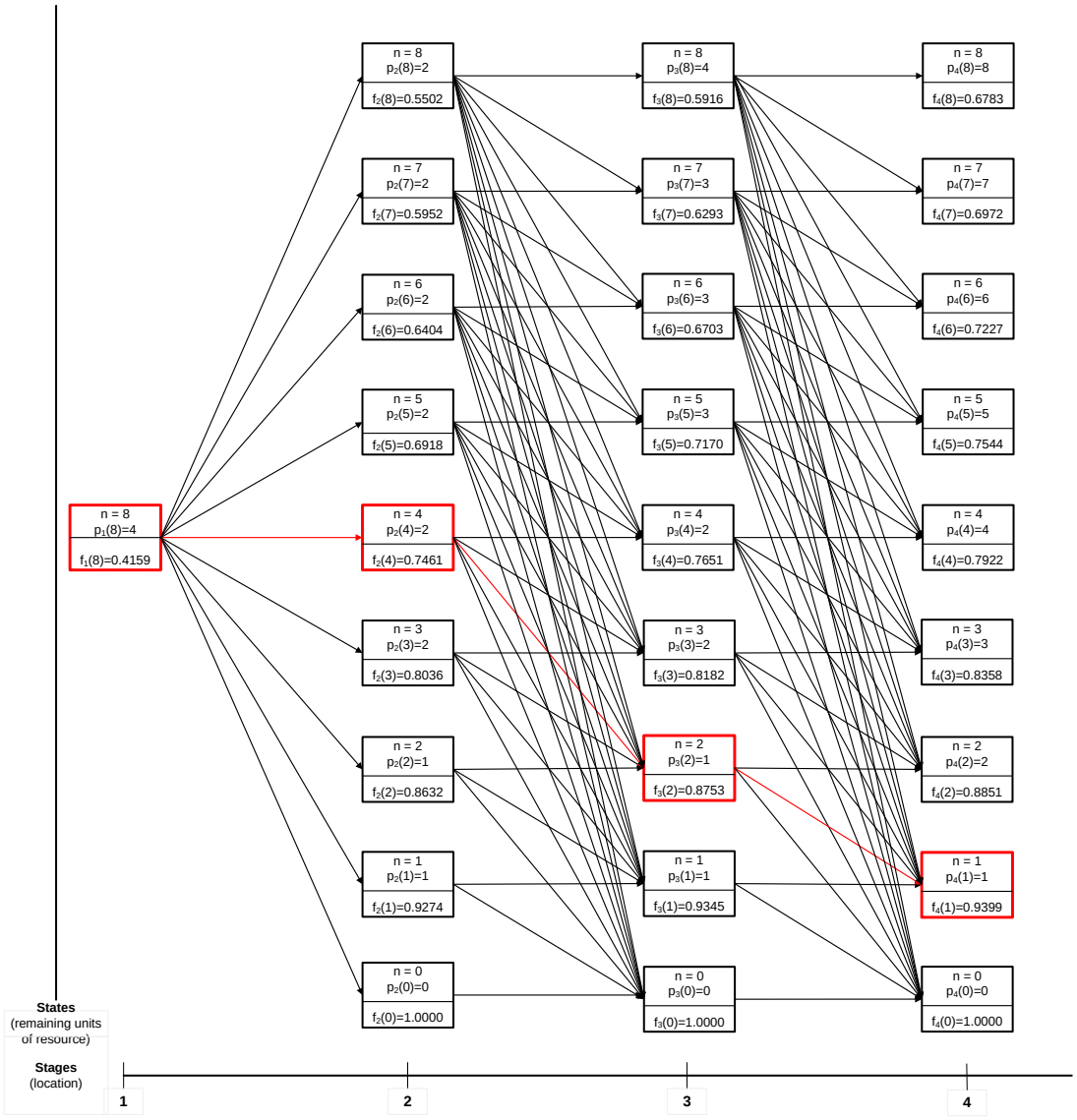

Figure 9.127: Graphic representation of the dynamic programming approach for the VAr resource allocation problem.

Therefore, the optimal solution involves installing 4 modules, i.e. 2 MVAr, of reactive support at the bus where motors 1 and 4 are connected. Then install two more modules, i.e. 1MVAr, of reactive support at the bus where motor 2 is connected. And finally installing one more module, 500 kVAr, at buses MOTOR3 and D03-2. This improves the voltage performance index by almost 60% by leveling the voltage profile of

the system. The new performance index value is 3.86188 and it's much less than half of the base-case value. The load flow solution of the system without reactive support was presented in section 9.3.2 at the beginning of this chapter. The provided reactive support significantly improves the system voltage profile, as illustrated in Figure 9.128 and Figure 9.129.

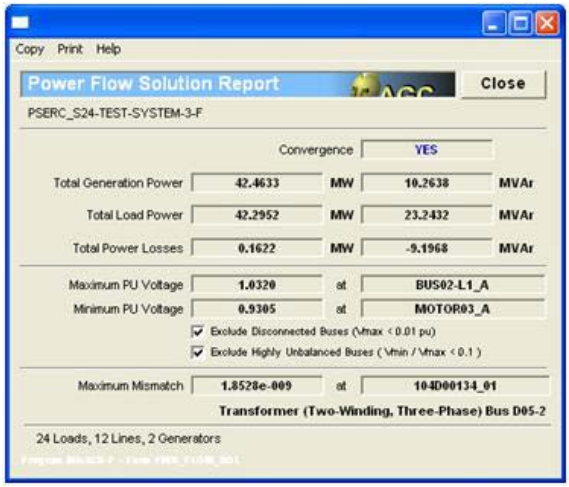

Figure 9.128: Steady-state solution report after the VAr module additions.

Bus Voltage – Min = 0.9305 p.u. Max = 1.0320 p.u.

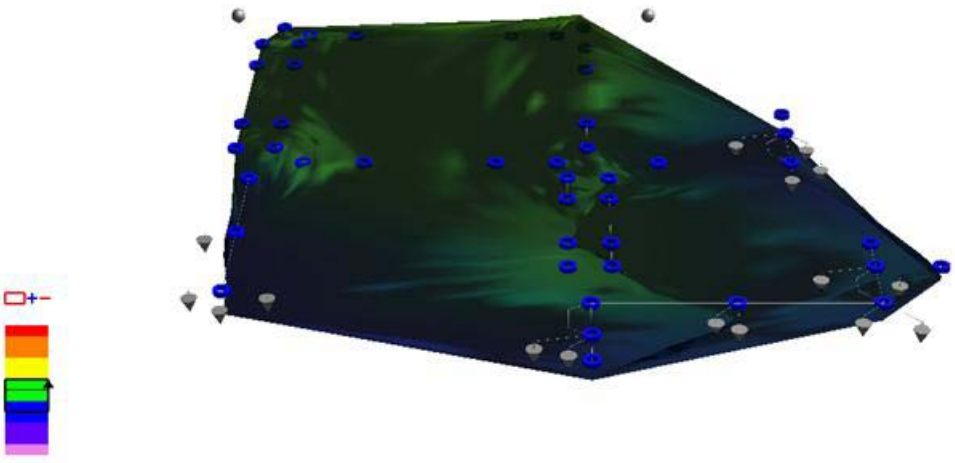

Figure 9.129: Surface plot of system voltage profile (positive sequence) after application of reactive support.

9.7 Summary

This chapter provided some illustrative examples to demonstrate the various methodologies developed in this work. Some simple cases were presented at the beginning, to clearly demonstrate the “quadratized” modeling approach and the utilization of the quadratic integration methodology for time-domain simulation. The performance of the proposed method was demonstrated in several cases and quantified both in terms of accuracy and computational efficiency. Next, some more complicated cases were considered including the simulation of voltage-recovery phenomena in transmission and distribution test systems. The phenomena were analyzed utilizing both the quasi-steady-state and the full-transient type of analysis. Then, in the following section, some examples of the contingency ranking algorithms were presented. Finally, some simple numerical examples were presented and thoroughly analyzed for the demonstration and explanation of the proposed procedure for the optimal allocation of reactive resources.

CHAPTER 10

CONCLUSIONS AND FUTURE RESEARCH DIRECTION

10.1 Conclusions

The work performed in this research was focused on power system modeling and analysis techniques and their application for the characterization of voltage-recovery phenomena in both transmission and distribution systems as well as the alleviation of problems related to such phenomena. The phenomena affecting voltage recovery are in general well known. Specifically, motor start-up or accelerating current and in-rush currents in transformers drastically affect the voltage recovery behavior of the system. Therefore, this work was focused on these issues. The approach followed was to develop and implement appropriate models and analysis methodologies that allow the simulation and analytical characterization of such events. Subsequently, a methodology was described for the mitigation of such phenomena by optimal allocation and operation of static and dynamic VAr resources over a planning horizon. This problem is solved with successive dynamic programming techniques with the following two innovations: (a) the states at each stage (candidate solutions) are obtained with static and dynamic (trajectory) sensitivity analysis and (b) each candidate solution is evaluated by considering the optimal operation of installed static and dynamic VAr sources utilizing concepts from the theory of applied optimal control and trajectory optimization.

In terms of power system modeling this research emphasized on developing and implementing appropriate mathematical models of the key system components, like

generating unit, transmission and distribution line, underground cable, transformer and load models, associated with voltage-recovery phenomena, capable of capturing the events of interest. More specifically the main part of the work concentrated on developing models of dynamic loads, saturable-core transformers, and dynamic VAr sources. The dynamic loads included three- and single-phase induction machines. The transformer models included single- and three-phase transformers with saturable-core reactors to model the transformer core. The dynamic VAr models included single- and three-phase static VAr systems (SVS) in the form of a thyristoc-controlled reactor (TCR) in parallel with a fixed capacitor (FC). Each of the developed models has been presented in detail in this dissertation, concentrating on both the theoretical model and on implementation issues and features of it.

In terms of analysis methodologies the study of only motor start-up currents and acceleration currents and their impact on voltage recovery requires a quasi-transient model, i.e., a model that considers the electromechanical transients, but neglects the fast electrical transients. Such a model only considers the essential slow dynamics of the load and assumes sinusoidal, quasi-steady-state conditions for the electrical network. Therefore, phasor representation is utilized for the electrical quantities and the changes in phasor magnitude and phase are only of interest. This was the primary type of analysis proposed and utilized in this work. However, the study of the simultaneous effect of motor start-up and acceleration currents and transformer in-rush current in distribution systems requires a more detailed, full transient model, i.e., a model that captures the electromechanical transients as well as the fast electrical transients. Such a model is also capable of capturing the waveform distortion from the sinusoidal form and the harmonic

pollution of the waveform due to the existing nonlinearities. The two analysis approaches, along with the steady-state analysis, have been presented and analyzed in detail in the dissertation. They are all based on the "quadratized" power system model described in detail in this work. In mathematical terms all three analysis approaches are essentially the same, once the differential equations of the dynamical models are converted to algebraic equations by application of some numerical integration rule. This work introduced a new numerical-integration methodology for power systems and dynamical systems in general, referred to as quadratic integration method.

Using the proposed modeling and analysis techniques, it was observed and verified that the dynamics of induction-motor loads are the primary cause of delayed voltage recovery. When a disturbance occurs in the system motors typically decelerate from their nominal or near-nominal operating point. Once the disturbance is removed and the system is restored motors tend to accelerate again. However, during the acceleration phase the current absorption of the motors increases tremendously compared to the normal operating current values. This current is primarily of reactive nature, meaning that the reactive power absorption of the motor increases substantially. This high reactive power demand results in a significant voltage drop at the motor terminals and, therefore, a significantly delayed voltage recovery. The main parameters affecting this phenomenon are the motor inertia and the motor design and electrical parameters, which determine the motor torque-slip, or torque-current characteristic. Some motor designs perform better compared to others in this respect. The amount and type of mechanical loading of the motor also plays a very important role. Motors operating under nearly constant-torque loading conditions are more affected by a prolonged voltage recovery period than motors

that operate under a speed-dependent loading mode. Stalling motors or motors that exhibit long recovery delays may also affect other nearby dynamic loads and cause additional motor stalling at nearby areas. It is also important to note that for motors that stall, the reactive power and the absorbed current remain to a high level compared to their nominal value during the whole recovery period and never come back to lower levels. The active power absorbed by such motor remains low, even lower than the nominal, and the motors cannot accelerate back to their nominal speed. Both single-phase and three-phase induction motors exhibit similar behavior. Three-phase motors are usually larger and of larger inertia and thus react more slowly and present a more stable behavior. Single-phase motors are usually smaller and demonstrate a very fast response time. They are, therefore, more likely to stall in case of prolonged voltage suppression and there are more likely to be affected by other nearby motors. It was also observed during the performed studies that voltage-recovery phenomena are in general very localized at specific areas or sections of the system. This means that, for example in a distribution system, even though the feeder may recover after a severe fault and the voltage at the beginning of the feeder may build back up to an acceptable level locally, at some section of the feeder the voltage may remain suppressed and there might be events like stalling motors isolated only at that particular area of the feeder.

Studies of voltage recovery phenomena were performed assuming both near-symmetric and balanced cases as well as completely unbalanced cases. Such cases were also including balanced three-phase faults or unbalanced two- and single-phase faults. In both situations the exhibited system behavior was similar. An interesting observation was that imbalances observed in the system operation and in particular in the induction motor

operation were amplified during the transient fault conditions and the transient recovery phase. Therefore, it was concluded that the behavior of dynamic loads may amplify imbalances in the system during transient operation.

Regarding the issue of in-rush currents in distribution systems the studies revealed that in-rush currents appear mainly during the energization phase of a system and in particular the energization of the transformers when core saturation is very profound. Such phenomena depend strongly on the moment of energization and they affect differently each phase of the system resulting in significantly unbalanced conditions. In-rush currents decay with time, but could last up to several seconds. The simulation studies considered cold-load pick-up, where induction motors were starting up along with the transformer energization. The combination of the motor start-up and transformer in-rush was of particular interest. During such conditions and depending on the saturation parameters and the energization time severe in-rush currents may flow in the network for up to a several second after the energization time. These current increase the harmonic pollution of the line currents in the network and result in significant waveform distortion. Such a harmonic signature is quite typical of saturation currents and this observation could be used to identify such conditions using estimation procedures.

Simulation of the combined motor start-up and in-rush phenomena using a full transient analysis provided results similar in nature to the results obtained using the quasi-steady-state model when only the motor transients were considered. This fact provided an insight on the close agreement of the two models and on the validity of using the simplified quasi-steady-state model under specific condition, when there is no need of

knowledge of the waveform distortion and of the harmonic pollution of the electrical system quantities.

Accurate modeling and simulation of voltage-recovery phenomena allows the development of mitigation methodologies by computing the optimal design of a voltage support system to alleviate the non-recoverable operating conditions. Specifically, voltage recovery can be assisted by dynamic VAr sources, such as generators, static VAr compensator, dynamic voltage restorers, etc. The algorithms can be structured to compute the optimal (minimal) amount of dynamic VAR sources (in addition to static sources such as capacitors) and how they should be placed in the system in order to make the system capable of recovery voltage with rates that will not cause any secondary effects such as relay operation. This problem is approached utilizing both static and dynamic sensitivity analysis techniques combined with a methodology based on successive dynamic programming for the optimal allocation and operation of static and dynamic VAr resources over the planning horizon.

The main contributions of this research work lie in the areas of power system modeling, power system simulation and analysis techniques, and decision making. Such contributions are both theoretical, introducing and validating some new concepts, and practical, addressing some more specific application and implementation issues.

More specifically, a new generalized framework was developed for power system modeling and simulation for steady-state, quasi-steady-state, and full transient analysis. The framework is based on the quadratic modeling of systems (both static and dynamic). Such a framework presents specific implementation advantages as well as improved computational efficiency for highly nonlinear systems. This approach was utilized to

develop and implement specific models of power system components and in particular dynamic load models that are essential for the study of voltage recovery phenomena. Implementation and simulation of such models clearly demonstrated the practicality of the proposed modeling approach as well as the advantages of this modeling framework.

Furthermore, a new numerical integration scheme was introduced in power system transient analysis. The method is based on the assumption that the system states vary quadraticaly within an integration time step and appears to be very promising presenting significant advantages compared to other numerical methods used in power system transient simulation.

Moreover, this work presented a new methodology for addressing the planning problem of optimal allocation of new static and dynamic reactive resources. The methodology is based on a successive dynamic programming technique. The proposed approach makes use of the notions of static and dynamic (trajectory) sensitivities, introducing also advances in the way of efficiently computing these sensitivities, especially for large-scale systems.

Finally, this work also introduced some basic concepts on the operational problem of optimal operation of existing static and dynamic reactive resources, utilizing concepts from the theory of applied optimal control and trajectory optimization.

10.2 Future Work

The present research work resulted in advanced modeling and simulation techniques for power-system analysis, both steady-state and dynamic and in application of these techniques for the development of a framework of studying voltage-recovery

phenomena. Furthermore, a methodology was proposed that selects the optimal mix of static and dynamic reactive power sources to meet specific design criteria. The design criteria ensure that there will be no load interruption by action of protective relaying due to voltage-recovery phenomena. The methodology uses dynamic load models, which are defined by physical considerations such as percentage of induction motor loads and percentage of other static and dynamic loads. In real time, the composition of the electric load model is determined by the actions of the customers. In addition the exact parameters of the dynamics of the loads may not be known. Considering these facts two important extensions of this work could be expected:

A first extension will be the ability to determine the dynamics of the electric load on-line. For this purpose, one can utilize waveform recordings of load response during a disturbance, for example a voltage dip. The recorded waveforms during a disturbance can be utilized to provide the parameter of the real-time dynamic-load model. The dynamic load models developed in this project could be utilized. The parameters of these models can be identified by fitting the recorded waveform data during the disturbance to the dynamic load model. This procedure will provide the parameters of a dynamic load model that best fits the actual response of the system. Since the present reality is that disturbance recorders and relays with oscillography are plentiful in a substation, the proposed approach could be implemented in real-time utilizing the existing infrastructure.

A second extension would be to further develop the prototype analysis software into production grade software capable of dealing with very large systems. As a first step will be the application of the methodology using the software on a very large system. The major task (and time consuming) will be the development of the model for such a system.

This application will provide a better feeling of performance and computational efficiency of the methodology. Considering the importance of the voltage-recovery phenomena, it appears that pursuing this goal would be worthwhile.

An important extension of the results obtained from the full time-domain transient analysis in distribution feeders would be the utilization of these results to identify the fault-induced delayed voltage recovery and to characterize the transients as stable or as non-recovery. This identification procedure is useful in protective relaying schemes. Specifically, the algorithms can be used to inhibit relay operation in cases of stable voltage recovery (even if it is delayed by the load dynamics) and to isolate the system partially in case of voltage collapse (non-recovery).

An evident further extension of the presented work lies in the area of the optimal operation of existing reactive support resources. This work laid the theoretical foundation for addressing this issue, however, did not proceed in the actual implementation of the proposed methodologies and algorithms and, therefore, did not address any practical implementation issues. Thus, this constitutes a clear future research direction.

Finally, a more thorough investigation of the proposed novel numerical integration scheme would also be of interest. This work presented the basic notion of the quadratic integration method and the main advantages and drawbacks the method possesses compared to other method and mainly compared to the trapezoidal integration rule. A more systematic theoretical presentation of the method and a more detailed comparison with other commonly used methods could be of interest, both on theoretical and practical basis.

APPENDIX A

DESCRIPTION AND IMPLEMENTATION OF DEVELOPED COMPONENT MODELS

A.1 Three-Phase Induction-Motor Model

A.1.1 Overview

This section of Appendix A describes the developed induction-machine model for three-phase network analysis. Models for steady-state, quasi-static, and full transient analysis are developed. One of the main features of this model is that it includes speed-dependent representation of the electric parameters of the rotor circuit. This feature is important since some motor types strongly demonstrate such behavior. The purpose of these models is to allow a more realistic and accurate, yet computationally simple, representation of the load in power system analysis.

A.1.2 Model Parameters and User Interface

This section presents the input parameters for defining the model of a three-phase induction motor as well as the user interface to define these parameters. The model input data include typical motor nominal (nameplate) data, plus electrical parameters, and mechanical load data. The user interface of the model is presented in Figure A.1 which also shows the model parameters. Figure A.2 presents the slip-torque characteristic of the motor of Figure A.1. The model supports three mechanical-loading modes: (a) constant torque, (b) constant slip, and (c) speed-dependent torque. In the later case the mechanical

torque can be either constant, or depend linearly or quadratically on the mechanical speed. The constant slip mode is only applicable to steady-state analysis.

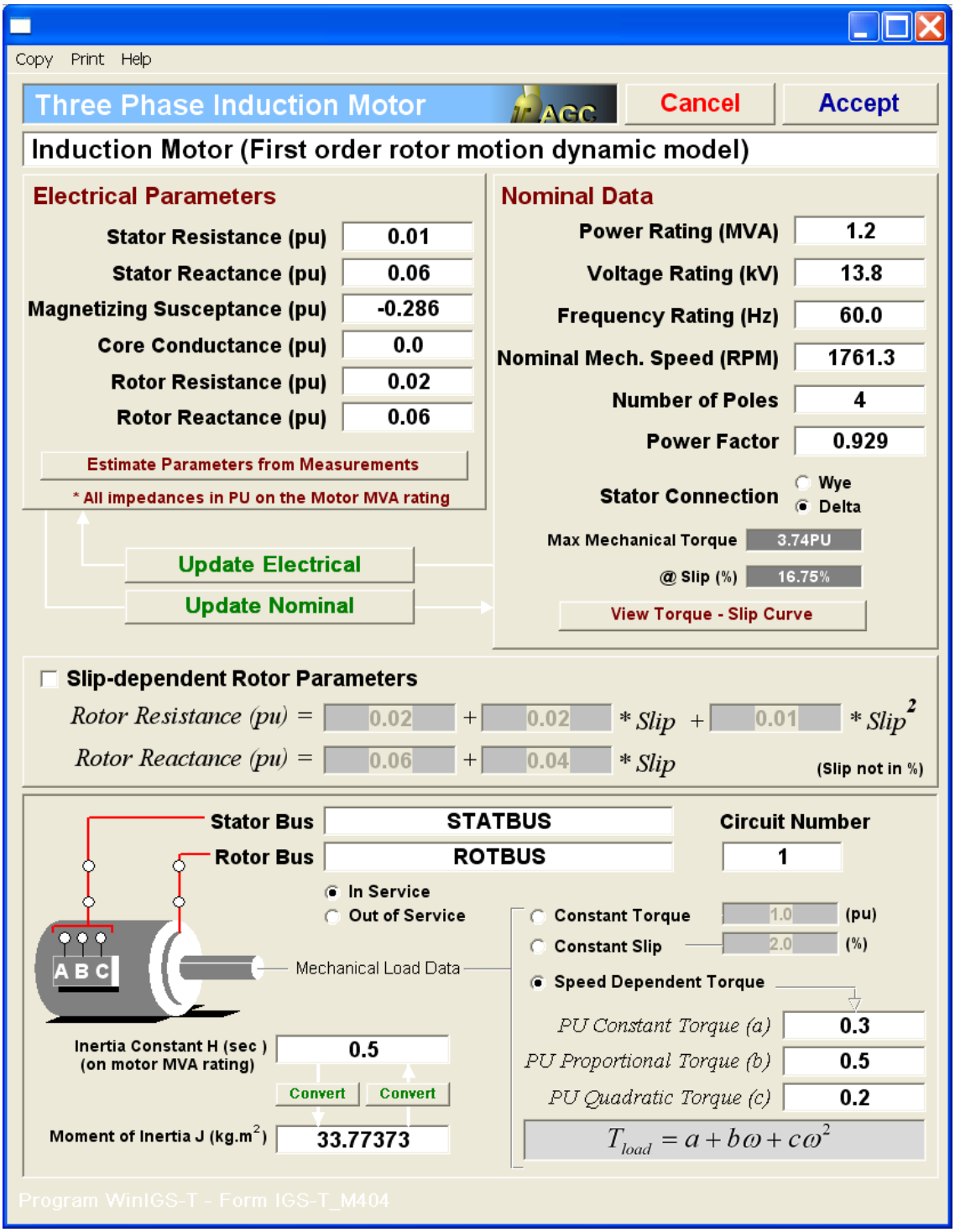

Figure A.1: Three-phase induction-motor parameters and user interface.

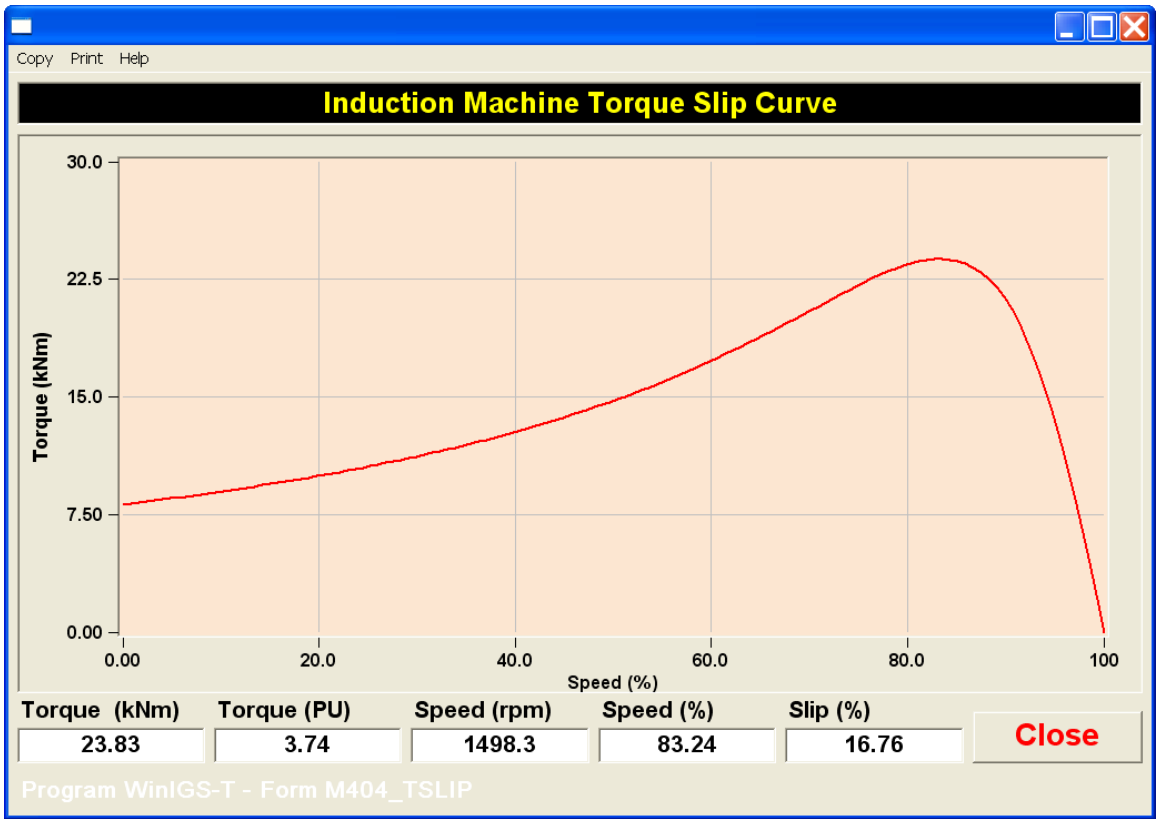

Figure A.2: Form of slip-torque characteristic of induction-motor model.

A.1.3 Steady-State Model

A.1.3.1 Compact Model

The compact model is based on the sequence equivalent circuits of an induction motor, illustrated in Figure A.3. This is an accurate way of modeling since the motor by construction is very symmetric, presenting little asymmetry. The circuit parameters include the stator resistant r_s, the stator reactance x_s, the rotor resistance r_r, the rotor reactance x_r, the core resistance r_m, the magnetizing reactance x_m, and the slip s.

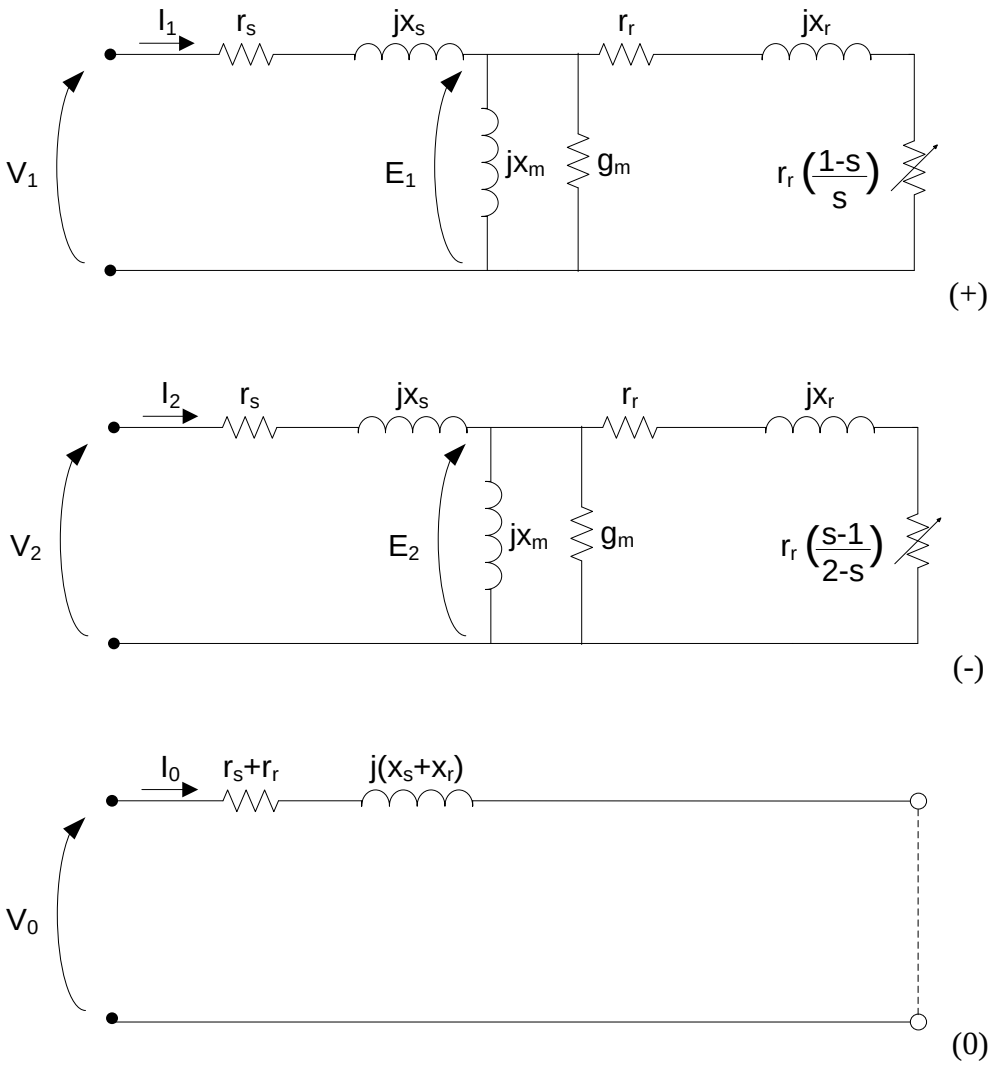

Figure A.3: Induction motor sequence networks.

Circuit analysis yields the following equations in complex form:

$$\tilde{I}_{abc} = T^{-1}\tilde{I}_{120}, \tag{A.1}$$

$$0 = \tilde{V}_{abc} - T^{-1}\tilde{V}_{120}, \tag{A.2}$$

$$0 = \tilde{I}_1 + (g_s + jb_s)\left(\tilde{E}_1 - \tilde{V}_1\right), \tag{A.3}$$

$$0 = \tilde{I}_2 + (g_s + jb_s)\left(\tilde{E}_2 - \tilde{V}_2\right), \tag{A.4}$$

$$0 = \tilde{I}_0 - (g_0 + jb_0)\tilde{V}_0, \tag{A.5}$$

$$0 = (g_m + jb_m)\tilde{E}_1 + \tilde{E}_1 \frac{s}{r_r + jx_r s} - (g_s + jb_s)\left(\tilde{V}_1 - \tilde{E}_1\right), \tag{A.6}$$

$$0 = (g_m + jb_m)\tilde{E}_2 + \tilde{E}_2 \frac{2-s}{r_r + jx_r(2-s)} - (g_s + jb_s)\left(\tilde{V}_2 - \tilde{E}_2\right), \tag{A.7}$$

where

$$T^{-1} = \begin{bmatrix} 1 & 1 & 1 \\ e^{j240^0} & e^{j120^0} & 1 \\ e^{j120^0} & e^{j240^0} & 1 \end{bmatrix}, \text{ with } e^{j\theta} = cos\theta + jsin\theta,$$

$$g_s + jb_s = \frac{1}{r_s + jx_s},$$

$$g_m + jb_m = \frac{1}{r_m + jx_m},$$

$$g_0 + jb_0 = \frac{1}{r_s + r_r + jx_s + jx_r} \qquad \text{for grounded Y, and 0 otherwise.}$$

If a neutral exists at the stator side (wye connection) the neutral voltage, $\tilde{V}_n$, is added as state, along with the equation

$$\tilde{I}_n = \tilde{I}_A + \tilde{I}_B + \tilde{I}_C = 3\tilde{I}_0 \,. \tag{A.8}$$

(a) Constant Slip Model (Linear)

No additional equations are needed and the above model is consistent.

(b) Torque Equilibrium Model (Nonlinear)

An additional equation links the electrical state variables to the mechanical torque. This equation is derived by equating the mechanical power (torque times mechanical frequency) to the power consumed by the variable resistors in the positive and negative circuits of Figure A.3.

$$0 = \left|\frac{\tilde{E}_1}{r_r + jx_r s}\right|^2 s r_r - \left|\frac{\tilde{E}_2}{r_r + jx_r(2-s)}\right|^2 (2-s) r_r - T_m \omega_s \tag{A.9}$$

and the slip, s, becomes a state variable.

If the mechanical torque is not constant, but depends on the speed (slip), the third operating mode of speed-dependent torque is defined which is similar to the torque equilibrium with the addition of equation (D-5), which creates a more general model.

$$0 = T_m - a - b\omega_s - c\omega_s^2 + (b\omega_s + 2c\omega_s^2)s - c\omega_s^2 s^2 \tag{A.10}$$

If the rotor model parameters depend on slip, as presented in Chapter 4, equations (A.1.11) are appended to the model and the rotor resistance and impedance become state variables.

$$\begin{aligned} r_r(s) &= \alpha + \beta s + \gamma s^2, \\ x_r(s) &= \delta + \varepsilon s. \end{aligned} \tag{A.11}$$

A.1.3.2 Equivalent Quadratic Model

The constant-slip model is linear and, thus, there is no need for model "quadratization." The torque-equilibrium model is a nonlinear model of high degree of nonlinearity. Therefore, the model is subsequently "quadratized" by the introduction of additional state variables. The case of the speed-dependent torque model with slip-dependent rotor parameters is shown here, which is the most complicated case. In order to "quadratize" the model equations, eight additional complex state variables are introduced, namely $\tilde{Y}_1$, $\tilde{Y}_2$, $\tilde{W}_1$, $\tilde{W}_2$, U_1, U_2, $\tilde{Z}_r$, and $\tilde{Z}_{rn}$ defined as follows:

$$\tilde{Y}_1 = \frac{1}{r_r + jx_r s},$$

$$\tilde{Y}_2 = \frac{1}{r_r + jx_r(2-s)},$$

$\widetilde{W}_1 = \tilde{Y}_1\tilde{E}_1$,

$\widetilde{W}_2 = \tilde{Y}_2\tilde{E}_2$,

$U_1 = \widetilde{W}_1\widetilde{W}_1^*$,

$U_2 = \widetilde{W}_2\widetilde{W}_2^*$,

$\tilde{Z}_r = r_r + jx_r$,

$\tilde{Z}_{rn} = s\tilde{Z}_r = r_r s + jx_r s$.

The model equations now become:

$$\tilde{I}_{abc} = T^{-1}\tilde{I}_{120}, \tag{A.12}$$

$$0 = -T_m\omega_s + U_1 s r_r - U_2(2-s)r_r, \tag{A.13}$$

$$0 = T_m - a - b\omega_s - c\omega_s^2 + (b\omega_s + 2\omega_s^2)s - \omega_s^2 s^2, \tag{A.14}$$

$$0 = \tilde{V}_{abc} - T^{-1}\tilde{V}_{120}, \tag{A.15}$$

$$0 = \tilde{I}_1 + (g_s + jb_s)(\tilde{E}_1 - \tilde{V}_1), \tag{A.16}$$

$$0 = \tilde{I}_2 + (g_s + jb_s)(\tilde{E}_2 - \tilde{V}_2), \tag{A.17}$$

$$0 = \tilde{I}_0 - (g_0 + jb_0)\tilde{V}_0, \tag{A.18}$$

$$0 = -(g_s + jb_s)\tilde{V}_1 + \big(g_s + g_m + j(b_s + b_m)\big)\tilde{E}_1 + \widetilde{W}_1 s, \tag{A.19}$$

$$0 = -(g_s + jb_s)\tilde{V}_2 + \big(g_s + g_m + j(b_s + b_m)\big)\tilde{E}_2 + \widetilde{W}_2(2-s), \tag{A.20}$$

$$0 = Re\{\tilde{Z}_r\}\tilde{Y}_1 + jIm\{\tilde{Z}_{rn}\}\tilde{Y}_1 - 1, \tag{A.21}$$

$$0 = Re\{\tilde{Z}_r\}\tilde{Y}_2 + j2Im\{\tilde{Z}_r\}\tilde{Y}_2 - jIm\{\tilde{Z}_{rn}\}\tilde{Y}_2 - 1, \tag{A.22}$$

$$0 = \widetilde{W}_1 - \tilde{Y}_1\tilde{E}_1, \tag{A.23}$$

$$0 = \widetilde{W}_2 - \tilde{Y}_2\tilde{E}_2, \tag{A.24}$$

$$0 = \widetilde{W}_1\widetilde{W}_1^* - U_1, \tag{A.25}$$

$$0 = \widetilde{W}_2\widetilde{W}_2^* - U_2, \tag{A.26}$$

$$0 = \tilde{Z}_r - \alpha - \beta s - \gamma s^2 - j\delta - j\varepsilon s, \tag{A.27}$$

$$0 = \tilde{Z}_{rn} - s\tilde{Z}_r\ . \tag{A.28}$$

The state vector is defined as

$$\tilde{X}^T = [\tilde{V}_a \quad \tilde{V}_b \quad \tilde{V}_c \quad s + jT_m \quad \tilde{V}_1 \quad \tilde{V}_2 \quad \tilde{V}_0 \quad \tilde{I}_1 \quad \tilde{I}_2 \quad \tilde{I}_0 \quad \tilde{E}_1 \quad \tilde{E}_2 \quad \tilde{Y}_1 \quad \tilde{Y}_2 \quad \widetilde{W}_1 \quad \widetilde{W}_2 \quad U_1 + jU_2 \quad \tilde{Z}_r \quad \tilde{Z}_{rn}]$$

The through-variable vector is

$$\tilde{I}^T = [\tilde{I}_a \quad \tilde{I}_b \quad \tilde{I}_c \quad 0 \quad 0 \quad 0 \quad 0 \quad 0 \quad 0 \quad 0 \quad 0 \quad 0 \quad 0 \quad 0 \quad 0 \quad 0 \quad 0 \quad 0 \quad 0]$$

By separating real and imaginary parts the model equations and state and through-variable vectors can be obtained in real form.

A.1.4 Quasi-Static Model

A.1.4.1 Compact Model

The compact model is based on the steady-state model with the addition of a dynamical equation describing the rotation of the rotor. The case of the speed-dependent torque model with slip-dependent rotor parameters is shown here, which is the most complicated case.

$$\tilde{I}_{abc} = T^{-1}\tilde{I}_{120}, \tag{A.29}$$

$$0 = \tilde{V}_{abc} - T^{-1}\tilde{V}_{120}, \tag{A.30}$$

$$0 = \tilde{I}_1 + (g_s + jb_s)(\tilde{E}_1 - \tilde{V}_1), \tag{A.31}$$

$$0 = \tilde{I}_2 + (g_s + jb_s)(\tilde{E}_2 - \tilde{V}_2), \tag{A.32}$$

$$0 = \tilde{I}_0 - (g_0 + jb_0)\tilde{V}_0, \tag{A.33}$$

$$0 = (g_m + jb_m)\tilde{E}_1 + \tilde{E}_1 \frac{s}{r_r + jx_r s} - (g_s + jb_s)\left(\tilde{V}_1 - \tilde{E}_1\right), \tag{A.34}$$

$$0 = (g_m + jb_m)\tilde{E}_2 + \tilde{E}_2 \frac{2-s}{r_r + jx_r(2-s)} - (g_s + jb_s)\left(\tilde{V}_2 - \tilde{E}_2\right), \tag{A.35}$$

$$0 = \left|\frac{\tilde{E}_1}{r_r + jx_r s}\right|^2 s r_r - \left|\frac{\tilde{E}_2}{r_r + jx_r(2-s)}\right|^2 (2-s) r_r - T_m \omega_s, \tag{A.36}$$

$$0 = T_L(t) - a - b\omega(t) - c\omega^2(t), \tag{A.37}$$

$$0 = \omega(t) + s\omega_s - \omega_s, \tag{A.38}$$

$$0 = r_r - \alpha - \beta s - \gamma s^2, \tag{A.39}$$

$$0 = x_r - \delta - \varepsilon s, \tag{A.40}$$

$$\frac{2H}{\omega_s}\frac{d\omega(t)}{dt} = T_{acc}(t) = T_{em}(t) - T_L(t). \tag{A.41}$$

A.1.4.2 Equivalent Quadratic Model

The same "quadratization" procedure as in the steady-state model is followed. The case of the speed-dependent torque model with slip-dependent rotor parameters is shown here, which is the most complicated case.

$$\tilde{I}_{abc} = T^{-1}\tilde{I}_{120}, \tag{A.42}$$

$$\frac{d\omega(t)}{dt} = \frac{\omega_s}{2H} T_{acc}(t), \tag{A.43}$$

$$0 = \omega(t) + s\omega_s - \omega_s, \tag{A.44}$$

$$0 = T_{acc}(t) - T_m(t) + T_L(t), \tag{A.45}$$

$$0 = -T_m\omega_s + U_1 s r_r - U_2(2-s)r_r, \tag{A.46}$$

$$0 = T_m - a - b\omega(\mathrm{t}) - c\omega^2(\mathrm{t}), \tag{A.47}$$

$$0 = \tilde{V}_{abc} - T^{-1}\tilde{V}_{120}, \tag{A.48}$$

$$0 = \tilde{I}_1 + (g_s + jb_s)(\tilde{E}_1 - \tilde{V}_1), \tag{A.49}$$

$$0 = \tilde{I}_2 + (g_s + jb_s)(\tilde{E}_2 - \tilde{V}_2), \tag{A.50}$$

$$0 = \tilde{I}_0 - (g_0 + jb_0)\tilde{V}_0, \tag{A.51}$$

$$0 = -(g_s + jb_s)\tilde{V}_1 + \big(g_s + g_m + j(b_s + b_m)\big)\tilde{E}_1 + \widetilde{W}_1 s, \tag{A.52}$$

$$0 = -(g_s + jb_s)\tilde{V}_2 + \big(g_s + g_m + j(b_s + b_m)\big)\tilde{E}_2 + \widetilde{W}_2(2-s), \tag{A.53}$$

$$0 = Re\{\tilde{Z}_r\}\tilde{Y}_1 + jIm\{\tilde{Z}_{rn}\}\tilde{Y}_1 - 1, \tag{A.54}$$

$$0 = Re\{\tilde{Z}_r\}\tilde{Y}_2 + j2Im\{\tilde{Z}_r\}\tilde{Y}_2 - jIm\{\tilde{Z}_{rn}\}\tilde{Y}_2 - 1, \tag{A.55}$$

$$0 = \widetilde{W}_1 - \tilde{Y}_1\tilde{E}_1, \tag{A.56}$$

$$0 = \widetilde{W}_2 - \tilde{Y}_2\tilde{E}_2, \tag{A.57}$$

$$0 = \widetilde{W}_1\widetilde{W}_1^* - U_1, \tag{A.58}$$

$$0 = \widetilde{W}_2\widetilde{W}_2^* - U_2, \tag{A.59}$$

$$0 = \tilde{Z}_r - \alpha - \beta s - \gamma s^2 - j\delta - j\varepsilon s, \tag{A.60}$$

$$0 = \tilde{Z}_{rn} - s\tilde{Z}_r. \tag{A.61}$$

By separating real and imaginary parts the model equations can be obtained in real form. Finally, the form of Figure A.4, shows an example of the motor operating state at steady-

state conditions. The form also depicts the actual slip-torque characteristic at the operating voltage level and the current operating point.

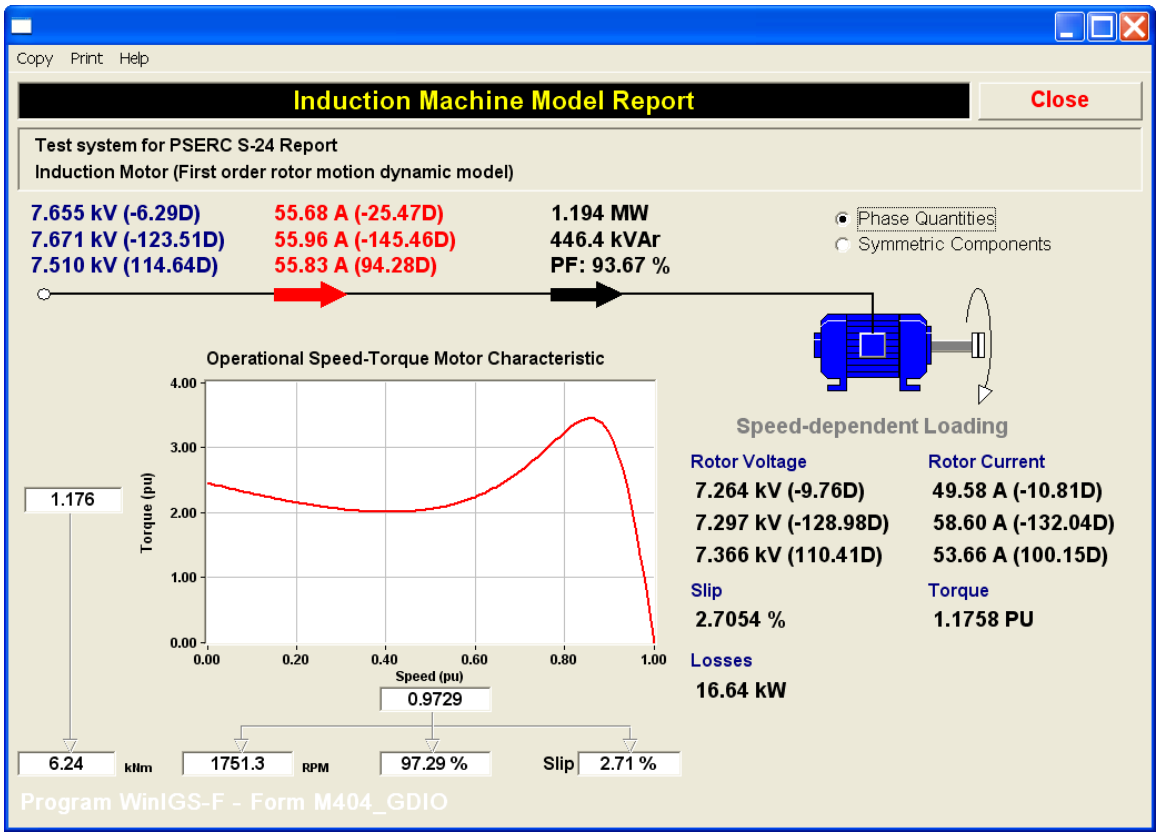

Figure A.4: Form of motor operating conditions at steady-state.

A.1.5 Full Transient Model

A.1.5.1 Compact Model

The compact model is based on representing an induction motor as a set of six mutually coupled windings, three for the phases of the stator and three for the rotor phases, as illustrated in Figure A.5.

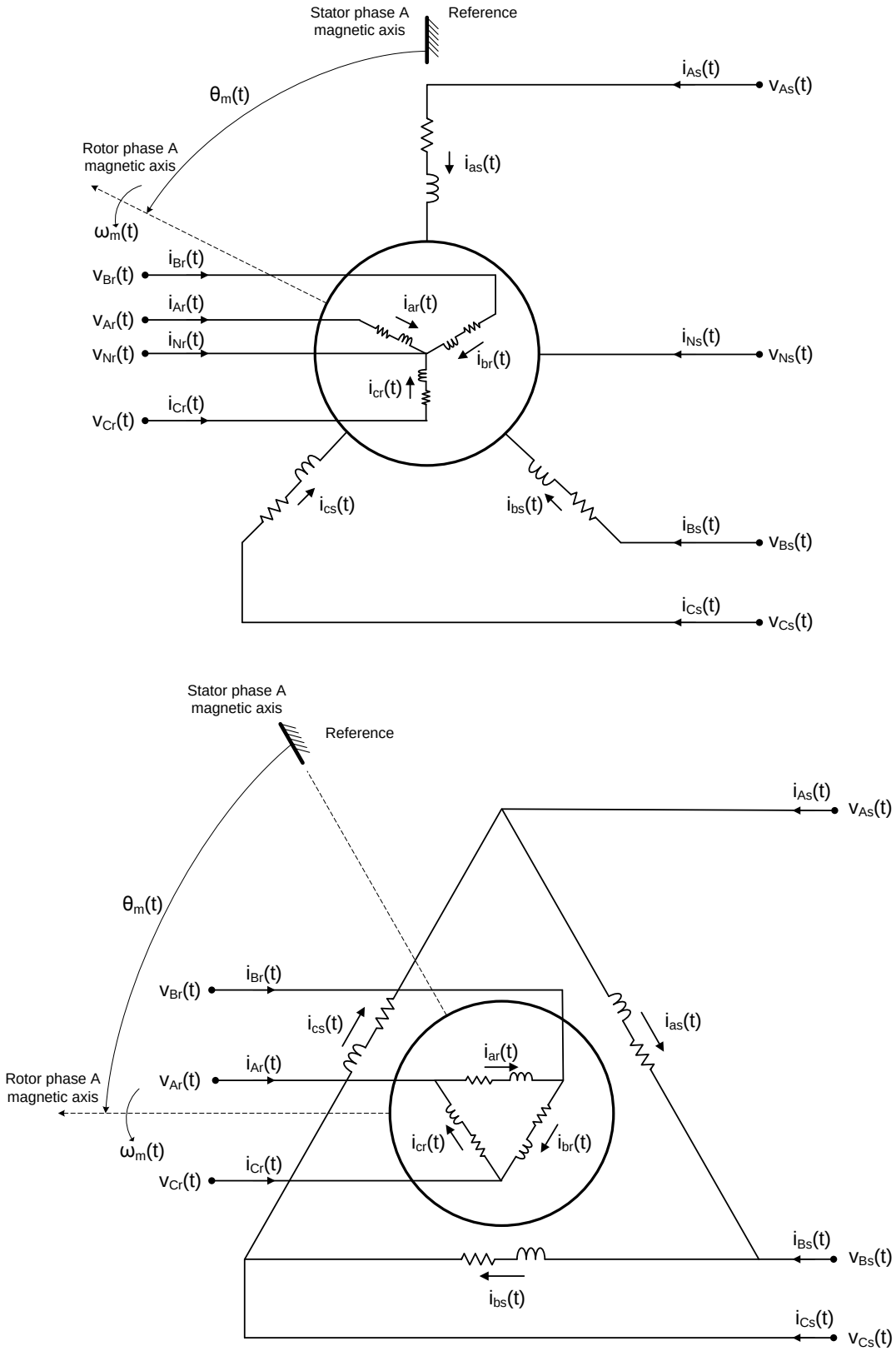

Figure A.5: Three-phase induction motor models for wye and delta connections.

The compact model of the motor is:

External equations:

$$i_{ABCN,s}(t) = E_1 i_{abc,s}(t), \tag{A.62}$$

$$i_{ABCN,r}(t) = E_2 i_{abc,r}(t). \tag{A.63}$$

Internal differential equations:

$$\frac{d\lambda_{as}(t)}{dt} = v_{as}(t) - r_s i_{as}(t), \tag{A.64}$$

$$\frac{d\lambda_{bs}(t)}{dt} = v_{bs}(t) - r_s i_{bs}(t), \tag{A.65}$$

$$\frac{d\lambda_{cs}(t)}{dt} = v_{cs}(t) - r_s i_{cs}(t), \tag{A.66}$$

$$\frac{d\lambda_{ar}(t)}{dt} = v_{ar}(t) - r_r i_{ar}(t), \tag{A.67}$$

$$\frac{d\lambda_{br}(t)}{dt} = v_{br}(t) - r_r i_{br}(t), \tag{A.68}$$

$$\frac{d\lambda_{cr}(t)}{dt} = v_{cr}(t) - r_r i_{cr}(t), \tag{A.69}$$

$$\frac{d\theta_m(t)}{dt} = \omega_m(t), \tag{A.70}$$

$$J\frac{d\omega_m(t)}{dt} = T_e(t) - T_L(t). \tag{A.71}$$

Internal algebraic equations:

$$0 = v_{abc,s}(t) - E_3 v_{ABCN,s}(t), \tag{A.72}$$

$$0 = v_{abc,r}(t) - E_4 v_{ABCN,r}(t), \tag{A.73}$$

$$0 = \lambda_{as}(t) - (L_{ls} + L_{ss}) i_{as}(t) - L_{sm} i_{bs}(t) - L_{sm} i_{cs}(t) - L_{sr}^{aa}(t) i_{ar}(t) - L_{sr}^{ab}(t) i_{br}(t) - L_{sr}^{ac}(t) i_{cr}(t), \tag{A.74}$$

$$0 = \lambda_{bs}(t) - L_{sm}i_{as}(t) - (L_{ls} + L_{ss})i_{bs}(t) - L_{sm}i_{cs}(t) - L_{sr}^{ba}(t)i_{ar}(t) - L_{sr}^{bb}(t)i_{br}(t) - L_{sr}^{bc}(t)i_{cr}(t), \quad \text{(A.75)}$$

$$0 = \lambda_{cs}(t) - L_{sm}i_{as}(t) - L_{sm}i_{bs}(t) - (L_{ls} + L_{ss})i_{cs}(t) - L_{sr}^{ca}(t)i_{ar}(t) - L_{sr}^{cb}(t)i_{br}(t) - L_{sr}^{cc}(t)i_{cr}(t), \quad \text{(A.75)}$$

$$0 = \lambda_{ar}(t) - L_{rs}^{aa}(t)i_{as}(t) - L_{rs}^{ab}i_{bs}(t) - L_{rs}^{ac}i_{cs}(t) - (L_{lr} + L_{rr})(t)i_{ar}(t) - L_{rm}(t)i_{br}(t) - L_{rm}(t)i_{cr}(t), \quad \text{(A.76)}$$

$$0 = \lambda_{br}(t) - L_{rs}^{ba}(t)i_{as}(t) - L_{rs}^{bb}i_{bs}(t) - L_{rs}^{bc}i_{cs}(t) - L_{rm}(t)i_{ar}(t) - (L_{lr} + L_{rr})(t)i_{br}(t) - L_{rm}(t)i_{cr}(t), \quad \text{(A.77)}$$

$$0 = \lambda_{cr}(t) - L_{rs}^{ca}(t)i_{as}(t) - L_{rs}^{cb}i_{bs}(t) - L_{rs}^{cc}i_{cs}(t) - L_{rm}(t)i_{ar}(t) - L_{rm}(t)i_{br}(t) - (L_{lr} + L_{rr})(t)i_{cr}(t), \quad \text{(A.78)}$$

$$L_{sr}^{abc}(t) = [L_{rs}^{abc}(t)]^T = L_{sr}\begin{bmatrix} cos\left(\frac{p}{2}\theta_m(t)\right) & cos\left(\frac{p}{2}\theta_m(t) + \frac{2\pi}{3}\right) & cos\left(\frac{p}{2}\theta_m(t) - \frac{2\pi}{3}\right) \\ cos\left(\frac{p}{2}\theta_m(t) - \frac{2\pi}{3}\right) & cos\left(\frac{p}{2}\theta_m(t)\right) & cos\left(\frac{p}{2}\theta_m(t) + \frac{2\pi}{3}\right) \\ cos\left(\frac{p}{2}\theta_m(t) + \frac{2\pi}{3}\right) & cos\left(\frac{p}{2}\theta_m(t) - \frac{2\pi}{3}\right) & cos\left(\frac{p}{2}\theta_m(t)\right) \end{bmatrix}, \quad \text{(A.79)}$$

$$T_e(t) = \frac{p}{2}\frac{1}{\sqrt{3}}(i_{as}(t)\lambda_{cs}(t) - i_{as}(t)\lambda_{bs}(t) + i_{bs}(t)\lambda_{as}(t) - i_{bs}(t)\lambda_{cs}(t) + i_{cs}(t)\lambda_{bs}(t) - i_{cs}(t)\lambda_{as}(t)), \quad \text{(A.80)}$$

$$T_L(t) = a + b\omega_m(t) + c\omega_m^2(t), \quad \text{(A.81)}$$

$$slip(t) = \frac{\omega_{m,s} - \omega_m(t)}{\omega_{m,s}}, \quad \text{(A.82)}$$

where the connectivity matrices are defined as

(a) wye connected motor

$$E_1 = \begin{bmatrix} 1 & 0 & 0 \\ 0 & 1 & 0 \\ 0 & 0 & 1 \\ 1 & 1 & 1 \end{bmatrix}, E_2 = \begin{bmatrix} 1 & 0 & 0 \\ 0 & 1 & 0 \\ 0 & 0 & 1 \\ 1 & 1 & 1 \end{bmatrix}, E_3 = \begin{bmatrix} 1 & 0 & 0 & -1 \\ 0 & 1 & 0 & -1 \\ 0 & 0 & 1 & -1 \end{bmatrix}, E_4 = \begin{bmatrix} 1 & 0 & 0 & -1 \\ 0 & 1 & 0 & -1 \\ 0 & 0 & 1 & -1 \end{bmatrix}$$

and

(b) delta connected motor

$$E_1 = \begin{bmatrix} 1 & 0 & -1 \\ -1 & 1 & 0 \\ 0 & -1 & 0 \\ 0 & 0 & 0 \end{bmatrix}, E_2 = \begin{bmatrix} 1 & 0 & -1 \\ -1 & 1 & 0 \\ 0 & -1 & 0 \\ 0 & 0 & 0 \end{bmatrix}, E_3 = \begin{bmatrix} 1 & -1 & 0 & 0 \\ 0 & 1 & -1 & 0 \\ -1 & 0 & 1 & 0 \end{bmatrix},$$

$$E_4 = \begin{bmatrix} 1 & -1 & 0 & 0 \\ 0 & 1 & -1 & 0 \\ -1 & 0 & 1 & 0 \end{bmatrix}.$$

The states are defined as follows:

$v_{As}(t)$: Stator terminal voltage, phase A;

$v_{Bs}(t)$: Stator terminal voltage, phase B;

$v_{Cs}(t)$: Stator terminal voltage, phase C;

$v_{Ns}(t)$: Stator terminal voltage, neutral; (wye connection only)

$v_{Ar}(t)$: Rotor terminal voltage, phase A;

$v_{Br}(t)$: Rotor terminal voltage, phase B;

$v_{Cr}(t)$: Rotor terminal voltage, phase C;

$v_{Nr}(t)$: Rotor terminal voltage, neutral; (wye connection only)

$\lambda_{as}(t)$: Stator winding A flux;

$\lambda_{bs}(t)$: Stator winding B flux;

$\lambda_{cs}(t)$: Stator winding C flux;

$\lambda_{ar}(t)$: Rotor winding A flux;

$\lambda_{br}(t)$: Rotor winding B flux;

$\lambda_{cr}(t)$: Rotor winding C flux;

$\theta_m(t)$: Rotor position angle, mechanical;

$\omega_m(t)$: Rotor mechanical speed;

$v_{as}(t)$: Stator winding A across voltage;

$v_{bs}(t)$: Stator winding B across voltage;

$v_{cs}(t)$: Stator winding C across voltage;

$v_{ar}(t)$: Rotor winding A across voltage;

$v_{br}(t)$: Rotor winding B across voltage;

$v_{cr}(t)$: Rotor winding C across voltage;

$i_{as}(t)$: Stator winding A current;

$i_{bs}(t)$: Stator winding B current;

$i_{cs}(t)$: Stator winding C current;

$i_{ar}(t)$: Rotor winding A current;

$i_{br}(t)$: Rotor winding B current;

$i_{cr}(t)$: Rotor winding C current;

$L_{sr}^{aa}(t)$: Stator-to-rotor mutual inductance, phase A-to-A;

$L_{sr}^{ab}(t)$: Stator-to-rotor mutual inductance, phase A-to-B;

$L_{sr}^{ac}(t)$: Stator-to-rotor mutual inductance, phase A-to-C;

$L_{sr}^{ba}(t)$: Stator-to-rotor mutual inductance, phase B-to-A;

$L_{sr}^{bb}(t)$: Stator-to-rotor mutual inductance, phase B-to-B;

$L_{sr}^{bc}(t)$: Stator-to-rotor mutual inductance, phase B-to-C;

$L_{sr}^{ca}(t)$: Stator-to-rotor mutual inductance, phase C-to-A;

$L_{sr}^{cb}(t)$: Stator-to-rotor mutual inductance, phase C-to-B;

$L_{sr}^{cc}(t)$: Stator-to-rotor mutual inductance, phase C-to-C;

$T_e(t)$: Motor electrical torque;

$T_L(t)$: Mechanical load torque;

$slip(t)$: Motor slip;

For the slip dependent rotor parameter case r_r and L_{lr} become states and the following equations are also added to the model:

$0 = r_r(t) - \alpha - \beta.slip(t) - \gamma.slip^2(t)$,

$0 = L_{lr}(t) - \frac{\delta}{\omega_s} - \frac{\varepsilon}{\omega_s} slip(t)$.

The model electrical parameters are related to the user-supplied parameters of the motor equivalent circuit (described in section 1) as follows:

r_s is provided directly by the user;

r_r is provided directly by the user;

$L_{ls} = \frac{x_s}{\omega_s}$, where x_s is the stator reactance provided by the user.

$L_{lr} = \frac{x_r}{\omega_s}$, where x_r is the stator reactance provided by the user.

$L_m = \frac{x_m}{\omega_s}$, where x_m is the magnetizing reactance provided by the user; in fact the user provides the core admittance value $G_m + jB_m = \frac{1}{r_m + jx_m}$.

$L_{ss} = \frac{2}{3} L_m$;

$L_{rr} = \frac{2}{3} L_m \left(\frac{N_r}{N_s}\right)$;

$L_{sr} = \frac{2}{3} L_m \left(\frac{N_r}{N_s}\right)$;

$L_{sm} = -\frac{1}{2} L_{ss}$;

$L_{rm} = -\frac{1}{2} L_{rr}$.

The ratio $\frac{N_r}{N_s}$ is the turns ratio between the rotor and stator windings, and is used if the values of L_{rr} and L_{sr} are referred to the rotor. Since in the analysis all the quantities are referred to the stator side this ratio is not used and is set to 1, therefore $L_{ss} = L_{rr} = L_{sr} = \frac{2}{3} L_m$.

A.1.5.2 Equivalent Quadratic Model

The compact model is subsequently "quadratized" so that it results to a model of at most quadratic equations, as described in Chapter 3.

External equations:

$$i_{ABCN,s}(t) = E_1 i_{abc,s}(t), \tag{A.83}$$

$$i_{ABCN,r}(t) = E_2 i_{abc,r}(t). \tag{A.84}$$

Internal differential equations:

$$\frac{d\lambda_{as}(t)}{dt} = e_{as}(t), \tag{A.85}$$

$$\frac{d\lambda_{bs}(t)}{dt} = e_{bs}(t), \tag{A.86}$$

$$\frac{d\lambda_{cs}(t)}{dt} = e_{cs}(t), \tag{A.87}$$

$$\frac{d\lambda_{ar}(t)}{dt} = e_{ar}(t), \tag{A.88}$$

$$\frac{d\lambda_{br}(t)}{dt} = e_{br}(t), \tag{A.89}$$

$$\frac{d\lambda_{cr}(t)}{dt} = e_{cr}(t), \tag{A.90}$$

$$\frac{d\theta_m(t)}{dt} = \omega_m(t), \tag{A.91}$$

$$J\frac{d\omega_m(t)}{dt} = T_{acc}(t), \tag{A.92}$$

$$\frac{ds(t)}{dt} = s\_dot(t), \tag{A.93}$$

$$\frac{dc(t)}{dt} = c\_dot(t). \tag{A.94}$$

Internal algebraic equations:

$$0 = v_{abc,s}(t) - E_3 v_{ABCN,s}(t), \tag{A.95}$$

$$0 = v_{abc,r}(t) - E_4 v_{ABCN,r}(t), \tag{A.96}$$

$$0 = e_{as}(t) - v_{as}(t) + r_s i_{as}(t), \tag{A.97}$$

$$0 = e_{bs}(t) - v_{bs}(t) + r_s i_{bs}(t), \tag{A.98}$$

$$0 = e_{cs}(t) - v_{cs}(t) + r_s i_{cs}(t), \tag{A.99}$$

$$0 = e_{ar}(t) - v_{ar}(t) + r_r i_{ar}(t), \tag{A.100}$$

$$0 = e_{br}(t) - v_{br}(t) + r_r i_{br}(t), \tag{A.101}$$

$$0 = e_{cr}(t) - v_{cr}(t) + r_r i_{cr}(t), \tag{A.102}$$

$$0 = L_{sr}^{aa}(t) - L_{sr}c(t), \tag{A.103}$$

$$0 = L_{sr}^{ab}(t) - L_{sr}\cos\left(\frac{2\pi}{3}\right)c(t) + L_{sr}\sin\left(\frac{2\pi}{3}\right)s(t), \tag{A.104}$$

$$0 = L_{sr}^{ac}(t) - L_{sr}\cos\left(\frac{2\pi}{3}\right)c(t) - L_{sr}\sin\left(\frac{2\pi}{3}\right)s(t), \tag{A.105}$$

$$0 = L_{sr}^{ba}(t) - L_{sr}^{ac}(t), \tag{A.106}$$

$$0 = L_{sr}^{bb}(t) - L_{sr}^{aa}(t), \tag{A.107}$$

$$0 = L_{sr}^{bc}(t) - L_{sr}^{ab}(t), \tag{A.108}$$

$$0 = L_{sr}^{ca}(t) - L_{sr}^{ab}(t), \tag{A.109}$$

$$0 = L_{sr}^{cb}(t) - L_{sr}^{ac}(t), \tag{A.110}$$

$$0 = L_{sr}^{cc}(t) - L_{sr}^{aa}(t), \tag{A.111}$$

$$0 = L_{rs}^{aa}(t) - L_{sr}^{aa}(t), \tag{A.112}$$

$$0 = L_{rs}^{ab}(t) - L_{sr}^{ba}(t), \tag{A.113}$$

$$0 = L_{rs}^{ac}(t) - L_{sr}^{ca}(t), \tag{A.114}$$

$$0 = L_{rs}^{ba}(t) - L_{sr}^{ab}(t), \tag{A.115}$$

$$0 = L_{rs}^{bb}(t) - L_{sr}^{bb}(t), \tag{A.116}$$

$$0 = L_{rs}^{bc}(t) - L_{sr}^{cb}(t), \tag{A.117}$$

$$0 = L_{rs}^{ca}(t) - L_{sr}^{ac}(t), \tag{A.118}$$

$$0 = L_{rs}^{cb}(t) - L_{sr}^{bc}(t), \tag{A.119}$$

$$0 = L_{rs}^{cc}(t) - L_{sr}^{cc}(t), \tag{A.120}$$

$$0 = T_{acc}(t) - T_e(t) + T_L(t), \tag{A.121}$$

$$0 = \omega_{m,s} slip(t) + \omega_m(t) - \omega_{m,s}, \quad \text{(A.122)}$$

$$0 = s\_dot(t) - \frac{p}{2} c(t)\omega_m(t), \quad \text{(A.123)}$$

$$0 = c\_dot(t) + \frac{p}{2} s(t)\omega_m(t), \quad \text{(A.124)}$$

$$0 = T_L(t) - a - b\omega_m(t) - c\omega_m^2(t), \quad \text{(A.125)}$$

$$0 = T_e(t) - \frac{p}{2}\frac{1}{\sqrt{3}}(i_{as}(t)\lambda_{cs}(t) - i_{as}(t)\lambda_{bs}(t) + i_{bs}(t)\lambda_{as}(t) - i_{bs}(t)\lambda_{cs}(t) + i_{cs}(t)\lambda_{bs}(t) - i_{cs}(t)\lambda_{as}(t)), \quad \text{(A.126)}$$

$$0 = \lambda_{as}(t) - (L_{ls} + L_{ss})i_{as}(t) - L_{sm}i_{bs}(t) - L_{sm}i_{cs}(t) - L_{sr}^{aa}(t)i_{ar}(t) - L_{sr}^{ab}(t)i_{br}(t) - L_{sr}^{ac}(t)i_{cr}(t), \quad \text{(A.127)}$$

$$0 = \lambda_{bs}(t) - L_{sm}i_{as}(t) - (L_{ls} + L_{ss})i_{bs}(t) - L_{sm}i_{cs}(t) - L_{sr}^{ba}(t)i_{ar}(t) - L_{sr}^{bb}(t)i_{br}(t) - L_{sr}^{bc}(t)i_{cr}(t), \quad \text{(A.128)}$$

$$0 = \lambda_{cs}(t) - L_{sm}i_{as}(t) - L_{sm}i_{bs}(t) - (L_{ls} + L_{ss})i_{cs}(t) - L_{sr}^{ca}(t)i_{ar}(t) - L_{sr}^{cb}(t)i_{br}(t) - L_{sr}^{cc}(t)i_{cr}(t), \quad \text{(A.129)}$$

$$0 = \lambda_{ar}(t) - L_{rs}^{aa}(t)i_{as}(t) - L_{rs}^{ab}i_{bs}(t) - L_{rs}^{ac}i_{cs}(t) - (L_{lr} + L_{rr})(t)i_{ar}(t) - L_{rm}(t)i_{br}(t) - L_{rm}(t)i_{cr}(t), \quad \text{(A.130)}$$

$$0 = \lambda_{br}(t) - L_{rs}^{ba}(t)i_{as}(t) - L_{rs}^{bb}i_{bs}(t) - L_{rs}^{bc}i_{cs}(t) - L_{rm}(t)i_{ar}(t) - (L_{lr} + L_{rr})(t)i_{br}(t) - L_{rm}(t)i_{cr}(t), \quad \text{(A.131)}$$

$$0 = \lambda_{cr}(t) - L_{rs}^{ca}(t)i_{as}(t) - L_{rs}^{cb}i_{bs}(t) - L_{rs}^{cc}i_{cs}(t) - L_{rm}(t)i_{ar}(t) - L_{rm}(t)i_{br}(t) - (L_{lr} + L_{rr})(t)i_{cr}(t), \quad \text{(A.132)}$$

where the connectivity matrices are defined as

(a) wye connected motor

$$E_1 = \begin{bmatrix} 1 & 0 & 0 \\ 0 & 1 & 0 \\ 0 & 0 & 1 \\ 1 & 1 & 1 \end{bmatrix}, E_2 = \begin{bmatrix} 1 & 0 & 0 \\ 0 & 1 & 0 \\ 0 & 0 & 1 \\ 1 & 1 & 1 \end{bmatrix}, E_3 = \begin{bmatrix} 1 & 0 & 0 & -1 \\ 0 & 1 & 0 & -1 \\ 0 & 0 & 1 & -1 \end{bmatrix}, E_4 = \begin{bmatrix} 1 & 0 & 0 & -1 \\ 0 & 1 & 0 & -1 \\ 0 & 0 & 1 & -1 \end{bmatrix}$$

and

(b) delta connected motor

$$E_1 = \begin{bmatrix} 1 & 0 & -1 \\ -1 & 1 & 0 \\ 0 & -1 & 0 \\ 0 & 0 & 0 \end{bmatrix}, E_2 = \begin{bmatrix} 1 & 0 & -1 \\ -1 & 1 & 0 \\ 0 & -1 & 0 \\ 0 & 0 & 0 \end{bmatrix}, E_3 = \begin{bmatrix} 1 & -1 & 0 & 0 \\ 0 & 1 & -1 & 0 \\ -1 & 0 & 1 & 0 \end{bmatrix},$$

$$E_4 = \begin{bmatrix} 1 & -1 & 0 & 0 \\ 0 & 1 & -1 & 0 \\ -1 & 0 & 1 & 0 \end{bmatrix}.$$

The states of the quadratic model are defined as follows:

$v_{As}(t)$: Stator terminal voltage, phase A;

$v_{Bs}(t)$: Stator terminal voltage, phase B;

$v_{Cs}(t)$: Stator terminal voltage, phase C;

$v_{Ns}(t)$: Stator terminal voltage, neutral; (wye connection only)

$v_{Ar}(t)$: Rotor terminal voltage, phase A;

$v_{Br}(t)$: Rotor terminal voltage, phase B;

$v_{Cr}(t)$: Rotor terminal voltage, phase C;

$v_{Nr}(t)$: Rotor terminal voltage, neutral; (wye connection only)

$\lambda_{as}(t)$: Stator winding A flux;

$\lambda_{bs}(t)$: Stator winding B flux;

$\lambda_{cs}(t)$: Stator winding C flux;

$\lambda_{ar}(t)$: Rotor winding A flux;

$\lambda_{br}(t)$: Rotor winding B flux;

$\lambda_{cr}(t)$: Rotor winding C flux;

$\theta_m(t)$: Rotor position angle, mechanical;

$\omega_m(t)$: Rotor mechanical speed;

$s(t)$: Sinus of electrical angle ($\frac{p}{2}\theta_m(t)$);

$c(t)$: Cosinus of electrical angle ($\frac{p}{2}\theta_m(t)$);

$v_{as}(t)$: Stator winding A across voltage;

$v_{bs}(t)$: Stator winding B across voltage;

$v_{cs}(t)$: Stator winding C across voltage;

$v_{ar}(t)$: Rotor winding A across voltage;

$v_{br}(t)$: Rotor winding B across voltage;

$v_{cr}(t)$: Rotor winding C across voltage;

$e_{as}(t)$: Stator winding A emf;

$e_{bs}(t)$: Stator winding B emf;

$e_{cs}(t)$: Stator winding C emf;

$e_{ar}(t)$: Rotor winding A emf;

$e_{br}(t)$: Rotor winding B emf;

$e_{cr}(t)$: Rotor winding C emf;

$L_{sr}^{aa}(t)$: Stator-to-rotor mutual inductance, phase A-to-A;

$L_{sr}^{ab}(t)$: Stator-to-rotor mutual inductance, phase A-to-B;

$L_{sr}^{ac}(t)$: Stator-to-rotor mutual inductance, phase A-to-C;

$L_{sr}^{ba}(t)$: Stator-to-rotor mutual inductance, phase B-to-A;

$L_{sr}^{bb}(t)$: Stator-to-rotor mutual inductance, phase B-to-B;

$L_{sr}^{bc}(t)$: Stator-to-rotor mutual inductance, phase B-to-C;

$L_{sr}^{ca}(t)$: Stator-to-rotor mutual inductance, phase C-to-A;

$L_{sr}^{cb}(t)$: Stator-to-rotor mutual inductance, phase C-to-B;

$L_{sr}^{cc}(t)$: Stator-to-rotor mutual inductance, phase C-to-C;

$L_{rs}^{aa}(t)$: Rotor-to-stator mutual inductance, phase A-to-A;

$L_{rs}^{ab}(t)$: Rotor-to-stator mutual inductance, phase A-to-B;

$L_{rs}^{ac}(t)$: Rotor-to-stator mutual inductance, phase A-to-C;

$L_{rs}^{ba}(t)$: Rotor-to-stator mutual inductance, phase B-to-A;

$L_{rs}^{bb}(t)$: Rotor-to-stator mutual inductance, phase B-to-B;

$L_{rs}^{bc}(t)$: Rotor-to-stator mutual inductance, phase B-to-C;

$L_{rs}^{ca}(t)$: Rotor-to-stator mutual inductance, phase C-to-A;

$L_{rs}^{cb}(t)$: Rotor-to-stator mutual inductance, phase C-to-B;

$L_{rs}^{cc}(t)$: Rotor-to-stator mutual inductance, phase C-to-C;

$T_{acc}(t)$: Accelerating torque;

$slip(t)$: Motor slip;

$s\_dot(t)$: Derivative of sin;

$c\_dot(t)$: Derivative of cos (rad/s);

$T_L(t)$: Mechanical load torque;

$T_e(t)$: Motor electrical torque;

$i_{as}(t)$: Stator winding A current;

$i_{bs}(t)$: Stator winding B current;

$i_{cs}(t)$: Stator winding C current;

$i_{ar}(t)$: Rotor winding A current;

$i_{br}(t)$: Rotor winding B current;

$i_{cr}(t)$: Rotor winding C current.

A.2 Single-Phase Induction-Motor Model

A.2.1 Overview

This section describes the single-phase induction machine model developed for three-phase network analysis. The motor can be connected either between a phase and neutral or between two phases of the system. One of the main features of this model is that it includes various starting modes of the single-phase motor and in particular split-phase, capacitor-start, permanent-split-capacitor, and capacitor-start, capacitor-run. Models for steady-state, quasi-static, and full transient analysis are developed. The purpose of this model is to allow a more realistic and accurate, yet computationally simple, representation of unbalanced loading condition in power system analysis, and especially in distribution networks. More particular this model is also used to represent large AC units connected to distribution feeders.

A.2.2 Model Parameters and User Interface

This section presents the input parameters for defining the model of the single-phase induction motor as well as the user interface to define these parameters.

The model input data include typical motor nominal (nameplate) data, plus electrical parameters, and mechanical load data. The model supports four mechanical-loading modes in steady state: (a) constant-torque, (b) constant-power, (c) constant-slip, and (d) speed-dependent-torque. For dynamic analysis the constant-power and constant-slip modes have no meaning and, therefore, only the constant-torque or slip-dependent-torque modes are used. The model also supports the options of including a running and a starting capacitor. The model incorporates four starting methods: (a) split-phase, (b) capacitor-start, (c) permanent-split-capacitor, and (d) capacitor-start, capacitor-run. The input data form is illustrated in Figure A.6.

The nominal slip-torque, slip-current, slip-power-factor, and slip-power curves can also be immediately plotted as illustrated in Figure A.7, for the motor of Figure A.6.

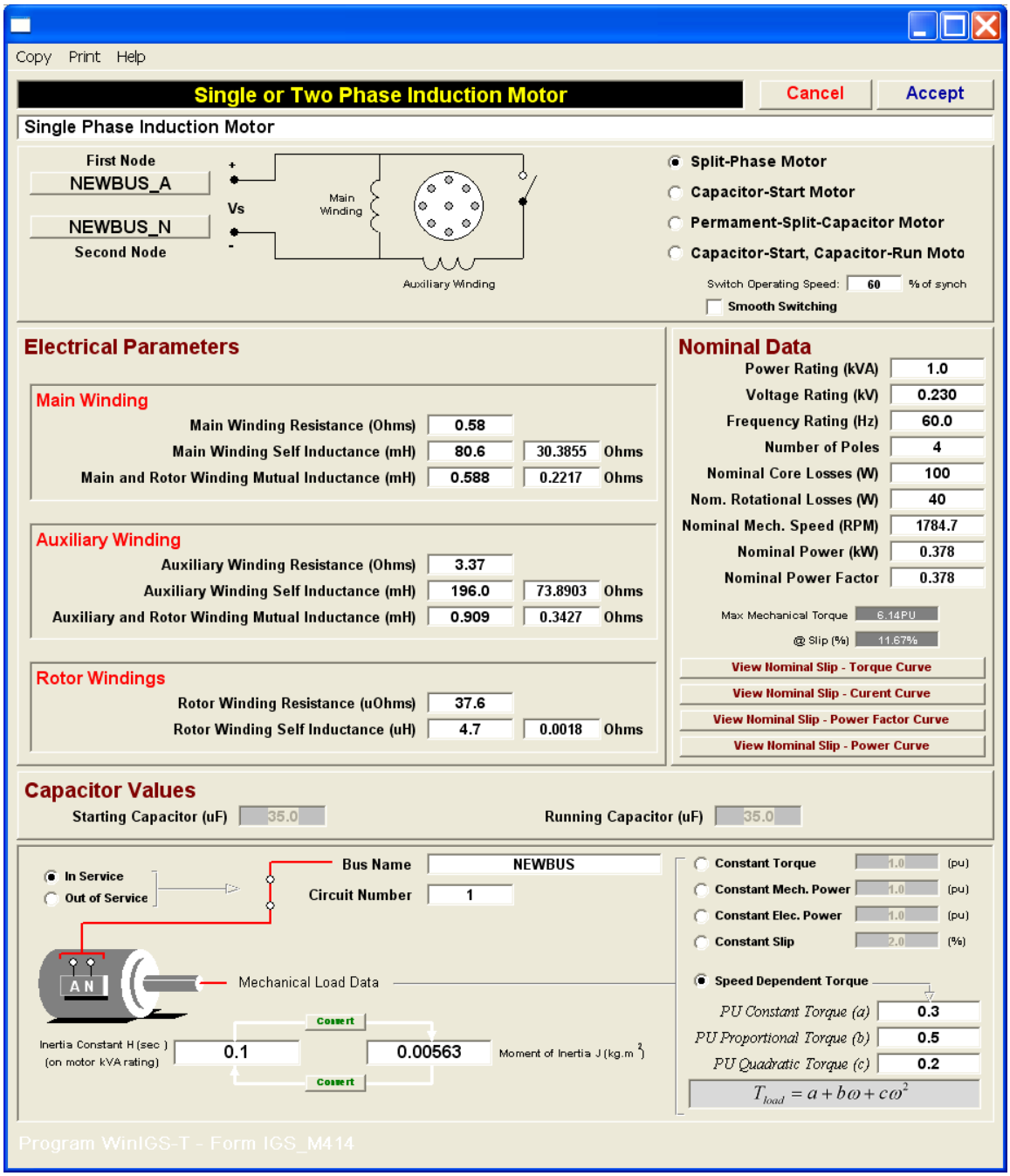

Figure A.6: Single-phase induction-motor parameters and user interface.

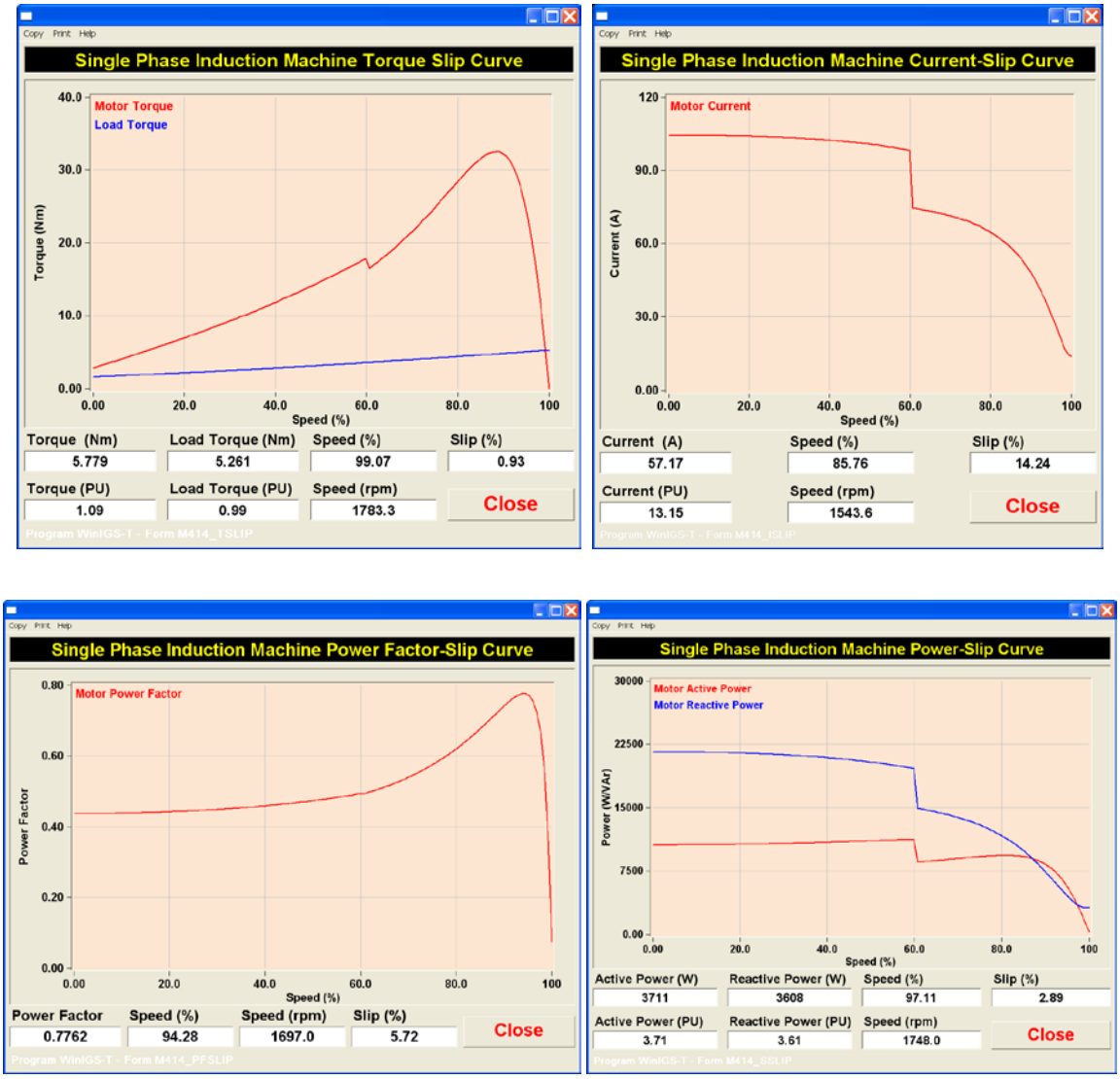

Figure A.7: Single-phase induction motor characteristics for motor of Figure A.6.

A.2.3 Steady-State Model

The model is based on the revolving field theory of a single phase induction motor. The physical circuit, is presented in Figure A.8, showing the case of both main and auxiliary windings and starting and running capacitors. The equations for simpler cases are simply derived by removing the elements (and thus equations and states) that are not present in each case. In the cases of split-phase, capacitor-start, and capacitor-start,

capacitor-run motors the corresponding models are switching models depending on the status of the starting switch illustrated in Figure A.8.

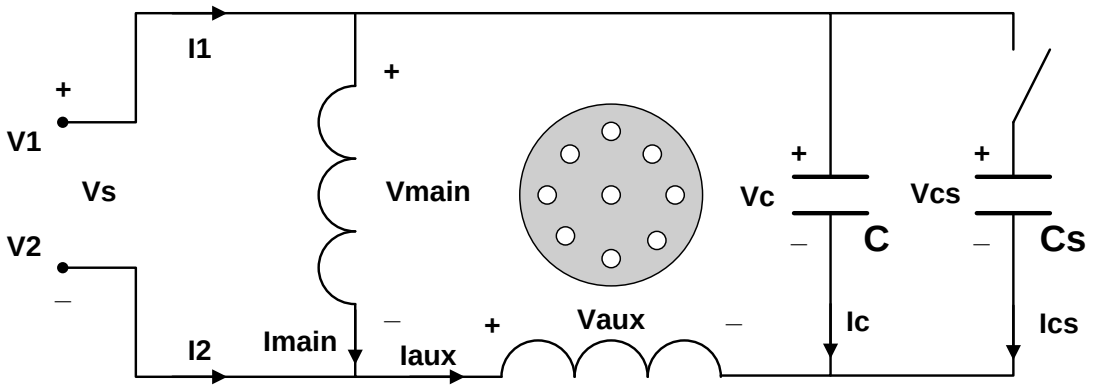

Figure A.8: Single-phase induction motor physical circuit.

Depending on the mechanical loading mode, circuit analysis yields the following equations, for the full case of a capacitor-start, capacitor-run motor:

$$\tilde{I}_1 = \tilde{I}_{main} + \tilde{I}_C + \tilde{I}_{CS} \,, \tag{A.133}$$

$$\tilde{I}_2 = -\tilde{I}_{main} - \tilde{I}_C - \tilde{I}_{CS} \,, \tag{A.134}$$

$$\tilde{V}_S = \tilde{V}_1 - \tilde{V}_2 \,, \tag{A.135}$$

$$\tilde{V}_{main} = \tilde{V}_S \,, \tag{A.136}$$

$$\tilde{V}_C = \tilde{V}_{main} + \tilde{V}_{aux} \,, \tag{A.137}$$

$$\tilde{I}_C = \frac{\tilde{V}_C}{j\omega_e C} \,. \tag{A.138}$$

Starting capacitor on:

$$\tilde{V}_{CS} = \tilde{V}_C \,, \tag{A.139}$$

$$\tilde{I}_{CS} = \frac{\tilde{V}_{CS}}{j\omega_e C_S} \,. \tag{A.140}$$

Starting capacitor off (normal operation):

$$\tilde{V}_{CS} = 0, \tag{A.141}$$

$$\tilde{I}_{CS} = 0\ . \tag{A.142}$$

$$\tilde{I}_C + \tilde{I}_{CS} + \tilde{I}_{aux} = 0\ , \tag{A.143}$$

$$\tilde{V}_{main} = \tilde{I}_{main}R_{main} + j\omega_e\tilde{\lambda}_{main}\ , \tag{A.144}$$

$$\tilde{V}_{aux} = \tilde{I}_{aux}R_{aux} + j\omega_e\tilde{\lambda}_{aux}\ , \tag{A.145}$$

$$\tilde{\lambda}_{main} = \left[L_{main} - jL_{main,r}^2\left(\widetilde{K}^+ + \widetilde{K}^-\right)\right]\tilde{I}_{main} + L_{main,r} + L_{main,r}L_{aux,r}\left(\widetilde{K}^+ - \widetilde{K}^-\right)\tilde{I}_{aux}\ , \tag{A.146}$$

$$\tilde{\lambda}_{aux} = -L_{main,r}L_{aux,r}\left(\widetilde{K}^+ - \widetilde{K}^-\right)\tilde{I}_{main} + \left[L_{aux} - jL_{aux,r}^2\left(\widetilde{K}^+ + \widetilde{K}^-\right)\right]\tilde{I}_{aux}\ , \tag{A.147}$$

$$\tilde{I}_{r1}^+ = \frac{-js\omega_e\left[L_{main,r}\tilde{I}_{main} + jL_{aux,r}\tilde{I}_{aux}\right]}{2(R_r + js\omega_e L_r)}\ , \tag{A.148}$$

$$\tilde{I}_{r1}^- = \frac{-j(2-s)\omega_e\left[L_{main,r}\tilde{I}_{main} - jL_{aux,r}\tilde{I}_{aux}\right]}{2(R_r + j(2-s)\omega_e L_r)}\ , \tag{A.149}$$

$$\tilde{I}_{r2}^+ = -j\tilde{I}_{r1}^+\ , \tag{A.150}$$

$$\tilde{I}_{r2}^- = j\tilde{I}_{r1}^-\ , \tag{A.151}$$

$$\widetilde{K}^+ = \frac{s\omega_e}{2(R_r + js\omega_e L_r)}\ , \tag{A.152}$$

$$\widetilde{K}^- = \frac{(2-s)\omega_e}{2(R_r + j(2-s)\omega_e L_r)}\ . \tag{A.153}$$

Constant-slip mode:

No additional equations.

Constant-torque mode:

$$T_e =$$

$$\left(\frac{poles}{2}\right) Re\{\left(L_{main,r}^2 \tilde{I}_{main} \tilde{I}_{main}^* + L_{aux,r}^2 \tilde{I}_{aux} \tilde{I}_{aux}^*\right)\left(\widetilde{K}^+ - \widetilde{K}^-\right)^* +$$

$$jL_{main,r} L_{aux,r} (\tilde{I}_{main}^* \tilde{I}_{aux} - \tilde{I}_{main} \tilde{I}_{aux}^*)\left(\widetilde{K}^+ + \widetilde{K}^-\right)\}\,, \tag{A.154}$$

$$T_e = T_m\,. \tag{A.155}$$

Constant-power mode:

$$T_e =$$

$$\left(\frac{poles}{2}\right) Re\{\left(L_{main,r}^2 \tilde{I}_{main} \tilde{I}_{main}^* + L_{aux,r}^2 \tilde{I}_{aux} \tilde{I}_{aux}^*\right)\left(\widetilde{K}^+ - \widetilde{K}^-\right)^* +$$

$$jL_{main,r} L_{aux,r} (\tilde{I}_{main}^* \tilde{I}_{aux} - \tilde{I}_{main} \tilde{I}_{aux}^*)\left(\widetilde{K}^+ + \widetilde{K}^-\right)\}\,, \tag{A.156}$$

$$P_e = T_e \omega_m + P_{rot.} + P_{core}\,, \tag{A.157}$$

$$P_e = P_{spec.}\,, \tag{A.158}$$

$$s = \frac{\omega_{sm} - \omega_m}{\omega_{sm}}\,. \tag{A.159}$$

Speed-dependent-torque mode:

$$T_e =$$

$$\left(\frac{poles}{2}\right) Re\{\left(L_{main,r}^2 \tilde{I}_{main} \tilde{I}_{main}^* + L_{aux,r}^2 \tilde{I}_{aux} \tilde{I}_{aux}^*\right)\left(\widetilde{K}^+ - \widetilde{K}^-\right)^* +$$

$$jL_{main,r} L_{aux,r} (\tilde{I}_{main}^* \tilde{I}_{aux} - \tilde{I}_{main} \tilde{I}_{aux}^*)\left(\widetilde{K}^+ + \widetilde{K}^-\right)\}\,, \tag{A.160}$$

$$T_m = a + b\omega_m + c\omega_m^2 \tag{A.161}$$

$$T_e = T_m\,, \tag{A.162}$$

$$s = \frac{\omega_{sm} - \omega_m}{\omega_{sm}}\,. \tag{A.163}$$

where

ω_e is the synchronous electrical angular velocity, in electrical rad/s,

ω_{sm} is the synchronous mechanical speed in rad/s,

ω_m is the motor mechanical speed in rad/s,

T_m is the specified constant mechanical torque,

$P_{spec.}$ is the specified constant power value.

A.2.4 Quasi-Static Model

The model is based on the frequency-domain model, presented in the previous section, with the addition of a dynamic equation to describe the rotor motion. An additional equation links the electrical state variables to the electrical torque produced by the motor, T_e. The mechanical-load torque, T_L, can be either constant or related to the motor speed, ω_m. This leads to two models based on the motor loading: (a) constant-torque model and (b) speed-dependent-torque model. Note that the second model can contain the first as a special case. The motor speed is linearly related to the slip, s. For the full case of a capacitor-start, capacitor-run motor, the model is:

$$\tilde{I}_1 = \tilde{I}_{main} + \tilde{I}_C + \tilde{I}_{CS} \,, \tag{A.164}$$

$$\tilde{I}_2 = -\tilde{I}_{main} - \tilde{I}_C - \tilde{I}_{CS} \,, \tag{A.165}$$

$$\tilde{V}_S = \tilde{V}_1 - \tilde{V}_2 \,, \tag{A.166}$$

$$\tilde{V}_{main} = \tilde{V}_S \,, \tag{A.167}$$

$$\tilde{V}_C = \tilde{V}_{main} + \tilde{V}_{aux} \,, \tag{A.168}$$

$$\tilde{I}_C = \frac{\tilde{V}_C}{j\omega_e C}\,. \tag{A.169}$$

Starting capacitor on:

$$\tilde{V}_{CS} = \tilde{V}_C\,, \tag{A.170}$$

$$\tilde{I}_{CS} = \frac{\tilde{V}_{CS}}{j\omega_e C_s}\,. \tag{A.171}$$

Starting capacitor off (normal operation):

$$\tilde{V}_{CS} = 0, \tag{A.172}$$

$$\tilde{I}_{CS} = 0\,. \tag{A.173}$$

$$\tilde{I}_C + \tilde{I}_{CS} + \tilde{I}_{aux} = 0\,, \tag{A.174}$$

$$\tilde{V}_{main} = \tilde{I}_{main}R_{main} + j\omega_e\tilde{\lambda}_{main}\,, \tag{A.175}$$

$$\tilde{V}_{aux} = \tilde{I}_{aux}R_{aux} + j\omega_e\tilde{\lambda}_{aux}\,, \tag{A.176}$$

$$\tilde{\lambda}_{main} = \left[L_{main} - jL_{main,r}^2\left(\widetilde{K}^+ + \widetilde{K}^-\right)\right]\tilde{I}_{main} + L_{main,r} + L_{main,r}L_{aux,r}\left(\widetilde{K}^+ - \widetilde{K}^-\right)\tilde{I}_{aux}\,, \tag{A.177}$$

$$\tilde{\lambda}_{aux} = -L_{main,r}L_{aux,r}\left(\widetilde{K}^+ - \widetilde{K}^-\right)\tilde{I}_{main} + \left[L_{aux} - jL_{aux,r}^2\left(\widetilde{K}^+ + \widetilde{K}^-\right)\right]\tilde{I}_{aux}\,, \tag{A.178}$$

$$\tilde{I}_{r1}^+ = \frac{-js\omega_e\left[L_{main,r}\tilde{I}_{main} + jL_{aux,r}\tilde{I}_{aux}\right]}{2(R_r + js\omega_e L_r)}\,, \tag{A.179}$$

$$\tilde{I}_{r1}^- = \frac{-j(2-s)\omega_e\left[L_{main,r}\tilde{I}_{main} - jL_{aux,r}\tilde{I}_{aux}\right]}{2(R_r + j(2-s)\omega_e L_r)}\,, \tag{A.180}$$

$$\tilde{I}_{r2}^+ = -j\tilde{I}_{r1}^+\,, \tag{A.181}$$

$$\tilde{I}_{r2}^- = j\tilde{I}_{r1}^-\,, \tag{A.182}$$

$$\widetilde{K}^{+} = \frac{s\omega_e}{2(R_r + js\omega_e L_r)}\,, \tag{A.183}$$

$$\widetilde{K}^{-} = \frac{(2-s)\omega_e}{2(R_r + j(2-s)\omega_e L_r)}\,. \tag{A.184}$$

Constant-torque mode:

$$s = \frac{\omega_{sm} - \omega_m}{\omega_{sm}}\,. \tag{A.185}$$

$$T_e(t) =$$

$$\left(\frac{poles}{2}\right) Re\{\left(L_{main,r}^2 \tilde{I}_{main}\tilde{I}_{main}^* + L_{aux,r}^2 \tilde{I}_{aux}\tilde{I}_{aux}^*\right)\left(\widetilde{K}^{+} - \widetilde{K}^{-}\right)^* +$$

$$jL_{main,r}L_{aux,r}(\tilde{I}_{main}^*\tilde{I}_{aux} - \tilde{I}_{main}\tilde{I}_{aux}^*)\left(\widetilde{K}^{+} + \widetilde{K}^{-}\right)\}\,, \tag{A.186}$$

$$T_{acc}(t) = T_e(t) - T_m\,, \tag{A.187}$$

$$\frac{d\omega_m(t)}{dt} = \frac{1}{J}T_{acc.}(t)\,. \tag{A.188}$$

Speed-dependent-torque mode:

$$s = \frac{\omega_{sm} - \omega_m}{\omega_{sm}}\,. \tag{A.189}$$

$$T_e =$$

$$\left(\frac{poles}{2}\right) Re\{\left(L_{main,r}^2 \tilde{I}_{main}\tilde{I}_{main}^* + L_{aux,r}^2 \tilde{I}_{aux}\tilde{I}_{aux}^*\right)\left(\widetilde{K}^{+} - \widetilde{K}^{-}\right)^* +$$

$$jL_{main,r}L_{aux,r}(\tilde{I}_{main}^*\tilde{I}_{aux} - \tilde{I}_{main}\tilde{I}_{aux}^*)\left(\widetilde{K}^{+} + \widetilde{K}^{-}\right)\}\,, \tag{A.190}$$

$$T_m(t) = a + b\omega_m(t) + c\omega_m^2(t) \tag{A.191}$$

$$T_{acc}(t) = T_e(t) - T_m(t)\,, \tag{A.192}$$

$$\frac{d\omega_m(t)}{dt} = \frac{1}{J}T_{acc.}(t)\,, \tag{A.193}$$

where

ω_e is the synchronous electrical angular velocity, in electrical rad/s,

ω_{sm} is the synchronous mechanical speed in rad/s,

ω_m is the motor mechanical speed in rad/s,

T_m is the specified constant mechanical torque.

A.2.5 Full Transient Model

The model is based on the time-domain analysis of the schematic diagram of Figure A.8. The rotor is represented by two perpendicular windings. The analysis below assumes that both main and auxiliary windings are present and also both starting and running capacitors are connected. The simpler cases are obtained by simply removing the equations of the components that are not present. An additional equation links the electrical state variables to the electrical torque produced by the motor, T_e. The mechanical load torque, T_L, can be either constant or related to the motor speed, ω_m. This leads to two models based on the motor loading: (a) constant-torque model and (b) speed-dependent-torque model. Note that the second model can contain the first as a special case. The motor speed is linearly related to the slip, s. The model is appended with an additional differential equation describing the motor rotor acceleration. Therefore, the model of the capacitor-start, capacitor run motor, with speed-dependent torque loading is:

External equations:

$$i_1(t) = i_{main}(t) - i_{aux}(t), \tag{A.194}$$

$$i_2(t) = -i_{main}(t) + i_{aux}(t). \tag{A.195}$$

Internal differential equations:

$$\frac{d\theta_m(t)}{dt} = \omega_m(t), \tag{A.196}$$

$$\frac{d\omega_m(t)}{dt} = \frac{1}{J} T_{acc}(t), \tag{A.197}$$

$$\frac{ds(t)}{dy} = s_{dot}(t), \tag{A.198}$$

$$\frac{dc(t)}{dt} = c_{dot}(t), \tag{A.199}$$

$$\frac{d\lambda_{main}(t)}{dt} = e_{main}(t), \tag{A.200}$$

$$\frac{d\lambda_{aux}(t)}{dt} = e_{aux}(t), \tag{A.201}$$

$$\frac{d\lambda_{r1}(t)}{dt} = e_{r1}(t), \tag{A.202}$$

$$\frac{d\lambda_{r2}(t)}{dt} = e_{r2}(t), \tag{A.203}$$

$$\frac{dv_C(t)}{dt} = \frac{1}{C} i_C(t), \tag{A.204}$$

$$\frac{dv_{Cs}(t)}{dt} = \frac{1}{Cs} i_{Cs}(t). \tag{A.205}$$

Internal linear algebraic equations:

$$0 = \theta_e(t) - \frac{p}{2} \theta_m(t), \tag{A.206}$$

$$0 = \omega_e(t) - \frac{p}{2} \omega_m(t), \tag{A.207}$$

$$0 = T_{acc}(t) - T_e(t) + T_m(t) + T_{rot}, \quad \text{(A.208)}$$

$$0 = e_{main}(t) - v_{main}(t) + R_{main} i_{main}(t), \quad \text{(A.209)}$$

$$0 = e_{aux}(t) - v_{aux}(t) + R_{aux} i_{aux}(t), \quad \text{(A.210)}$$

$$0 = e_{r1}(t) + R_r i_{r1}(t), \quad \text{(A.211)}$$

$$0 = e_{r2}(t) + R_r i_{r2}(t), \quad \text{(A.212)}$$

$$0 = v_{main}(t) - v_1(t) + v_2(t), \quad \text{(A.213)}$$

$$0 = v_{aux}(t) - v_C(t) + v_{main}(t), \quad \text{(A.214)}$$

$$0 = i_C(t) + i_{aux}(t) + i_{Cs}(t), \quad \text{(A.215)}$$

Starting capacitor is on:

$$0 = v_C(t) - v_{Cs}(t). \quad \text{(A.216)}$$

Starting capacitor is off:

$$0 = i_{Cs}(t). \quad \text{(A.217)}$$

$$0 = L_{main,r1}(t) - L_{mr} c(t), \quad \text{(A.218)}$$

$$0 = L_{main,r2}(t) + L_{mr} s(t), \quad \text{(A.219)}$$

$$0 = L_{aux,r1}(t) - L_{aux,r} s(t), \quad \text{(A.220)}$$

$$0 = L_{aux,r2}(t) - L_{aux,r} c(t). \quad \text{(A.221)}$$

Internal quadratic algebraic equations:

$$0 = T_m(t) - a - b\omega_m(t) - c\omega_m^2(t), \quad \text{(A.222)}$$

$$0 = T_e(t) - L_{main,r2}(t)i_{mr1}(t) + L_{main,r1}(t)i_{mr2}(t) - L_{aux,r2}(t)i_{ar1}(t) + L_{aux,r1}(t)i_{ar2}(t), \quad \text{(A.223)}$$

$$0 = i_{mr1}(t) - i_{main}(t)i_{r1}(t), \quad \text{(A.224)}$$

$$0 = i_{mr2}(t) - i_{main}(t)i_{r2}(t), \quad \text{(A.225)}$$

$$0 = i_{ar1}(t) - i_{aux}(t)i_{r1}(t), \quad \text{(A.226)}$$

$$0 = i_{ar2}(t) - i_{aux}(t)i_{r2}(t), \quad \text{(A.227)}$$

$$0 = \lambda_{main}(t) - L_{main}i_{main}(t) - L_{main,r1}(t)i_{r1}(t) - L_{main,r2}(t)i_{r2}(t), \quad \text{(A.228)}$$

$$0 = \lambda_{aux}(t) - L_{aux}i_{aux}(t) - L_{aux,r1}(t)i_{r1}(t) - L_{aux,r2}(t)i_{r2}(t), \quad \text{(A.229)}$$

$$0 = \lambda_{r1}(t) - L_{main,r1}i_{main}(t) - L_{aux,r1}(t)i_{aux}(t) - L_r i_{r1}(t), \quad \text{(A.230)}$$

$$0 = \lambda_{r2}(t) - L_{main,r2}i_{main}(t) - L_{aux,r2}(t)i_{aux}(t) - L_r i_{r2}(t), \quad \text{(A.231)}$$

$$0 = s_{dot}(t) - c(t)\omega_e(t), \quad \text{(A.232)}$$

$$0 = c_{dot}(t) + s(t)\omega_e(t). \quad \text{(A.233)}$$

A.3 Three-Phase Synchronous Generating Unit Model

A.3.1 Overview

This section of Appendix A describes the model of a three-phase synchronous generating unit. A single-axis model is used for steady-state and quasi-steady-state analysis. A two-axis, physically-based model is implemented for full transient analysis. The mathematical models are presented in compact form in the subsequent sections. Models of the control subsystems of the unit, like prime mover and excitation system are also included.

A.3.2 Model Parameters and User Interface

The synchronous machine parameters are defined in p.u. and in the standard d-q-0 frame, as they are usually available. In the implementation the program itself computes the physical parameters as required by the model, by converting the user defined parameters to physical parameters. The user interface of the generating unit is shown in Figure A.9. The user interface of the synchronous generator is presented in Figure A.10. and the physical parameters that are used in the mathematical model are presented in the form in Figure A.11. The user interface of the prime-mover and excitation subsystem models are presented in Figure A.12 through Figure A.19.

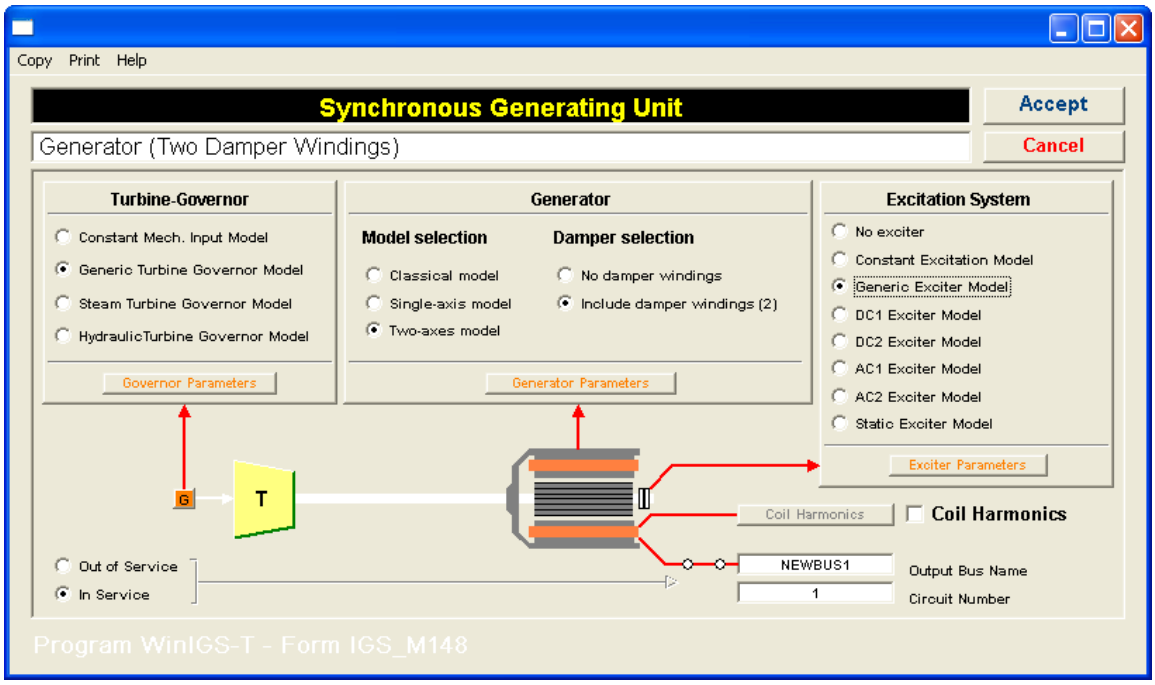

Figure A.9: Generating unit user interface.

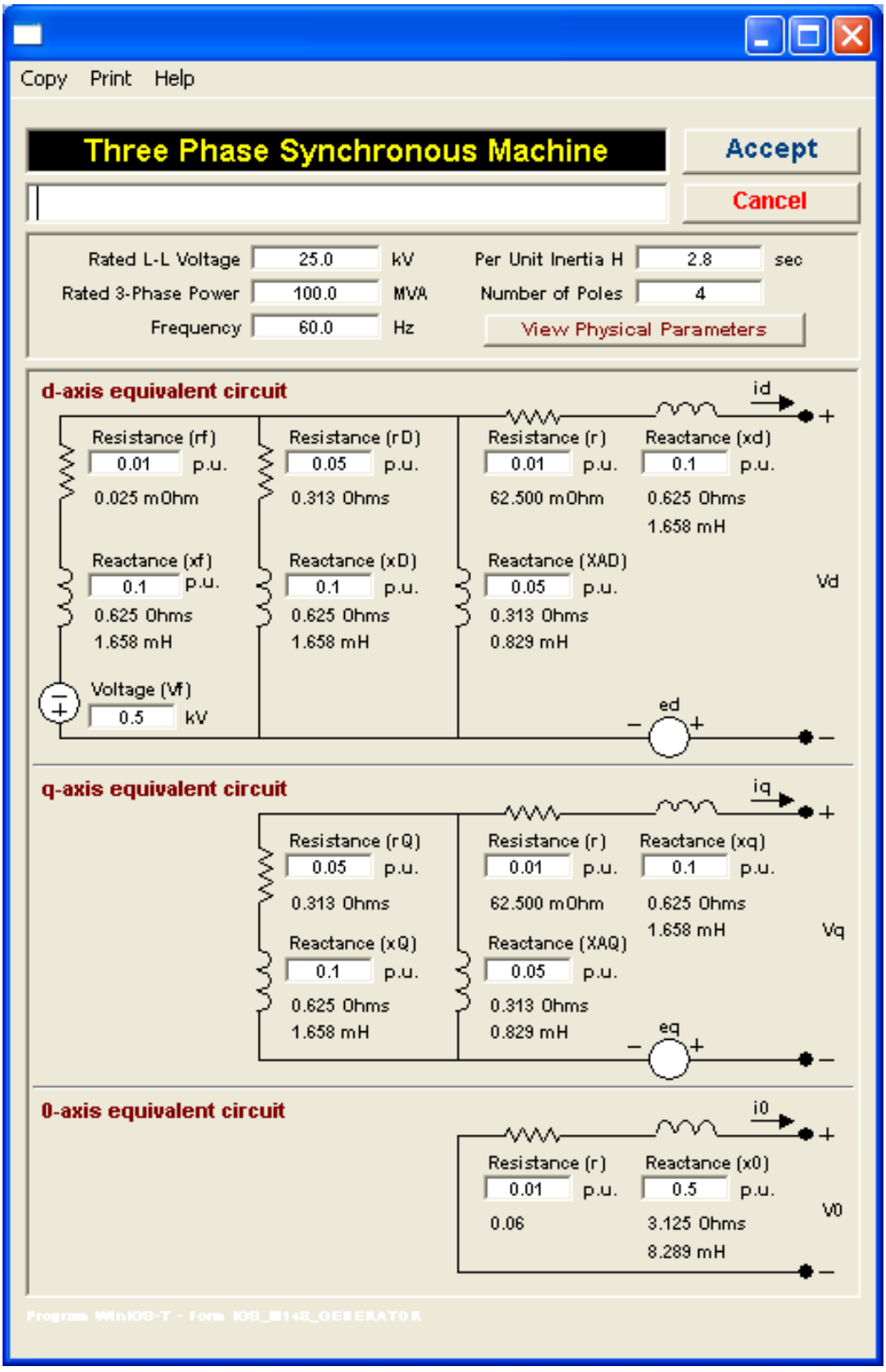

Figure A.10: Synchronous-machine user interface.

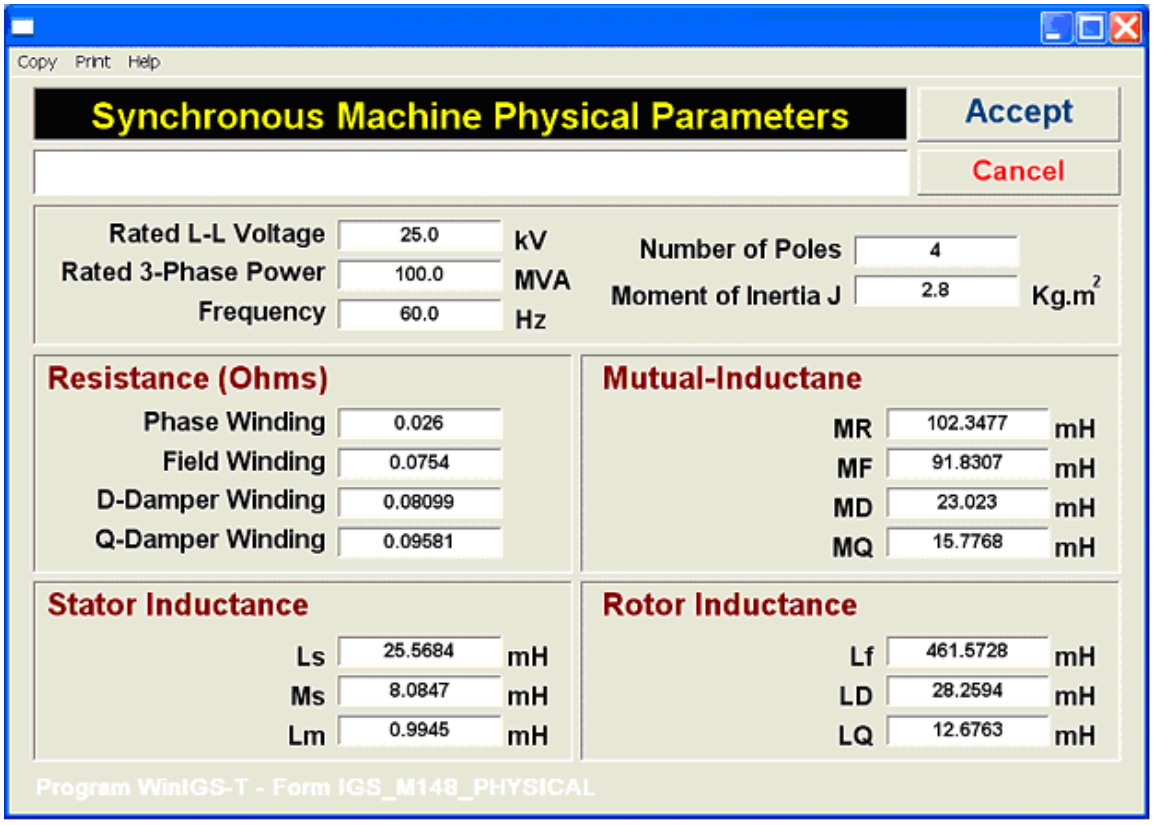

Figure A.11: Synchronous-machine physical parameters.

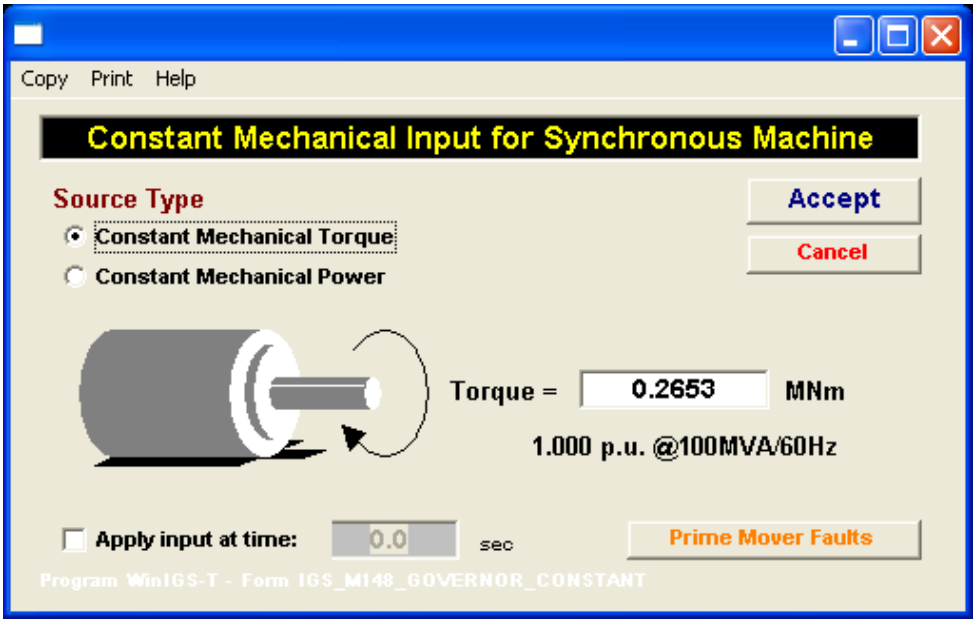

Figure A.12: Constant-torque-input prime-mover model interface.

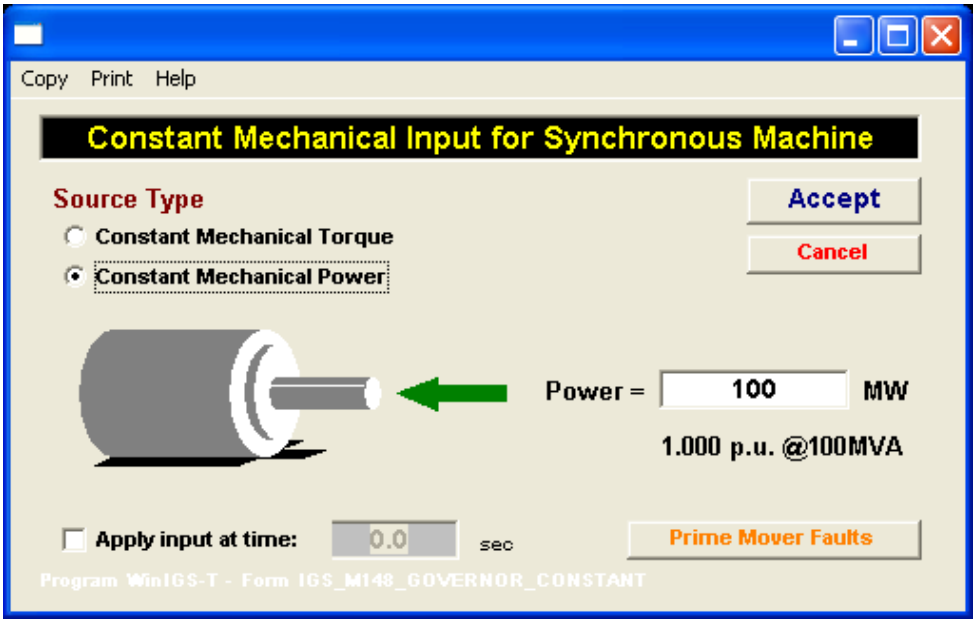

Figure A.13: Constant-power-input prime-mover model interface.

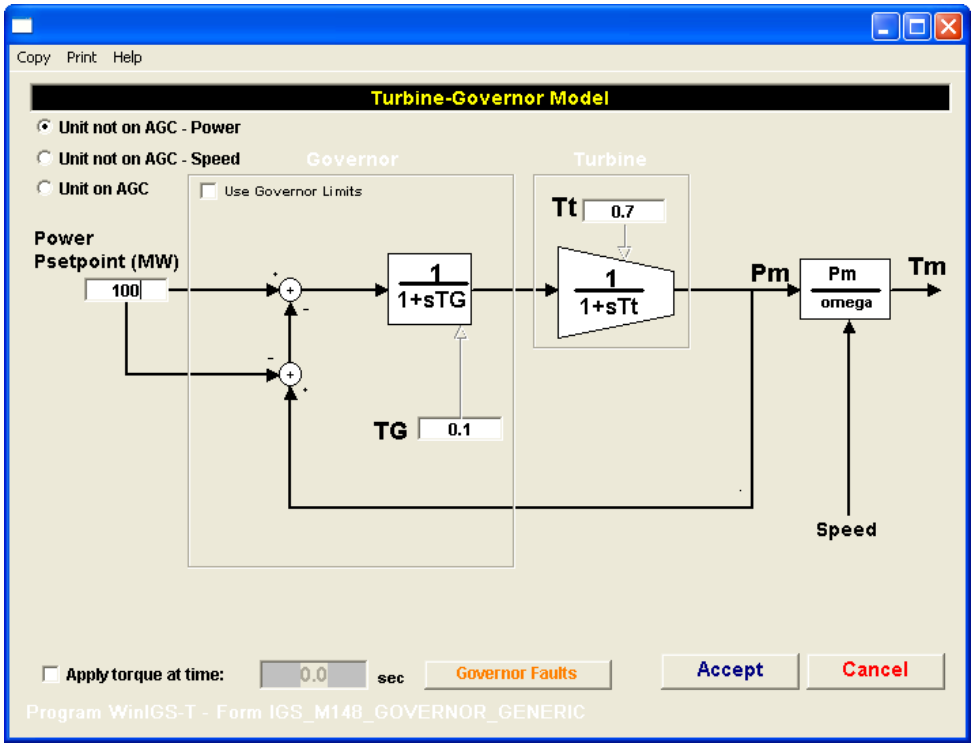

Figure A.14: Generic prime-mover model interface. Unit not on AGC, power-controlled.

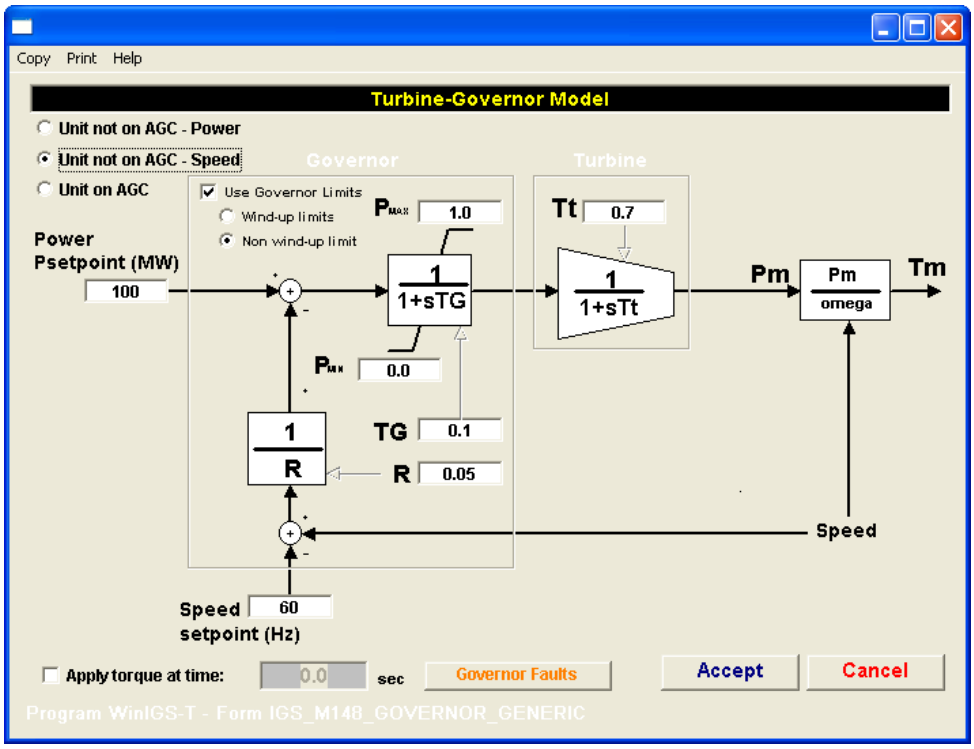

Figure A.15: Generic prime-mover model interface. Unit not on AGC, speed-controlled.

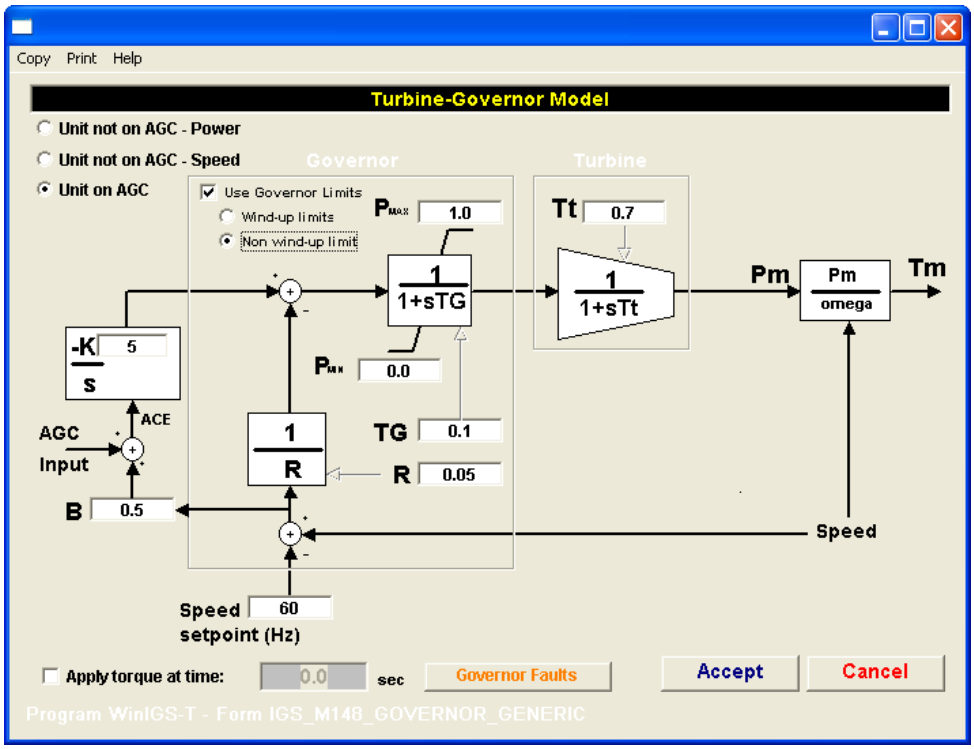

Figure A.16: Generic prime-mover model interface. Unit on AGC mode.

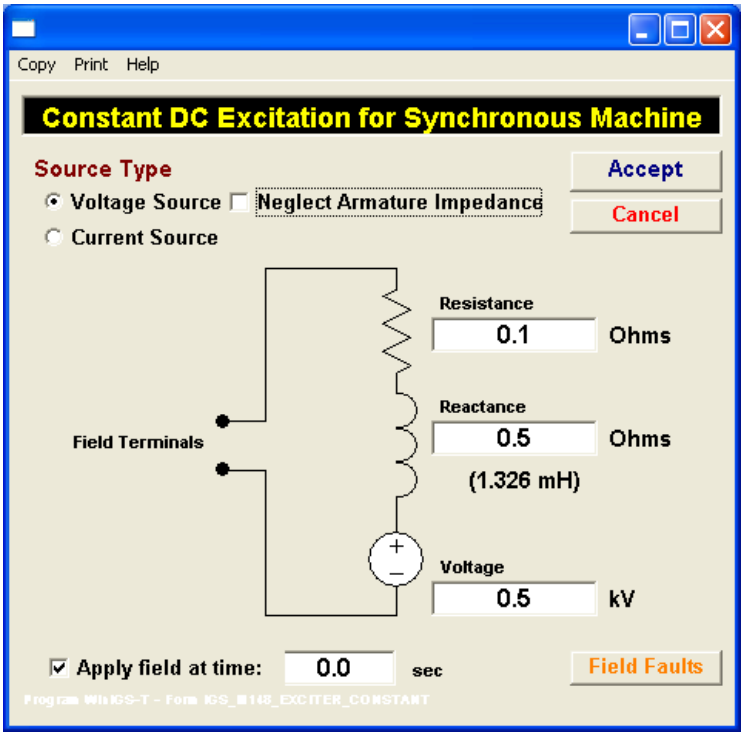

Figure A.17: Constant-voltage-source excitation system.

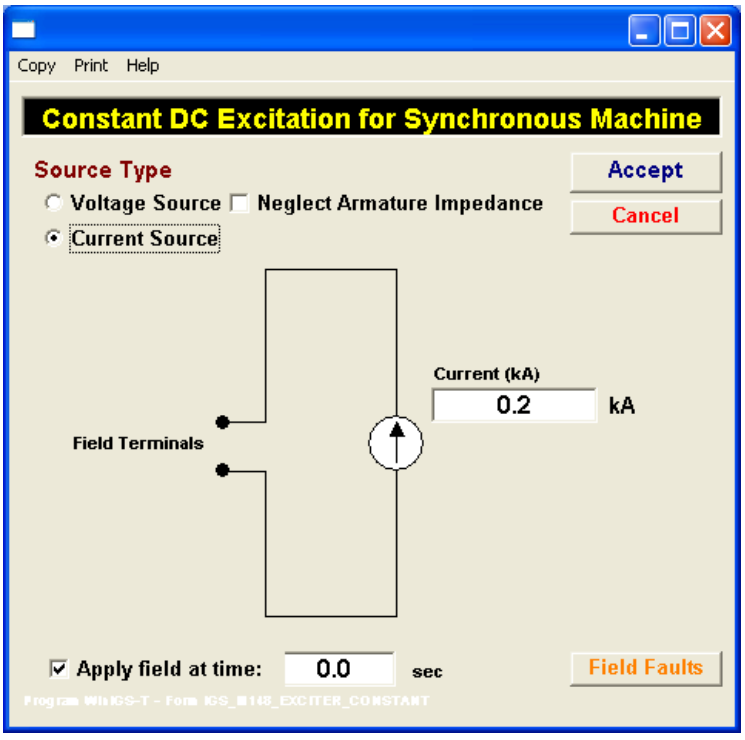

Figure A.18: Constant-current-source excitation system.

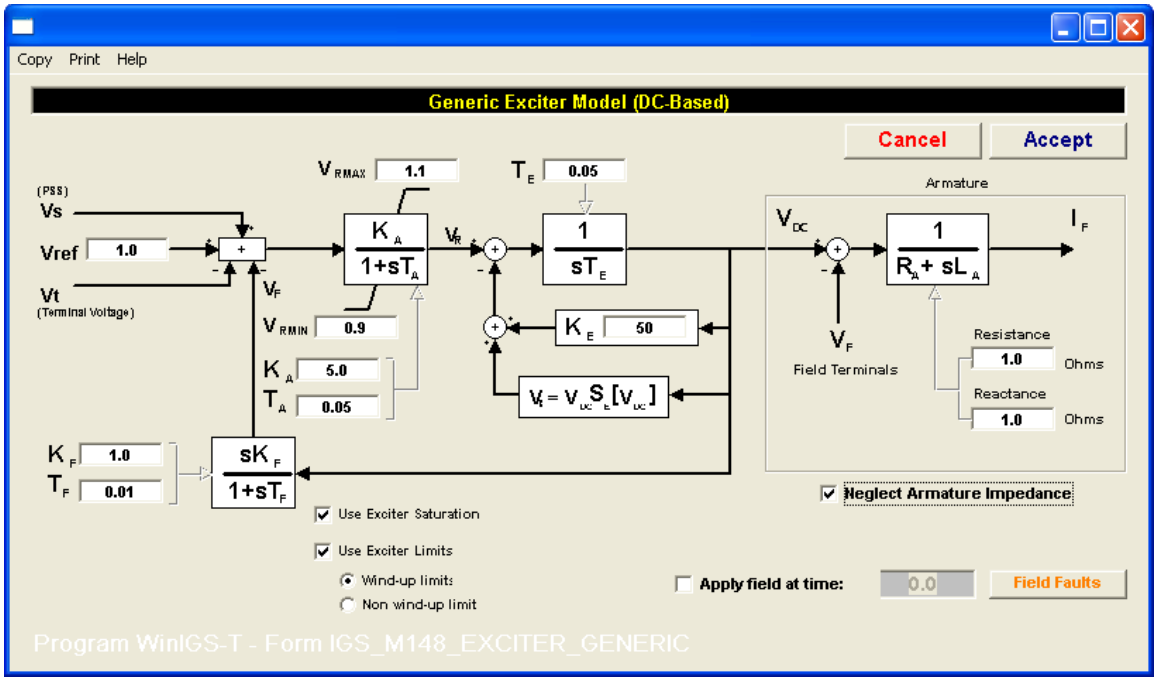

Figure A.19: User interface of generic exciter model.

A.3.3 Single-Axis Steady-State Model

This section presents the compact steady-state model of a single-axis synchronous generator. The model includes three control options: (a) PQ mode, (b) PV mode, and (c) slack-bus mode. The device equivalent circuit is illustrated in Figure A.20. The internal sources provide a set of balanced three phase voltages, described with the state variables E and δ, or equivalently with the real and imaginary parts of the complex variable $\tilde{E}$.

The state vector is $x = [V_{ar} \quad V_{ai} \quad V_{br} \quad V_{bi} \quad V_{cr} \quad V_{ci} \quad V_{nr} \quad V_{ni} \quad E_r \quad E_i]$. The model equations for each control mode are described next.

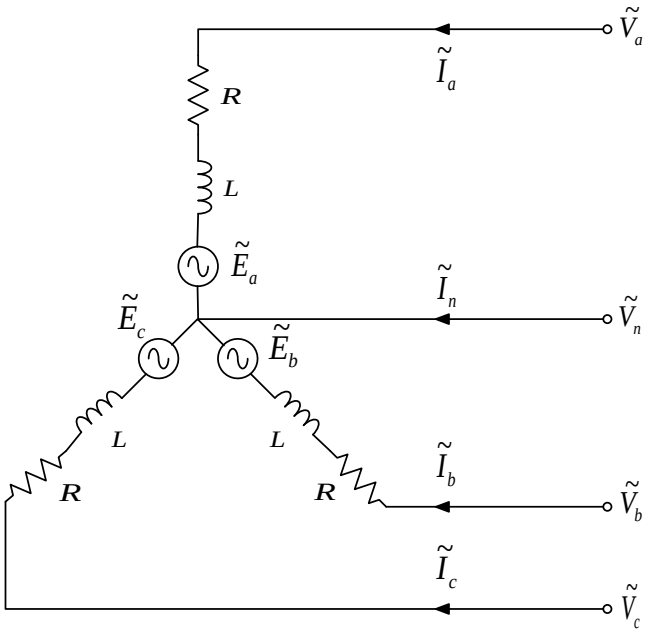

Figure A.20: Equivalent circuit of single axis synchronous generator model.

$$\tilde{I}_a = (g + jb)(\tilde{V}_a - \tilde{V}_n - \tilde{E}_a)\ , \tag{A.234}$$

$$\tilde{I}_b = (g + jb)(\tilde{V}_b - \tilde{V}_n - \tilde{E}_b)\ , \tag{A.235}$$

$$\tilde{I}_c = (g + jb)(\tilde{V}_c - \tilde{V}_n - \tilde{E}_c), \tag{A.236}$$

$$\tilde{I}_n = (g + jb)(-\tilde{V}_a - \tilde{V}_b - \tilde{V}_c + 3\tilde{V}_n)\ ; \tag{A.237}$$

For PQ mode:

$$Re\{\tilde{V}_a I_a^* + \tilde{V}_b I_b^* + \tilde{V}_c I_c^*\} = -P_{specified}\ , \tag{A.238}$$

$$Im\{\tilde{V}_a I_a^* + \tilde{V}_b I_b^* + \tilde{V}_c I_c^*\} = -Q_{specified}\ ; \tag{A.239}$$

For PV mode:

$$Re\{\tilde{V}_a I_a^* + \tilde{V}_b I_b^* + \tilde{V}_c I_c^*\} = -P_{specified}\ , \tag{A.240}$$

$$\left|\tilde{V}_a - \tilde{V}_b\right| = V_{specified}; \tag{A.241}$$

For slack mode:

$$\delta = 0\ , \tag{A.242}$$

$$\left|\tilde{V}_a - \tilde{V}_b\right| = V_{specified}\ , \tag{A.243}$$

where

$g = -\frac{R}{R^2+\omega^2L^2}$,

$b = -\frac{\omega L}{R^2+\omega^2L^2}$,

and

$\tilde{E}_a = Ee^{j\delta}$,

$\tilde{E}_b = Ee^{j(\delta-\frac{2\pi}{3})}$,

$\tilde{E}_c = Ee^{j(\delta-\frac{4\pi}{3})}$.

A.3.4 Single-Axis Quasi-Static Model

The quasi-static model is based on a the steady-state model along with the rotor mechanical system dynamics; therefore, the steady state-equations described in the previous section also hold, with the augmentation of the system with the swing equation of the rotor rotational movement. This equation defines the mechanical rotational speed $\omega(t)$ as well as the internal voltage angle $\delta(t)$ which is now a time varying quantity. The internal voltage magnitude $E(t)$ is specified by the excitation system, or may have constant value. Therefore the model compact equations are as follows:

$$\tilde{I}_a = (g + jb)(\tilde{V}_a - \tilde{V}_n - \tilde{E}_a)\ , \tag{A.244}$$

$$\tilde{I}_b = (g + jb)(\tilde{V}_b - \tilde{V}_n - \tilde{E}_b)\ , \tag{A.245}$$

$$\tilde{I}_c = (g + jb)(\tilde{V}_c - \tilde{V}_n - \tilde{E}_c), \tag{A.246}$$

$$\tilde{I}_n = (g + jb)(-\tilde{V}_a - \tilde{V}_b - \tilde{V}_c + 3\tilde{V}_n)\ , \tag{A.247}$$

$$\frac{d\delta(t)}{dt} = \omega(t) - \omega_s\ , \tag{A.248}$$

$$J\frac{d\omega(t)}{dt} = T_m(t) - T_e(t) - D(\omega(t) - \omega_s)\ , \tag{A.249}$$

$$0 = P_e(t) + Re\{\tilde{E}_a\tilde{I}_a^* + \tilde{E}_b\tilde{I}_b^* + \tilde{E}_c\tilde{I}_c^*\}\ , \tag{A.250}$$

$$0 = T_e(t)\omega(t) - P_e(t)\ , \tag{A.251}$$

$$0 = E(t) - KE_f(t)\ , \tag{A.252}$$

where

$g = -\frac{R}{R^2+\omega^2L^2}$,

$b = -\frac{\omega L}{R^2+\omega^2L^2}$,

J is the moment of inertia of the generator,

D is a damping coefficient,

ω_s is the synchronous speed, and

K is a constant of proportionality.

Furthermore,

$\tilde{E} = E(t)e^{j\delta(t)} = E(t)cos\delta(t) + jE(t)sin\delta(t)$,

$\tilde{E}_a = Ee^{j\delta}$,

$\tilde{E}_b = Ee^{j(\delta - \frac{2\pi}{3})}$,

$\tilde{E}_c = Ee^{j(\delta - \frac{4\pi}{3})}$.

The state vector is defined as

$x = [V_{ar} \quad V_{ai} \quad V_{br} \quad V_{bi} \quad V_{cr} \quad V_{ci} \quad V_{nr} \quad V_{ni} \quad \delta(t) \quad \omega(t) \quad P_e(t) \quad T_e(t) \quad E(t)]$.

A.3.5 Two-Axis Full Transient Model

Figure A.21 illustrates the electrical subsystem model of a synchronous machine with two damper windings as a set of mutually coupled circuits.

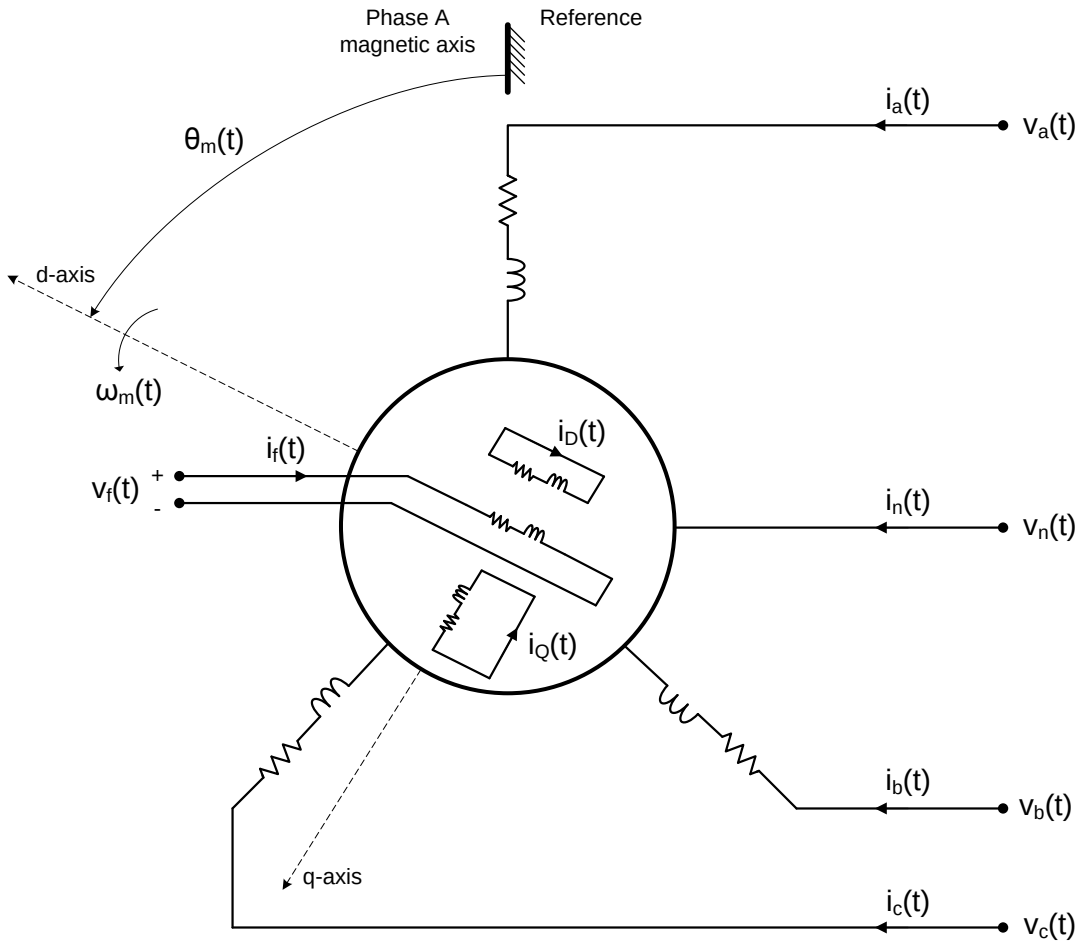

Figure A.21: Electrical model of a synchronous machine as a set of mutually coupled windings.

A.3.5.1 Compact model

Analysis of the model and inclusion of the rotor motion equations yields the following compact model of the generator. A detailed presentation of the analysis can be found in [135].

$$v_{abc}(t) = R_{abc} i_{abc}(t) + \frac{d}{dt}\lambda_{abc}(t) + \Gamma v_n(t) \,, \tag{A.253}$$

$$i_n(t) = -i_a(t) - i_b(t) - i_c(t) \,, \tag{A.254}$$

$$0 = r_f i_f(t) + \frac{d\lambda_f(t)}{dt} - v_f(t) + v_{fn}(t) \,, \tag{A.255}$$

$$i_{fn}(t) = -i_f(t) \,, \tag{A.256}$$

$$T_m(t) = J\frac{d\omega_m(t)}{dt} - T_e(t) - T_{wf}(t) \,, \tag{A.257}$$

$$0 = \frac{d\theta_m(t)}{dt} - \omega_m(t) \,, \tag{A.258}$$

$$0 = \theta(t) - \frac{p}{2}\theta_m(t) \,, \tag{A.259}$$

$$0 = \omega(t) - \frac{p}{2}\omega_m(t) \,, \tag{A.260}$$

$$0 = -\theta(t) + \omega_s t + \delta(t) + \frac{\pi}{2} \,, \tag{A.261}$$

$$0 = R_{DQ} i_{DQ}(t) + \frac{d\lambda_{DQ}(t)}{dt} \,, \tag{A.262}$$

$$0 = \lambda_{abc}(t) - L_{ss}\big(\theta(t)\big) i_{abc}(t) - L_{sr}\big(\theta(t)\big) i_{fDQ}(t) \,, \tag{A.263}$$

$$0 = \lambda_{fDQ}(t) - L_{rs}\big(\theta(t)\big) i_{abc}(t) - L_{rr} i_{fDQ}(t) \,, \tag{A.264}$$

$$0 = T_e(t) + \frac{1}{\sqrt{3}} i_{abc}(t) \begin{bmatrix} 0 & 1 & -1 \\ -1 & 0 & 1 \\ 1 & -1 & 0 \end{bmatrix} \lambda_{abc}(t) \,, \tag{A.265}$$

$$0 = T_{wf}(t) + \left(D_{wf} + D'_{wf}\omega_m(t) + D''_{wf}\omega_m^2(t)\right), \quad \text{(A.266)}$$

where

$v_{abc}(t) = [v_a(t) \quad v_b(t) \quad v_c(t)]^T$,

$v_{fDQ}(t) = [v_f(t) \quad v_D(t) \quad v_Q(t)]^T = [v_f(t) \quad 0 \quad 0]^T$,

$i_{abc}(t) = [i_a(t) \quad i_b(t) \quad i_c(t)]^T$,

$i_{fDQ}(t) = [i_f(t) \quad i_D(t) \quad i_Q(t)]^T$,

$\lambda_{abc}(t) = [\lambda_a(t) \quad \lambda_b(t) \quad \lambda_c(t)]^T$,

$\lambda_{fDQ}(t) = [\lambda_f(t) \quad \lambda_D(t) \quad \lambda_Q(t)]^T$,

$R_{abc} = diag(r_a \quad r_b \quad r_c) = diag(r \quad r \quad r)$,

$R_{fDQ} = diag(r_f \quad r_D \quad r_Q)$,

$\Gamma = [1 \quad 1 \quad 1]^T$,

$E = [1 \quad 0 \quad 0]^T$,

J is the rotor moment of inertia,

$T_m(t)$ is the mechanical torque applied on the rotor shaft by a prime mover system,

$T_e(t)$ is the electromagnetic torque developed by the generator,

$T_{fw}(t)$ is the friction and windage torque,

$\theta_m(t)$ is the mechanical rotor position,

$\omega_m(t)$ is the mechanical rotor speed,

$\theta(t)$ is the mechanical rotor position,

$\omega(t)$ is the mechanical rotor speed,

$$L_{ss}\big(\theta(t)\big) = \begin{bmatrix} L_{aa}(\theta(t)) & L_{ab}(\theta(t)) & L_{ac}(\theta(t)) \\ L_{ab}(\theta(t)) & L_{bb}(\theta(t)) & L_{bc}(\theta(t)) \\ L_{ac}(\theta(t)) & L_{bc}(\theta(t)) & L_{cc}(\theta(t)) \end{bmatrix},$$

$$L_{sr}(\theta(t)) = \begin{bmatrix} L_{af}(\theta(t)) & L_{aD}(\theta(t)) & L_{aQ}(\theta(t)) \\ L_{bf}(\theta(t)) & L_{bD}(\theta(t)) & L_{bQ}(\theta(t)) \\ L_{cf}(\theta(t)) & L_{cD}(\theta(t)) & L_{cQ}(\theta(t)) \end{bmatrix},$$

$$L_{rs}(\theta(t)) = L_{sr}^{T}(\theta(t)),$$

$$L_{rr} = \begin{bmatrix} L_{ff} & L_{fD} & L_{fQ} \\ L_{fD} & L_{DD} & L_{DQ} \\ L_{fQ} & L_{DQ} & L_{QQ} \end{bmatrix}.$$

Detailed description of the above inductances is as follows:

Stator Self-Inductances

The stator self-inductances, L_{aa}, L_{bb}, and L_{cc}, in general depend on rotor position. An approximate expression of this dependence is

$$L_{aa}(t) = L_s + L_m cos(2\theta(t)), \tag{A.267}$$

$$L_{bb}(t) = L_s + L_m cos\left(2\theta(t) - \frac{2\pi}{3}\right), \tag{A.268}$$

$$L_{cc}(t) = L_s + L_m cos\left(2\theta(t) + \frac{2\pi}{3}\right), \tag{A.269}$$

where L_s is the self-inductance due to space-fundamental air-gap flux and the armature leakage flux; the additional component that varies with 2θ is due to the rotor saliency.

A typical variation of L_{ii} is shown in Figure A.22.

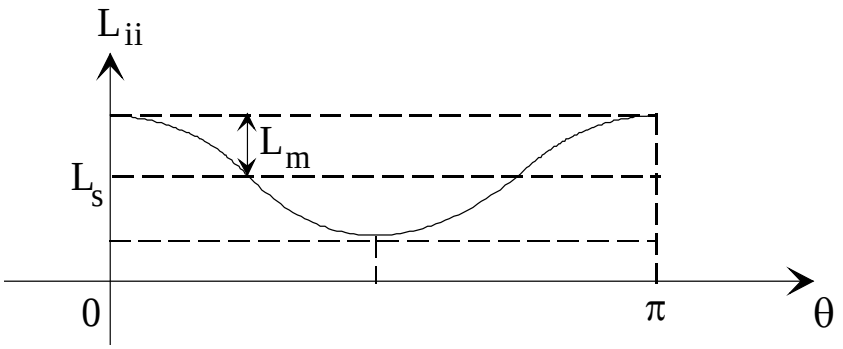

Figure A.22: Stator self-inductance as a function of θ.

Rotor Self-Inductances

The rotor self-inductances, L_{ff}, L_{DD}, and L_{QQ}, are approximately constant and can be represented by the symbols $L_{ff} = L_f$, $L_{DD} = L_D$, and $L_{QQ} = L_Q$.

Stator Mutual Inductances

The stator mutual inductances, L_{ab}, L_{bc}, and L_{ca}, are negative. They are functions of the rotor position $\theta(t)$. Approximate expressions for these functions are

$$L_{ab}(t) = L_{ba}(t) = -M_s - L_m cos2\left(\theta(t) + \frac{\pi}{6}\right) = -M_s - L_m cos\left(2\theta(t) + \frac{\pi}{3}\right), \quad \text{(A.270)}$$

$$L_{bc}(t) = L_{cb}(t) = -M_s - L_m cos2\left(\theta(t) - \frac{\pi}{2}\right) = -M_s - L_m cos(2\theta(t) - \pi), \quad \text{(A.271)}$$

$$L_{ca}(t) = L_{ac}(t) = -M_s - L_m cos2\left(\theta(t) - \frac{7\pi}{6}\right) = -M_s - L_m cos\left(2\theta(t) - \frac{\pi}{3}\right). \quad \text{(A.272)}$$

A typical variation of L_{ij} is shown in Figure A.23.

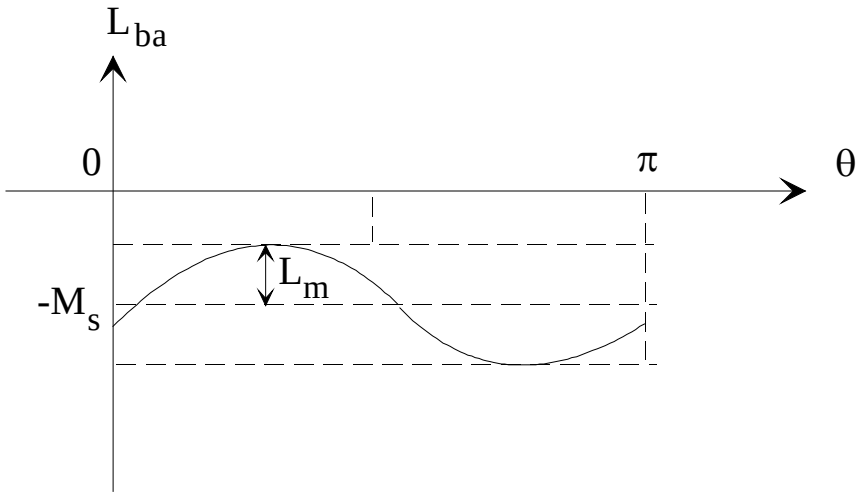

Figure A.23: Mutual inductance between stator windings.

Rotor Mutual Inductances

The rotor mutual inductances, L_{fD}, L_{DQ}, and L_{Qf}, are constant and independent of $\theta(t)$, because the rotor windings are stationary with one another. Therefore, there are denoted as $L_{fD} = L_{Df} = M_R$, $L_{DQ} = L_{QD} = 0$, and $L_{Qf} = L_{fQ} = 0$.

Mutual Inductances between Stator and rotor

The mutual inductances between stator and rotor windings, L_{af}, L_{bf}, and L_{cf} are dependent upon the rotor position $\theta(t)$ as follows:

$$L_{af}(t) = L_{fa}(t) = M_F cos\theta(t)\,, \tag{A.273}$$

$$L_{bf}(t) = L_{fb}(t) = M_F cos\left(\theta(t) - \frac{2\pi}{3}\right), \tag{A.274}$$

$$L_{cf}(t) = L_{fc}(t) = M_F cos\left(\theta(t) - \frac{4\pi}{3}\right) = M_F cos\left(\theta(t) + \frac{2\pi}{3}\right). \tag{A.275}$$

Similarly

$$L_{aD}(t) = L_{Da}(t) = M_D cos\theta(t)\,, \tag{A.276}$$

$$L_{bD}(t) = L_{Db}(t) = M_D cos\left(\theta(t) - \frac{2\pi}{3}\right), \quad \text{(A.277)}$$

$$L_{cD}(t) = L_{Dc}(t) = M_D cos\left(\theta(t) - \frac{4\pi}{3}\right) = M_D cos\left(\theta(t) + \frac{2\pi}{3}\right). \quad \text{(A.278)}$$

The damper winding Q is orthogonal to the D winding. According to our definition of rotor d-axis and q-axis, it holds that:

$$L_{aQ}(t) = L_{Qa}(t) = M_Q cos\left(\theta(t) - \frac{\pi}{2}\right) = M_Q sin\theta(t), \quad \text{(A.279)}$$

$$L_{bQ}(t) = L_{Qb}(t) = M_Q cos\left(\theta(t) - \frac{\pi}{2} - \frac{2\pi}{3}\right) = M_Q sin\left(\theta(t) - \frac{2\pi}{3}\right), \quad \text{(A.280)}$$

$$L_{cQ}(t) = L_{Qc}(t) = M_Q cos\left(\theta(t) - \frac{\pi}{2} - \frac{4\pi}{3}\right) = M_Q sin\left(\theta(t) - \frac{4\pi}{3}\right) = M_Q sin\left(\theta(t) + \frac{2\pi}{3}\right). \quad \text{(A.281)}$$

Actually, the inductances are perturbed from sinusoidal variation with harmonics. Generally speaking, these harmonics are kept low with the use of distributed coils, double layers and fractional pitch. The inclusion and effect of harmonics can be included in the above formulation. In the current model, however, these phenomena are omitted.

A.3.5.2 Equivalent Quadratic Model

External equations:

$$i_a = i_a(t), \quad \text{(A.282)}$$

$$i_b = i_b(t), \quad \text{(A.283)}$$

$$i_c = i_c(t), \quad \text{(A.284)}$$

$$i_n = -i_a(t) - i_b(t) - i_c(t), \quad \text{(A.285)}$$

$$i_f = i_f(t), \quad \text{(A.286)}$$

$$i_{fn} = -i_f(t)\ , \tag{A.287}$$

$$T_m = T_m(t)\ . \tag{A.288}$$

State: $v(t) = [v_a(t) \quad v_b(t) \quad v_c(t) \quad v_n(t) \quad v_f(t) \quad v_{fn}(t) \quad T_m(t)]^T$.

Internal linear differential equations:

$$\frac{d\lambda_a(t)}{dt} = e_a(t)\ , \tag{A.289}$$

$$\frac{d\lambda_b(t)}{dt} = e_b(t)\ , \tag{A.290}$$

$$\frac{d\lambda_c(t)}{dt} = e_c(t)\ , \tag{A.291}$$

$$\frac{d\lambda_f(t)}{dt} = e_f(t)\ , \tag{A.292}$$

$$\frac{d\lambda_D(t)}{dt} = e_D(t)\ , \tag{A.293}$$

$$\frac{d\lambda_Q(t)}{dt} = e_Q(t)\ , \tag{A.294}$$

$$\frac{d\theta_m(t)}{dt} = \omega_m(t)\ , \tag{A.295}$$

$$\frac{d\omega_m(t)}{dt} = \frac{1}{J}T_{acc}(t)\ , \tag{A.296}$$

$$\frac{dc(t)}{dt} = y_1(t)\ , \tag{A.297}$$

$$\frac{ds(t)}{dt} = y_2(t)\ . \tag{A.298}$$

State:

$x(t) = [\lambda_a(t) \quad \lambda_b(t) \quad \lambda_c(t) \quad \lambda_f(t) \quad \lambda_D(t) \quad \lambda_Q(t) \quad \theta_m(t) \quad \omega_m(t) \quad c(t) \quad s(t)]^T$.

Internal linear algebraic equations:

$$0 = T_{acc}(t) - T_e(t) - T_m(t) - T_{fw}(t)\,, \tag{A.299}$$

$$0 = \theta(t) - \frac{p}{2}\theta_m(t)\,, \tag{A.300}$$

$$0 = \omega(t) - \frac{p}{2}\omega_m(t)\,, \tag{A.301}$$

$$0 = \delta(t) - \theta(t) + \omega_s t + \frac{\pi}{2}\,, \tag{A.302}$$

$$0 = e_a(t) + r_a i_a(t) - v_a(t) + v_n(t)\,, \tag{A.303}$$

$$0 = e_b(t) + r_b i_b(t) - v_b(t) + v_n(t)\,, \tag{A.304}$$

$$0 = e_c(t) + r_c i_c(t) - v_c(t) + v_n(t)\,, \tag{A.305}$$

$$0 = e_f(t) + r_f i_f(t) - v_f(t) + v_{fn}(t)\,, \tag{A.306}$$

$$0 = e_D(t) + r_D i_D(t)\,, \tag{A.307}$$

$$0 = e_Q(t) + r_Q i_Q(t)\,. \tag{A.308}$$

State:

$$y(t) = \begin{bmatrix} T_{acc}(t) & \theta(t) & \omega(t) & \delta(t) & e_a(t) & e_b(t) & e_c(t) & e_f(t) & e_D(t) & e_Q(t) \end{bmatrix}^T.$$

Internal nonlinear algebraic equations:

$$0 = T_e(t) + \frac{1}{\sqrt{3}}(i_a(t)\lambda_b(t) - i_a(t)\lambda_c(t) + i_b(t)\lambda_c(t) - i_b(t)\lambda_a(t) + i_c(t)\lambda_b(t) - i_c(t)\lambda_b(t))\,, \tag{A.309}$$

$$0 = T_{wf}(t) + a + b\omega_m(t) + c\omega_m^2(t)\,, \tag{A.310}$$

$$0 = P_e(t) - e_a(t)i_a(t) - e_b(t)i_b(t) - e_c(t)i_c(t) - e_f(t)i_f(t) - e_D(t)i_D(t) - e_Q(t)i_Q(t)\,, \tag{A.311}$$

$$0 = y_1(t) + s(t)\omega(t)\,, \tag{A.312}$$

$$0 = y_2(t) - c(t)\omega(t)\,, \tag{A.313}$$

$$0 = \lambda_a(t) - L_{aa}(t)i_a(t) - L_{ab}(t)i_b(t) - L_{ac}(t)i_c(t) - L_{af}(t)i_f(t) - L_{aD}(t)i_D(t) - L_{aQ}(t)i_Q(t)\,, \tag{A.314}$$

$$0 = \lambda_b(t) - L_{ba}(t)i_a(t) - L_{bb}(t)i_b(t) - L_{bc}(t)i_c(t) - L_{bf}(t)i_f(t) - L_{bD}(t)i_D(t) - L_{bQ}(t)i_Q(t)\,, \tag{A.315}$$

$$0 = \lambda_c(t) - L_{ca}(t)i_a(t) - L_{cb}(t)i_b(t) - L_{cc}(t)i_c(t) - L_{cf}(t)i_f(t) - L_{cD}(t)i_D(t) - L_{cQ}(t)i_D(t) - L_{cQ}(t)i_Q(t)\,, \tag{A.316}$$

$$0 = \lambda_f(t) - L_{fa}(t)i_a(t) - L_{fb}(t)i_b(t) - L_{fc}(t)i_c(t) - L_f i_f(t) - M_R i_D(t) - L_{fQ}i_Q(t)\,, \tag{A.317}$$

$$0 = \lambda_D(t) - L_{Da}(t)i_a(t) - L_{Db}(t)i_b(t) - L_{Dc}(t)i_c(t) - M_R i_f(t) - L_D i_D(t) - L_{DQ}i_Q(t), \tag{A.318}$$

$$0 = \lambda_Q(t) - L_{Qa}(t)i_a(t) - L_{Qb}(t)i_b(t) - L_{Qc}(t)i_c(t) - L_{Qf}i_f(t) - L_{QD}i_D(t) - L_Q i_Q(t)\,, \tag{A.319}$$

$$0 = L_{aa}(t) - L_s - L_m c^2(t) + L_m s^2(t)\,, \tag{A.320}$$

$$0 = L_{bb}(t) - L_s - L_m cos\left(\frac{2\pi}{3}\right)c^2(t) + L_m cos\left(\frac{2\pi}{3}\right)s^2(t) + 2L_m sin\left(\frac{2\pi}{3}\right)c(t)s(t)\,, \tag{A.321}$$

$$0 = L_{cc}(t) - L_s - L_m cos\left(\frac{2\pi}{3}\right)c^2(t) + L_m cos\left(\frac{2\pi}{3}\right)s^2(t) - 2L_m sin\left(\frac{2\pi}{3}\right)c(t)s(t)\,, \tag{A.322}$$

$$0 = L_{ab}(t) + M_s + L_m cos\left(\frac{\pi}{3}\right)c^2(t) - L_m cos\left(\frac{\pi}{3}\right)s^2(t) - 2L_m sin\left(\frac{2\pi}{3}\right)c(t)s(t)\,, \tag{A.323}$$

$$0 = L_{ac}(t) + M_s + L_m cos\left(\frac{7\pi}{3}\right)c^2(t) - L_m cos\left(\frac{7\pi}{3}\right)s^2(t) + 2L_m sin\left(\frac{7\pi}{3}\right)c(t)s(t)\,, \tag{A.324}$$

$$0 = L_{bc}(t) + M_s + L_m cos(\pi) c^2(t) - L_m cos(\pi) s^2(t) + 2L_m sin(\pi) c(t) s(t) \,, \quad \text{(A.325)}$$

$$0 = L_{af}(t) - M_F c(t) \,, \quad \text{(A.326)}$$

$$0 = L_{bf}(t) - M_F cos\left(\frac{2\pi}{3}\right) c(t) - M_F sin\left(\frac{2\pi}{3}\right) s(t) \,, \quad \text{(A.327)}$$

$$0 = L_{cf}(t) - M_F cos\left(\frac{4\pi}{3}\right) c(t) - M_F sin\left(\frac{4\pi}{3}\right) s(t) \,, \quad \text{(A.328)}$$

$$0 = L_{aD}(t) - M_D c(t) \,, \quad \text{(A.329)}$$

$$0 = L_{bD}(t) - M_D cos\left(\frac{2\pi}{3}\right) c(t) - M_D sin\left(\frac{2\pi}{3}\right) s(t) \,, \quad \text{(A.330)}$$

$$0 = L_{cD}(t) - M_D cos\left(\frac{4\pi}{3}\right) c(t) - M_D sin\left(\frac{4\pi}{3}\right) s(t) \,, \quad \text{(A.331)}$$

$$0 = L_{aQ}(t) - M_Q s(t) \,, \quad \text{(A.332)}$$

$$0 = L_{bQ}(t) - M_Q cos\left(\frac{2\pi}{3}\right) s(t) + M_Q sin\left(\frac{2\pi}{3}\right) c(t) \,, \quad \text{(A.333)}$$

$$0 = L_{cQ}(t) - M_Q cos\left(\frac{4\pi}{3}\right) s(t) + M_Q sin\left(\frac{4\pi}{3}\right) c(t) \,. \quad \text{(A.334)}$$

State:

$$z(t) = \begin{bmatrix} T_e(t) & T_{fw}(t) & P_e(t) & y_1(t) & y_2(t) & i_a(t) & i_b(t) & i_c(t) & i_f(t) \\ i_D(t) & i_Q(t) & L_{aa}(t) & L_{bb}(t) & L_{cc}(t) & L_{ab}(t) & L_{ac}(t) & L_{bc}(t) & L_{af}(t) \\ L_{bf}(t) & L_{cf}(t) & L_{aD}(t) & L_{bD}(t) & L_{cD}(t) & L_{aQ}(t) & L_{bQ}(t) & L_{cQ}(t) & \end{bmatrix}^T$$

Implicit Equations (linear – do not introduce additional states):

$$0 = L_{ba}(t) - L_{ab}(t) \,, \quad \text{(A.335)}$$

$$0 = L_{cb}(t) - L_{bc}(t) \,, \quad \text{(A.336)}$$

$$0 = L_{ca}(t) - L_{ac}(t) \,, \quad \text{(A.337)}$$

$$0 = L_{fa}(t) - L_{af}(t) \,, \quad \text{(A.338)}$$

$$0 = L_{fb}(t) - L_{bf}(t)\ , \tag{A.339}$$

$$0 = L_{fc}(t) - L_{cf}(t)\ , \tag{A.340}$$

$$0 = L_{Da}(t) - L_{aD}(t)\ , \tag{A.341}$$

$$0 = L_{Db}(t) - L_{bD}(t)\ , \tag{A.342}$$

$$0 = L_{Dc}(t) - L_{cD}(t)\ , \tag{A.343}$$

$$0 = L_{Qa}(t) - L_{aQ}(t)\ , \tag{A.344}$$

$$0 = L_{Qb}(t) - L_{bQ}(t)\ , \tag{A.345}$$

$$0 = L_{Qc}(t) - L_{cQ}(t)\ . \tag{A.346}$$

Note that $L_{fQ} = L_{Qf} = 0$ and $L_{DQ} = L_{QD} = 0$ since the Q and D windings are perpendicular.

The model is formulated as a 53-order quadratic model consisting of 53 states: 7 external states and 46 internal. Of the internal states 10 are dynamic and 36 algebraic. The model consists of 7 external equations, 10 linear differential and 36 algebraic equations. Of the algebraic equations 10 are linear, 26 nonlinear (there are 12 more linear equations that are implicit and will be eliminated from the final model). The number of equations is equal to the number of states, thus the model is consistent. The total state vector is defined as

$$X(t) = [v^T \quad x^T \quad y^T \quad z^T]^T$$

where

$$v(t) = [v_a \quad v_b \quad v_c \quad v_n \quad v_f \quad v_{fn} \quad T_m]^T\ ,$$

$$x(t) = [\lambda_a \quad \lambda_b \quad \lambda_c \quad \lambda_f \quad \lambda_D \quad \lambda_Q \quad \theta_m \quad \omega_m \quad c \quad s]^T ,$$

$$y(t) = [T_{acc} \quad \theta \quad \omega \quad \delta \quad e_a \quad e_b \quad e_c \quad e_f \quad e_D \quad e_Q]^T ,$$

$$z(t) = \begin{bmatrix} T_e & T_{fw} & P_e & y_1 & y_2 & i_a & i_b & i_c & i_f & i_D & I_Q & L_{aa} & L_{bb} \\ L_{cc} & L_{ab} & L_{ac} & L_{bc} & L_{af} & L_{bf} & L_{cf} & L_{aD} & L_{bD} & L_{cD} & L_{aQ} & L_{bQ} & L_{cQ} \end{bmatrix}^T .$$

The through variables are

$$I = [i_a \quad i_b \quad i_c \quad i_n \quad i_f \quad i_{fn} \quad T_m \quad 0 \quad ... \quad 0]^T .$$

A.3.6 Governor, Prime-Mover Model

The compact model of a generic turbine-governor system is a second-order dynamical system. The governor is represented as a single-time-delay unit and the turbine as a second single-time-delay until. Nonlinearities are introduced in the system by the conversion of mechanical power to mechanical torque and by adding a non-windup limiter that limits the output of the governor. Three operating modes are defined: (a) the unit is not on AGC (automatic generation control) and controls the produced output power, (b) the unit is not on AGC (automatic generation control) and controls its speed, and (c) the unit is on AGC. In the first case a feedback is taken from the electrical power produced by the unit; this is compared to a power production setpoint and the error is the input of the governor system. In the second case, where the unit is controlling its speed, the speed setpoint is provided as reference and it is compared to a speed feedback. The error is fed to the governor system after being amplified by the droop of the unit. In the third case, where the unit is on AGC, apart from the speed setpoint an additional control signal is provided from the AGC system and goes though and integral control defining the unit power setpoint, so that the frequency error is zero. Based on the above

description six modes of operation are defined: 1. Unit is not on AGC, power controlled, limits are not considered; 2. unit is not on AGC, power controlled, limits are considered; 3. unit is not on AGC, speed controlled, limits are not considered; 4. unit is not on AGC, speed controlled, limits are considered; 5. unit is on AGC, limits are not considered; 6. unit is on AGC, limits are considered.

1. Unit is not on AGC, power-controlled, limits are not considered

The compact model is of the form:

$$T_G \frac{dP_T(t)}{dt} = 2P_{set} - P_m(t) - P_T(t)\ , \tag{A.347}$$

$$T_t \frac{dP_m(t)}{dt} = P_T(t) - P_m(t)\ , \tag{A.348}$$

$$0 = T_m(t)\omega_m(t) - P_m(t)\ . \tag{A.349}$$

2. Unit is not on AGC, power-controlled, limits are considered

The compact model is of the form:

For non-windup limits

If $P^{min} \leq P_T(t) \leq P^{max}$

$$T_G \frac{dP_T(t)}{dt} = 2P_{set} - P_m(t) - P_T(t)\ , \tag{A.350}$$

else if $P_T(t) < P^{min}$ and $\frac{dP_T(t)}{dt} < 0$

$$P_T(t) = P^{min}, \tag{A.351}$$

$$\frac{dP_T(t)}{dt} = 0 \Leftrightarrow 2P_{set} - P_m(t) - P_T(t) = 0, \tag{A.352}$$

else if $P_T(t) > P^{max}$ and $\frac{dP_T(t)}{dt} > 0$

$$P_T(t) = P^{max}, \tag{A.353}$$

$$\frac{dP_T(t)}{dt} = 0 \Leftrightarrow 2P_{set} - P_m(t) - P_T(t) = 0, \tag{A.354}$$

$$T_t \frac{dP_m(t)}{dt} = P_T(t) - P_m(t)\ , \tag{A.355}$$

$$0 = T_m(t)\omega_m(t) - P_m(t)\ . \tag{A.356}$$

For windup limits

$$T_G \frac{dP_T(t)}{dt} = 2P_{set} - P_m(t) - P_T(t)\ , \tag{A.357}$$

$$T_t \frac{dP_m(t)}{dt} = P_T^*(t) - P_m(t)\ , \tag{A.358}$$

$$0 = T_m(t)\omega_m(t) - P_m(t)\ , \tag{A.359}$$

If $P^{min} \le P_T(t) \le P^{max}$

$$0 = P_T^*(t) - P_T(t)\ , \tag{A.360}$$

else if $P_T(t) < P^{min}$

$$P_T^*(t) = P^{min}, \tag{A.361}$$

else if $P_T(t) > P^{max}$

$$P_T^*(t) = P^{max}. \tag{A.362}$$

3. Unit is not on AGC, speed-controlled, limits are not considered

The compact model is of the form:

$$T_G \frac{dP_T(t)}{dt} = P_{set} - \frac{1}{R}(\omega_m(t) - \omega_{set})\ , \tag{A.363}$$

$$T_t \frac{dP_m(t)}{dt} = P_T(t) - P_m(t)\ , \tag{A.364}$$

$$0 = T_m(t)\omega_m(t) - P_m(t)\ . \tag{A.365}$$

4. Unit is not on AGC, speed-controlled, limits are considered

The compact model is of the form:

For non-windup limits

If $P^{min} \le P_T(t) \le P^{max}$

$$T_G \frac{dP_T(t)}{dt} = P_{set} - \frac{1}{R}(\omega_m(t) - \omega_{set})\ , \tag{A.366}$$

else if $P_T(t) < P^{min}$ and $\frac{dP_T(t)}{dt} < 0$

$$P_T(t) = P^{min}, \tag{A.367}$$

$$\frac{dP_T(t)}{dt} = 0 \Leftrightarrow P_{set} - \frac{1}{R}(\omega_m(t) - \omega_{set}) = 0, \tag{A.368}$$

else if $P_T(t) > P^{max}$ and $\frac{dP_T(t)}{dt} > 0$

$$P_T(t) = P^{max}, \tag{A.369}$$

$$\frac{dP_T(t)}{dt} = 0 \Leftrightarrow P_{set} - \frac{1}{R}(\omega_m(t) - \omega_{set}) = 0, \tag{A.370}$$

$$T_t \frac{dP_m(t)}{dt} = P_T(t) - P_m(t)\ , \tag{A.371}$$

$$0 = T_m(t)\omega_m(t) - P_m(t)\ . \tag{A.372}$$

For windup limits

$$T_G \frac{dP_T(t)}{dt} = P_{set} - \frac{1}{R}(\omega_m(t) - \omega_{set})\ , \tag{A.373}$$

$$T_t \frac{dP_m(t)}{dt} = P_T^*(t) - P_m(t)\ , \tag{A.374}$$

$$0 = T_m(t)\omega_m(t) - P_m(t)\ . \tag{A.375}$$

If $P^{min} \le P_T(t) \le P^{max}$

$$0 = P_T^*(t) - P_T(t), \tag{A.376}$$

else if $P_T(t) < P^{min}$

$$P_T^*(t) = P^{min}, \tag{A.377}$$

else if $P_T(t) > P^{max}$

$$P_T^*(t) = P^{max}. \tag{A.378}$$

5. Unit is on AGC, limits are not considered

The compact model is of the form:

$$T_G \frac{dP_T(t)}{dt} = P_{set}(t) - \frac{1}{R}(\omega_m(t) - \omega_{set})\ , \tag{A.379}$$

$$T_t \frac{dP_m(t)}{dt} = P_T(t) - P_m(t)\ , \tag{A.380}$$

$$\frac{dP_{set}(t)}{dt} = -K(B(\omega_m(t) - \omega_s) + P_{AGC})\ , \tag{A.381}$$

$$0 = T_m(t)\omega_m(t) - P_m(t)\ . \tag{A.382}$$

6. Unit is on AGC, limits are considered

The compact model is of the form:

For non-windup limits

If $P^{min} \le P_T(t) \le P^{max}$

$$T_G \frac{dP_T(t)}{dt} = P_{set}(t) - \frac{1}{R}(\omega_m(t) - \omega_{set}), \tag{A.383}$$

else if $P_T(t) < P^{min}$ and $\frac{dP_T(t)}{dt} < 0$

$$P_T(t) = P^{min}, \tag{A.384}$$

$$\frac{dP_T(t)}{dt} = 0 \Leftrightarrow P_{set}(t) - \frac{1}{R}(\omega_m(t) - \omega_{set}) = 0\ , \tag{A.385}$$

else if $P_T(t) > P^{max}$ and $\frac{dP_T(t)}{dt} > 0$

$$P_T(t) = P^{max}, \tag{A.386}$$

$$\frac{dP_T(t)}{dt} = 0 \Leftrightarrow P_{set}(t) - \frac{1}{R}(\omega_m(t) - \omega_{set}) = 0, \tag{A.387}$$

$$T_t \frac{dP_m(t)}{dt} = P_T(t) - P_m(t)\ , \tag{A.388}$$

$$\frac{dP_{set}(t)}{dt} = -K(B(\omega_m(t) - \omega_s) + P_{AGC})\ , \tag{A.389}$$

$$0 = T_m(t)\omega_m(t) - P_m(t)\ . \tag{A.390}$$

For windup limits

$$T_G \frac{dP_T(t)}{dt} = P_{set}(t) - \frac{1}{R}(\omega_m(t) - \omega_{set})\ , \tag{A.391}$$

$$T_t \frac{dP_m(t)}{dt} = P_T^*(t) - P_m(t)\ , \tag{A.392}$$

$$\frac{dP_{set}(t)}{dt} = -K(B(\omega_m(t) - \omega_s) + P_{AGC})\ , \tag{A.393}$$

$$0 = T_m(t)\omega_m(t) - P_m(t)\ . \tag{A.394}$$

If $P^{min} \le P_T(t) \le P^{max}$

$$0 = P_T^*(t) - P_T(t), \tag{A.395}$$

else if $P_T(t) < P^{min}$

$$P_T^*(t) = P^{min}, \tag{A.396}$$

else if $P_T(t) > P^{max}$

$$P_T^*(t) = P^{max}. \tag{A.397}$$

A.3.7 Excitation System Model

A.3.7.1 Constant Voltage/Current Excitation System Model

In this model the dynamic effects of the excitation and voltage-regulation system are ignored. In steady-state and quasi-static analysis it is assumed that the generator terminal voltage is maintained constant, by a voltage-regulating system that acts practically instantaneously. For more detailed transient analysis it is assumed that a constant DC voltage source is connected to the field terminal that can act as an ideal voltage source, a voltage source with internal resistance, or as an ideal current source. However, since the transients of such a source are very fast compared to the time scales of interest for quasi-steady-state analysis they will be normally neglected if such a model is used.

Three operating modes are specified:

(a) The model provides a constant DC field voltage to the generator field terminal. The field voltage does not change during transient operation of the generator, but is kept constant. It is equivalent to connecting an ideal constant DC source to the generator field.

(b) The model operates as a constant DC voltage source behind an internal impedance. It is equivalent to connecting a DC voltage source with an internal impedance to the

field terminal of the generator. The internal EMF of the DC source is constant, but the field voltage is not constant, as there is a voltage drop across the internal source impedance that is proportional to the field current.

(c) The model provides a constant DC field current value to the generator field winding. The field current is kept constant during the transient operation of the generator. It is equivalent to connecting an ideal current source to the generator field winding. This mode may cause numerical problems in the time domain simulation, because of the step changes in the field winding current, due to the series connection of a current source with an inductor. Therefore, its implementation might not be very practical.

The above three modes of operation are defined as (a) constant field-voltage mode, (b) DC-voltage-source mode, and (c) current-source mode.

(a) Constant field-voltage mode

The constant field voltage mode assumes that the field voltage is specified and remains constant. The two equations for this model are

$$v_f(t) = V_{specified} \,, \tag{A.398}$$

$$v_{fn}(t) = 0 \,. \tag{A.399}$$

Note, that special care needs to be taken in this case, in case a loss of excitation fault is to be applied. In that case, the only possible and meaningful fault that can be considered is a full loss of excitation, in which case the applied voltage becomes zero. This is equivalent to replacing the above two equations by

$$v_f(t) = 0 \,, \tag{A.400}$$

$$v_{fn}(t) = 0. \tag{A.401}$$

(b) DC-voltage -source mode

The DC-voltage-source mode assumes that a constant, non-ideal DC source, with an internal impedance is connected to the field terminal, supplying the field voltage. The compact equations for this model are

1. Pure resistive internal impedance model

The voltage source with internal resistance is illustrated in Figure A.24.

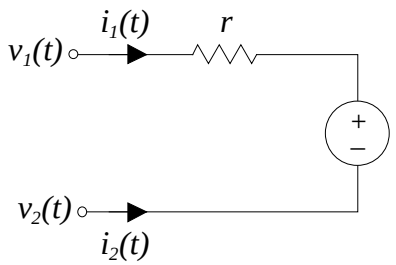

Figure A.24: Voltage source with internal resistance.

The compact model is

$$i_1(t) = g(v_1(t) - v_2(t) - V_{DC}) , \tag{A.402}$$

$$i_2(t) = -i_1(t) , \tag{A.403}$$

where $g = \frac{1}{r}$ is the conductance of the resistor and V_{DC} denotes the voltage value of the source.

2. Pure Inductive Internal Impedance Model

The voltage source with internal resistance is illustrated in Figure A.25.

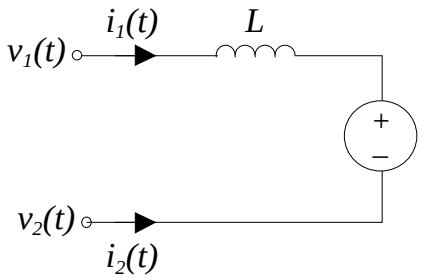

Figure A.25: Voltage source with internal inductance.

The compact model is

$$0 = v_1(t) - v_2(t) - L\frac{di_1(t)}{dt} - V_{DC}\ , \tag{A.404}$$

$$i_2(t) = -i_1(t)\ . \tag{A.405}$$

V_{DC} denotes the voltage value of the source.

3. Resistive-Inductive Internal Impedance Model

The voltage source with internal resistance is illustrated in Figure A.26.

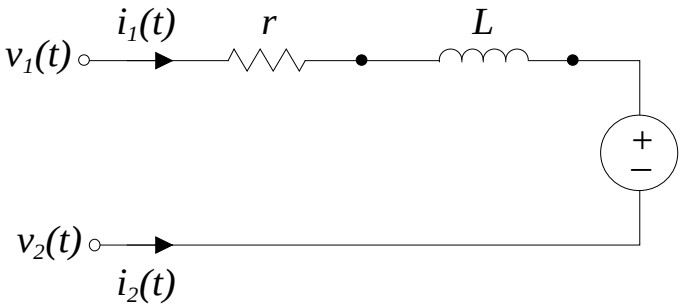

Figure A.26: Voltage source with internal impedance.

The compact model is

$$i_1(t) = g(v_1(t) - v_2(t)) - gL\frac{di_1(t)}{dt} - gV_{DC}\ , \tag{A.406}$$

$$i_2(t) = -i_1(t)\ . \tag{A.407}$$

V_{DC} denotes the voltage value of the source.

(c) Current Source

The current source diagram is illustrated in Figure A.27.

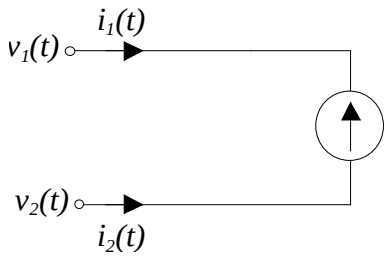

Figure A.27: Current-source circuit.

The compact model is

$$i_1(t) = -I_{DC}\ , \tag{A.408}$$

$$i_2(t) = -i_1(t). \tag{A.409}$$

I_{DC} denotes the value of the current source.

A.3.7.2 Generic Excitation System Model

This model of the excitation system assumes that a DC generator is acting as the excitation system of the unit. The exciter is modeled as a DC source with internal impedance connected to the field terminal, as in the previous section. However, now the DC source is not constant, but a DC motor whose armature is connected to the field terminals of the generator. The source impedance is simply the armature impedance of the DC machine.

Three cases are defined based on the armature impedance of the DC exciter: pure resistive, pure inductive and resistive inductive. The DC armature circuit of these three

cases is illustrated the same way as in Figure A.24 through Figure A.26. The following sets of DAEs describe the model of the excitation system in compact form.

If no limits are imposed:

Pure resistive model

$$i_1(t) = g(v_1(t) - v_2(t) - V_{DC}(t)), \tag{A.410}$$

$$i_2(t) = -i_1(t). \tag{A.411}$$

Pure inductive model

$$0 = v_1(t) - v_2(t) - L\frac{di_1(t)}{dt} - V_{DC}(t), \tag{A.412}$$

$$i_2(t) = -i_1(t). \tag{A.413}$$

Resistive inductive model

$$i_1(t) = g(v_1(t) - v_2(t)) - gL\frac{di_1(t)}{dt} - gV_{DC}, \tag{A.414}$$

$$i_2(t) = -i_1(t). \tag{A.415}$$

$$T_E\frac{dV_{DC}(t)}{dt} = -\Big(K_E + S_E\big(V_{DC}(t)\big)\Big)V_{DC}(t) + V_R(t), \tag{A.416}$$

$$T_A\frac{dV_R(t)}{dt} = -V_R(t) + K_A R_f(t) - \frac{K_A K_F}{T_F}V_{DC}(t) + K_A\big(V_{ref} - V_t(t) + V_s(t)\big), \tag{A.417}$$

$$T_F\frac{dR_f(t)}{dt} = -R_f(t) + \frac{K_F}{T_F}V_{DC}(t), \tag{A.418}$$

where $g = \frac{1}{r}$ is the conductance of the resistor. The function $S_E(V_{DC})$ models the saturation of the exciter [133]. If no exciter saturation is modeled then $S_E(V_{DC}) = 0$. The first differential equation represents the dynamics of the DC machine. The armature dynamics are neglected. The second differential equation models the voltage regulator.

V_{ref} is a model input, while $V_t(t)$ is a feedback of the unit terminal voltage that is to be regulated. It can be uncompensated or compensated, to accommodate parallel operation of two units connected at the same bus, using load compensation. The last differential equation models the dynamic behavior of the stabilizing transformer of the system.

If non-windup limits are imposed to the voltage regulator output the compact model is modified as follows:

If $V_R^{min} < V_R(t) < V_R^{max}$

$$T_A \frac{dV_R(t)}{dt} = -V_R(t) + K_A R_f(t) - \frac{K_A K_F}{T_F} V_{DC}(t) + K_A\big(V_{ref} - V_t(t) + V_s(t)\big), \quad \text{(A.419)}$$

else if $V_R(t) \leq V_R^{min}$ and $\frac{dV_R(t)}{dt} < 0$

$$V_R(t) = V_R^{min}, \quad \text{(A.420)}$$

$$\frac{dV_R(t)}{dt} = 0 \Leftrightarrow 0 = -V_R(t) + K_A R_f(t) - \frac{K_A K_F}{T_F} V_{DC}(t) + K_A\big(V_{ref} - V_t(t) - V_s(t)\big), \quad \text{(A.421)}$$

else if $V_R(t) \geq V_R^{max}$ and $\frac{dV_R(t)}{dt} > 0$

$$V_R(t) = V_R^{max}, \quad \text{(A.422)}$$

$$\frac{dV_R(t)}{dt} = 0 \Leftrightarrow 0 = -V_R(t) + K_A R_f(t) - \frac{K_A K_F}{T_F} V_{DC}(t) + K_A\big(V_{ref} - V_t(t) - V_s(t)\big), \quad \text{(A.423)}$$

else if $V_R(t) \leq V_R^{min}$ and $\frac{dV_R(t)}{dt} \geq 0$

$$T_A \frac{dV_R(t)}{dt} = -V_R(t) + K_A R_f(t) - \frac{K_A K_F}{T_F} V_{DC}(t) + K_A\big(V_{ref} - V_t(t) + V_s(t)\big), \quad \text{(A.424)}$$

$$V_R(t) = V_R^{min}, \quad \text{(A.425)}$$

else if $V_R(t) \geq V_R^{max}$ and $\frac{dV_R(t)}{dt} \leq 0$

$$T_A \frac{dV_R(t)}{dt} = -V_R(t) + K_A R_f(t) - \frac{K_A K_F}{T_F} V_{DC}(t) + K_A\big(V_{ref} - V_t(t) + V_s(t)\big), \quad \text{(A.426)}$$

$$V_R(t) = V_R^{max}. \quad \text{(A.427)}$$

If windup limits are imposed to the voltage regulator output the compact model is modified as follows:

If $V_R^{min} < V_R(t) < V_R^{max}$

$$T_E \frac{dV_{DC}(t)}{dt} = -\Big(K_E + S_E\big(V_{DC}(t)\big)\Big) V_{DC}(t) + V_R(t), \quad \text{(A.428)}$$

$$T_A \frac{dV_R(t)}{dt} = -V_R(t) + K_A R_f(t) - \frac{K_A K_F}{T_F} V_{DC}(t) + K_A\big(V_{ref} - V_t(t) + V_s(t)\big), \quad \text{(A.429)}$$

else if $V_R(t) \leq V_R^{min}$

$$T_E \frac{dV_{DC}(t)}{dt} = -\Big(K_E + S_E\big(V_{DC}(t)\big)\Big) V_{DC}(t) + V_R^*(t), \quad \text{(A.430)}$$

$$V_R^*(t) = V_R^{min}, \quad \text{(A.431)}$$

$$T_A \frac{dV_R(t)}{dt} = -V_R(t) + K_A R_f(t) - \frac{K_A K_F}{T_F} V_{DC}(t) + K_A\big(V_{ref} - V_t(t) + V_s(t)\big), \quad \text{(A.432)}$$

else if $V_R(t) \geq V_R^{max}$

$$T_E \frac{dV_{DC}(t)}{dt} = -\Big(K_E + S_E\big(V_{DC}(t)\big)\Big) V_{DC}(t) + V_R^*(t), \quad \text{(A.433)}$$

$$V_R^*(t) = V_R^{max}, \quad \text{(A.434)}$$

$$T_A \frac{dV_R(t)}{dt} = -V_R(t) + K_A R_f(t) - \frac{K_A K_F}{T_F} V_{DC}(t) + K_A\big(V_{ref} - V_t(t) + V_s(t)\big). \quad \text{(A.435)}$$

A.4 Single-Phase Static VAr Compensator Model

A.4.1 Overview

This section describes a simplified model of a single-phase static VAr compensator (SVC). The SVC system, including its control subsystems, is modeled as a variable susceptance, controlled via a terminal-voltage feedback loop. Two models are considered: (a) a total susceptance model and (b) a conductance-angle model. Models for steady-state and quasi-static analysis are developed.

A.4.2 Model Parameters and User Interface

This section presents the input parameters for defining the model of the single-phase static VAr system as well as the user interface to define these parameters. The model parameters are illustrated in Figure A.28.

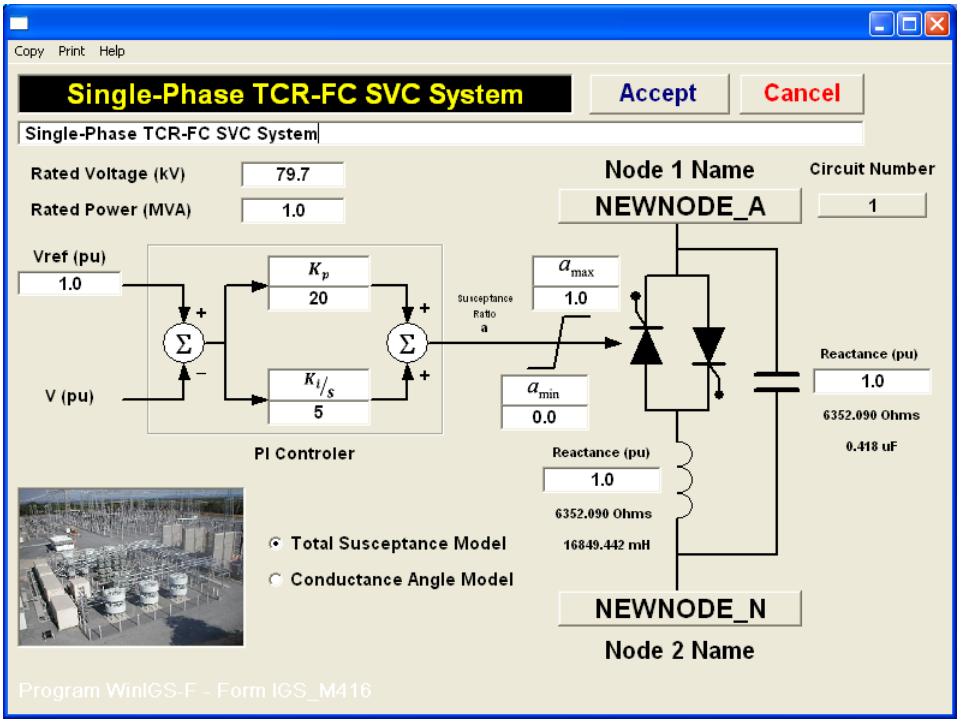

Figure A.28: User interface of SVC model.

A.4.3 Steady-State Model

A.4.3.1 Compact Model

(a) Total susceptance model

The steady-state model in compact form is described by equations (A.336) to (A.341).

$$\tilde{I}_{SVC1} = jB_C\left(\tilde{V}_1 - \tilde{V}_2\right) - jB_R\left(\tilde{V}_1 - \tilde{V}_2\right), \quad \text{(A.336)}$$

$$\tilde{I}_{SVC2} = jB_C\left(\tilde{V}_2 - \tilde{V}_1\right) - jB_R\left(\tilde{V}_2 - \tilde{V}_1\right), \quad \text{(A.337)}$$

$$0 = B_R - \frac{1}{X_L}\alpha. \quad \text{(A.338)}$$

If $\alpha_{min} < \alpha < \alpha_{max}$

$$0 = \left|\tilde{V}_1 - \tilde{V}_2\right| - V_R, \quad \text{(A.339)}$$

else if $\alpha \leq \alpha_{min}$

$$0 = \alpha - \alpha_{min}, \quad \text{(A.340)}$$

else if $\alpha \geq \alpha_{max}$

$$0 = \alpha - \alpha_{max}, \quad \text{(A.341)}$$

where

$\tilde{I}_{SVC1}$: is the phasor of the injected current by the SVC at terminal 1;

$\tilde{I}_{SVC2}$: is the phasor of the injected current by the SVC at terminal 2;

$\tilde{V}_1$: is the phasor of the terminal 1 voltage of the SVC;

$\tilde{V}_2$: is the phasor of the terminal 2 voltage of the SVC;

B_R : is the equivalent susceptance of the TCR;

B_C : is the susceptance of the fixed capacitor;

V_R : is the regulated voltage setpoint;

X_L : is the reactance of the TCR;

α : is the factor with value between 0 and 1 determining the TCR susceptance;

α_{min} : is the minimum value of factor α;

α_{max} : is the maximum value of factor α.

(b) Conductance-angle model

The steady-state model in compact form is described by equations (A.342) to (A.347).

$$\tilde{I}_{SVC1} = jB_C\left(\tilde{V}_1 - \tilde{V}_2\right) - jB_R\left(\tilde{V}_1 - \tilde{V}_2\right), \quad \text{(A.342)}$$

$$\tilde{I}_{SVC2} = jB_C\left(\tilde{V}_2 - \tilde{V}_1\right) - jB_R\left(\tilde{V}_2 - \tilde{V}_1\right), \quad \text{(A.343)}$$

$$0 = B_R - \frac{1}{\pi X_L}\sigma + \frac{1}{\pi X_L} sin\sigma. \quad \text{(A.344)}$$

If $\sigma_{min} < \sigma < \sigma_{max}$

$$0 = \left|\tilde{V}_1 - \tilde{V}_2\right| - V_R, \quad \text{(A.345)}$$

else if $\sigma \leq \sigma_{min}$

$$0 = \sigma - \sigma_{min}, \quad \text{(A.346)}$$

else if $\sigma \geq \sigma_{max}$

$$0 = \sigma - \sigma_{max}, \quad \text{(A.347)}$$

where

$\tilde{I}_{SVC1}$: is the phasor of the injected current by the SVC at terminal 1;

$\tilde{I}_{SVC2}$: is the phasor of the injected current by the SVC at terminal 2;

$\tilde{V}_1$: is the phasor of the terminal 1 voltage of the SVC;

$\tilde{V}_2$: is the phasor of the terminal 2 voltage of the SVC;

B_R : is the equivalent susceptance of the TCR;

B_C : is the susceptance of the fixed capacitor;

V_R : is the regulated voltage setpoint;

σ : is the conductance angle in rad;

X_L : is the reactance of the TCR;

σ_{min} : is the minimum conductance angle of the TCR;

σ_{max} : is the maximum conductance angle of the TCR.

A.4.3.2 Equivalent Quadratic Model

(a) Total susceptance model

The steady-state equivalent quadratic model is described by equations (A.348) through (A.356).

$$I_{SVC1,r} = -B_C V_{1i} + B_C V_{2i} + B_R V_{1i} - B_R V_{2i}, \quad \text{(A.348)}$$

$$I_{SVC1,i} = B_C V_{1r} - B_C V_{2r} - B_r V_{1r} + B_R V_{2r}, \quad \text{(A.349)}$$

$$I_{SVC2,r} = B_C V_{1i} - B_C V_{2i} - B_R V_{1i} + B_R V_{2i}, \quad \text{(A.350)}$$

$$I_{SVC2,i} = -B_C V_{1r} + B_C V_{2r} + B_R V_{1r} - B_R V_{2r}, \quad \text{(A.351)}$$

$$0 = B_R - \frac{1}{X_L}\alpha. \quad \text{(A.352)}$$

If $\alpha_{min} < \alpha < \alpha_{max}$

$$0 = V_m - V_R, \quad \text{(A.353)}$$

else if $\alpha \leq \alpha_{min}$

$$0 = \alpha - \alpha_{min}, \quad \text{(A.354)}$$

else if $\alpha \geq \alpha_{max}$

$$0 = \alpha - \alpha_{max}, \quad \text{(A.355)}$$

$$0 = V_m^2 - V_{1r}^2 - V_{2r}^2 + 2V_{1r}V_{2r} - V_{1i}^2 - V_{2i}^2 + 2V_{1i}V_{2i}, \quad \text{(A.356)}$$

where the subscripts r and i denote the real and imaginary parts. The state vector is defined as

$x^T = [V_{1r} \quad V_{1i} \quad V_{2r} \quad V_{2i} \quad B_R \quad \sigma \quad V_m]$.

The through variables are I_{1r}, I_{1i}, I_{2r}, I_{2i}.

The external states are V_{1r}, V_{1i}, V_{2r}, V_{2i}.

The internal states are B_R, σ, V_m.

(b) Conductance-angle model

The steady-state equivalent quadratic model is described by equations (A.357) through (A.373). Notice that the only way to "quadratize" the model is by introducing a Taylor series approximation for the $sin\sigma$ term.

$$I_{SVC1,r} = -B_C V_{1i} + B_C V_{2i} + B_R V_{1i} - B_R V_{2i}, \quad \text{(A.357)}$$

$$I_{SVC1,i} = B_C V_{1r} - B_C V_{2r} - B_r V_{1r} + B_R V_{2r}, \quad \text{(A.358)}$$

$$I_{SVC2,r} = B_C V_{1i} - B_C V_{2i} - B_R V_{1i} + B_R V_{2i}, \quad \text{(A.359)}$$

$$I_{SVC2,i} = -B_C V_{1r} + B_C V_{2r} + B_R V_{1r} - B_R V_{2r}. \quad \text{(A.360)}$$

If $\sigma_{min} < \sigma < \sigma_{max}$

$$0 = V_m - V_R, \quad \text{(A.361)}$$

else if $\sigma \leq \sigma_{min}$

$$0 = \sigma - \sigma_{min}, \quad \text{(A.362)}$$

else if $\sigma \geq \sigma_{max}$

$$0 = \sigma - \sigma_{max}, \quad \text{(A.363)}$$

$$0 = B_R - \frac{1}{\pi X_L}\sigma + \frac{1}{\pi X_L}s, \quad \text{(A.364)}$$

$$0 = s - \sigma + \frac{1}{6}y_3 - \frac{1}{120}y_5 + \frac{1}{7!}y_7 - \frac{1}{9!}y_9 + \frac{1}{11!}y_{11} - \frac{1}{13!}y_{13}\ , \quad \text{(A.365)}$$

$$0 = y_2 - \sigma^2, \quad \text{(A.366)}$$

$$0 = y_3 - \sigma y_2, \quad \text{(A.367)}$$

$$0 = y_5 - y_3 y_2, \quad \text{(A.368)}$$

$$0 = y_7 - y_5 y_2, \quad \text{(A.369)}$$

$$0 = y_9 - y_7 y_2, \quad \text{(A.370)}$$

$$0 = y_{11} - y_9 y_2, \quad \text{(A.371)}$$

$$0 = y_{13} - y_{11} y_2, \quad \text{(A.372)}$$

$$0 = V_m^2 - V_{1r}^2 - V_{2r}^2 + 2V_{1r}V_{2r} - V_{1i}^2 - V_{2i}^2 + 2V_{1i}V_{2i}, \quad \text{(A.373)}$$

where the subscripts r and i denote the real and imaginary parts. The state vector is defined as

$$x^T = [V_{1r} \quad V_{1i} \quad V_{2r} \quad V_{2i} \quad \sigma \quad B_R \quad s \quad y_2 \quad y_3 \quad y_5 \quad y_7 \quad y_9 \quad y_{11} \quad y_{13} \quad V_m] .$$

The through variables are I_{1r}, I_{1i}, I_{2r}, I_{2i}.

The external states are V_{1r}, V_{1i}, V_{2r}, V_{2i}.

The internal states are: σ, B_R, s, y_2, y_3, y_5, y_7, y_9, y_{11}, y_{13}, V_m.

A.4.4 Quasi-Static Model

A.4.4.1 Compact Model

(a) Total susceptance model

The quasi-static model in compact form is described by equations (A.374) to (A.380).

$$\tilde{I}_{SVC1} = jB_C\big(\tilde{V}_1(t) - \tilde{V}_2(t)\big) - jB_R\big(\tilde{V}_1(t) - \tilde{V}_2(t)\big), \quad \text{(A.374)}$$

$$\tilde{I}_{SVC2} = jB_C\big(\tilde{V}_2(t) - \tilde{V}_1(t)\big) - jB_R\big(\tilde{V}_2(t) - \tilde{V}_1(t)\big), \quad \text{(A.375)}$$

$$\dot{x}(t) = K_i\big(V_R - \big|\tilde{V}_1(t) - \tilde{V}_2(t)\big|\big), \quad \text{(A.376)}$$

$$0 = x(t) + K_p\big(V_R - \big|\tilde{V}_1(t) - \tilde{V}_2(t)\big|\big) - \alpha(t). \quad \text{(A.377)}$$

If $\alpha_{min} < \alpha(t) < \alpha_{max}$

$$0 = B_R - \frac{1}{X_L}\alpha, \quad \text{(A.378)}$$

else if $\alpha \leq \alpha_{min}$

$$0 = B_R - \frac{1}{X_L}\alpha_{min}, \tag{A.379}$$

else if $\alpha \geq \alpha_{max}$

$$0 = B_R - \frac{1}{X_L}\alpha_{max}, \tag{A.380}$$

where

$\tilde{I}_{SVC1}$: is the phasor of the injected current by the SVC at terminal 1;

$\tilde{I}_{SVC2}$: is the phasor of the injected current by the SVC at terminal 2;

$\tilde{V}_1(t)$: is the phasor of the terminal 1 voltage of the SVC;

$\tilde{V}_2(t)$: is the phasor of the terminal 2 voltage of the SVC;

$B_R(t)$: is the equivalent susceptance of the TCR;

B_C : is the susceptance of the fixed capacitor;

V_R : is the regulated voltage setpoint;

X_L : is the reactance of the TCR;

$\alpha(t)$: is the factor with value between 0 and 1 determining the TCR susceptance;

α_{min} : is the minimum value of factor α;

α_{max}: is the maximum value of factor α;

K_i : is the integral gain of the PI controller;

K_p : is the proportional gain of the PI controller.

(b) Conductance-angle model

The steady-state model in compact form is described by equations (A.381) to (A.387).

$$\tilde{I}_{SVC1} = jB_C\left(\tilde{V}_1(t) - \tilde{V}_2(t)\right) - jB_R\left(\tilde{V}_1(t) - \tilde{V}_2(t)\right), \quad \text{(A.381)}$$

$$\tilde{I}_{SVC2} = jB_C\left(\tilde{V}_2(t) - \tilde{V}_1(t)\right) - jB_R\left(\tilde{V}_2(t) - \tilde{V}_1(t)\right), \quad \text{(A.382)}$$

$$\dot{x}(t) = K_i\left(V_R - \left|\tilde{V}_1(t) - \tilde{V}_2(t)\right|\right), \quad \text{(A.383)}$$

$$0 = x(t) + K_p\left(V_R - \left|\tilde{V}_1(t) - \tilde{V}_2(t)\right|\right) - \sigma(t). \quad \text{(A.384)}$$

If $\sigma_{min} < \sigma < \sigma_{max}$

$$0 = B_R(t) - \frac{1}{\pi X_L}\sigma(t) + \frac{1}{\pi X_L} sin\sigma(t), \quad \text{(A.385)}$$

else if $\sigma \leq \sigma_{min}$

$$0 = B_R(t) - \frac{1}{\pi X_L}\sigma_{min} + \frac{1}{\pi X_L} sin\sigma_{min}, \quad \text{(A.386)}$$

else if $\sigma \geq \sigma_{max}$

$$0 = B_R(t) - \frac{1}{\pi X_L}\sigma_{max} + \frac{1}{\pi X_L} sin\sigma_{max}, \quad \text{(A.387)}$$

where

$\tilde{I}_{SVC1}$: is the phasor of the injected current by the SVC at terminal 1;

$\tilde{I}_{SVC2}$: is the phasor of the injected current by the SVC at terminal 2;

$\tilde{V}_1(t)$: is the phasor of the terminal 1 voltage of the SVC;

$\tilde{V}_2(t)$: is the phasor of the terminal 2 voltage of the SVC;

$B_R(t)$: is the equivalent susceptance of the TCR;

B_C : is the susceptance of the fixed capacitor;

V_R : is the regulated voltage setpoint;

$\sigma(t)$: is the conductance angle in rad;

X_L : is the reactance of the TCR;

σ_{min} : is the minimum conductance angle of the TCR;

σ_{max} : is the maximum conductance angle of the TCR;

K_i : is the integral gain of the PI controller;

K_p : is the proportional gain of the PI controller.

A.4.4.2 Equivalent Quadratic Model

(a) Total susceptance model

The steady-state equivalent quadratic model is described by equations (A.388) through (A.397).

$$I_{SVC1,r} = -B_C V_{1i}(t) + B_C V_{2i}(t) + B_R(t)V_{1i}(t) - B_R(t)V_{2i}(t), \quad \text{(A.388)}$$

$$I_{SVC1,i} = B_C V_{1r}(t) - B_C V_{2r}(t) - B_R(t)V_{1r}(t) + B_R(t)V_{2r}(t), \quad \text{(A.389)}$$

$$I_{SVC2,r} = B_C V_{1i}(t) - B_C V_{2i}(t) - B_R(t)V_{1i}(t) + B_R(t)V_{2i}(t), \quad \text{(A.390)}$$

$$I_{SVC2,i} = -B_C V_{1r}(t) + B_C V_{2r}(t) + B_R(t)V_{1r}(t) - B_R(t)V_{2r}(t), \quad \text{(A.391)}$$

$\dot{x}(t) = x'(t)$,

$0 = x'(t) - K_i(V_R - V_m(t))$, (A.392)

$$0 = x(t) + K_p(V_R - V_m(t)) - \sigma(t)\ . \tag{A.393}$$

If $\alpha_{min} < \alpha(t) < \alpha_{max}$

$$0 = B_R(t) - \frac{1}{X_L}\alpha(t), \tag{A.394}$$

else if $\alpha(t) \leq \alpha_{min}$

$$0 = B_R(t) - \frac{1}{X_L}\alpha_{min}, \tag{A.395}$$

else if $\alpha \geq \alpha_{max}$

$$0 = B_R(t) - \frac{1}{X_L}\alpha_{max}, \tag{A.396}$$

$$0 = V_m^2(t) - V_{1r}^2(t) - V_{2r}^2(t) + 2V_{1r}(t)V_{2r}(t) - V_{1i}^2(t) - V_{2i}^2(t) + 2V_{1i}(t)V_{2i}(t), \tag{A.397}$$

where the subscripts r and i denote the real and imaginary parts. The state vector is defined as

$$x^T = [V_{1r}(t) \quad V_{1i}(t) \quad V_{2r}(t) \quad V_{2i}(t) \quad x(t) \quad x'(t) \quad \sigma(t) \quad B_R(t) \quad V_m(t)]\ .$$

The through variables are I_{1r}, I_{1i}, I_{2r}, I_{2i}.

The external states are $V_{1r}(t)$, $V_{1i}(t)$, $V_{2r}(t)$, $V_{2i}(t)$.

The internal states are $x(t)$, $x'(t)$, $\sigma(t)$, $B_R(t)$, $V_m(t)$.

(b) Conductance angle model

The steady-state equivalent quadratic model is described by equations (A.398) through (A.413). Notice that the only way to "quadratize" the model is by introducing a Taylor series approximation for the $sin\sigma$ term.

$$I_{SVC1,r} = -B_C V_{1i}(t) + B_C V_{2i}(t) + B_R(t)V_{1i}(t) - B_R(t)V_{2i}(t), \tag{A.398}$$

$$I_{SVC1,i} = B_C V_{1r}(t) - B_C V_{2r}(t) - B_R(t) V_{1r}(t) + B_R(t) V_{2r}(t), \quad \text{(A.399)}$$

$$I_{SVC2,r} = B_C V_{1i}(t) - B_C V_{2i}(t) - B_R(t) V_{1i}(t) + B_R(t) V_{2i}(t), \quad \text{(A.400)}$$

$$I_{SVC2,i} = -B_C V_{1r}(t) + B_C V_{2r}(t) + B_R(t) V_{1r}(t) - B_R(t) V_{2r}(t). \quad \text{(A.401)}$$

If $\sigma_{min} < \sigma(t) < \sigma_{max}$

$$0 = B_R(t) - \frac{1}{\pi X_L}\sigma(t) + \frac{1}{\pi X_L} s(t), \quad \text{(A.402)}$$

else if $\sigma(t) \leq \sigma_{min}$

$$0 = B_R(t) - \frac{1}{\pi X_L}\sigma_{min} + \frac{1}{\pi X_L} sin\sigma_{min}, \quad \text{(A.403)}$$

else if $\sigma(t) \geq \sigma_{max}$

$$0 = B_R(t) - \frac{1}{\pi X_L}\sigma_{max} + \frac{1}{\pi X_L} sin\sigma_{max}, \quad \text{(A.404)}$$

$$0 = s(t) - \sigma(t) + \frac{1}{6} y_3(t) - \frac{1}{120} y_5(t) + \frac{1}{7!} y_7(t) - \frac{1}{9!} y_9(t) + \frac{1}{11!} y_{11}(t) - \frac{1}{13!} y_{13}(t)\ , \quad \text{(A.405)}$$

$$0 = y_2(t) - \sigma^2(t), \quad \text{(A.406)}$$

$$0 = y_3(t) - \sigma(t) y_2(t), \quad \text{(A.407)}$$

$$0 = y_5(t) - y_3(t) y_2(t), \quad \text{(A.408)}$$

$$0 = y_7(t) - y_5(t) y_2(t), \quad \text{(A.409)}$$

$$0 = y_9(t) - y_7(t) y_2(t), \quad \text{(A.410)}$$

$$0 = y_{11}(t) - y_9(t) y_2(t), \quad \text{(A.411)}$$

$$0 = y_{13}(t) - y_{11}(t) y_2(t), \quad \text{(A.412)}$$

$$0 = V_m^2(t) - V_{1r}^2(t) - V_{2r}^2(t) + 2V_{1r}(t)V_{2r}(t) - V_{1i}^2(t) - V_{2i}^2(t) + 2V_{1i}(t)V_{2i}(t), \quad \text{(A.413)}$$

where the subscripts r and i denote the real and imaginary parts.

The through variables are I_{1r}, I_{1i}, I_{2r}, I_{2i}.

The external states are $V_{1r}(t)$, $V_{1i}(t)$, $V_{2r}(t)$, $V_{2i}(t)$.

The internal states are: $\sigma(t)$, $B_R(t)$, $s(t)$, $y_2(t)$, $y_3(t)$, $y_5(t)$, $y_7(t)$, $y_9(t)$, $y_{11}(t)$, $y_{13}(t)$, $V_m(t)$.

A.5 Three-Phase Static VAr Compensator Model

A.5.1 Overview

This section of Appendix A presents the model of a three-phase static VAr system. The model extends the single-phase model presented in the previous section. Three modules of the single-phase model are used and only their connection needs to be additionally specified. The model equations for each of the three single-phase modules are the same as in section A.4, for both steady-state and quasi-static models. The possible connection types considered are wye and delta.

A.5.2 Wye Connection

The overall physical model of a wye-connected SVC is illustrated in Figure A.29.

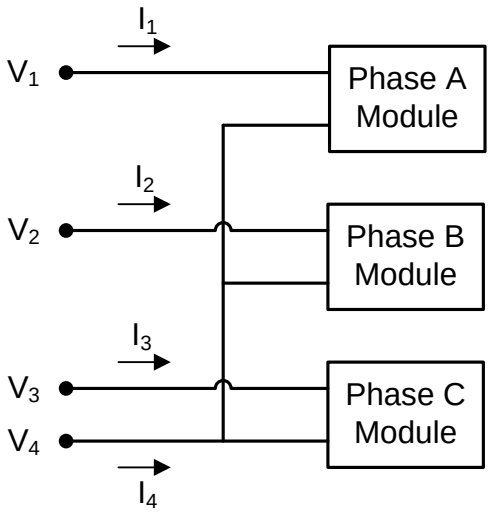

Figure A.29: Wye-connected SVC model.

Based on the connections of Figure A.29 the following relations hold that relate the new through variables (currents) and new external states with the variables of each individual module. It can be assumed that the external states and the through variables of each module become internal states of the three-phase device. There are 4 new external voltage variables, $\tilde{V}_1$ through $\tilde{V}_4$ and 2 new complex variables for each module (the through currents that now become states), so in total 4+6=10 new variables. The 10 new equations are

$$\tilde{I}_1 = \tilde{I}_{1A}, \tag{A.414}$$

$$\tilde{I}_2 = \tilde{I}_{1B}, \tag{A.415}$$

$$\tilde{I}_3 = \tilde{I}_{1C}, \tag{A.416}$$

$$\tilde{I}_4 = \tilde{I}_{2A} + \tilde{I}_{2B} + \tilde{I}_{2C}, \tag{A.417}$$

$$0 = \tilde{V}_1 - \tilde{V}_{1A}, \tag{A.418}$$

$$0 = \tilde{V}_4 - \tilde{V}_{2A}, \tag{A.419}$$

$$0 = \tilde{V}_2 - \tilde{V}_{1B}, \tag{A.420}$$

$$0 = \tilde{V}_4 - \tilde{V}_{2B}, \tag{A.421}$$

$$0 = \tilde{V}_3 - \tilde{V}_{1C}, \tag{A.422}$$

$$0 = \tilde{V}_4 - \tilde{V}_{2C}. \tag{A.423}$$

A.5.3 Delta Connection

The overall physical model of a delta-connected SVC is illustrated in Figure A.30.

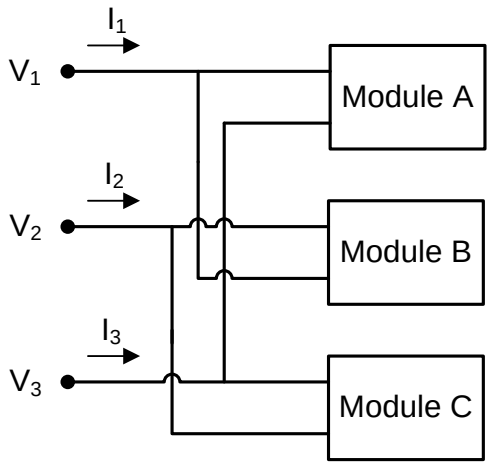

Figure A.30: Delta-connected SVC model.

Based on these connections of Figure A.30 the following relations hold that relate the new through variables (currents) and new external states with the variables of each individual module. It can be assumed that the external states and the through variables of each module become internal states of the three phase device. There are 3 new external voltage variables, $\tilde{V}_1$ through $\tilde{V}_6$ and 2 new complex variables for each module (the

through currents that now become states), so in total 3+6=9 new variables. The 9 new equations are

$$\tilde{I}_1 = \tilde{I}_{1A} + \tilde{I}_{2B}, \tag{A.424}$$

$$\tilde{I}_2 = \tilde{I}_{1B} + \tilde{I}_{2C}, \tag{A.425}$$

$$\tilde{I}_3 = \tilde{I}_{1C} + \tilde{I}_{2A}, \tag{A.426}$$

$$0 = \tilde{V}_1 - \tilde{V}_{1A}, \tag{A.427}$$

$$0 = \tilde{V}_3 - \tilde{V}_{2A}, \tag{A.428}$$

$$0 = \tilde{V}_2 - \tilde{V}_{1B}, \tag{A.429}$$

$$0 = \tilde{V}_1 - \tilde{V}_{2B}, \tag{A.430}$$

$$0 = \tilde{V}_3 - \tilde{V}_{1C}, \tag{A.431}$$

$$0 = \tilde{V}_2 - \tilde{V}_{2C}. \tag{A.432}$$

A.6 Nonlinear Inductor Model

A.6.1 Overview

This part of Appendix A presents the nonlinear, time-domain model of a saturable-core inductor. The model is used to capture nonlinearities that might occur during energization of transformers. Such condition may appear during cold-load pick-up after severe disturbances and transients in distribution feeders. The inductor is modeled by an analytical polynomial function of high degree. A full time-domain model is presented and implemented. The user specifies the parameters of the current-flux characteristic, which is assumed to have a fixed closed form. Subsequently, using the quadratic

equivalent model, the algebraic companion forms can be developed based on the quadratic integration or any other numerical integration rule.

A.6.2 Model Parameters and User Interface

The input parameters for defining the model of a nonlinear saturable-core inductor, as well as the user interface to define these parameters are presented in Figure A.31.

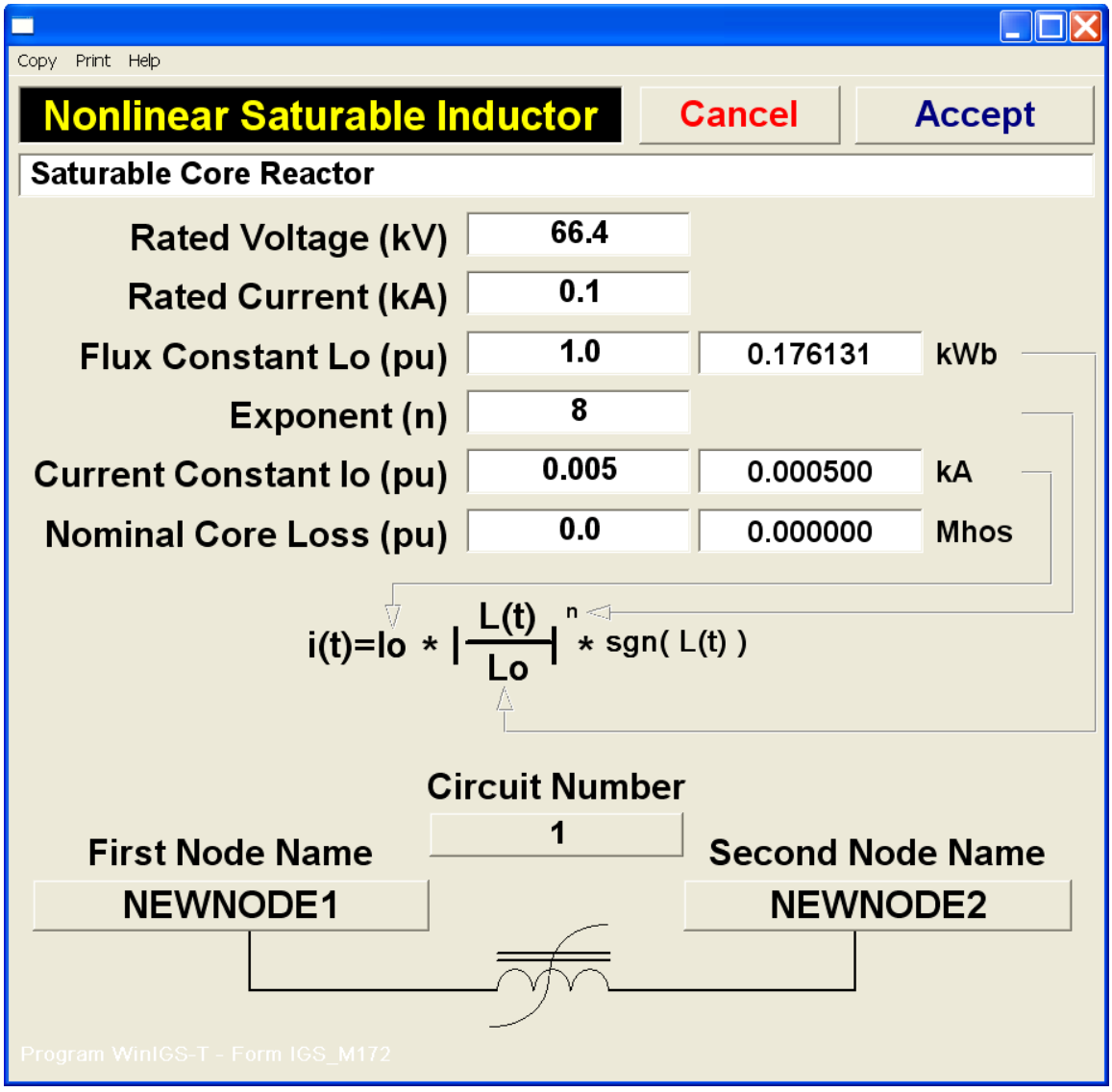

Figure A.31: Saturable-core inductor parameters and user interface.

A.6.3 Full Transient Model

A.6.3.1 Compact Model

The overall physical model of a saturable-core inductor is illustrated in Figure A.32. Two cases are considered: (a) pure (ideal) inductor and (b) inductor with core-loss modeling.

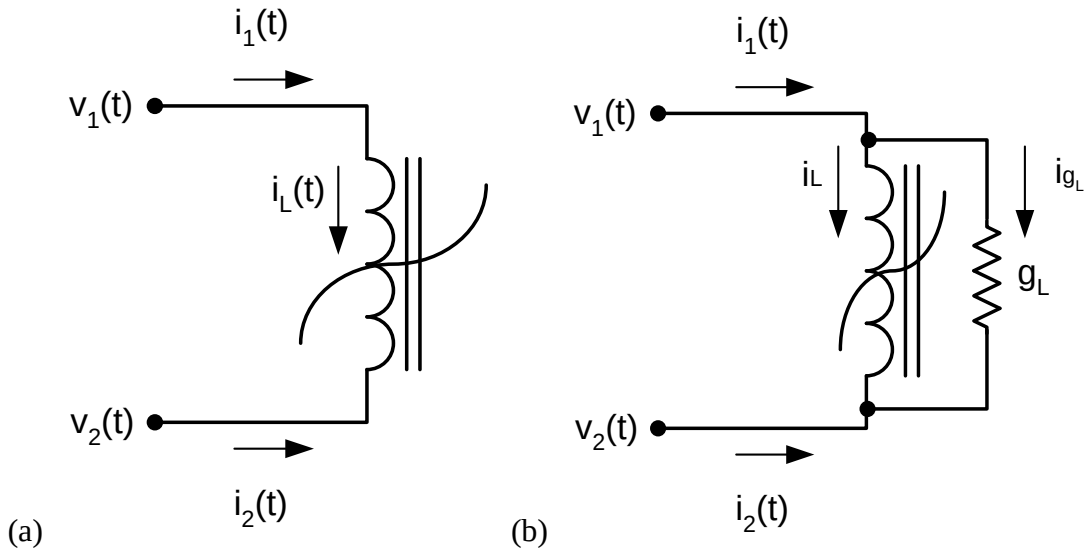

Figure A.32: Saturable-core inductor model: (a) pure inductor, (b) inductor with core-loss modeling.

(a) Pure Inductor Model

$$i_1(t) = i_L(t), \tag{A.433}$$

$$i_2(t) = -i_1(t), \tag{A.434}$$

$$\frac{d\lambda(t)}{dt} = v_L(t), \tag{A.435}$$

$$0 = v_L(t) - v_1(t) + v_2(t), \tag{A.436}$$

$$i_L(t) = i_0 \left|\frac{\lambda(t)}{\lambda_0}\right|^n sgn(\lambda(t)). \tag{A.437}$$

(b) Inductor Model with Core-Loss Modeling

$$i_1(t) = i_L(t) + i_{g_L}(t), \tag{A.438}$$

$$i_2(t) = -i_1(t), \tag{A.439}$$

$$\frac{d\lambda(t)}{dt} = v_L(t), \tag{A.440}$$

$$0 = i_{g_L}(t) - g_L v_L(t), \tag{A.441}$$

$$0 = v_L(t) - v_1(t) + v_2(t), \tag{A.442}$$

$$i_L(t) = i_0 \left|\frac{\lambda(t)}{\lambda_0}\right|^n sgn(\lambda(t)). \tag{A.443}$$

A.6.3.2 Equivalent Quadratic Model

The model is quadratized by introducing additional internal state variables, so that the n-th exponent is replaced by equations of at most quadratic degree. Since the exact degree of nonlinearity is not known until the user specifies it, the model performs automatic quadratization of the equations. A special procedure is used, so that the model is quadratized using the minimum number of additional internal states, while also maintaining the sparsity of the resulting equations. The methodology is based on expressing the exponent in binary form. The binary representation provides all the information about the number of new variables and equations that need to be introduced and about the form of the equations (products of new variables). The procedure is described later. Following this procedure the model can be converted into the standard quadratized form:

(a) Pure Inductor Model

$$i_1(t) = i_L(t), \tag{A.444}$$

$$i_2(t) = -i_1(t), \tag{A.445}$$

$$\frac{d\lambda(t)}{dt} = v_L(t), \tag{A.446}$$

$$0 = v_L(t) - v_1(t) + v_2(t), \tag{A.447}$$

$$i_L(t) = \frac{i_0}{|\lambda_0|^n} y_m(t)[sgn(\lambda(t))]^{n+1}, \tag{A.448}$$

$$0 = y_1(t) - \lambda^2(t), \tag{A.449}$$

$$0 = y_2(t) - y_1^2(t), \tag{A.450}$$

…

$$0 = y_{m1}(t) - y_{m1-1}^2(t), \tag{A.448+m_1}$$

$$0 = y_{m1+1}(t) - y_{i1}(t)y_{j1}(t), \tag{A.448+m_1+1}$$

$$0 = y_{m1+2}(t) - y_{m1+1}(t)y_{j2}(t), \tag{A.448+m_1+2}$$

…

$$\begin{cases} 0 = y_m(t) - y_{m-1}(t)y_{jm2}(t), & \text{if } n \text{ even,} \\ 0 = y_m(t) - y_{m-1}(t)\lambda(t), & \text{if } n \text{ odd.} \end{cases} \tag{A.448+m_1+m2}$$

(b) Inductor Model with Core-Loss Modeling

$$i_1(t) = i_L(t) + i_{g_L}(t), \tag{A.451}$$

$$i_2(t) = -i_1(t), \tag{A.452}$$

$$\frac{d\lambda(t)}{dt} = v_L(t), \tag{A.453}$$

$$0 = i_{g_L}(t) - g_L v_L(t), \tag{A.454}$$

$$0 = v_L(t) - v_1(t) + v_2(t), \tag{A.455}$$

$$i_L(t) = \frac{i_0}{|\lambda_0|^n} y_m(t)[sgn(\lambda(t))]^{n+1}, \tag{A.456}$$

$$0 = y_1(t) - \lambda^2(t), \tag{A.457}$$

$$0 = y_2(t) - y_1^2(t), \tag{A.458}$$

…

$$0 = y_{m1}(t) - y_{m1-1}^2(t), \tag{A.456+m_1}$$

$$0 = y_{m1+1}(t) - y_{i1}(t)y_{j1}(t), \tag{A.456+m_1+1}$$

$$0 = y_{m1+2}(t) - y_{m1+1}(t)y_{j2}(t), \tag{A.456+m_1+2}$$

…

$$\begin{cases} 0 = y_m(t) - y_{m-1}(t)y_{jm2}(t), & \text{if } n \text{ even,} \\ 0 = y_m(t) - y_{m-1}(t)\lambda(t), & \text{if } n \text{ odd.} \end{cases} \tag{A.456+m_1+m2}$$

Based on the above formulation, the number of additional internal states and equations m is computed as follows:

$m = m_1 + m_2$,

where

$m_1 = int(log_2(n))$,

m_2 = (# of ones in the binary representation of n) – 1.

The sets of indices i and j in the last set of equations (A.448+m_1+1 to A.448+m and A.456+m1+1 to A.456+m) are provided by positions of ones in the binary representation

of n. The values of these indices are equal to the values of the power of 2 corresponding to that position, meaning that the right most positions is indexed 0 and the left most indexed $int(log_2(n))$. The variable y_0 is by definition equal to λ, so it is not used and appears as λ in the equations. If the symbol y_0 was used instead of λ then only the first case in equations (A.448+m_1+m_2) and (A.456+m1+m2) would have been necessary, since this would include the second when the index becomes 0. However, since λ is physically related to flux, for the time being the use of this symbol is preferred instead.

A.7 Single-Phase Saturable-Core Transformer Model

A.7.1 Overview

This section of Appendix A presents the nonlinear, time-domain model of a single-phase, saturable-core transformer. The model utilizes the inductor model presented in the previous section and is used to represent nonlinearities that might occur during energization of transformers. Such condition may appear during cold load pick-up after severe disturbances and transients in distribution feeders. A full time-domain model is presented and implemented. The user specifies the parameters of the standard transformer as well as the parameters of the current-flux characteristic of the nonlinear inductor, referred to the primary side. Subsequently, using the quadratic equivalent model, the algebraic companion forms can be easily developed based on the quadratic integration rule or any other integration rule.

A.7.2 Model Parameters and User Interface

The input parameters for defining the model of a single-phase, saturable-core transformer, as well as the user interface to define these parameters are presented in Figure A.33.

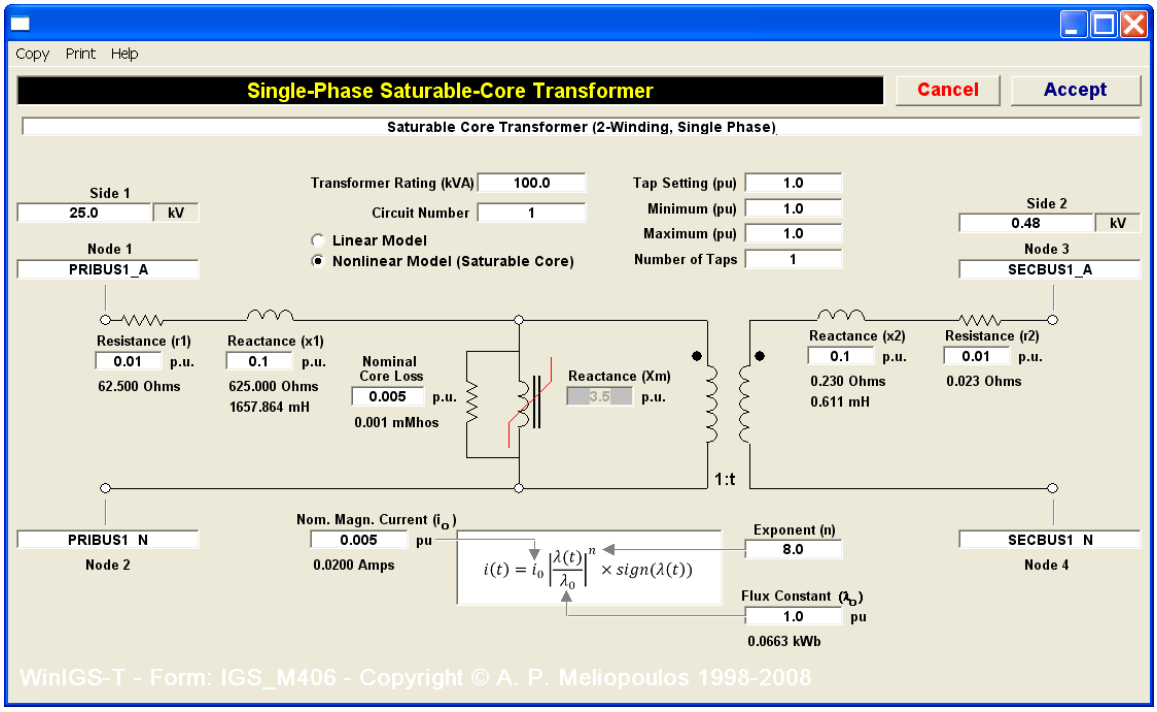

Figure A.33: Single-phase, saturable-core transformer parameters and user interface.

A.7.3 Full Transient Model

A.7.3.1 Compact Model

The overall physical model of a single-phase, saturable-core transformer is illustrated in Figure A.34. Core losses are also considered in the model, expressed by the conductance g_L.

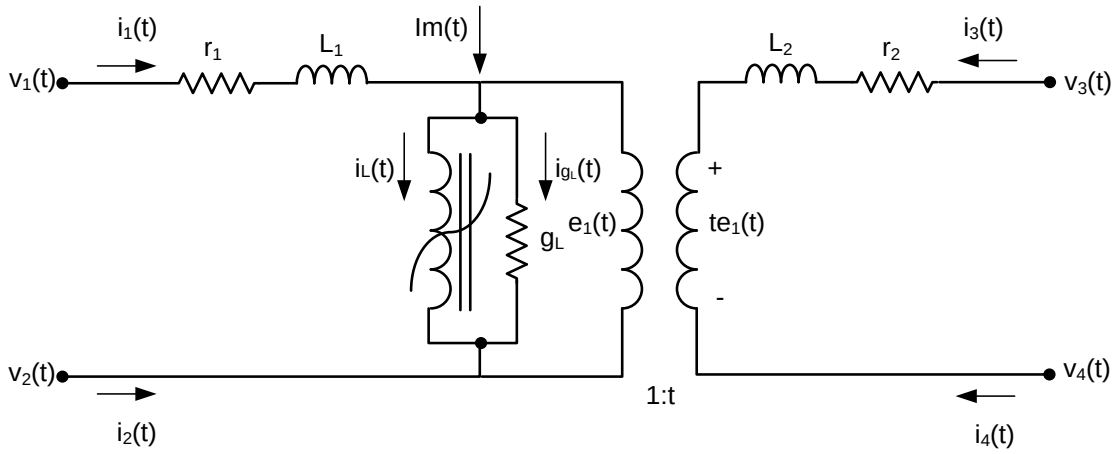

Figure A.34: Single-phase, saturable-core transformer model.

The model with the nonlinear magnetizing inductor in compact form is described by equations (A.459) through (A.467).

$$i_1 = i_1(t), \tag{A.459}$$

$$i_2 = -i_1(t), \tag{A.460}$$

$$i_3 = i_3(t), \tag{A.461}$$

$$i_4 = -i_3(t), \tag{A.462}$$

$$\frac{d\lambda(t)}{dt} = e_1(t), \tag{A.463}$$

$$L_1 \frac{di_1(t)}{dt} = v_1(t) - r_1 i_1(t) - e_1(t) - v_2(t), \tag{A.464}$$

$$L_2 \frac{di_3(t)}{dt} = v_3(t) - r_2 i_3(t) - te_1(t) - v_4(t), \tag{A.465}$$

$$0 = i_m(t) - i_0 \left|\frac{\lambda(t)}{\lambda_0}\right|^n sgn(\lambda(t)) - g_L e_1(t), \tag{A.466}$$

$$0 = i_1(t) + ti_3(t) - i_m(t). \tag{A.467}$$

The linear version of the model in compact form is described by equations (A.468) through (A.475).

$$i_1 = i_1(t), \tag{A.468}$$

$$i_2 = -i_1(t), \tag{A.469}$$

$$i_3 = i_3(t), \tag{A.470}$$

$$i_4 = -i_3(t), \tag{A.471}$$

$$L_m \frac{di_L(t)}{dt} = e_1(t), \tag{A.472}$$

$$L_1 \frac{di_1(t)}{dt} = v_1(t) - r_1 i_1(t) - e_1(t) - v_2(t), \tag{A.473}$$

$$L_2 \frac{di_3(t)}{dt} = v_3(t) - r_2 i_3(t) - te_1(t) - v_4(t), \tag{A.474}$$

$$0 = i_1(t) + ti_3(t) - i_L(t) - g_L e_1(t), \tag{A.475}$$

where

i_1 is the terminal 1 current;

i_2 is the terminal 2 current;

i_3 is the terminal 3 current;

i_4 is the terminal 4 current;

$v_1(t)$ is the terminal 1 voltage;

$v_2(t)$ is the terminal 2 voltage;

$v_3(t)$ is the terminal 3 voltage;

$v_4(t)$ is the terminal 4 voltage;

$i_L(t)$ is the current through the magnetizing inductor (linear model);

$i_m(t)$ is the magnetizing current (nonlinear model);

$\lambda(t)$ is the nonlinear inductor flux;

$e_1(t)$ is the emf across the inductor;

t is the transformation ratio.

A.7.3.2 Equivalent Quadratic Model

The model with the nonlinear magnetizing inductor in quadratic form is described by equations (A.476) through (A.487+m1+m2).

$$i_1 = i_1(t), \tag{A.476}$$

$$i_2 = -i_1(t), \tag{A.477}$$

$$i_3 = i_3(t), \tag{A.478}$$

$$i_4 = -i_3(t), \tag{A.479}$$

$$L_1 \frac{di_1(t)}{dt} = v_{L1}(t), \tag{A.480}$$

$$L_2 \frac{di_3(t)}{dt} = v_{L2}(t), \tag{A.481}$$

$$\frac{d\lambda(t)}{dt} = e_1(t), \tag{A.482}$$

$$0 = -i_L(t) + g_L e_1(t) + i_m(t), \tag{A.483}$$

$$0 = i_m(t) - i_1(t) - t i_3(t), \tag{A.484}$$

$$0 = i_1(t) r_1 + v_{L1}(t) + e_1(t) - v_1(t) + v_2(t), \tag{A.485}$$

$$0 = i_3(t) r_2 + v_{L2}(t) + t e_1(t) - v_3(t) + v_4(t), \tag{A.486}$$

$$0 = i_L(t) - \frac{i_0}{|\lambda_0|^n} y_m(t)[sgn(\lambda(t))]^{n+1}, \quad \text{(A.487)}$$

$$0 = y_1(t) - \lambda^2(t), \quad \text{(A.488)}$$

$$0 = y_2(t) - y_1^2(t), \quad \text{(A.489)}$$

…

$$0 = y_{m1}(t) - y_{m1-1}^2(t), \quad \text{(A.487+m1)}$$

$$0 = y_{m1+1}(t) - y_{i1}(t)y_{j1}(t), \quad \text{(A.487+m1+1)}$$

$$0 = y_{m1+2}(t) - y_{m1+1}(t)y_{j2}(t), \quad \text{(A.487+m1+2)}$$

……

$$\begin{cases} 0 = y_m(t) - y_{m-1}(t)y_{jm2}(t), & \text{if } n \text{ even,} \\ 0 = y_m(t) - y_{m-1}(t)\lambda(t), & \text{if } n \text{ odd.} \end{cases} \quad \text{(A.487+m1+m2)}$$

The state vector is defined as

$$x(t) = \begin{bmatrix} v_1(t) \\ v_2(t) \\ v_3(t) \\ v_4(t) \\ i_1(t) \\ i_3(t) \\ \lambda(t) \\ i_m(t) \\ e(t) \\ v_{L1}(t) \\ v_{L2}(t) \\ i_L(t) \\ y_1(t) \\ y_2(t) \\ \cdots \\ y_m(t) \end{bmatrix}$$

The through variables are: i_1, i_2, i_3, i_4.

The external states are: $v_1(t)$, $v_2(t)$, $v_3(t)$, $v_4(t)$.

The internal states are: $i_1(t)$, $i_3(t)$, $\lambda(t)$, $i_m(t)$, $e(t)$, $v_{L1}(t)$, $v_{L2}(t)$, $i_L(t)$, $y_1(t)$, $y_2(t)$, ..., $y_m(t)$.

A.8 Three-Phase Saturable-Core Transformer Model

A.8.1 Overview

This section of Appendix A presents the nonlinear, time-domain model of a saturable-core, three-phase, two-winding transformer. The model extends the single-phase model presented in the previous section. Three modules of the single-phase model are used and only their connection needs to be additionally specified. The model equations for each of the three single-phase modules are the same as in section A.7. The possible connection types considered are Y-Y, Y-Δ, Δ-Y, and Δ-Δ. The model can be used to represent nonlinearities that might occur during energization of feeder transformers. Such condition may appear during cold load pick-up after severe disturbances and transients in distribution feeders. A full time-domain model is presented and implemented. The user specifies the parameters of the standard transformer as well as the parameters of the current-flux characteristic of the nonlinear inductor. Subsequently, using the quadratic equivalent model, the algebraic companion forms can be developed based on the quadratic integration rule, or any other integration rule.

A.8.2 Model Parameters and User Interface

This section presents the input parameters for defining the model of a three-phase, saturable-core transformer, as well as the user interface to define these parameters. The

user interface of the model is presented in Figure A.35, which also illustrates the parameters specified by the user:

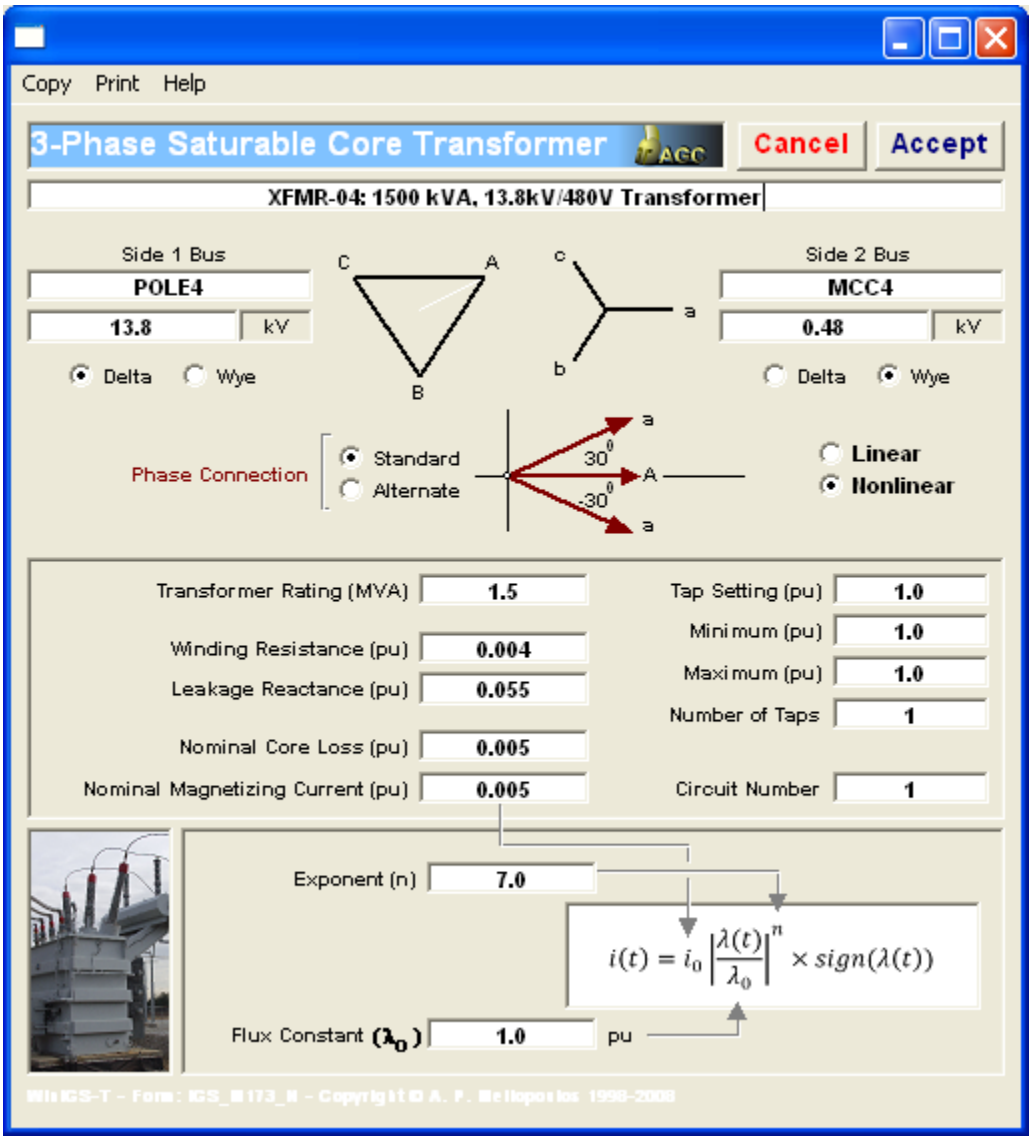

Figure A.35: Three-phase, saturable-core transformer parameters and user interface.

A.8.3 Full Transient Model

A.8.3.1 Wye-Wye Connection

The overall physical model of a wye-wye-connected three-phase transformer is illustrated in Figure A.36.

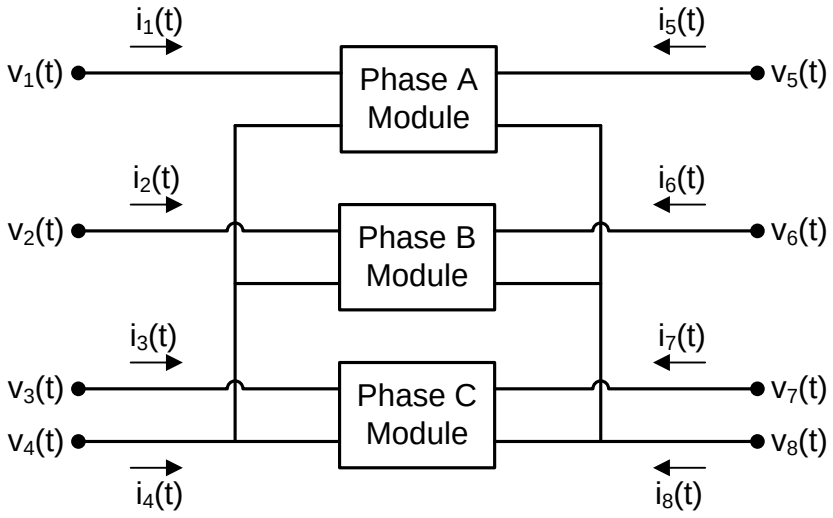

Figure A.36: Wye-wye transformer connection.

Based on the connections of Figure A.36 the following relations hold that relate the new through variables (currents) and new external states with the variables of each individual module. It can be assumed that the external states and the through variables of each module become internal states of the three phase device. There are 8 new external voltage variables, $v_1(t)$ through $v_8(t)$ and 4 new variables for each module (the through currents that now become states), so in total 8+12=20 new variables. The 20 new equations are

$$i_1 = i_{1A}(t), \tag{A.490}$$

$$i_2 = i_{1B}(t), \tag{A.491}$$

$$i_3 = i_{1C}(t), \tag{A.492}$$

$$i_4 = i_{2A}(t) + i_{2B}(t) + i_{2C}(t), \tag{A.493}$$

$$i_5 = i_{3A}(t), \tag{A.494}$$

$$i_6 = i_{3B}(t), \tag{A.495}$$

$$i_7 = i_{3C}(t), \tag{A.496}$$

$$i_8 = i_{4A}(t) + i_{4B}(t) + i_{4C}(t), \tag{A.497}$$

$$0 = v_1(t) - v_{1A}(t), \tag{A.498}$$

$$0 = v_4(t) - v_{2A}(t), \tag{A.499}$$

$$0 = v_5(t) - v_{3A}(t), \tag{A.500}$$

$$0 = v_8(t) - v_{4A}(t), \tag{A.501}$$

$$0 = v_2(t) - v_{1B}(t), \tag{A.502}$$

$$0 = v_4(t) - v_{2B}(t), \tag{A.503}$$

$$0 = v_6(t) - v_{3B}(t), \tag{A.504}$$

$$0 = v_8(t) - v_{4B}(t), \tag{A.505}$$

$$0 = v_3(t) - v_{1C}(t), \tag{A.506}$$

$$0 = v_4(t) - v_{2C}(t), \tag{A.507}$$

$$0 = v_7(t) - v_{3C}(t), \tag{A.508}$$

$$0 = v_8(t) - v_{4C}(t). \tag{A.509}$$

A.8.3.2 Wye-Delta Connection

The overall physical model of a wye-delta-connected three-phase transformer is illustrated in Figure A.37.

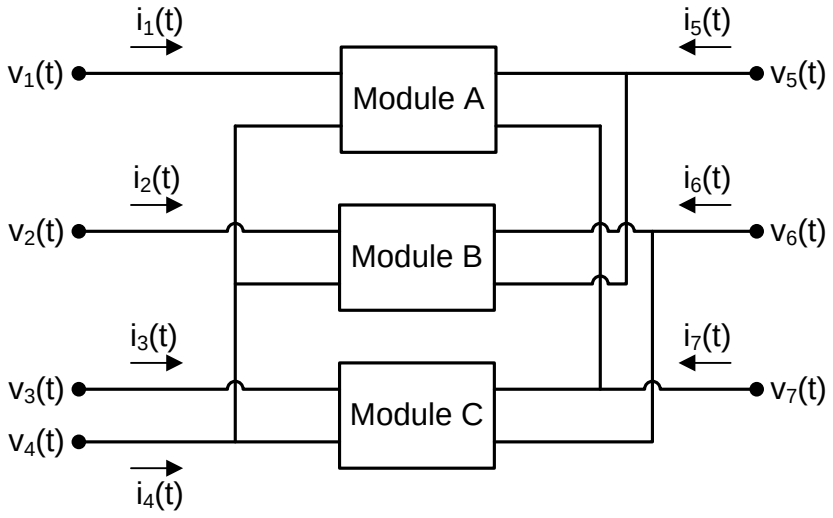

Figure A.37: Wye-delta transformer connection.

Based on the connections of Figure A.37 the following relations hold that relate the new through variables (currents) and new external states with the variables of each individual module. It can be assumed that the external states and the through variables of each module become internal states of the three phase device. There are 7 new external voltage variables, $v_1(t)$ through $v_7(t)$ and 4 new variables for each module (the through currents that now become states), so in total 7+12=19 new variables. The 19 new equations are

$$i_1 = i_{1A}(t), \tag{A.510}$$

$$i_2 = i_{1B}(t), \tag{A.511}$$

$$i_3 = i_{1C}(t), \tag{A.512}$$

$$i_4 = i_{2A}(t) + i_{2B}(t) + i_{2C}(t), \tag{A.513}$$

$$i_5 = i_{3A}(t) + i_{4B}(t), \tag{A.514}$$

$$i_6 = i_{3B}(t) + i_{4C}(t), \tag{A.515}$$

$$i_7 = i_{3C}(t) + i_{4A}(t), \tag{A.516}$$

$$0 = v_1(t) - v_{1A}(t), \tag{A.517}$$

$$0 = v_4(t) - v_{2A}(t), \tag{A.518}$$

$$0 = v_5(t) - v_{3A}(t), \tag{A.519}$$

$$0 = v_7(t) - v_{4A}(t), \tag{A.520}$$

$$0 = v_2(t) - v_{1B}(t), \tag{A.521}$$

$$0 = v_4(t) - v_{2B}(t), \tag{A.522}$$

$$0 = v_6(t) - v_{3B}(t), \tag{A.523}$$

$$0 = v_5(t) - v_{4B}(t), \tag{A.524}$$

$$0 = v_3(t) - v_{1C}(t), \tag{A.525}$$

$$0 = v_4(t) - v_{2C}(t), \tag{A.526}$$

$$0 = v_7(t) - v_{3C}(t), \tag{A.527}$$

$$0 = v_6(t) - v_{4C}(t). \tag{A.528}$$

A.8.3.3 Delta-Wye Connection

The overall physical model of a delta-wye-connected three-phase transformer is illustrated in Figure A.38.

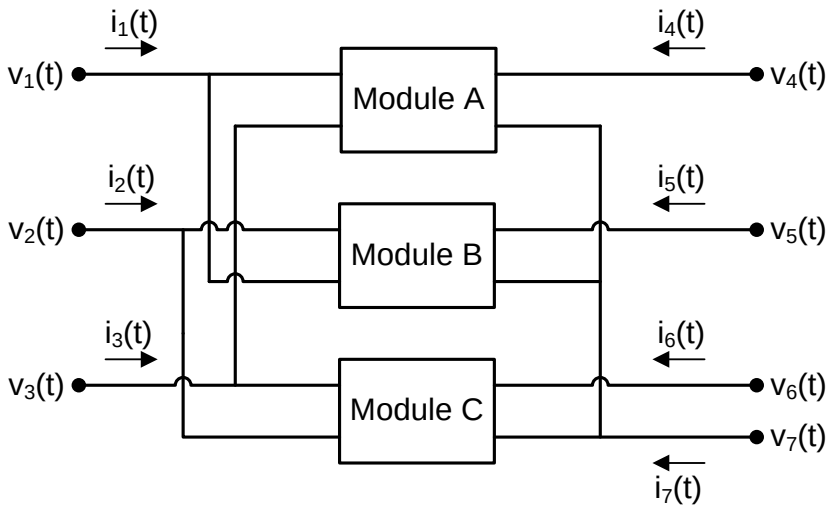

Figure A.38: Delta-wye transformer connection.

Based on these connections of Figure A.38 the following relations hold that relate the new through variables (currents) and new external states with the variables of each individual module. It can be assumed that the external states and the through variables of each module become internal states of the three phase device. There are 7 new external voltage variables, $v_1(t)$ through $v_7(t)$ and 4 new variables for each module (the through currents that now become states), so in total 7+12=19 new variables. The 19 new equations are

$$i_1 = i_{1A}(t) + i_{2B}(t), \tag{A.529}$$

$$i_2 = i_{1B}(t) + i_{2C}(t), \tag{A.530}$$

$$i_3 = i_{1C}(t) + i_{2A}(t), \tag{A.531}$$

$$i_4 = i_{3A}(t), \tag{A.532}$$

$$i_5 = i_{3B}(t), \tag{A.533}$$

$$i_6 = i_{3C}(t), \tag{A.534}$$

$$i_7 = i_{4A}(t) + i_{4B}(t) + i_{4C}(t), \tag{A.535}$$

$$0 = v_1(t) - v_{1A}(t), \tag{A.536}$$

$$0 = v_3(t) - v_{2A}(t), \tag{A.537}$$

$$0 = v_4(t) - v_{3A}(t), \tag{A.538}$$

$$0 = v_7(t) - v_{4A}(t), \tag{A.539}$$

$$0 = v_2(t) - v_{1B}(t), \tag{A.540}$$

$$0 = v_1(t) - v_{2B}(t), \tag{A.541}$$

$$0 = v_5(t) - v_{3B}(t), \tag{A.542}$$

$$0 = v_7(t) - v_{4B}(t), \tag{A.543}$$

$$0 = v_3(t) - v_{1C}(t), \tag{A.544}$$

$$0 = v_2(t) - v_{2C}(t), \tag{A.545}$$

$$0 = v_6(t) - v_{3C}(t), \tag{A.546}$$

$$0 = v_7(t) - v_{4C}(t). \tag{A.547}$$

A.8.3.4 Delta-delta connection

The overall physical model of a delta-wye-connected three-phase transformer is illustrated in Figure A.39.

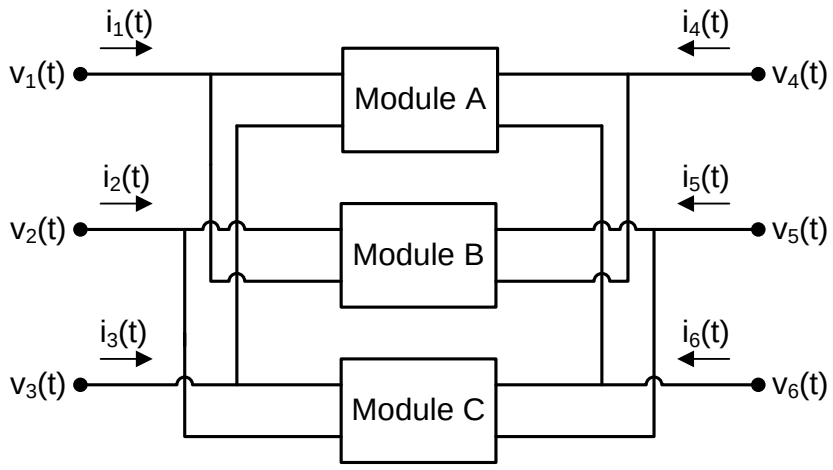

Figure A.39: Delta-delta transformer connection.

Based on these connections of Figure A.39 the following relations hold that relate the new through variables (currents) and new external states with the variables of each individual module. It can be assumed that the external states and the through variables of each module become internal states of the three phase device. There are 6 new external voltage variables, $v_1(t)$ through $v_6(t)$ and 4 new variables for each module (the through currents that now become states), so in total 6+12=18 new variables. The 18 new equations are

$$i_1 = i_{1A}(t) + i_{2B}(t), \tag{A.548}$$

$$i_2 = i_{1B}(t) + i_{2C}(t), \tag{A.549}$$

$$i_3 = i_{1C}(t) + i_{2A}(t), \tag{A.550}$$

$$i_4 = i_{3A}(t) + i_{4B}(t), \tag{A.551}$$

$$i_5 = i_{3B}(t) + i_{4C}(t), \tag{A.552}$$

$$i_6 = i_{3C}(t) + i_{4A}(t), \tag{A.553}$$

$$0 = v_1(t) - v_{1A}(t), \tag{A.554}$$

$$0 = v_3(t) - v_{2A}(t), \tag{A.555}$$

$$0 = v_4(t) - v_{3A}(t), \tag{A.556}$$

$$0 = v_6(t) - v_{4A}(t), \tag{A.557}$$

$$0 = v_2(t) - v_{1B}(t), \tag{A.558}$$

$$0 = v_1(t) - v_{2B}(t), \tag{A.559}$$

$$0 = v_5(t) - v_{3B}(t), \tag{A.560}$$

$$0 = v_4(t) - v_{4B}(t), \tag{A.561}$$

$$0 = v_3(t) - v_{1C}(t), \tag{A.562}$$

$$0 = v_2(t) - v_{2C}(t), \tag{A.563}$$

$$0 = v_6(t) - v_{3C}(t), \tag{A.564}$$

$$0 = v_5(t) - v_{4C}(t). \tag{A.565}$$

APPENDIX B

ADVANCED PROBABILISTIC POWER FLOW METHODOLOGY

B.1 Introduction

The operation of a power system is determined to a great extend by the load demand it has to satisfy. The use of traditional load-flow analysis to simulate the system operation is based on the assumption that the system loading at each bus is precisely known. That is, the electric load and additionally the generating-unit outputs are deterministically known quantities. This can be considered quite accurate when on-line measurements are used for real-time analysis. However, in many cases the load needs to be assumed stochastic in nature and therefore the power system operation has to be studied based on estimates of this demand and taking into consideration the probabilistic nature of the load. Therefore, an important issue in reliability studies is the inherent uncertainty in the knowledge of the electric load demand. The demand is in general unknown and stochastic in nature and, therefore, the power-system operation has to be studied and planned based on estimates of this demand and taking into consideration the probabilistic nature of the load. This issue can be handled either by performing several studies under various loading levels or by directly treating the stochastic nature of the load. This is performed using the stochastic load-flow analysis, also referred to as probabilistic power-flow analysis. Probabilistic power flow is a term that refers to power-flow analysis methods that directly treat the uncertainty of electric load and generation.

The first notions of probabilistic power flow analysis appeared in the early 1970s [198] – [200]. In [199] and [200] a simplified probabilistic load flow is proposed, based on the assumptions that the active bus loads are independent random variables and the transmission system is represented by the DC network model (thus the reactive-power flow is neglected). The generation-dispatch procedure is modeled with an arbitrary function that allocates the variation of the total electric load to specific generation buses. Since the variables of the active electric load at each bus are assumed independent, the probability density function of the circuit flows can be computed with a series of convolutions. Later, this basic method was extended and it was also applied to the AC network model [201], [202]. A conventional deterministic power-flow analysis is performed initially, assuming net bus loads equal to their mean values. This solution determines the operating point about which the load-flow equations are subsequently linearized.

The assumption of independence of the nodal electric loads is, however, quite unrealistic. In [203] a linear dependence between nodal powers in probabilistic load flow is suggested. This assumption is also implied by Allan *et al.* in [204]. In [205], a linear dependence model of electric loads is proposed, again, along with a method which combines Monte Carlo simulation and convolutions, using a linearized power flow model. In [206], Dopazo *et al.* used a method which models the correlation between the loads at any two buses. Their proposed method assumes that circuit flows and bus voltage magnitudes are Gaussian distributed and, thus, only their variance should be computed. However, Monte Carlo simulations indicate that it is unrealistic to assume, a priori, Gaussian distributions of circuit flows and bus voltages [204], [205], [207]. For this

reason, Sauer and Heydt [208] have proposed the use of higher moments (third and fourth) for accurate representation of the probability distribution functions. The topic of probabilistic power flow was further investigated in the mid and late 80's. Some typical extensions and improvements can be found in [209] – [212]. An extended literature review on power system probabilistic analysis (until the late 80's) can be found in [213].

An efficient method for treating the correlation among bus loads and the generation dispatch procedure is proposed in [214]. The model assumes Gaussian distribution of bus loads and a linearized economic dispatch model. The circuit flows and bus voltages are expressed as a linear combination of the bus loads only, and are assumed to be normally distributed. The linearized equations are utilized to determine the moments of probability density function of circuit flows and bus voltages. The inclusion of this model in a reliability analysis method resulted in more accurate representation of the electric load at reduced computational requirements [214]. While this approach models the economic redispatch of generating units due to electric load variations, it is based on the linearized power-flow equations and the linearized economic dispatch model. In [215] the method was further extended addressing the issues of the economic dispatch of the generating units, the effects of nonlinearities of the power system model and the uncertainty associated with the availability of the generating units. Furthermore the a priori assumption that the circuit loadings and bus voltages are normally distributed was waived.

The work presented in this appendix extends some of the ideas presented in [214], [215] and [216]. More specifically this paper applies a stochastic load flow methodology to the "quadratized" power flow model, as described in this dissertation, and in addition it

introduces a non-conforming stochastic electric load representation. Based on this load model, the electric load is accurately and realistically represented with a few independent stochastic processes, $[v]$. These processes are determined by historical bus-load data. The type of probabilistic models to be used depends on the context in which the methodology is used. Currently the methodology is developed for operation planning. However, it can be easily extended to long term planning or on-line operation. The statistics of the quantities under study are computed from their linearized models with respect to the independent load variables $[v]$, around the expected value of the non-conforming load. Emphasis is given in the ability of taking into consideration major operating practices such as economic dispatch and possibly congestion management or observation of network constraints.

B.2 Problem Statement

Consider an electric power system consisting of the power grid, the loads, and the generating units, as illustrated in Figure B.1. Given the probabilistic load model, it is desired to calculate the statistics of the voltage magnitude at each bus and of the current magnitude and power flow at each system branch considering the operating constraints and optimization practices of the system.

More specifically it is desired to compute the statistics of the current magnitude I_{km} (or the apparent power flow T_{km}) of any circuit connecting buses k and m, or the voltage magnitude at any bus k, V_k. The operation of the system is constraint by the capacities of the circuits, the need for voltage regulations and the need to optimize the operation of the system (minimize operating cost). The statistics of circuit flows and voltage magnitudes become functionals of the parameters affecting the operation. Major operating practices

such as economic dispatch and congestion management should be accounted for in the evaluation of these statistics.

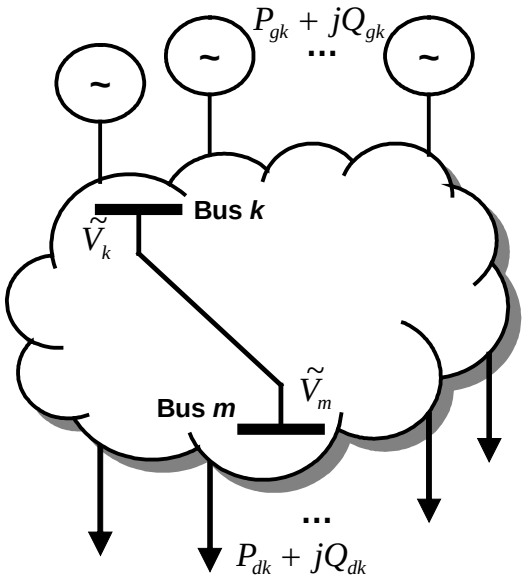

Figure B.1: Schematic illustration of an electric power system.

The proposed solution methodology consists of the following steps. First, a non-conforming probabilistic load model is assumed. The load model is described with a small set of independent random variables (typically two or three). This model realistically captures the stochastic nature of the load, and the strong correlation of electric loads at each bus. The total increase or decrease in the required system generation is a dependant random variable. In fact it depends on the independent load random variables via an economic dispatch operation. The output of each generating unit is expressed as a function of the total generation change using linearization assuming the computed values of the participation factors of each unit at the base case operating point. Therefore the statistics (probability distribution functions) of the total generation of generation buses are computed.

Second, circuit currents, circuit power flows and bus voltage magnitudes are expressed as linear combinations of the defined random variables. The appropriate coefficients are the sensitivities of each quantity with respect to the corresponding random variable and can be simply and efficiently computed using the costate method, as described in Chapter 6. This linearized relationship allows the computation of the statistics of circuit currents, circuit power flows and bus voltage magnitudes.

The proposed approach and methodology is validated with an independent method based on Monte Carlo simulation. Specifically, the same problem is also solved via Monte Carlo simulations in which each random sample is fully solved, thus incorporating nonlinearities resulting from the AC power flow equations and major operating practices such as economic dispatch and possibly congestion management. Both the linearization solution and the Monte Carlo approach are based on the quadratic power flow model.

B.3 Proposed Model Description

Models of the various components of the system are presented in this section. Based on the approach described in the previous section, three main subsystems need to be modeled: (1) the electric load, (2) the generation system, and (3) the transmission network.

B.3.1 Non-conforming Electric Load Stochastic Model

The electric load representation is a key issue in a probabilistic load flow methodology. Total independence of bus loads has been extensively assumed in the literature [199], [200], [202], [204], [206], [207]. This assumption, in combination with linearized power-flow equations results in the solution of the probabilistic load flow

being a sum of independent random variables weighted by sensitivity coefficients. Therefore, it can be obtained by a series of convolutions. However, this assumption of independence is quite far from being realistic [201], [203], [205], [215], [216], since there are various reasons for correlation to exist between loads [205].

A typical probabilistic load model is a conforming electric load model, i.e. a specific bus load is a fixed percentage of the total system load. Statistically, this means that the bus loads are correlated one hundred percent. This practice fails to represent the fact that the actual loads are not fully correlated. For a more realistic representation of the electric load, it is necessary to represent the bus electric load as a non-conforming load. For this purpose a generalized nonconforming electric load model is proposed, which is defined in terms of n independent and zero-mean random processes (typically no more than three to five). At a certain instance of time (or certain time interval) the stochastic processes become random variables with specific probability distribution functions and of zero mean. The characterization of the random variables and thus the determination of the non-conforming load model can be obtained from bus historical data using load forecasting methods, which are, however, outside the scope of this work. Here it is assumed that the model of the independent stochastic processes is given. If the number of bus loads in the system is L the entire system active and reactive loading can be represented as two L-dimensional vectors:

$$\vec{P}_d = \vec{P}_d^0 + \vec{v}\bar{P}_d, \tag{B.1}$$

$$\vec{Q}_d = A\vec{P}_d, \tag{B.2}$$

where

$\vec{P}_d$: L-dimensional active load vector, $\vec{P}_d = [P_{dk}]$,

$\vec{P}_d^0$: L-dimensional base case load vector, $\vec{P}_d^0 = [P_{dk}^0]$,

$\vec{v}$: n-dimensional vector of stochastic load variables,

$\bar{P}_d$: nxL matrix of participation coefficients,

$\bar{P}_d = \left[p_{dk}^i\right]$, $i = 1, \dots, n$ and $k = 1, \dots, L$,

$\vec{Q}_d$: L-dimensional reactive load vector,

A : LxL diagonal matrix of proportionality constants,

$A = diag(a_k)$, k=1,…,L.

It is assumed that the load at each bus k maintains a constant power factor; therefore the reactive power consumption at bus k is proportional to the active power consumption, with a constant of proportionality a_k depending on the power factor. This assumption may be rather limitative, however, it is a commonly made assumption is many cases (including actual utility practices and studies) and provides a good starting point. It can be waived by slightly complicating the load model by possibly introducing some additional stochastic processes, which will enable a realistic representation of both active and reactive power demand variations and the variable correlation among them.

The presented non-conforming load model assumes variable correlation between the various bus loads. However, the bus loads are not fully correlated, as it would be the case in a conventional conforming load model. This depicts a more realistic situation. If $v_i = 0$ for $i = 2, \dots, n$ then the above model becomes a simple conforming load. The load variations at every bus have the exact same statistics, imposed by the single random

variable v_1. If $n \geq 2$ then the above model becomes a non-conforming load model. The ability of this model to represent the variable correlation between bus loads is illustrated with a very simple system in Figure B.2.

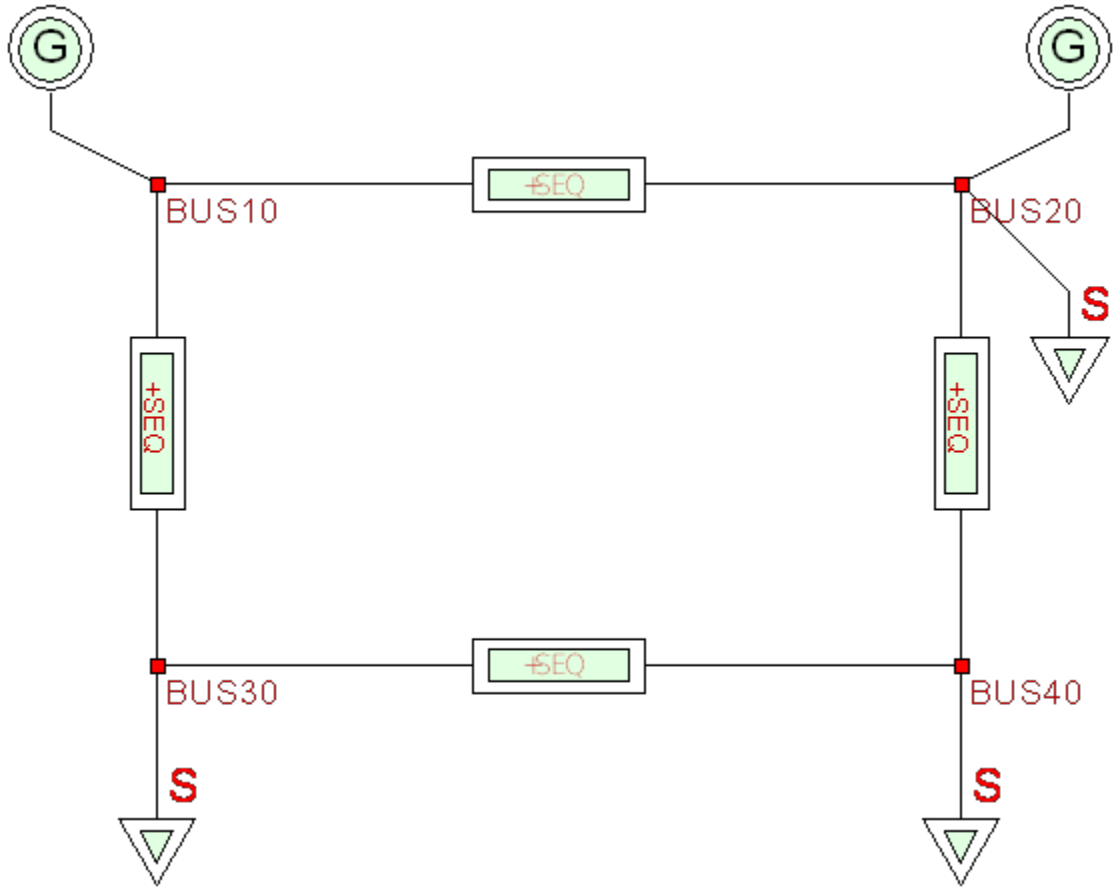

Figure B.2: System for illustration of the correlation among bus loads when using non-conforming load representation.

Assume that the bus loads are given by

$$P_1 = 100 + 4v_1 + v_2, \tag{B.3}$$

$$P_2 = 50 + 2v_1 + 5v_2, \tag{B.4}$$

$$P_3 = 200 + 8v_1, \tag{B.5}$$

where $v_1 \sim N(0,1)$ and $v_2 \sim N(0,2)$.

Computation of the correlation of the bus loads gives:

$$Cor[P_2, P_3] = 0.577, \quad \text{(B.6)}$$

$$Cor[P_2, P_4] = 0.943, \quad \text{(B.7)}$$

$$Cor[P_3, P_4] = 0.272, \quad \text{(B.8)}$$

which indicates that there is variable correlation among the loads. Note that if a conforming load model of one random variable was used then every bus load would be 100% correlated with each other.

B.3.2 Probabilistic Generation Model

B.3.2.1 Introduction

The probabilistic nature of the load imposes variations to the total generation required by the system. This is mainly due to the variation of the demand, and to a lesser degree on changes in transmission losses. Therefore, the variations in transmission losses due to the load fluctuations are also another factor that needs to be considered. To deal with the random load variation from the generation viewpoint the following different approaches are considered.

a) The generation of each unit can be considered constant at its base case value. Therefore, the slack bus picks up all the required generation variation, in order to compensate for the load changes and the changes in losses. This approach is very simplified and quite unrealistic.

b) The total change in load demand can be calculated as the sum of the change at each bus. Therefore, based on equation (B.1), for example, this is the sum of the L elements of the vector $\vec{v}\bar{P}_d$. Alternative and in more detail

$$\Delta P_d = \sum_{k=1}^{L} \sum_{i=1}^{n} p_{dk}^{i} v_i. \quad \text{(B.9)}$$

This is a sum of random variables, thus it is also a random variable, but dependent on v_i's. Since the total change can be either positive or negative, two such new random variables can be defined, called w^+ and w^-, one for load increase and one for load decrease. However, for any sample realization of the independent random variables, only one of these two variables is nonzero, since we can have either an increase in the demand compared to the expected demand or a decrease. Ignoring the changes in losses, this can be assumed the total generation change that needs to be dispatched between the units. This can be done, by assuming that each unit is dispatched an amount of the total change (increase or decrease) proportional to its participation factor, computed at the base case. The participation factor of each unit can be computed as a by-product of an economic dispatch algorithm at base case, for either increase or decrease in generation. For units operating in PQ mode, constant power-factor operation is assumed. The advantage of this case is that there is an explicit and exact linear relation between the independent random variables v_i's and the dependent random variables of the total generation change. More specifically it holds that

$$w^+ - w^- = \sum_{k=1}^{L} \sum_{i=1}^{n} p_{dk}^{i} v_i, \quad \text{(B.10)}$$

with $w^+, w^- \geq 0$ and $w^+ w^- = 0$.

However, the disadvantage is that this model ignores the dispatch of changes in losses, and therefore it is assumed that the slack bus is picking up all the losses.

c) The total change in generation is considered to be the load change plus the change in losses. This is to be dispatched among the units of the system. The dispatch is performed assuming linearization and using the participation factors of each unit computed by an economic dispatch at base case. Again the units operating in PQ mode are assumed to work with constant power factor. This approach is very similar to the previous one; however, it assumes the changes in demand as well as the consequent changes in the losses. Again two new dependent random variables are assumed for the required increase or decrease in generation, say w^+ and w^- respectively. Again, for any sample realization of the independent random variables, only one of these two variables is nonzero, since we can have either an increase in the demand compared to the expected demand or a decrease. Assuming that the losses can be expressed as a percentage of the load it holds that

$$\frac{w^+}{\gamma^+} - \frac{w^-}{\gamma^-} = \sum_{k=1}^{L} \sum_{i=1}^{n} p_{dk}^i v_i, \tag{B.11}$$

with $w^+, w^- \geq 0$ and $w^+ w^- = 0$. Furthermore, $\gamma^+, \gamma^- \geq 1$.

This model includes the losses in the dispatch, however, it is more difficult to find a relation between the independent and the dependent random variables. This will be the model that will be mostly used in the rest of the work. Note that for $\gamma^+ = 1$ or $\gamma^- = 1$ the approach described in (b) is obtained. This is the approach that will be used from now on in this work.

d) The full economic dispatch problem is considered. In the two previous cases, a linearized generation dispatch was assumed based on participation factors. In this approach the full economic dispatch model is assumed. This provides the more accurate results, however, it seems to be impractical for theoretical probabilistic studies, because of its complexity. Furthermore, since an attempt to approach the probabilistic power flow problem via linearization is made, the previous approach is considered more than accurate, and no need to incorporate an economic dispatch algorithm is necessary. In addition, such a method would not result in significant improvement, since linearization would be applied to the problem anyway. Nevertheless, this method can be used in a Monte Carlo simulation approach, where all the nonlinearities are included in the calculations. Therefore, the generation dispatch problem using full-scale economic dispatch can be addressed for validation purposes in a Monte Carlo approach.

B.3.2.2 Mathematical Details

In this section some more mathematical details on the generation model are presented, for the approaches discussed in the previous section.

a) Deterministic generation model – Slack bus picks all variations

If it is assumed that the slack bus will pick all the load variations then no additional random variables are introduced and no additional equations are necessary. A new load flow will adjust the output of the slack bus so that there is a total power balance in the system. Furthermore, the same assumption will hold for the linearization procedure and the computed values of the sensitivities will implicitly have the information that the slack bus takes all the variations. It is assumed that this method will provide some valid first approximation.

b) Probabilistic generation model – Load demand is dispatched linearly, slack bus picks variations in losses

Based on the non-conforming load model described previously the electric load at each system bus is given by equations (B.1) and (B.2). The generation of each unit is adjusted to the load changes based on its participation factor. For units on PQ operation mode a constant power factor assumption is made. The total change in generation that is to be dispatched among the units is set equal to the total change in load, thus by equation (B.9) it hold that

$$\Delta P_g = \sum_{k=1}^{L} \sum_{i=1}^{n} p_{dk}^{i} \, v_i. \tag{B.12}$$

This quantity is a random variable (not independent though since it depends on the v_i's) and it can get either a positive or negative values. To distinguish between the two cases two different random variables are assumed one for each case, w^+ and w^-. The distinction is necessary since we will assume a linearized unit dispatch and the participation factors for increase and decrease in load are in general different for each unit, especially if for example a unit is operating close to its limits or at its limits. At each time one of w^+ or w^- is nonzero, therefore it holds that

$$w^+ w^- = 0 \tag{B.13}$$

and in addition

$$w^+, w^- \geq 0. \tag{B.14}$$

Thus the active power generation of each unit k is given by

$$P_{gk} = P_{gk}^0 + p_{gk}^+ w^+ - p_{gk}^- w^-, \tag{B.15}$$

where

P_{gk} : the new active power production of unit k ;

P_{gk}^{0} : the base case active power production of unit k ;

P_{gk}^{+} : the participation factor of unit k for a total demand increase;

P_{gk}^{-} : the participation factor of unit k for a total demand decrease;

w^{+} : the dependent random variable of total demand increase;

w^{-} : the dependent random variable of total demand decrease.

In addition equation (B.10) can be written as

$$w^{+} - w^{-} = \sum_{k=1}^{L} \sum_{i=1}^{n} p_{dk}^{i} v_i \qquad \text{(B.16)}$$

since (B.13) holds and this introduces a linear relation between the independent and the dependent random variables. This relation can be simplified by combining the coefficients corresponding to the same random variables.

$$w^{+} - w^{-} = \sum_{i=1}^{n} \theta_i v_i, \qquad \text{(B.17)}$$

where $\theta_i = \sum_{k=1}^{L} p_{dk}^{i}$, L being the total number of loads.

For the generated reactive power of units operating in PQ mode, we assume that the power factor is constant; therefore, the change in their reactive production is proportional to the change the active power production so that the power factor is kept constant.

The additional losses (or the decrease in losses) introduced by the load change are assumed to be picked up by the slack bus. Thus the slack bus picks up some additional

load and all the additional losses. This is quite unrealistic, however, it can be considered as a valid assumption.

c) Probabilistic generation model – Load demand and losses are dispatched linearly

In this approach the same concepts as in the previous one apply, with the exception that losses are also considered in the generation dispatch. Based on the non-conforming load model described earlier the electric load at each system bus is given by equations (B.1) and (B.2). Therefore, the total change in generation is now given by

$$\frac{w^+}{\gamma^+} - \frac{w^-}{\gamma^-} = \sum_{k=1}^{L} \sum_{i=1}^{n} p_{dk}^{i} v_i = \sum_{i=1}^{n} \theta_i v_i, \tag{B.18}$$

where $\theta_i = \sum_{k=1}^{L} p_{dk}^{i}$, L being the total number of loads, and $\gamma^+, \gamma^- \geq 1$.

The generation of each unit is adjusted to the load and losses changes based on its participation factor. Therefore, the active power generation of each unit is given by

$$P_{gk} = P_{gk}^{0} + p_{gk}^{+} w^+ - p_{gk}^{-} w^-, \tag{B.19}$$

where

P_{gk} : the new active power production of unit k;

P_{gk}^{0} : the base case active power production of unit k;

P_{gk}^{+} : the participation factor of unit k for a net total demand increase;

P_{gk}^{-} : the participation factor of unit k for a net total demand decrease;

w^+ : the dependent random variable of net total demand increase (load + losses);

w^- : the dependent random variable of net total demand decrease (load + losses).

Note that in every case one of either w^+ or w^- will be zero, since the demand will either increase or decrease. Thus,

$$w^+w^- = 0, \tag{B.20}$$

w^+ and w^- are random variables that depend on the independent random variables v_i's and the relation between them is rather complicated, since w^+ and w^- also include changes in system losses. Equation (B.18) does not practically provide this relation since the parameters γ^+ and γ^- are unknown.

For the generated reactive power of units operating in PQ mode, the power factor is considered constant; therefore, the change in their reactive production is proportional to the change the active power production so that the power factor is kept constant.

In order to simply identify a relation between w^+, w^- and v_i's (γ^+ and γ^- in equation B.18 are unknown) let's assume for a moment that there is a fictitious generator located at bus *fict*. In this case it holds from the power balance equation that

$$P_{g,fict} = \sum_{lines(fict)} P_{line} + \sum_{loads(fict)} P_{load} - \sum_{gen(fict)} P_{gen}, \tag{B.21}$$

where

$P_{g,fict}$: the power produced by the fictitious generator;

P_{line} : the line flow for each line connected to the fictitious generator bus;

P_{load} : the demand of each load connected to the fictitious generator bus;

P_{gen} : the active power production of each generator connected to the fictitious generator bus;

$lines(fict)$: the set of lines connected to the fictitious generator bus;

$loads(fict)$: the set of loads connected to the fictitious generator bus;

$gen(fict)$: the set of generators connected to the fictitious generator bus.

Equation (B.21) can be linearized with respect to the random variables introduced in the problem. The loads are by definition linear functions of the introduced independent random variables. The line flows and the generator outputs can also be expressed as linearized functions of the random variables. However, it should be mentioned that it is preferable to assume a fictitious generator at a bus that does not have any other generators connected, or even at a bus without any loads, since this will simplify the problem considerably. For now it is assumed that $P_{g,fict}$ can be written as

$$P_{g,fict} = \sum_{i=1}^{n} a_i v_i + b^+ w^+ + b^- w^-, \tag{B.22}$$

where

$P_{g,fict}$: the power produced by the fictitious generator,

v_i : i[th] random variable from the set of independent variables,

w^+ : the dependent random variable of net total demand increase (load + losses),

w^- : the dependent random variable of net total demand decrease (load + losses),

and $a_i = \frac{dP_{g,fict}}{dv_i}$, $b^+ = \frac{dP_{g,fict}}{dw^+}$, $b^- = \frac{dP_{g,fict}}{dw^-}$.

However, since $P_{g,fict}$ is in fact produced by a fictitious generator we want it to be equal to zero. Therefore, setting $P_{g,fict} = 0$ we get the desired relation between the independent random variables v_i's and the dependent w^+ and w^-:

$$0 = \sum_{i=1}^{n} a_i v_i + b^+ w^+ + b^- w^-. \quad \text{(B.22)}$$

B.3.3 Transmission Network Model

The network quantities (circuit currents, power flows or bus voltages) are also treated as random variables that depend on the stochastic load variables, v_i's. Linear dependence is assumed for small deviations around a base-case operating point, and therefore the circuit currents and flows as well as the bus voltages are linearized with respect to the probabilistic control variables. The derived linear functions are used for the calculation of the statistical properties of each quantity.

More specifically, a network quantity F (i.e. a line current, power flow or a bus voltage) is expressed as a linear combination of the load random variables as

$$F = F^0 + \sum_{i=1}^{n} (c_i \Delta v_i), \quad \text{(B.23)}$$

where

F^0 : base case value of F,

c_i : linearization coefficient of quantity F with respect to v_i.

Based on equation (B.23) and since v_i's are independent random variables the statistics of the quantity F can be derived from the statistics of the load random variables by simply performing a series of convolutions on the probability density functions of v_i's.

The proposed method is based on the concept of utilizing a linearized model around a specific value of electric load as defined by a sample of the electric load model variables. The linearized model is constrained with the operational practices such as

economic dispatch, congestion management and others. Using the linearized model and the electric load model the performance of the system in terms of distributions of bus voltage magnitudes, circuit currents and flows are derived. To further improve on the accuracy of the proposed method the non-conforming load model is sectionalized into a small number of segments as it is depicted in Figure B.3. This results in multiple linearization points and therefore better handling of the nonlinearities arising from the electric network equations. A specific combination of a segment from each variable defines an electric load event. Such an event C_i is illustrated in Figure B.3. We then consider the conditional probability of the electric load given that the electric load belongs to the electric load event C_i. Subsequently, we consider the conditional expected value of the electric load given that the load belongs to event C_i. The operating conditions of the system at the conditional expected value are determined by simulation of the electric power network. Then the linearized model of the system is computed around this operating point. Finally, the conditional (given event C_i) performance of the system in terms of distributions of bus voltage magnitudes, circuit flows and total operating cost are derived from the linearized model and the known conditional electric load model. The procedure is applied to all possible electric load events and the results are weighted with the probabilities of the electric load events and summarized into an overall probabilistic model. It is important to note that at each expected value of a load event congestion management or any other type of remedial actions can be applied, if necessary, as well as the effect of possible contingencies can be accounted for.

The basis of this idea is depicted in Figure B.3. Three stochastic load variables are assumed, namely v_1, v_2 and v_3 following some probability distribution in the interval

$[a, b]$. This interval is divided into three sections, and the expected value of each load random variable is calculated in each section. The triplet of such expected values of each load variables defines a specific load profile and therefore a base case operating point. Furthermore, a triplet of such sections, one for each variable, defines a possible event, i.e. event ε of Figure B.3 is defined as

$$C_i = \{v_1 \in (d_{12}, b_1) \cap v_2 \in (d_{21}, d_{22}) \cap v_3 \in (d_{31}, d_{32})\}. \quad \text{(B.24)}$$

For each electric load event, the base case conditions of the electric power network are computed as well as the linearized model around the base case conditions. This linearization is illustrated in Figure B.4. Assuming n random processes and m sections for each process the total number of events to be considered is m^n. Although the number of events can be very large, leading to bulky computations, in practice we anticipate that no more than three to five random processes will be needed and three to five sections for each variable can provide adequate results. This results in several hundreds or maybe a few thousand events and, thus, load-flow computations. This is still typically one or two orders of magnitude better than Monte Carlo simulation, where several tenths or even hundreds of thousands of trials might be necessary in a typical situation to get credible results. It should be clarified, however, that since linearization are involved there is always some approximation involved in the results, which is greater as the degree of nonlinearity increases. Multi-linearization mitigate this effect, but cannot eliminate it.

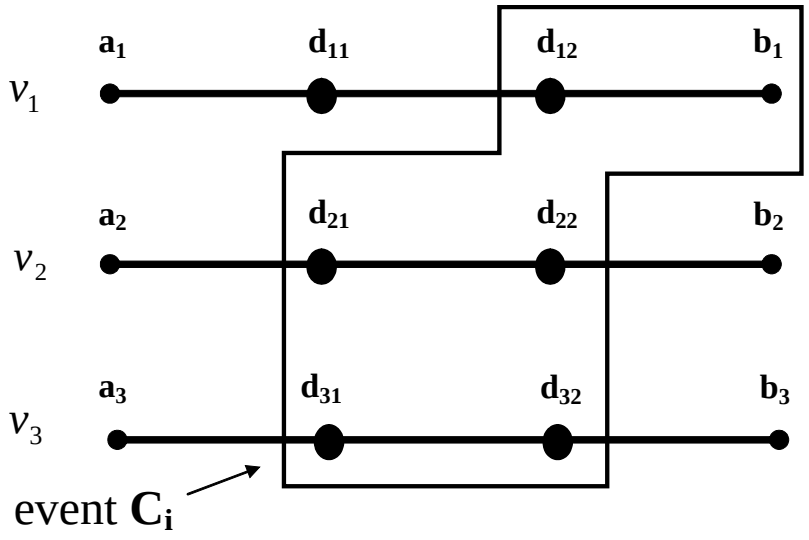

Figure B.3: Schematic representation of non-conforming load sectionalization.

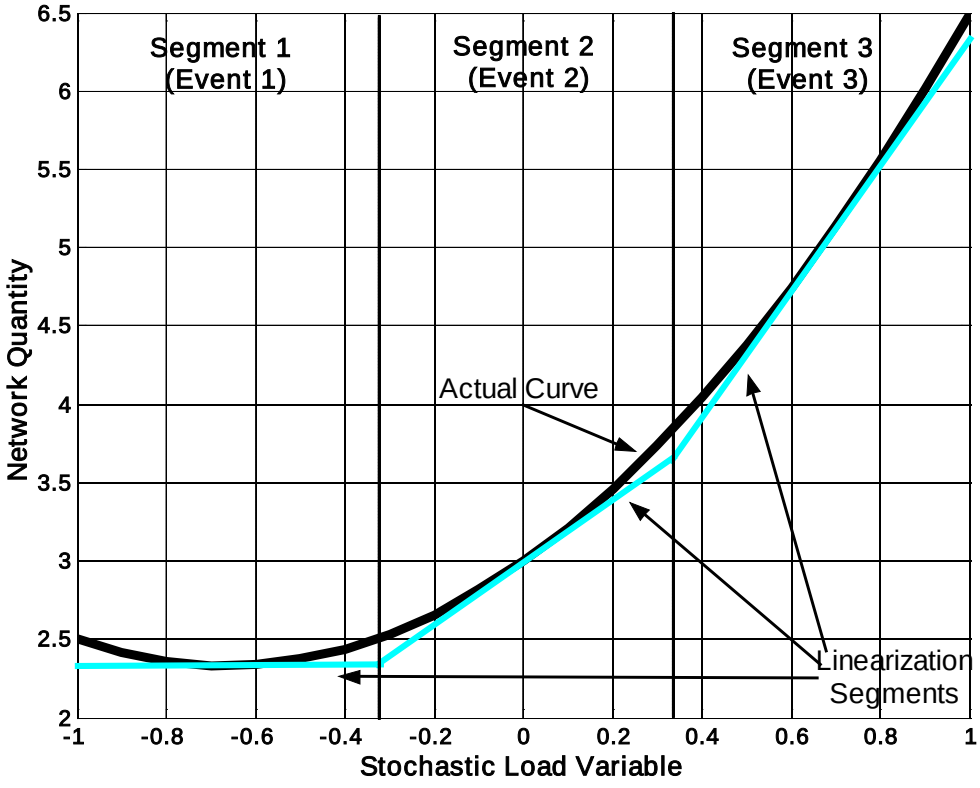

Figure B.4: Illustration of multi-point linearization.

B.4 Monte Carlo Simulation

The proposed multiple-point-linearization based methodology is validated with an independent method based on Monte Carlo simulation. Specifically, the same problem is also solved via Monte Carlo simulations in which each random sample is fully solved, thus incorporating nonlinearities resulting from the AC power flow equations and major operating practices, such as economic dispatch and congestion management or other necessary remedial actions. Both the linearization solution and the Monte Carlo approach are based on the quadratic power flow model.

The basic idea of Monte Carlo simulation is to simulate a specified system with a reasonable number of random draws of all possible system states according to their probability distributions. In this model, the circuit currents, line power flows and bus voltages are computed for a system state determined from a random draw of the state of electric load, that is, by a random draw of the values of the stochastic load variables. Economic dispatch and congestion management, or other possible remedial actions take place at any state that it is necessary, in order to bring the system to an acceptable and secure operational condition. In the Monte Carlo simulation a large number of random draws are generated. The process generates the statistics of circuit currents and the bus voltages. Specifically the cumulative probability distribution function of these quantities is generated. From this distribution, other quantities, such as the probability density function, the expected value, the variance, the standard deviation, etc. can be computed.

B.5 Numerical Results

The proposed method has been applied to the IEEE 24-bus reliability test system (RTS-24), illustrated in Figure B.5. The system is operating at peak loading, at base case.

The detailed system data for each system component can be found in [36]. The nonconforming load model consists of two zero mean stochastic load variables namely v_1 and v_2, which are assumed to be normally distributed with zero mean and variance of 0.1. Therefore, each bus load is expressed as a linear function of these two random variables, i.e.,

$$P_{dk} = P_{dk}^0 + p_{dk}^1 v_1 + p_{dk}^2 v_2, \tag{B.25}$$

where

P_{dk} : active power demand (load) at bus k,

P_{dk}^0 : base case load value at bus k,

p_{dk}^1 : participation coefficient for the 1st random variable,

p_{dk}^2 : participation coefficient for the 2nd random variable.

Three cases are considered for the proposed multi-linearization approach. The stochastic load variables are segmented into one, three and five sections. Comparative results from all the cases are presented. Some sample input forms of the analysis parameters are presented in Figure B.6 and Figure B.7. Sample output results are presented in Figure B.8.

For validation purposes and for the small IEEE RTS-24 20000 Monte Carlo trials are used. Since Monte Carlo simulation is used only for validation purposes, at this stage, no attempt was made to formally estimate the required number of trials, for a particular confidence level.

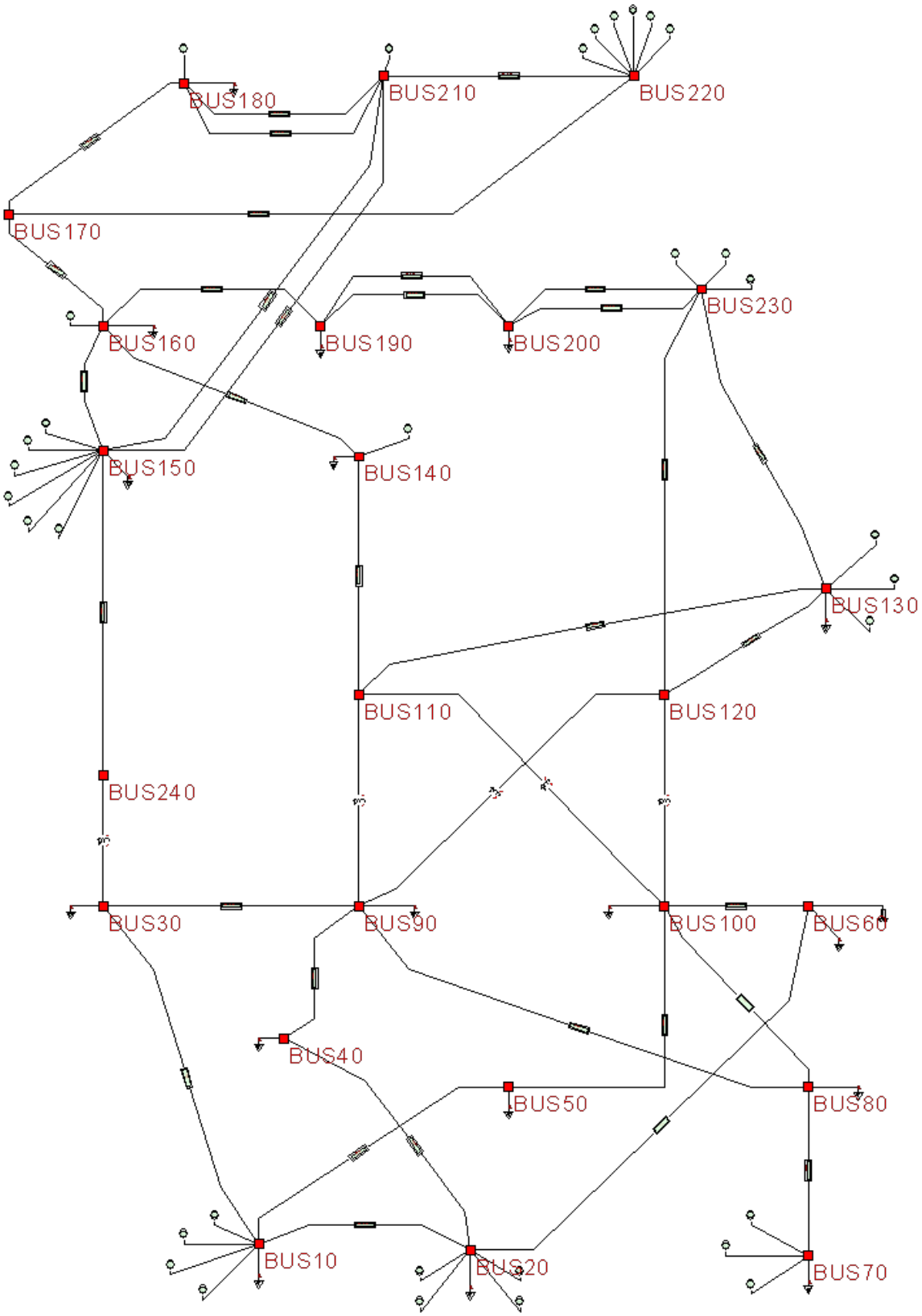

Figure B.5: The IEEE 24-bus reliability test system.

Table B.1 and Table B.2 provide a comparison between the mean value, standard deviation and third and fourth moments for several network quantities, as calculated using the proposed approach and using the Monte Carlo (MC) simulation results. A close agreement between the results is observed for the voltage magnitudes of the PQ system buses, even when using single point linearization. A very close agreement, even when using single linearization, is also observed for the majority of the circuit currents, as shown in Table B.2. Figure B.9 shows the probability density and distribution function for the current magnitude at circuit 200-230 as obtained using the proposed multi-point-linearization method and Monte Carlo simulation.

In only few of the circuits was there a significant mismatch between the proposed method with single linearization and the MC simulation results. This mismatch is minimized or even eliminated when multi-linearizations are used. Results from these circuits are shown in Table B.3 and probability distribution plots of such a case are presented in Figure B.10 through Figure B.12.

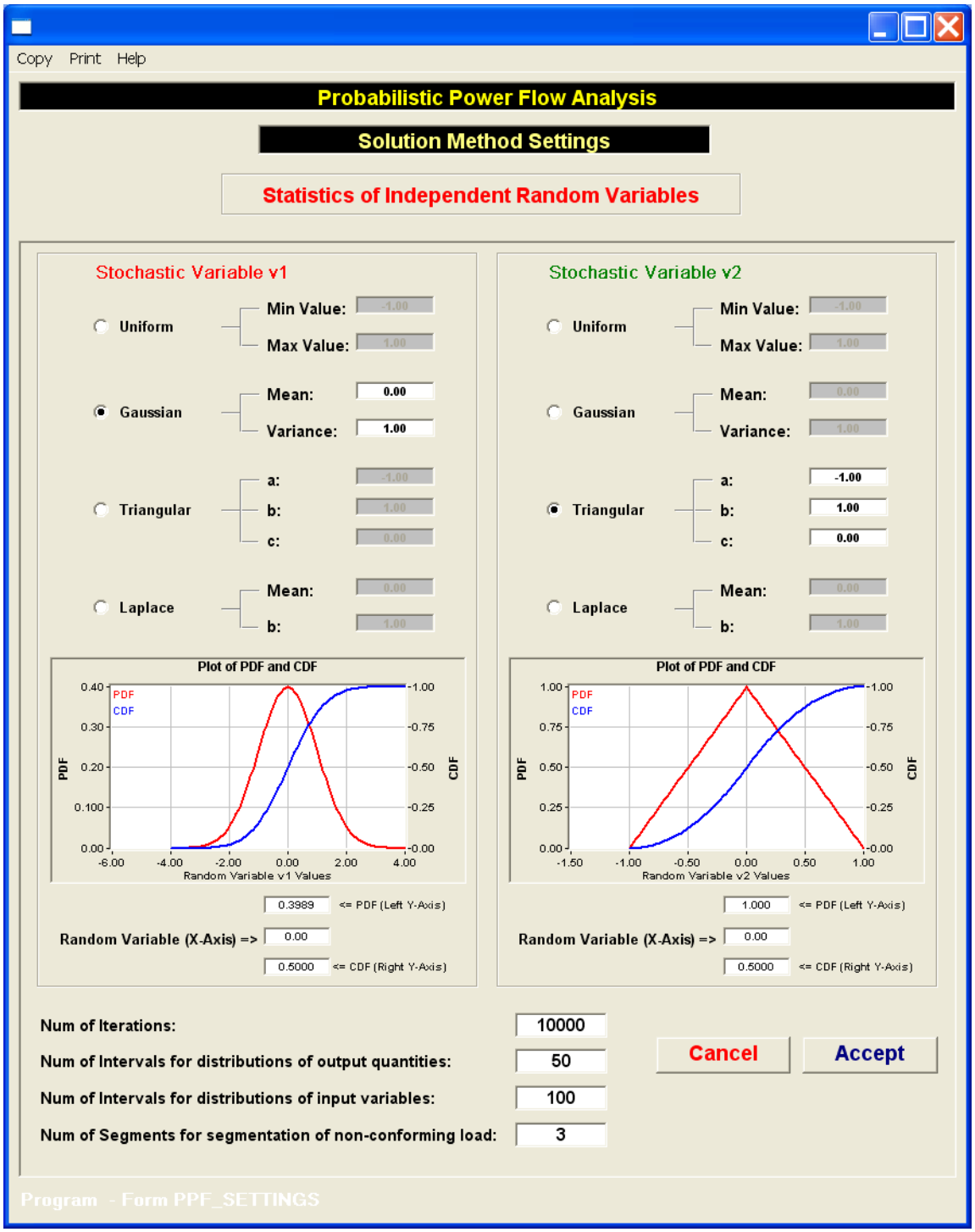

Figure B.6: Definition of stochastic load variables for probabilistic load-flow analysis.

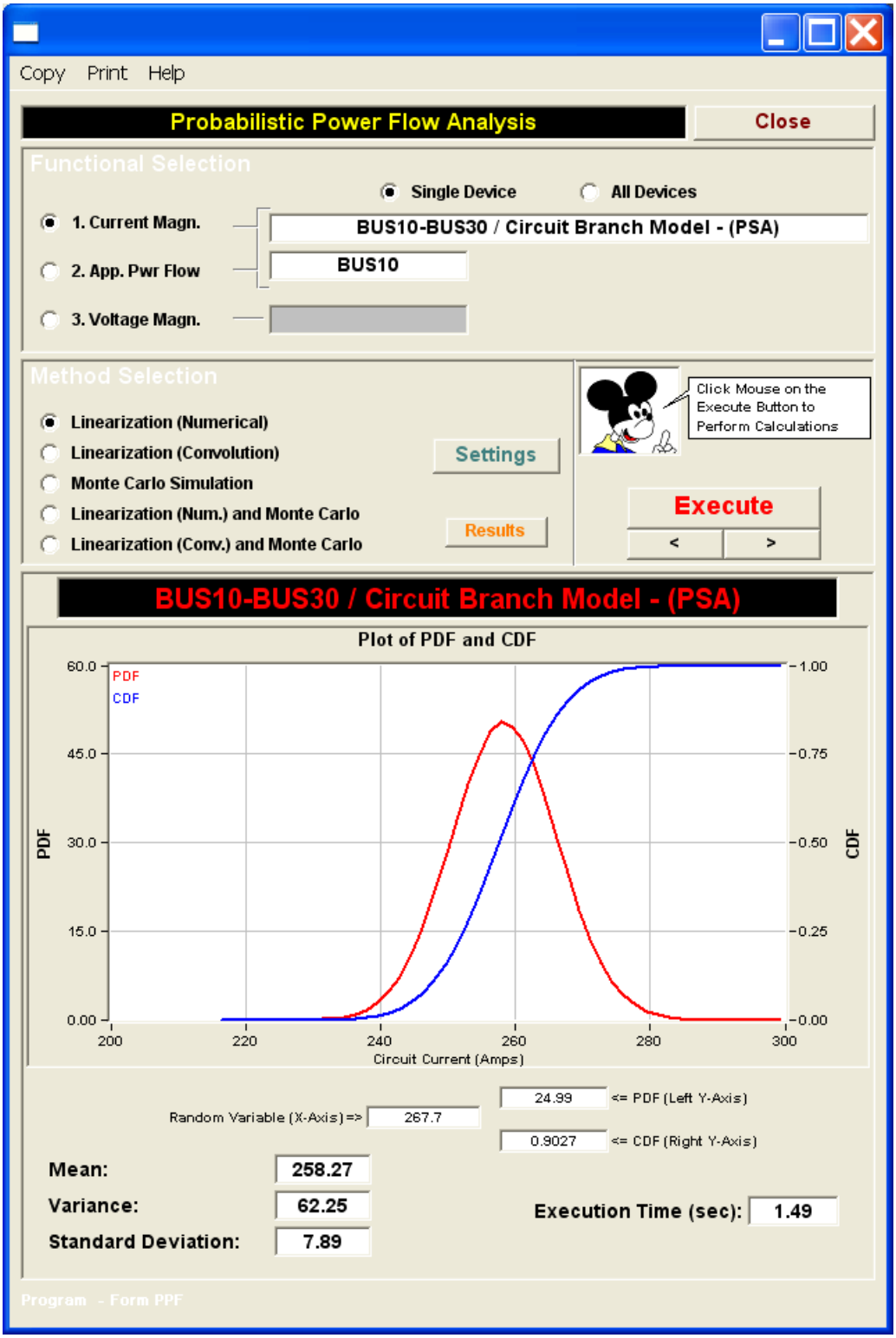

Figure B.7: Sample input/output form for probabilistic load-flow analysis.

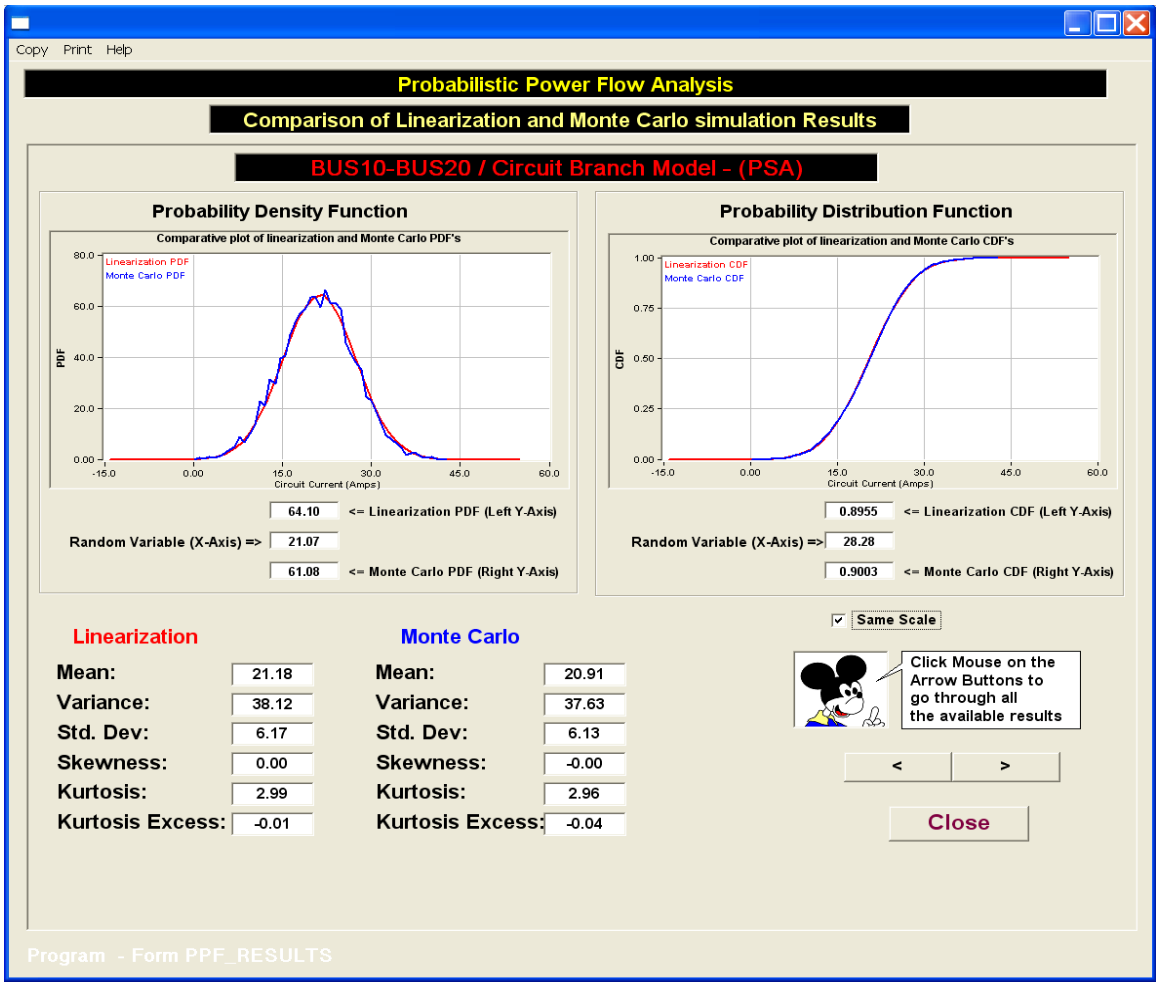

Figure B.8: Detailed output form for probabilistic load-flow analysis.

Table B.1: Comparison of proposed linearization method and Monte-Carlo simulation results for PQ bus voltage magnitudes.

Bus		Proposed Method			MC
		1 Lin.	3 Lin.	5 Lin.	
90	Mean (kV)	131.96	131.91	131.90	131.86
	Std. Dev. (kV)	0.71	0.73	0.73	0.73
	Skewness	0.02	-0.54	-0.59	-0.65
	Kurtosis	2.99	3.52	3.58	3.79
100	Mean (kV)	133.04	132.99	132.98	132.93
	Std. Dev. (kV)	0.81	0.83	0.83	0.83
	Skewness	0.02	-0.50	-0.55	-0.59
	Kurtosis	3.00	3.45	3.50	3.67
110	Mean (kV)	223.77	223.70	223.68	223.62
	Std. Dev. (kV)	1.09	1.12	1.11	1.11
	Skewness	0.03	-0.57	-0.63	-0.68
	Kurtosis	3.00	3.57	3.63	3.84
120	Mean (kV)	224.79	224.73	224.71	224.65
	Std. Dev. (kV)	1.15	1.17	1.17	1.17
	Skewness	0.03	-0.49	-0.54	-0.59
	Kurtosis	3.00	3.43	3.48	3.64

Table B.2: Comparison of proposed linearization method and Monte-Carlo simulation results for circuit currents.

Circuit		Proposed Method			MC
		1 Lin.	3 Lin.	5 Lin.	
210-220	Mean (A)	332.51	332.52	332.52	332.51
	Std. Dev. (A)	1.96	1.96	1.96	1.95
	Skewness	0.03	0.06	0.06	0.04
	Kurtosis	3.00	3.00	3.01	3.01
200-230	Mean (A)	358.74	359.04	359.12	358.30
	Std. Dev. (A)	54.68	54.74	54.71	54.38
	Skewness	0.00	0.05	0.06	0.07
	Kurtosis	3.00	3.00	3.00	3.00
40-90	Mean (A)	207.29	207.73	207.93	207.36
	Std. Dev. (A)	37.66	37.81	37.80	37.61
	Skewness	0.00	0.09	0.10	0.12
	Kurtosis	3.00	3.03	3.04	3.04
60-100	Mean (A)	459.47	460.02	460.21	459.61
	Std. Dev. (A)	46.29	46.38	46.35	46.08
	Skewness	0.00	0.11	0.12	0.13
	Kurtosis	3.00	3.02	3.02	3.03

Table B.3: Comparison of proposed linearization method and Monte-Carlo simulation results for circuit currents.

Circuit		Proposed Method			MC
		1 Lin.	3 Lin.	5 Lin.	
20-40	Mean (A)	164.35	166.33	167.06	166.96
	Std. Dev. (A)	0.70	3.42	3.48	3.51
	Skewness	0.06	2.76	2.74	2.79
	Kurtosis	3.00	14.65	15.52	14.80
20-60	Mean (A)	185.02	186.05	186.38	186.48
	Std. Dev. (A)	3.53	3.82	3.87	3.77
	Skewness	0.06	1.70	1.76	1.81
	Kurtosis	3.00	7.21	6.94	7.45
70-80	Mean (A)	564.66	565.93	566.42	566.26
	Std. Dev. (A)	16.43	16.15	16.18	15.90
	Skewness	0.02	0.73	0.79	0.81
	Kurtosis	3.00	3.62	3.61	3.69
80-100	Mean (A)	76.05	77.72	78.66	78.77
	Std. Dev. (A)	31.68	30.06	29.35	28.74
	Skewness	0.01	0.60	0.71	0.77
	Kurtosis	3.00	3.14	3.22	3.25
160-190	Mean (A)	87.97	95.70	98.16	99.43
	Std. Dev. (A)	55.33	48.06	46.20	43.37
	Skewness	0.02	0.77	0.99	1.11
	Kurtosis	3.00	3.53	3.61	3.96

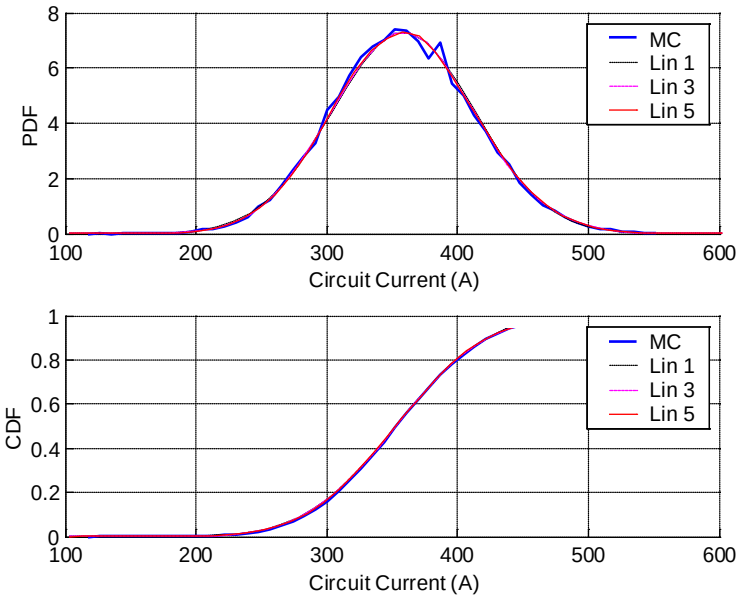

Figure B.9: Comparison of proposed method and Monte Carlo simulation results. Probability density and cumulative distributiion function of circuit 200-230 current.

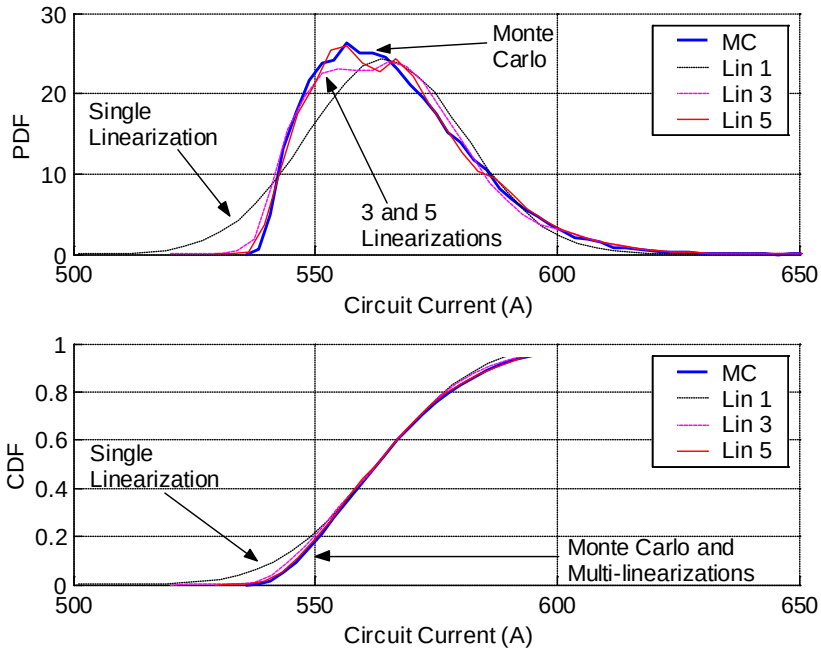

Figure B.10: Comparison of proposed method and Monte Carlo simulation results. Probability density and cumulative distribution function of circuit 70-80 current.

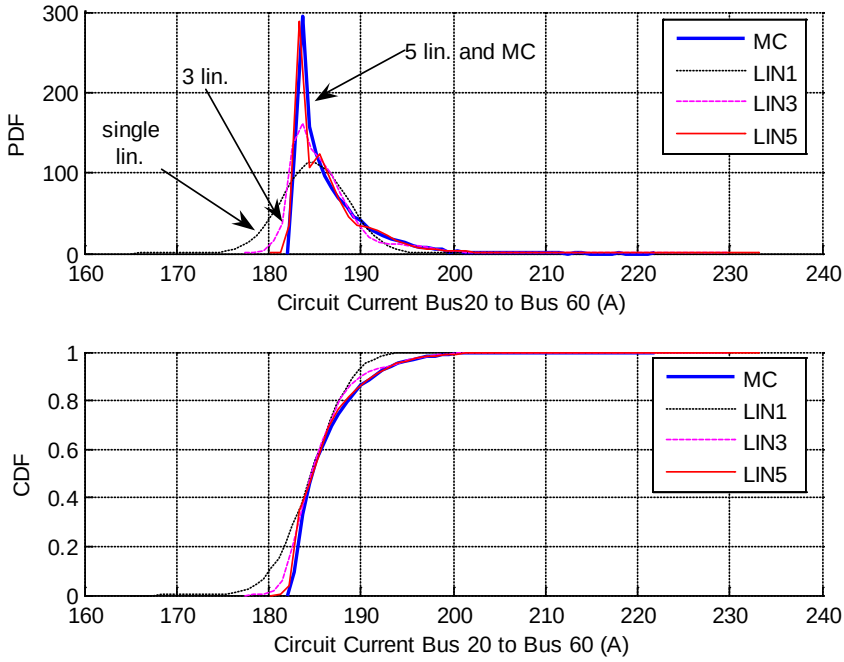

Figure B.11: Comparison of proposed method and Monte Carlo simulation results. Probability density and cumulative distribution function of circuit 20-60 current.

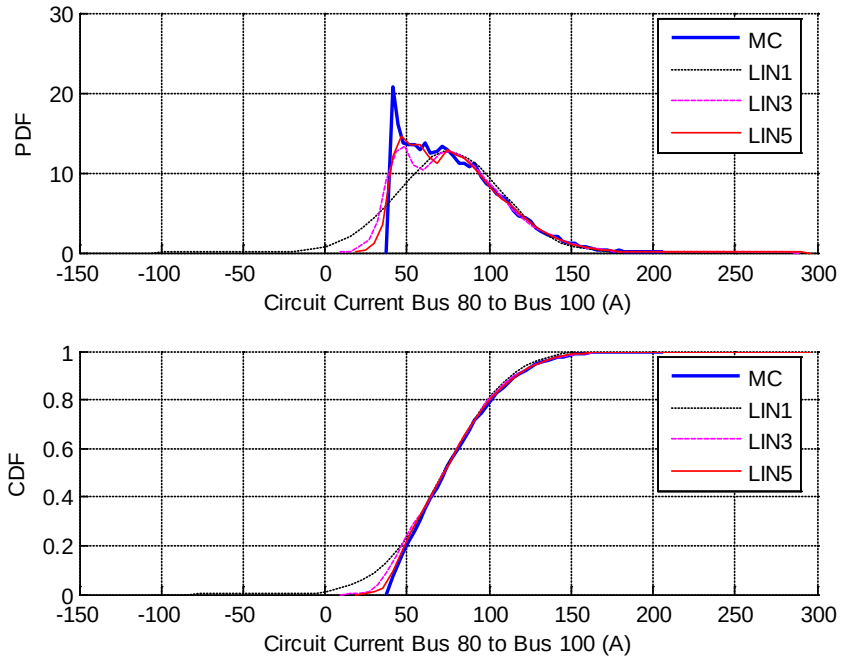

Figure B.12: Comparison of proposed method and Monte Carlo simulation results. Probability density and cumulative distribution function of circuit 80-100 current.

REFERENCES

[1] IEEE Task Force Report, "Load representation for dynamic performance analysis," *IEEE Transactions on Power Systems*, Vol. 8, No 2, May 1993, pp. 472 – 482.

[2] IEEE Task Force Report, "Standard load models for power flow and dynamic performance simulation," *IEEE Transactions on Power Systems*, Vol. 10, No. 3, Aug. 1995, pp. 1302 – 1313.

[3] IEEE Std. 493 2007, IEEE Recommended Practices for the Design of Reliable Industrial and Commercial Power Systems.

[4] M. H. J. Bollen, "Voltage recovery after unbalanced and balanced voltage dips in three-phase systems," *IEEE Transactions on Power Systems*, Vol. 18, Issue 4, Oct. 2003, pp. 1376 – 1381.

[5] B. R. Williams, W. R. Schmus and D. C. Dawson, "Transmission voltage recovery delayed by stalled air conditioner compressors," *IEEE Transactions on Power Systems*, Vol. 7, No. 3, Aug. 1992, pp. 1173 – 1181.

[6] L. Y. Taylor, and S. -M. Hsu, "Transmission voltage recovery following a fault event in the Metro Atlanta area," in *Proceedings of the 2000 IEEE-PES Summer Meeting*, July 16 – 20, 2000, pp. 537 – 542.

[7] T. Sun, Z. Chen and F. Blaabjerg, "Voltage recovery of grid-connected wind turbines after a short-circuit fault," in *Proceedings of the 29th Annual Conference of the IEEE Industrial Electronics Society (IECON '03)*, Vol. 3, Nov. 2 – 6, 2003, pp. 2723 – 2728.

[8] T. Sun, Z. Chen and F. Blaabjerg, "Voltage recovery of grid-connected wind turbines with DFIG after a short-circuit fault," in *Proceedings of the 35th Annual IEEE Power Electronics Specialists Conference (PESC '04)*, Vol. 3, June 20 – 25, 2004, pp. 1991 – 1997.

[9] L. Haijun and H. W. Renzhen, “Preventing of transient voltage instability due to induction motor loads by static condenser,” in *Proceedings of the 1994 IEEE Conference on Industrial Technology*, Dec. 5 – 9, 1994, pp. 827 – 831.

[10] E. Hammad and M. Z. El-Sadek, “Prevention of transient voltage instabilities due to induction motor loads by static VAr compensators,” *IEEE Transactions on Power Systems*, Vol. 4, No. 3, Aug. 1989, pp. 1182 – 1190.

[11] I.A. Hamzah and J. A. Yasin, “Static VAr compensators (SVC) required to solve the problem of delayed voltage recovery following faults in the power system of the Saudi electricity company, western region (SEC-WR),” in *Proceedings of the 2003 IEEE PowerTech Conference*, Vol. 4, Bologna, Italy, June 23 – 26, 2003.

[12] F. P. de Mello and J. W. Feltes, “Voltage oscillatory instability caused by induction motor loads,” *IEEE Transactions on Power Systems*, Vol. 11, No. 3, Aug. 1996, pp. 1279 – 1285.

[13] A. A. Mahmoud, T. H. Ortmeyer, R. G. Harley, and C. Calabrese, “Effects of reactive compensation on induction motor dynamic performance,” *IEEE Transactions on Power Apparatus and Systems*, Vol. PAS-99, No. 3, May/June 1980, pp. 841 – 846.

[14] N. Martins, S. Gomes Jr., R. M. Henriques, C. B. Gomes, A. de Andrade Barbosa, and A. C. B. Martins, “Impact of induction motor loads in system loadability margins and damping of inter-area modes,” in *Proceedings of the 2003 IEEE-PES General Meeting*, Toronto, Canada, July 13 – 17, 2003.

[15] J. Undrill, A. Renno, and G. Drobnjak, “Dynamics of a large induction motor load system,” in *Proceedings of the 2003 IEEE-PES General Meeting*, Toronto, Canada, July 13 – 17, 2003.

[16] K. Morison, H. Hamadani, and L. Wang, “Practical issues in load modeling for voltage stability studies,” in *Proceedings of the 2003 IEEE-PES General Meeting*, Toronto, Canada, July 13 – 17, 2003.

[17] K. Tomiyama, S. Ueoka, T. Takano, I. Iyoda, K. Matsuno, K. Temma, and J. J. Paserba, “Modeling of load during and after system faults based on actual field

data," in *Proceedings of the 2003 IEEE-PES General Meeting*, Toronto, Canada, July 13 – 17, 2003.

[18] R. Navarro, O. Samuelsson, and S. Lindahi, "Automatic determination of parameters in dynamic load models from normal operation data," in *Proceedings of the 2003 IEEE-PES General Meeting*, Toronto, Canada, July 13 – 17, 2003.

[19] R. Navarro, O. Samuelsson, and S. Lindahi, "Influence of normalization in dynamics reactive load models," *IEEE Transactions on Power Systems*, Vol. 18, Issue 2, May 2003, pp. 972 – 973.

[20] C. -J. Lin, A. Y. -T. Chen, C. -Y. Chiou, C. -H. Huang, H. -D. Chiang, J. -C. Wang and L. Fekih-Ahmed, "Dynamic load models in power systems using the measurement approach," *IEEE Transactions on Power Systems*, Vol. 8, Issue 1, Feb. 1993, pp. 309 – 315.

[21] D. J. Hill, "Nonlinear dynamic load models with recovery for voltage stability studies," *IEEE Transactions on Power Systems*, Vol. 8, No. 1, Feb. 1993, pp. 166 – 176.

[22] D. Karlsson and D. J. Hill, "Modeling and identification of nonlinear dynamic loads in power systems," *IEEE Transactions on Power Systems*, Vol. 9, No. 1, Feb. 1994, pp. 157 – 166.

[23] V. Stewart and E. H. Camm, "Modeling of stalled motor loads for power system short-term voltage stability analysis," in *Proceedings of the 2005 IEEE-PES General Meeting*, San Francisco, CA, USA, June 12 – 16, 2005, pp. 1887 – 1892.

[24] S. J. Ranade, D. R. Sagi, R. Adapa, "Load understanding and model development," in *Proceedings of the 2005/2006 IEEE-PES Transmission and Distribution Conference and Exposition*, Dallas, TX, USA, May 21 – 26, 2006, pp. 1315 – 1319.

[25] A. Ellis, D. Kosterev, A. Meklin, "Dynamic load models: Where are we," in *Proceedings of the 2005/2006 IEEE-PES Transmission and Distribution Conference and Exposition*, Dallas, TX, USA, May 21 – 26, 2006, pp. 1320 – 1324.

[26] S. J. Ranade, D. R. Sagi, A. Ellis, “Identifying load inventory from measurements,” in *Proceedings of the 2005/2006 IEEE-PES Transmission and Distribution Conference and Exposition*, Dallas, TX, USA, May 21 – 26, 2006, pp. 1329 – 1333.

[27] S. M. Halpin, “Advanced load models in power system dynamic studies: Application issues,” in *Proceedings of the 2005/2006 IEEE-PES Transmission and Distribution Conference and Exposition*, Dallas, TX, USA, May 21 – 26, 2006, pp. 1334 – 1336.

[28] T. E. McDermott, R. Juchem, D. Devarajan, “Distribution feeder and induction motor modeling with VHDL-AMS,” in *Proceedings of the 2005/2006 IEEE-PES Transmission and Distribution Conference and Exposition*, Dallas, TX, USA, May 21 – 26, 2006, pp. 141 – 146.

[29] G. L. Chinn, “Modeling stalled induction motors,” *Proceedings of the 2005/2006 IEEE-PES Transmission and Distribution Conference and Exposition*, Dallas, TX, USA, May 21 – 26, 2006, pp. 1325 – 1328.

[30] W. H. Kersting, W. Carr, “Induction machine phase frame model,” in *Proceedings of the 2005/2006 IEEE-PES Transmission and Distribution Conference and Exposition*, Dallas, TX, USA, May 21 – 26, 2006, pp. 568 – 574.

[31] T. E. McDermott, “Induction machine test case for distribution feeders: Steady state and dynamic solutions,” in *Proceedings of the 2005/2006 IEEE-PES Transmission and Distribution Conference and Exposition*, Dallas, TX, USA, May 21 – 26, 2006, pp. 575 – 577.

[32] R. C. Dugan, “Induction machine modeling for distribution system analysis – Test case description,” in *Proceedings of the 2005/2006 IEEE-PES Transmission and Distribution Conference and Exposition*, Dallas, TX, USA, May 21 – 26, 2006, pp. 578 – 582.

[33] S. Santoso, Kyeon Hur, Zheng Zhou, “Induction machine modeling for distribution system analysis – A time domain solution,” in *Proceedings of the*

2005/2006 IEEE-PES Transmission and Distribution Conference and Exposition, Dallas, TX, USA, May 21 – 26, 2006, pp. 583 – 587.

[34] J. Mahseredjian, S. Dennetiere, B. Khodabakhchian, A. Xemard, "Induction machine modeling for distribution system analysis using initialization and time-domain methods," in *Proceedings of the 2005/2006 IEEE-PES Transmission and Distribution Conference and Exposition*, Dallas, TX, USA, May 21 – 26, 2006, pp. 588 – 591.

[35] A. P. Sakis Meliopoulos, Wenzhong Gao, Shengyuan Li, G. J. Cokkinides and Roger Dougal, "Quadratized induction machine model for power flow analysis," in *Proceedings of the Second IASTED International Conference, EuroPES,* Crete, Greece, June 25 – 28, 2002, pp 194 – 199.

[36] IEEE Committee Report, "IEEE Reliability Test System," *IEEE Transactions Power Apparatus and Systems*, Vol. PAS-98, No. 6, Nov./Dec. 1979, pp. 2047 – 2054.

[37] A. P. Meliopoulos and G. J. Cokkinides, *Power Systems Modeling, Analysis, and Control*. Unpublished.

[38] S. W. Kang, "A new approach for power transaction evaluation and transfer capability analysis," Ph.D. dissertation, Georgia Institute of Technology, Atlanta, GA, USA, 2001.

[39] Sun Wook Kang, A. P. Meliopoulos, "Contingency selection via quadratized power flow sensitivity analysis," in *Proceedings of the IEEE 2002 Power Engineering Society Summer Meeting*, Vol. 3, pp.1494 – 1499.

[40] G. K. Stefopoulos, A. P. Sakis Meliopoulos, and G. J. Cokkinides, "Probabilistic power flow with non-conforming electric loads," in *Proceedings of the 8th International Conference on Probabilistic Methods Applied to Power Systems (PMAPS 2004),* Ames, IA, Sept. 12 – 16, 2004, pp. 525 – 531.

[41] F. Yang, "A comprehensive approach for bulk power system reliability assessment," Ph.D. dissertation, Georgia Institute of Technology, Atlanta, GA, USA, 2007.

[42] Z. Zhang, G. E. Dawson, and T. R. Eastham, “Evaluation of dynamic parameters and performance of deep-bar induction machines,” in *Proceedings of the IEEE-IAS Annual Meeting*, 1993, pp. 62 – 66.

[43] S. I. Moon and A. Keyhani, “Estimation of induction machine parameters from standstill time domain data,” in *Proceedings of the IEEE-IAS Annual Meeting*, 1993, pp. 336 – 342.

[44] J. R. Willis, G. J. Brock, and J. S. Edmonds, “Derivation of induction motor models form standstill frequency response tests,” *IEEE Transactions on Energy Conversion*, Vol. 4, Dec. 1989, pp. 608 – 615.

[45] T. A. Lipo and A. Consoli, “Modeling and simulation of induction motors with saturable leakage reactances,” *IEEE Transactions on Industry Applications*, Vol. IA-21, Jan./Feb. 1984, pp. 180 – 189.

[46] A. Keyani and H. Tsai, “IGSPICE simulation of induction machines with saturable inductances,” *IEEE Transactions on Energy Conversion*, Vol. 4, Mar. 1989, pp. 118 – 125.

[47] L. Zai, C. L. de Marco, and T. A. Lipo, “An extended Kalman filter approach to rotor time constant measurement in PWM induction motor drives,” *IEEE Transactions on Industry Applications*, Vol. 28, Jan./Feb. 1992, pp. 96 – 104.

[48] J. Holtz and T. Thim, “Identification of the machine parameters in a vector controlled induction motor drive,” *IEEE Transactions on Industry Applications*, Vol. 27, Nov./Dec., 1991, pp. 1111 – 1118.

[49] J. A. de Koch, F. S. van der Merwe, and H. J. Vermeuler, “Induction motor parameter estimation through and output error technique,” presented at the *IEEE-PES Winter Meeting*, Columbus, OH, 1993, Paper 93-WM 01909 EC.

[50] P. Pillay, R. Nolan, and T. Haque, “Application of genetic algorithm to motor parameter determination for transient torque calculations,” *IEEE Transactions on Industry Applications*, Vol. 33, No 5, Sept./Oct. 1997, pp. 1273 – 1282.

[51] T. Phumiphak and C. Chat-uthai, “Estimation of induction motor parameters based on field test coupled with genetic algorithm,” in *Proceedings of the*

International Conference on Power System Technology 2002 (PowerCon 2002), pp. 1199 – 1203.

[52] H. Weatherford and C. W. Brice, "Estimation of induction motor parameters by a genetic algorithm," in *Proceedings of the 2003 Annual Pulp and Paper Industry Technical Conference*, pp. 21 – 28.

[53] P. Nangsue, P. Pillay, S. Conry, "Evolutionary algorithms for induction motor parameter determinations," *IEEE Transactions on Energy Conversion*, Vol. 14, No 3, Sept.1999, pp. 447 – 453.

[54] B. K. Johnson and J. R. Willis, "Tailoring induction motor analytical models to fit known motor performance characteristics and satisfy particular study needs," *IEEE Transactions on Power Systems*, Vol. 6, No 3, Aug. 1991, pp. 959 – 965.

[55] J. Pedra and F. Corcoles, "Estimation of induction motor double-cage model parameters from manufacturer data," *IEEE Transactions on Energy Conversion*, Vol. 19, No 2, June 2004, pp. 310 – 317.

[56] M. Cirrincione, M. Pucci, G. Cirrincione, and G-A Capolino, "A new experimental application of least squares techniques for the estimation of the induction motor parameters," *IEEE Transactions on Industry Applications*, Vol. 39, No 5, Sept./Oct. 2003, pp. 1247 – 1256.

[57] P. Ju, E. Handschin, Z. N. Wei, U. Schluecking, "Sequential parameter estimation of a simplified induction motor load model," *IEEE Transactions on Power Systems*, Vol. 11, No 1, Feb. 1996, pp. 319 – 324.

[58] U. M. Ascher and L. R. Petzold, *Computer methods for ordinary differential and differential-algebraic equations*. Society for Industrial and Applied Mathematics (SIAM), 1998.

[59] E. Hairer, S. P. Norsett and G. Wanner, *Solving ordinary differential equations I: Nonstiff problems*. 2nd edition, New York: Springer-Verlag, 1993.

[60] E. Hairer and G. Wanner, *Solving ordinary differential equations II: Stiff and differential-algebraic problems*. 2nd edition, New York: Springer-Verlag, 1996.

[61] H. W. Dommel, “Digital computer simulation of electromagnetic transients in single- and multiphase networks,” *IEEE Transactions on Power Apparatus and Systems*, Vol. PAS-88, No. 4, Apr. 1969, pp. 388 – 399.

[62] R. B. I. Johnson, B. J. Cory and M. J. Short, “A tunable integration method for the simulation of power system dynamics,” *IEEE Transactions on Power Systems*, Vol. 3, No. 4, Nov. 1988, pp. 1530 – 1537.

[63] K. K. Yen, Z. Hu and J. Andrian, “Stability study of parallel predictor-corrector numerical integration algorithm and redesign,” in *Proceedings of the 1989 IEEE Energy and Information Technologies in the Southeast Conference*, 9 – 12 April 1989, Vol. 2, pp. 417 – 420.

[64] P. P. J. van den Bosch and H. R. Visser, “Simulation of state-events in power electronic devices,” in *Proc. of the 4th International Conference on Power Electronics and Variable-Speed Drives*, 17 – 19 July 1990, pp. 184 – 189.

[65] T. Kato and K. Ikeuchi, “Variable order and variable step-size integration method for transient analysis programs,” *IEEE Transactions on Power Systems*, Vol. 6, No. 1, Feb. 1991, pp. 206 – 213.

[66] T. Kato and T. Kataoka, “Computer-aided analysis of a power electronic circuit by a new multirate method,” in *Proceedings of the 29th Annual IEEE Power Electronics Specialists Conference (PESC 98)*, May 1998, Vol. 2, pp. 1076 – 1083.

[67] H. Takano, S. M. Ulhaq and M. Nakaoka, “Computer-aided simulation technique of digitally controlled switched-mode power conversion circuits and systems using state variable matrices,” in *Proceedings of the 1997 Power Conversion Conference*, 3 – 6 Aug. 1997, Vol. 1, pp. 411 – 418.

[68] P. Pejovic, D. Maksimovic, “PETS-A simulation tool for power electronics,” *1996 IEEE Workshop on Computers in Power Electronics*, 11 – 14 Aug. 1996, pp. 1 – 8.

[69] V. R. Dinavahi, M. R. Iravani and R. Bonert, “Real-time digital simulation of power electronic apparatus interfaces with digital controllers,” *IEEE Transactions on Power Delivery*, Vol. 16, No. 4, Oct. 2001, pp. 775 – 781.

[70] W. Gao, E. Solodovnik, R. Dougal, G. Cokkinides, and A. P. Meliopoulos, “Elimination of numerical oscillations in power system dynamic simulation,” in *Proceedings of the 18th Annual IEEE Applied Power Electronics Conference and Exposition (APEC ‘03)*, 9 – 13 Feb. 2003, Vol. 2, pp. 790 – 794.

[71] J. R. Marti and J. Lin, “Suppression of numerical oscillations in the EMTP,” *IEEE Transactions on Power Systems*, Vol. 4, No. 2, May 1989, pp. 739 – 747.

[72] J. Lin and J. R. Marti, “Implementation of the CDA procedure in the EMTP,” *IEEE Transactions on Power Systems*, Vol. 5, No. 2, May 1990, pp. 394 – 402.

[73] F. L. Alvarado, R. H. Lasseter, and J. J. Sanchez, “Testing of trapezoidal integration with damping for the solution of power transient problems,” *IEEE Transactions on Power Apparatus and Systems*, Vol. PAS-102, No. 12, Dec. 1983, pp. 3783 – 3790.

[74] K. Strunz, “Position variant integration in digital real time simulators for electromagnetic transients,” in *Proceedings of the 2002 International Conference on Power System Technology (PowerCon 2002)*, 13-17 Oct. 2002, Vol. 4, pp. 2019 – 2025.

[75] K. Strunz, “Flexible numerical integration for efficient representation of switching in real time electromagnetic transients simulation,” *IEEE Transactions on Power Delivery*, Vol. 19, No. 3, July 2004, pp. 1276 – 1283.

[76] K. Strunz, “Position-dependent control of numerical integration in circuit simulation,” IEEE Transactions on Circuits and Systems II: Express Briefs [see also Circuits and Systems II: Analog and Digital Signal Processing], Vol. 51, Issue 10, Oct. 2004, pp. 561 – 565.

[77] K. Strunz, Numerical methods for real time simulation of electromagnetics in AC/DC network systems. Dusseldorf, Germany: VDI Verlag, 2002.

[78] C.-T. Liu and W.-L. Chang, “Synchronized solution of power electronics system equations using flexible MODELS component connected to the EMTP,” *IEEE Transactions on Power Delivery*, Vol. 11, No. 4, Oct. 1996, pp. 1868 – 1873.

[79] X. Cao, A. Kurita, T. Yamanaka, Y. Tada and H. Mitsuma, “Suppression of numerical oscillation caused by the EMTP-TACS interface using filter interpolation,” *IEEE Transactions on Power Delivery*, Vol. 11, No. 4, Oct. 1996, pp. 2049 – 2055.

[80] M. Roitman and P. S. R. Diniz, “Simulation of non-linear and switching elements for transient analysis based on wave digital filters,” *IEEE Transactions on Power Delivery*, Vol. 11, No. 4, Oct. 1996, pp. 2042 – 2048.

[81] J. J. Grainger and S. H. Lee, “Optimum size and location of shunt capacitors for reduction of losses on distribution feeders,” *IEEE Transactions on Power Apparatus and Systems*, Vol. PAS-100, Mar. 1981, pp. 1105 – 1118.

[82] J. J. Grainger, S. H. Lee, “Capacity release by shunt capacitor placement on distribution feeders: A new voltage-dependent model,” *IEEE Transactions on Power Apparatus and Systems*, Vol. 101, Issue 5, May 1982, pp. 1236 – 1244.

[83] J. J. Grainger, A. A. El-Kib, S. H. Lee, “Optimal capacitor placement on three-phase primary feeders: Load and feeder unbalance effects,” *IEEE Transactions on Power Apparatus and Systems*, Vol. PAS-102, Issue 10, Oct. 1983, pp. 3296 – 3305.

[84] R. E. Rinker, D. L. Rembert, “Using the reactive current profile of a feeder to determine optimal capacitor placement,” *IEEE Transactions on Power Delivery*, Vol. 3, Issue 1, Jan. 1988, pp. 411 – 416.

[85] M. E. Baran, F. F. Wu, “Optimal capacitor placement on radial distribution systems,” *IEEE Transactions on Power Delivery*, Vol. 4, Issue 1, Jan. 1989, pp. 725 – 734.

[86] H. -D. Chiang, J. -C. Wang, O. Cockings, H. -D. Shin, “Optimal capacitor placements in distribution systems. I. A new formulation and the overall

problem," *IEEE Transactions on Power Delivery*, Vol. 5, Issue 2, Apr. 1990, pp. 634 – 642.

[87] H. -D. Chiang, J. -C. Wang, O. Cockings, H. -D. Shin, "Optimal capacitor placements in distribution systems. II. Solution algorithms and numerical results," *IEEE Transactions on Power Delivery*, Vol. 5, Issue 2, Apr. 1990, pp. 643 – 649.

[88] H. -D Chiang, J. -C Wang, J. Tong, G. Darling, "Optimal capacitor placement, replacement and control in large-scale unbalanced distribution systems: system modeling and a new formulation," in *Proceedings of the 1994 IEEE PES Transmission and Distribution Conference*, Apr. 10 – 15 1994, pp. 173 – 179.

[89] H. -D Chiang, J. -C Wang, J. Tong, G. Darling, "Optimal capacitor placement, replacement and control in large-scale unbalanced distribution systems: system solution algorithms and numerical studies," in *Proceedings of the 1994 IEEE PES Transmission and Distribution Conference*, Apr. 10 – 15, 1994, pp. 180 – 186.

[90] H. -D Chiang, J. -C Wang, J. Tong, G. Darling, "Optimal capacitor placement, replacement and control in large-scale unbalanced distribution systems: modeling and a new formulation," *IEEE Transactions on Power Systems*, Vol. 10, Issue 1, Feb. 1995, pp. 356 – 362.

[91] H. -D Chiang, J. -C Wang, J. Tong, G. Darling, "Optimal capacitor placement, replacement and control in large-scale unbalanced distribution systems: system solution algorithm and numerical studies," *IEEE Transactions on Power Systems*, Vol. 10, Issue 1, Feb. 1995, pp. 363 – 369.

[92] H. -T. Yang, Y. -C. Huang, C. -L. Huang, "Solution to capacitor placement problem in a radial distribution system using tabu search method," in *Proceedings of the 1995 International Conference on Energy Management and Power Delivery*, Nov. 21 – 23, 1995, pp. 388 – 393.

[93] Y. -C. Huang, H. -T. Yang, C. -L. Huang, "Solving the capacitor placement problem in a radial distribution system using Tabu search approach," *IEEE Transactions on Power Systems*, Vol. 11, Issue 4, Nov. 1996, pp. 1868 – 1873.

[94] J. -C. Wang, H. -D Chiang, K. N. Miu, G. Darling, “Capacitor placement and real time control in large-scale unbalanced distribution systems: loss reduction formula, problem formulation, solution methodology and mathematical justification,” *IEEE Transactions on Power Delivery*, Vol. 12, Issue 2, Apr. 1997, pp. 953 – 958.

[95] J. -C. Wang, H. -D Chiang, K. N. Miu, G. Darling, “Capacitor placement and real time control in large-scale unbalanced distribution systems: numerical studies,” *IEEE Transactions on Power Delivery*, Vol. 12, Issue 2, Apr. 1997, pp. 959 – 964.

[96] K. N. Miu, H. -D Chiang, G. Darling, “Capacitor placement and control in large-scale distribution systems by a GA-based two-stage algorithm,” *IEEE Transactions on Power Delivery*, Vol. 12, Issue 3, Aug. 1997, pp. 1160 – 1166.

[97] K. -H. Kim, S. -K. You, “Voltage profile improvement by capacitor placement and control in unbalanced distribution systems using GA,” in *Proceedings of the 1999 IEEE PES Summer Meeting*, July 18 – 22, 1999, pp. 800-805.

[98] H. Mori, Y. Ogita, “Parallel tabu search for capacitor placement in radial distribution systems,” in *Proceedings of the 2000 IEEE PES Winter Meeting*, Jan. 23 – 27, 2000, pp. 2334 – 2339.

[99] R. A. Gallego, A. J. Monticelli, R. Romero, “Optimal capacitor placement in radial distribution networks,” *IEEE Transactions on Power Systems*, Vol. 16, Issue 4, Nov. 2001, pp. 630 – 637.

[100] K. -H. Kim, S. -B. Rhee, S. -N. Kim, S. -K You, “Application of ESGA hybrid approach for voltage profile improvement by capacitor placement,” *IEEE Transactions on Power Delivery*, Vol. 18, Issue 4, Oct. 2003, pp. 1516 – 1522.

[101] M. H. Shwehdi, A. Mantawi, S. Selim, A. Al-Shehri, G. K. Al-Bassam, “Capacitor placement in distribution systems, a new formulation,” in *Proceedings of the IEEE 2003 Power Tech Conference*, June 23 – 26, 2003, Vol.4.

[102] B. Milosevic, M. Begovic, "Capacitor placement for conservative voltage reduction on distribution feeders," *IEEE Transactions on Power Delivery*, Vol. 19, Issue 3, July 2004, pp. 1360 – 1367.

[103] V. Ajjarapu, Z. Albanna, "Application of genetic based algorithm to optimal capacitor placement," in *Proceedings of the First International Forum on Applications of Neural Networks to Power Systems*, July 23 – 26, 1991, pp. 251 – 255.

[104] M. Delfanti, G. P. Granelli, P. Marannino, M. Montagna, "Optimal capacitor placement using deterministic and genetic algorithms," in *Proceedings of the 21st IEEE International Conference on Power Industry Computer Applications*, May 16 – 21, 1999, pp. 331 – 336.

[105] M. Delfanti, G. P. Granelli, P. Marannino, M. Montagna, "Optimal capacitor placement using deterministic and genetic algorithms," *IEEE Transactions on Power Systems*, Vol. 15, Issue 3, Aug. 2000, pp. 1041 – 1046.

[106] S. R. Iyer, K. Ramachandran, S. Hariharan, "Optimal reactive power allocation for improved system performance," *IEEE Transactions on Power Apparatus and Systems*, Vol. 103, Issue 6, June 1984, pp.1509 – 1515.

[107] R. Kenarangui, N. M. Tabatabaye, "Decision based VAr compensators placement in electric power systems," in *Proceedings of the 1991 IEEE International Conference on Systems, Man, and Cybernetics*, Oct. 13 – 16, 1991, Vol. 3, pp. 1912 – 1924.

[108] B. Kermanshahi, K. Takahashi, Yicheng Zhou, "Optimal operation and allocation of reactive power resources considering static voltage stability," in *Proceedings of the 1998 International Conference on Power System Technology*, Aug. 18 – 21, 1998, Vol. 2, pp. 1473 – 1477.

[109] S. Ahmed, G. Strbac, L. Yao, A. Dixon, A. Chebbo, A. Ekwue, D. T. Y. Cheng, "Method for green field security-constrained allocation of reactive support," *IEE Proceedings on Generation, Transmission and Distribution*, Vol. 146, Issue 1, Jan. 1999, pp. 65 – 71.

[110] S. H. Goh, T. K. Saha, Z. Y. Dong, "Optimal reactive power allocation for power system transfer capability assessment," presented at the *2006 IEEE PES General Meeting*, June 18 – 22, 2006.

[111] A. A. El-Dip, H. K. M. Youssef, M. M. El-Metwally, Z. Osman, "Optimum VAr sizing & Allocation using particle swarm optimization," in *Proceedings of the 2005 – 2006 IEEE PES T&D Conference and Exposition*, Dallas, TX, May 21 – 26, 2006, pp. 1108 – 1115.

[112] A. A. El-Dip, H. K. M. Youssef, M. M. El-Metwally, Z. Osman, "Optimum VAr sizing & Allocation using particle swarm optimization," in *Proceedings of the* 2006 *IEEE PES General Meeting*, June 18 – 22, 2006.

[113] M. M. Begovic, B. Radibratovic, F. C. Lambert, "On multi-objective volt-VAr optimization in power systems," in *Proceedings of the 37th Annual Hawaii International Conference on System Sciences*, Jan. 5 – 8, 2004.

[114] B. Radibratovic, "Reactive optimization of transmission and distribution networks," Ph.D. dissertation, Georgia Institute of Technology, Atlanta, GA, USA, 2009.

[115] B. Gou, A. Abur, "Optimal capacitor placement for improving power quality," in *Proceedings of the 1999 IEEE PES Summer Meeting*, July 18 – 22, 1999, pp. 488 – 492.

[116] P. M. Hogan, J. D. Rettkowski, J. L. Bala Jr., "Optimal capacitor placement using branch and bound," in *Proceedings of the 37th Annual North American Power Engineering Symposium*, Oct. 23 – 25, 2005.

[117] S. F. Mekhamer, M. E. El-Hawary, S. A. Soliman, M. A. Moustafa, M. M. Mansour, "New heuristic strategies for reactive power compensation of radial distribution feeders," *IEEE Transactions on Power Delivery*, Vol. 17, Issue 4, Oct. 2002, pp. 1128 – 1135.

[118] A. H. H. Al-Mohammed, I. Elamin, "Capacitor placement in distribution systems using artificial intelligence techniques," in *Proceedings of the 2003 IEEE Bologna Power Tech Conference*, Vol. 4, Jun. 23 – 26, 2003.

[119] H. N. Ng, M. M. A. Salama, A. Y. Chikhani, "Capacitor allocation by approximate reasoning: fuzzy capacitor placement," *IEEE Transactions on Power Delivery*, Vol. 15, Issue 1, Jan. 2000, pp. 393 – 398.

[120] S. F. Mekhamer, S. A. Soliman, M. A. Moustafa, M. E. El-Hawary, "Application of fuzzy logic for reactive-power compensation of radial distribution feeders," *IEEE Transactions on Power Systems*, Vol. 18, Issue 1, Feb. 2003, pp. 206 – 213.

[121] K. Prakash, M. Sydulu, "Particle swarm optimization based capacitor placement on radial distribution systems," in *Proceedings of the 2007 IEEE PES General Meeting*, Jun. 24 – 28, 2007.

[122] P.K. Dash, S. Saha, P. K. Nanda, "Artificial neural net approach for capacitor placement in power system," in *Proceedings of the First International Forum on Applications of Neural Networks to Power Systems*, July 23 – 26, 1991, pp. 247 – 250.

[123] S. F. Mekhamer, M. E. El-Hawary, M. E. Mansour, M. A. Moustafa, S. A. Soliman, "State of the art in optimal allocation for reactive power compensation in distribution feeders," in *Proceedings of the 2002 Large Engineering Systems Conference on Power Engineering*, Jun. 2002, pp. 61 – 75.

[124] M. A. Golkar, D. Jalali, R. Berahmand-pour, "Optimal placement of static VAr compensators in power systems for stability improvement," in *Proceedings of the 1993 Athens Power Tech Conference*, Sept. 5 – 8, 1993, Vol. 2, pp. 542 – 546.

[125] R. H. Lasseter, R. Wang, "The impact of generation mix on placement of static VAr compensators," *IEEE Transactions on Power Delivery*, Vol. 14, Issue 3, July 1999, pp. 1018 – 1023.

[126] T. V. Menezes, L. C. P. da Silva, V. F. da Costa, "Dynamic VAr sources scheduling for improving voltage stability margin," *IEEE Transactions on Power Systems*, Vol. 18, Issue 2, May 2003, pp. 969 – 971.

[127] G. K. Venayagamoorthy, Y. del Valle, S. Mohagheghi, W. Qiao, S. Ray, R. G. Harley, D. M. Falcao, G. N. Taranto, T. M. L. Assis, "Effects of a STATCOM, a SCRC and a UPFC on the dynamic behavior of a 45 bus section of the Brazilian

power system," in *Proceedings of the Inaugural 2005 IEEE PES Conference and Exposition in Africa*, July 11 – 15, 2005, pp. 305 – 312.

[128] S. Mohagheghi, Y. del Valle, G. K. Venayagamoorthy, R. G. Harley, "Hierarchical control scheme for two static compensators in the Brazilian 45-bus power system," in *Proceedings of the 2006 IEEE PES Power Systems Conference and Exposition*, Oct. 29 – Nov. 1, 2006, pp. 860 – 864.

[129] Y. del Valle, J. C. Hernandez, G. K. Venayagamoorthy, R. G. Harley, "Optimal STACOM sizing and placement using particle swarm optimization," presented at the *2006 IEEE PES Transmission and Distribution Conference and Exposition: Latin America*, Aug. 2006.

[130] A. A. Alabduljabbar, J. V. Milanovic, "Genetic algorithm based optimization for allocation of static VAr compensators," in *Proceedings of the 8th IEE International Conference on AC and DC Power Transmission*, Mar. 28 – 31, 2006, pp. 115 – 120.

[131] J. G. Singh, S. N. Singh, S. C. Srivastava, "An approach for optimal placement of static VAr compensators based on reactive power spot price," *IEEE Transactions on Power Systems*, Vol. 22, Issue 4, Nov. 2007, pp. 2021 – 2029.

[132] P. Kundur, *Power System Stability and Control*. New York: McGraw-Hill, 1994.

[133] P. W. Sauer, M. A. Pai, Power System Dynamics and Stability.

[134] P. M. Anderson, A. A. Fouad, *Power System Control and Stability*, IEEE Press, 2003.

[135] W. Gao, "New methodology for power system modeling and its application in machine modeling and simulation," Ph.D. dissertation, Georgia Institute of Technology, Atlanta, GA, USA, 2002.

[136] W. Gao, A. P. Meliopoulos, E. V. Solodovnik, R. Dougal, "A nonlinear model for studying synchronous machine dynamic behavior in phase coordinates," in *Proceedings of the 2005 IEEE International Conference on Industrial Technology (ICIT 2005)*, Dec. 14 – 17, 2005, Hong Kong, pp. 1092 – 1097.

[137] A. P. Sakis Meliopoulos and George J. Cokkinides, "A virtual environment for protective relaying evaluation and testing", *IEEE Transactions of Power Systems*, Vol. 19, No. 1, Feb., 2004, pp. 104 – 111.

[138] R. G. Harley, E. B. Makram, E. G. Duran, "The effects of unbalanced network and unbalanced faults on induction motor transient stability," *IEEE Transactions on Energy Conversion*, Vol. 3, No. 2, June 1988, pp. 398 – 403.

[139] E. B. Makram, V. O. Zambrano, R. G. Harley, J. C. Balda, "Three-phase modeling for transient stability of large scale unbalanced distribution systems," *IEEE Transactions on Power Systems*, Vol. 4, No. 2, May 1989, pp. 487 – 493.

[140] E. B. Makram, V. O. Zambrano, R. G. Harley, J. C. Balda, "Three-phase modeling for transient stability of large scale unbalanced distribution systems," *IEEE Power Engineering Review*, Vol. 9, Issue 5, May 1989, pp. 47 – 47.

[141] J. E. Dennis, Jr., R. B. Schnabel, Numerical methods for unconstrained optimization and nonlinear equations. SIAM 1996.

[142] G. K. Stefopoulos and A. P. Meliopoulos, "Quadratized three-phase induction motor model for steady-state and dynamic analysis," in *Proceedings of the 38th North America Power Symposium*, Carbondale, IL, USA, Sept. 17 – 19, 2006, pp. 79 – 89.

[143] G. K. Stefopoulos and A. P. Meliopoulos, "Induction motor load dynamics: Impact on voltage recovery phenomena," presented at the *2005 – 2006 IEEE PES T&D Conference and Exposition*, Dallas, TX, May 21 – 26, 2006.

[144] P. Meliopoulos, G. J. Cokkinides, and G. K. Stefopoulos, "Voltage stability and voltage recovery: Effects of electric load dynamics," presented at the *2006 IEEE International Symposium on Circuits and Systems*, Island of Kos, Greece, May 21 – 24, 2006.

[145] A. P. Meliopoulos, G. J. Cokkinides, and G. K. Stefopoulos, "Voltage stability and voltage recovery: load dynamics and dynamic VAr sources," presented at the *2006 IEEE PES General Meeting*, Montréal, Quebec, Canada, June 18 – 29, 2006.

[146] A. P. Meliopoulos, G. J. Cokkinides, and G. K. Stefopoulos, "Voltage stability and voltage recovery: Load dynamics and dynamic VAr sources," in Proceedings of the 2006 IEEE PES Power Systems Conference and Exposition (PSCE 2006), Atlanta, GA, USA, Oct. 29 – Nov. 1, 2006, pp. 124 – 131.

[147] G. K. Stefopoulos, A. P. Meliopoulos, and G. J. Cokkinides, "Voltage-load dynamics: Modeling and control," in *Proceedings of the 2007 iREP Symposium on Bulk Power System Dynamics and Control – VII (iREP 2007)*, Charleston, SC, USA, Aug. 19 – 24, 2007.

[148] G. K. Stefopoulos and A. P. Meliopoulos, "Numerical parameter estimation procedure for three phase induction motor models," in *Proceedings of the 2007 PowerTech Conference*, Lausanne, Switzerland, July 1 – 5, 2007.

[149] A. E. Fitzgerald, C. Kingsley Jr., and S. D. Umans, *Electric Machinery Analysis.* McGraw-Hill, 6th edition, 2002.

[150] IEEE Special Stability Controls Working Group, "Static Var compensator models for power flow and dynamic performance simulation," *IEEE Transactions Power Systems*, Vol. 9, No. 1, Feb. 1994, pp. 229 – 240.

[151] H. Ambriz-Pérez, E. Acha, and C. R. Fuerte-Esquivel, "Advanced SVC models for Newton-Raphson load flow and Newton optimal power flow studies," *IEEE Transactions Power Systems*, Vol. 15, No. 1, Feb. 2000, pp. 129 – 136.

[152] H. Su, K. K. W. Chan, and L. A. Snider, "Interfacing an electromagnetic SVC model into the transient stability simulation," in *Proceedings of the 2002 International Conference on Power System Technology (PowerCon '02)*, Oct. 13 – 17, 2002, pp. 1568 – 1572.

[153] E. Zhijun, K. W. Chan, D. Z. Fang, "A practical dynamic phasor model of static VAR compensator," in *Proceedings of the 2nd International Conference on Power Electronics Systems and Applications*, 2006, pp. 23 – 27.

[154] S. Mohagheghi, "Adaptive critic designs based neurocontrollers for local and wide area control of a multimachine power system with a static compensator," Ph.D. dissertation, Georgia Institute of Technology, Atlanta, GA, USA, 2006.

[155] Q. B. Dam, "Operating strategies to preserve the adequacy of power systems circuit breakers," Ph.D. dissertation, Georgia Institute of Technology, Atlanta, GA, USA, 2009.

[156] P. Sakis Meliopoulos, G. J. Cokkinides, and G. K. Stefopoulos, "Symbolic integration of dynamical systems by collocation methods," in *Proceedings of the 2005 IEEE-PES General Meeting*, San Francisco, CA, June 12 – 16, 2005, pp. 2387 – 2392.

[157] A. P. Sakis Meliopoulos, G. J. Cokkinides, and G. K. Stefopoulos, "Quadratic integration method," in *Proceedings of the 8th Int. Conference on Power System Transients (IPST 05)*, Montréal, Canada, June 19 – 23, 2005.

[158] G. K. Stefopoulos, G. J. Cokkinides, and A. P. Meliopoulos, "Expert symbolic transient simulator based on quadratic integration method," presented at the *13th International Conference on Intelligent System Application to Power Systems (ISAP 2005)*, Washington DC, Nov. 6 – 10, 2005.

[159] A. P. Meliopoulos, G. J. Cokkinides, and G. K. Stefopoulos, "Improved numerical integration method for power/power electronic systems based on three-point collocation," presented at the *44th IEEE Conference on Decision and Control (CDC 2005)*, Seville, Spain, Dec. 12 – 15, 2005.

[160] A. P. Meliopoulos, G. J. Cokkinides, and G. K. Stefopoulos, "Symbolic integration of dynamical systems by collocation methods," in *Proceedings of the 2006 IEEE PES Power Systems Conference and Exposition (PSCE 2006)*, Atlanta, GA, USA, Oct. 29 – Nov. 1, 2006, pp. 362 – 367.

[161] J. J. Sanchez Gasca, C. J. Bridenbaugh, C. E. J. Bowler, J. S. Edmonds, "Trajectory sensitivity based identification of synchronous generator and excitation system parameters," *IEEE Transactions on Power Systems*, Vol. 3, Issue 4, Nov. 1988, pp. 1814 – 1822.

[162] S. M. Benchluch and J. H. Chow, "A trajectory sensitivity method for the identification of nonlinear excitation system models," *IEEE Transactions on Energy Conversion*, Vol. 8, Issue 2, June 1993, pp. 159 – 164.

[163] M. J. Laufenberg and M. A. Pai, "A new approach to dynamic security assessment using trajectory sensitivities," presented at the *20th International Conference on Power Industry Computer Applications (PICA '97)*, 1997.

[164] M. J. Laufenberg and M. A. Pai, "A new approach to dynamic security assessment using trajectory sensitivities," *IEEE Transactions on Power Systems*, Vol. 13, Issue 3, Aug. 1998, pp. 953 – 958.

[165] I. A. Hiskens and M. Akke, "Analysis of the Nordel power grid disturbance of January 1, 1997 using trajectory sensitivities," *IEEE Transactions on Power Systems*, Vol. 14, Issue 3, Aug. 1999, pp. 987 – 994.

[166] I. A. Hiskens and M. A. Pai, "Trajectory sensitivity analysis of hybrid systems," *IEEE Transactions on Circuits and Systems I: Fundamental Theory and Applications*, Vol. 47, No. 2, Feb. 2000, pp. 204 – 220.

[167] T. B. Nguyen, M. A. Pai, and I. A. Hiskens, "Direct computation of critical clearing time using trajectory sensitivities," in *Proceedings of the 2000 IEEE PES Summer Meeting*, July 16 – 20, 2000, pp. 604 – 608.

[168] I. A. Hiskens and M. A. Pai, "Power system applications of trajectory sensitivities," in *Proceedings of the 2002 IEEE PES Winter Meeting*, Jan. 27 – 31, 2002, pp. 1200 – 1205.

[169] T. B. Nguyen, M. A. Pai and I. A. Hiskens, "Sensitivity approaches for direct computation of critical clearing time," *International Journal of Electrical Power and Energy Systems*, Vol. 24, 2002, pp. 337 – 343.

[170] M. Zima and G. Andersson, "Stability assessment and emergency control method using trajectory sensitivities," presented at the *2003 IEEE PowerTech Conference*, Bologna, Italy, June 23 – 26, 2003.

[171] T. B. Nguyen and M. A. Pai, "Dynamic security-constrained rescheduling of power systems using trajectory sensitivities," *IEEE Transactions on Power Systems*, Vol. 18, Issue 2, May 2003, pp. 848 – 854.

[172] Z. Baorong, D. Z. Fang, and T. S. Chung, "Computation of trajectory sensitivities of power systems with respect to parameters of PSS," in *Proceedings of the 6th*

International Conference on Advances in Power System Control, Operation and Management (APSCOM 2003), Hong Kong, November 2003, pp. 280 – 284.

[173] A. Ghosh, D. Chatterjee, P. Bhandiwad, and M. A. Pai, "Trajectory sensitivity analysis of TCSC compensated power systems," in *Proceedings of the 2004 IEEE PES General Meeting*, Denver, CO, USA, June 6 – 12, 2004, pp. 1515 – 1520.

[174] C. M. Machado Ferreira, J. A. Dias Pinto, and F. P. Maciel Barbosa, "Transient stability assessment of an electric power system using trajectory sensitivity analysis," in *Proceedings of the 39th International Universities Power Engineering Conference (UPEC 2004)*, Sept. 6 – 8, 2004, pp. 1091 – 1095.

[175] K. N. Shubhanga and A. M. Kulkarni, "Determination of effectiveness of transient stability controls using reduced number of trajectory sensitivity computations," *IEEE Transactions on Power Systems*, Vol. 19, Issue 1, Feb. 2004, pp. 473 – 482.

[176] D. Chatterjee, A. Ghosh, and M. A. Pai, "Trajectory sensitivity analysis in distributed generation systems," presented at the *2006 International Conference on Power Electronics, Drives, and Energy Systems (PEDES '06)*, Dec. 12 – 15, 2006.

[177] E. P. T. Cari, L. F. C. Alberto, and N. G. Bretas, "A methodology for parameter estimation of synchronous generators based on trajectory sensitivity and synchronization technique," in *Proceedings of the 2006 IEEE PES General Meeting*, Montreal, Quebec, Canada, June 18 – 22, 2006.

[178] A. P. Sakis Meliopoulos and C. Cheng, "A hybrid contingency selection method," in *Proceedings of the 10th Power System Computation Conference*, Graz, Austria, Aug. 1990, pp. 605 – 612.

[179] A. P. Sakis Meliopoulos, Carol S. Cheng, Feng Xia, "Performance evaluation of static security analysis methods," *IEEE Transactions on Power Systems*, Vol. 9, No. 3, Aug. 1994, pp. 1441 – 1449.

[180] G. K. Stefopoulos, F. Yang and A. P. Meliopoulos, "An improved contingency ranking method," in *Proceedings of the 35th Annual North American Power Symposium*, Oct. 20 – 21, 2003, Rolla, MO.

[181] G. K. Stefopoulos, F. Yang, G. J. Cokkinides, and A. P. Meliopoulos, "Advanced contingency selection methodology," presented at the *37th North American Power Symposium (NAPS 2005)*, Ames, IA, Oct. 23 – 25, 2005.

[182] S. H. Horowitz, A. G. Phadke, *Power System Relaying*, 2nd Edition, RSP Press, 2000.

[183] ABB – *Protective Relaying Theory and Applications* edited by W. A. Elmore, Marcel Dekker Inc., New York, 1994.

[184] D. P. Bertsekas, *Dynamic Programming and Optimal Control*, Vol. 1 and 2, Athena Scientific.

[185] S. E. Dreyfus and A. M. Law, *The Art and Theory of Dynamic Programming*, Vol. 130 in Mathematics in Science and Engineering, Academic Press, Inc, 1977.

[186] G.C. Ejebe and B. F. Wollenberg, "Automatic contingency selection," *IEEE Transactions on Power Apparatus and Systems*, Vol. PAS-98, No. 1, Jan./Feb. 1979, pp. 92 – 104.

[187] J. Zaborszky, F.W. Whang and K. Prasad, "Fast contingency evaluation using concentric relaxation," *IEEE Transactions on Power Apparatus and Systems*, Vol. PAS-99, No. 1, Jan./Feb. 1980, pp. 28 – 36.

[188] V. Brandwajn, "Efficient bounding method for linear contingency analysis," *IEEE Transactions on Power Systems*, Vol. PWRS-3, No. 1, Feb. 1988, pp. 38 – 43.

[189] V. Brandwajn and M. G. Lauby, "Complete bounding for ac contingency analysis," *IEEE Transactions on Power Systems*, Vol. PWRS-4, No. 2, May 1990, pp. 724 – 729.

[190] B. Stott and O. Alsac, "Fast decoupled power flow," *IEEE Transactions on Power Apparatus and Systems*, Vol. PAS-93, No. 3, May/June 1974, pp. 859 – 869.

[191] O. Alsac, B. Stott and M. F. Tinney, "Sparsity-oriented compensation methods for modified network solutions," *IEEE Transactions on Power Apparatus and Systems*, Vol. PAS-102, No. 5, May 1983, pp. 1050 – 1060.

[192] W. F. Tinney, V. Brandwajn and S. M. Chan, "Sparse vector method," *IEEE Transactions on Power Apparatus and Systems*, Vol. PAS-104, No. 2, Feb. 1985, pp. 295 – 301.

[193] S. M. Chan and V. Brandwajn, "Partial matrix refactorization," *IEEE Transactions on Power Systems*, Vol. PWRS-1, No. 1, Feb. 1986, pp. 193 – 200.

[194] R. Bacher and W. F. Tinney, "Faster local power solutions: The zero mismatch approach," *IEEE Transactions on Power Systems*, Vol. PWRS-4, No. 4, Feb. 1989, pp. 1345 – 1354.

[195] G. Irisarri, A. M. Sasson and D. Levner, "Automatic contingency selection for on-line security analysis – Real time tests," *IEEE Transactions on Power Apparatus and Systems*, Vol. PAS-98, No. 5, Sept./Oct. 1979, pp. 1552 – 1559.

[196] J. T. Betts, Practical Methods for Optimal Control Using Nonlinear Programming. SIAM 2001.

[197] J. T. Betts, "Survey of numerical methods for trajectory optimization," *AIAA Journal of Guidance, Control, and Dynamics*, Vol. 21, 1998, pp. 193 – 207.

[198] R. R. Booth, "Power system simulation methods based on probability analysis," *IEEE Transactions on Power Apparatus and Systems*, vol. PAS-91, Jan./Feb. 1972, pp. 62 – 69.

[199] B. Borkowska, "Probabilistic load flow", *IEEE Transactions on Power Apparatus and Systems*, vol. PAS-93, No. 3, May/June 1974, pp. 752 – 759.

[200] R. N. Allan, B. Borkowska, and C. H. Grigg, "Probabilistic analysis of power flows," *Proceedings of the IEE*, vol. 121, No. 12, Dec. 1974, pp. 1551 – 1556.

[201] R. N. Allan, C. H. Grigg, D. A. Newey, and R. F. Simmons, "Probabilistic power flow techniques extended and applied to operational decision making," *Proceedings of the IEE*, vol. 123, No. 12, Dec. 1976, pp. 1317 – 1324.

[202] R. N. Allan and M. R. G. Al-Shakarchi, “Probabilistic techniques in AC load flow analysis,” *Proceedings of the IEE*, vol. 124, No. 2, Feb. 1977, pp. 154 – 160.

[203] R. N. Allan and M. R. G. Al-Shakarchi, “Linear dependence between nodal powers in probabilistic AC load flow,” *Proceedings of the IEE*, vol. 124, No. 6, June 1977, pp. 529 – 534.

[204] R. N. Allan, A. M. Leite da Silva, and R. C. Burchett, “Evaluation methods and accuracy in probabilistic load flow solutions,” *IEEE Transactions on Power Apparatus and Systems*, vol. PAS-100, No. 5, May 1981, pp. 2539 – 2546.

[205] A. M. Leite da Silva, V. L. Arienti, and R. N. Allan, “Probabilistic load flow considering dependence between input nodal powers,” *IEEE Transactions on Power Apparatus and Systems*, vol. PAS-103, No. 6, June 1984, pp. 1524 – 1530.

[206] J. F. Dopaso, O. A. Klitin, and A. M. Sasson, “Stochastic load flows,” *IEEE Transactions on Power Apparatus and Systems*, vol. PAS-94, No. 2, Mar./Apr. 1975, pp. 299 – 309.

[207] R. N. Allan and A. M. Leite da Silva, “Probabilistic load flow using multilinearisations,” *Proceedings of the IEE*, vol. 128, Pt. C, No. 5, Sep. 1981, pp. 280 – 287.

[208] P. W. Sauer and G. T. Heydt, “A generalized stochastic power flow algorithm,” presented at the IEEE/PES Summer Meeting, July 1978, Paper A78-544-9.

[209] A. M. Leite da Silva, R. N. Allan, S. M. Soares, and V. L. Arienti, “Probabilistic load flow considering network outages,” *Proceedings of the IEE*, vol. 123, Pt. C, May 1985, pp. 139 – 145.

[210] A. M. Leite da silva, V. L. Arienti, and M. H. Barbosa, “Probabilistic techniques in load flow analysis – A practical application,” *Proceedings of the 1st International Symposium on Systems (ISPMAEPS)*, Toronto, Canada, pp. 643 – 651, July 1986.

[211] A. M. Leite da Silva, S. M. P. Ribeiro, V. L. Arienti, R. N. Allan, and M. B. Do Coutto Filho, “Probabilistic load flow techniques applied to power system

expansion planning," *IEEE Transactions on Power System*, vol. 5, No. 4, Nov. 1990, pp. 1047 – 1053.

[212] A. M. Leite da Silva and V. L. Arienti, "Probabilistic load flow by multilinear simulation algorithm," *Proceedings of the IEE*, vol. 137, Pt. C, No 4, July 1990, pp. 276 – 282.

[213] M. Th. Schilling, A. M. Leite da Silva, R. Billinton, and M. A. El-Kady, "Bibliography on power system probabilistic analysis (1962-1988)," *IEEE Transactions on Power Systems*, vol. 5, No. 1, Feb. 1990, pp. 1 – 11.

[214] A. P. Meliopoulos, A. G. Bakirtzis, and R. Kovacs, "Power system reliability evaluation using stochastic load flows," *IEEE Transactions on Power Apparatus and Systems*, vol. PAS-103, No. 5, May 1984, pp. 1084 – 1091.

[215] A. P. Sakis Meliopoulos, George J. Cokkinides, and Xing Yong Chao, "A new probabilistic power flow analysis method," *IEEE Transactions on Power Systems*, vol. 5, No. 1, Feb. 1990, pp. 182 – 190.

[216] A. P. Meliopoulos, X. Chao, George J. Cokkinides, and R. Monsalvatge, "Transmission loss evaluation based on probabilistic power flow," *IEEE Transactions on Power Systems*, vol. 6, No. 1, Feb. 1991, pp. 364 – 371.

VITA

GEORGE K. STEFOPOULOS

GEORGE STEFOPOULOS (*Greek: Γιώργος Στεφόπουλος*) was born in Athens, Greece in 1977. He attended public schools in Athens and received his high-school diploma in June 1995. In September 1995 he joined the school of Electrical and Computer Engineering at the National Technical University of Athens, in Athens, Greece, where he received his Diploma in 2001. He then moved to the USA and joined the Georgia Institute of Technology, in Atlanta, Georgia, in Fall 2001, receiving a M.S. in Electrical and Computer Engineering in 2003, before continuing to pursue a doctorate in Electrical Engineering, again at Georgia Tech.

Since the beginning of his studies at Georgia Tech, Mr. Stefopoulos has been a graduate research assistant working on topics in the area of operation and control of electric power systems under the supervision of Professor A. P. Sakis Meliopoulos. He has been a member of several professional organizations, such as the Institute of Electrical and Electronics Engineers, the Institute of Engineering Technology, and the Society of Industrial and Applied Mathematics. He is also an active member of several student organizations or local professional societies, like the Hellenic Society at Georgia Tech, Eta Kappa Nu, and the Hellenic Academic Society.